

NASA Conference Publication 2243

NASA
CP
2243
c.1

Flow Visualization and Laser Velocimetry for Wind Tunnels



LOAN COPY: RETURN TO
AFWL TECHNICAL LIBRARY
KIRTLAND AFB, N.M.



*Proceedings of a workshop held at
NASA Langley Research Center
Hampton, Virginia
March 25-26, 1982*

NASA



NASA Conference Publication 2243

Flow Visualization and Laser Velocimetry for Wind Tunnels

Edited by
William W. Hunter, Jr., and Jerome T. Foughner, Jr.
Langley Research Center
Hampton, Virginia

Proceedings of a NASA workshop held at
Langley Research Center
Hampton, Virginia
March 25-26, 1982

NASA

National Aeronautics
and Space Administration

Scientific and Technical
Information Branch

1982

Use of trade names or names of manufacturers in this report does not constitute an official endorsement of such products or manufacturers, either expressed or implied, by the National Aeronautics and Space Administration.

PREFACE

The principal motivating factor for the Workshop on Flow Visualization and Laser Velocimetry for Wind Tunnels was the construction and approaching commissioning of the National Transonic Facility (NTF) at the Langley Research Center (LaRC). Because the NTF will achieve significantly higher simulated Reynolds number flight conditions than any other wind tunnel in the world and therefore will occupy a unique position among ground test facilities, every effort is being made to ensure that it is equipped or provisions are made for those flow field diagnostic techniques that potential users from industry, universities, and government feel are necessary. The need for flow visualization and laser velocimetry were highlighted in a workshop held at LaRC and reported in NASA Conference Publication 2183 entitled "High Reynolds Number Research - 1980." As a result of the high Reynolds number workshop, this workshop was organized, and its purpose was threefold: 1) provide a state-of-the-art overview; 2) provide a forum for industry, universities, and government agencies to address problems in developing useful and productive flow visualization and laser velocimetry measurement techniques; and 3) provide discussion of recent developments and applications of flow visualization and laser velocimetry measurement techniques and instrumentation systems for LaRC wind tunnels including the Langley 0.3-Meter Transonic Cryogenic Tunnel and plans for the NTF.

The papers presented herein are grouped according to session. Some of the papers contained color photographs which are printed in black and white. Those photographs with an LaRC photo number included in the lower right-hand corner are available as color prints by contacting Jerome T. Foughner, Jr., Langley Research Center, Mail Stop 285, Hampton, Virginia, 23665 (telephone: (804) 827-2961). Please order prints by number, and prints are available through August 1983.

A list of attendees is included at the end of the document. Grateful appreciation is expressed to the invited speakers and the authors who shared their experiences and their views with the workshop participants and to those who contributed to many useful exchanges of information.

William W. Hunter, Jr.
Jerome T. Foughner, Jr.
Conference Cochairmen



CONTENTS

PREFACE iii

SESSION I - NTF OPERATION PLANS

1. PROVISIONS FOR NONINTRUSIVE FLOW-EVALUATION TOOLS IN THE NATIONAL
TRANSONIC FACILITY 1
Dennis E. Fuller

SESSION II - FLOW VISUALIZATION

2. THE STATE OF THE ART OF CONVENTIONAL FLOW VISUALIZATION
TECHNIQUES FOR WIND TUNNEL TESTING 9
Gary S. Settles

3. THE NEED FOR AN OPTICAL TRANSITION DETECTION SYSTEM IN THE NTF 27
M. F. Fancher

4. SURFACE FLOW VISUALIZATION REQUIREMENTS FOR TESTING IN NTF 31
Ronald L. Bengelink

5. SURFACE FLOW VISUALIZATION USING INDICATORS 37
James P. Crowder

6. A COLOR VIDEO DISPLAY TECHNIQUE FOR FLOW FIELD SURVEYS 47
Allen E. Winkelmann and Chen P. Tsao

7. NEW VERSIONS OF OLD FLOW VISUALIZATION SYSTEMS 59
Walton L. Howes

8. OPERATIONAL FLOW VISUALIZATION TECHNIQUES IN THE LANGLEY
UNITARY PLAN WIND TUNNEL 65
William A. Corlett

9. PROPELLER FLOW VISUALIZATION TECHNIQUES 75
George L. Stefko, F. J. Paulovich, J. P. Greissing,
and E. D. Walker

10. IN-FLIGHT PROPELLER FLOW VISUALIZATION USING FLUORESCENT
MINITUFTS 91
James P. Crowder

11. SHADOWGRAPH TECHNIQUES IN TRANSONIC TESTS WITH POWERED
NACELLES 97
P. G. Hutton

12. FLOW VISUALIZATION OF SHOCK-BOUNDARY LAYER INTERACTION 101
Warren R. Hingst and Mark Jurkovich

13. TRANSONIC APPLICATIONS OF THE WAKE IMAGING SYSTEM 109
James P. Crowder

14. FLOW VISUALIZATION IN THE LANGLEY 0.3-METER TRANSONIC CRYOGENIC TUNNEL AND PRELIMINARY PLANS FOR THE NATIONAL TRANSONIC FACILITY	117
D. B. Rhodes and S. B. Jones	

15. "SEEING" THROUGH FLOWS IN LANGLEY'S 0.3-METER TRANSONIC CRYOGENIC TUNNEL	133
W. L. Snow, A. W. Burner, and W. K. Goad	

SESSION III - HOLOGRAPHY/TOMOGRAPHY

16. HOLOGRAPHIC FLOW VISUALIZATION - STATE-OF-THE-ART OVERVIEW	149
J. D. Trolinger	

17. MEASUREMENT OF THREE-DIMENSIONAL DENSITY DISTRIBUTIONS BY HOLOGRAPHIC INTERFEROMETRY AND COMPUTER TOMOGRAPHY	159
C. M. Vest	

18. HOLOGRAPHIC CINEMATOGRAPHY AND OTHER DYNAMIC FLOW VISUALIZATION METHODS	175
Arthur J. Decker	

19. HOLOGRAPHIC INTERFEROMETRY AND TOMOGRAPHY AT AMES RESEARCH CENTER	179
George Lee	

20. FLOW FIELD STUDIES USING HOLOGRAPHIC INTERFEROMETRY AT LANGLEY	193
A. W. Burner, W. L. Snow, W. K. Goad, V. T. Helms and P. B. Gooderum	

SESSION IV - LASER VELOCIMETRY

21. LASER VELOCIMETRY - A STATE-OF-THE-ART OVERVIEW	205
Warren H. Stevenson	

22. COHERENT RAMAN SPECTROSCOPIES FOR MEASURING MOLECULAR FLOW VELOCITY	215
C. Y. She	

23. MEASUREMENT POTENTIAL OF LASER SPECKLE VELOCIMETRY	219
Ronald J. Adrian	

24. STATUS OF LASER ANEMOMETRY IN TURBOMACHINERY RESEARCH AT THE LEWIS RESEARCH CENTER	227
Richard G. Seasholtz	

25. FLOW VISUALIZATION EFFORTS AND PILOT MEASUREMENTS WITH A LASER-DOPPLER ANEMOMETER IN BACKSCATTER MODE	235
K. A. Butefisch	

26. DEVELOPMENT OF A LASER VELOCIMETER FOR A LARGE TRANSONIC WIND TUNNEL	243
John P. Greissing and Daniel L. Whipple	
27. SEEDING CONSIDERATIONS FOR AN LV SYSTEM IN A LARGE TRANSONIC WIND TUNNEL	249
Robert J. Freedman	
28. LV MEASUREMENTS WITH AN ADVANCED TURBOPROP	253
H. E. Neumann and J. S. Serafini	
29. 16-FOOT TRANSONIC TUNNEL LASER VELOCIMETER SYSTEM	257
J. M. Franke	
30. LASER VELOCIMETER APPLICATIONS TO HIGH-LIFT RESEARCH	273
R. R. Whipkey, G. Jones, and J. A. Braden	
31. APPLICATIONS OF A LASER VELOCIMETER IN THE LANGLEY 4- BY 7-METER TUNNEL	283
William L. Sellers and Joe W. Elliott	
32. APPLICATION OF THE LASER DOPPLER VELOCIMETER IN AERODYNAMIC FLOWS	295
William J. Yanta and Donald W. Ausherman	
33. COMPARISON OF HOT WIRE/LASER VELOCIMETER TURBULENCE INTENSITY MEASUREMENTS	303
J. F. Meyers and S. P. Wilkinson	
34. LASER DOPPLER VELOCIMETRY APPLICATION IN THE LANGLEY 0.3-METER TRANSONIC CRYOGENIC TUNNEL	323
Luther R. Gartrell	
35. VELOCITY AND FLOW ANGLE MEASUREMENTS IN THE LANGLEY 0.3-METER TRANSONIC CRYOGENIC TUNNEL USING A LASER TRANSIT ANEMOMETER	335
W. C. Honaker	
36. SOME NTF LASER VELOCIMETER INSTALLATION AND OPERATION CONSIDERATIONS	343
W. W. Hunter, Jr., L. R. Gartrell, and W. C. Honaker	
ATTENDEES	359

PROVISIONS FOR NONINTRUSIVE FLOW-EVALUATION
TOOLS IN THE NATIONAL TRANSONIC FACILITY

Dennis E. Fuller
NASA Langley Research Center
Hampton, Virginia

NATIONAL TRANSONIC FACILITY - GENERAL DESCRIPTION

The National Transonic Facility (refs. 1 to 4) is a fan-driven, closed-circuit, continuous-flow, pressurized wind tunnel (fig. 1). The test section is 2.500 m x 2.500 m and 7.620 m long with a slotted-wall configuration. There are six slots each in the top and bottom walls and two slots per sidewall.

In order to maintain good flow quality and aerodynamic efficiency over the wide range of test capabilities the test-section geometry is variable. The position of the test-section top and bottom walls, the reentry flaps at the rear of the test-section slots, and the step height for reentering slot flow are remotely controlled.

The test gas may be dry air or nitrogen. For the elevated-temperature (340 K) mode of operation the test medium is normally air, and heat removal is by means of a water-cooled heat exchanger (cooling coil) located at the upstream end of the settling chamber. For the cryogenic mode of operation, heat removal is by means of evaporation of liquid nitrogen, which is sprayed into the circuit upstream of the fan. By utilizing liquid nitrogen as a coolant, the tunnel test-temperature range is variable from 340 to 78 K. When nitrogen is injected into the circuit, venting must occur to maintain a constant pressure. Thermal insulation is installed internal to the pressure shell to minimize energy consumption.

The pressure range for the National Transonic Facility is from 1 to 9 bar. The Reynolds number range (based on $\bar{c} = .25M$) is up to 120×10^6 at Mach = 1.0. The Mach number range is from .2 to 1.2.

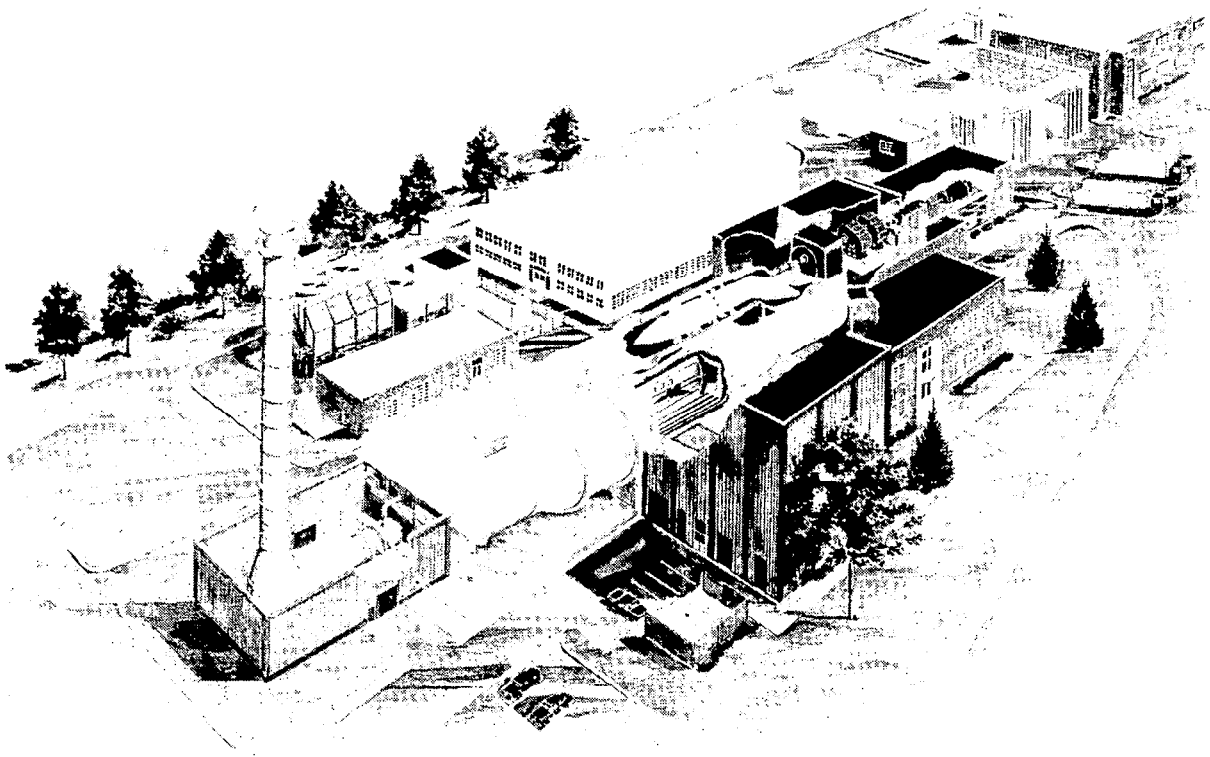


Figure 1

TEST PLENUM ISOLATION SYSTEM

To facilitate model access during a test series, with a minimum loss of nitrogen (energy) and time, gate valves upstream and downstream of the test section are provided which isolate the plenum (fig. 2). When the plenum is isolated it will be vented to the atmosphere and thermally conditioned to provide a work environment. This configuration provides personnel access to the plenum and any attendant instrumentation which may be mounted around the test section in either the floor, ceiling, or sidewalls.

Conditioning of the plenum area for access is estimated to take up to four hours, the time depending on the tunnel operational temperature. Approximately the same amount of time will be required to recondition the plenum to test conditions.

The relatively slow warmup/cooldown times of the plenum result from the structural components inside which must undergo large temperature swings without being subjected to excessive thermal gradients.

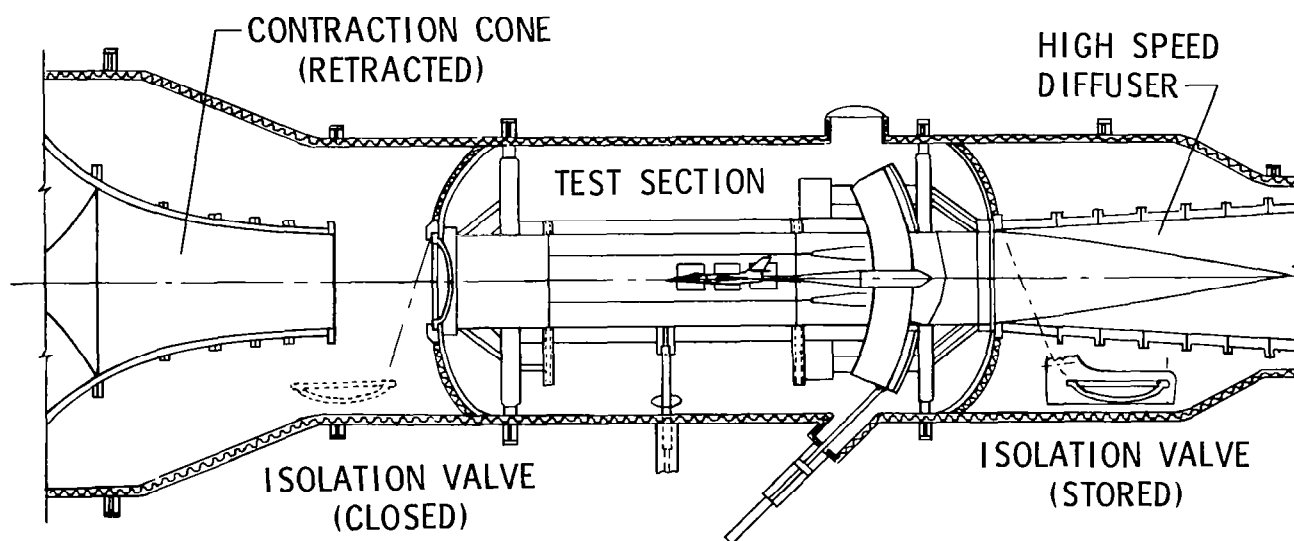


Figure 2

MODEL ACCESS SYSTEM

In addition to the plenum access mode shown in Figure 2, the test model, mounted in the test section, may be accessed by using two 7 X 10 ft access tubes (fig. 3). These tubes are inserted from either side of the plenum and close around the model to form a thermally insulated enclosure. This enclosure provides for personnel entry while the plenum is cold and circuit pressure is maintained behind the gate valves. Model access using the tubes is estimated to take about 45 minutes with another 45 minutes required to return the test section to the testing configuration.

The plenum and its associated instrumentation cannot be serviced during this mode of access.

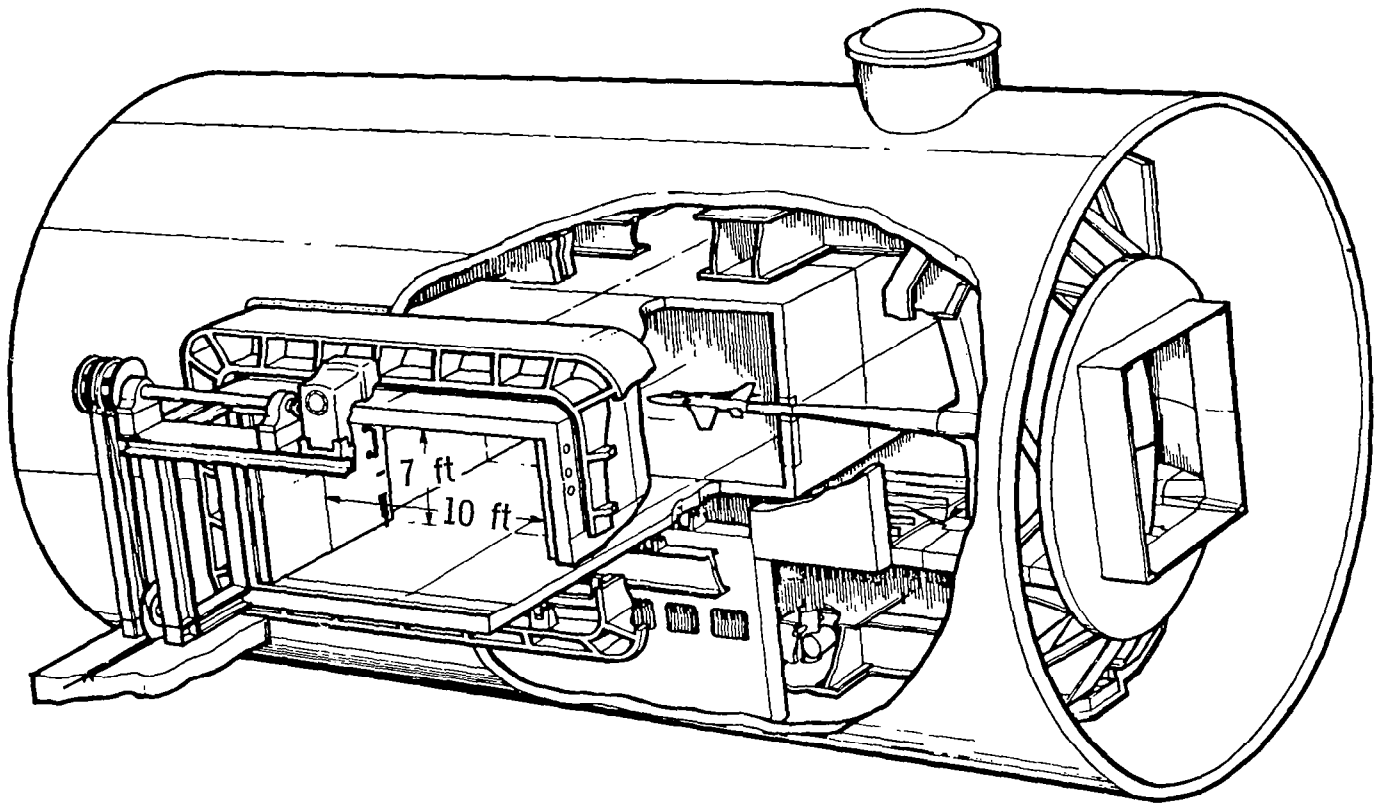


Figure 3

SECTION VIEW OF MODEL ACCESS SYSTEM

Figure 4 shows a section through the plenum/test section area with one model access tube inserted and one extracted. Viewing and lighting ports are located adjacent to the flow stream in the hollow beams located in the test section floor and ceiling. Space for instrumentation to be located inside the floor and ceiling beams is somewhat limited. The nominal dimensions inside the beams are 5 1/2 in. wide by 30 in. deep.

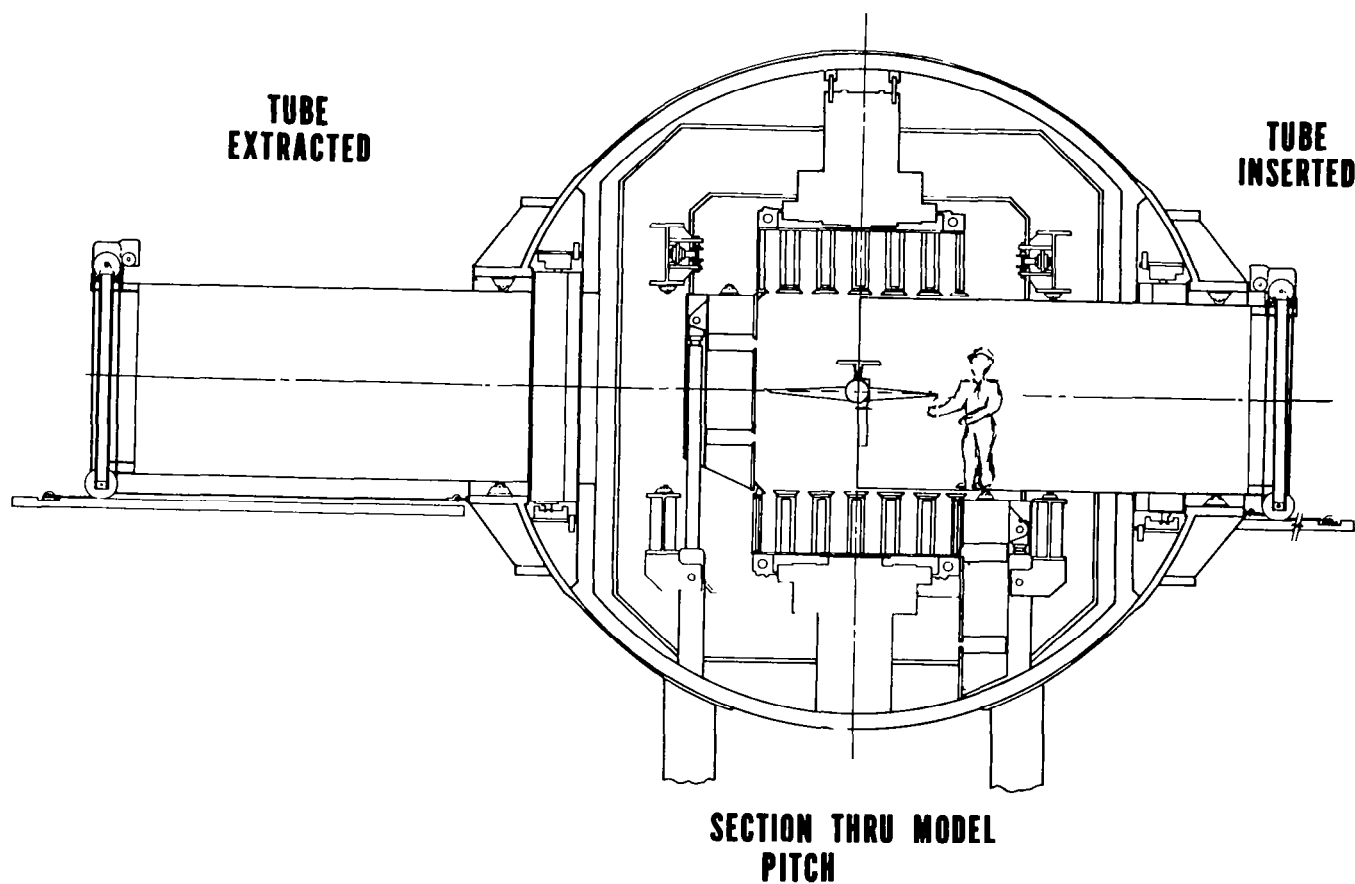


Figure 4

VIEWING PORTS FOR SIDEWALL DOORS

Viewing ports are also provided in the test section sidewall doors as shown in Figure 5. Each door has provision for three 24 X 30 in. windows (cross-hatched area). The length (or depth) of the instrumentation package that might use these windows is limited to 32 in. (see end view in fig. 5). Anything longer will not clear plenum structure when the door is lowered for plenum access. The window openings currently are filled with metal blanks which are fitted with smaller viewing/lighting ports.

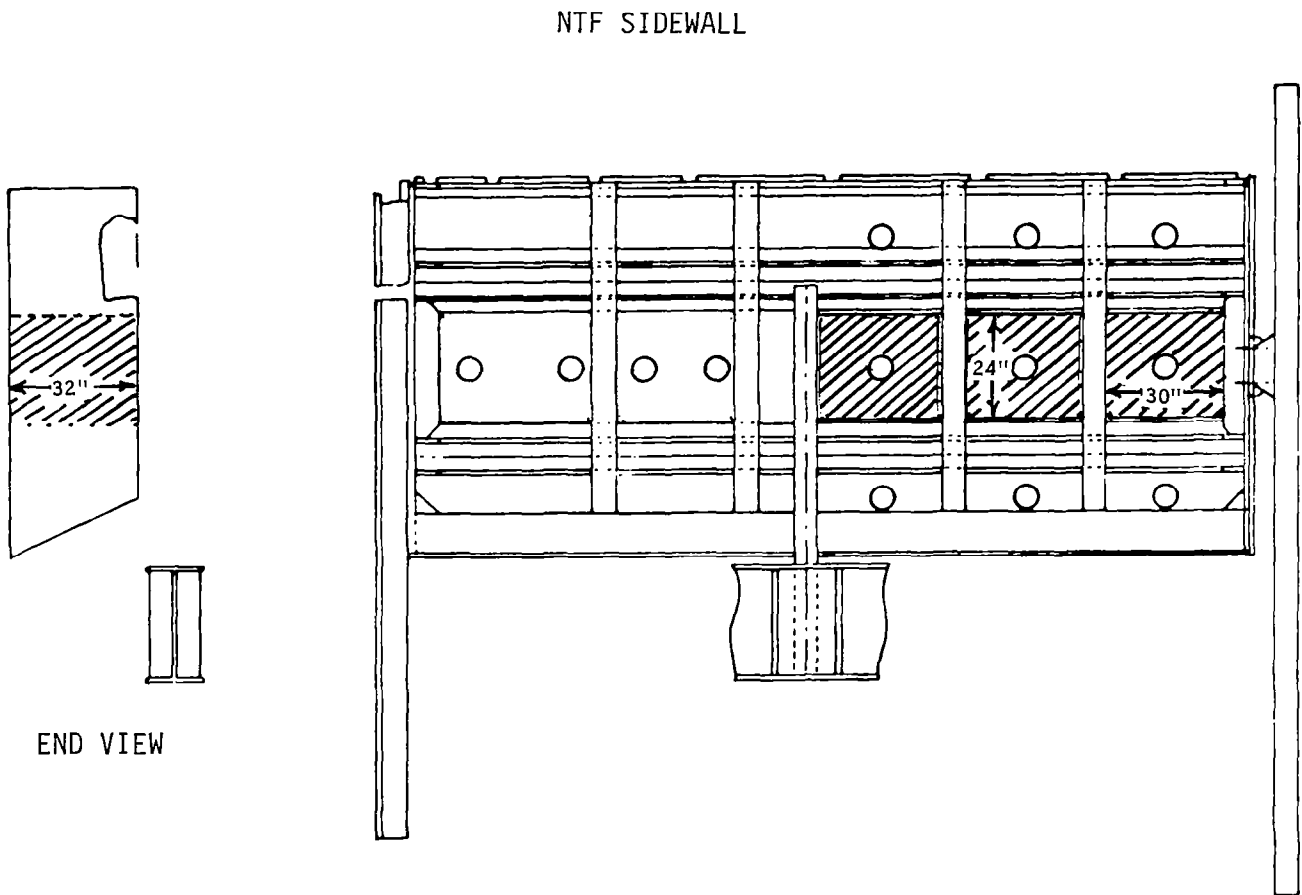


Figure 5

OVERALL WINDOW CAPABILITIES

The overall window capabilities for the NTF are illustrated in Figure 6 which is a folded-out view of the test section. There are a total of 56 openings around the test section that may be used for viewing or lighting. This includes the large sidewall window blanks which are currently fitted with smaller viewing/lighting ports.

LOOKING DOWNSTREAM

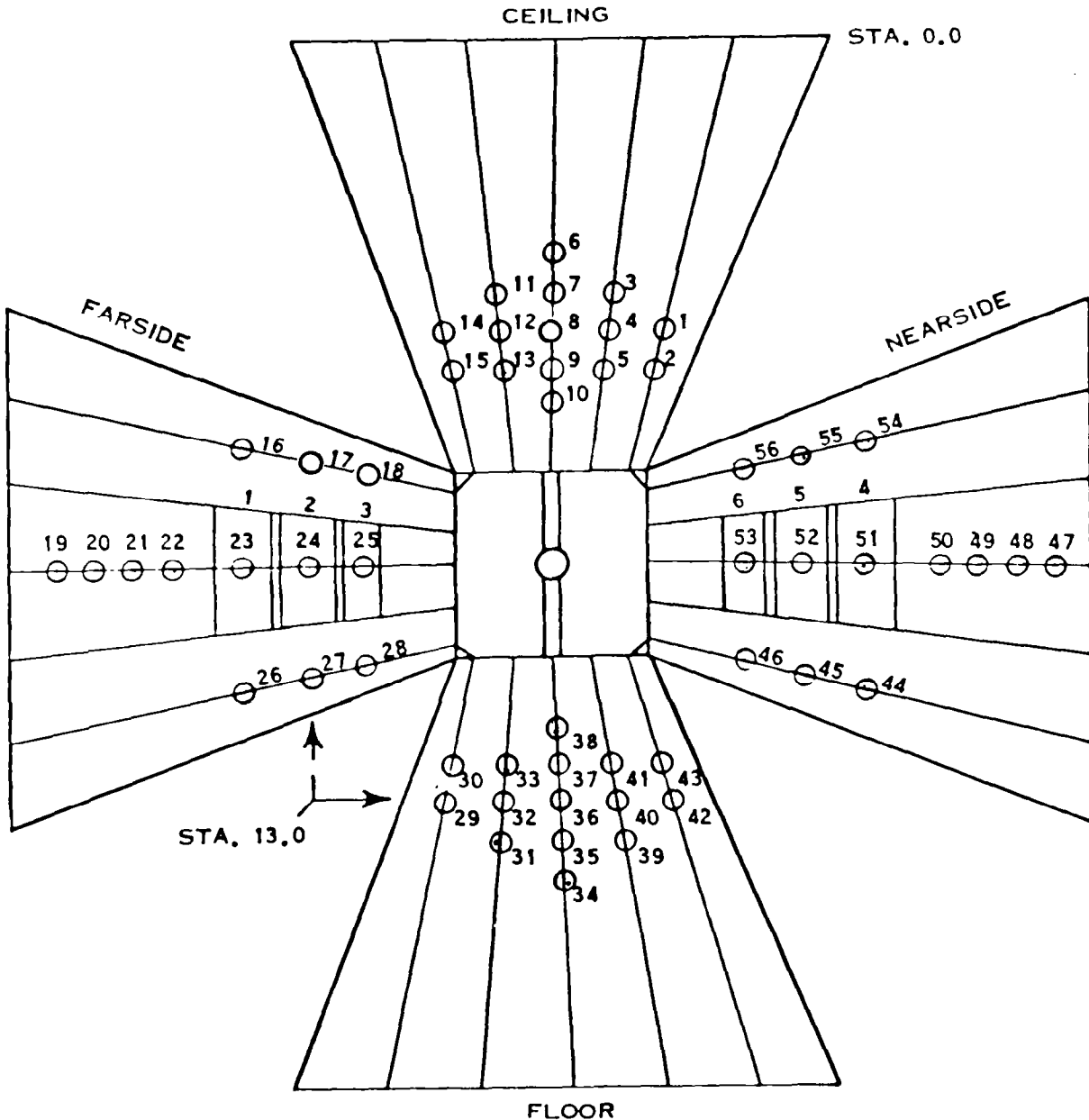


Figure 6

REFERENCES

1. McKinney, Linwood W.; and Howell, Robert R.: The Characteristics of the Planned National Transonic Facility. Proceedings - AIAA 9th Aerodynamic Testing Conference, June 1976, pp. 176-184.
2. Howell, Robert R.; and McKinney, Linwood W.: The U.S. 2.5-Meter Cryogenic High Reynolds Number Tunnel. ICAS Paper No. 76-04, Oct. 1976.
3. Nicks, Oran W.; and McKinney, Linwood W.: Status and Operational Characteristics of the National Transonic Facility. AIAA Paper 78-770, Apr. 1978.
4. Howell, Robert R.: The National Transonic Facility: Status and Operational Planning. A Collection of Technical Papers - AIAA 11th Aerodynamic Testing Conference, Mar. 1980, pp. 1-9. (Available as AIAA-80-0415.)

THE STATE OF THE ART OF CONVENTIONAL
FLOW VISUALIZATION TECHNIQUES
FOR WIND TUNNEL TESTING

by

Gary S. Settles
Princeton University
Princeton, NJ

CONVENTIONAL WIND TUNNEL
'FLOW VISUALIZATION TECHNIQUES'

- 1) SURFACE-FLOW METHODS
- 2) TRACERS
- 3) OPTICAL METHODS

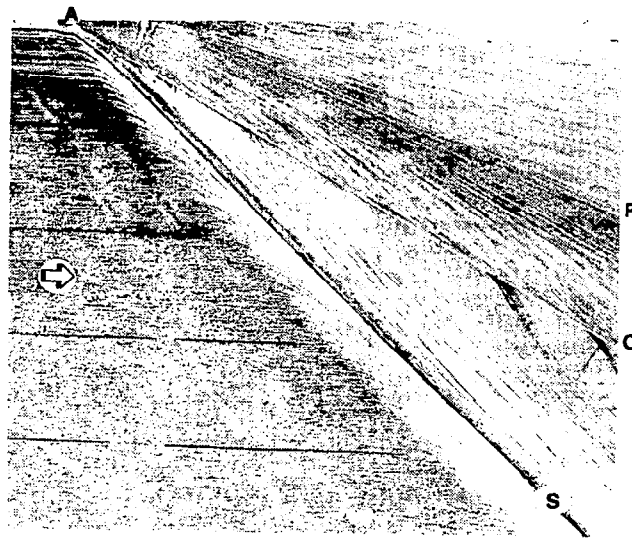
PHOTOGRAPHY AND VIDEOGRAPHY

SURFACE-FLOW METHODS

- 1) LIQUID FILMS
 - OIL + FLUORESCENT DYE, UV LIGHTING
 - RENEWABLE FILM VIA POROUS DISPENSER IN MODEL
 - VOLATILE CARRIER FLUID: DRY TRACE
 - CRYOGENIC: LIQUID PROPANE + PIGMENT
 - COLORED OIL DOTS
 - OIL FILM INTERFEROMETRY YIELDS C_f
- 2) REACTIVE SURFACE TREATMENTS
 - REACTIVE GAS INJECTION
 - REVERSIBLE DYE
- 3) TRANSITION & HEAT TRANSFER DETECTORS
 - EVAPORATION
 - SUBLIMATION
 - LIQUID CRYSTALS
 - PHASE-CHANGE PAINTS
 - IR THERMOGRAPHY
- 4) TUFTS
 - FLUORESCENT MINI-TUFTS
 - CRYOGENIC SUITABILITY

KEROSENE-LAMPBLACK SURFACE STREAK TRACES

A mixture of kerosene and lampblack has been useful for many years in producing dry traces of surface flow patterns, which are not disturbed when the wind is stopped. Rather than photographing these patterns, a novel method of preserving them is to press 8"-wide "Scotch Magic Transparent Tape" onto the model and actually peel the pattern off. The result is a full-scale, highly-detailed trace from which quantitative measurements can be made of surface streak features and angles. This example is from a series of 3D shock/turbulent boundary layer experiments done by the author.

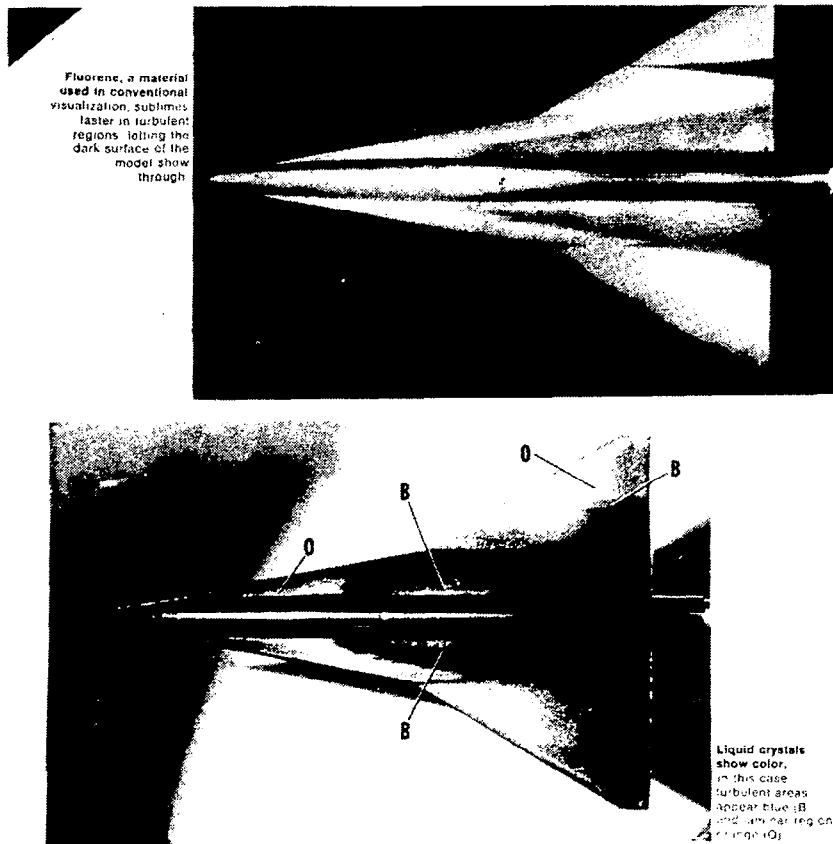


Kerosene-Lampblack Surface Streak Trace
for $\lambda = 60^\circ$; A = apex, C = corner,
R = reattachment, S = separation.

Source: Settles, G. S. and Teng, H. Y., AIAA Paper 82-0229,
Jan. 1982.

SUBLIMATION AND LIQUID CRYSTALS FOR TRANSITION DETECTION

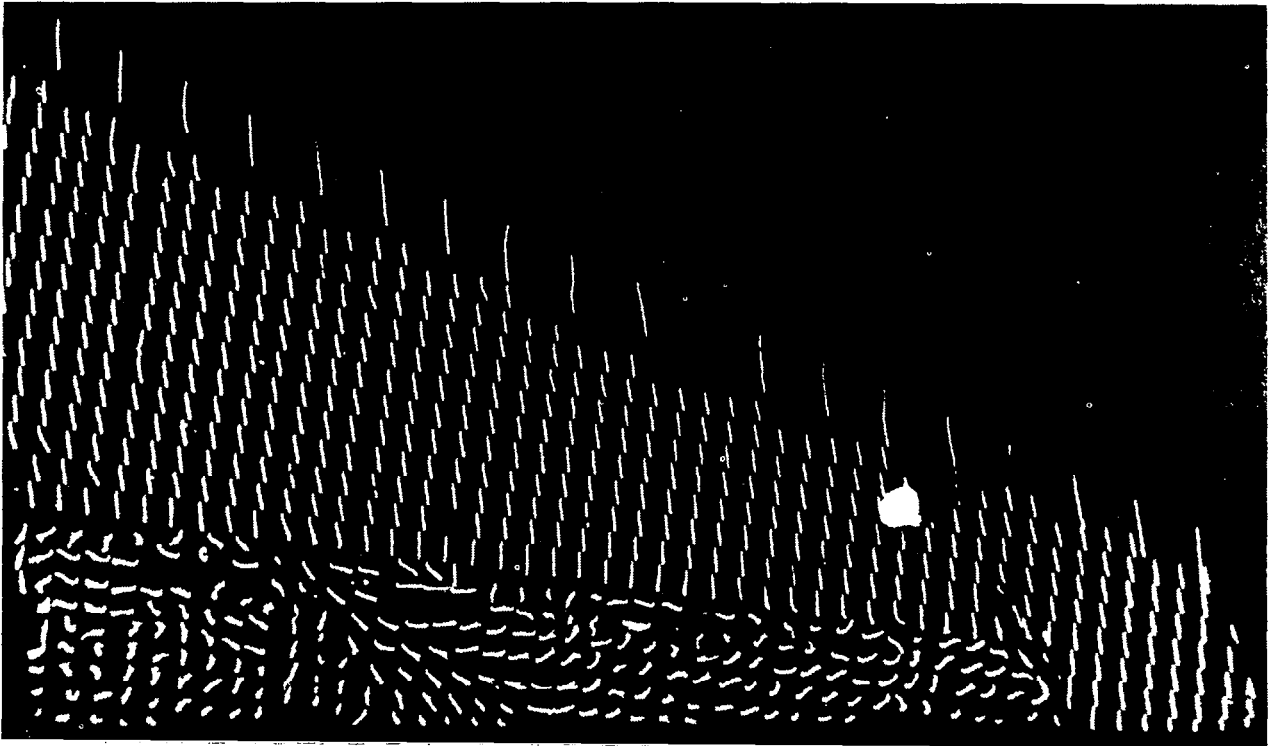
Liquid crystals are by far the most optically active substances available. They respond with a perceived color change to minute differences in temperature. Thus, as in this example, they have been proved useful for detecting the temperature change at transition. Liquid crystals have some advantages over traditional sublimation techniques in that the transition pattern is displayed with color contrast and is able to indicate changes due to, say, a change in model attitude during a single wind tunnel run.



Source: Klein, E. J., "Liquid Crystals in Aerodynamic Testing," Astronautics & Aeronautics, July 1968, pp. 70-73.

FLUORESCENT MINI-TUFTS

Fluorescent mini-tufts are a recent advance in the state-of-the-art of tuft visualization for flow near a solid surface. Extremely thin fluorescent nylon monofilament is glued to the model surface in short lengths according to a regular grid pattern. Under UV lighting these mini-tufts can be photographed despite their small size. The results, as in this example, give a graphic indication of surface flow angles and separation. Further, the inventor of this technique (J. P. Crowder of Boeing) has shown by rigorous tests that the mini-tufts do not produce a significant disturbance to the flow.



Source: Crowder, J. P., Astronautics & Aeronautics, Nov. 1980, pp. 54-56.

TRACERS

1) SMOKE

- SMOKE-WIRE TECHNIQUE
- SMOKE FILAMENTS AT HIGH SPEEDS

2) "VAPOR SCREEN"

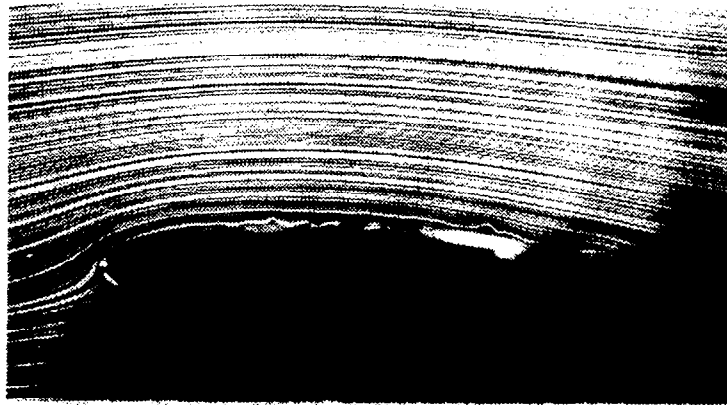
- GLOBAL SEEDING W/LASER LIGHT SHEET
- LOCAL SEEDING W/LASER OR STROBE
- CRYOGENIC: LIQUID HE YIELDS N_2 "FOG"?

3) OTHER METHODS

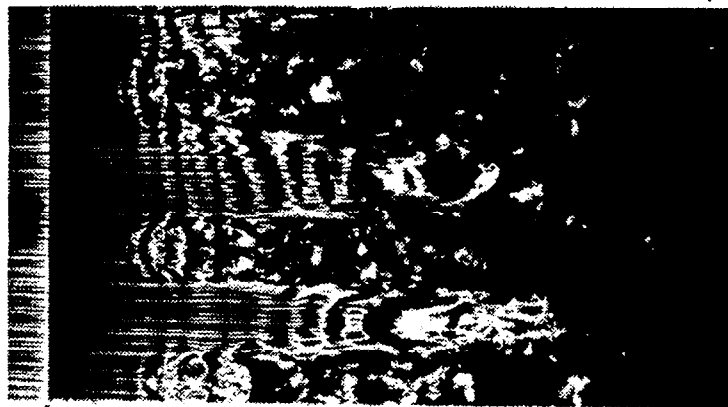
- FLUORESCENT AEROSOLS, PARTICLES, OR ATOMS
- NEUTRALLY BOUYANT BUBBLES
- SPARK TRACING
- PROBE SURVEYS + GRAPHICS

SMOKE-WIRE TECHNIQUE

For low-speed flows the smoke-wire technique is a simple and elegant means to produce high-quality smoke filaments for flow visualization. A fine resistive wire on the order of 0.1 mm diameter is coated with oil and heated by electrical current, whereupon the oil forms beads and ejects filaments of aerosol particles. Given proper lighting and a low level of free-stream turbulence, these filaments can dramatically reveal, for example, boundary layer transition on a wing.



PROFILE VIEW



PLANFORM VIEW

L.E.

Smoke-wire visualization for $\alpha = 8$ deg and $Re_c = 55,000$.

Source: Batill, S. M. and Mueller, T. J., AIAA Journal,
March 1981, pp. 340-345.

HIGH-SPEED SMOKE

Recent efforts by various investigators — notably including the group at Notre Dame University — have extended the range of smoke visualization techniques to include transonic and supersonic speeds. While extra precautions may be necessary in assuming a large contraction ratio and flow smoothing, the results are quite good. This photograph, for example, clearly shows the leading-edge vortices of a delta wing at angle of attack and Mach 0.9. It was obtained by introducing a single smoke filament along the flow centerline in the wind tunnel stilling chamber.

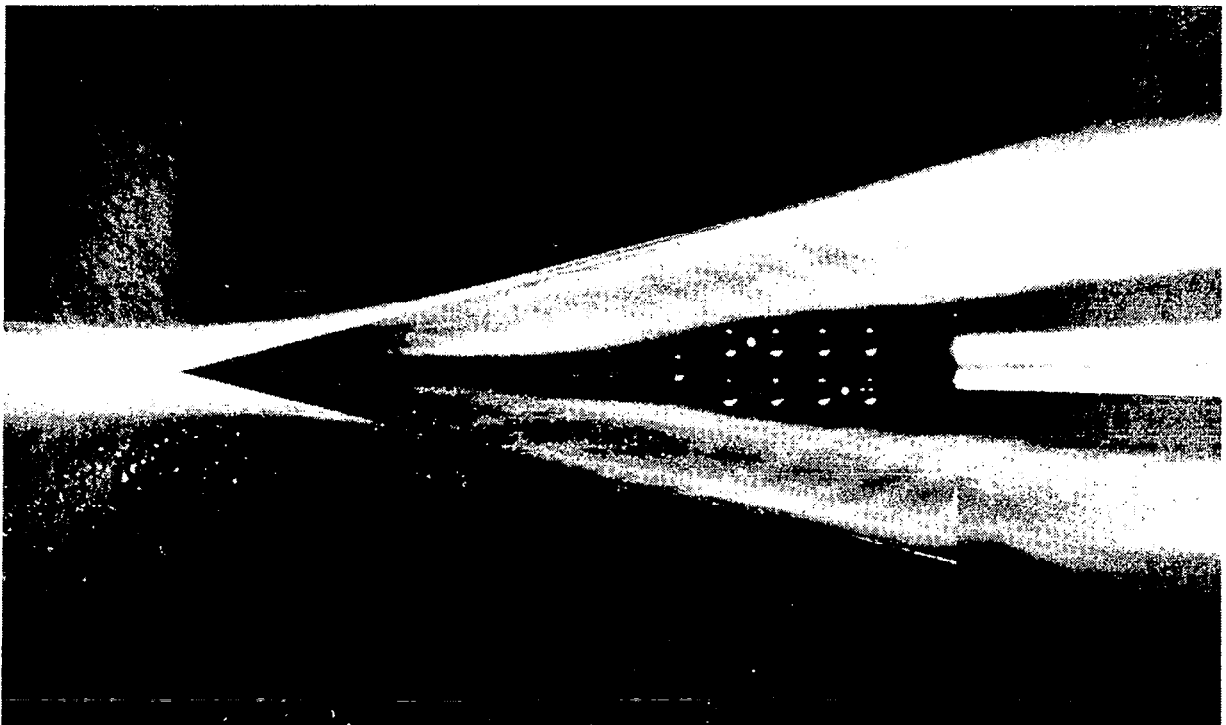


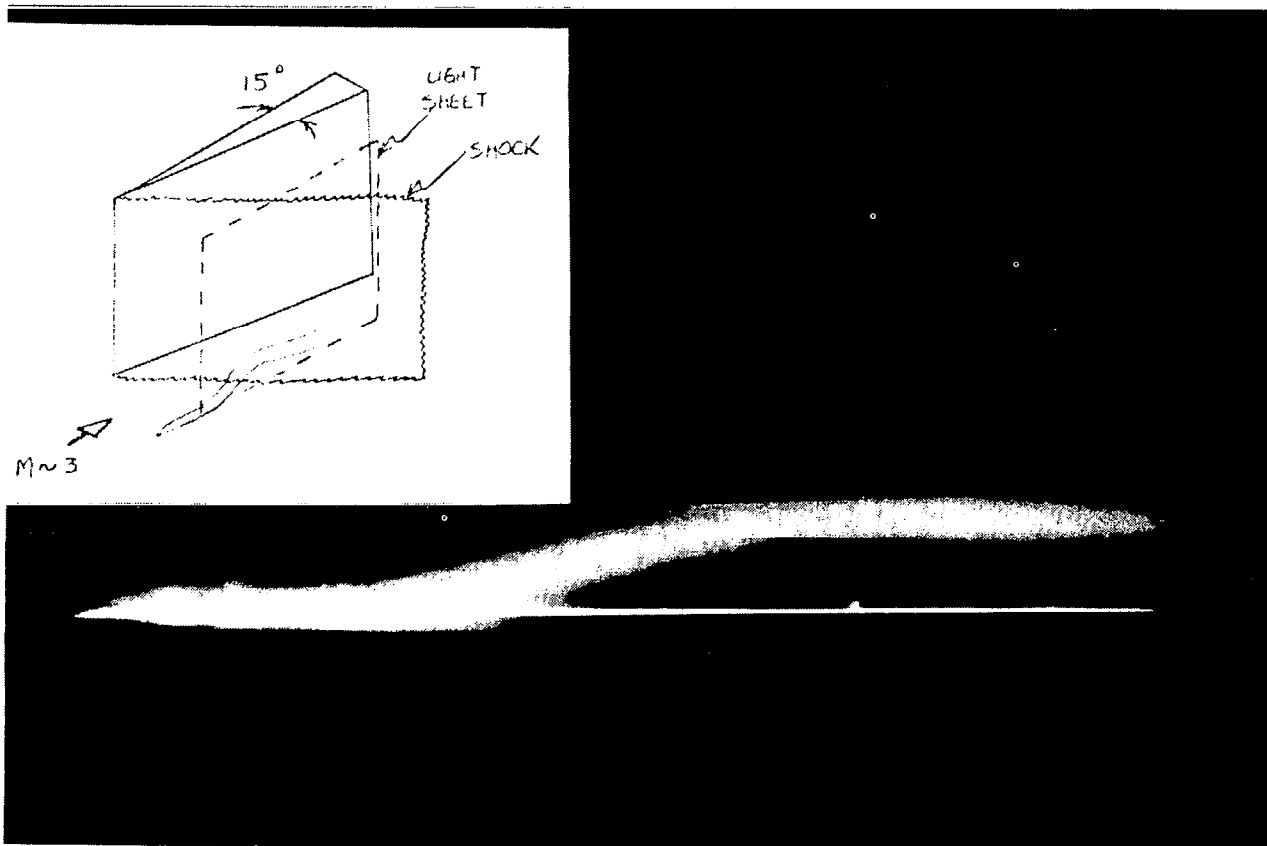
Bild 7: $Ma_{\infty} = 0,9$; $\alpha = 18^{\circ}$

70 A 45

Source: Stahl, W., "Zur Sichtbarmachung von Strömungen um schlanke Deltaflügel bei hohen Unterschallgeschwindigkeiten," DFVLR-AVA-70-A-45, Oct. 1970.

LOCALIZED VAPOR SCREEN

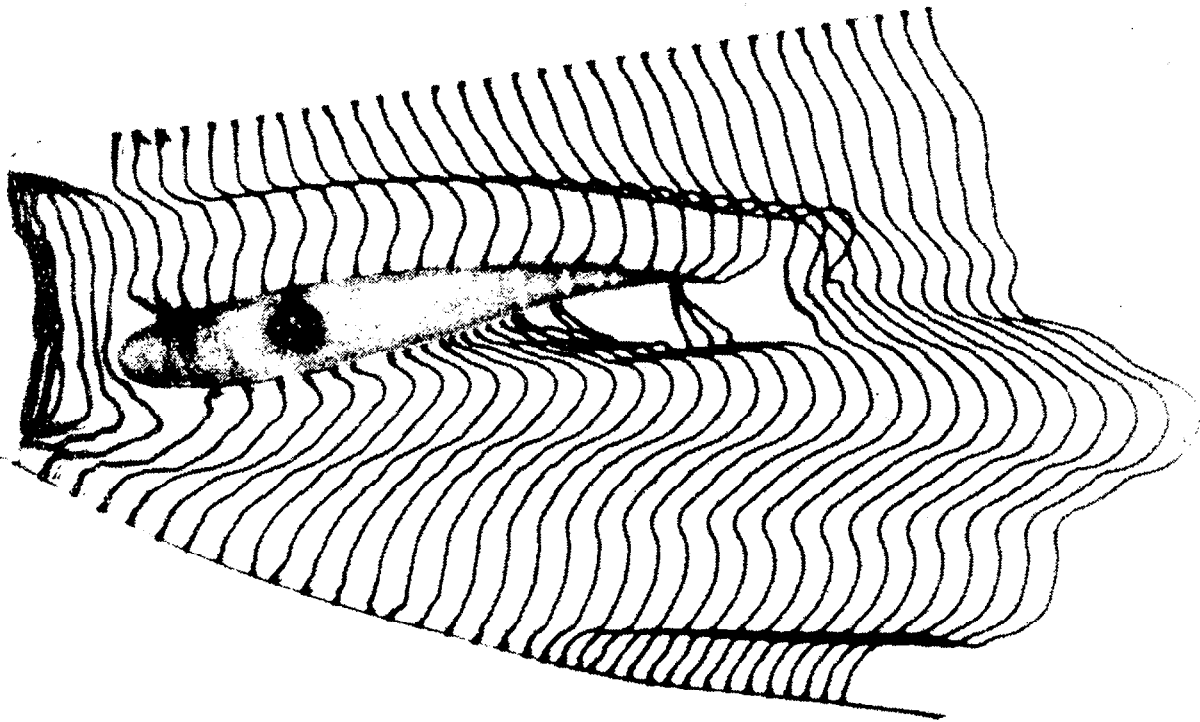
The vapor screen method can be highly useful for investigating complex flows and obtaining flowfield "cuts" which are impossible with standard optical methods. The usual vapor screen technique involves global flow seeding with an aerosol such as water fog. However, vapor screen results can also be had with localized seeding, as shown in this example. Here, a small quantity of acetone was injected through a pressure tap upstream of a 3D shock/turbulent boundary layer interaction. The acetone boiled and atomized, filling the incoming turbulent layer with fog. A streamwise light sheet was generated by spreading the beam of a 1-watt argon-ion laser with a cylindrical lens. The resulting vapor screen photo clearly shows the turbulent boundary layer lifting off the surface. (For more details of the technique, see AIAA Paper 82-0229 by Settles and Teng.)



Source: G. S. Settles and F. Lu, Princeton University.

SPARK TRACING

Profiles of flow velocities from incompressible to supersonic speeds can be obtained by the spark tracing method. Electrical pulses at up to 250 kV and 100 kHz generate periodically luminous spark plasma trails which are convected with the flow. This example shows the flow pattern over a transonic airfoil (spark frequency: 10 kHz). The equipment is made by IMPULSPHYSIK GmbH, Hamburg FRG.



Source: Sales literature, IMPULSPHYSIK GmbH.

OPTICAL METHODS

1) SHADOWGRAPH

- CONVENTIONAL PARALLEL BEAM
- CONICAL SHADOWGRAPH
- RETROREFLECTIVE MODEL SURFACE
- SPECULAR MODEL SURFACE
- WIDE-FIELD MOIRE-GRID PROJECTION

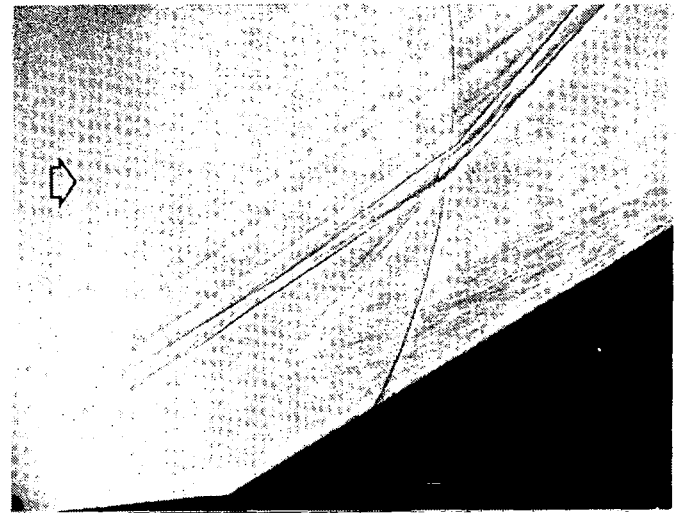
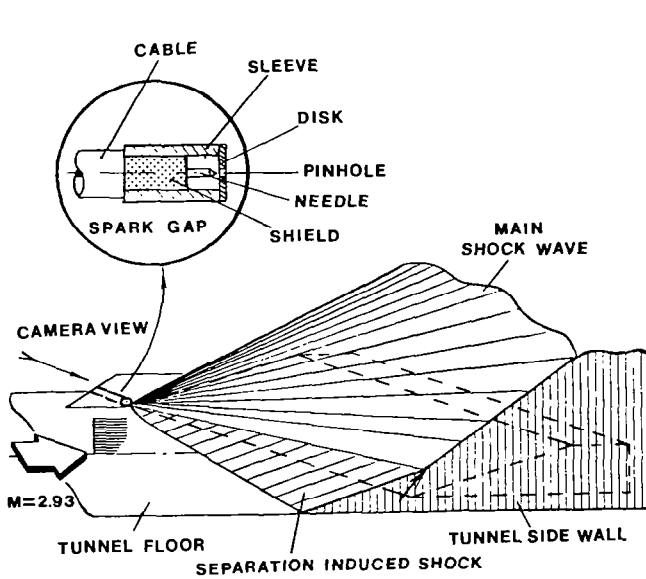
2) SCHLIEREN

- CONVENTIONAL PARALLEL BEAM, KNIFE-EDGE
- COLOR-CODING
- MULTIPLE-SOURCE, SHARP-FOCUSING
- STEREOSCOPIC
- SIMPLE GRID BACKGROUND
- SPECULAR MODEL SURFACE
- QUALITATIVE VS. QUANTITATIVE EVALUATION
- RELATED METHODS: PHASE CONTRAST,
RESONANT REFRACTIVITY, LASER DEFLECTOMETRY,
HOLOGRAPHY

3) INTERFEROMETER

CONICAL SHADOWGRAPH

A variation of the traditional parallel-beam shadowgraph can be used to investigate quasi-conical flowfields. The light source (in this case a spark generated at the end of a coaxial cable inserted into the flow) is positioned near the apex of the conical flow. The shadowgram is cast upon the tunnel wall downstream, where it may be photographed.



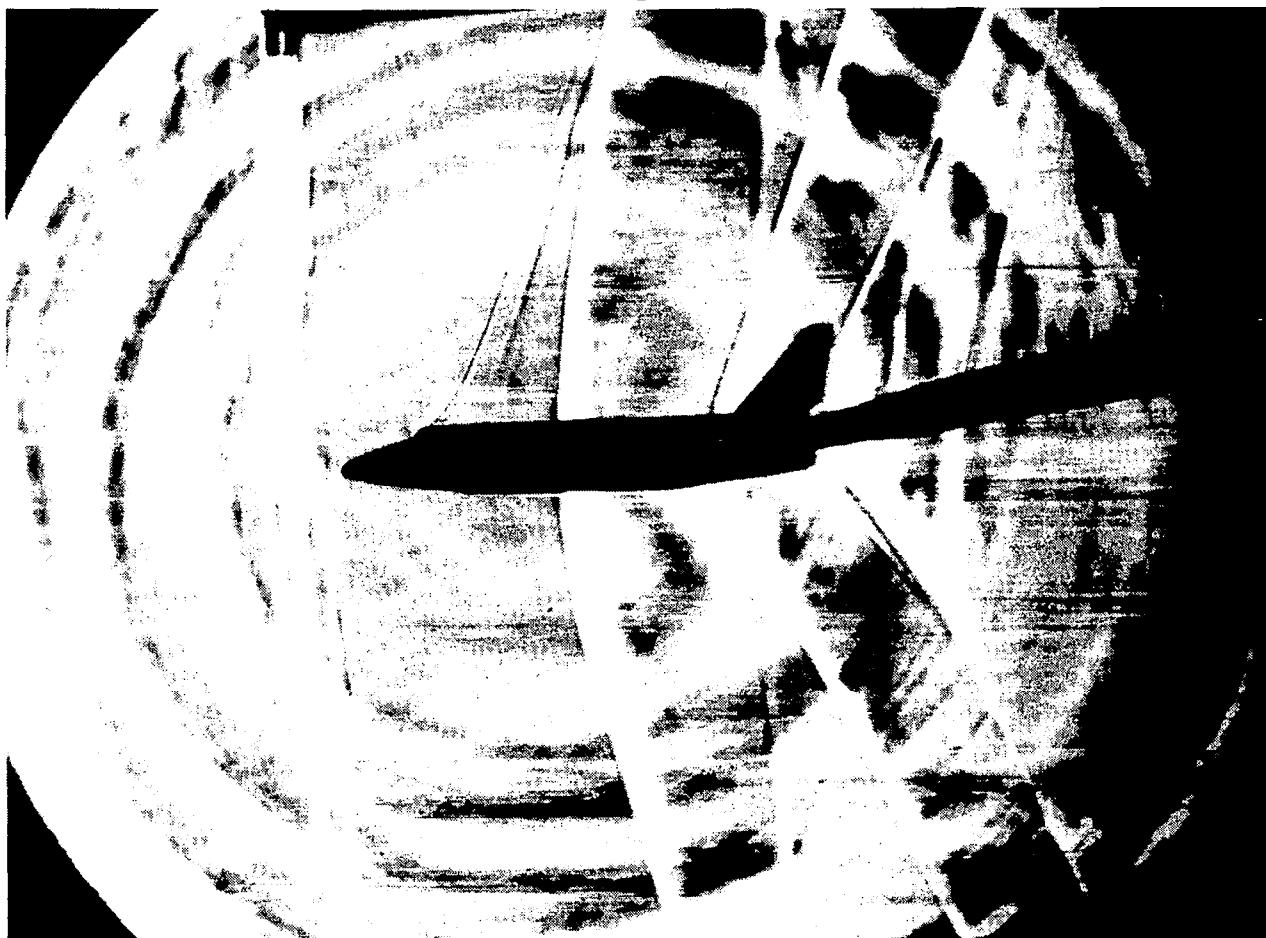
Conical Shadowgram

Sketch of Experimental Arrangement for
Conical Shadowgraph, Showing Shock
Wave Shape for $\lambda = 40^\circ$.

Source: Settles, G. S. and Teng, H. Y., AIAA Paper 82-0229, Jan. 1982.

SCHLIEREN: COLOR-CODING

A variety of modifications (usually simple) to existing schlieren equipment can convey useful flow visualization data by color-coding the schlieren image. This example shows a 1970-vintage Shuttle Orbiter model in the NASA-Ames 6 x 6-foot supersonic tunnel. Here the color-coding serves to provide contrast between the flowfield and the model, and to combine both vertical (yellow-blue) and horizontal (red-green) knife-edge settings in a single photograph. Additionally, the color schlieren arrangement used here has sensitivity equal to that of black-and-white schlieren using the same optics. At least a dozen different color-coding schemes are available to highlight different types of information in the schlieren image. (See Settles, G. S., "Color Schlieren Optics - A Review of Techniques and Applications," in Flow Visualization II, ed. W. Merzkirch, Hemisphere Pub. Corp., 1982, pp. 749-763.

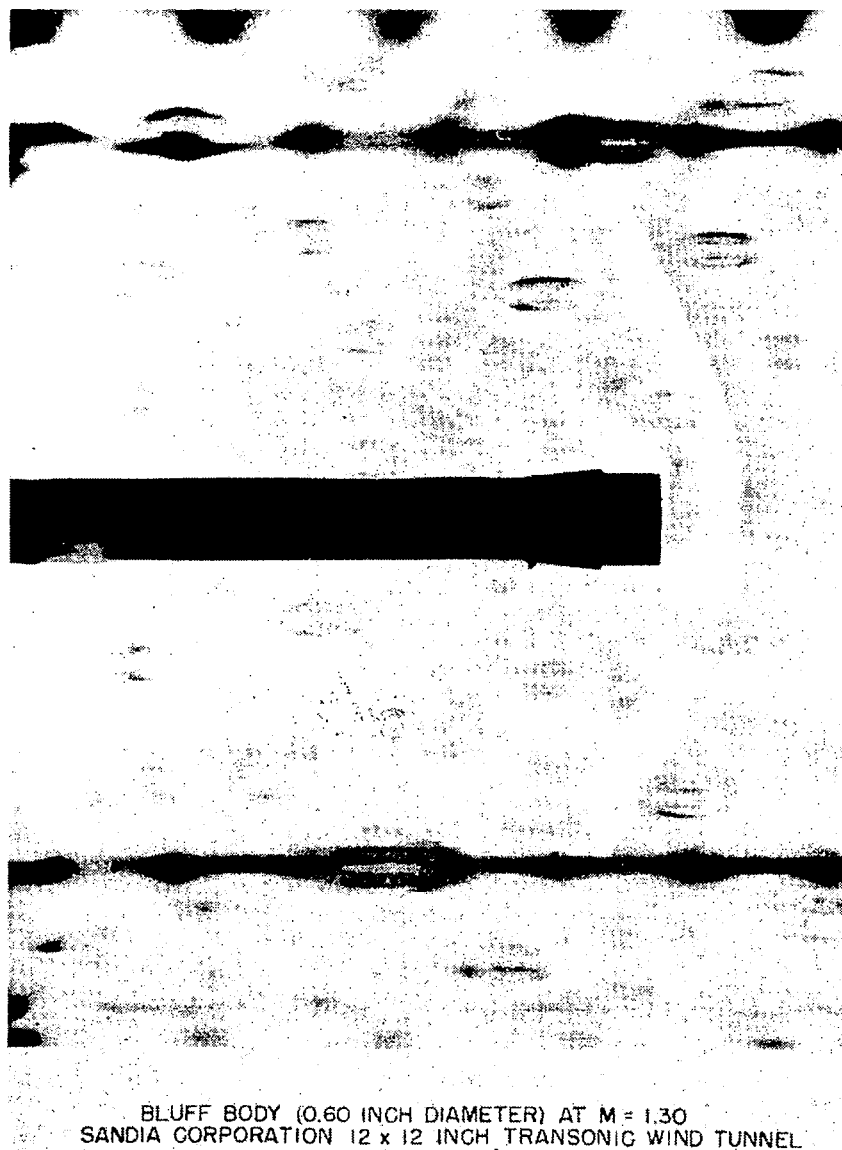


L-82-5674

Source: G. S. Settles/NASA Ames Research Center.

MULTIPLE-SOURCE SCHLIEREN

While conventional schlieren methods generally use small single light sources, there are reasons to use multiple sources for some applications. An extended light source gives a sharp-focusing capability, allowing one to concentrate, say, on the centerline of a complex 3D flowfield. Perhaps even more important for transonic testing is the ability to configure a multiple-source schlieren system to look through slotted or perforated tunnel walls, as in this example.

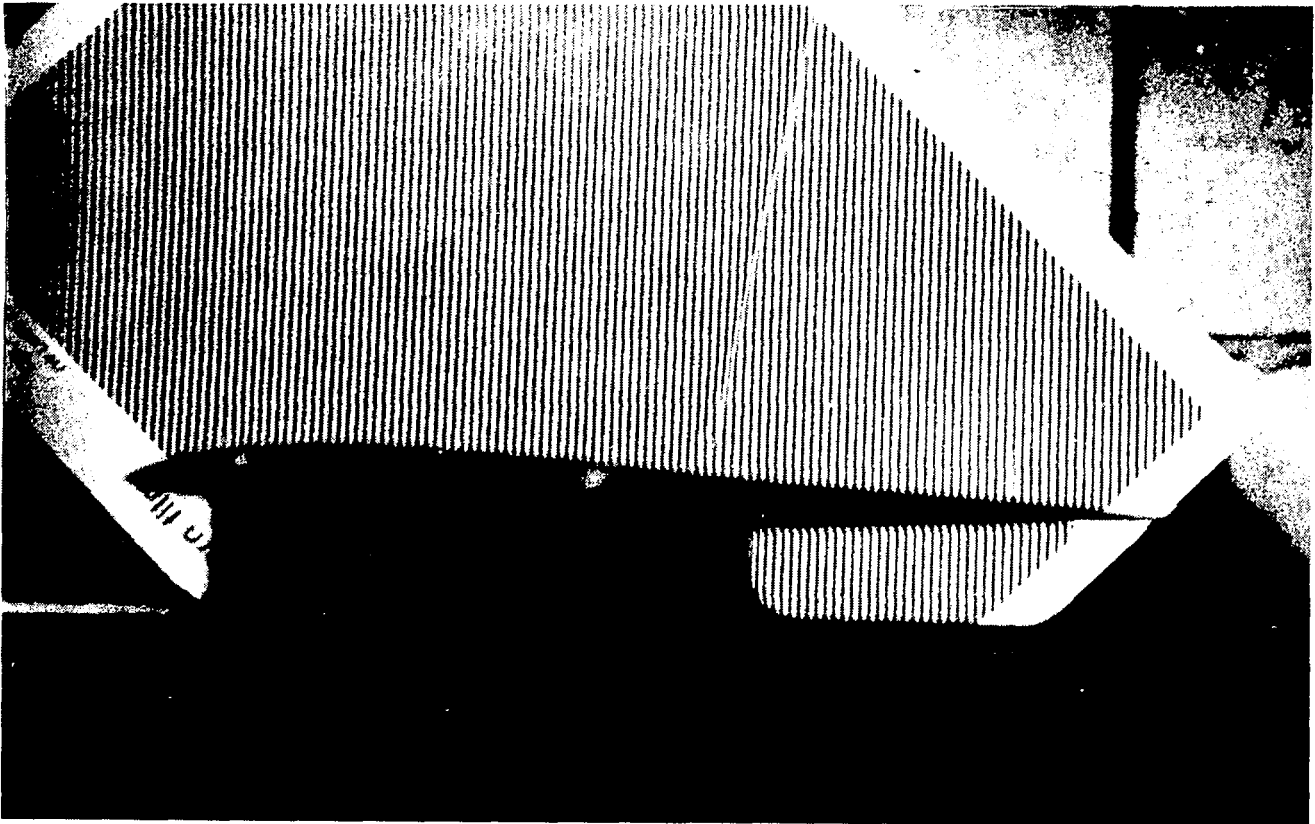


BLUFF BODY (0.60 INCH DIAMETER) AT $M = 1.30$
SANDIA CORPORATION 12 x 12 INCH TRANSONIC WIND TUNNEL

Source: R. C. Maydew, Sandia Corp.

SIMPLE BACKGROUND-GRID SCHLIEREN

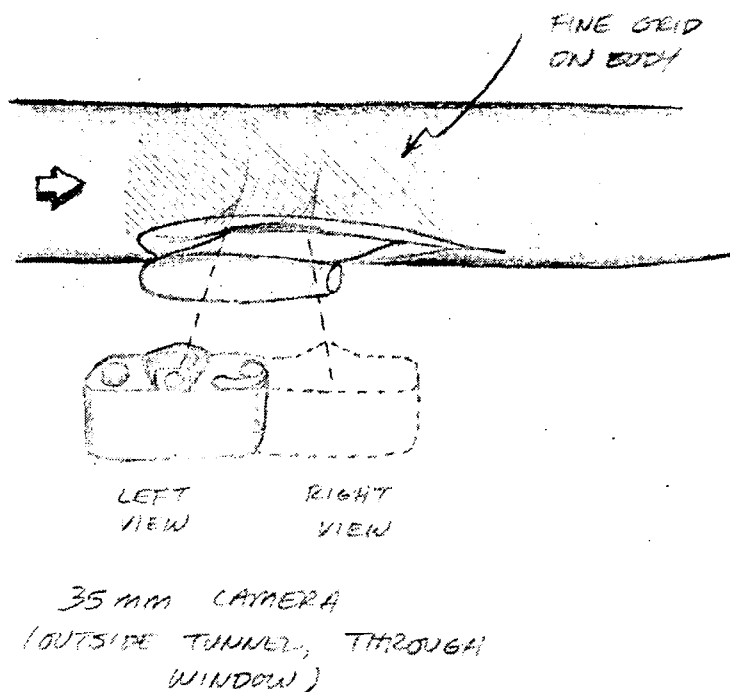
Shock wave locations and shapes can often be found by the simple expedient of viewing through the wind tunnel test section toward a background grid. This technique lacks the sensitivity of more sophisticated optical methods, but requires no equipment and is adaptable to a wide range of viewing angles and to tunnels not originally designed for flow visualization. Here, an airfoil is tested at Mach 0.8 in the Boeing Model Transonic Wind Tunnel. A sheet of ordinary drafting grid was placed a few feet in back of the test section. Stroboscopic backlighting was used to visualize the shock, which appears clearly at about 60% chord.



Source: G. S. Settles/Boeing Aerodynamic Laboratory, Boeing Commercial Airplane Company.

STEREOSCOPIC SCHLIEREN

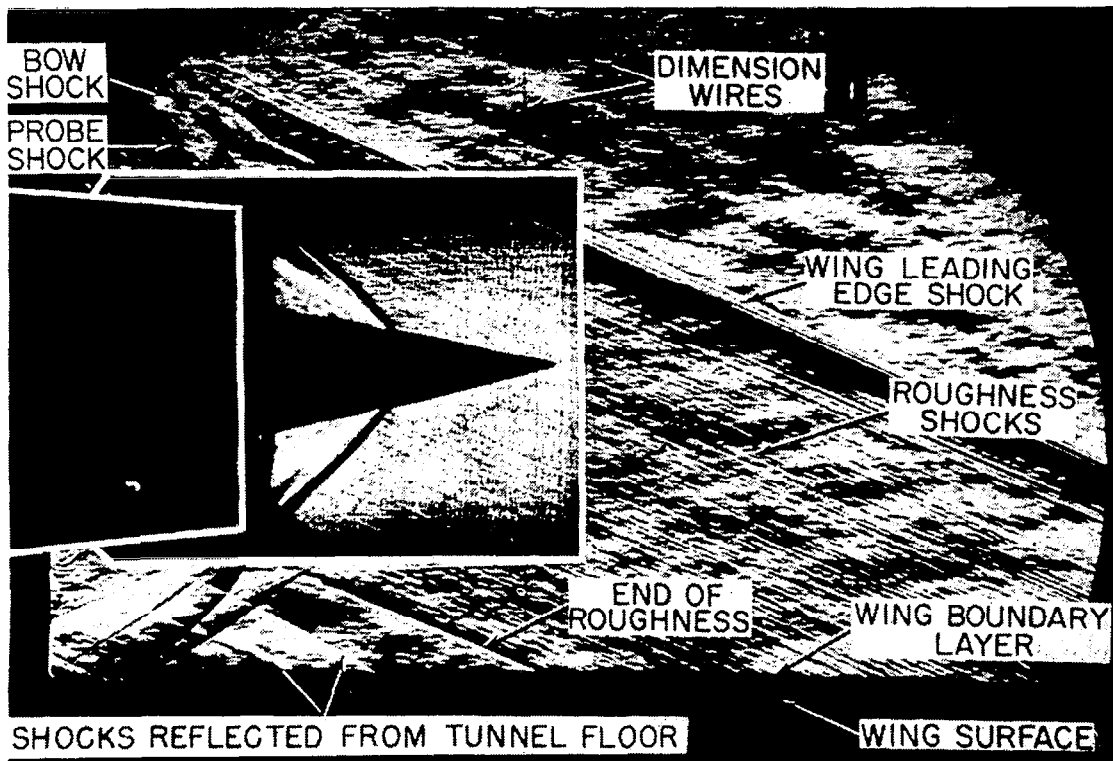
Various arrangements are possible for taking stereoscopic schlieren views of 3D flow phenomena. These methods overcome the inherent disadvantage of conventional schlieren visualizations: the integration of 3D flow information into a 2D image. The simplest stereo schlieren method involves taking stereo photos with the grid background described earlier. As shown in this sketch, the method can be used, for example, to visualize the 3D transonic shock pattern on the wing of a commercial air transport model. Such visualizations were carried out by the author and J. P. Crowder of Boeing's Aerodynamic Laboratory during 1981 tests in the Boeing Transonic Wind Tunnel.



Source: G. S. Settles/Boeing Aerodynamic Laboratory, Boeing Commercial Airplane Company.

SCHLIEREN AND SHADOWGRAPH USING REFLECTING MODEL SURFACES

Test models appear only in silhouette in most optical flow visualizations. This is a disadvantage in observing complex 3D flows, where the model may obscure important parts of the flowfield. Specular model surfaces can sometimes be used to overcome this problem by allowing one to collect the reflected light and form an image of the normally-obscured flow. In this example a reflecting splitter-plate was used to visualize an inlet shock pattern that would otherwise have been obscured. Such techniques have the potential to visualize transition on polished wings by planform schlieren or shadowgraphy. Further, in NTF the model surfaces may need to be specular for other reasons as well.



Composite shadowgraph and schlieren of the flow. Splitter plate 1; high pylon; $\phi = 0^\circ$; $\dot{m}_2/\dot{m}_1 = 0.72$.

L-66-1003

Source: Moseley, G. W., et al., NASA TN D-3385, April 1966.

PHOTOGRAPHY AND VIDEOGRAPHY

1) LIGHT SOURCES

- CONVENTIONAL, STROBOSCOPIC, & LASER

2) CAMERAS

- HIGH-SPEED: > 1 MHz
- STANDARD VIDEO: 30 Hz
- HIGH-SPEED VIDEO: 12 kHz B&W, 200 Hz COLOR

THE NEED FOR AN OPTICAL TRANSITION
DETECTION SYSTEM IN THE NTF

M. F. Fancher
Douglas Aircraft Company
Long Beach, CA

TRANSITION DETECTION IN THE NTF

The very high test and model costs which will be associated with the NTF as well as the limited access of commercial transport aircraft manufacturers to the facility will necessitate testing of any new configuration over a range of Reynolds numbers for correlation with data obtained in conventional tunnels, where most development testing will continue to be done. These Reynolds number variations will be carried out at constant dynamic pressure, i.e., constant aeroelastic condition, by varying test temperature. Boundary-layer transition cannot be expected to occur at the full-scale location at significantly less than full-scale Reynolds numbers, and transition patterns will change with varying Reynolds number. Knowledge of the location of transition on model surfaces is essential for correct interpretation of drag data, however, so that a means of determining transition location in the NTF is essential if the testing requirements of transport manufacturers are to be satisfied. The importance of transition, the limitations of artificial transition fixing, and their relation to the NTF are further reviewed in Reference 1.

Transition detection techniques used on model transport configurations in conventional tunnels are restricted to surface flow visualization methods such as oil flow and sublimation. Even if problems associated with very low temperatures are overcome, adaptation of these methods for transition detection in the NTF is not practical because of the very small critical roughness heights encountered. Figure 1 shows the calculated minimum roughness height to instantaneously trip transition on a model transport wing over a range of Reynolds numbers of interest in the NTF. Clearly, any material placed on a model surface would be very likely to affect transition at many important conditions. A nonintrusive method of transition detection is required.

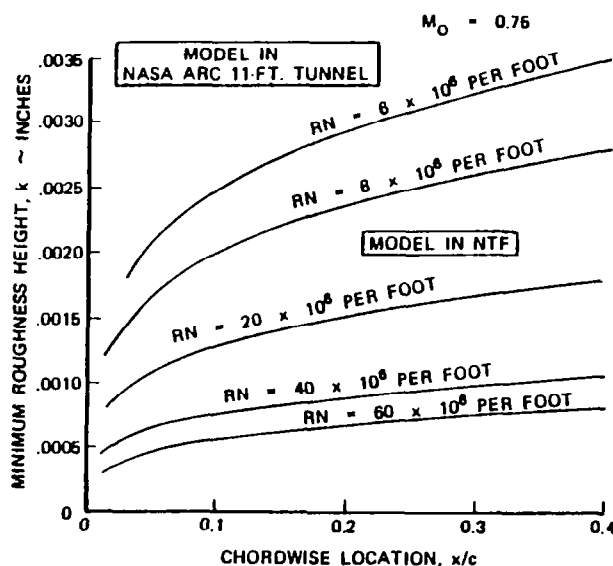
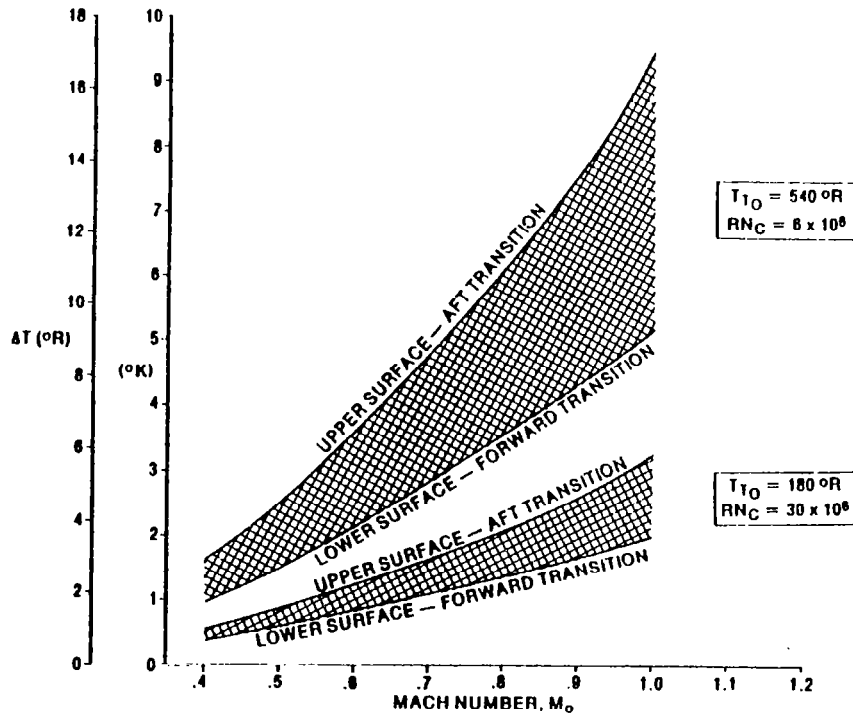


Figure 1

THE NEED FOR A NEW OPTICAL METHOD

To date, no fully satisfactory method for transition detection in the NTF has been identified. A uniquely nonintrusive configuration of hot-film gages described in Reference 2 appears to at least partially satisfy the firm requirement for transition detection on transport models in the NTF. However, only an optical method offering nonintrusive and total coverage of model surfaces will be completely satisfactory. One such approach is infrared thermography. However, both fundamental and practical limitations appear to prevent its use for transition detection in the NTF. Figure 2 shows the calculated range of temperature change across the transition region on a model transport wing over the Mach number range of interest. It is seen that the temperature changes associated with transition in conventional wind tunnels, in which only marginal results have been obtained, are far larger than those at conditions of interest in the NTF. This consideration and other complications of low temperature infrared measurement eliminate these methods from consideration. An innovative alternative is needed, perhaps based on properties of coherent light reflected from model surfaces or transmitted through the model boundary layer from sources in the model surface.

In summary, a method for boundary-layer transition detection on models tested on the NTF is necessary if the requirements of transport aircraft manufacturers are to be satisfied. Current methods are not applicable, and the only workable approach proposed to date, the hot-film system of Reference 2, is not ideal. Identification and development of a nonintrusive method, preferably optical, must be given high priority now if this critical capability is to be on hand when the NTF becomes available to industrial users.



REFERENCES

1. Lynch, F. T. and Patel, D. R.: Some Important New Instrumentation Needs and Testing Requirements for Testing in a Cryogenic Wind Tunnel Such as the NTF. AIAA Paper No. 82-0605, presented at AIAA 12th Aerodynamic Testing Conference, Williamsburg, VA, March 1982.
2. Fancher, M. F.: Aspects of Cryogenic Wind Tunnel Testing Technology at Douglas. AIAA Paper No. 82-0606, presented at AIAA 12th Aerodynamic Testing Conference, Williamsburg, VA, March 1982.

SURFACE FLOW VISUALIZATION REQUIREMENTS
FOR TESTING IN NTF

Ronald L. Bengelink
Boeing Aerodynamic Laboratory
The Boeing Company
Seattle, Washington

NASA/Industry panels have addressed the question of wind tunnel to flight correlation using the National Transonic Facility in both 1976 and 1980. The 1976 panel (ref. 1) recommended very strongly that users should "avoid absolute drag comparisons (model to flight) because of thrust measuring uncertainties." The 1980 panel (ref. 2) recommended in a more positive vein, "an early priority for the NTF should be the definition and conducting of an experiment or experiments to provide user confidence in tunnel-to-tunnel measurements (comparing existing facilities to the NTF)." It is just this type of experiment which is currently being developed by Boeing, comparing the Boeing Transonic Wind Tunnel (BTWT), the Calspan 8 Foot Transonic Tunnel, the NASA-Ames 11 Foot Unitary Transonic Tunnel, and the NTF using a swept-strut mounted full model of the 767.

By carefully tailoring the instrumentation package and the test program in each tunnel, this tunnel-to-tunnel correlation can be made using drag level, drag rise due to compressibility, and buffet boundary (fig. 1). At the same time, the variation of drag with Mach number and the buffet boundaries can also be correlated with full-scale in-flight measurements.

These parameters are expected to vary with Reynolds number. Figure 2 schematically indicates this expected variation of drag coefficient for two Mach numbers of interest. The effect of forced boundary layer transition as a function of Reynolds number is well known. To allow a tunnel-to-tunnel correlation, the shape of the various "tripped" boundary layer curves shown in figure 2 and the Reynolds number at which they coalesce should not be a function of the wind tunnel in which the test is run. Yet, turbulence level and distribution, local upflow distribution, test section noise, model surface deterioration, and other factors will affect boundary layer transition. Therefore it is necessary to know the untripped transition location, the shock location, and the trip effectiveness in order to be able to assure a consistent model surface flow condition in the various wind tunnels to be correlated. These are certainly factors which need to be controlled during such a tunnel correlation study.

In the past (ref. 3) very few surface flow measurement schemes have been suggested which offer the potential for application to this problem. Yet it is obvious that surface flow visualization is required at all the facilities to be correlated, including the NTF, in order to allow the following (fig. 3):

1. an understanding of the chordwise and spanwise extent of laminar flow
2. the change in shock location for various trip configurations
3. the effectiyeness of the chosen boundary layer trip (since its specifications will change as a function of Reynolds number)
4. a comparison of the separation patterns at the buffet conditions.

It is not the purpose of this paper to offer a solution to this requirement, but merely to point out that it is a requirement to tunnel-to-tunnel correlation testing involving the NTF. Figure 4 is an attempt to define a specification for a surface flow visualization system to be used in the NTF. Recognition of the special limitations in the NTF including physical and visual accessibility, high operating cost, flow contamination requirements, as well as the need for on-line review of the results in order to develop the final trip configurations in a timely manner, leads to the requirements listed.

It is recommended that a high priority be given to the development of such a surface flow visualization system by NASA and all potential users.

References

1. Baals, Donald D. ed.: High Reynolds Number Research, NASA CP-2009, 1976.
2. Ayers, Theodore G.: Report of the Wind Tunnel/Flight Correlation Panel. High Reynolds Number Research - 1980, McKinney, L. Wayne; and Baals, Donald D.; eds., NASA CP-2183, 1981, pp. 249-263.
3. Bobbitt, Percy J.: Report of the Panel on Fluid Dynamics. High Reynolds Number Research - 1980, McKinney, L. Wayne; and Baals, Donald D.; eds., NASA CP-2183, 1981, pp. 169-195.

- **Drag Level at "Incompressible" Mach Number**
 - Comparison with other wind tunnels at a constant Reynolds Number
 - Comparison with other wind tunnels as a function of Reynolds Number
- **Compressible Drag Rise**
 - Comparison with other wind tunnels as a function of Reynolds Number
 - Comparison with flight at a constant Reynolds Number
- **Lift & Drag Buffet Boundaries**
 - Comparison with other wind tunnels as a function of Reynolds Number
 - Comparison with flight at a constant Reynolds Number

Figure 1.- Output of correlation testing at NTF for transport-type configurations.

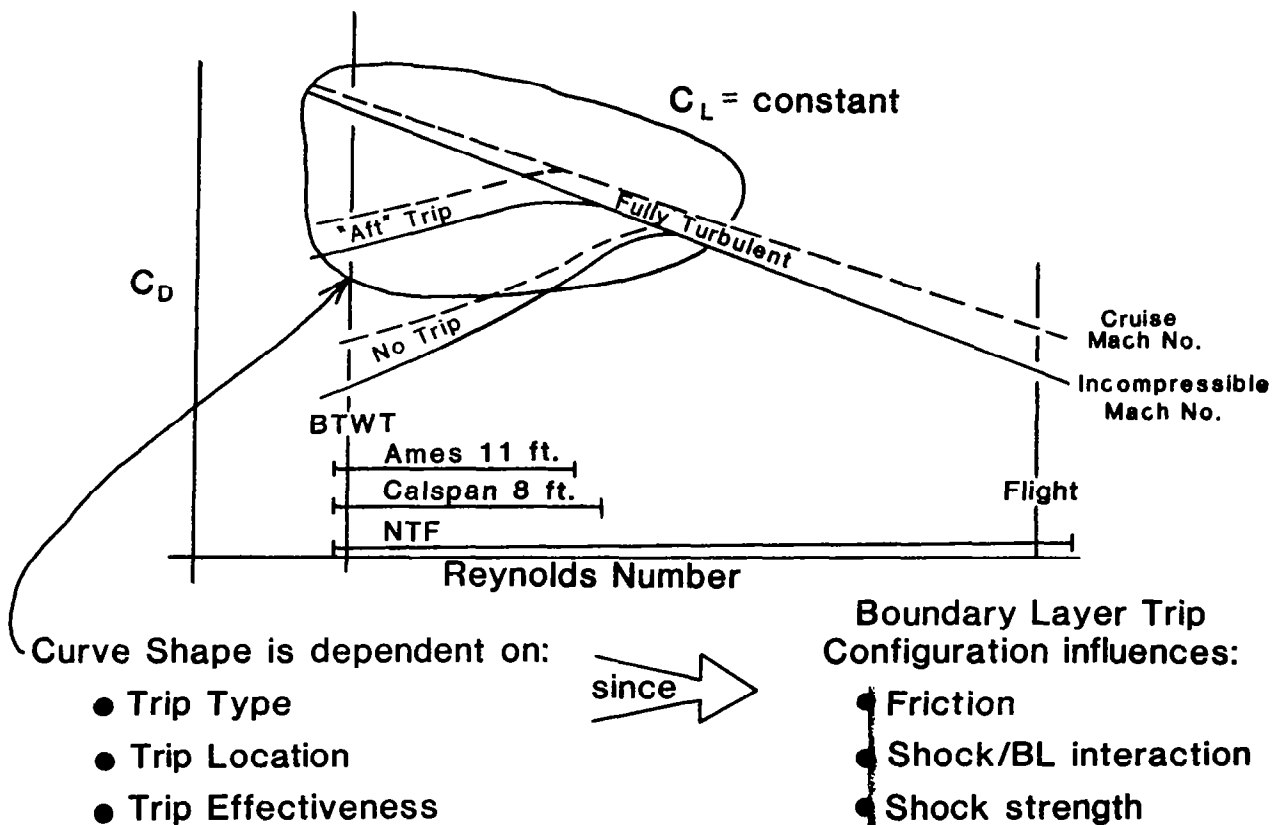


Figure 2.- Expected drag variation with Reynolds number.

● **Meaningful Testing at NTF will require Surface Flow Visualization to identify:**

- **Extent of Laminar Flow (Aft trip location requirements)**
- **Shock Location**
- **Shock/Boundary Layer Interactions**
- **Trip Effectiveness**
- **Separation Patterns**

as a function of Mach Number and Angle of Attack.

Figure 3.- Correlation testing with NTF.

- **Application**
 - **Remote**
 - **Rapid**
- **Patterns**
 - **Rapid Development**
 - **Easily Recorded**
 - **Readily Interpreted**
- **Material**
 - **No measurable Impact on Flow Field**
 - **Non-contaminating**
- **Documentation**
 - **On-line visibility**
 - **Clear permanent records**

Figure 4.- Surface flow visualization requirements.

SURFACE FLOW VISUALIZATION
USING INDICATORS

James P. Crowder
Boeing Aerodynamic Laboratory
The Boeing Company
Seattle, Washington

Surface flow visualization using indicators in the cryogenic wind tunnel will remain as important an experimental procedure as the conventional "oil flow" methods, but with the extreme testing environment will require a fresh look at materials and procedures to accommodate the new test conditions. In a sense, these new conditions are welcome, as they provide an opportunity to identify new materials and reactions to provide better surface flow visualization opportunities.

Figure 1 summarizes several potential liquid and gaseous indicators that can be identified from a cursory examination of material tables, but their particular suitability can only be determined after actual trials in the test environment. These particular materials illustrate the various requirements an indicator must fulfill. Foremost among the requirements is that the indicator must exist in the proper state at the test condition. Keeping in mind that the test conditions can span the entire operating envelope of the NTF, it is probably too much to expect one material to be used over the entire range. Several different indicators must be selected.

Equally important are the requirements that the indicator must respond properly to the flow phenomenon of interest and must be observable. Boundary layer transition is the most important phenomenon for which flow visualization indicators may be employed and probably the most difficult application. Identification of surface flow direction and separation is a more easily achieved application, and is still sufficiently important to justify the development effort required.

The visibility of a particular indicator will depend on utilizing various optical or chemical reactions. For example, liquid nitrogen may be visible on a model surface by specular reflections from the liquid-gas interface or by

atomic emissions excited by tuneable laser illumination. The hydrocarbons such as propane and pentane will readily dissolve various fluorescent dyes and thus can be easily observed with ultraviolet illumination.

Gaseous indicators are probably more difficult to utilize, but because of their diversity, may present unusual and useful opportunities. Presumably they can be observed directly by resonant emissions, but other reactions can also be expected. For example, oxygen can quench the fluorescence of other materials so that one can imagine the model surface coated with a fluorescent paint which will produce a visible emission which is inhibited where the concentration of oxygen in the boundary layer is sufficiently high. Ozone has the property of strongly absorbing ultraviolet radiation and so can conceivably be used to cast a shadow on a fluorescent surface by blocking the ultraviolet excitation. At higher temperatures ammonia can be used in conjunction with pH indicators incorporated into a paint system to produce visible stains in regions of high concentration such as in Figure 2. In this example ammonia is dispensed from pressure orifices in the model surface.

Other factors that must be considered in selecting an indicator include handling safety, toxicity, potential for contamination of the tunnel, and cost.

Delivery of the indicator to the model surface is a major consideration, if not impediment, in any flow visualization system. It can be readily appreciated that a wind-on dispensing system is necessary for practical utilization of flow visualization indicators in the NTF. Not only would a one-shot pre-run application of indicator to the model surface be prohibitively expensive for routine use in the NTF, but most indicators would not even exist in the proper state at the application temperature and pressure.

Of the possible flow visualization indicator delivery systems, as summarized in Figure 3, the retractable spray bar approach is probably the least attractive. It has the advantage of being independent of the model, but it would require a complex facility installation. Its greatest disadvantage, however, may be the very inefficient delivery of indicator to the model surface which implies that large quantities of material are needed and hence the tunnel contamination may be very serious.

An onboard-model dispenser comprised of an array of orifices in the surface could be considered a conventional system, but this approach suffers several serious difficulties. The supply pressure drop of the indicator through an orifice of practical size is relatively small compared to typical aerodynamic pressure gradients across the model surface. Therefore, in order to maintain uniform delivery over the entire wing span, for example, a multiple manifold system is usually required. This complicates the installation of the system in the model and requires a complex control system. Figure 4 shows the narrow nature of liquid indicator plumes dispensed from orifices.

A delivery system comprised of a continuous strip of porous metal inset flush with the model surface offers many advantages. In particular, it is possible to achieve uniform dispensing over an entire wingspan with a single manifold at conveniently high supply pressures (on the order of 1000 psi) so there is little potential for interaction with model surface pressures. Figure 5 shows the typical appearance of an indicator dispensed from a relatively nonuniform porous strip. The model surface can be very smooth and thus presents less of a disturbance to the flow than individual orifices.

The greatest difficulty with this approach to date has been model fabrication. The porous metal has usually been in the form of sintered stock cut into strips and inset into a carefully machined groove in the model to achieve a close-fitting mechanical attachment. This has been relatively easy for conventional, 2-D models, but will be much more difficult for cryogenic, 3-D models.

A new method of fabricating a porous dispenser suitable for a 3-D, cryogenic model has been developed at the Boeing Aerodynamic Laboratory as reported here and is depicted in Figure 6. With this new method, a single spanwise slot is machined into the wing leading edge, but it need not be very straight nor of constant dimension. The sides of the slot should be widely spread and a narrow groove located in the bottom. The slot is then filled by a flame spray process which involves blowing semi-molten powdered metal from a high temperature gun. Figure 7 shows the appearance of the flame spray application before finishing.

Depending on the details of the material used, preparation of the model surface, and the particular application process, a very secure attachment of the porous material to the model can be achieved. The flame spray material is finished to the final model contour as if it were solid metal with a very smooth surface finish. Depending on the final finishing and porosity of the material, an electro-chemical etch of the surface may be required to open the pores a controlled amount for uniform dispensing of the indicator.

Experience with this process on small specimens has been very encouraging, but several important questions remain to be answered, as summarized in Figure 8. The major structural problem may be the effect of repeated temperature cycles on the porous material attachment. Thermal stressing of small samples

by alternate submersion in liquid nitrogen and hot water has so far shown no adverse effects. Another question which must await wind tunnel trials is the durability against erosion by wind-borne matter.

A final question which deserves careful study is a definition of surface roughness requirements. Even though these porous metal surfaces feel smooth to the fingertip, it is clear that they tend to have relatively large pores below the surface which would doubtless be perceived by conventional roughness inspection methods as similar to roughness features that protrude above a mean surface. It is unlikely, however, that the aerodynamic flow will react to such surface features similarly. It is probably not possible to resolve this question without actual wind tunnel trials, but conventional, and somewhat arbitrary, model surface roughness specifications should not be applied too rigorously and prematurely.

Clearly there are great potential benefits in developing surface flow visualization methods for cryogenic wind tunnel testing and there are many potential materials and reactions that deserve thorough study. Even though there appear to be a few practical techniques close at hand, the potential for even greater surface flow visualization productivity ought to justify a long term and complete development effort.

* Candidate Flow Visualization Indicators

LIQUID			GASEOUS	
	M.P.(K)	B.P.(K)		B.P.(K)(1 ATM)
NITROGEN	63	77	OXYGEN	90
PROPANE	83	229	OZONE	161
FREON-12	118	278	CARBON MONOXIDE	81
ACETONE	179	329	NITRIC OXIDE	120
PENTANE	143	309	AMMONIA	240

- * Pre-run application of indicator is impractical
 - access to model for one-shot flow vis involves great expense.
 - physical properties of most indicators are incompatible with standard temperature and pressure.
- * Cryogenic surface flow visualization using indicators requires wind-on dispensing system.

Figure 1.- Cryogenic surface flow visualization using indicators.

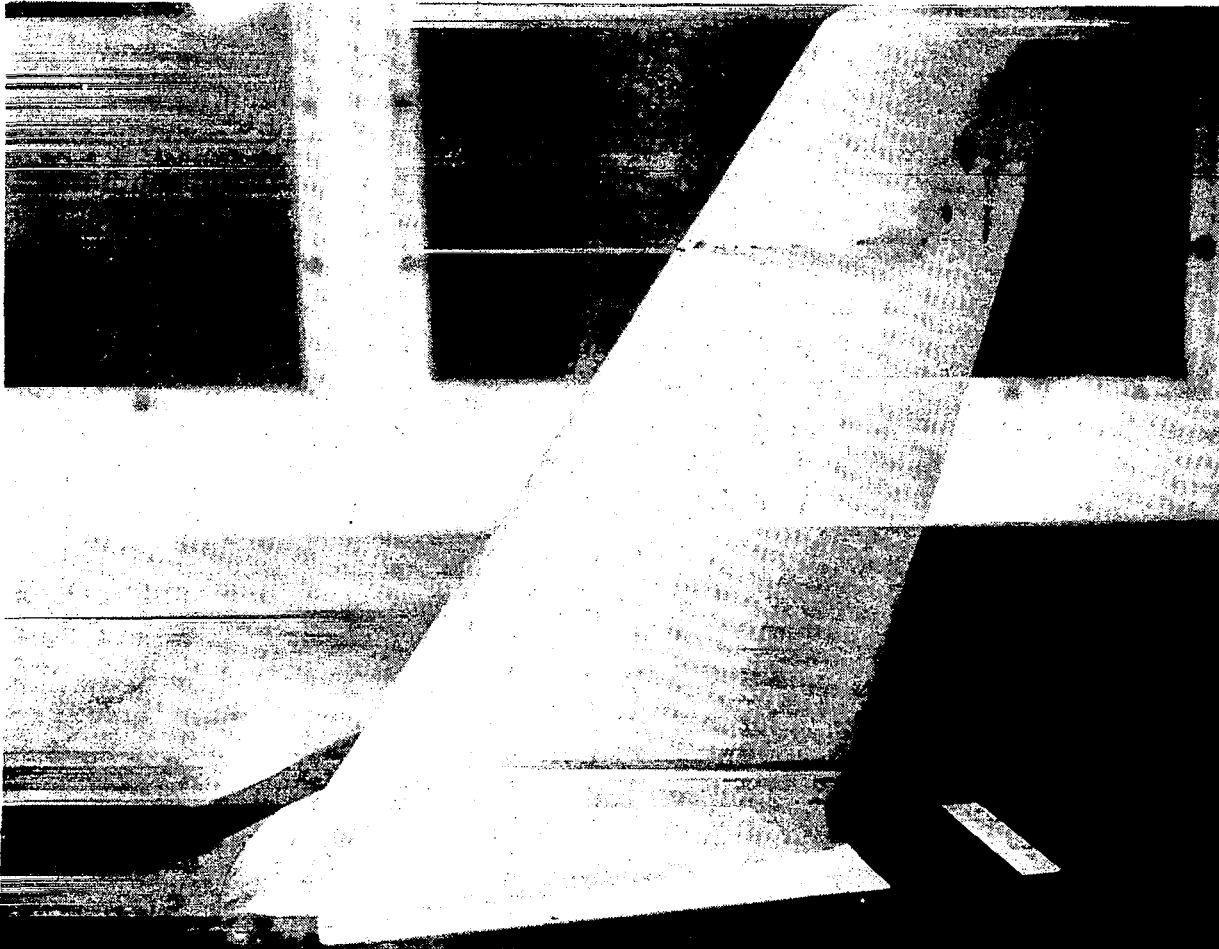


Figure 2.- Example of flow visualization using ammonia gas indicator.

- * Retractable Spray Bar
 - + Independent of model
 - Requires elaborate facility modification
 - Disturbs flow while dispensing
 - Large quantities of indicator--contaminates tunnel
- * Orifice Arrays in Model
 - + Present state-of-the-art baseline method
 - + Simple concept
 - Complicated multiple manifolds
 - Small pressure drop--interacts with model pressures
 - Orifice size disturbs boundary layer
- * Porous Surface
 - + Uniform distribution from single manifold
 - + High supply pressure (0~1000 psi)
 - + Smooth surface
 - Difficult to install sintered strips in 3-D model
 - Easily plugged by non-soluble pigments

Figure 3.- Cryogenic surface flow visualization dispenser systems.

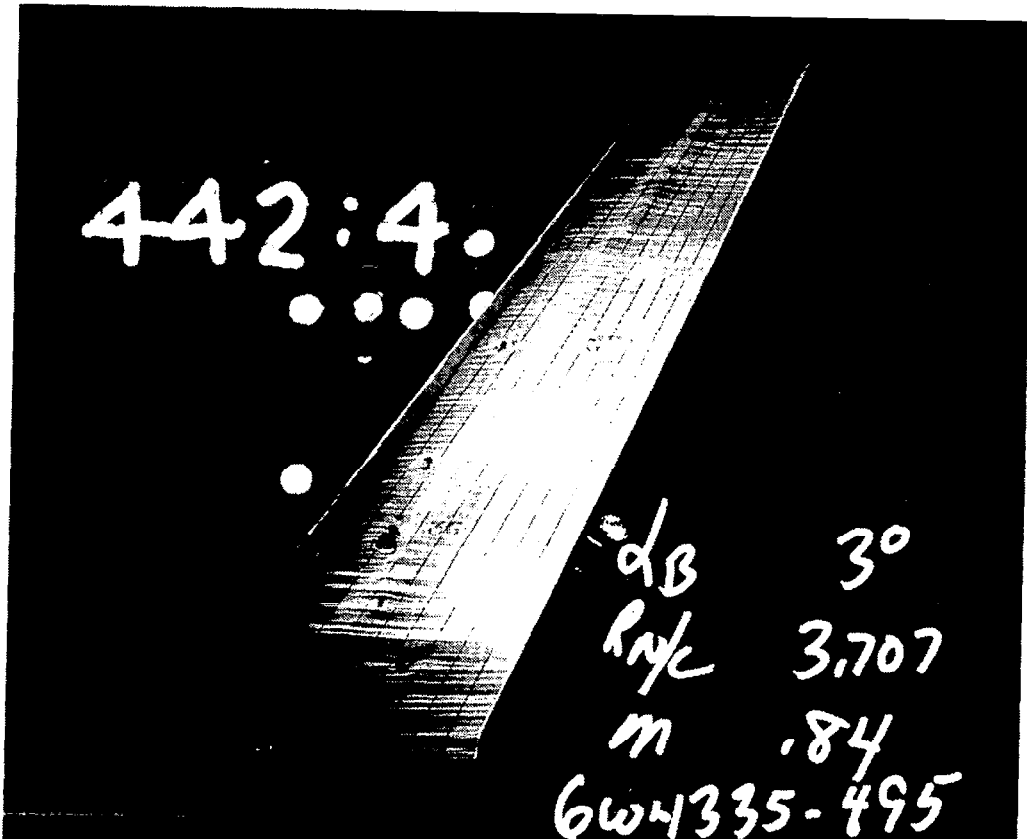


Figure 4.- Example of liquid indicator dispensed from orifices.

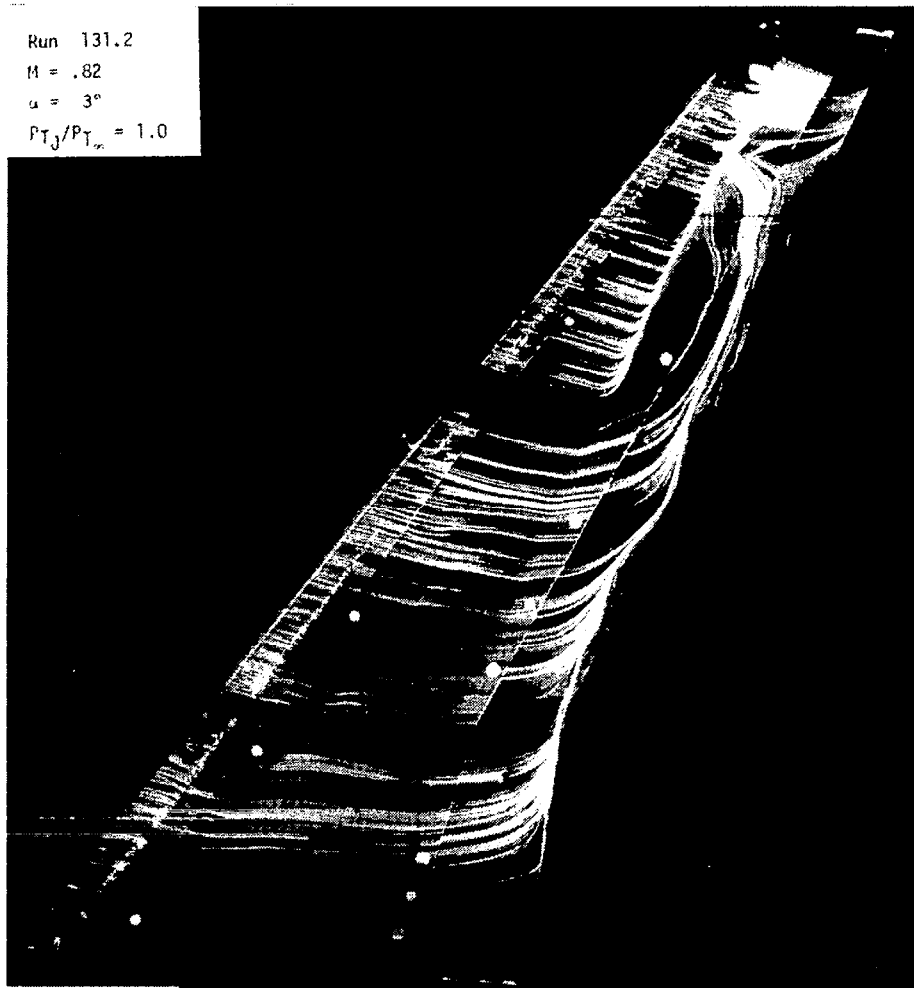
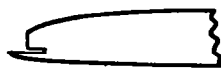


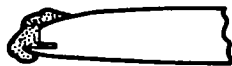
Figure 5.- Example of liquid indicator dispensed from porous strip.

* Machine one continuous spanwise slot in wing leading edge



- slot need not be straight nor constant dimension
- hand finishing can be used for transition regions
- narrow part of slot serves as distribution manifold

* Flame spray with powdered metal



- various materials (i.e. alum, nickel, s.s., etc.)
- various particle sizes—adjust for proper porosity, bonding strength, smoothness, etc.
- various processes (i.e. flame spray, plasma arc, etc.)
- various preparation steps (i.e. degrease, blast clean, masking, etc.)

* Finish to final contour

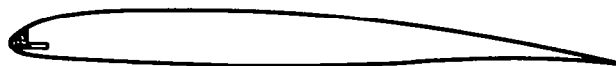


Figure 6.- New porous dispensing system for cryogenic surface flow visualization, developed by Boeing Aerodynamic Laboratory.

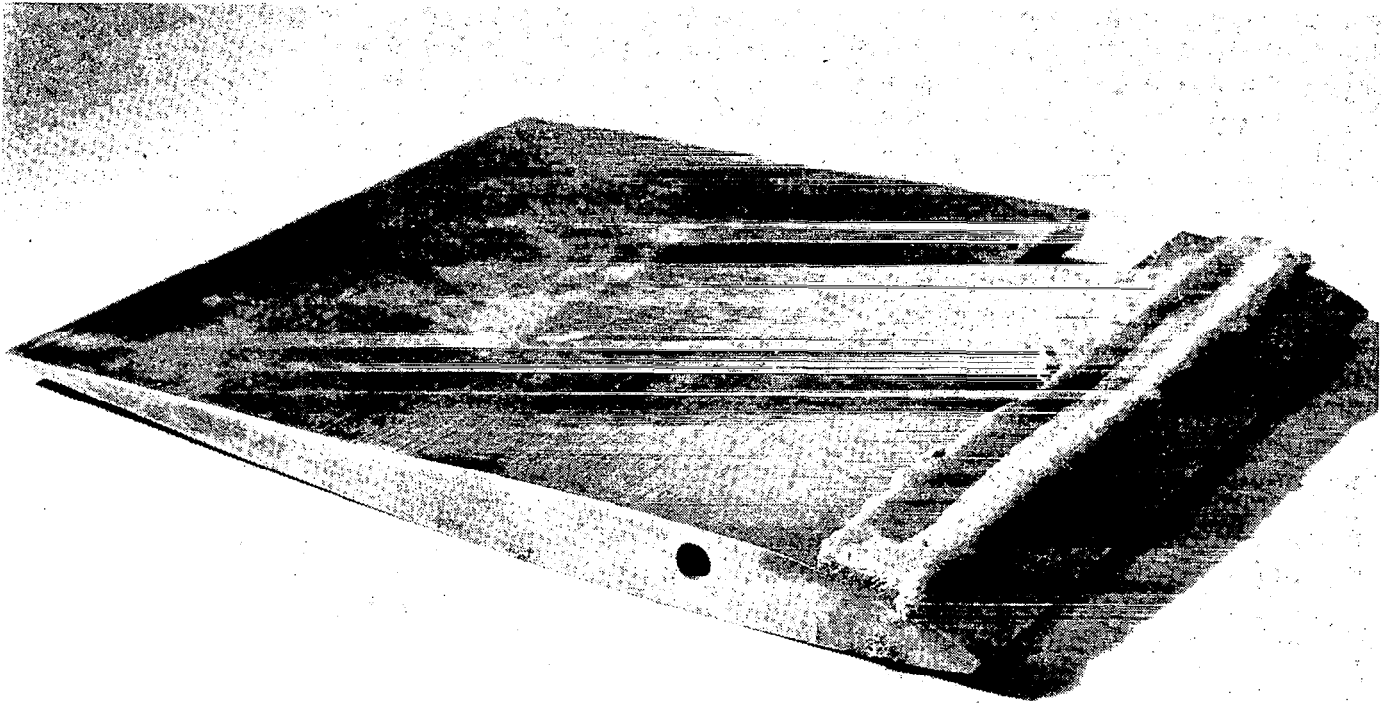


Figure 7.- Typical appearance of flame spray application.

- * Bond strength after repeated temperature cycles
- * Durability against erosion by wind-borne matter
- * "Effective Roughness" of roughness geometry, especially subsurface pits

Figure 8.- Cryogenic surface flow visualization questions to be investigated.

A COLOR VIDEO DISPLAY
TECHNIQUE FOR FLOW FIELD SURVEYS

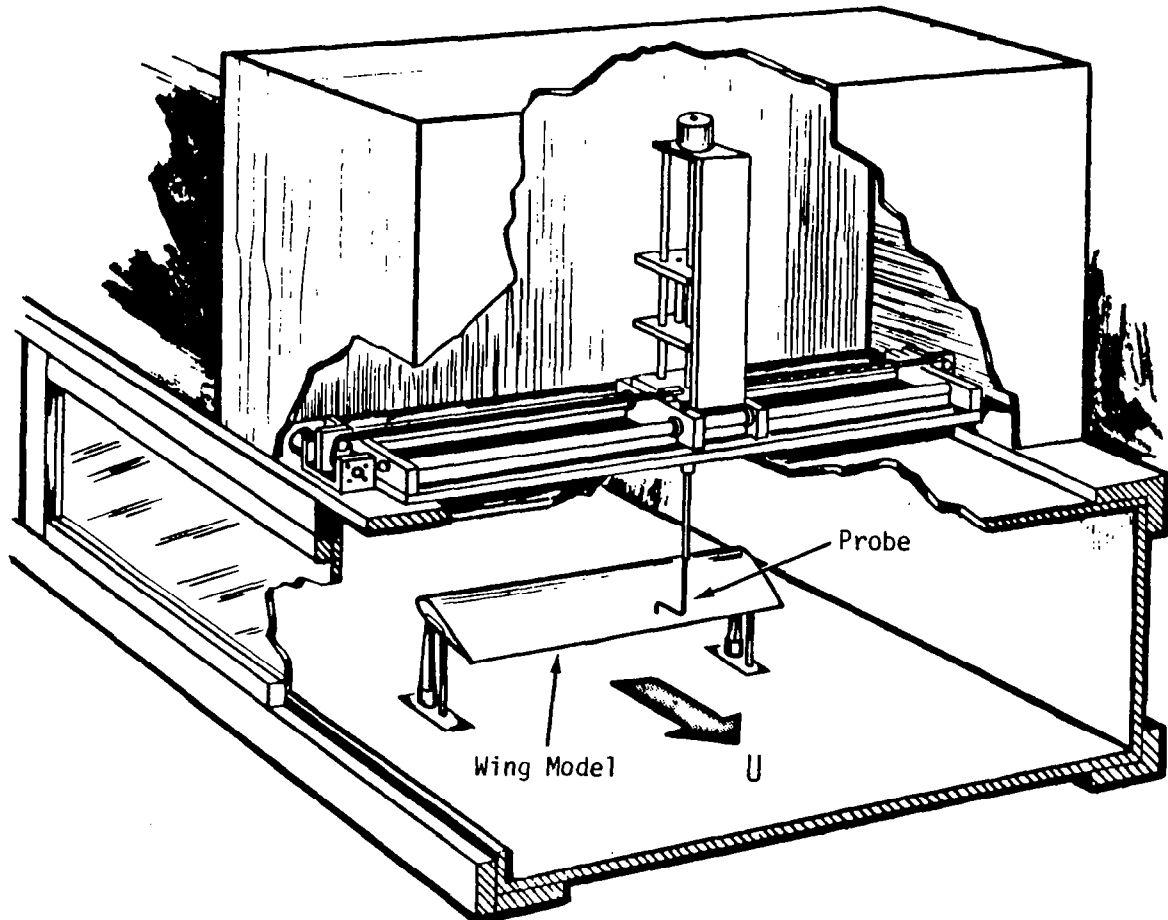
Allen E. Winkelmann
and
Chen P. Tsao

Department of Aerospace Engineering
University of Maryland
College Park, Maryland 20742

TRAVERSE DEVICE USED FOR FLOW FIELD SURVEYS
ABOVE AND BEHIND FINITE WING MODELS

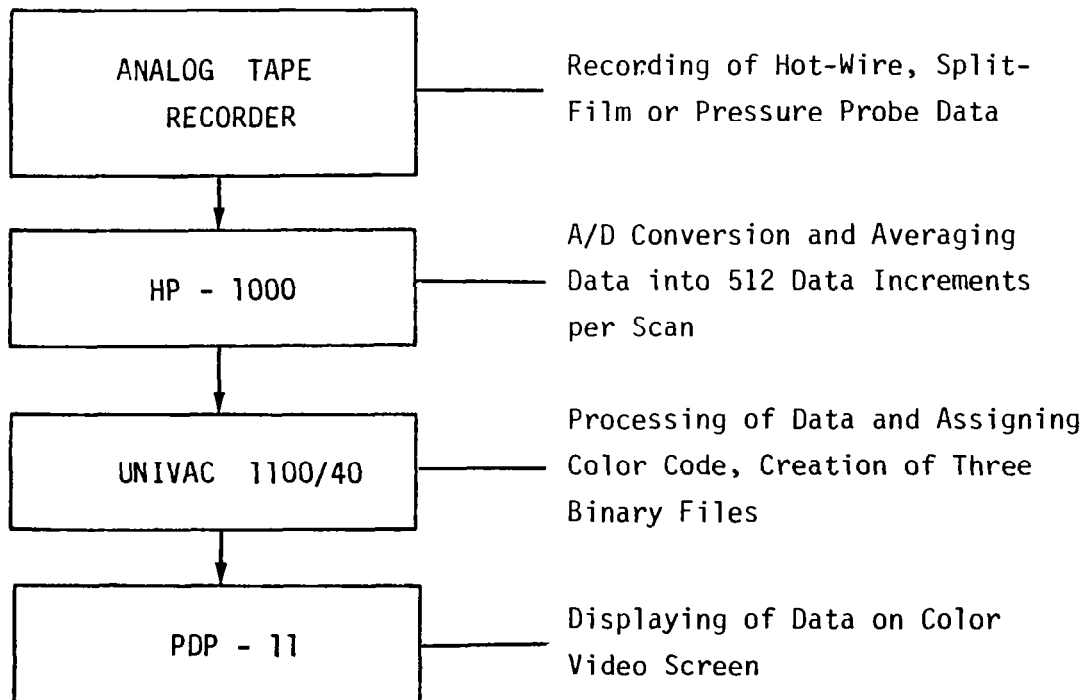
This figure shows a sketch of the traverse device used to obtain flow field survey data above and behind a wing model in the 1.17 x 0.46 m Aerospace Boundary Layer Tunnel at the University of Maryland. The wing model used in this test had an aspect ratio $AR=4.0$ with a 15.24 cm Clark Y-14 airfoil section. The traverse device allowed a probe to be scanned (spanwise) across the flow field generated by the wing. At the end of each scan, a secondary traverse unit was used to increment the probe location vertically. In addition to the hot-wire probe, surveys have also been made with a split-film probe, a Conrad (pitch) probe and a 5-tube probe. In the near future, a single channel laser velocimeter will also be used to scan the flow field generated by the wing.

The X-Y traverse device used in this study provided data in a direct analog to the video raster scan (i.e. in vertically incremented scan lines.) This simplified the computer processing since the data could be handled scan line by scan line. In some applications, such as flow field surveys in transonic or supersonic tunnels, where sting mounting systems are used, traverse devices which scan in circular arcs may be more appropriate. The data from such surveys will require additional computer processing since any given scan may cut across many different video raster lines.



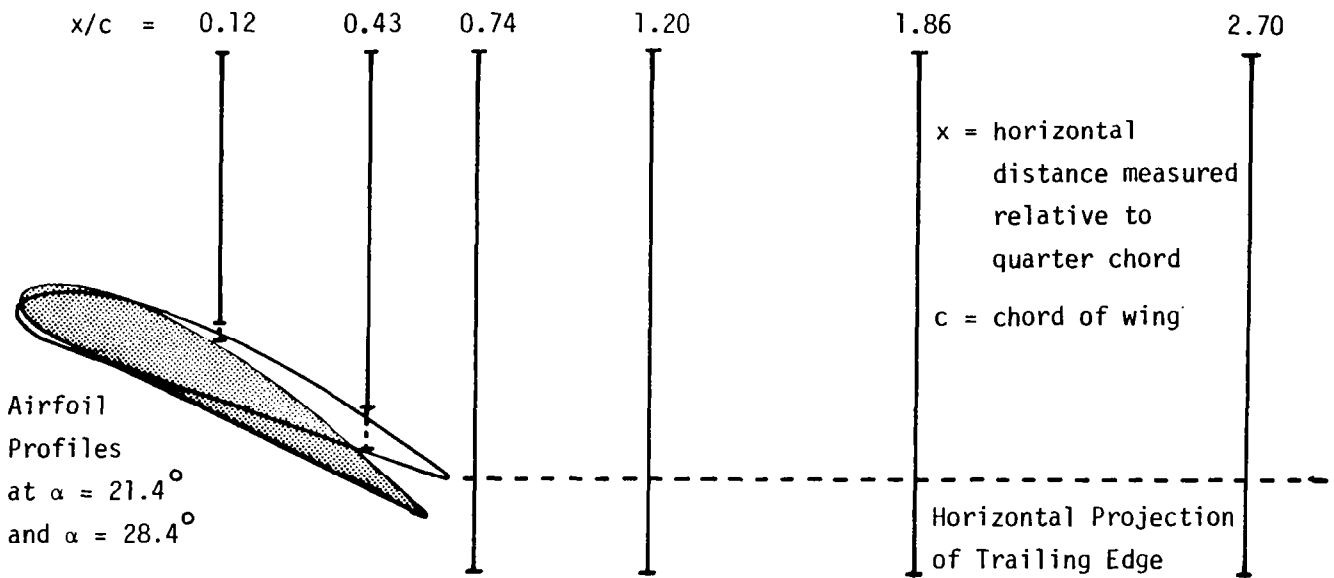
FLOW CHART OF DATA REDUCTION FOR
COLOR VIDEO DISPLAY TECHNIQUE

The data obtained in a flow field survey was initially recorded on analog tape. In addition to the spanwise location and probe transducer output, an on/off signal was recorded on one channel to identify the beginning and end of a scan. The analog tape was processed through the HP-1000 system which did the A/D conversion and averaged the 4000-7000 data points per scan into 512 spatial increments. Additional data processing (including color coding) was completed on the UNIVAC system. For qualitative data such as that obtained by the hot-wire probe, the voltage range from minimum to maximum was divided into 15 to 20 levels or windows and a color was assigned to each level. For qualitative data such as that obtained by the 5-tube probe, each data window or color corresponded to a specific range of flow direction, pressure, etc.. A PDP-11 computer system was finally used to display the data on a color monitor with 512 x 512 pixel resolution.



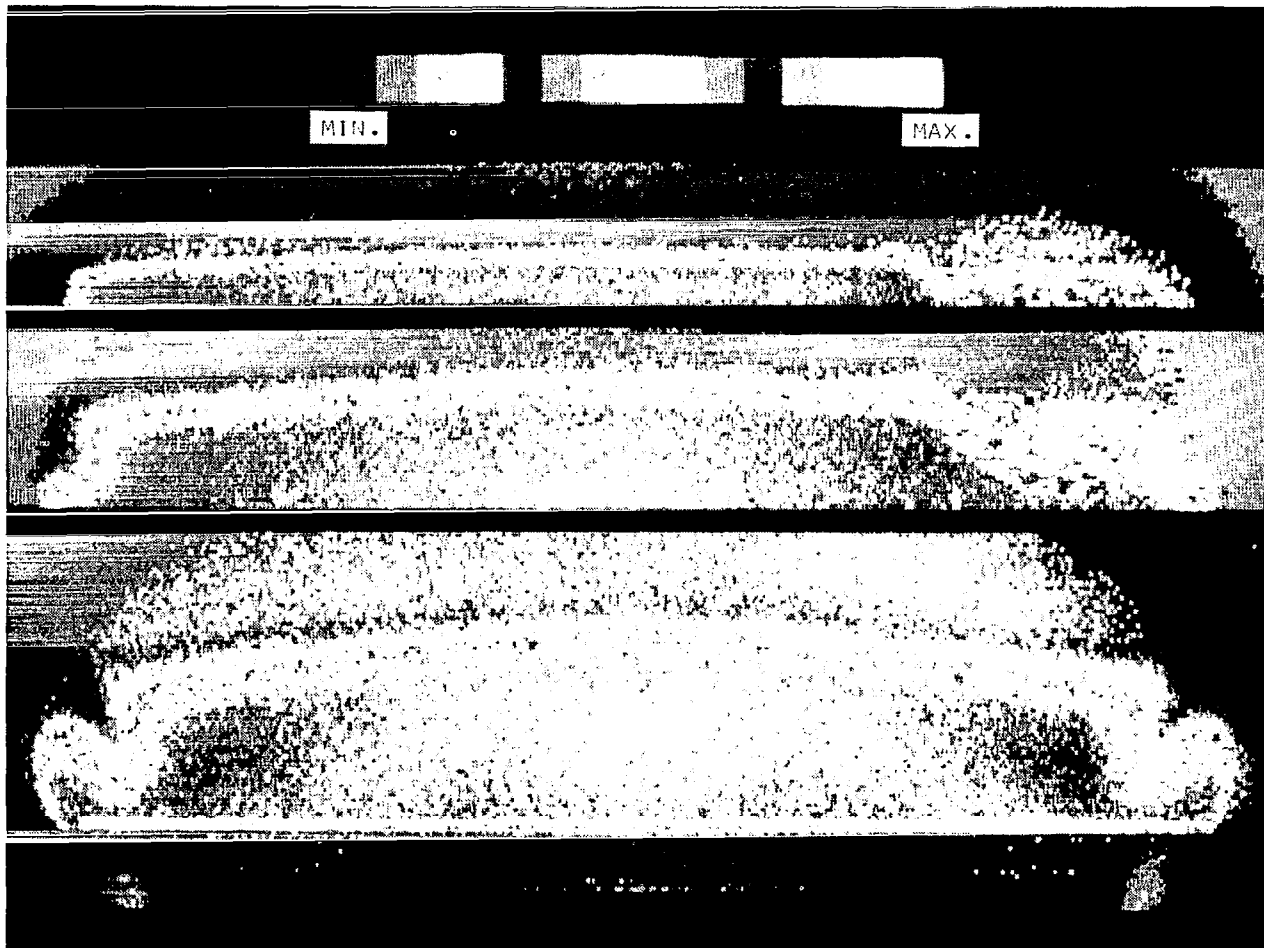
LOCATION OF SPANWISE SURVEY STATIONS ABOVE AND BEHIND WING

Flow field surveys were made at six stations above and behind the wing at two angles of attack. The wing was partially stalled at $\alpha = 21.4^\circ$ and fully stalled at $\alpha = 28.4^\circ$. Surface oil flow studies show the development of a well defined "mushroom" shaped trailing edge stall cell on the wing at $\alpha = 21.4^\circ$. For the fully stalled wing, oil flow studies indicate regions of reversed/recirculating flow over most of the upper surface.



HOT-WIRE DATA AT FIRST THREE SURVEY
STATIONS ON FULLY STALLED WING

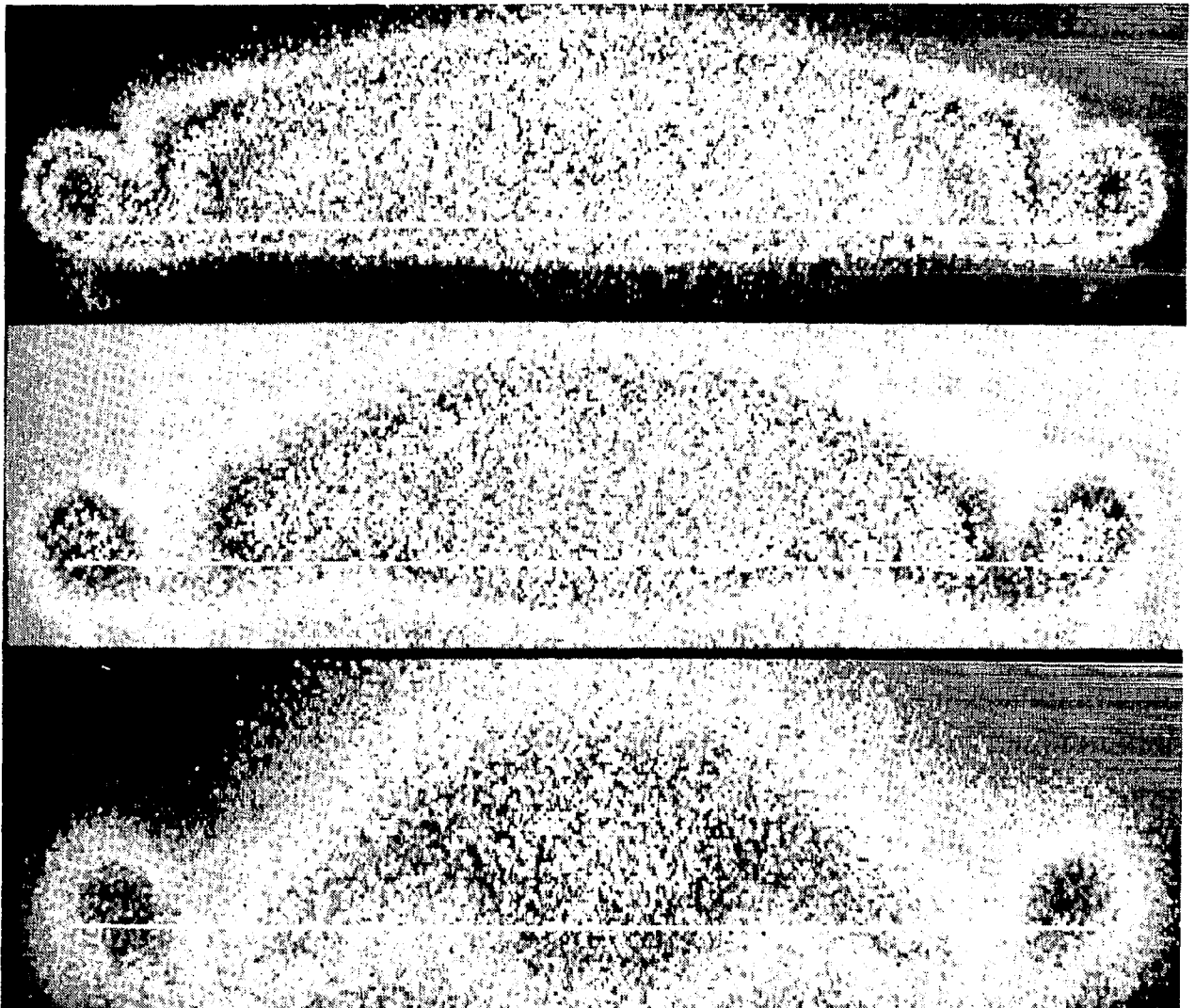
This photograph shows the hot-wire data (dc output) obtained at the first three stations on the fully stalled wing ($\alpha = 28.4^\circ$, $x/c = 0.12$, 0.43 , 0.74). The view of the data plane is from behind the wing--i.e. as if the viewer were in the diffuser. The white line in the bottom data image is the horizontal projection of the trailing edge of the wing. The separated wake region is characterized by shades of red and yellow indicating the minimum hot-wire output. This data display is highly qualitative since the hot-wire probe is sensitive to changes in flow speed and/or flow angle. The formation of a rather diffuse tip vortex can be seen in the bottom data image. Wake blockage above the separated region appears as shades of pink (maximum output). The wake flow from the mounting struts can be seen near each wing tip in the bottom data image. In some sense, this data display can be considered as a form of flow visualization.



L-82-5680

HOT-WIRE DATA AT LAST THREE STATIONS
BEHIND FULLY STALLED WING

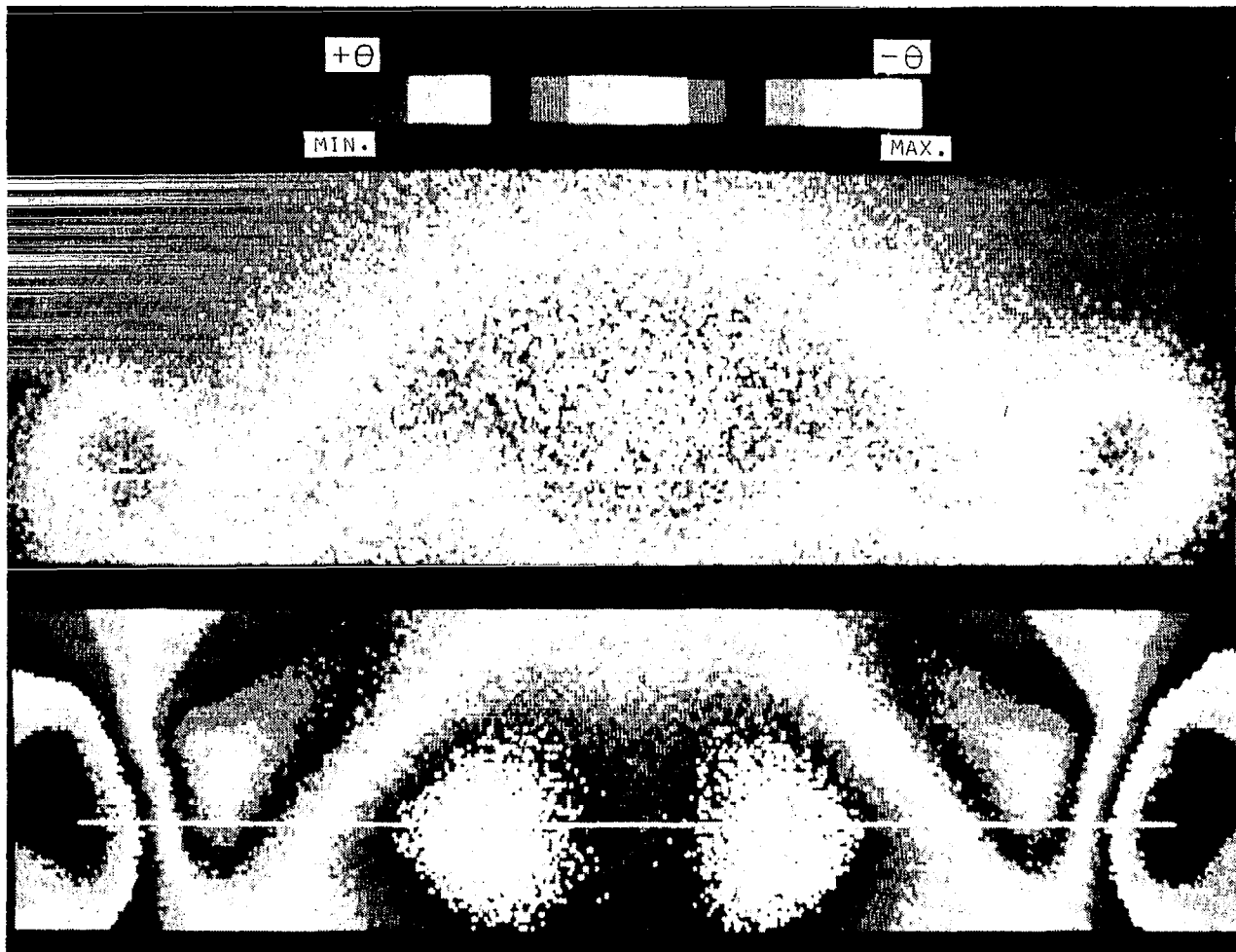
The hot-wire data at the last three stations on the fully stalled wing ($\alpha = 28.4^\circ$, $x/c = 1.20, 1.86, 2.70$) indicates the gradual dissipation of the separated wake region. The diffuse structure of the tip vortices may be an indication of a vortex "bursting" phenomenon.



L-82-5681

HOT-WIRE AND PITCH PROBE DATA AT
X/C = 2.70 BEHIND FULLY STALLED WING

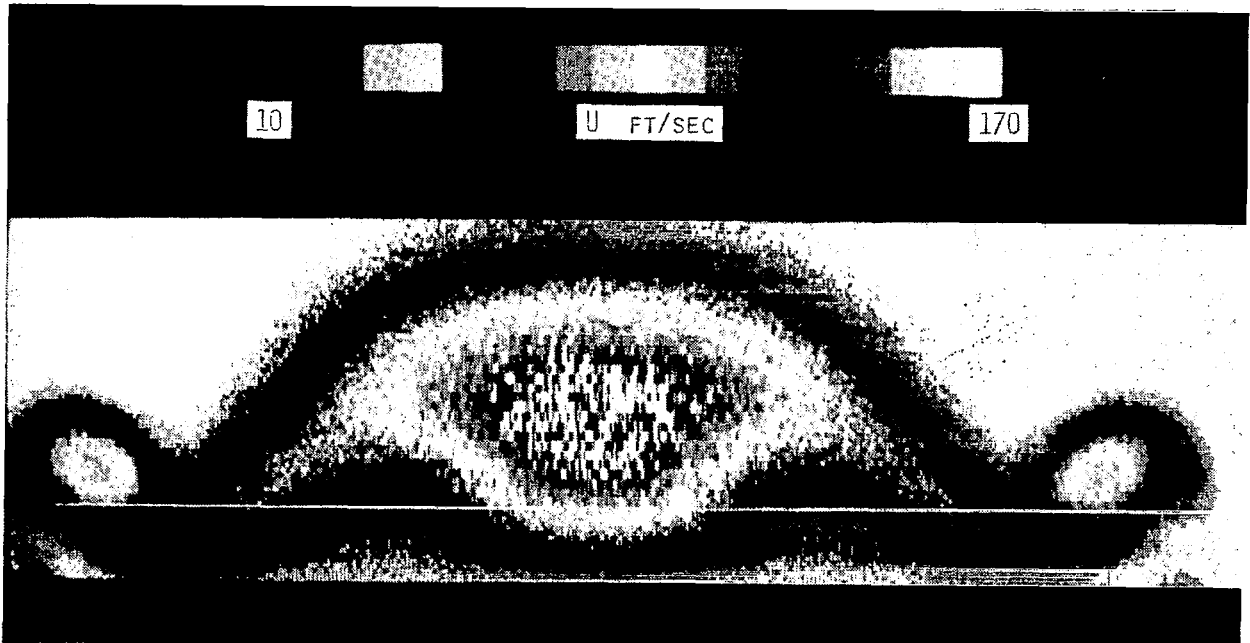
The hot-wire data and pitch probe data at the last survey station for the fully stalled wing are shown here for comparison. The tip vortex structure is very clearly shown by the pitch probe output. Shades of red and yellow outboard of the wing tips indicate a strong upward (+ θ) flow. Just inboard of the tips, shades of pink indicate a strong downward (- θ) flow. Because the pitch probe is also affected by cross flow, the data display from this probe is considered qualitative.



L-82-5682

MAGNITUDE OF VELOCITY FROM 5-TUBE SURVEY
AT $x/c = 2.70$ BEHIND FULLY STALLED WING

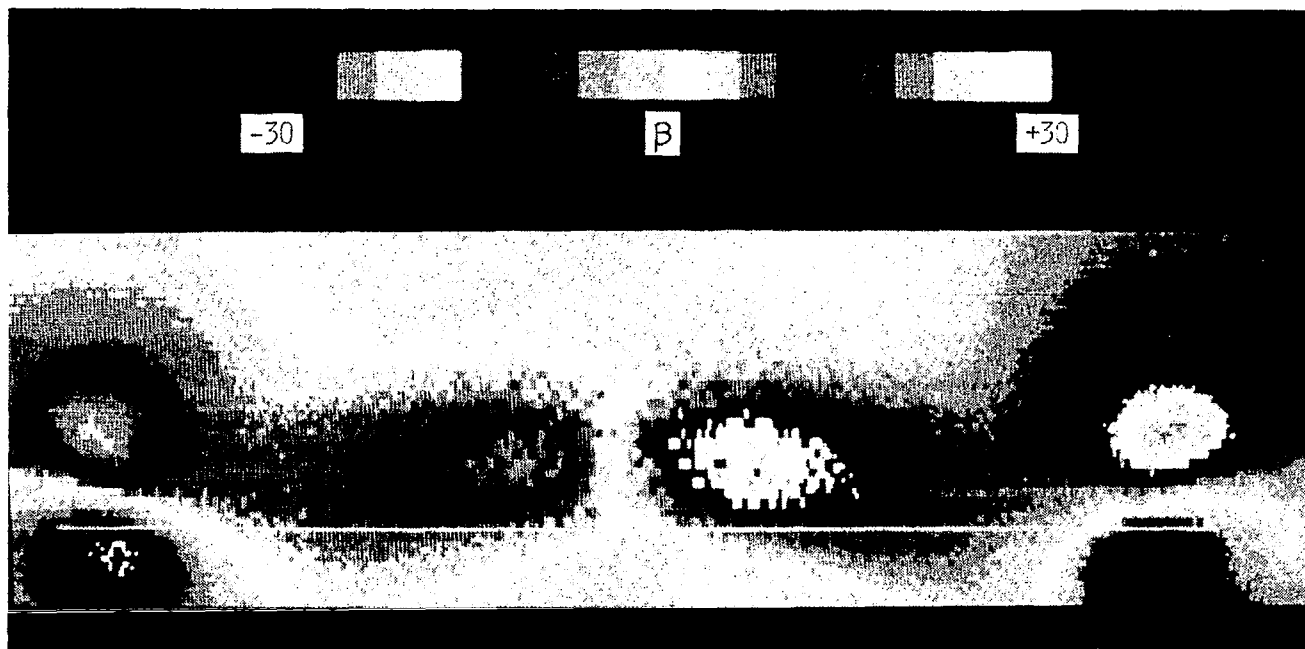
This photograph shows the magnitude of velocity obtained at the last survey station on the fully stalled wing ($\alpha = 28.4^\circ$, $x/c = 2.70$) using a scanning 5-tube probe. Each color covers a speed range of 8 ft/sec. The lowest speeds in shades of reds and yellows occur in the center of the wake region. It is interesting to note that the core of the tip vortex is relatively slow ($U \approx 90$ ft/sec). A similarity between this data display and the hot-wire data shown in the previous photograph is apparent.



L-82-5683

YAW ANGLE FROM 5-TUBE SURVEY AT X/C = 2.70
BEHIND FULLY STALLED WING

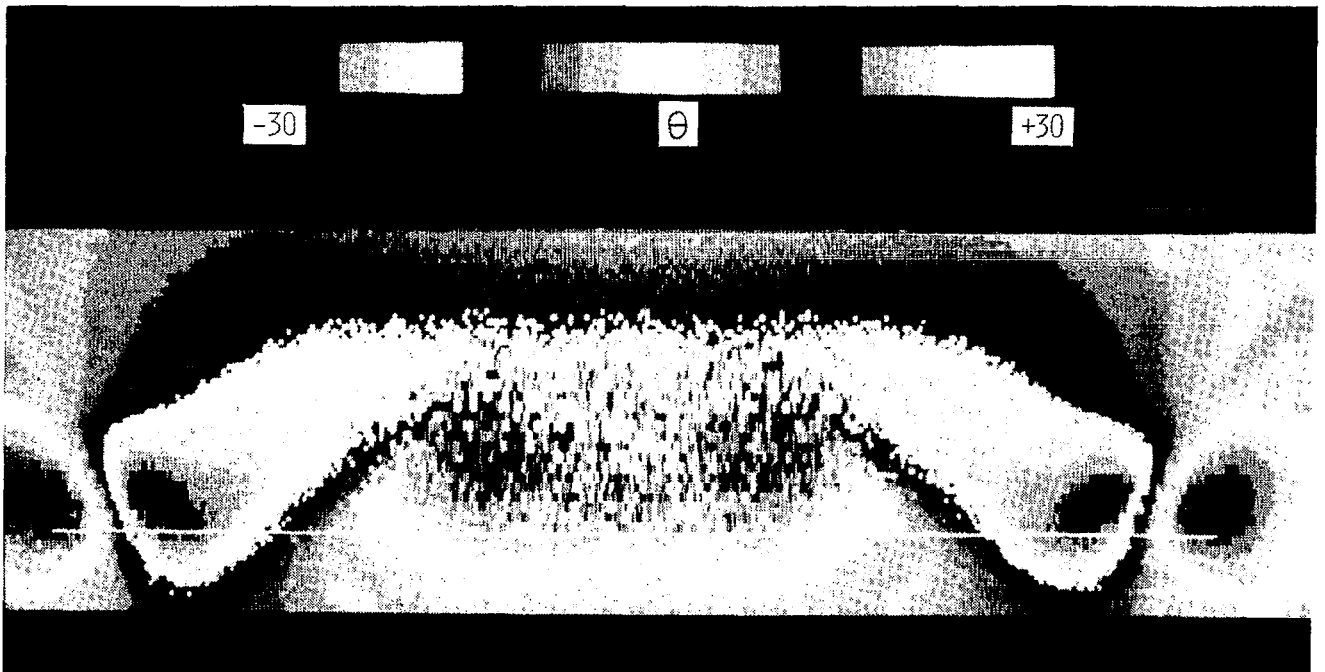
In this data display, flow to the right ($+\beta$) is indicated in shades of blues and pinks, where each shade of color is an increment of 3° . Flow to the left ($-\beta$) is in shades of greens and yellows. The inward (vortex) flow above the wing tips is clearly indicated in this display. The two regions of pink and yellow to either side of the center also indicate an inward flow.



L-82-5684

PITCH ANGLE FROM 5-TUBE SURVEY AT X/C = 2.70
BEHIND FULLY STALLED WING

This photograph looks quite similar to the pitch probe data shown on a previous page. The color code has been reversed so that shades of yellow and green indicate downward ($-\theta$) flow and shades of blue and pink indicate upward flow ($+\theta$). As before, the pitch data very clearly shows the tip vortices.

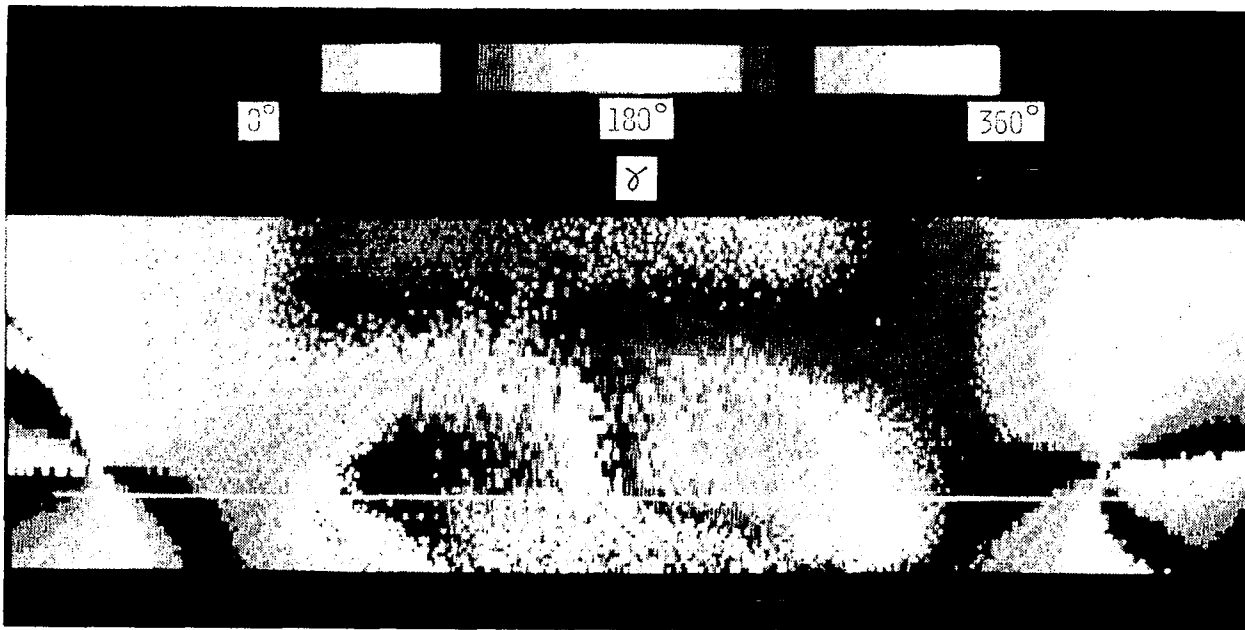


L-82-5685

CROSS-FLOW DIRECTION FROM 5-TUBE SURVEY AT
X/C = 2.70 BEHIND FULLY STALLED WING

This display shows the cross-flow direction γ at the $x/c = 2.70$ station of the fully stalled wing. Each color represents a flow angle increment of 18° . For example, any region showing the darkest shade of red is flow going off to the right side between $\gamma = 0^\circ$ (horizontally to the right) and $\gamma = 18^\circ$ (γ measured positive in the CCW direction). The border between the darkest shade of red and white is flow going horizontally to the right ($\gamma = 0^\circ$). The next lighter shade of red is for flow going to the upper right corner at flow angles γ between 18° and 36° to the horizon. In a similar manner, the subsequent colors are for flows (in 18° increments) going off in other pie shaped sectors. Obviously a circular pie sectored color chart would be appropriate here. The circular flow field generated by the tip vortices is very clearly shown in this display.

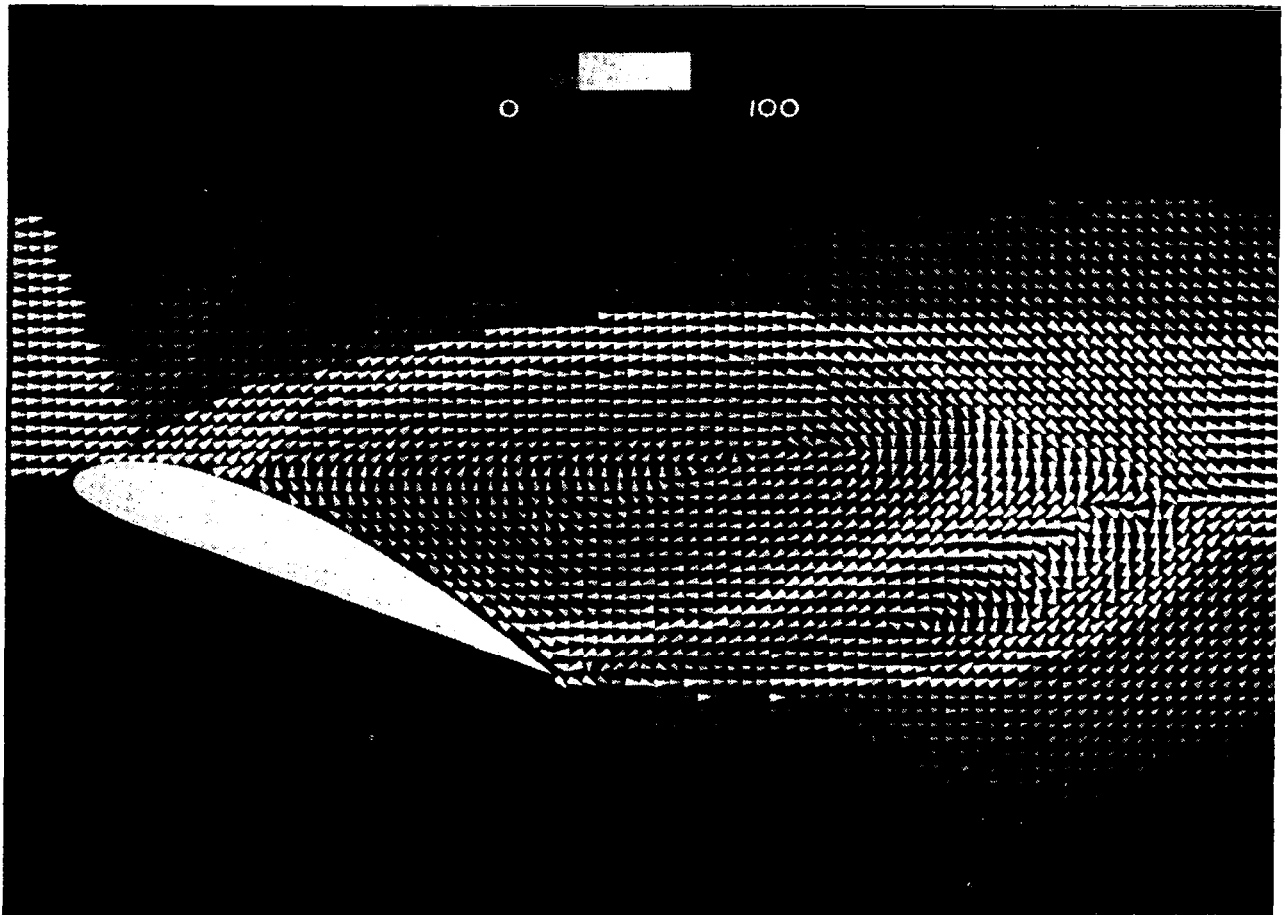
In addition to the data from the 5-tube probe shown in the above photographs, further data processing has been completed to show the total and static pressure fields. Further details of the technique presented here are given in AIAA Paper No. 82-0611.



L-82-5686

FUTURE DEVELOPMENTS FOR COLOR VIDEO
DISPLAY OF FLOW FIELD SURVEY DATA

With future advances in the resolution of computer driven color video monitors, someday a data display such as shown above may be possible. In this highly idealized artist's conception, color is used to indicate magnitude while the deltas show flow direction. Perhaps someday a wind tunnel operator will sit in the control room watching a large projection video monitor on which a view of the model has been dubbed in, and shimmering behind the model will be a real time data display being constantly updated with a rapidly scanning laser velocimeter. When the operator changes the model to a different angle of attack, the data image will gradually change to show the new flow field geometry.



L-82-5687

NEW VERSIONS OF OLD FLOW VISUALIZATION SYSTEMS

Walton L. Howes
NASA Lewis Research Center
Cleveland, Ohio 44135

Large Aperture Interferometer Using Local Reference Beam

The Mach-Zehnder interferometer is limited in size by the difficulty and cost of making large splitter plates. Alternatives still require a reference beam which circumvents the test section and is subject to differential vibrations. These problems can be overcome by means of a small, modified Mach-Zehnder interferometer placed in series with a much larger schlieren optical system spanning the test section (figs. 1 and 2). In one arm of the interferometer, light from the schlieren is focused through a pinhole and recollimating lens to produce a reference beam which interferes with the remaining object beam from the other arm. Sample interferograms from a lens schlieren and mirror schlieren are shown in figure 3. Because the object and reference beams are separated only over a small interval following the test section, differential vibrations should be greatly reduced.

Rainbow Schlieren

Color schlieren has technical, as well as aesthetic, advantages over black-and-white schlieren. Maximum advantage of color as an additional degree of freedom can be achieved by replacing the neutral filter (e.g., knife edge) with a radial-rainbow filter having a transparent center and opaque surround. Such filters are easily made photographically on color film. Since each color is associated with a specific amount of refraction, quantitative evaluation of certain refractive-index fields becomes possible using very simple equations derived from ray trace theory. Figure 4 shows a rainbow schlieren of an acetylene flame, and figure 5 shows the evaluated refractive-index distribution. Root-mean-square refractive-index fluctuations in homogeneous, isotropic turbulence have also been determined using the rainbow schlieren, since these fluctuations determine the root-mean-square refraction, which is indicated by the overall color of the image.

Further details on the local-reference-beam interferometer and rainbow schlieren are contained in two reports being processed for publication.

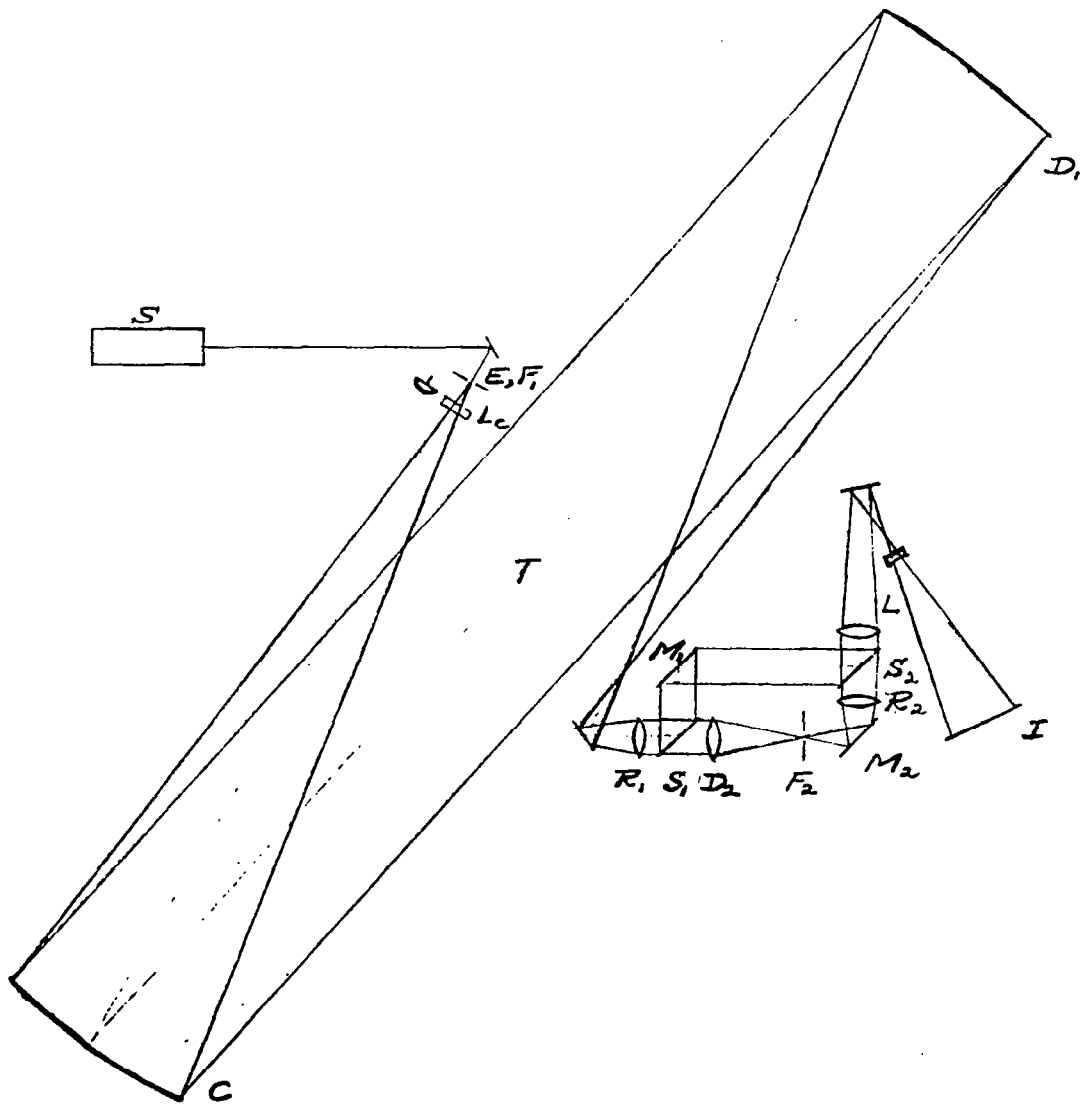


Figure 1.- Schematic of local-reference-beam interferometer coupled with schlieren optics.

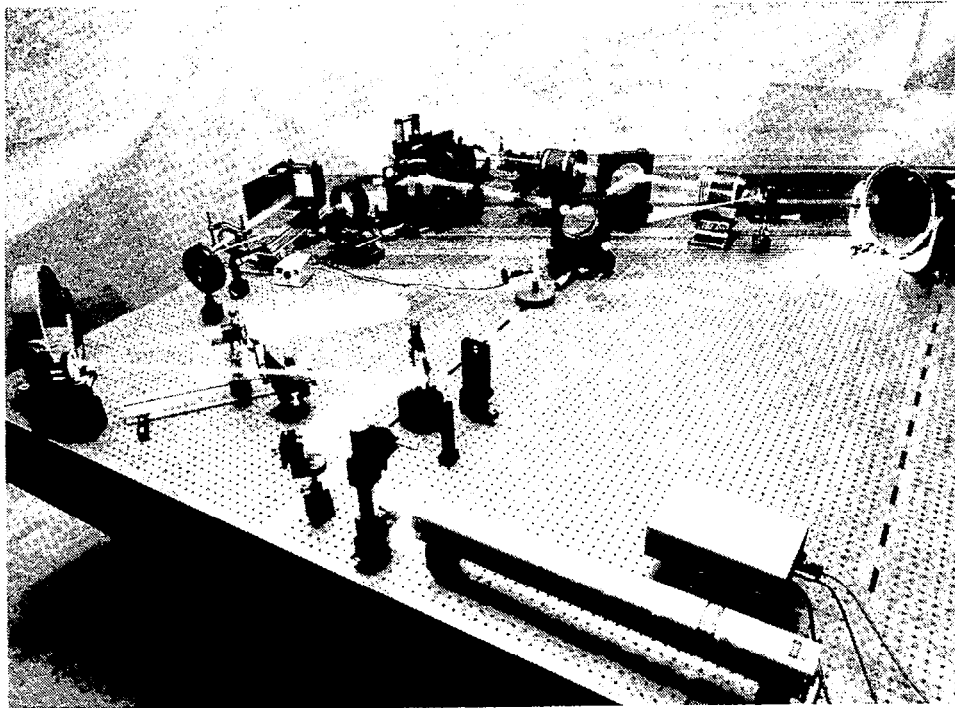
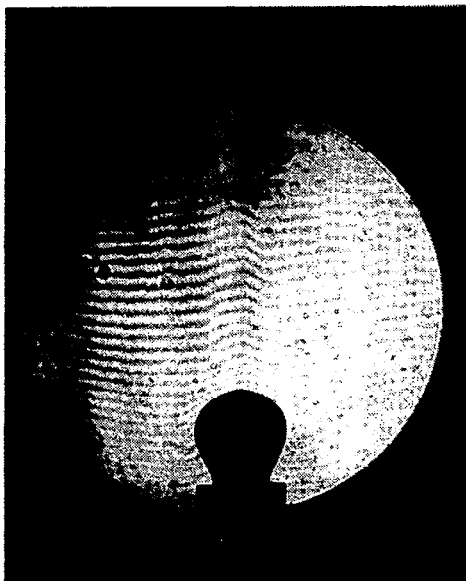
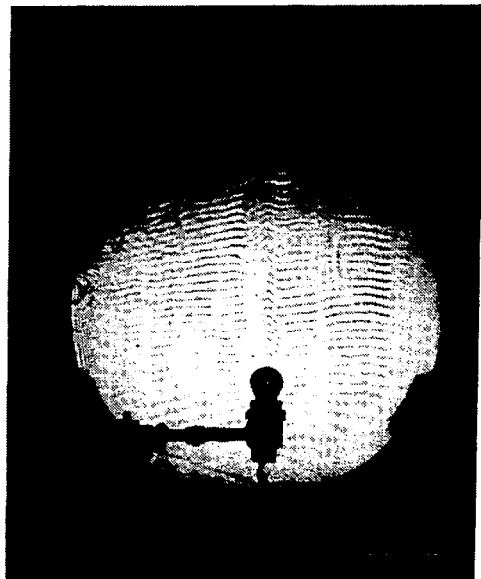


Figure 2.- Local-reference-beam interferometer coupled with mirror schlieren.

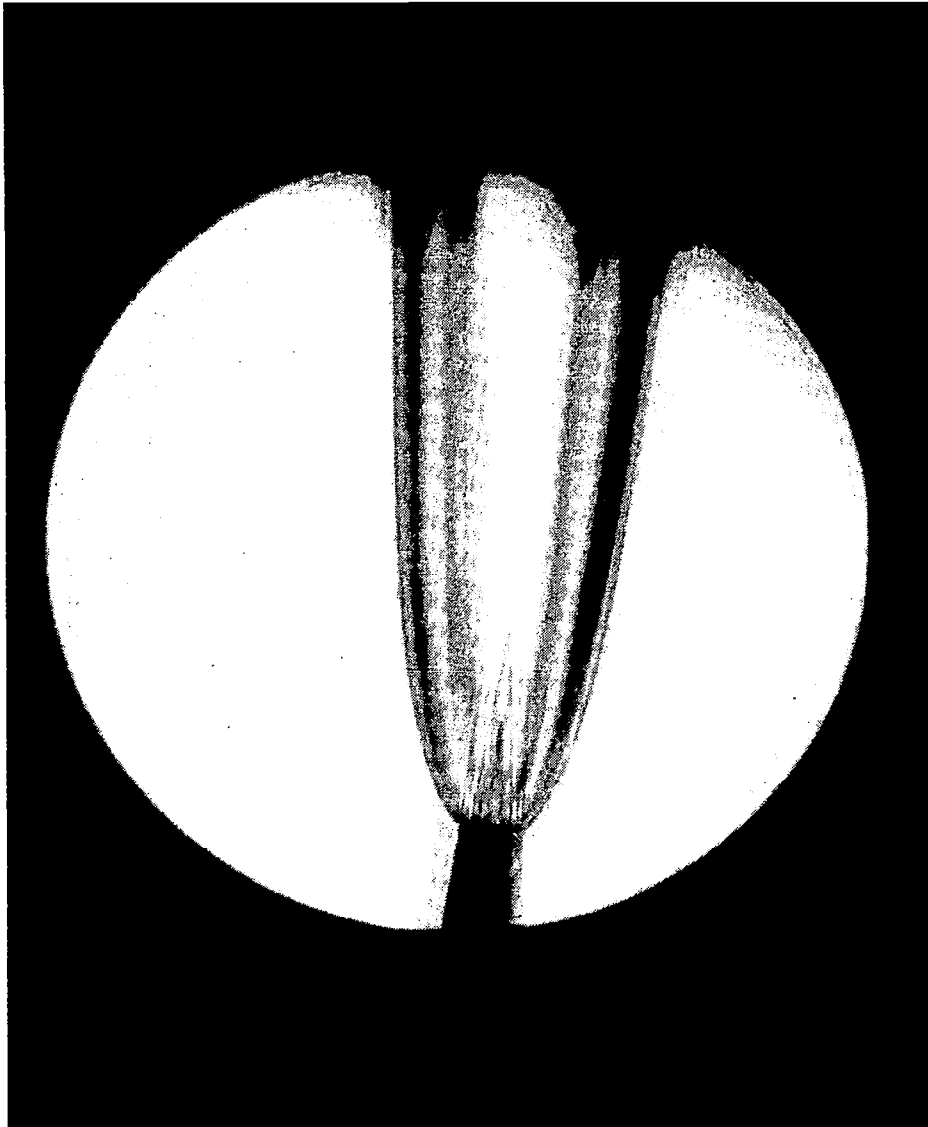


(a) 5-in. diam. lenses



(b) 12-in. diam. mirrors

Figure 3.- Interferograms obtained using local-reference-beam interferometer.



L-82-5675

Figure 4.- Rainbow schlieren of acetylene flame.

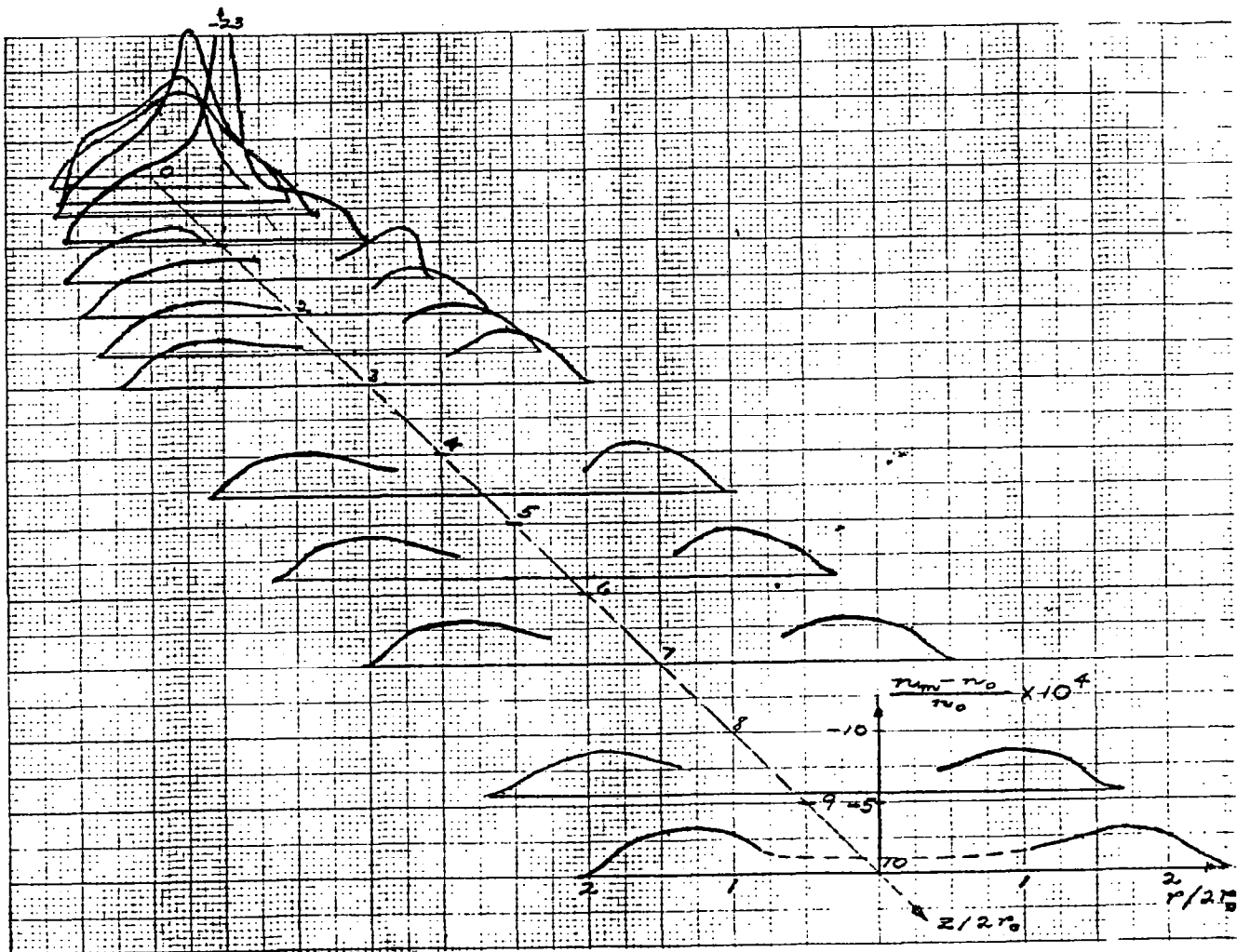


Figure 5.- Relative-refractive-index change $(n_m - n_0)/n_0$ above acetylene flame as determined using rainbow schlieren. Z , height; r_0 , nozzle radius.

OPERATIONAL FLOW VISUALIZATION TECHNIQUES
IN THE LANGLEY UNITARY PLAN WIND TUNNEL

William A. Corlett
NASA Langley Research Center
Hampton, Virginia

INTRODUCTION

The purpose of this paper is not to illustrate the latest innovations in flow visualization techniques, but to show what the Unitary Plan Wind Tunnel (UPWT) uses in daily operation. This paper is presented more from the viewpoint of a user than a pioneer. Although improvements have been made in several of the old techniques used in Unitary, there are still shortcomings. We are currently developing new ideas for improving the quality of established flow visualization methods and are pursuing cooperative programs on promising new flow visualization techniques.

The Unitary Plan Wind Tunnel is Langley's only supersonic facility. It is a highly productive facility and is normally referred to as a production facility, although the majority of our tests are inhouse basic research investigations. The facility has two 4 ft. by 4 ft. test sections which span a Mach range from 1.5 to 4.6. The cost of operation is about \$10 per minute (3rd shift power rate). Therefore, one of the problems is the time often required for a flow visualization test setup and the cost of an extensive investigation. Another is the ability to obtain consistently repeatable results; this is essential for qualitative analysis.

Following are examples of sublimation, vapor screen, oil flow, mini-tufts, schlieren, and shadowgraphs taken in UPWT. These results are from typical research investigations. All tests in UPWT employ one or more of these flow visualization techniques.

SUBLIMATION

Sublimation is used in the Unitary Plan Wind Tunnel as a flow visualization technique. This technique is based on areas of higher skin friction sublimating faster and is used to locate the laminar to turbulent transition region.

The procedure requires painting the model a flat black and then uniformly coating with a white sublimation chemical. In the tunnel, fluorine in a petroleum ether solvent is sprayed on the model.

An example at Mach 1.5 in the UPWT is shown below. As time progresses, the fluorine sublimates from the rear of the model toward the transition region. At the point where the fluorine sublimation rate becomes a minimum, a pattern of coated area is formed and the location of transition region is indicated. Figures (a) and (b), for example, show the same pattern after 3 minutes of elapsed time. The transition region is the juncture of the coated and clear portion of the model. (An area of high skin friction along the leading edge will also cause rapid sublimation.)

The problems encountered with this technique are the ability to apply the required uniform coating and the wind-tunnel time required to obtain the results.

$$M=1.5; RN/FT=2 \times 10^6; T_0=150^\circ F.$$



(a) $t=11$ minutes



(b) $t = 14$ minutes

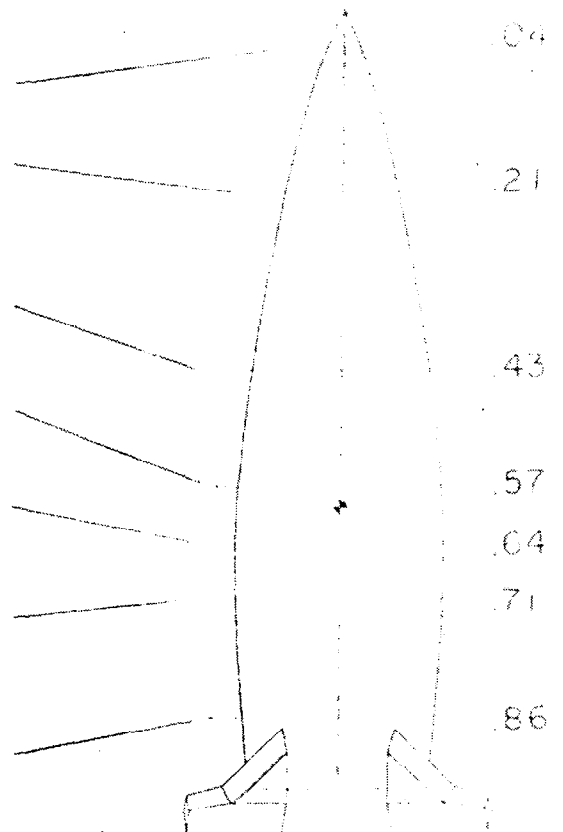
VAPOR SCREEN

The vapor screen method of flow visualization utilizes an intense sheet of light to illuminate water particles which have been induced into the air flow. A variation in particle density caused by a strong disturbance such as a shock or a vortex varies the intensity of the scattered light in the vapor screen resulting in a two-dimensional illustration of the flow field.

In an effort to obtain consistently high quality photographs, several light sources varying from a 1000 watt Hg arc lamp to a large 5 watt laser have been used in the UPWT. A 1 watt fanned argon laser source produces an excellent light screen. However, getting consistently good photographs with either the laser or Hg arc lamp is still a problem. The figure below represents several longitudinal stations using two 1000 watt Hg arc lamps. Photographs were taken with a Hassalblad 500 EL/M camera mounted inside the tunnel directly behind the model. Kodak ASA 400 tri-x pan film was used with an exposure time of 1/4 sec at f/2.8.

Currently, experiments using smoke instead of water vapor are being evaluated. A chloride flare produces a favorable smoke screen which is anticipated to have a lesser effect on flow properties than wet air (water added downstream of test section to raise dew point to approximately +20°F for vapor screen).

$$M = 2.50; \alpha = 16.2^\circ$$



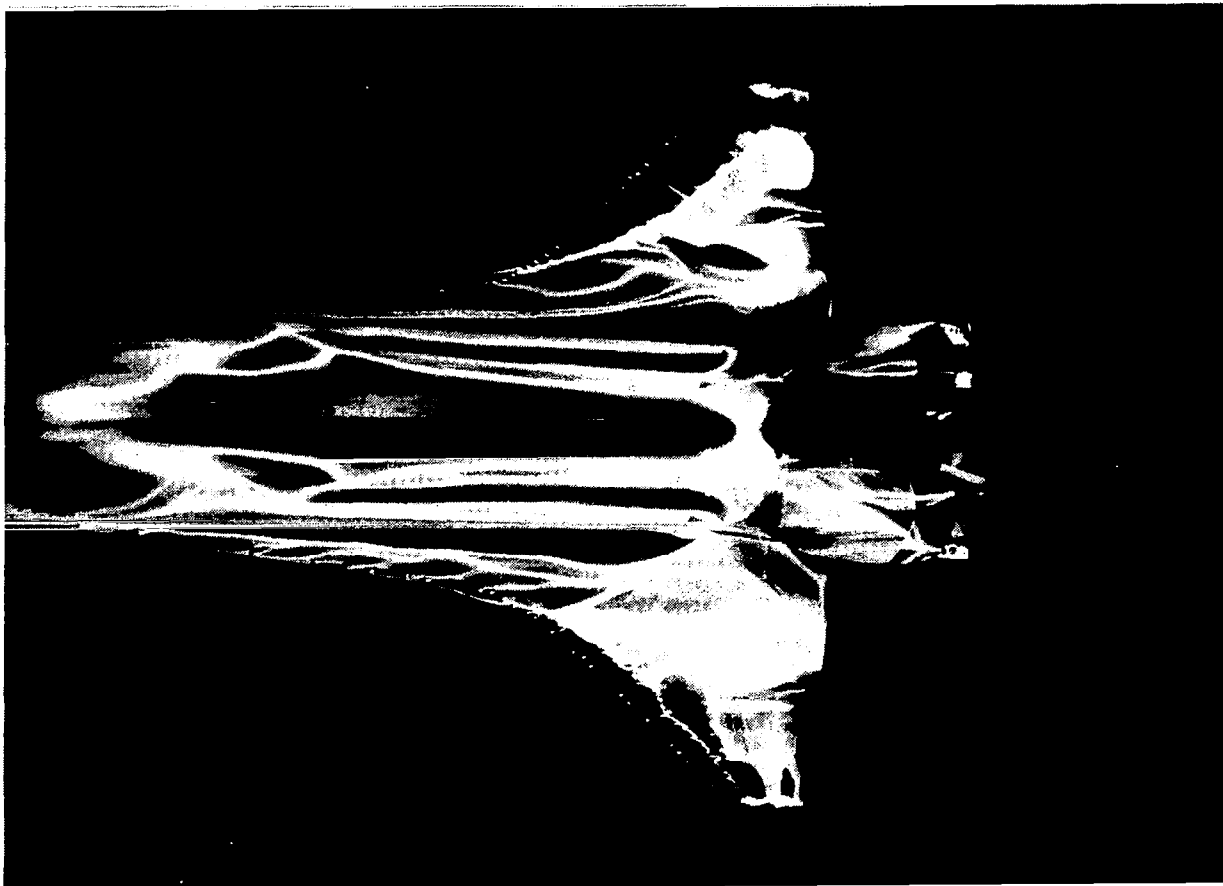
OIL FLOW

This visualization technique utilizes a fluorescent oil illuminated with ultraviolet light to show surface flow patterns.

The procedure uses a mixture of heavy oil and "fluorescent green" (3 tablespoons per pint of No. 600 w. oil). The model is painted a flat black, then a uniform coating of the fluorescent oil is brushed over the complete model. The heavy oil is required in order to maintain a uniform coating on the model during the supersonic start and required time to establish desired flow conditions. Once on point, 10 to 15 minutes are required to develop the flow pattern. Normally only two test conditions can be photographed before the model requires recoating. A technique to continuously supply a light weight fluorescent oil from the model leading edge during the tests is desired. This, however, adds to the model cost.

The photograph below shows the surface flow pattern on the shuttle configuration with aft reaction control jets firing. Compare separation regions on the left wing (jet on) with the right wing (jet off).

$$M = 2.5; \alpha = 20^\circ$$



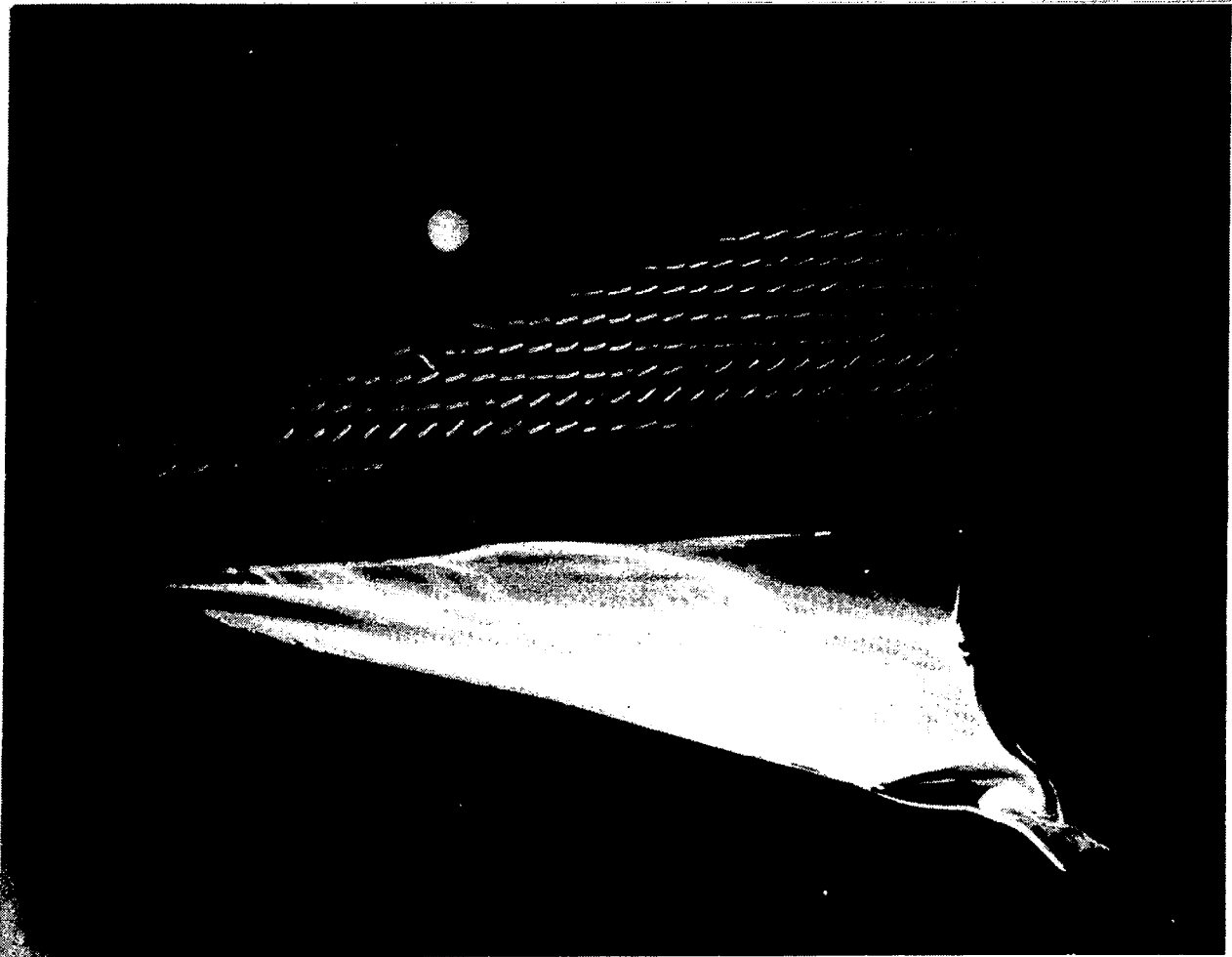
MINI-TUFTS

The mini-tuft flow visualization technique employs a grid of very fine monofilament tufts illuminated with ultraviolet light.

The procedure requires painting the model a flat black and attaching the desired grid of tufts. The tufts are 0.003 inch diameter nylon monofilament. The length is varied from 0.3 to 1 inch. Due to their very small size, there is no apparent tuft interference on the surface flow field. Tests have indicated that the mini-tufts have a negligible effect on model aerodynamic performance characteristics. There is also no delay in establishing the flow pattern.

The same camera and ultraviolet lamps are used for both the oil flow visualization technique and the mini-tufts. Therefore, both techniques can be readily employed at the same time as indicated in the figure below. Shown is an advanced supersonic transport model at Mach 2.7 and an angle of attack of 10° . Flow direction and instability are more apparent with the mini-tufts; however, the oil flow technique gives more distinct patterns.

AST 205 MODEL; $M = 2.7$; $\alpha = 10^\circ$



SCHLIEREN

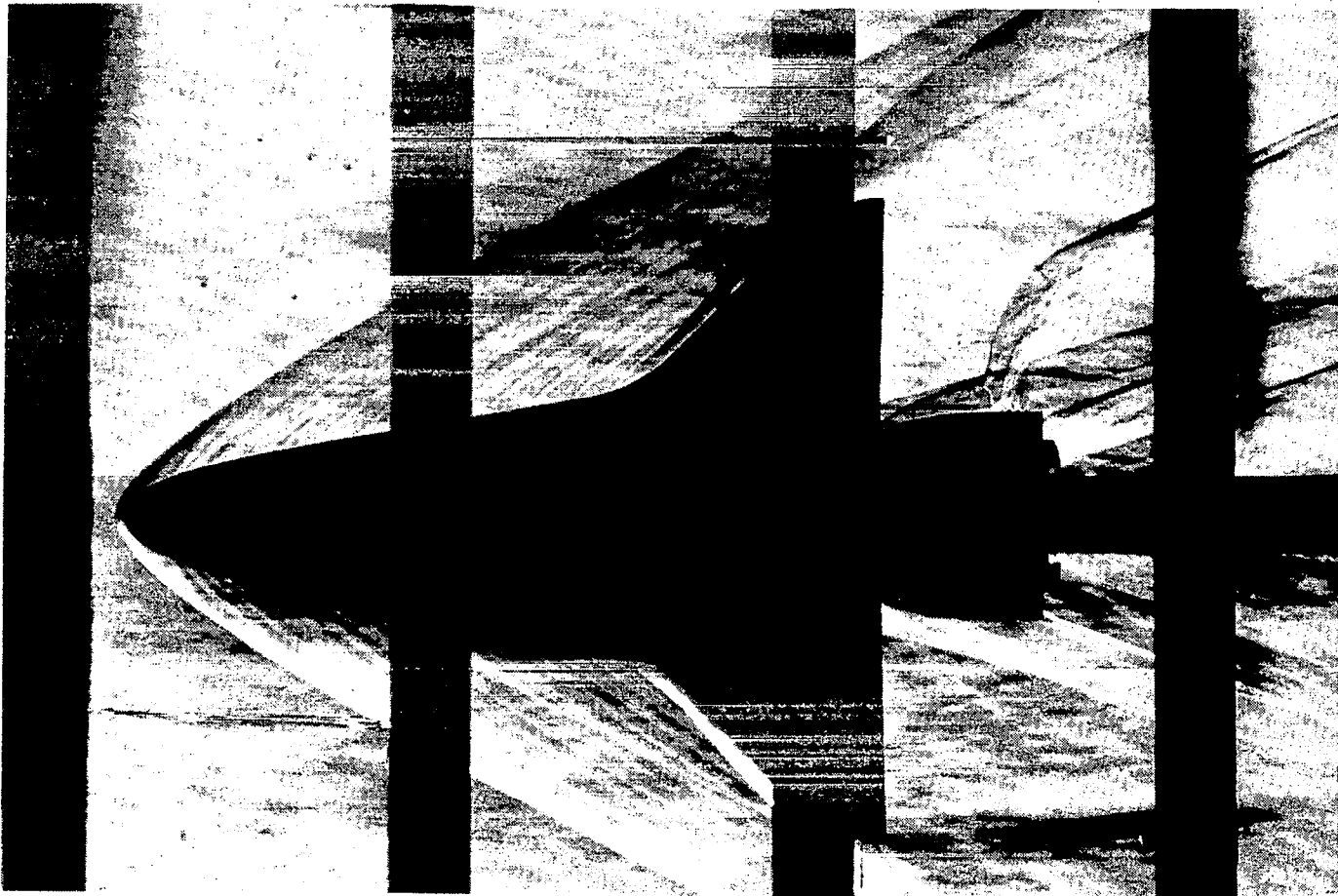
Schlieren is a flow visualization method based on the refraction of light while passing through a varying air density. Collimated rays of light are bent while passing obliquely through a density gradient.

Each test section in the Unitary Plan Wind Tunnel is equipped with a schlieren system having a 49-inch field of view. The system uses a silvered knife edge at the focal point to provide simultaneous viewing and recording of the image. The schlieren image is photographed with a 9-inch by 9-inch still camera or the image may be recorded on video tape. This system has the same problem that all optic systems have in that continuous focusing and aligning is required to obtain consistently good results. Vibration transmitted to the system also cannot be tolerated.

The schlieren system in UPWT is used to monitor all tests from establishing supersonic flow to dropping flow. (The only exception being tests that require installing steel doors.)

The photograph below is of the shuttle model showing the influence of the reaction control jets. (Shuttle control surfaces removed to show jet plume.)

$$M = 2.5 \quad \alpha = 20^\circ \quad W_j/W_\infty = 0.0071$$

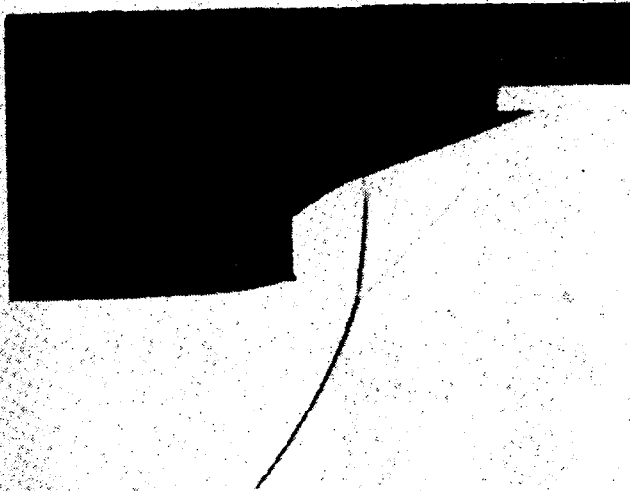


SHADOWGRAPH

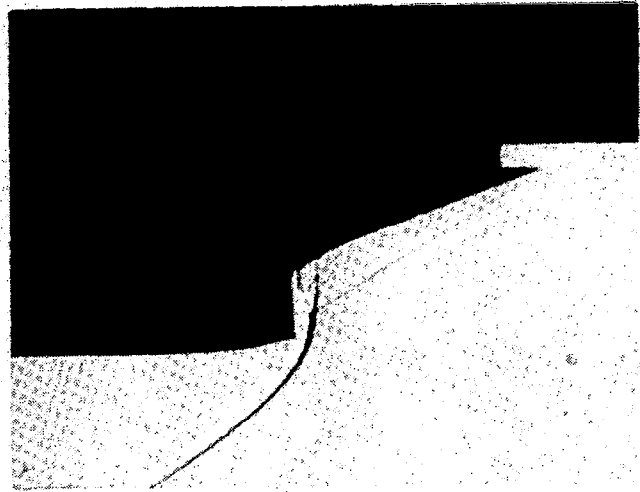
A shadowgraph shows steep pressure gradients in the air flow. The shadowgraph differs from a schlieren in that the schlieren depends on the first derivative of the refraction index while the shadowgraph depends on the second derivative.

Normally in a shadowgraph, only the shock waves and the model silhouette are visible. The most common use of the shadowgraph at UPWT is in monitoring model inlet flow conditions.

The photographs below show the variation of inlet shock location with change in Mach number. At Mach 1.6 the inlet appears completely choked with little air flow passing through the inlet.



(a) $M = 1.6$



(b) $M = 2.5$

CONCLUSIONS

The Langley Unitary Plan Wind Tunnel currently relies on the more conventional flow visualization techniques that are very familiar to test personnel. Some problems are apparent such as the time required for test setup and the cost when 10 to 15 minutes are required per data point. However, good quality results are obtained and one or more of these techniques are used for all investigations in the Unitary wind tunnel.

A continuous effort to improve the quality of established flow visualization methods and the development of new ideas is maintained.

PROPELLER FLOW VISUALIZATION TECHNIQUES

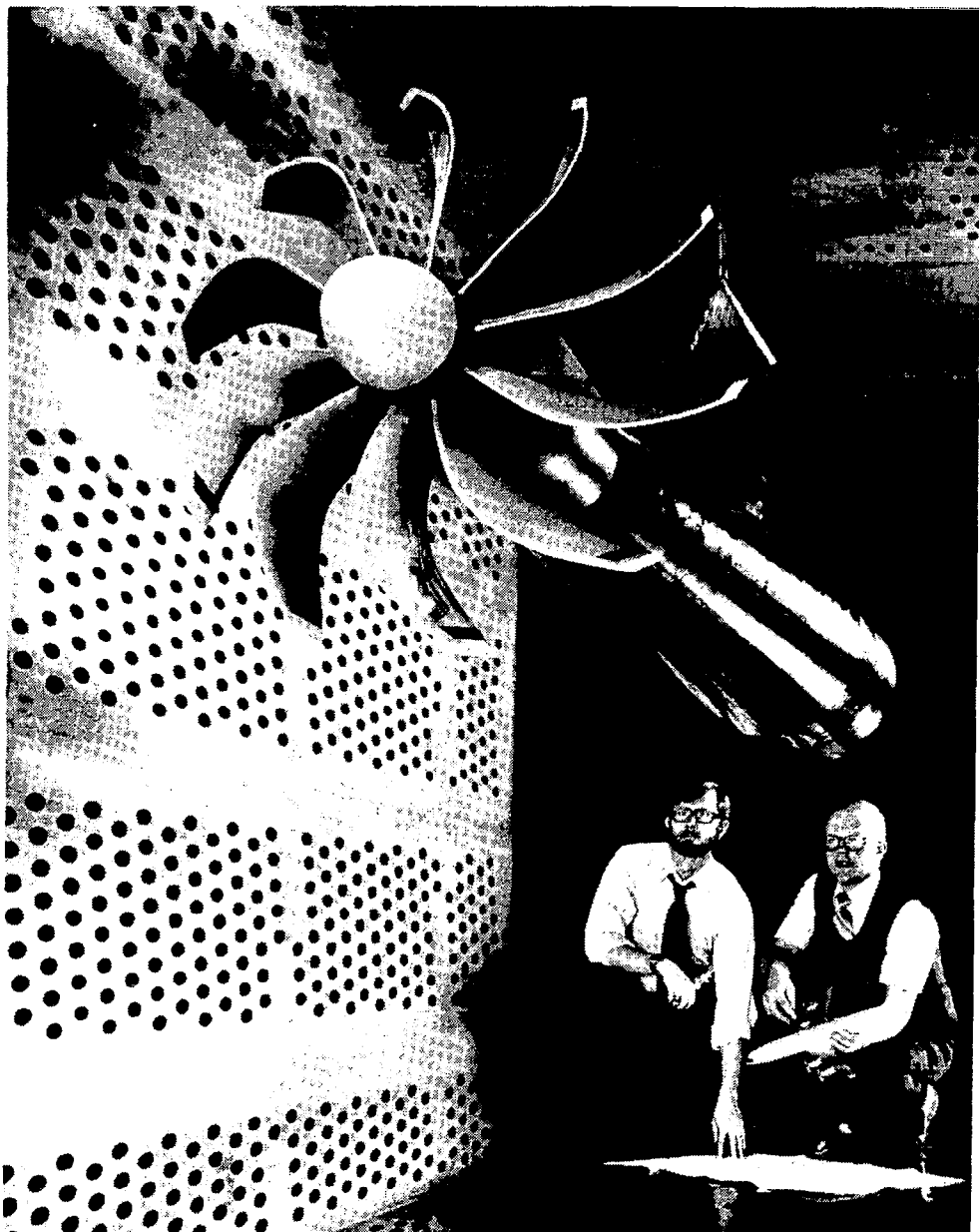
George L. Stefko, F. J. Paulovich, J. P. Greissing and E. D. Walker

NASA Lewis Research Center

Cleveland, Ohio

ADVANCED PROPELLER IN LEWIS 8 × 6 WIND TUNNEL

Advanced propeller designs for future fuel-efficient high-subsonic speed aircraft are being investigated in the Lewis 8 × 6 wind tunnel to determine their performance, noise, and aeroelastic characteristics. These advanced propeller designs have thin, highly swept blade shapes which can experience large structural deflections under the operating loads of high-speed flight. These blade deflections may significantly alter the propeller operating characteristics. To investigate this important area, new propeller stroboscopic measurement techniques have been developed. With these techniques, the flutter motion and blade deflected shape of a rotating propeller can be determined. In addition, tuft, oil, and paint flow visualization of the local blade flow field can be accomplished.



PROPELLER FLOW VISUALIZATION

Two propeller stroboscopic measurement systems were developed to perform propeller flow visualization work on advanced propellers in the Lewis wind tunnels. One propeller measurement system used a video photographic system while the other used a 35-mm photographic system.

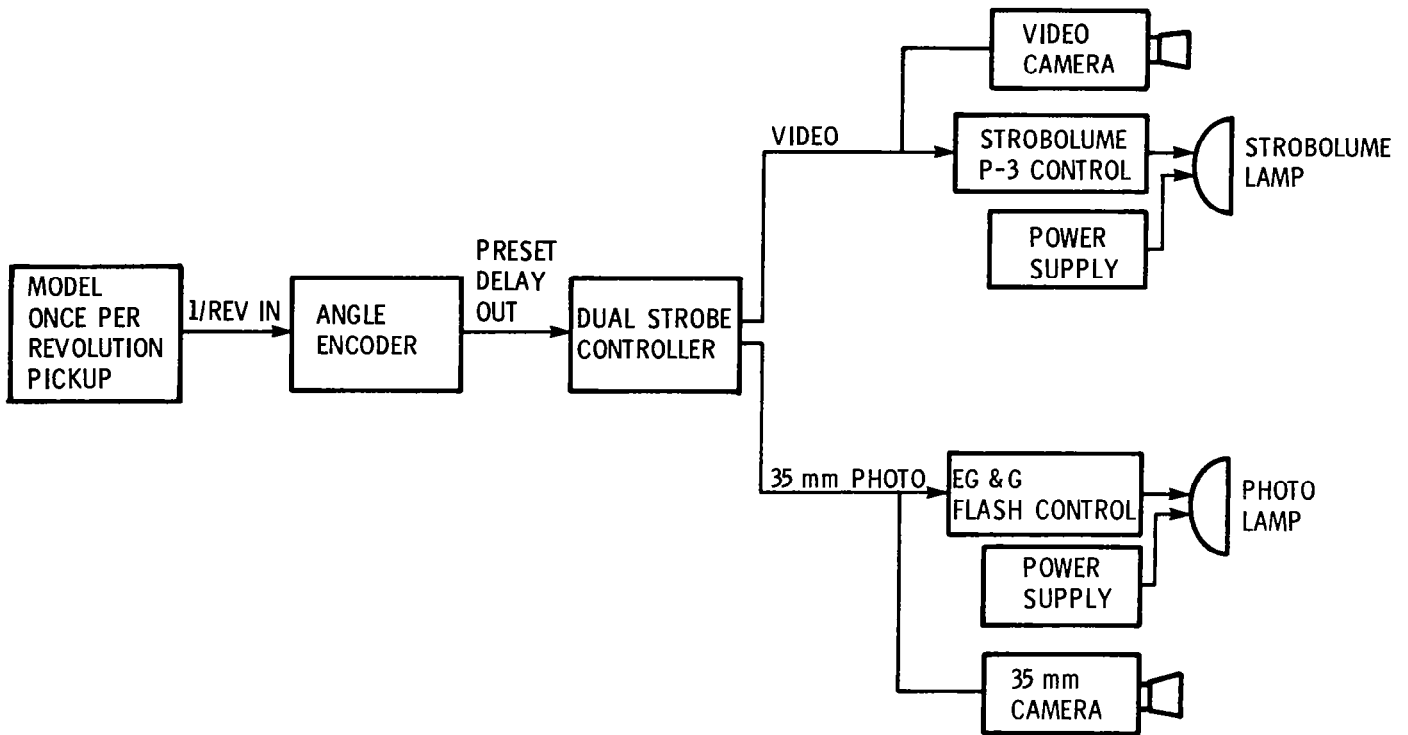
The video stroboscopic photographic system was used to record: (1) propeller flutter blade motions, (2) blade-to-blade differences in blade tip motion, and (3) the on-line television pictures to position the propeller for the 35-mm photographs.

The 35-mm stroboscopic photographic system was used to record: (1) propeller blade tip deflections under steady centrifugal and aerodynamic loads, (2) tuft patterns on the rotating propeller blade, and (3) surface flow patterns on the propeller blades including a new "paint flow" technique.

- EQUIPMENT
- FLUTTER MOTION
- BLADE TIP DEFLECTION
- TUFTS
- PAINT FLOW

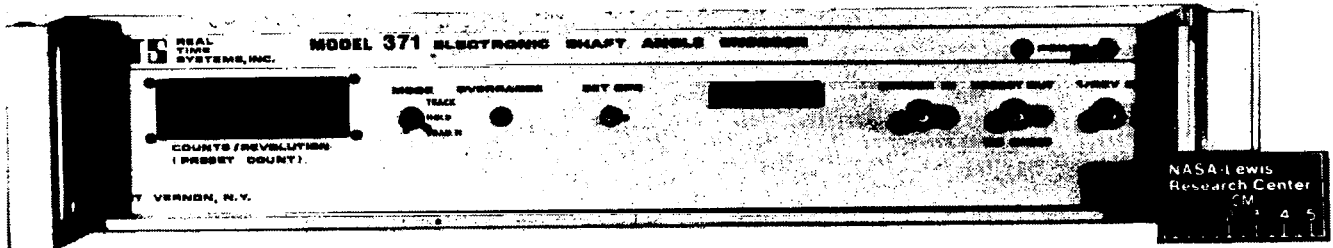
ELECTRONIC CONTROL DIAGRAM

This diagram illustrates the major pieces of equipment in the two photographic systems developed to take pictures of propellers in the wind tunnel at rotation speeds up to 10 000 revolutions per minute (RPM). The propeller's once-per-revolution signal is delayed by an Angle Encoder so that the propeller blades can be viewed in any desired angular position. The modified once-per-revolution signal is then sent to the Dual Strobe controller which allows one to take video or 35-mm pictures.

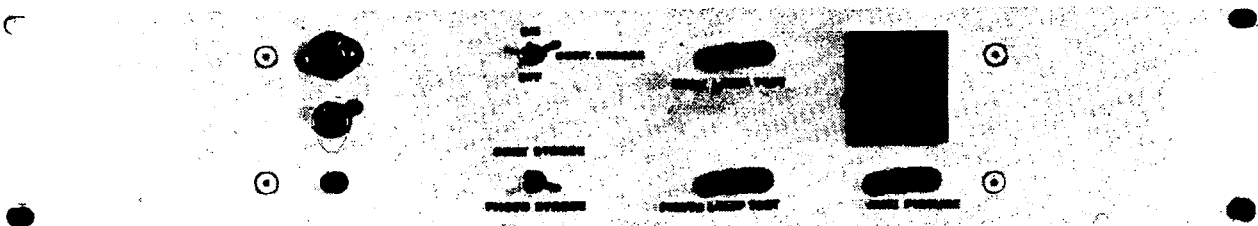


ELECTRONIC CONTROLLERS

The Angle Encoder controller and the Dual Strobe controller are shown in this figure. The Angle Encoder allowed the propeller blades to be positioned in any desired rotational position within 0.01° . The Dual Strobe controller allowed the pictures to be taken remotely from the wind tunnel control room.



ANGLE ENCODER CONTROLLER

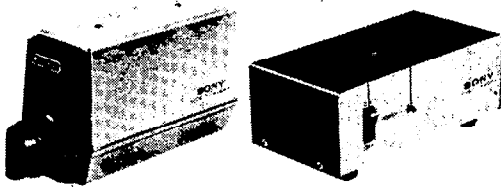


DUAL STROBE CONTROLLER

VIDEO PHOTOGRAPHIC SYSTEM

The video stroboscopic photographic system consisted of a Sony video camera (AVC-1400), a General Radio stroboscope (Strobolume 1540), a Sony videocassette recorder (Betamax SL-5400) and a television. Pictures of the hardware are shown in the figure.

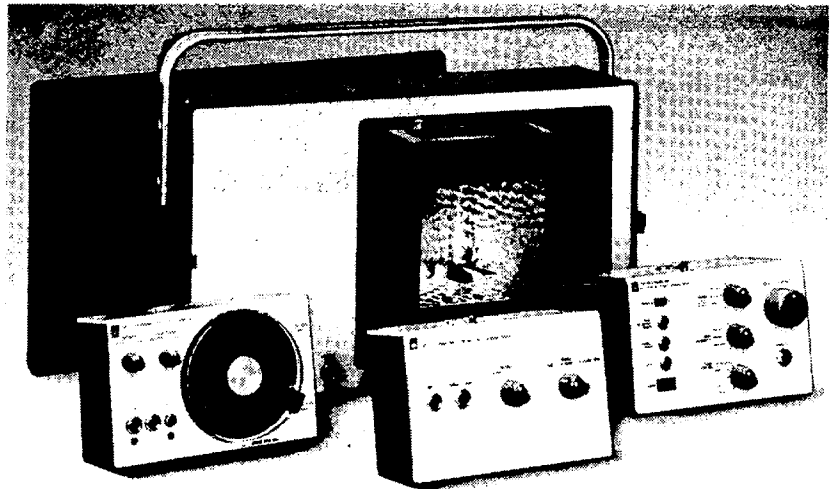
The camera was positioned 5 ft from the propeller centerline while the flash head was positioned 3 ft from the propeller centerline. The videocassette recorder and television monitor were located in the wind tunnel control room.



SONY VIDEO CAMERA



SONY VIDEO RECORDER

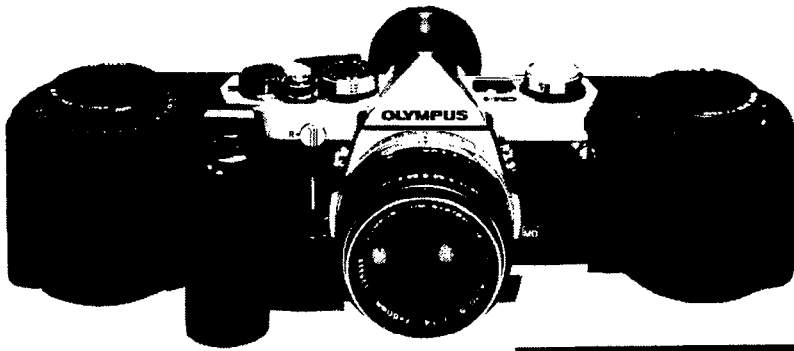


GR VIDEO STROBOSCOPE

35-mm PHOTOGRAPHIC SYSTEM

The 35-mm stroboscopic photographic system consisted of an Olympus 35-mm camera (OM-1) and an EG&G stroboscope (549 microflash). Pictures of this hardware are shown in this figure.

The best combination of camera variables were as follows: (1) an 85-mm lens, (2) an f-stop of 4.0, (3) an ASA 400 film processed at the equivalent speed of ASA 1200 film, (4) a 1 μ sec (1×10^{-6} sec) stroboscope flash duration, (5) a stroboscope flash head positioned 3 ft from the propeller centerline, and (6) a camera positioned 5 ft from the propeller centerline.



OLYMPUS CAMERA



EG & G STROBOSCOPE

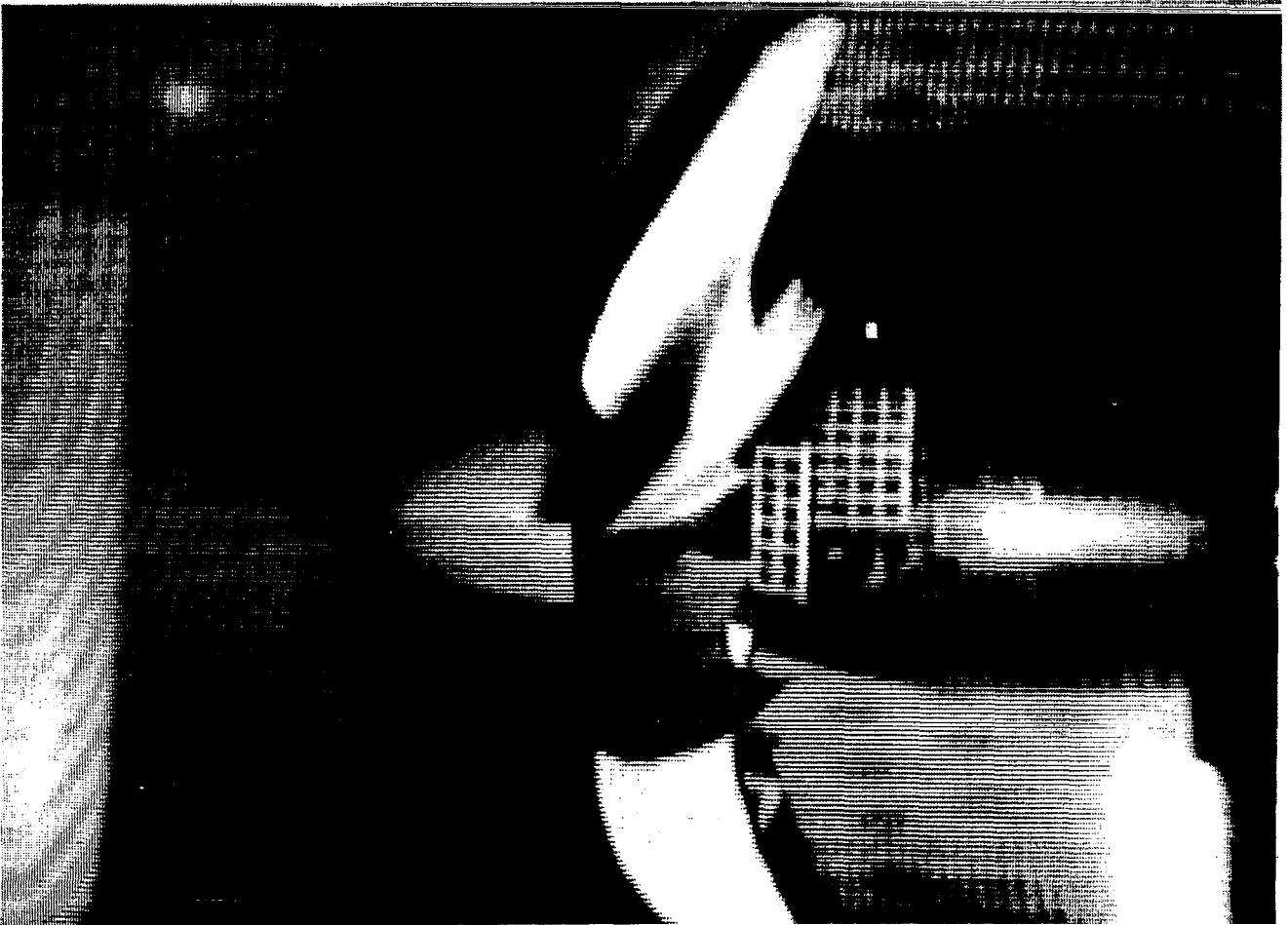
FLUTTER MOTION OF THE SR-5 PROPELLER

This figure shows the blade flutter that occurred with the SR-5 propeller model (i.e., 24 in. diameter) in the Lewis 8 × 6 wind tunnel. The video system recorded each blade in flutter so that the blade to blade variations in the vibration amplitude could be assessed. Also, the video recordings allowed the approximate shape of the blade motion to be assessed.

These video recordings were very useful in understanding the nature of the flutter instability. It was determined that the flutter was a coupled bending-torsion type of flutter and that the following factors were significant in causing the flutter: (1) high blade sweep, (2) cascade effect, and (3) compressibility. With this knowledge, analytical methods were developed to predict the flutter.

$M_0 = 0.70$

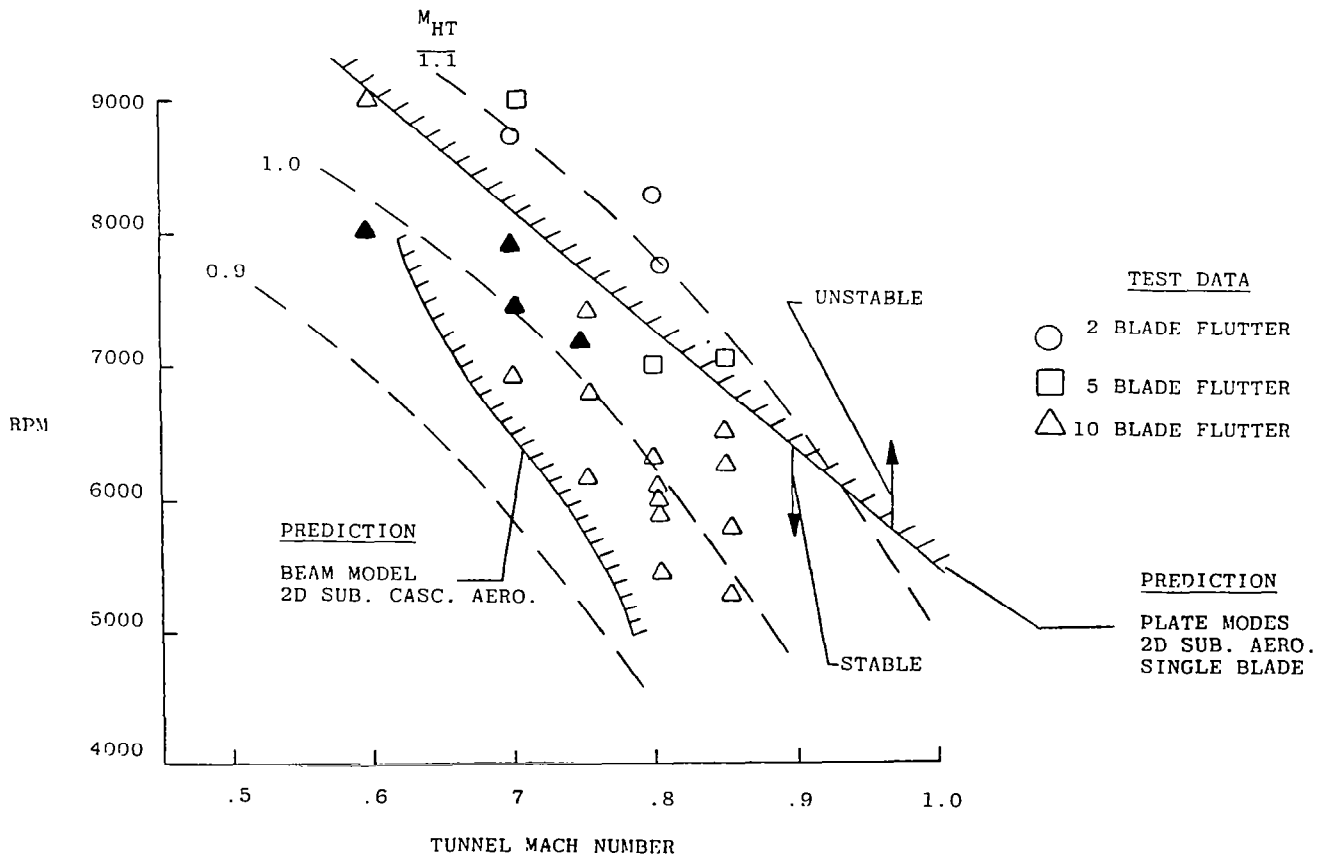
rpm = 7400



SR-5 CLASSICAL FLUTTER SUMMARY

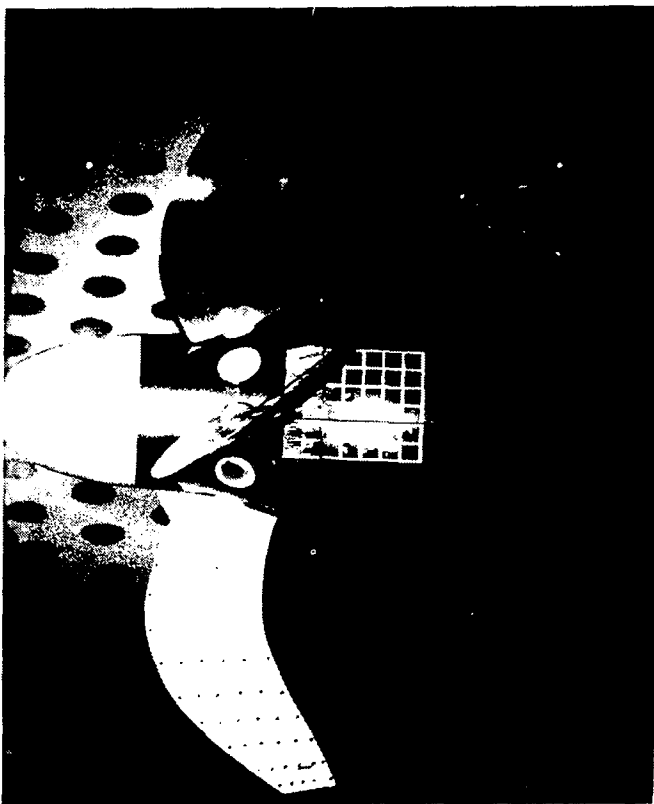
The conditions where three SR-5 propeller configurations were in the coupled bending-torsion flutter are plotted in terms of the propeller RPM, tunnel Mach number, and number of blades on the propeller. The number of blades on the SR-5 propeller hub was varied from two to five to ten blades to determine the blade cascade effect on the flutter. The larger number of blades caused the onset of flutter to occur earlier (i.e., at lower Mach numbers and RPM). This experimentally demonstrated that the blade aerodynamic cascade effects have an unfavorable effect on flutter. The places where video recordings were made of the flutter motion are indicated by the solid triangular symbols.

Two flutter boundaries are indicated by the cross-hatched lines. Two different flutter prediction methods were used to predict these boundaries as follows: (1) a modal analysis with plate modes in conjunction with two dimensional (2D) subsonic single blade unsteady aerodynamic theory, and (2) a beam model with 2D subsonic unsteady cascade aerodynamic theory. It can be seen that the flutter boundary predicted by the beam model is in better agreement with the measured data primarily because it accounted for cascade effects.

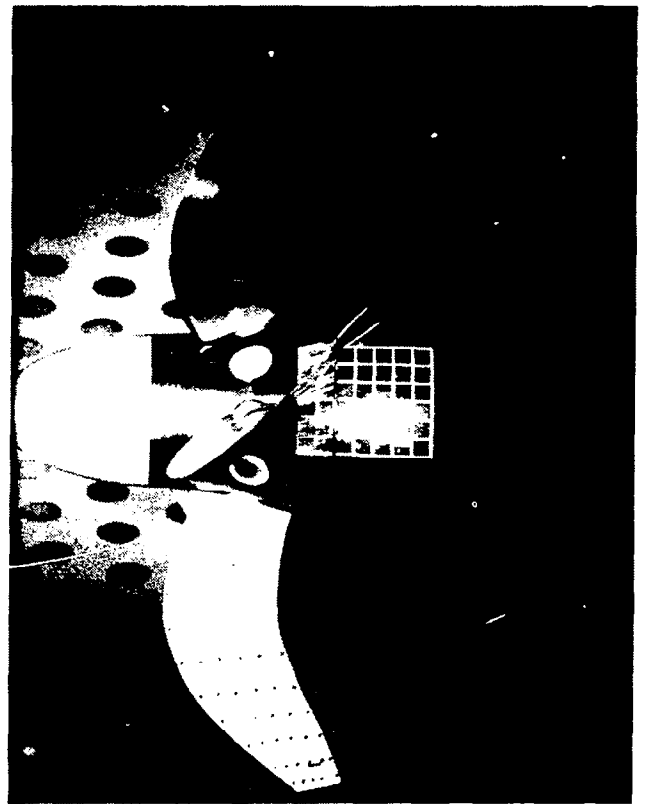


PROPELLER BLADE TIP DEFLECTION MEASUREMENT TECHNIQUE

It is very important to know the actual operating propeller blade shape as it determines the actual propeller performance and noise. Therefore, propeller blade tip movement under steady centrifugal and aerodynamic loading were measured using the 35-mm stroboscopic photographic system. In this figure, two photographs are shown of the SR-5 propeller (that incorporated 60° of tip sweep) operating at a blade angle of 59° ($\beta_{3/4} = 59^\circ$). The photograph on the left side was taken as the wind tunnel started running with the propeller at 750 RPM and the tunnel at a Mach number of approximately 0.10. The photograph on the right side illustrates the propeller at a rotational speed of 9000 RPM and a tunnel Mach number of 0.45. The blade tip deflections were determined by measuring displacements relative to the aligned grid pattern on the rotating hub and static nacelle. These initial results demonstrated the ability to photographically determine the advanced propeller blade steady state tip deflections. These blade tip deflections are compared with analytical predictions in the next figure.



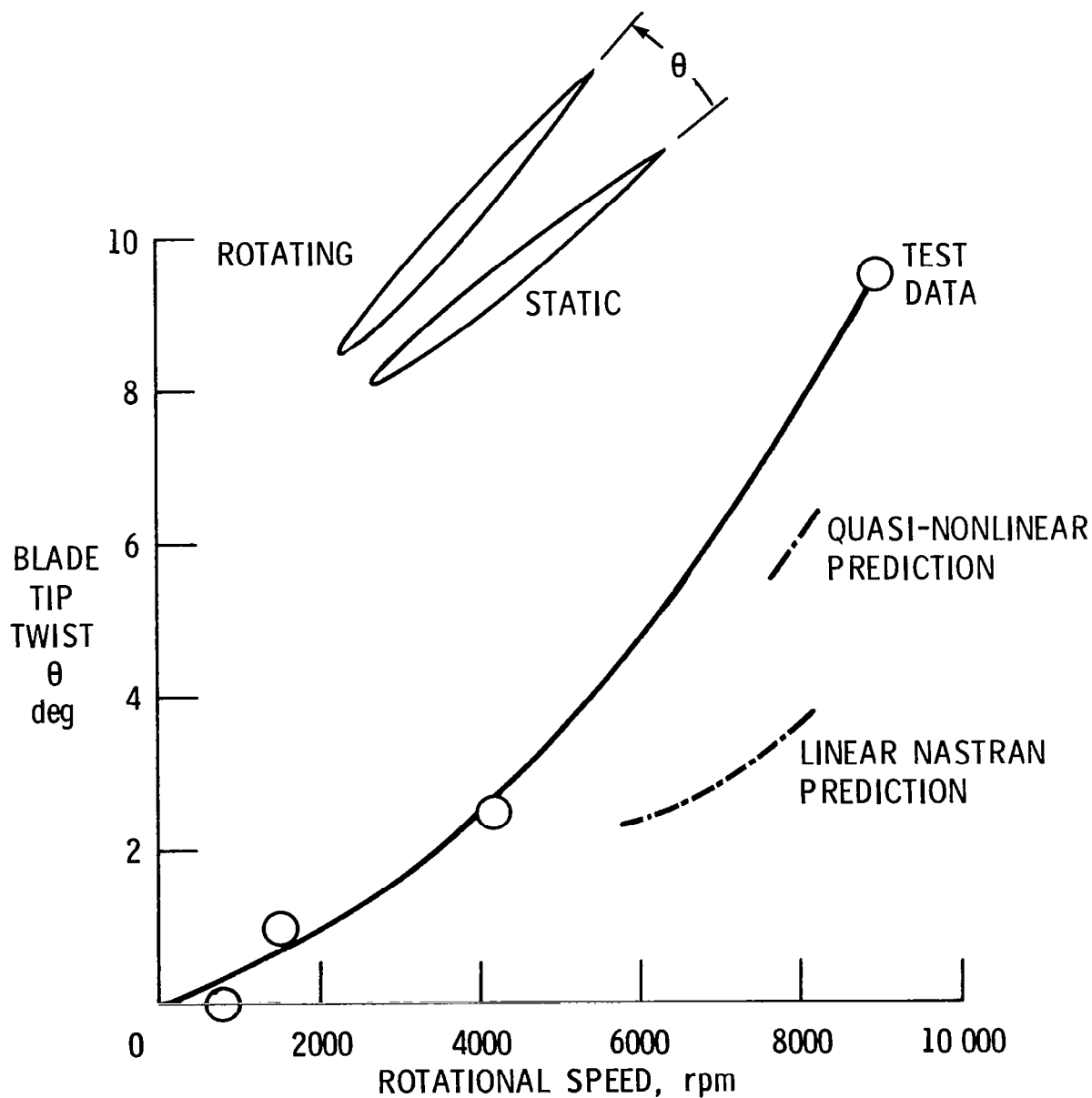
rpm = 750
 $M_0 \sim 0.1$



rpm = 9000
 $M_0 = 0.45$

SR-5 BLADE TIP MOVEMENT

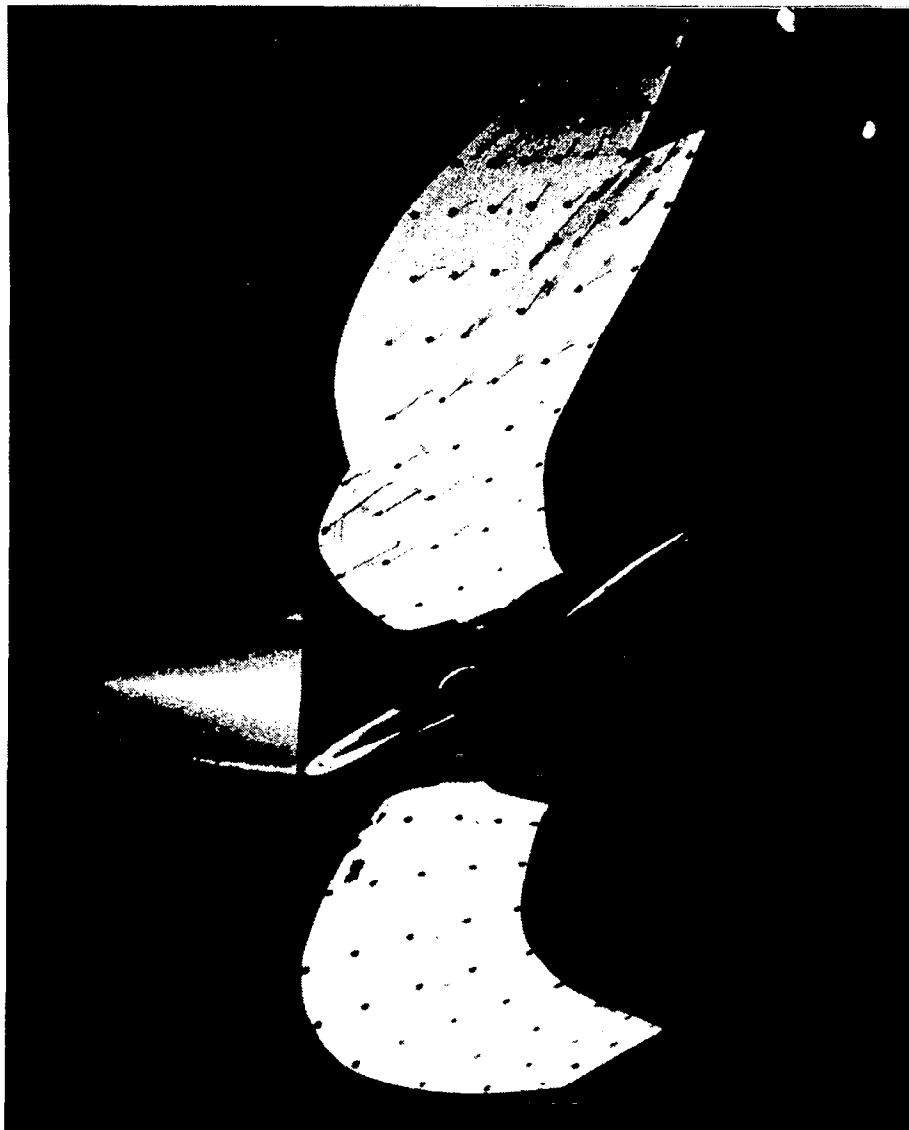
A comparison of the measured blade tip twist with finite element structural prediction methods is shown in this figure. At rotational speeds near 8000 RPM, the data shows that the structural prediction methods underestimated the blade twist about 1.5° to 4.0°. The figure also shows that as the propeller rotational speed was increased to 9000 RPM, the blade twist reached 9.5°. With the blade twisting to 9.5°, the blade tip trailing edge moved about 0.4 in. horizontally and 0.5 in. vertically. The sketch at the top of the figure shows the approximate positions of the blade tip at rotational speeds of 750 and 9000 RPM.



TUFT FLOW VISUALIZATION TECHNIQUE

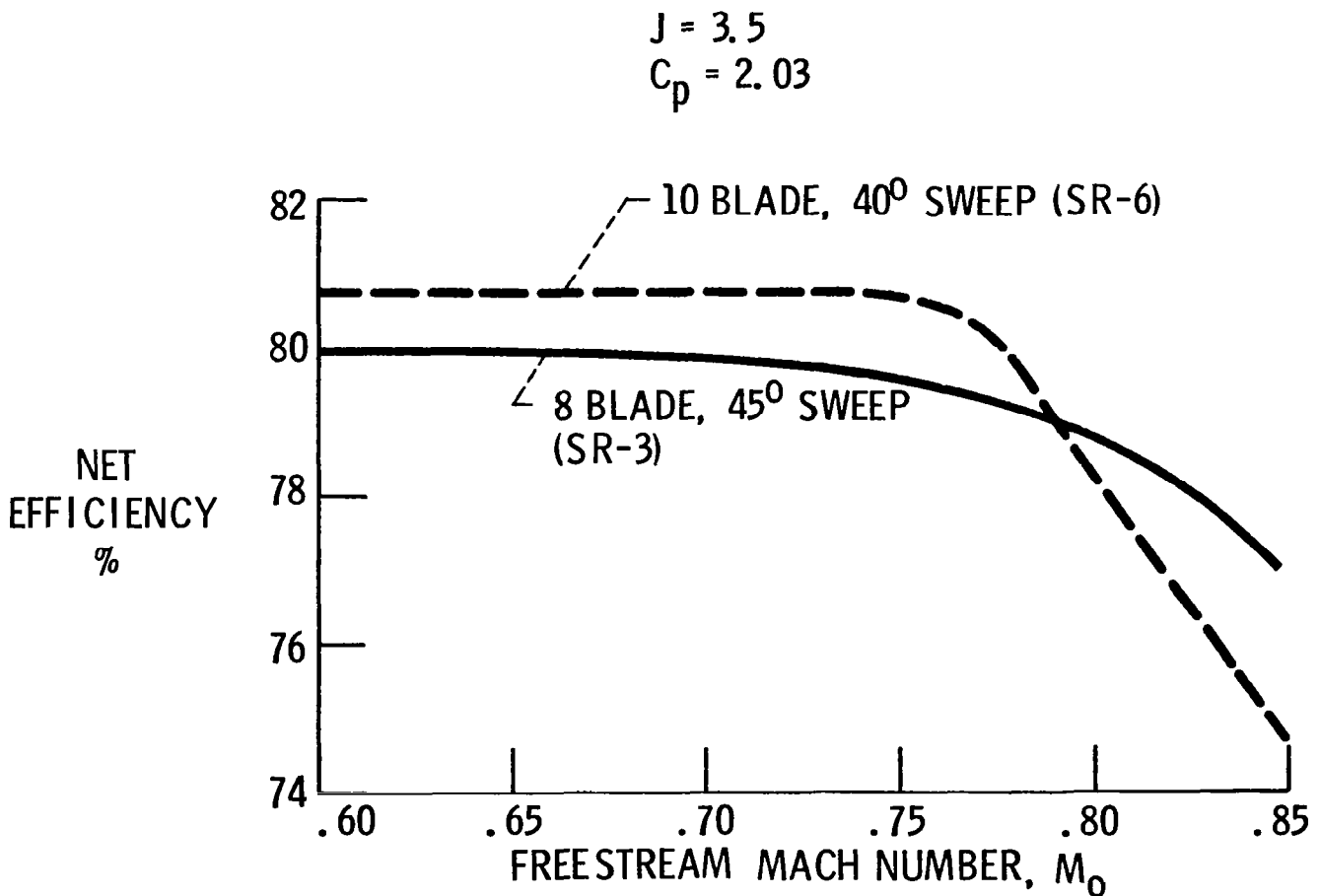
Tufts with a diameter of 0.007 were installed on the propeller blades. The tuft flow patterns due to aerodynamic and centrifugal forces are shown for the SR-5 propeller operating at 0.75 free-stream Mach number, 7200 RPM, and a blade angle of 64° (i.e., $\beta_{3/4} = 64^\circ$). The tufts radial alignment, especially near the blade tip, indicates that the centrifugal force on the tufts dominated the aerodynamic force. Consequently, the flow directions are more typical of the boundary layer flow directions than the free-stream aerodynamic flow directions over the blade. Further, at the conditions the tufts were tested, no stall regions were evident on the propeller blades.

$M_0 = 0.75$
rpm = 7200



COMPARISON OF 8 AND 10 BLADE PERFORMANCE

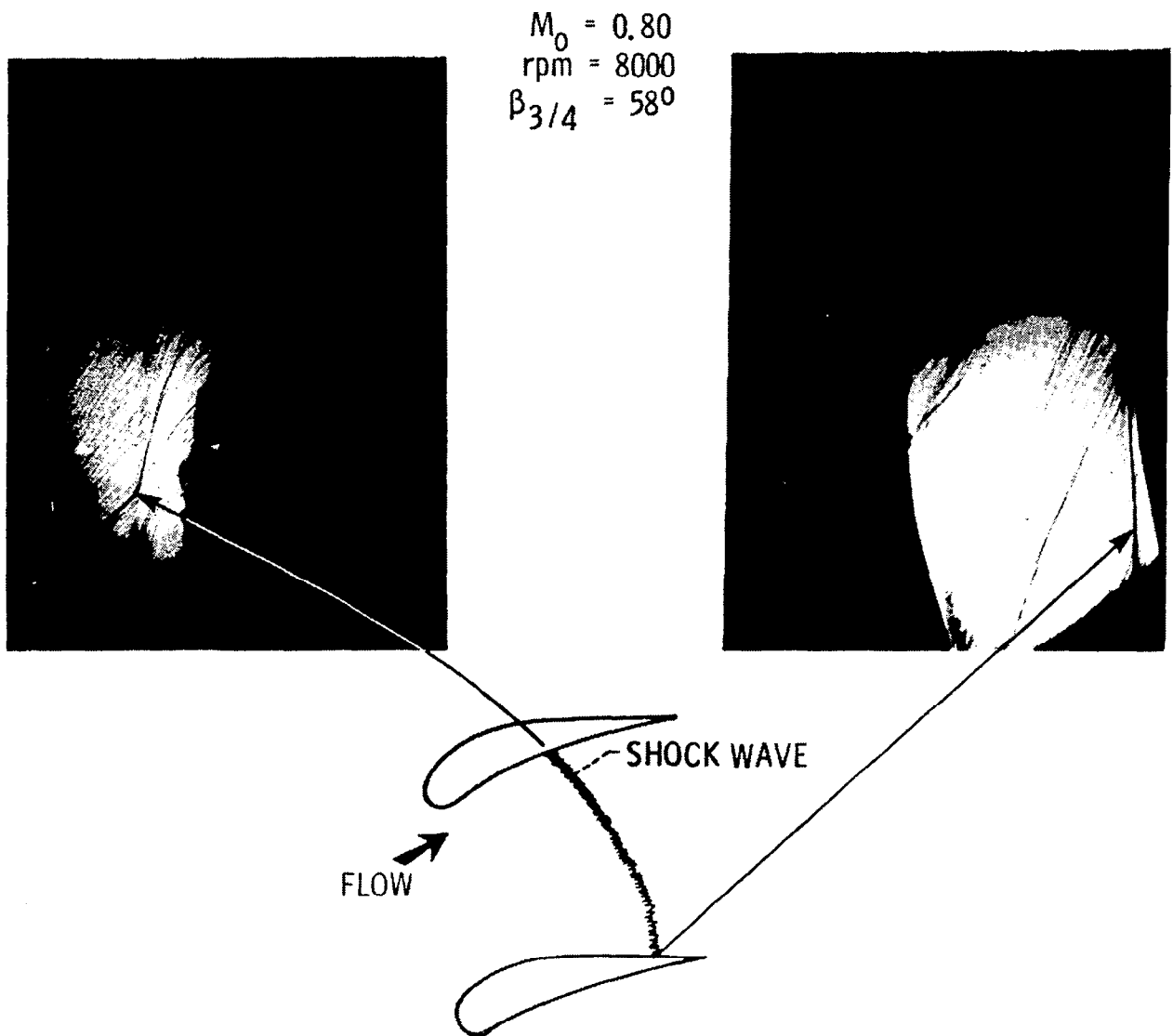
This figure shows the ten-blade SR-6 propeller performance loss due to shock waves in the root region. The propeller net efficiency for the ten-blade SR-6 and the eight-blade SR-3 propellers are presented versus free-stream Mach number for an advance ratio of 3.5 and a power coefficient of 2.03. The SR-6 ten-blade propeller indicates a rapid drop in efficiency for Mach numbers above 0.77. Although a couple of hypotheses for the efficiency loss existed previously, the paint flow test established blade root choking as the most probable cause of the propeller performance loss.



SHOCK WAVE LOCATIONS ON THE SR-6 PROPELLER BLADES

The paint flow technique was used on the ten-blade SR-6 propeller to determine if it could locate shock waves. The propeller was tested at a free-stream Mach number of 0.80, a rotational speed of 8000 RPM, a blade angle of 58° , an advanced ratio of 2.85, and a power coefficient of 1.35. The technique worked well. It showed shock waves located between the propeller blades which were especially strong in the blade root region. The figure shows the actual shock wave pattern on the propeller blades. Note the discontinuous change in flow direction behind the shock wave which is more clearly evident in the picture on the left side.

These shock waves show that the flow was choked in the propeller root regions. This flow choking gave rise to the shock waves which cause a loss of propeller efficiency at the higher Mach numbers.



RESULTS

It is very important to know the actual operating blade shape as it determines the actual propeller performance and noise. These results demonstrated the ability to photographically determine the advanced propeller blade tip deflections, local flow field conditions, and gain insight into aeroelastic instability.

With this new knowledge, the analytical prediction methods that are under development can be compared with experimental data. These comparisons will contribute to the verification of these improved methods and will give improved capability for designing future advanced propellers with enhanced performance and noise characteristics.

- TWO PROPELLER PHOTOGRAPHIC SYSTEMS WERE DEVELOPED
- FLUTTER MOVIES DETERMINED TYPE OF FLUTTER
- BLADE TIP DEFLECTIONS WERE MEASURED
- TUFTS SHOWED NO STALL REGIONS
- PAINT FLOW TECHNIQUE SHOWED SHOCK WAVES

IN-FLIGHT PROPELLER FLOW VISUALIZATION
USING FLUORESCENT MINITUFTS

James P. Crowder
X-Aero Company
Mercer Island, Washington

IN-FLIGHT PROPELLER FLOW VISUALIZATION USING FLUORESCENT MINITUFTS

The fluorescent minituft flow visualization technique (Crowder, J. P., *Astronautics & Aeronautics*, Nov. 1980, pp. 54-56) was originally developed for non-intrusive flow visualization in wind tunnel testing. This note describes a recent extension of the method to in-flight flow visualization on propellers.

The basis of the method is the use of extremely thin nylon monofilament for the minitufts, a process of attaching them to the test surface with small drops of lacquer-like adhesive, and the use of fluorescence photography for recording the minituft patterns. Using this method, thousands of minitufts can be applied to small, high speed wind tunnel models without affecting the airflow. Therefore, the minitufts can remain in place throughout a wind tunnel test, permitting non-intrusive flow visualization data to be acquired at any time.

The greatest problem in developing a flow visualization experiment for propellers is the high centrifugal acceleration which acts on any kind of indicator, such as oil or tufts. The very small size of fluorescent minitufts helps, in this regard, to make them relatively unaffected by centrifugal forces. Simple dimensional analysis suggests that the aerodynamic forces on a tuft, for a given velocity and radius, depend on the tuft diameter while the centrifugal forces depend on the cross-section area, or diameter squared. Therefore, as the tuft diameter is reduced, the centrifugal force will decrease at a greater rate than the aerodynamic force. Consequently, at some particular tuft size, the centrifugal loading will become insignificant.

Furthermore, the tuft airloads depend on the dynamic pressure, the rotational component of which is proportional to the rotational rate Ω squared, times the radius R squared, or $\Omega^2 R^2$, while the centrifugal forces on the tufts depend on $\Omega^2 R$. Thus the ratio of aerodynamic to centrifugal forces increases as the radius is increased.

From this reasoning it seems certain that for some combination of tuft diameter, rotational rate, radius and Reynolds number, fluorescent minitufts will properly indicate surface flow direction. These effects are difficult to determine analytically so actual demonstration of minituft behavior requires experimental trials.

The greatest difficulty in using the fluorescent minituft method is in providing sufficient ultraviolet illumination to make the very small tufts photographically visible. For stationary wind tunnel models, the usual illumination source is a pulsed xenon flash lamp with an electrical power for each pulse of 2000 Joule and a duration of about five milliseconds.

Propeller flow visualization and other rotating machinery applications typically involve motion rates so fast that the illumination duration must be on the order of one microsecond to produce an image with tolerable blur. This is very difficult to achieve for such high energy levels.

A test program to demonstrate the fluorescent minituft method for in-flight propeller flow visualization was sponsored by Machen, Inc. in support of their flight test program of the Machen Superstar. This airplane, shown in Figure 1, is a re-engined version of the Piper Aerostar. The airplane was experiencing high speed performance limitations attributable to the propeller performance. The

fluorescent minituft method was applied to help identify the propeller flow characteristics to aid in designing new propellers for the airplane.

The flashlamp power supply, weighing over one hundred pounds, including the a.c. inverter, and occupying several cubic feet is just visible in the cabin through the door. The flash lamp was placed in a forward fuselage compartment rather than in the cabin window because the plastic window material was opaque to the ultraviolet radiation. The lamp-to-propeller distance was about eight feet. The camera was located in the cabin door window, shown open in Figure 1.

Figure 2 shows the typical appearance of the in-flight minituft propeller flow visualization results. The flight condition in this case was close to maximum cruise speed with a propeller tip Mach number of 0.93. The line of local separation evident along the outer half-radius is most likely a shock wave induced separation bubble. From the reflections of the minitufts on the shiny aluminum surface of the spinner, one can get an indication of the centrifugal force biasing of the minituft direction.

Figure 3 shows the propeller flow condition during climb at high altitude, approaching the service ceiling. As expected, there is extensive separation on the propeller surface.

These pictures graphically show the type of flow visualization results that can routinely be achieved on rotating surfaces. This technique is suitable for a wide variety of aerodynamic problems including helicopter rotors, turbomachinery, and wind turbines, in addition to propeller flow visualization. The method is easy to implement and can produce data images over a wide range of conditions with little or no interference to the flow or test procedures.

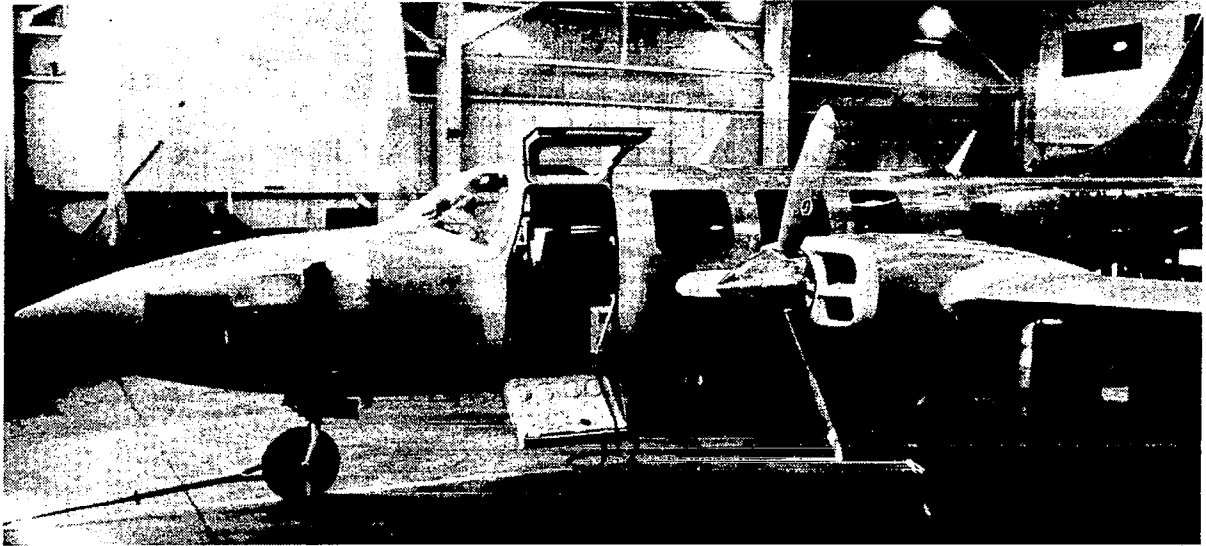


Figure 1.- Ultraviolet flash lamp installation in Machen Superstar.

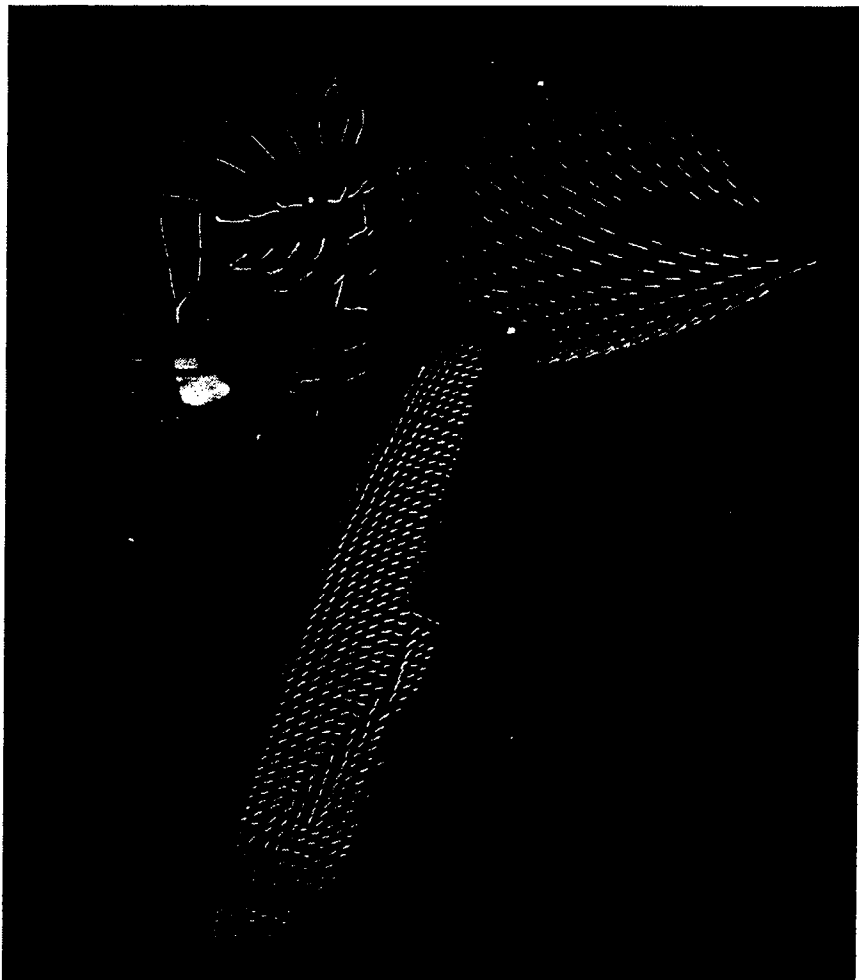


Figure 2.- Fluorescent minitufts on Machen Superstar propeller. 25,000 ft;
285 kt IAS; $M_{\text{tip}} = 0.93$; Advance ratio = 1.87; Power coef = 0.21.

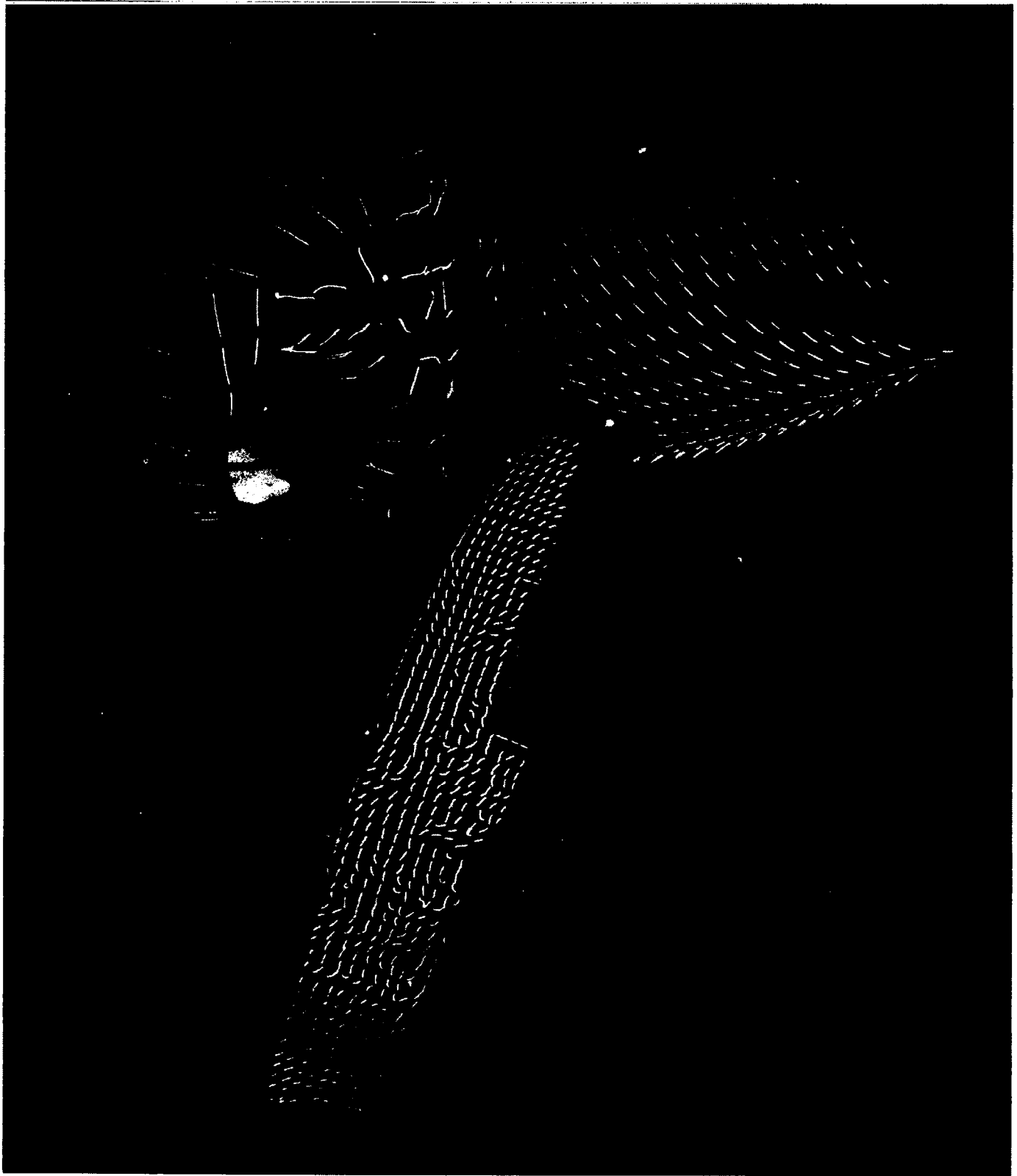


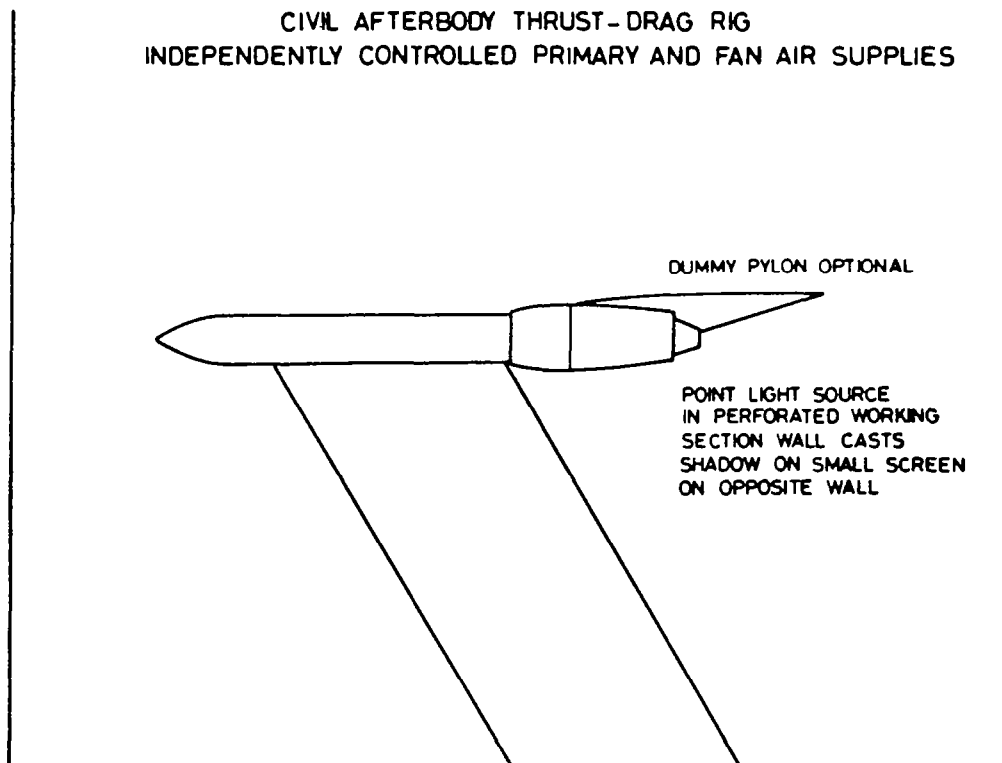
Figure 3.- Fluorescent minitufts on Machen Superstar propeller. 24,000 ft; Climbing; 120 kt IAS; Advance ratio = 1.18; Power coef = 0.27.

SHADOWGRAPH TECHNIQUES
IN TRANSONIC TESTS WITH
POWERED NACELLES

P. G. Hutton
Aircraft Research Association Ltd.
Bedford, England

The ARA 9' x 8' transonic tunnel has a working section with four perforated walls with normal holes of $\frac{1}{2}$ " diameter. In the application of the shadowgraph technique to this tunnel, one of the wall perforations is used to accommodate a high intensity point light source. The shadow showing shock wave patterns is then cast onto a suitable surface, normally the opposite wall.

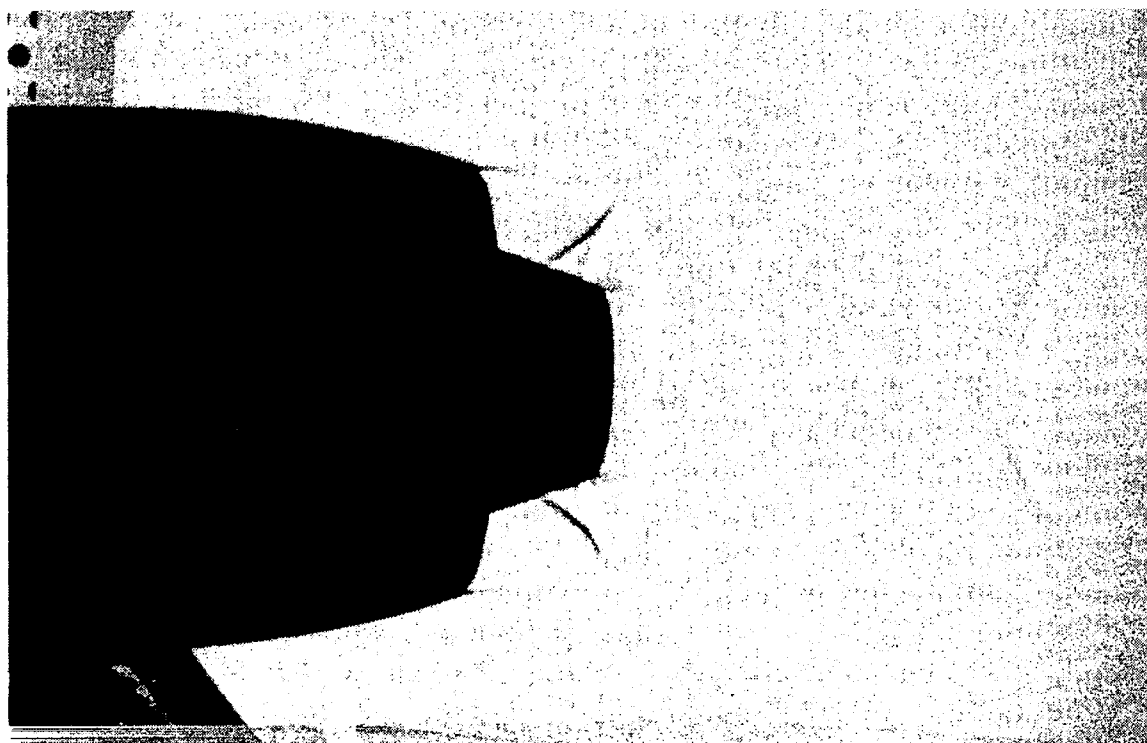
This system has been used in a number of tests with powered nacelle rigs to visualise the shock wave patterns in the exhaust flow. A blown rig on which the technique has been used is shown in this diagram.



This is a photograph taken during a test with the rig shown in the previous illustration, in this case without a dummy pylon.

A remote camera behind the perforated wall in which the light was installed was used to photograph a small screen attached to the opposite wall.

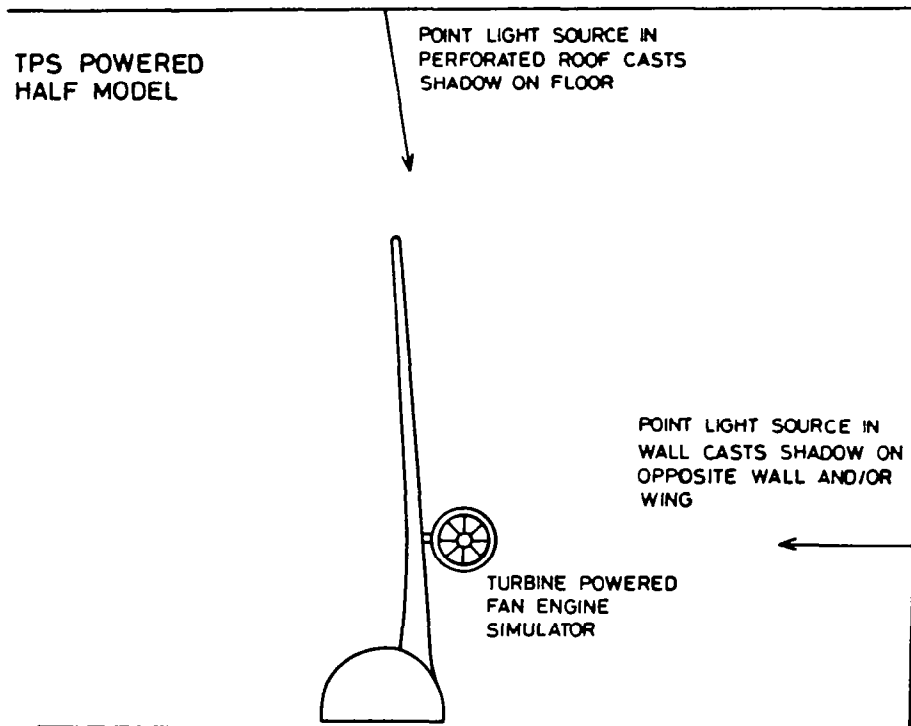
As an alternative to the photographic technique, a television camera and video recorder have been used successfully. The TV camera is mounted behind a small glass window near the aft end of the perforated wall.



The shadowgraph technique has also been used successfully for installed nacelle tests on a floor-mounted half model with a turbine powered fan-engine simulator.

In this case the light source was positioned in one of the roof perforations so that the shadow was projected onto the floor which is solid in this area. This, of course, shows the shock wave pattern near a plane normal to the wing.

To visualise the flow near a plane parallel to the wing it is proposed to use a light source in the side wall and project onto the opposite wall and/or the wing.



FLOW VISUALIZATION OF SHOCK-
BOUNDARY LAYER INTERACTION

Warren R. Hingst and Mark Jurkovich
NASA Lewis Research Center
Cleveland, Ohio

Figure 1. Experimental Program

An experimental program is underway in the Lewis 1 X 1 foot supersonic wind tunnel to obtain two and three-dimensional shock-boundary layer interaction data. These interactions are studied both with and without boundary layer bleed. The data are to be of sufficient detail for verification of computational fluid dynamic codes. In addition to the quantitative measurements such as surface static pressure, pitot pressure, flow angularity, and bleed rates, qualitative studies of the flow are made using flow visualization techniques. Surface oil flow using fluorescent dye and laser sheet using water droplets as the scattering material are being used for flow visualization.

SUPERSONIC FLOW VERIFICATION EXPERIMENTS

GLANCING SIDEWALL SHOCK - B. L.

2-D SHOCK - B. L.

3-D SEPARATED FLOW

EFFECTS OF B. L. BLEED

QUANTITATIVE MEASUREMENTS

PRESSURES

FLOW ANGULARITY

BLEED RATES

FLOW VISUALIZATION

SURFACE OIL FLOW

LASER SHEET

Figure 2. Schematic of Experimental Configuration

The experimental configuration consists of a shock generator that spans the tunnel. The shock generated produces a sidewall glancing interaction on the tunnel wall and a ramp interaction on the tunnel floor. The boundary layers in the interactions are those naturally occurring on the tunnel surfaces.

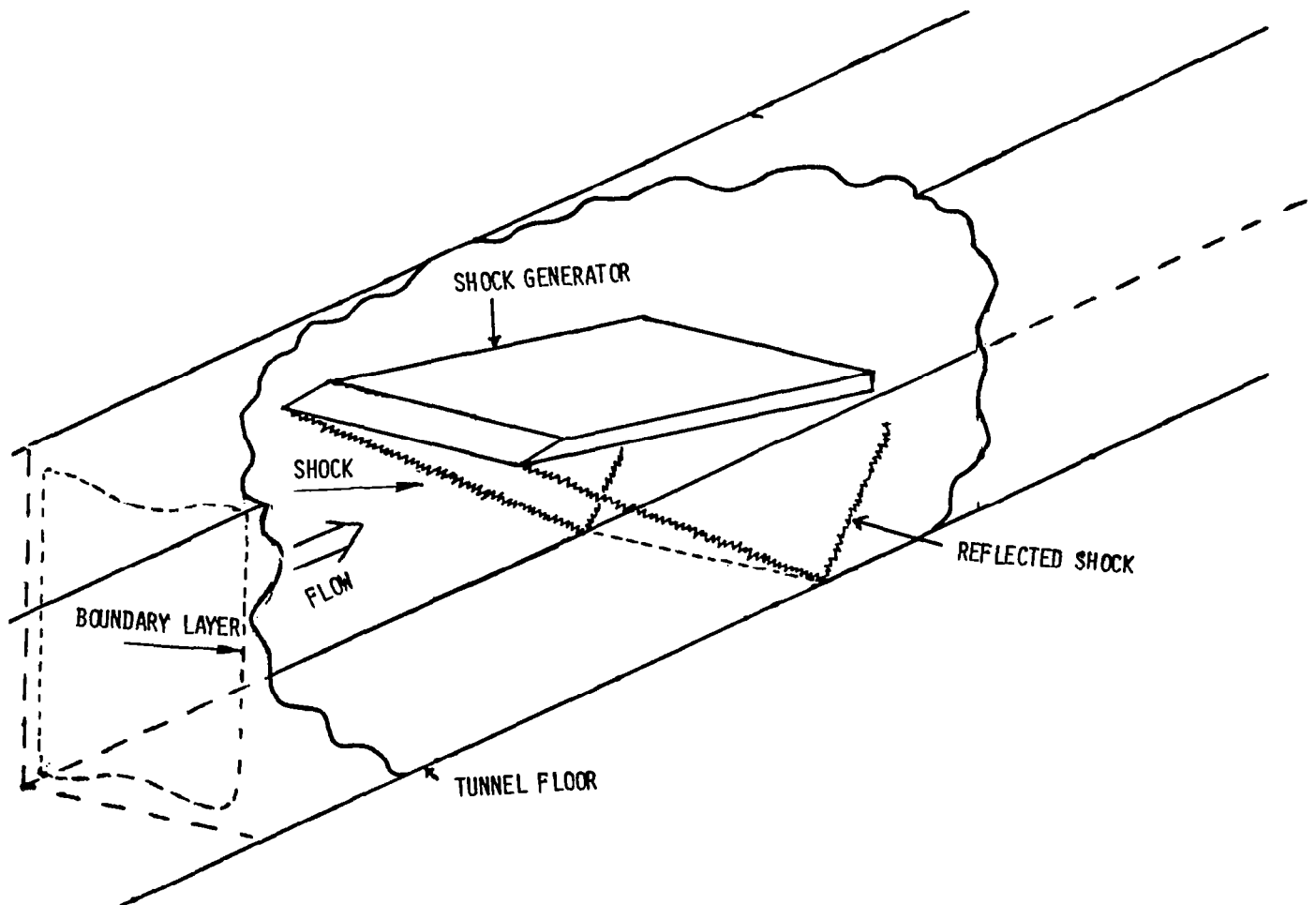


Figure 3. Surface Oil Flow Visualization of Glancing Sidewall Shock-Boundary Layer Interaction

This photograph shows the results of surface oil flow visualization using a fluorescent dye to suppress background reflections. The view is from upstream and across the tunnel. The shock generator can be seen on the upper part of the photograph. The turning of the oil flow shows the upstream influence of the shock propagating through the boundary layer. The results are for a Mach number of 2.5 and a shock generator angle of 8° .

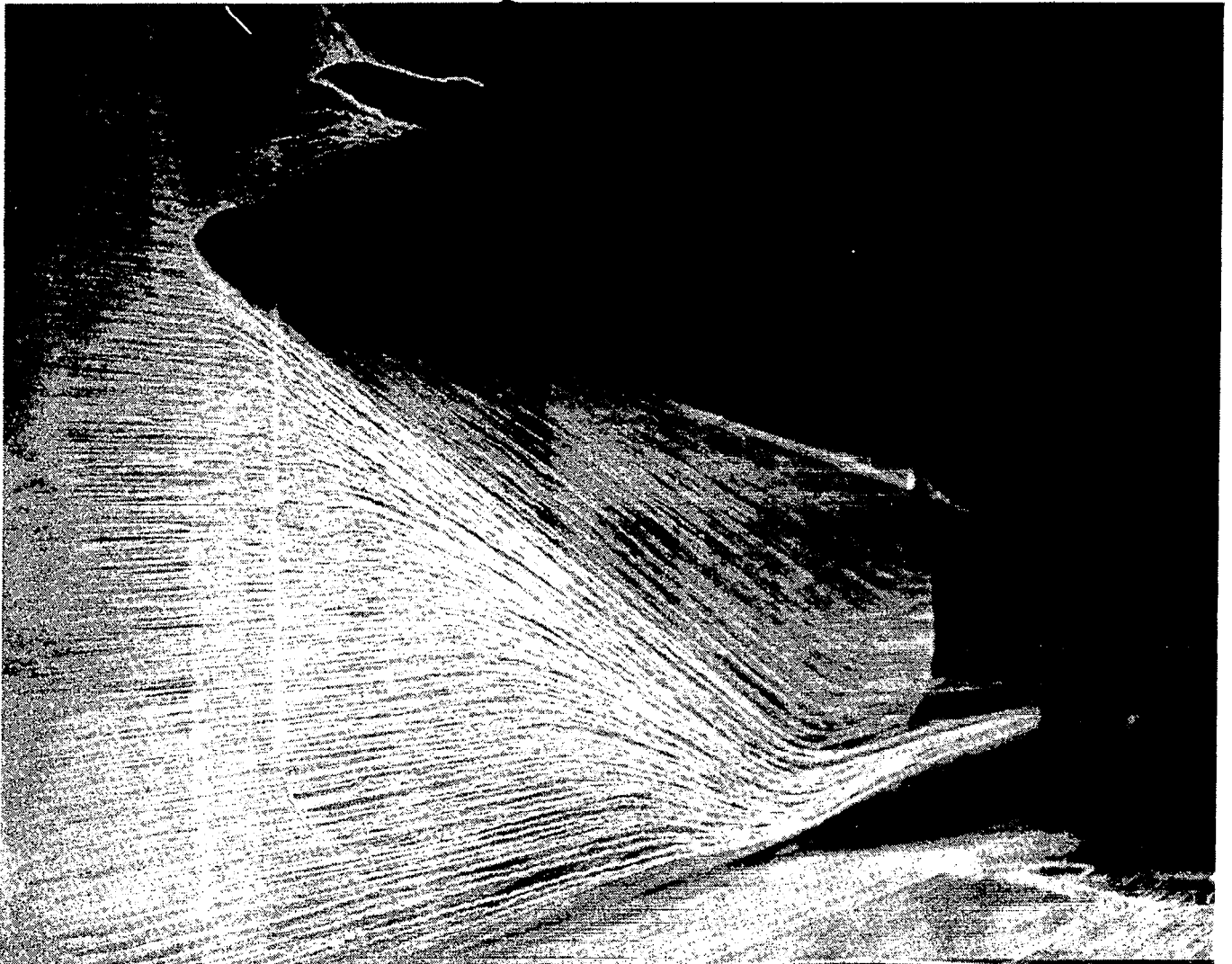


Figure 4. Surface Oil Flow of 3-D Separation on Tunnel Floor

This view of the surface oil flow visualization shows the shock-boundary layer interaction on the tunnel floor. The view is directly from the side. A large three-dimensional flow separation is shown. The flow conditions are the same as described for figure 3.



Figure 5. Schematic of Laser Sheet Configuration

This schematic shows the optical configuration used for the laser sheet flow visualization. The experimental configuration is that shown in figure 2. The laser beam enters the tunnel downstream of the test section. The beam enters an optics package that spreads the beam in one direction with a cylindrical lens and projects it upstream. This optics package is actuated to move the resulting laser sheet up and down or across the tunnel depending on the orientation of the sheet. The scattered light is recorded with a still or T.V. camera located to the side of the shock generator.

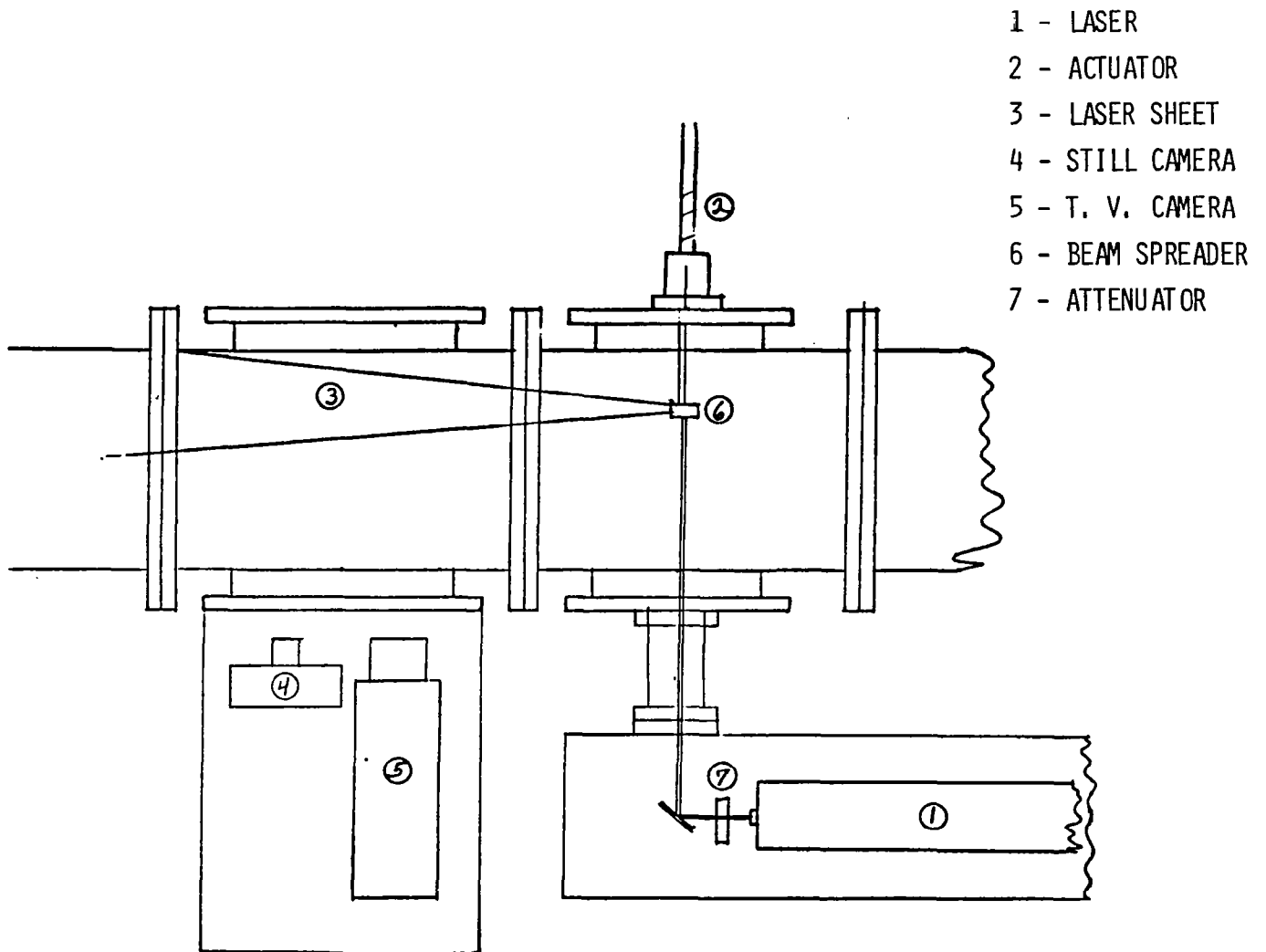


Figure 6. Laser Sheet Flow Visualization on Tunnel Centerline

This photograph shows the laser sheet along the tunnel centerline perpendicular to the tunnel floor. This would correspond to a plane through the center of the separated region on the floor shown in figure 4. The incident shock from the shock generator along with a shock induced by the separation are visible. The separated region is seen as the dark region near the floor. The flow conditions are the same as described for figure 3.

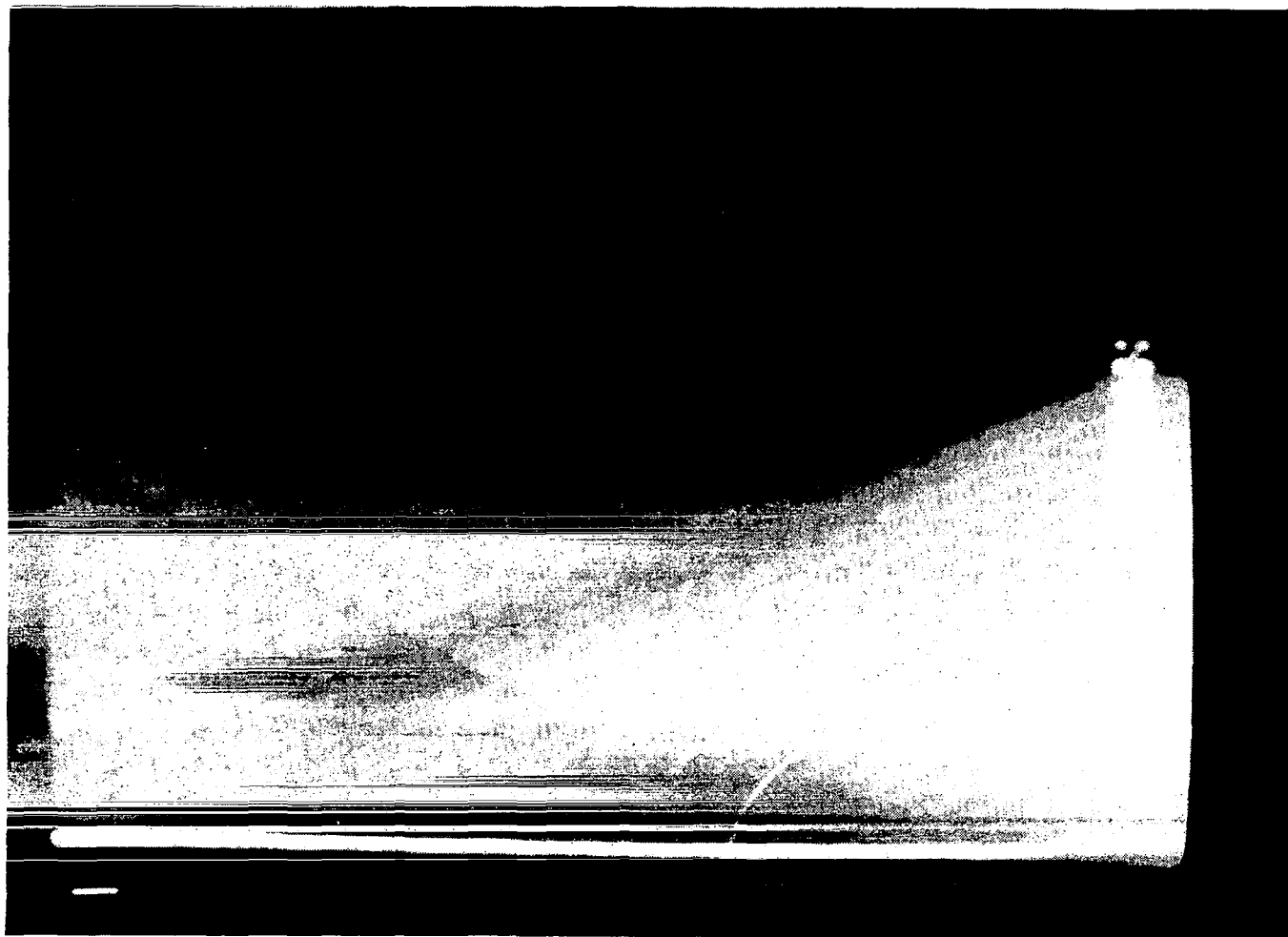
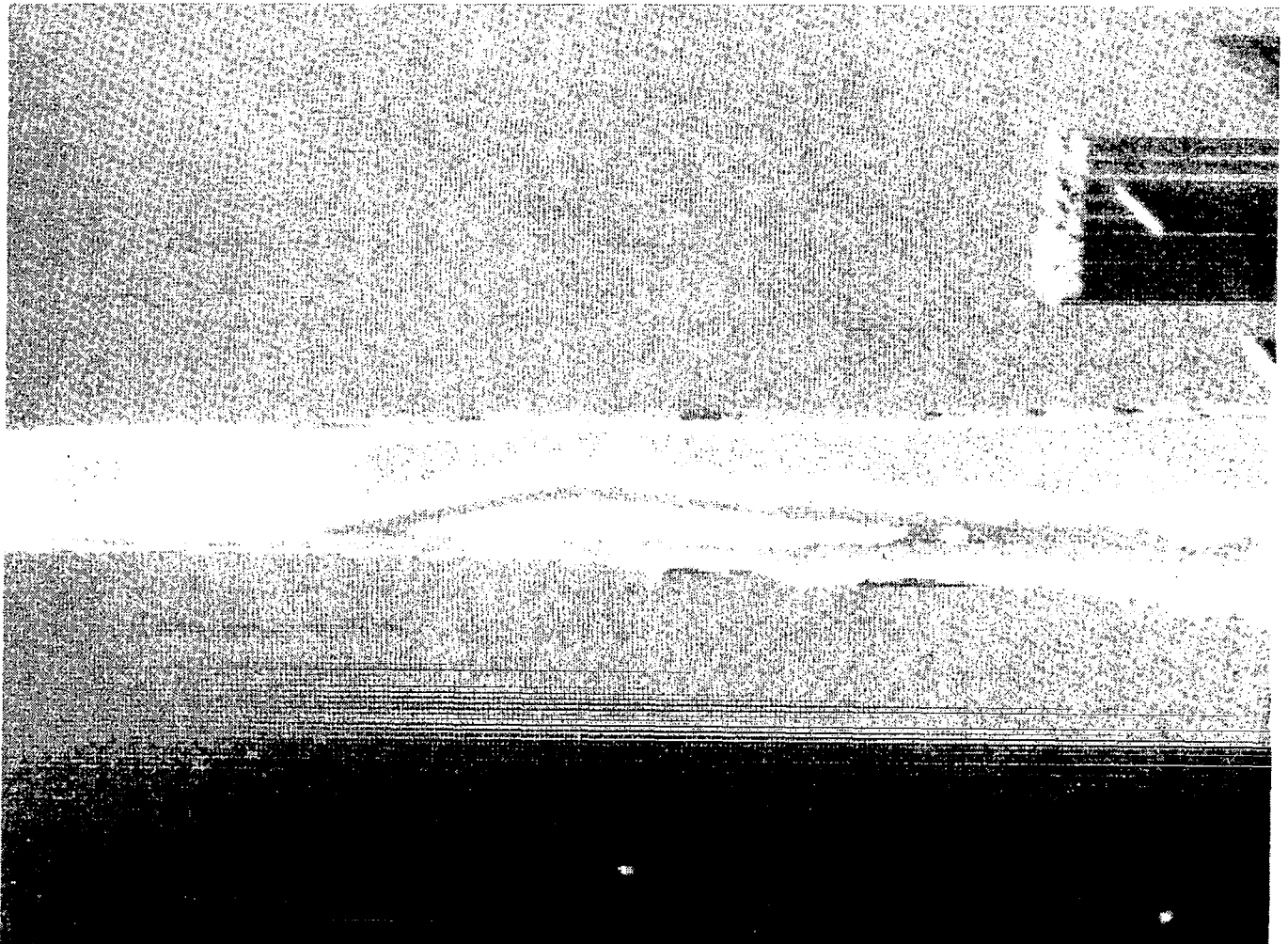


Figure 7. Laser Sheet Flow Visualization of Three-Dimensional Separation

This figure shows the laser sheet localized through the centerline of the three-dimensional flow separation shown by the surface oil flow in figure 4. Here the original laser sheet photograph has been enhanced by an image processor to bring out the density gradients in the scattered light. The various density gradients are represented by a false color image. By taking a series of these cuts through the separated region a three-dimensional representation of the separated flow can be obtained. The tunnel conditions are the same as described for figure 3.



L-82-5678

TRANSONIC APPLICATIONS OF
THE WAKE IMAGING SYSTEM

James P. Crowder
Boeing Aerodynamic Laboratory
The Boeing Company
Seattle, Washington

A rapid flow field survey method, known as the Wake Imaging System (WIS), originally developed for low speed wind tunnel operation, is being extended to transonic wind tunnel applications. The greatest difficulty in performing these flow field surveys at high dynamic pressures in transonic wind tunnels is the development of a relatively unobtrusive probe traversing system. The unique features of the WIS permits great flexibility in selecting a flow field traversing system.

Figure 1 shows a typical WIS data image from the Boeing 5 x 8 foot low speed wind tunnel. This photograph is the only form of the flow field data and is produced directly as a time-exposure photograph of a traversing colored signal light attached adjacent to the sensing probe. As the sensor, in this case a total pressure pickup, is traversed through the flow field, its output voltage goes to a level detector circuit which causes the signal light to turn on various colors in certain, preset pressure ranges. As the sensor and signal light sweep through the flow field, the light blinks on and off with different colors corresponding to the local total pressure level. A camera located in the wind tunnel, focused on the survey plane, records the trajectory of the signal light as colored streaks which merge into the total pressure isobars seen here. The results can be available immediately at the conclusion of a run in the form of color Polaroid photographs without any additional data manipulation.

The great advantage of the WIS, besides the simplicity and low cost of the data acquisition system, is that the probe position data are recorded as an optical image of the actual sensor and thus are unaffected by the inevitable deflections of the probe support. This permits traversing systems which are deliberately flexible and have unusual motions.

The traversing system developed for low speed tunnels has the sensor supported on the end of a high aspect ratio strut extending perpendicular to the flow, inserted through a small hole in the test section ceiling. The type of motion used is polar coordinate, with the center of azimuthal travel at the tunnel boundary.

The first transonic application of the WIS at Boeing uses, as one of the two degrees of motion, the main model support strut, which moves vertically. The second degree of motion is provided by a linear traverse drive rigged to move perpendicular to the main strut motion (or horizontally). This drive has 25 inches of travel and a traverse rate of 5 inches per second. The system can survey a 2-D plane, perpendicular to the flow, with rectangular motion. It is limited to surveying models not mounted on the sting, such as floor mounted or external balance plate mounted models.

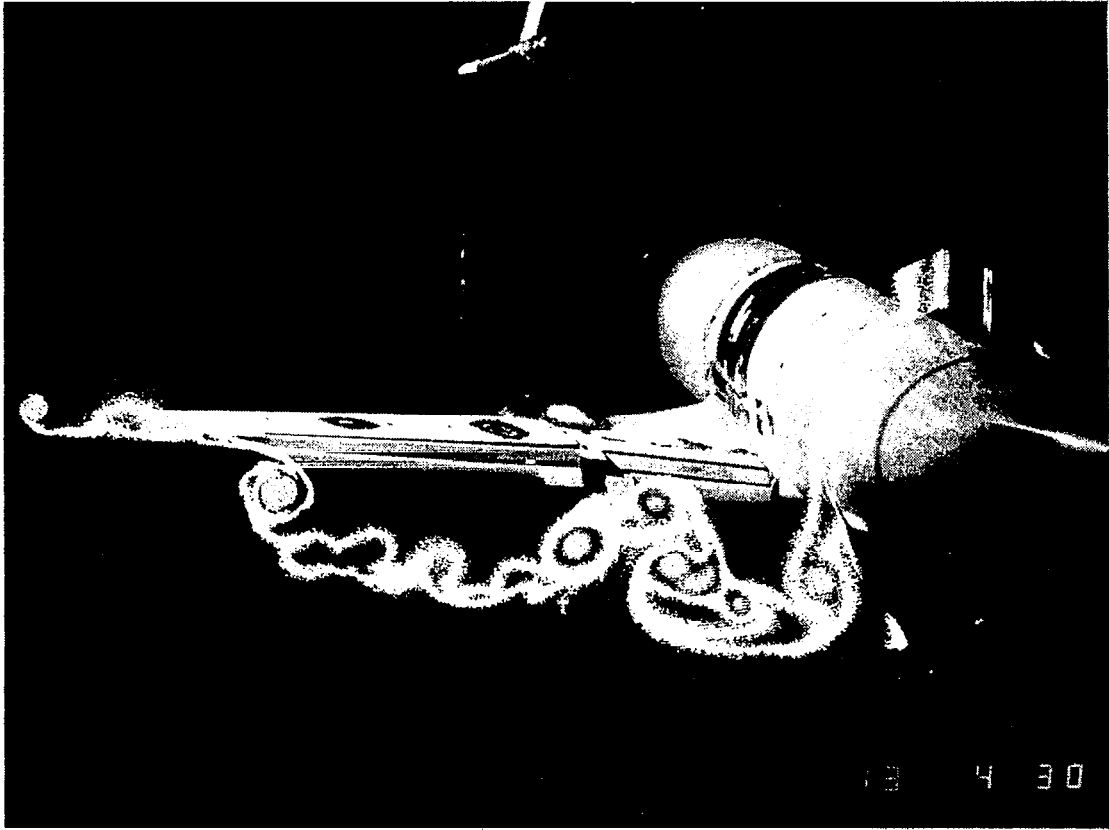
Since this system is relatively stiff and because we were not ready to install a camera in the tunnel, the position readout is by conventional electrical potentiometers. The data acquisition procedure uses an analog X-Y plotter driven by the two position potentiometers with the signal light mounted on the plotter pen arm. The plotter is placed inside a box and a camera located directly over it to take the time exposure photograph.

Figure 2 shows the system installed in the Ames 11-Foot Transonic Wind Tunnel behind a floor mounted half-span model of the 747. Notice the vortex generators attached to the wing surface. Figure 3 shows several typical data images from this installation and illustrates the type of details that can be resolved by the system. Keep in mind that these images are available on-line in the form of a Polaroid print after a ten-minute run.

Figure 4 shows WIS images acquired in the Boeing Transonic Wind Tunnel of the outboard nacelle flow field on the 747 with and without a wing-strut intersection fairing. The ability to resolve these local flow field details greatly enhances the ability to understand the aerodynamic effects of small configuration changes that way not be discernable in the overall model forces.

This particular traversing drive is far from optimum for this experiment. We are presently developing an all new 2-D traversing system utilizing a combination of linear and rotary motion as shown in Figures 5 and 6. This new traverser is called the Wide Area Rapid Traverser, or WART. It will use a slow moving, rigid, linear-traversing strut from the tunnel wall with a fast moving rotating strut on the end. The rotating strut relies on a self-trimming mechanism to automatically rotate its incidence angle to produce zero root bending moment on the strut as the rotational traverse motion carries it through the model flow field.

We are also developing a digital data acquisition and display system to replace the time exposure camera. An opto-electronic position sensor located inside the tunnel will produce electrical signals from a continuously illuminated light on the tip of the survey strut. The position signals and pressure transducer output will be connected to signal conditioners and a fast analog-to-digital converter and stored in a color graphics buffer. The color video display will show the traversing probe location in real time and so can aid in controlling the traverse motion. The completed image can be stored on a floppy disk and can be accessed for further analysis.



L-82-5676

Figure 1.- Typical WIS data image from 5 X 8 foot low speed wind tunnel.

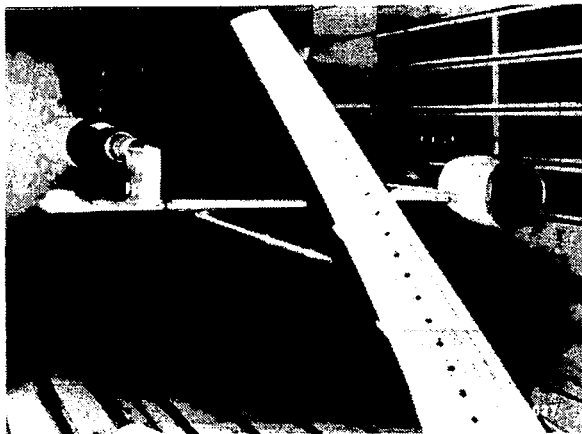
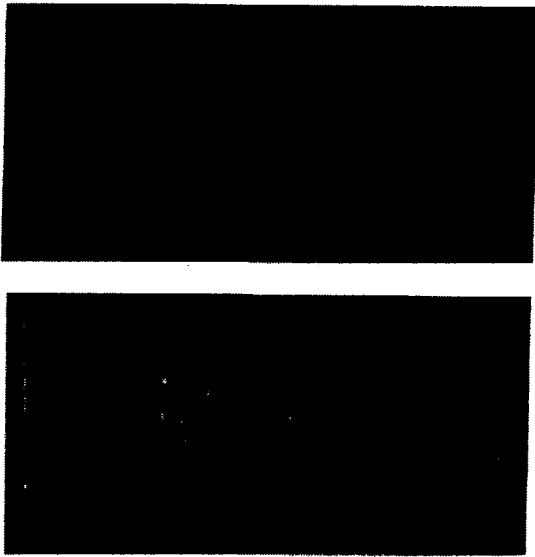


Figure 2.- Existing transonic WIS installed in Ames 11-Foot Transonic Wind Tunnel.

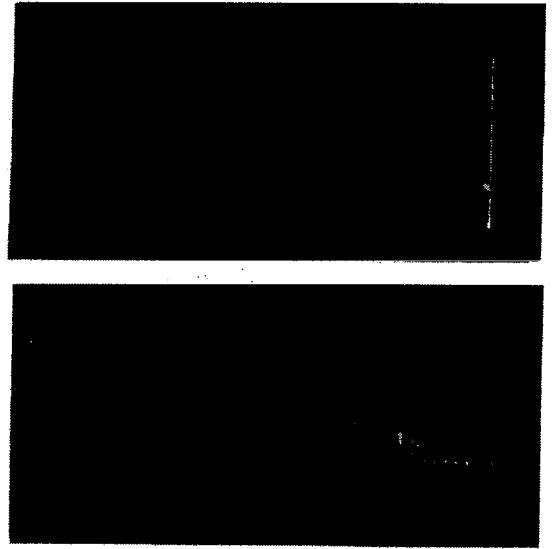
EFFECTS OF VORTEX GENERATORS

M=.84



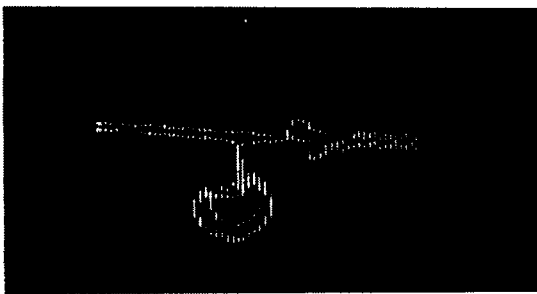
EFFECTS OF NACELLES

AT M=.88



L-82-5679

Figure 3.- WIS survey results.



FAIRING — OFF



FAIRING — ON

L-82-5677

Figure 4.- Effect of intersection fairing on 747 from WIS survey.

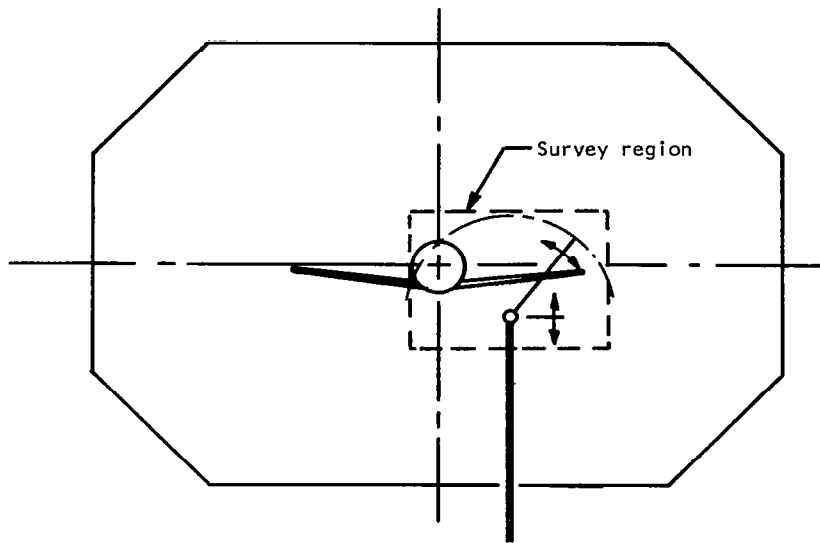


Figure 5.- Two-dimensional motion for wide area rapid traverser.

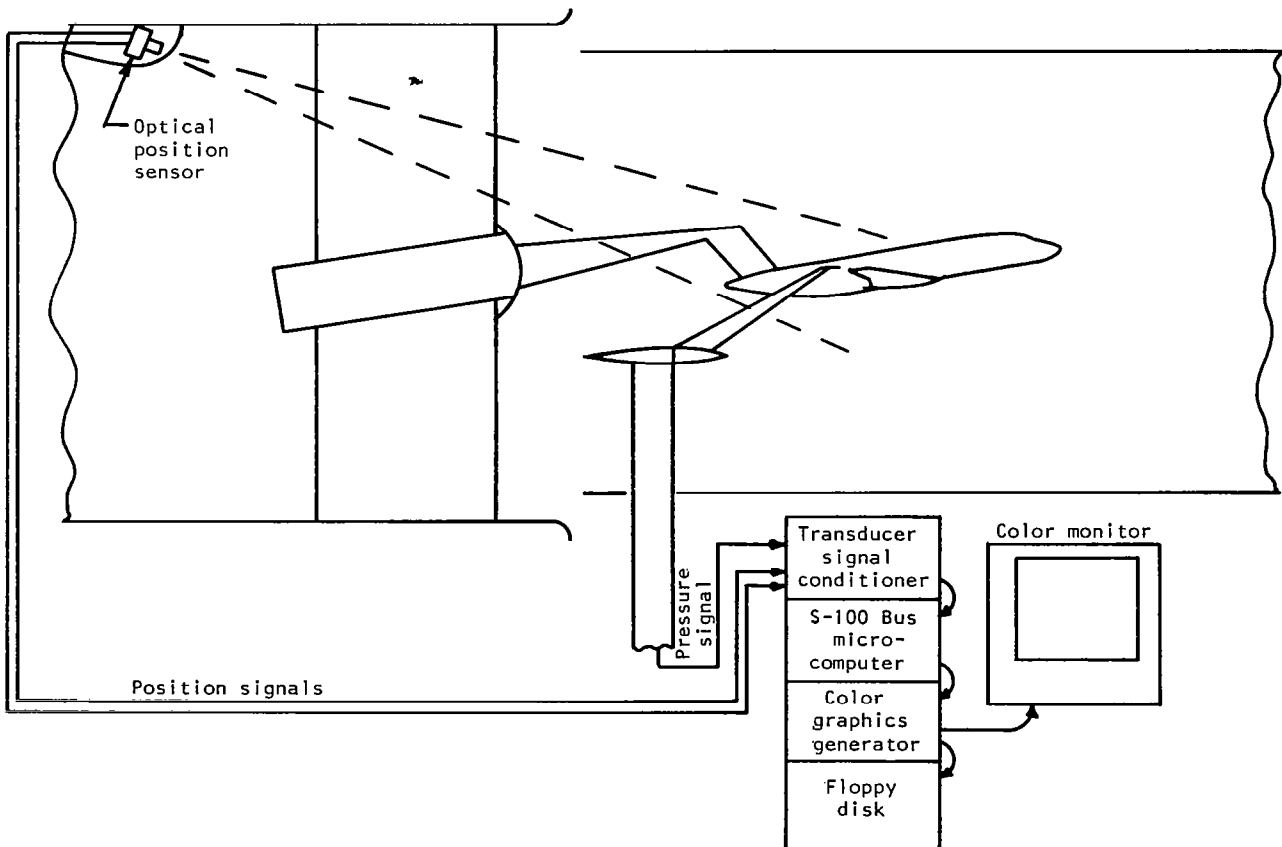
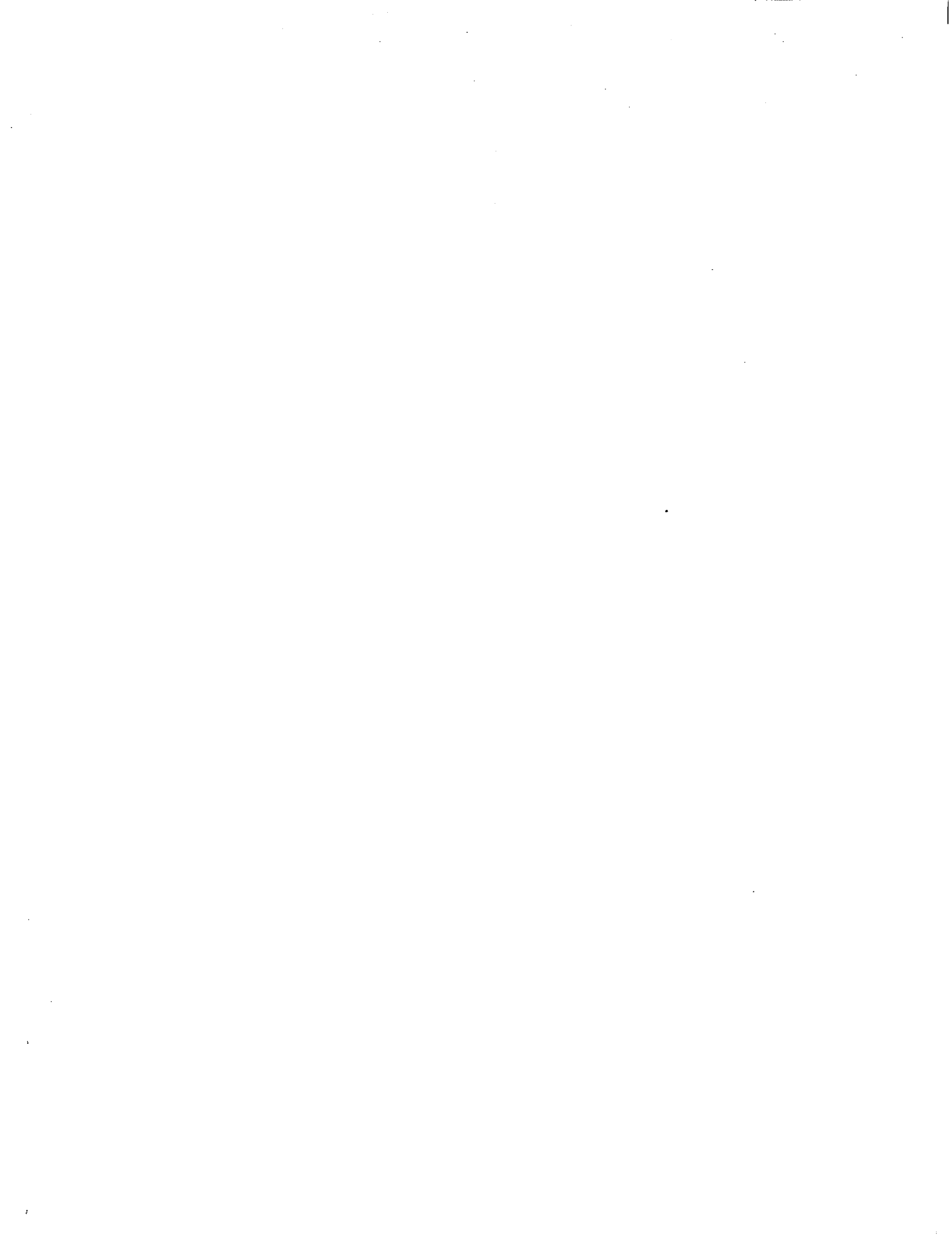


Figure 6.- Transonic wake imaging system - real time acquisition and display.



**FLOW VISUALIZATION IN THE LANGLEY 0.3-METER TRANSONIC CRYOGENIC TUNNEL
AND PRELIMINARY PLANS FOR THE NATIONAL TRANSONIC FACILITY**

**D. B. Rhodes and S. B. Jones
NASA Langley Research Center
Hampton, Virginia**

INTRODUCTION

The feasibility of flow visualization in cryogenic facilities is of interest at Langley with the anticipated start-up of the National Transonic Facility (NTF). The possible effects from the cryogenic environment (i.e., window distortion due to thermal contraction both in the mounts and in the window material itself and turbulence in the flow due to injected LN₂) need to be examined. The flow visualization techniques to be studied are schlieren, shadowgraph, moiré deflectometry and holographic interferometry. The test beds for this work are an in-house cryogenic test chamber and the 0.3-Meter Transonic Cryogenic Tunnel (TCT).

CRYOGENIC TEST CHAMBER DESIGN

The window material selected for the 0.3-Meter Transonic Cryogenic Tunnel and the National Transonic Facility was fused silica. This selection was based on the thermal shock properties, mechanical strength and good optical transmission. A chamber was constructed so that a schlieren system could be used to examine windows as they were subjected to the expected pressures and cryogenic temperatures. The chamber was fabricated from aluminum with double windows in each end. The inner windows were fused silica 12 inches in diameter and 2 inches thick while the outer windows were crown glass 10.5 inches in diameter and 1.56 inches thick (2.54 cm per inch). The chamber is shown in figure 1. The windows were mounted in AISI no. 304 stainless steel frames. The schlieren system had a sensitivity of 1 arc second under ambient conditions. The pressure load on the window would be controlled by venting LN₂ into the inner cavity while maintaining a reducing pressure in the cavity between the fused silica and the crown glass windows.

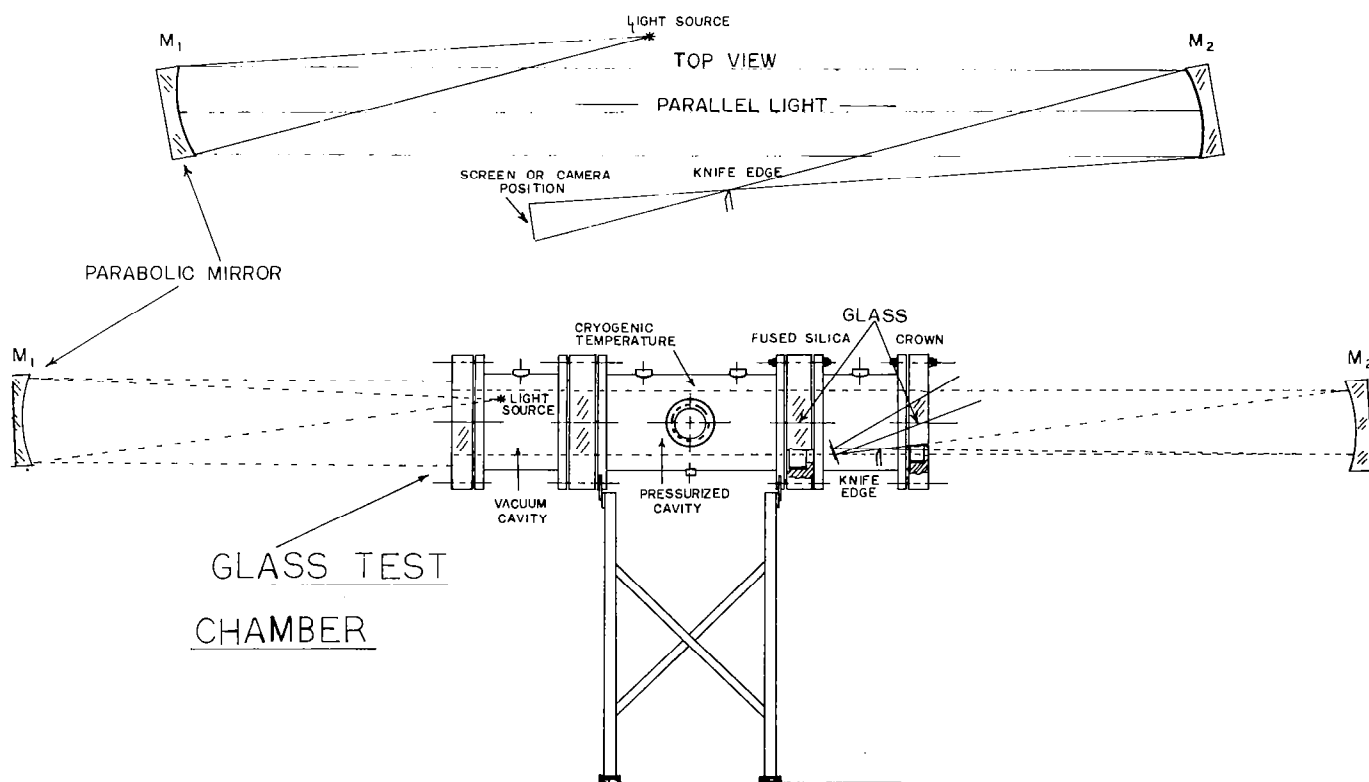


Figure 1

CRYOGENIC TEST CHAMBER

The cryogenic test chamber and schlieren system used to evaluate the window distortion at pressure differentials up to 50 psi and temperatures of 100° Kelvin are shown in figure 2. Changes in the detectable sensitivity of the system due to turbulence in the flow could be noted. The turbulence, however, was so severe it masked any possible "lens effects" due to window distortion.

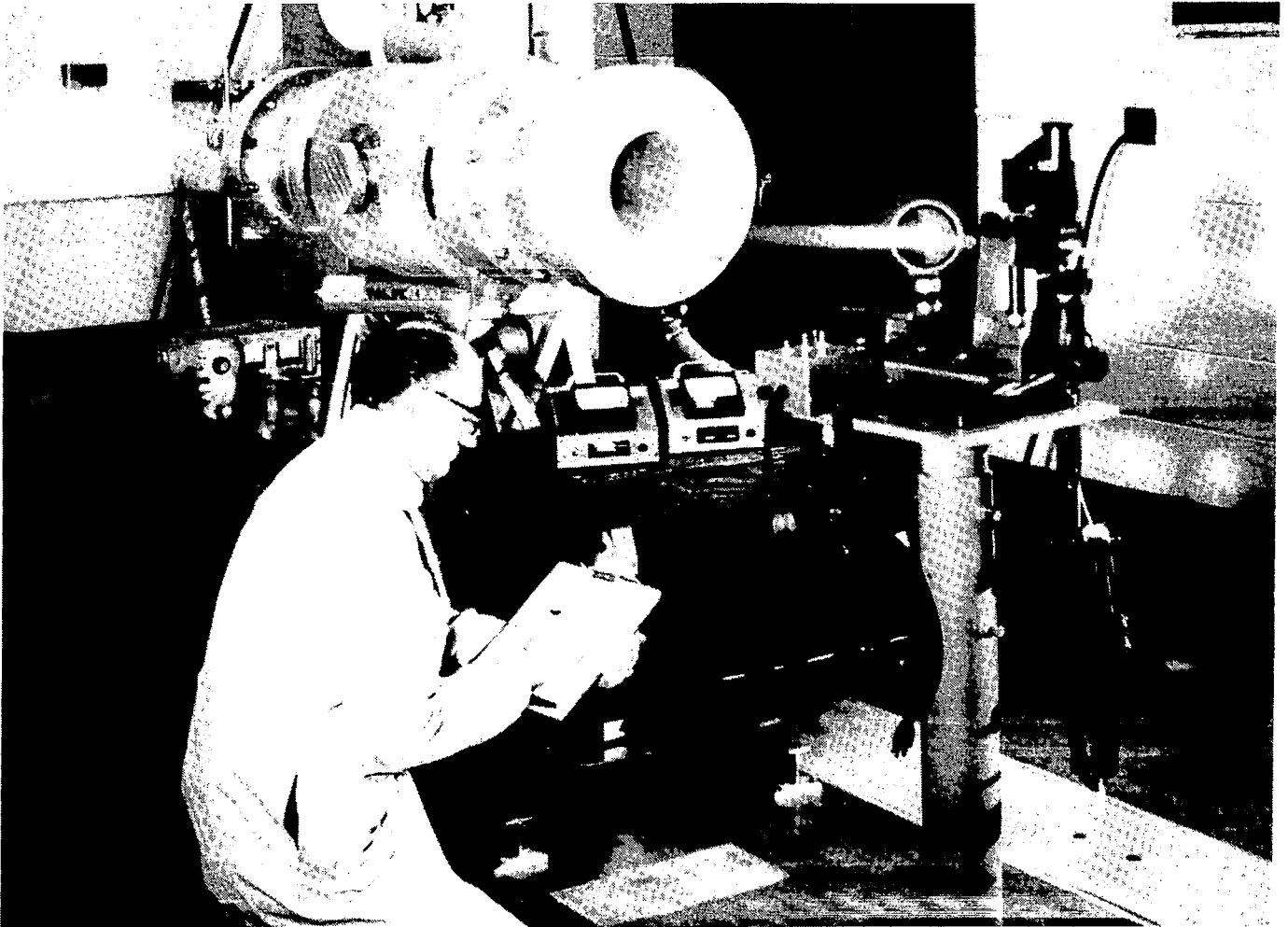


Figure 2

STRESS PATTERNS IN CRYO CHAMBER WINDOWS

The windows can be examined with polarizers and analyzers for stress concentrations during the cryogenic tests. This technique was not sensitive to the chamber turbulence and a heavy "cross" stress pattern was noted during the cooling of the chamber (fig. 3). The pattern and stress were determined to be in the outer crown glass window when the windows were individually checked. Since the window material to be used in the cryogenic tunnels is fused silica, which has a lower coefficient of expansion than crown glass, the distortion in the tunnel windows should be minimal.

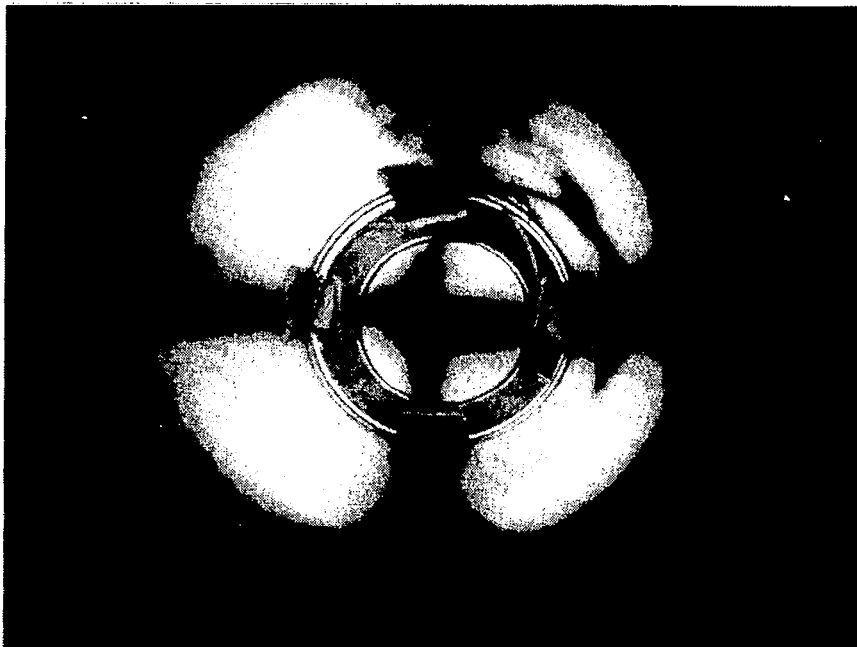
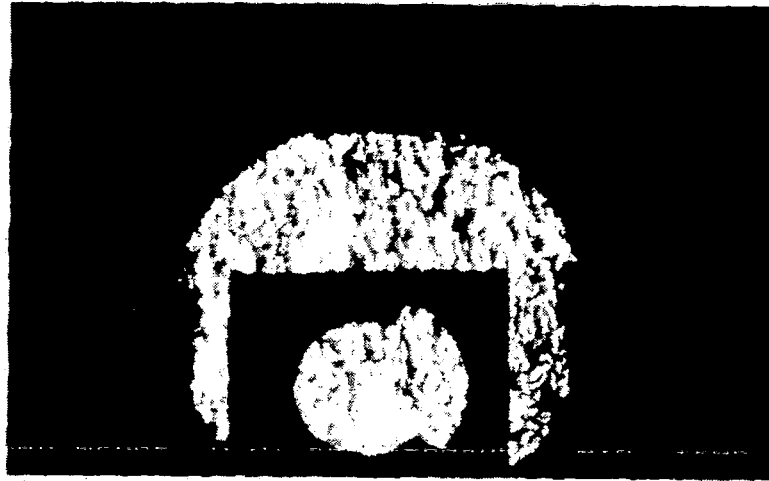


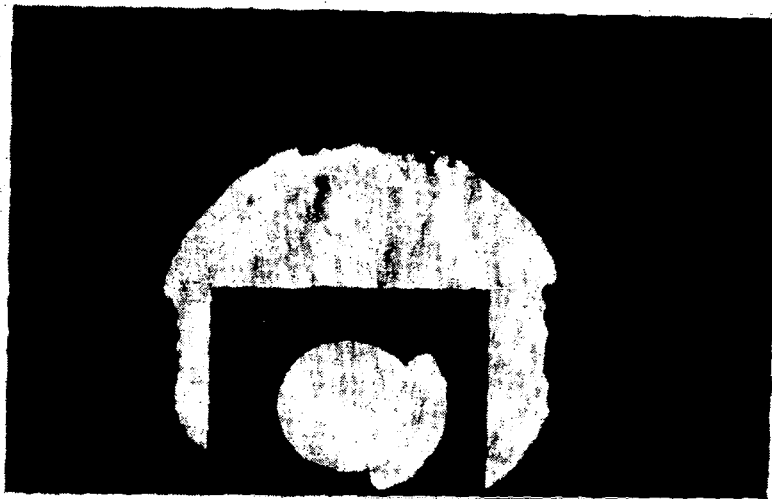
Figure 3

SCHLIEREN PHOTOGRAPHS IN THE CRYO CHAMBER

Schlieren test revealed the turbulence inherent in the chamber tests was a problem and masked the maximum angle of the sensitivity wedge (5 arc seconds). Although longer exposures integrate the turbulence the wedge angle is still obscured and no measurement of the system's sensitivity is possible. Frost and condensation on the chamber windows was a problem and indicated that flow visualization enclosures would be needed for the 0.3-Meter Transonic Cryogenic Tunnel (fig. 4).



3 ARC SECOND WEDGE, 0.01 SEC EXPOSURE, MIN. TEMP. -114°C



5 ARC SECOND WEDGE, 1 SEC EXPOSURE, MIN. TEMP. -123°C

Figure 4

DESIGN OF THE 2-D CRYO-TUNNEL

The schlieren housings were designed for the 0.3-m TCT to enclose the schlieren system. The enclosures or pods could be placed under a partial vacuum or flushed with dry nitrogen to eliminate the frost and condensation that would otherwise form on the plenum chamber windows (fig. 5).

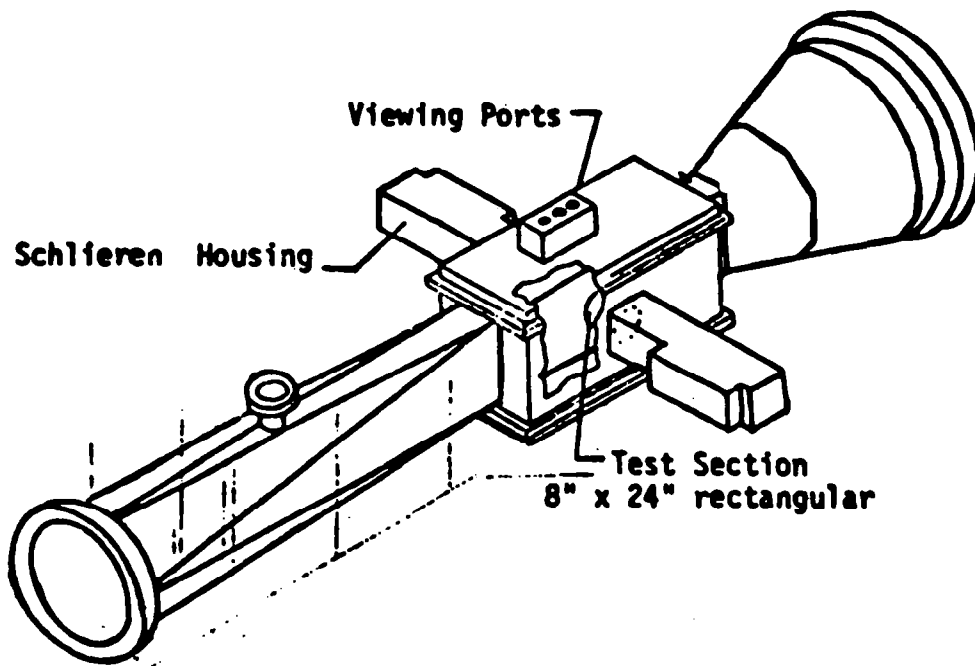


Figure 5

SCHLIEREN SYSTEM AT 0.3-METER TRANSONIC CRYOGENIC TUNNEL

The schematic in figure 6 shows a folded F/8 six inch diameter schlieren system enclosed in the schlieren pods. The light source and camera locations are external to the pods. The system's optical access to the test section is through two fused silica windows in each side of the tunnel. One window is a "D" shaped window mounted in the turntable holding the airfoil and the other window is in the outer plenum wall.

The schlieren system at the 0.3-m TCT has been configured to be similar to those envisioned for NTF and therefore restricted to using video cameras to record the flow visualization data. Alignment of the two pods for schlieren is more easily done at the 0.3-m TCT since the pods are not required to be mobile. The alignment problem will be significant for the NTF if schlieren is used; however, a shadowgraph system would be somewhat easier.

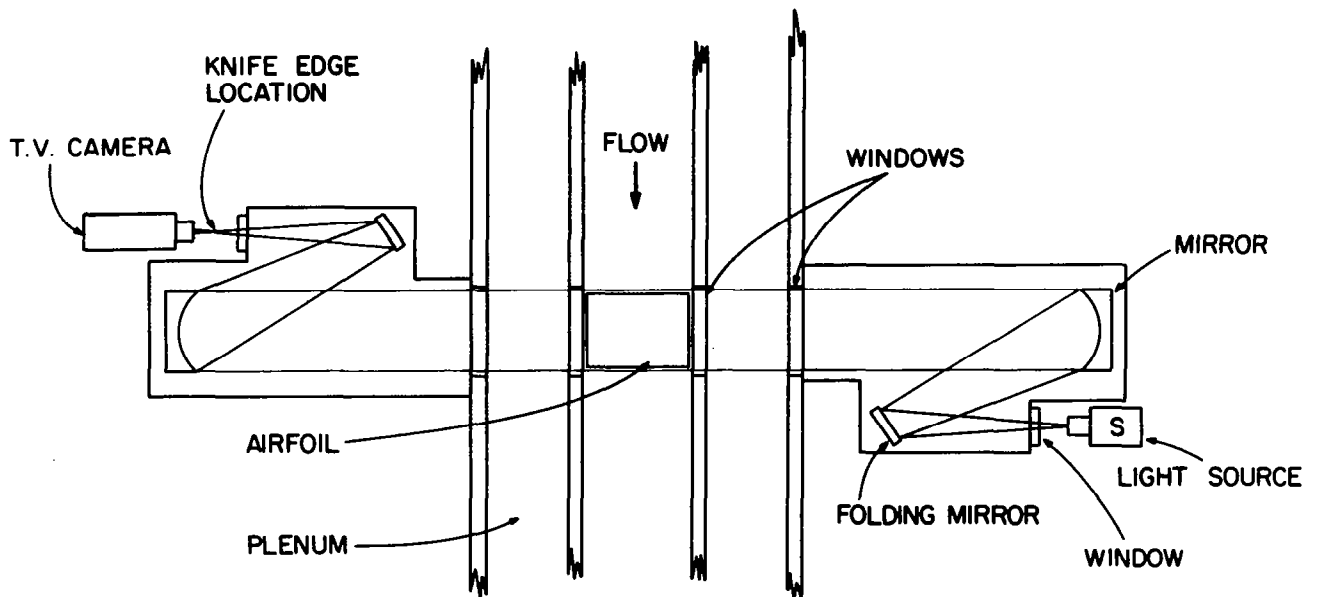


Figure 6

FLOW VISUALIZATION SYSTEM IN CRYOGENIC ENVIRONMENT

The schematic of the flow visualization system is shown at the top of figure 7. The photo on the left shows one of the pods mounted on the 0.3-m TCT. The right photograph shows two pods mounted on the tunnel which has the top of the test section removed to reveal the plenum area and the airfoil. The bottom photo shows the "D" shaped window mounted in the airfoil turntable which has been lifted out of the test section.

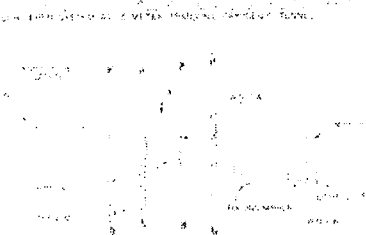
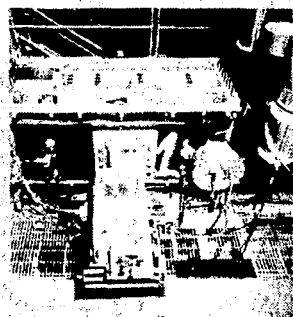


Figure 7

CRYO-TUNNEL WINDOW DESIGN

Prior to the tunnel runs in the 0.3-m TCT we experienced several window failures. One problem was the "D" window in the turntable was designed with an inside corner (fig. 8). Although the corner had a 0.063 inch radius it proved to be an area for crack growth. The window was changed to a double-beveled design having all outside edges. The window is mounted in a split frame which is bolted to the tunnel. Although none of the double beveled windows has failed the larger outer fused silica windows have experienced edge fractures and have been replaced. These fractures appeared to be due to compression so the AISI no. 304 stainless steel frames were enlarged and a foam teflon gasket was inserted to avoid any metal/glass contacts. As a result of this experience the windows for the NTF will have Invar frames and shall be doubled-beveled.

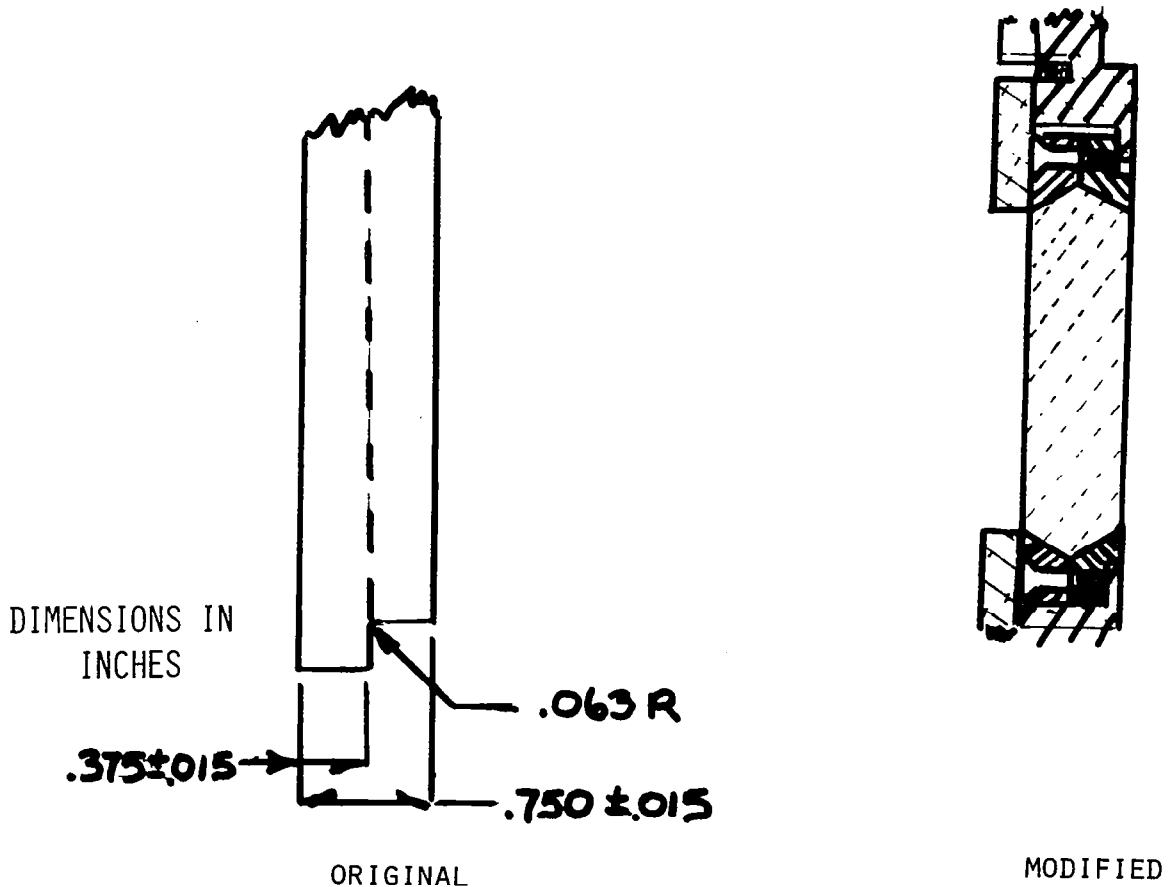


Figure 8

NTF TEST SECTION - TOP VIEW

There is a difference in the pod concept for the 0.3-m TCT and what will be necessary for NTF. Any NTF visualization system will have to be totally in the plenum area. The space constraints are shown in the NTF test section top view (fig. 9). The area that would be available for the protective pods is approximately 12.5 feet by 3 feet. The system can not be placed so as to block access to the test section so it will have to be mobile. The model may be as large as the six foot model shown. Optical access to the test section will be through windows mounted in the test section door, three windows on each side.

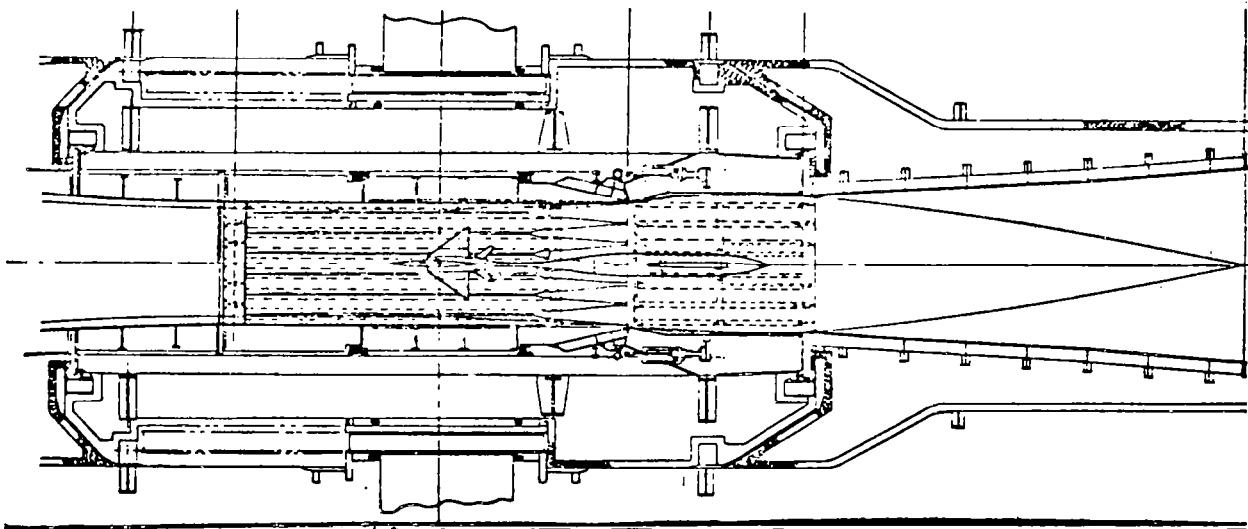


Figure 9

NTF TEST SECTION DOOR - END VIEW

The NTF test section door can have windows mounted in the central area. The door is hinged to move vertically. The area that is located in figure 10 to the left of the door in the plenum is the area available for the flow visualization system. There are about 3.5 feet from the center line through the door to the bottom of the upper "I" beam.

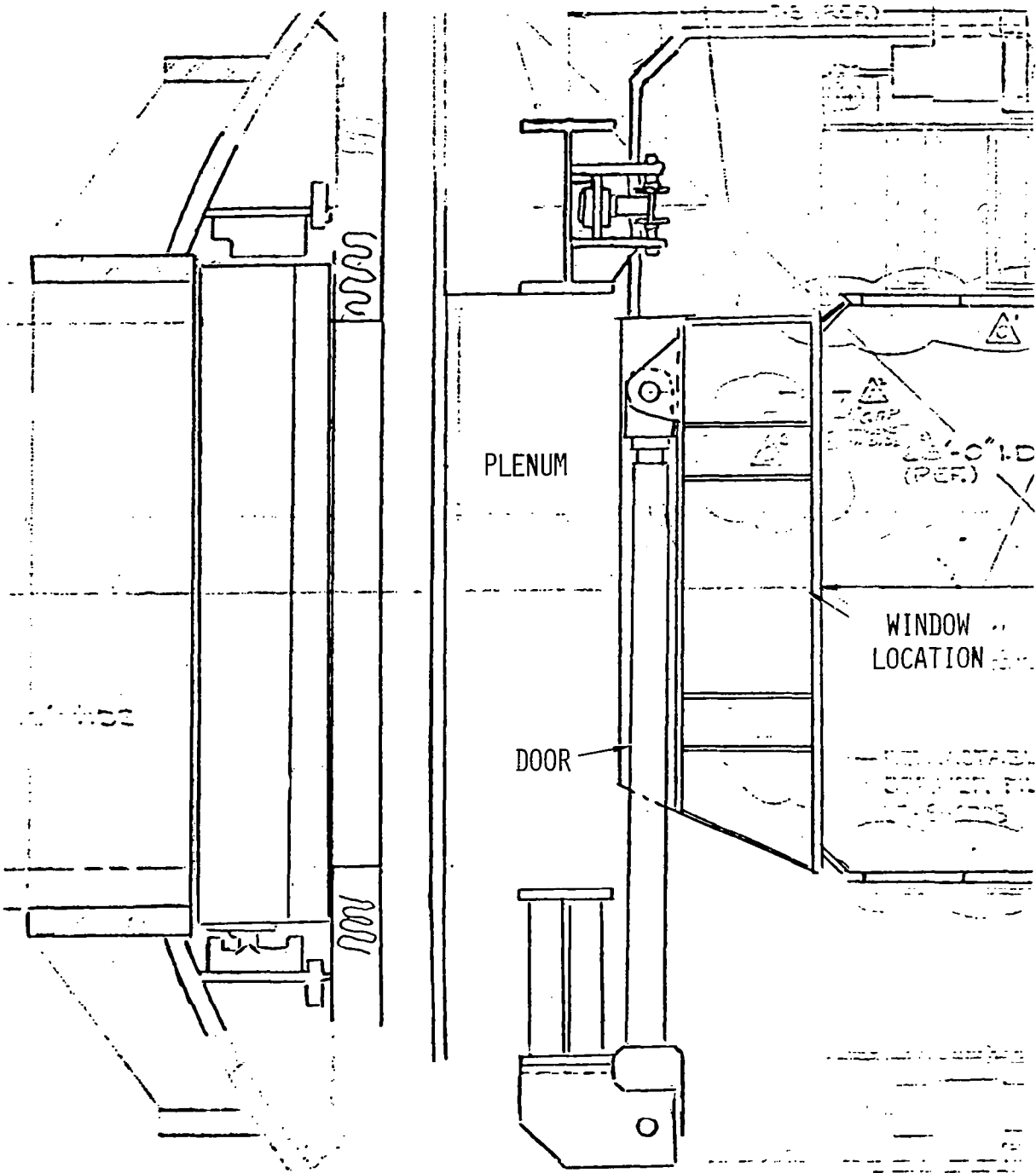


Figure 10

PRELIMINARY NTF SCHLIEREN SYSTEM CONCEPT

A conceptual design for the protective pods for the NTF system is shown in figure 11. The three quartz or fused silica windows are shown in the sides of the test section. The pods contain a 24-inch F/5 system which would allow about 2 feet of the model to be examined at any time. The data would be recorded on video cameras to permit rapid access to the data and avoid problems with the photographic films at cryogenic temperatures.

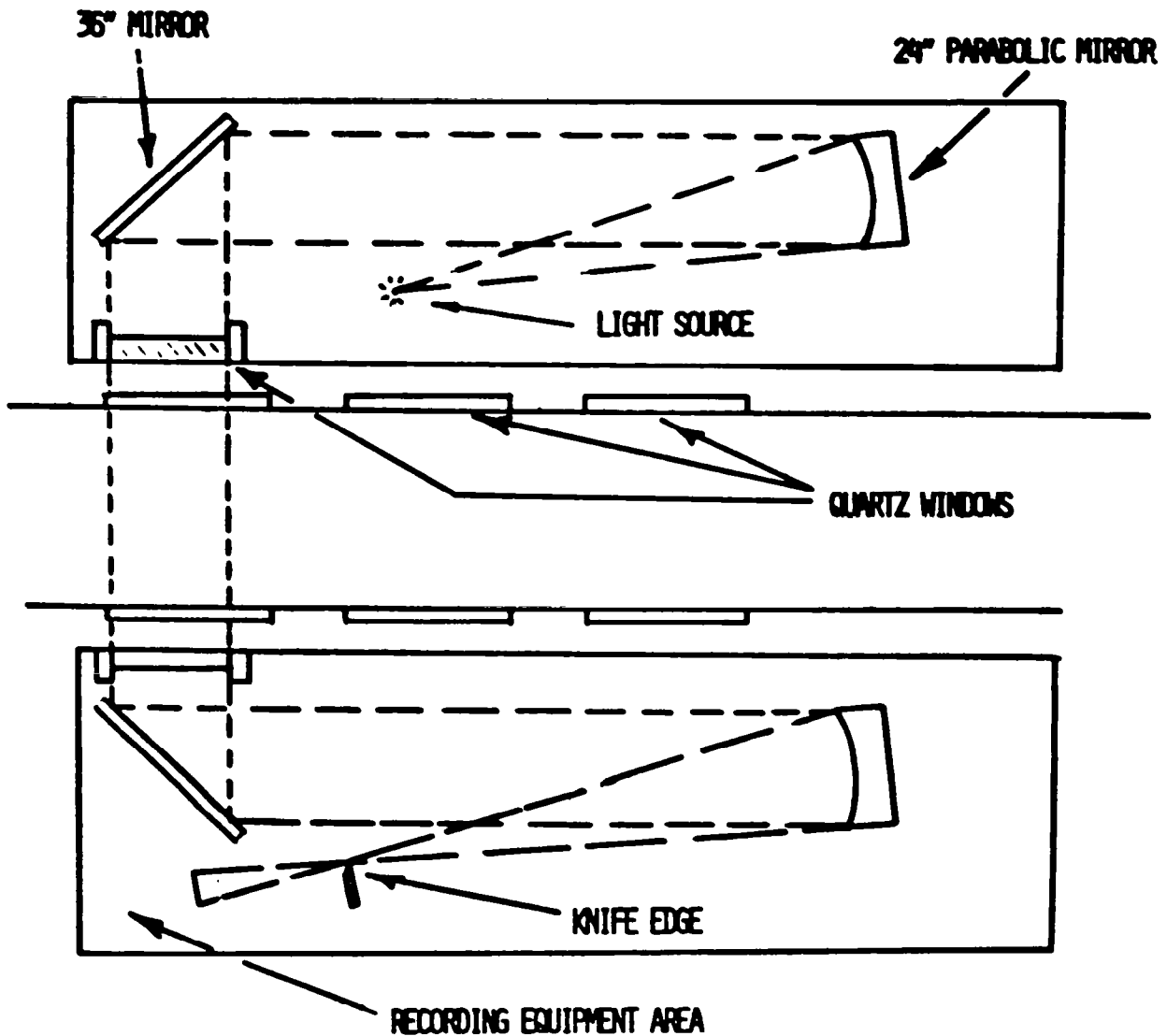


Figure 11

MOIRÉ DEFLECTOMETRY SYSTEM AT 0.3-m TCT

The pods could also be used for another technique that appeared to have promise: the moiré deflectometer (fig. 12). This technique uses the first pod with no changes from the schlieren system as a direct shadowgraph method. Refraction information can be encoded by two grids on the shadowgraph taken in the second pod by the video camera. The relative rotation between the two grids determines the direction and spacing of the resulting moiré pattern. The grid to grid spacing in the collimated light beam determines the sensitivity of the system for a particular grid frequency. In this test the grid frequency was about 2 lines per millimeter (50 lines per inch) and their separation was 131 millimeters. The sensitivity is calculated to be approximately 8×10^{-4} grams-cm⁻⁴ for a shift of one moiré fringe.

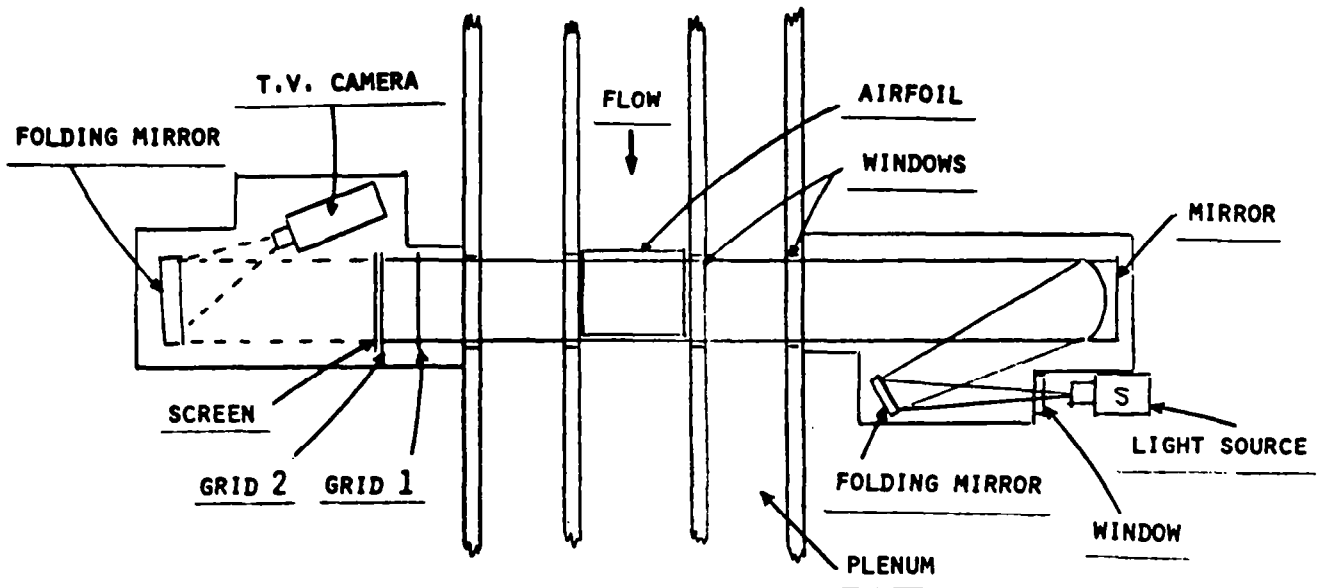


Figure 12

FLOW VISUALIZATION TECHNIQUES

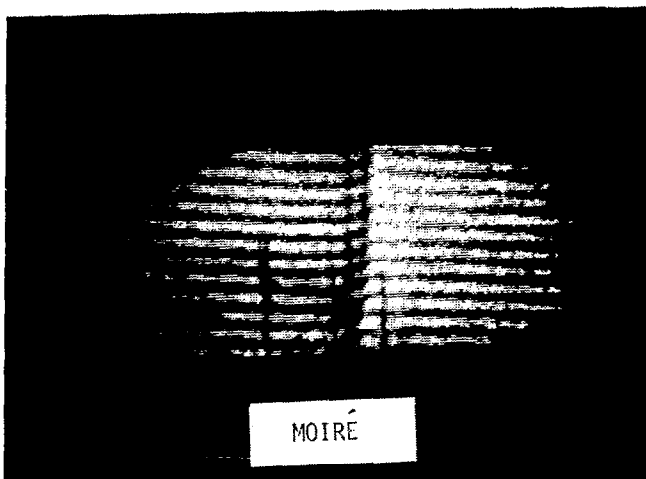
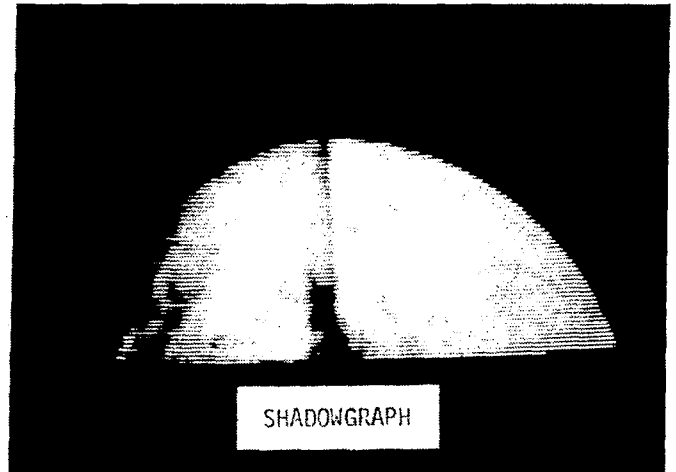
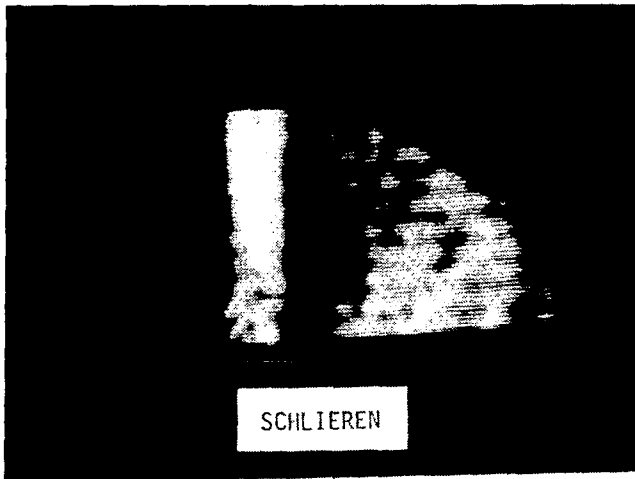
A generalization on the flow visualization techniques we studied is shown in figure 13. The column "simplicity" refers the ease of alignment and setup. The four techniques are shadowgraph, schlieren, interferometry and moiré. The interferometry (holographic) work was done by Al Burner and is covered in his presentation (paper 20 of this compilation). The shadowgraph system is the easiest to set up, least expensive and least sensitive, detecting mainly shocks. The schlieren technique is intermediate in all categories and can detect density gradients. The moiré technique is similar to the shadowgraph in simplicity and cost but has a sensitivity more like a schlieren system.

<u>TECHNIQUE</u>	<u>SIMPLICITY</u>	<u>RELATIVE COST</u>	<u>SENSITIVITY</u>
SHADOWGRAPH	SIMPLE	LOW	LEAST SENSITIVE
SCHLIEREN	INTERMEDIATE	INTERMEDIATE	INTERMEDIATE
INTERFEROMETRY	COMPLEX	EXPENSIVE	MOST SENSITIVE
MOIRÉ	SIMPLE	LOW	INTERMEDIATE

Figure 13

EXAMPLES OF FLOW VISUALIZATION AT 0.3-m TCT

The results of the three flow visualization techniques are shown in figure 14. The model was a NACA 0012 airfoil mounted about half an inch below the window. The angle of attack was 0 degrees, Mach number was 0.85, temperature was 190° Kelvin and the pressure was 30 psi. Flow is from left to right and the midpoint on the 6 inch chord is indicated by the taller line on the moiré photograph. For scale the shorter lines in the photograph are located one inch on either side of the midchord line. The schlieren photo is of lower quality than expected. The video camera maintains a constant current and as the knife edge is introduced the gain is increased and a good gray scale cannot be attained. The shadowgraph shows the heavy shock. The moiré deflectometry pattern remained stable and a shift of almost one fringe was detected through the shock which corresponds to a density gradient of nearly $8 \times 10^{-4}(\text{g}/\text{cm}^3)/\text{cm}$. The preliminary recommendation is for the selection of moiré deflectometry as the best technique for flow visualization at NTF.



PRESSURE - 30 PSI
TEMPERATURE - 190° K
MACH NUMBER - .85
ANGLE OF ATTACK - 0°

Figure 14

"SEEING" THROUGH FLOWS IN LANGLEY'S
0.3-METER TRANSONIC CRYOGENIC TUNNEL

W. L. Snow, A. W. Burner, and W. K. Goad
NASA Langley Research Center
Hampton, Virginia 23665

INTRODUCTION

Cryogenic wind tunnels are being developed to enable testing at realistic Reynolds numbers. Such facilities take advantage of the increasing density and decreasing viscosity associated with cooling. When coupled with high pressure operation, these tunnels can provide aeronautical engineers with full scale Reynolds number simulation. The high dynamic pressures available in many of these test environments coupled with reasonable large and slender models can effect considerable deformation. Wing tips are expected to deflect 2 to 3 inches over 30 inch spans for some configurations in the NTF. The test engineer is faced with the dilemma of having unique data on an unknown model geometry unless ancillary measurements can provide simultaneous topological information. Virtually all of the proposed techniques being considered to discern model deformation including stereo photogrammetry, moiré topology, or surface LED trackers presume that identifiable targets can be viewed clearly and unambiguously thru the flow field. The tests described herein were made to shed light on these problems and were conducted in the Langley 0.3-Meter Transonic Cryogenic Tunnel.

IDEALIZED TARGET PROFILES

For purposes of modelling the problem, it is convenient to represent the ideal target as a rectangular distribution of energy (or image density). When viewed under less than ideal circumstances the distribution will in general shift and or become diffuse as suggested in figure 1. These effects directly influence the accuracy of model deformation data.

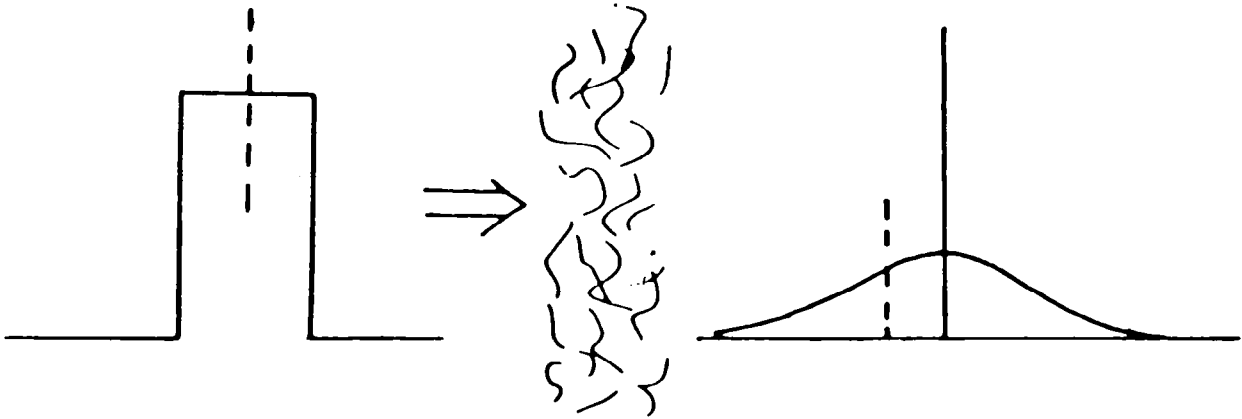


Figure 1

EFFECT OF CONDENSATION OVER AIRFOIL

Condensation and turbulence are potential problem areas. Cryogenic facilities work close to the condensation line to maximize the cryogenic advantage. Figure 2 shows the effect as saturation is increased by holding pressure constant and decreasing temperature. These areas will be avoidable by effective use of the operating envelope of the facility. As the condensation curve is approached, say by holding pressure constant and decreasing temperature, then 'fog' begins to appear. This is shown in figure 2 with density increasing from (a) to (d) with case (d) representing complete 'white out' as the liquid-vapor curve is crossed.

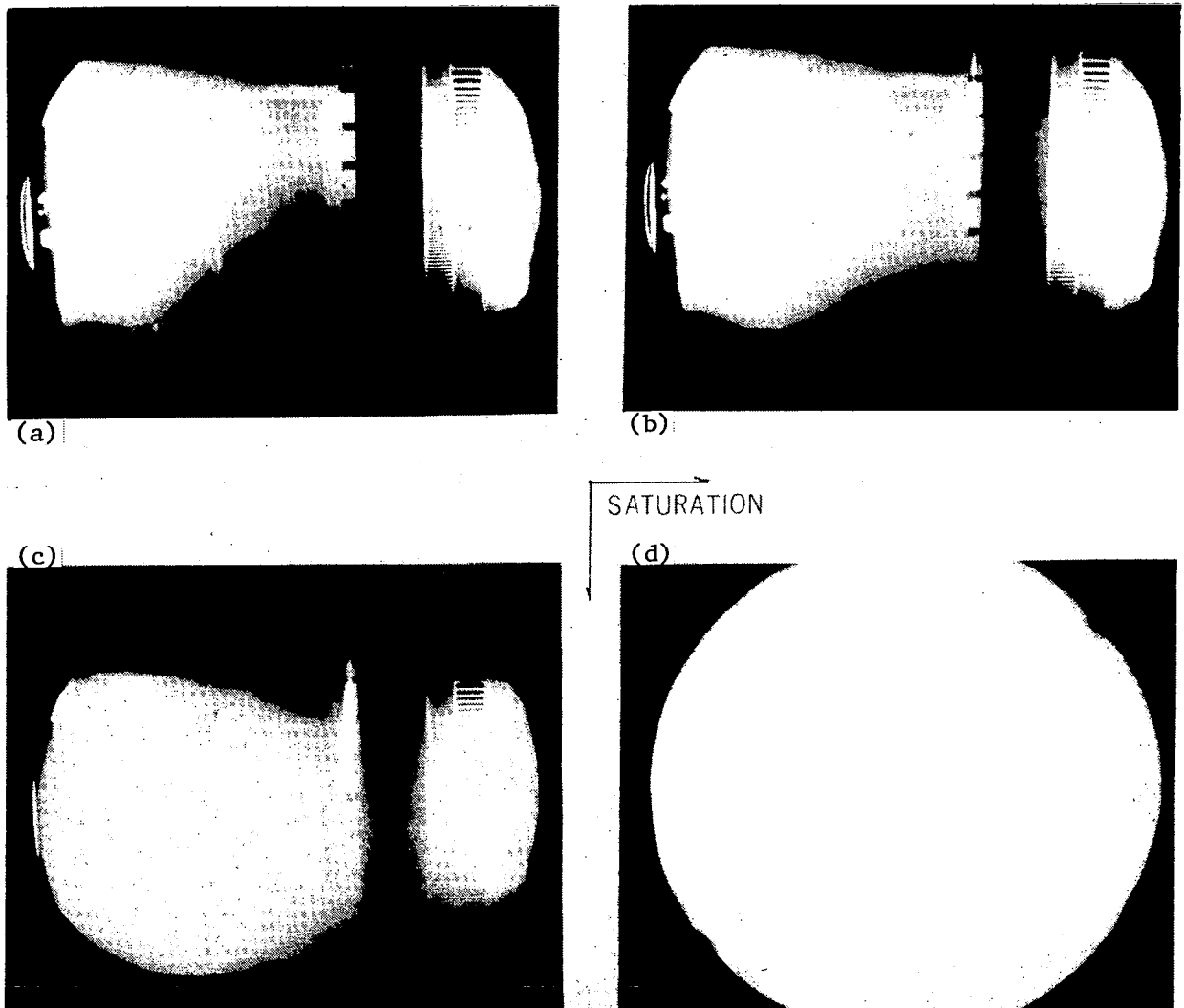
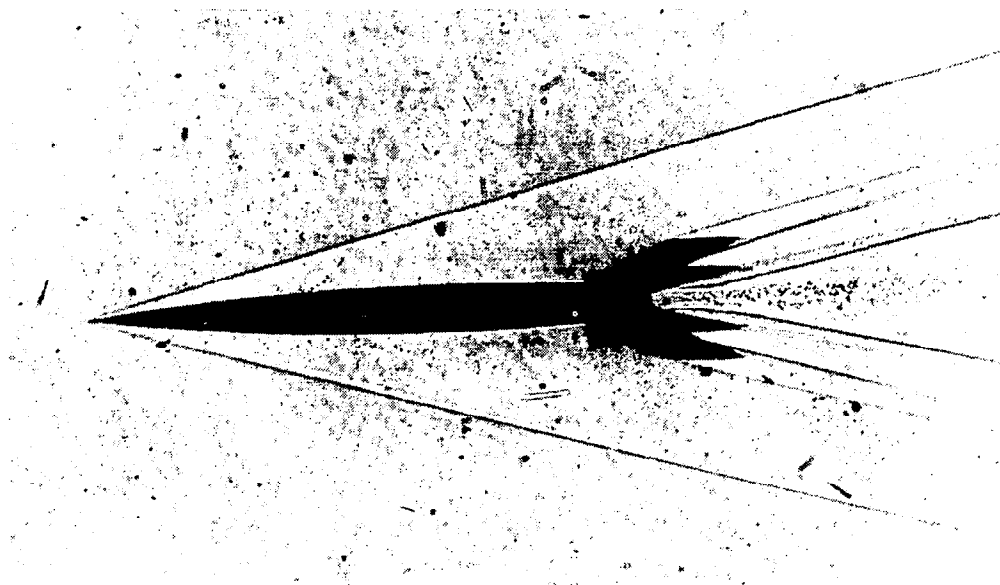


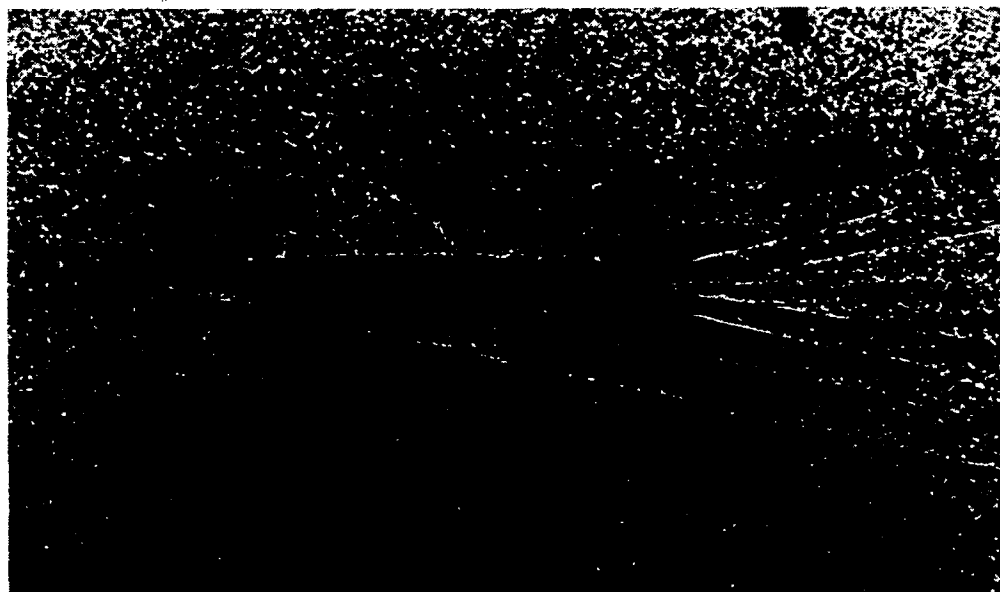
Figure 2

EFFECTS OF TURBULENT BOUNDARY LAYERS

Turbulence as suggested in figure 3 will be less forgiving and unavoidable. These photos from NACA RM A56B21 show focussed shadowgraphs for still air (a) and in the presence of flow induced turbulent boundary layers (b). Boundary layer effects will undoubtedly impose limits to image quality and will be assessed for NTF during the shakedown testing.



(a) Tunnel Mach number = 0; missile Mach number = 1.



(b) Tunnel Mach number = 2; missile Mach number = 5

Figure 3

PHOTOGRAPHY THROUGH THE SIDE WINDOWS

To quantitatively assess image quality, the Modulation Transfer Function (MTF) of the optical designer is used. An image can be decomposed into its two dimensional Fourier spatial frequencies. The MTF is a plot of the relative efficiency of the system to pass these frequencies. To measure the response, a logarithmically increasing density of bars (Sayce target) is photographed through the flow as shown in figure 4. The diffusely illuminated target is viewed through the flow using a 70 mm camera with telephoto lens. Equipment is housed in sidemounted schlieren pods.

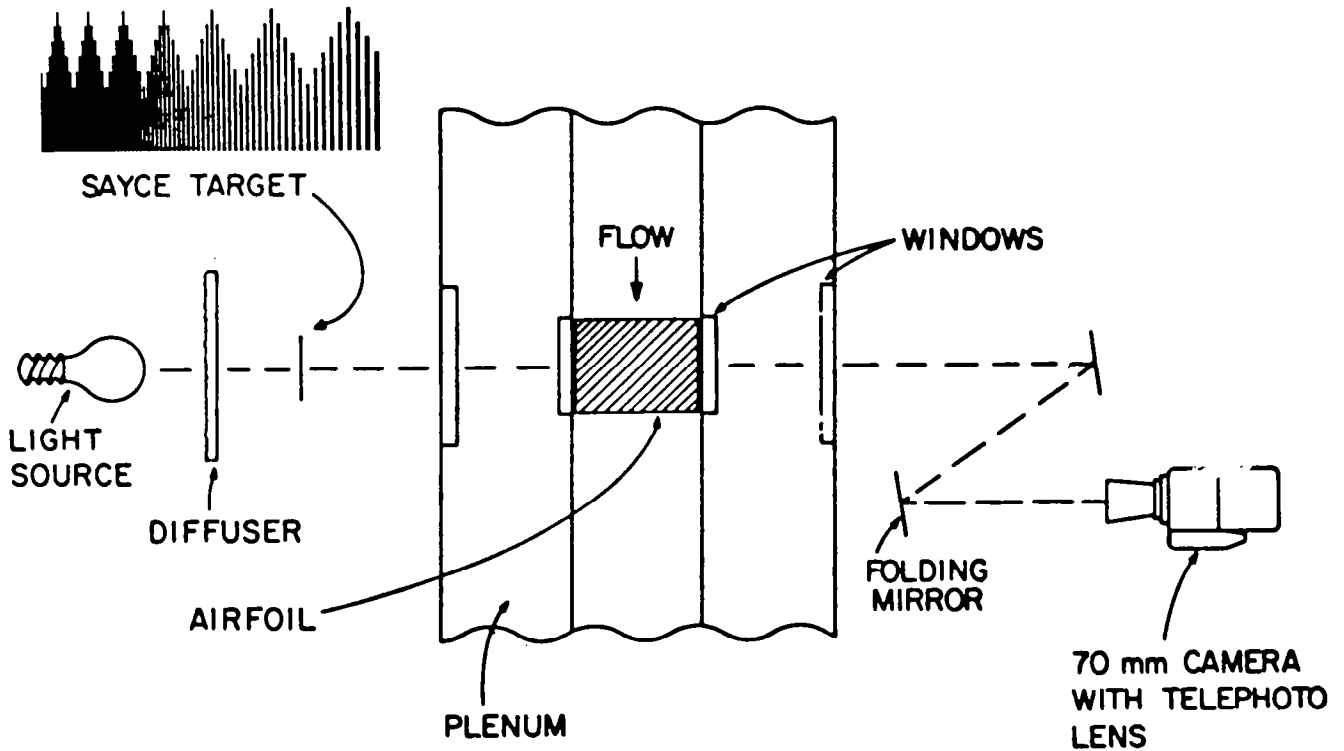


Figure 4

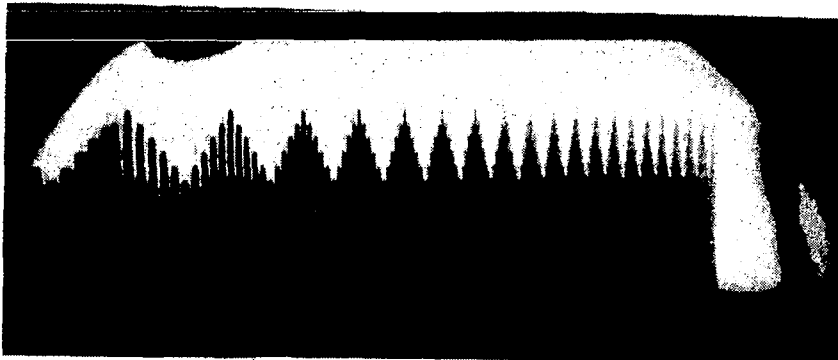
PHOTOGRAPHS OF SAYCE TARGETS

An ideal system would resolve even the finest lines. The upper photo in figure 5 represents the mildest flow condition encountered in this facility while the lower shot represents a temperature induced density increase of only 2.5. The coarsest grid lines are barely discernible even at these modest conditions.

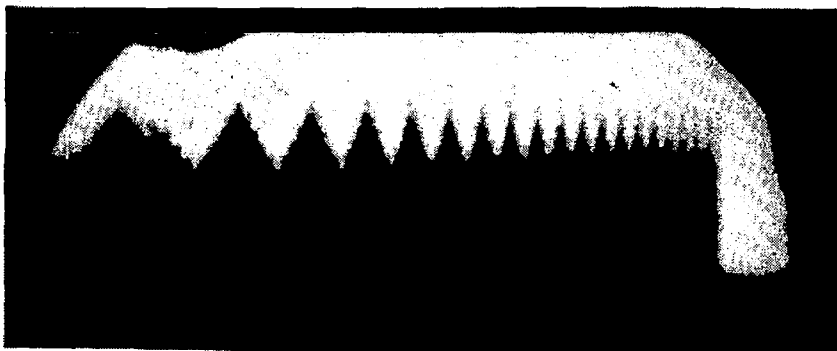
$$P = 1.2 \text{ ATM.}$$

$$M = 0.65$$

$$\alpha = 6^\circ$$



250 K



100 K

Figure 5

DENSITOMETER TRACES OF SAYCE TARGETS

Densitometer traces corresponding to figure 5 are shown in figure 6. The top trace is for 1.2 atmospheres and 250 K while the lower is for 1.2 atmospheres and 100 K. The vestiges of a shock can be seen against the Sayce background as a dip in the modulation near the coarse edge of the target.

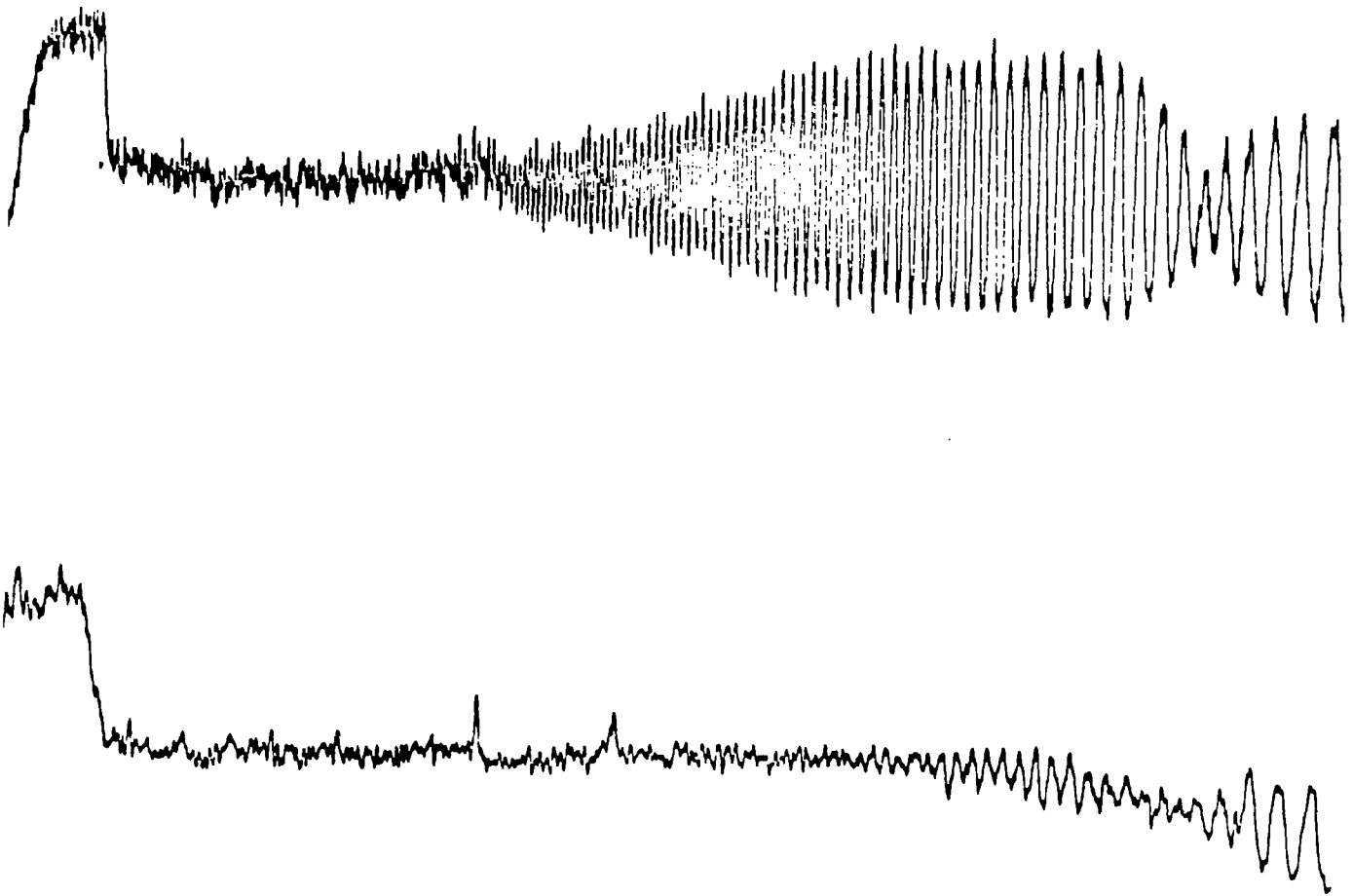


Figure 6

PHOTOGRAPHY THROUGH THE TOP WINDOW

To more closely approximate the model deformation format, a target was contact printed on stripping film and the film applied to the surface of an airfoil. The target was photographed using the relay system shown in figure 7.

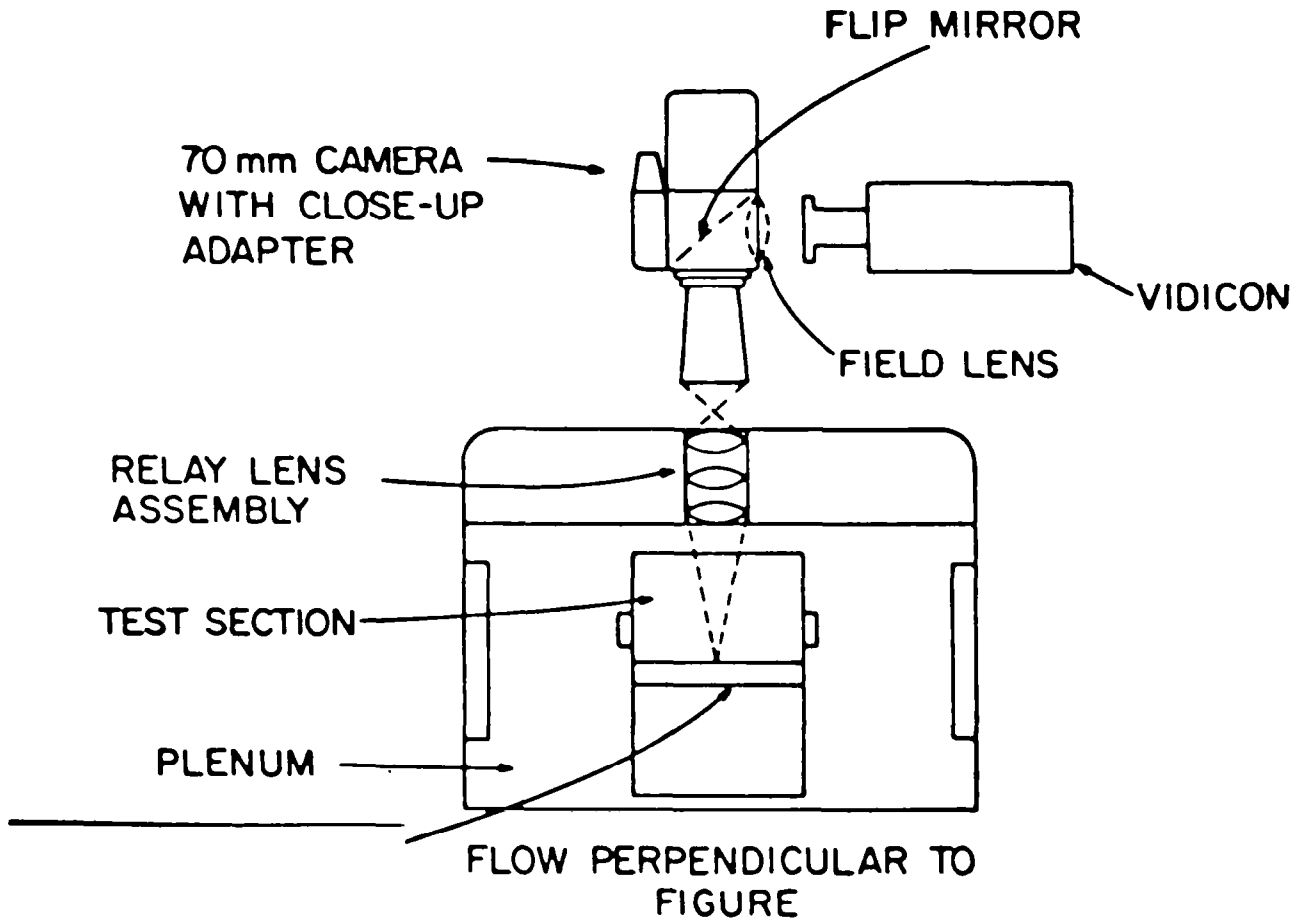
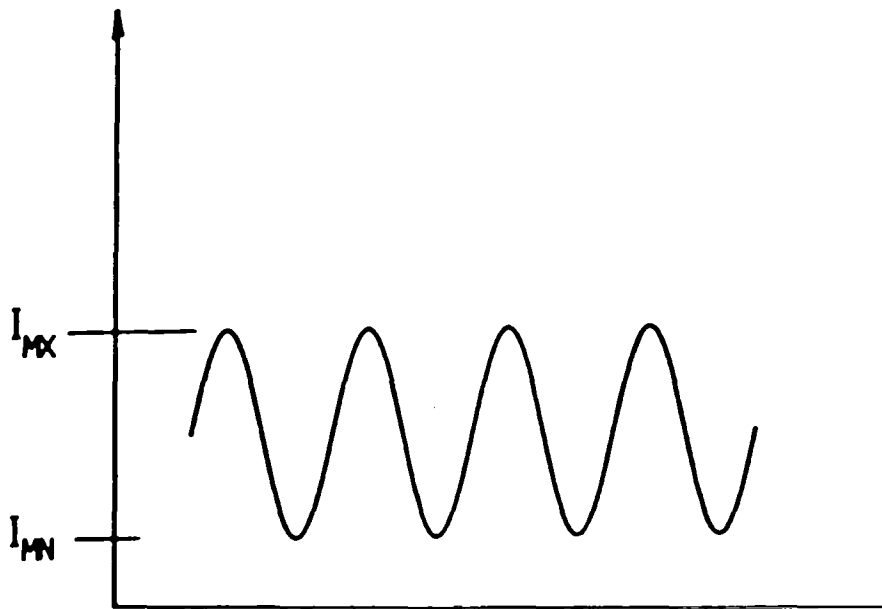


Figure 7

DEFINITION OF THE MODULATION FUNCTION

The photos made using the relay system were remarkably crisp. A quantitative evaluation was made by plotting the response as a function of spatial frequency. The contrast as defined in figure 8 was measured. If I_{mn} is zero then $V = 1.0$ and you have a perfect contrast whereas if I_{mn} equals I_{mx} there is a complete redistribution of energy to a dc value, the contrast is zero and results in complete information loss.



$$V = \frac{I_{MX} - I_{MN}}{I_{MX} + I_{MN}}$$

Figure 8

RESPONSE FUNCTIONS

Response functions for two test conditions obtained using both top and side viewing configurations are shown in figure 9. Some degradation is expected with increased density but the large discrepancy between top and side results were puzzling and prompted further investigation. The response is defined as the ratio of measured to reference modulation.

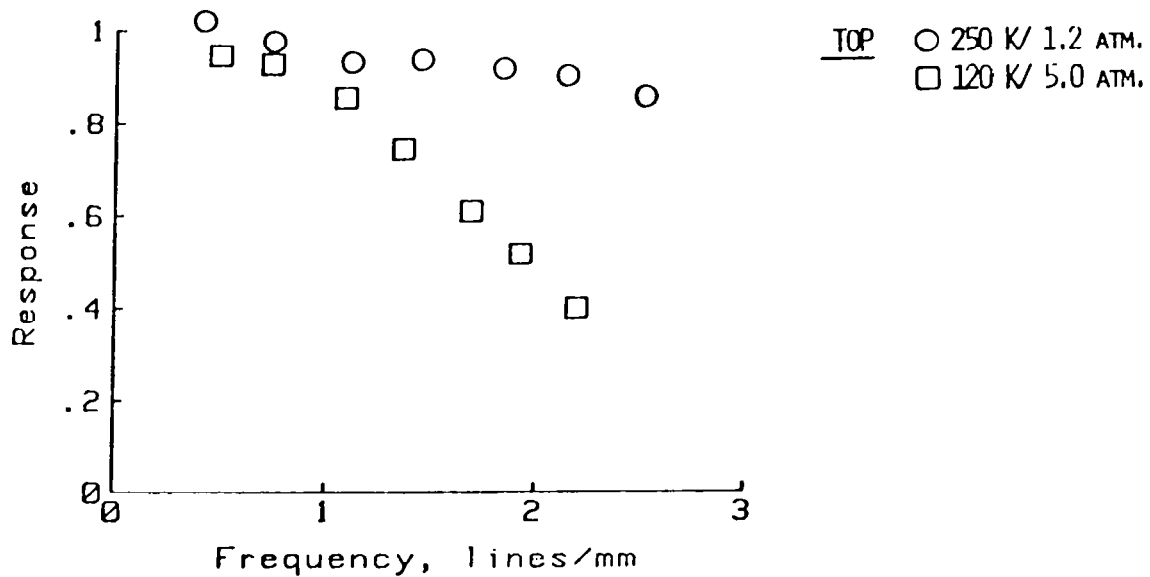
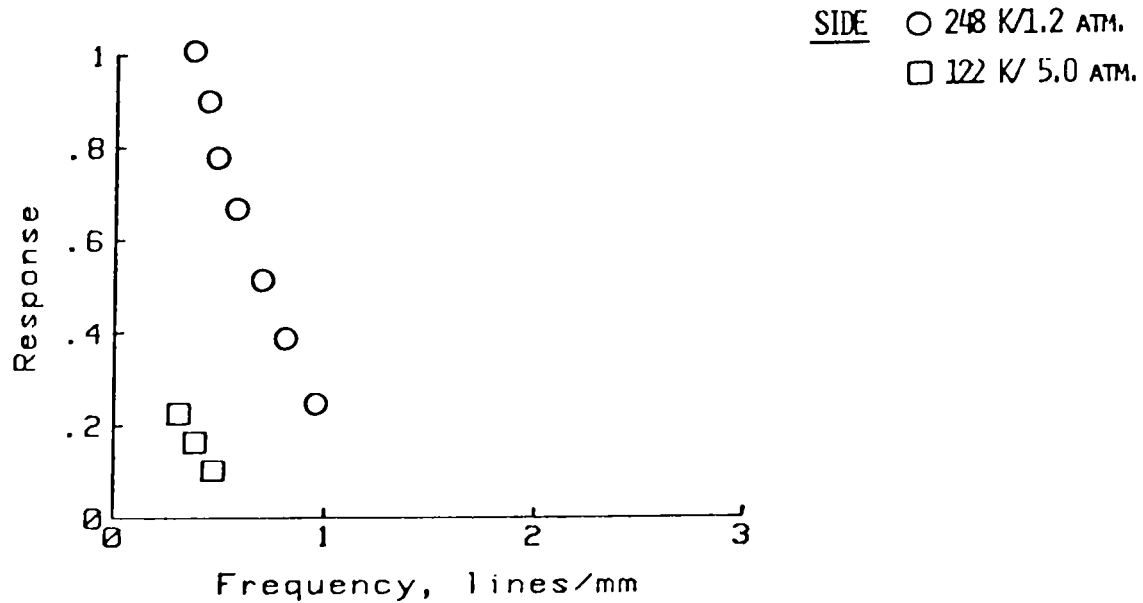


Figure 9

REPEAT OF SIDE WINDOW EXPERIMENT WITH EACH WINDOW TARGETTED

The discrepancy prompted a return to the pod experiment with targets affixed to each window (shown shaded in figure 10) and the camera mounted on a track to allow viewing of each target individually at each tunnel condition. The critical station proved to be that nearest the camera and outside of the flow. The effect was attributed to vibration which was progressively worse as the tunnel approached its operating envelope.

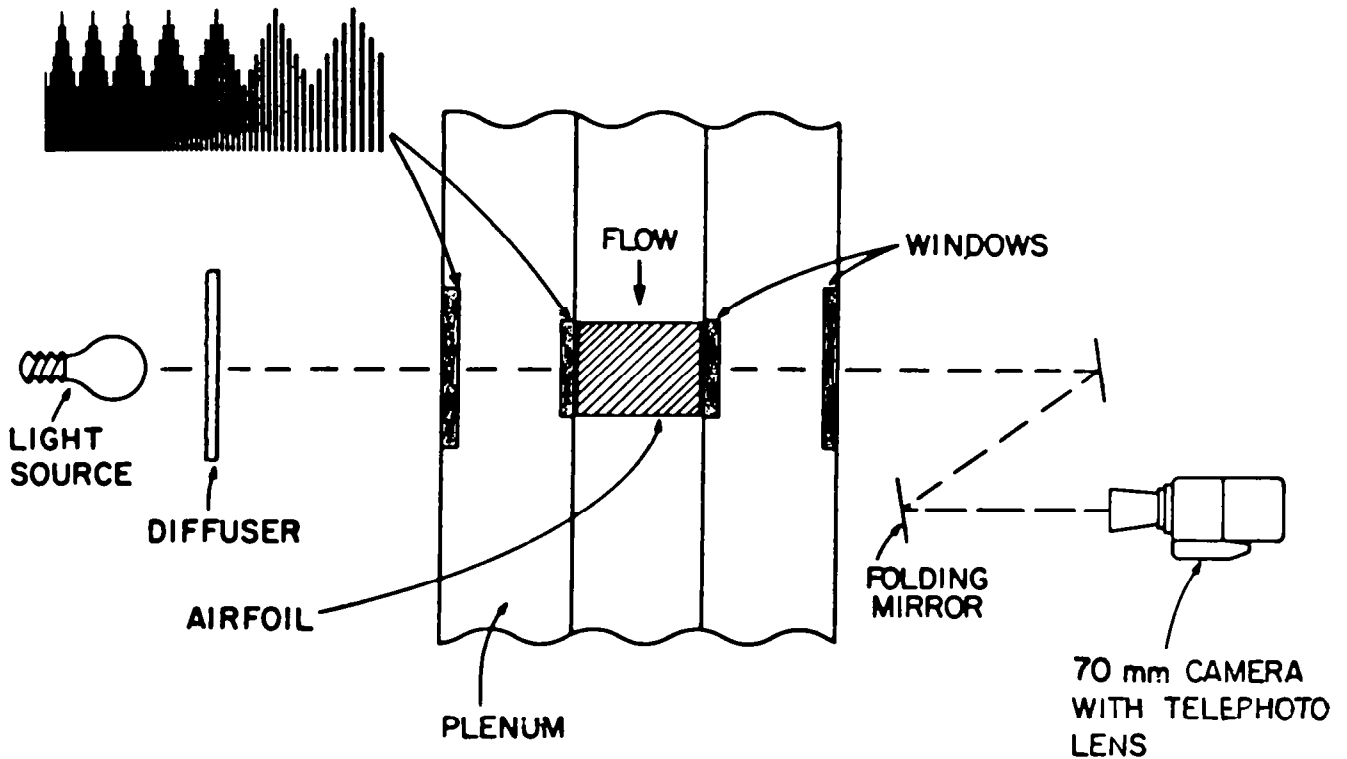


Figure 10

REVISED RESPONSE FUNCTIONS

When several independent mechanisms contribute, their MTF's multiply together to obtain the system MTF. The transfer function relating to vibration could be determined by examining the data for the nearest station to the camera since it was outside the flow. When this information was used to correct the earlier results (solid symbols) the data became consistent with that for the top shots as shown in figure 11.

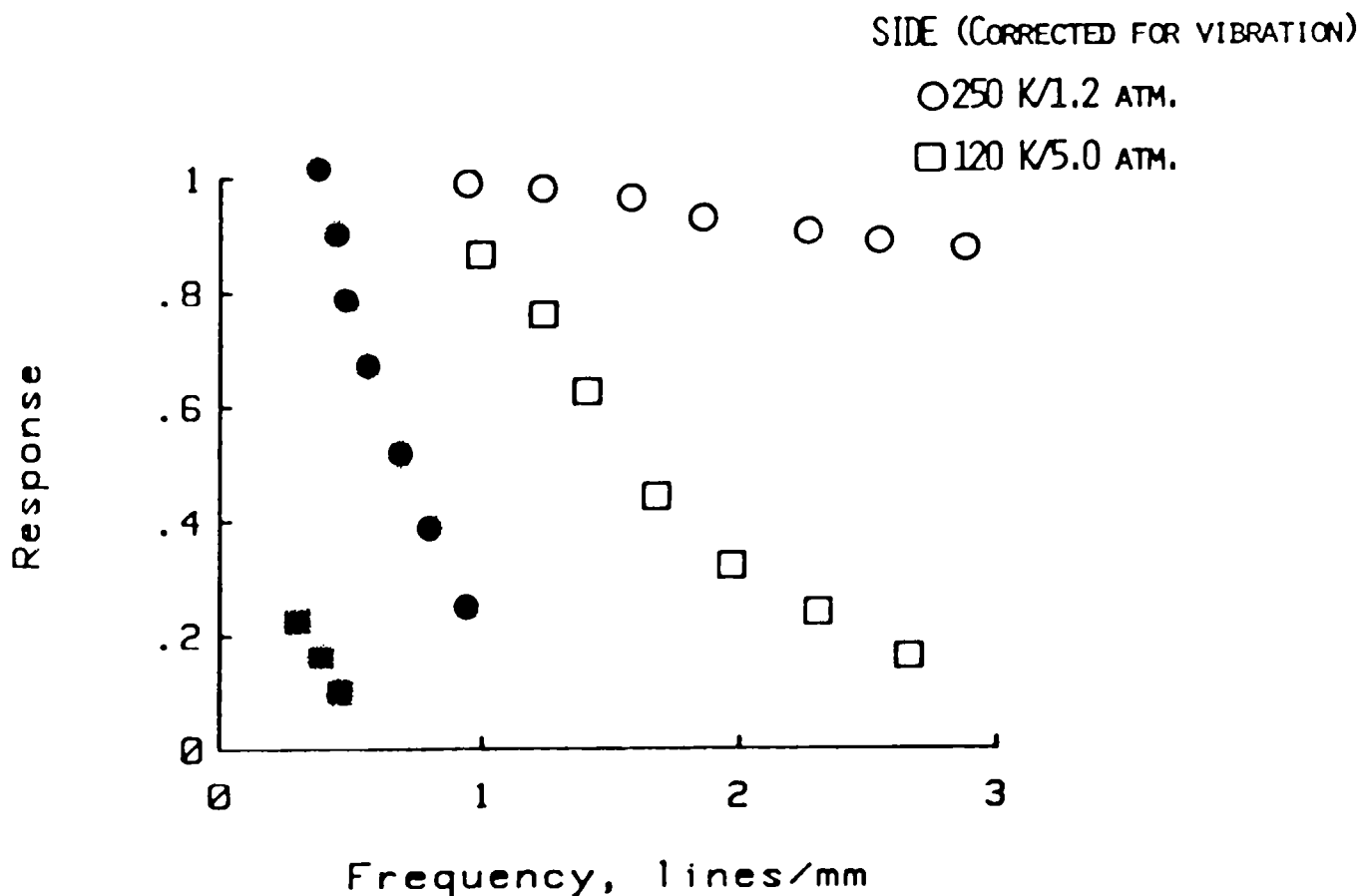


Figure 11

MODELLING IMAGE DEGRADATION USING EXPERIMENTAL RESULTS

The energy distribution for an ideal target can be represented by a step function as shown in figure 12. This distribution can be decomposed in a Fourier series. Each of these coefficients is tied to a spatial frequency. If the MTF is unity for a particular frequency then the corresponding coefficient is unchanged. Otherwise it is multiplied by the fractional response thus attenuating its contribution. If the square wave is reconstructed with coefficients modified by the MTF depicted by open squares in figure 11 the result is shown as the attenuated and extended curve in figure 12. The energy is redistributed and the contrast reduced. Note that this was for a flow-off condition and therefore does not include turbulence effects.

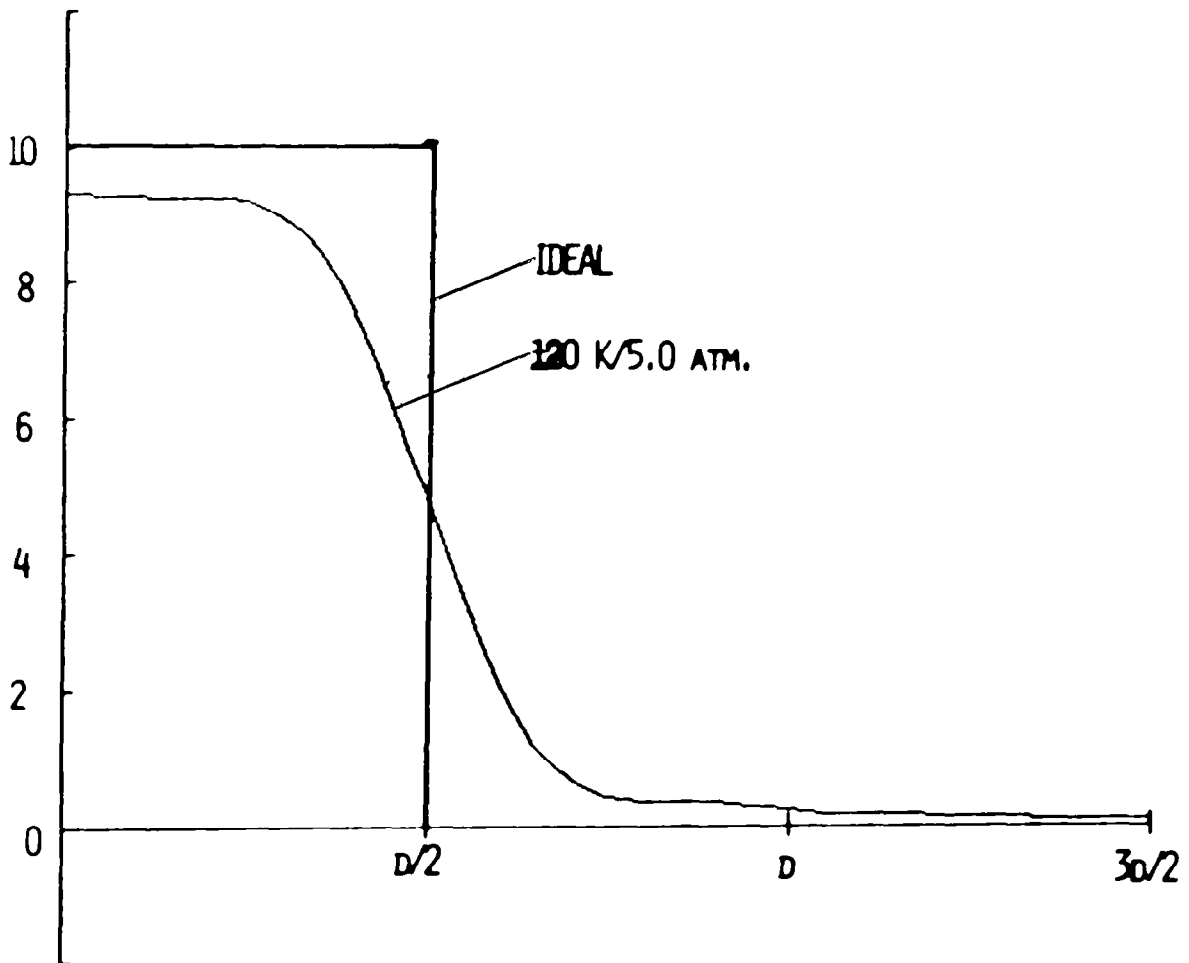


Figure 12

SUMMARY COMMENTS

DEGRADATION DUE TO INCREASED DENSITY, THOUGH MEASURABLE, SHOULD NOT IMPACT THE MODEL DEFORMATION APPROACHES.

EFFECTS OF TURBULENT BOUNDARY LAYERS ARE UNAVOIDABLE AND WILL BE ASSESSED ON SITE.

VIBRATIONAL DEGRADATION COULD DOMINATE THE PREVIOUS EFFECTS AND WILL BE MONITORED AND GUARDED AGAINST BY DESIGN OF CAMERA ENCLOSURES.

HOLOGRAPHIC FLOW VISUALIZATION -
STATE-OF-THE-ART OVERVIEW

J. D. Trolinger
Spectron Development Laboratories, Inc.
Costa Mesa, California

STATE-OF-THE-ART HOLOGRAPHY TECHNIQUES/FRONTIERS

- TOMOGRAPHY
- AUTOMATED DATA REDUCTION
- ON-LINE INTERFEROGRAM PRODUCTION
- HETERODYNE HOLOGRAPHIC INTERFEROMETRY
- CINE HOLOGRAPHY

APPROACHES TO AUTOMATED INTERFEROGRAM DATA REDUCTION

- (SEMI-AUTOMATIC) USE GRAPHIC TABLET TO DIGITIZE FRINGE POSITION
- USE IMAGE ANALYZING COMPUTER TO DIGITIZE FRINGES
- USE MOVING FRINGES WITH PHASE DETECTING ARRAY

LABORATORIES USING LARGE-SCALE HOLOGRAPHIC FLOW VISUALIZATION

NASA

- AMES
- LANGLEY
- LEWIS

US AIR FORCE

- AEDC
- KAFB/AFWL
- WPAFB/FDL

US ARMY

- MOFFET FIELD
- PICATINNY

US NAVY

- USN PGS
- USN SURFACE WEAPONS

INDUSTRIAL

- BOEING COMMERCIAL AIRPLANE CO.
- LOCKHEED
- ROLLS ROYCE
- SDL
- TRW

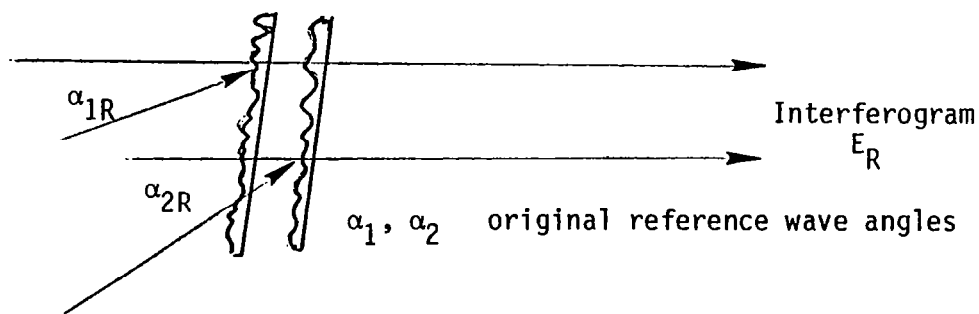
RECORDING MATERIALS FOR FLOW VISUALIZATION HOLOGRAPHY

TYPES	MANUFACTURER	RESOLUTION LINES/m	EXPOSURE REQUIRED ERGS/CM ²
PHOTOPLATES	AGFA 8E75, 10E75	2000 - 3000	50 - 200
PHOTO FILMS	8E56, 10E56		
THERMOPLASTIC FILMS	ROTTENKOLBER	1000 - 1500	~ 200
THERMOPLASTIC PLATES	HONEYWELL/ NEWPORT	1000 - 1500	~ 200

PULSED LASERS FOR FLOW VISUALIZATION HOLOGRAPHY

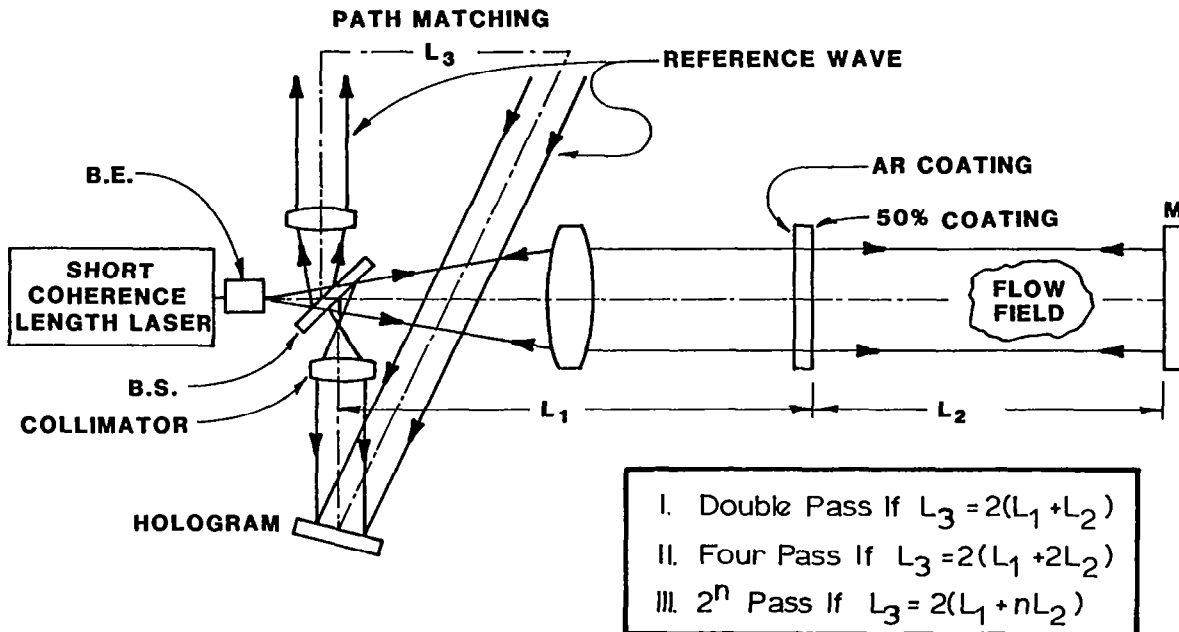
TYPE	TEM ₀₀ Q-SWITCHED ENERGY, MJ.	MULTIPULSE NUMBER	PULSE WIDTH SEC	PULSE SEPARATIONS, SEC	COHERENCE LENGTH	REP RATE, SEC ⁻¹
RUBY .694 MICRONS	50 500 4000	2,3,4	10 ⁻⁸	1 - 1000	1m	1
YAG .53 MICRONS	25 200 700	2	10 ⁻⁸	1 - 100	1m	30

DOUBLE REFERENCE WAVE HOLOGRAPHIC INTERFEROMETRY

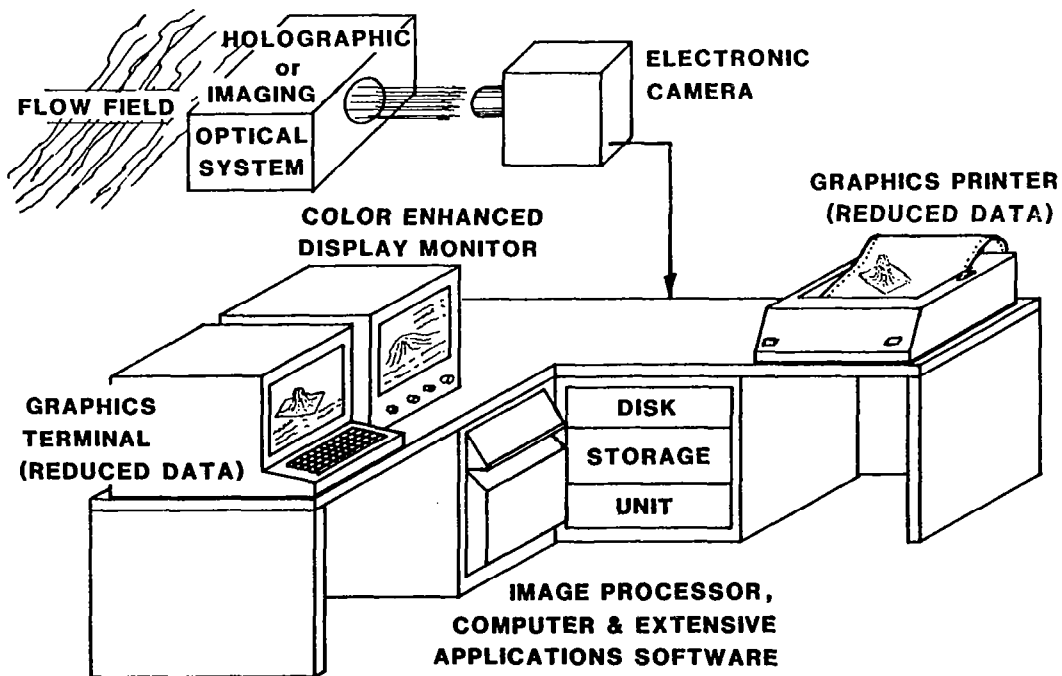


$$E_R = A \cos [kx(\sin \alpha_1 - \sin \alpha_{1R} + \sin \alpha_2 - \sin \alpha_{2R}) + \Delta \phi(x) - \Delta \phi_0 - \Delta \omega t]$$

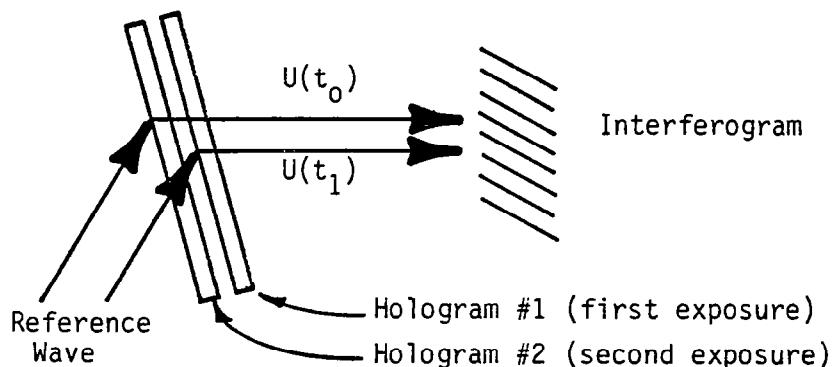
MULTI-PASS HOLOGRAPHIC FLOW VISUALIZATION



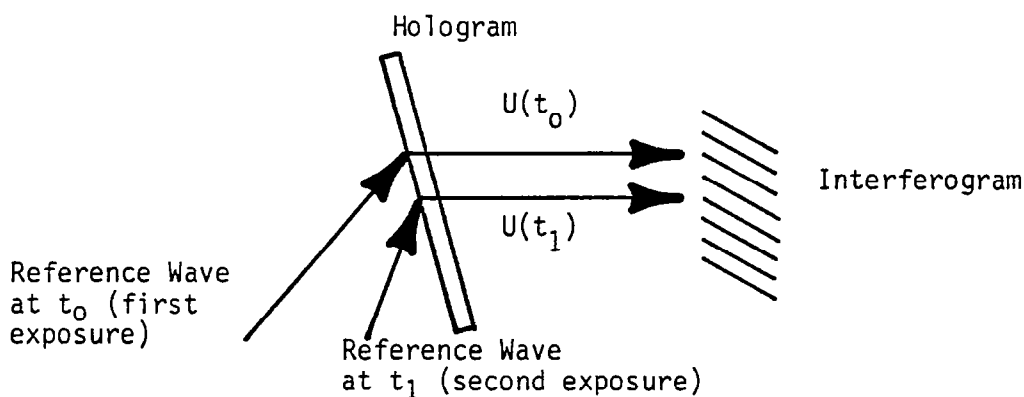
ELECTRONIC FLOW VISUALIZATION AND MEASUREMENT



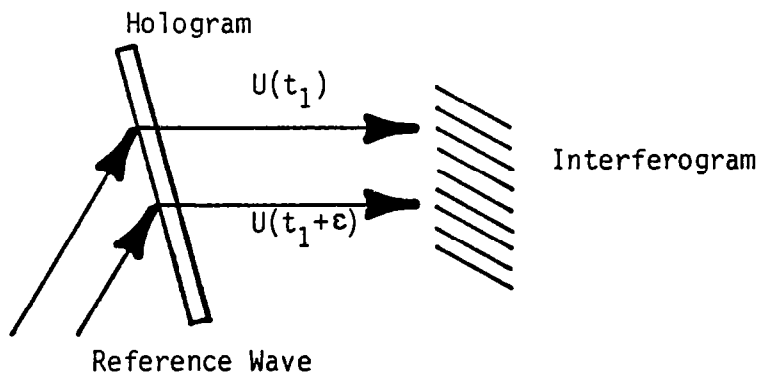
HOLOGRAPHIC INTERFEROMETRY WITH MULTIPLE RECORDINGS



A. DOUBLE PLATE HOLOGRAPHIC INTERFEROMETRY

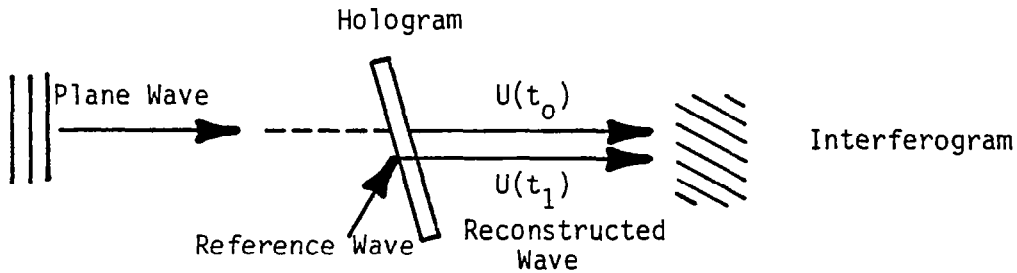


B. DOUBLE REFERENCE WAVE HOLOGRAPHIC INTERFEROMETRY

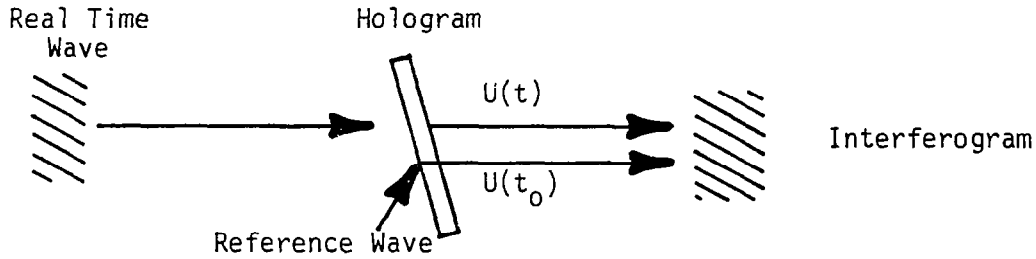


C. DOUBLE PULSED HOLOGRAPHIC INTERFEROMETRY

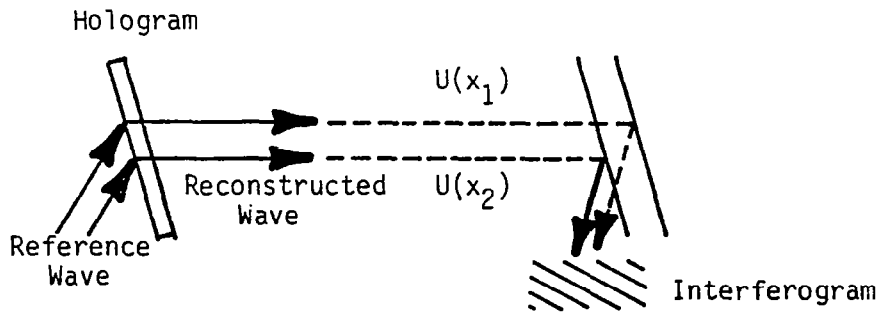
HOLOGRAPHIC INTERFEROMETRY WITH SINGLY EXPOSED HOLOGRAMS



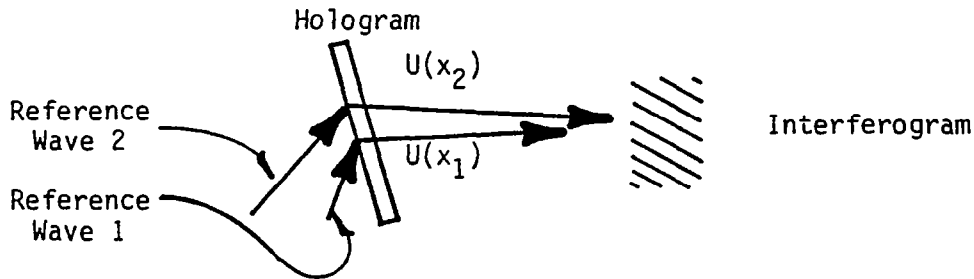
A. HOLOGRAPHIC INTERFEROMETRY WITH A SINGLE HOLOGRAM



B. REAL TIME HOLOGRAPHIC INTERFEROMETRY

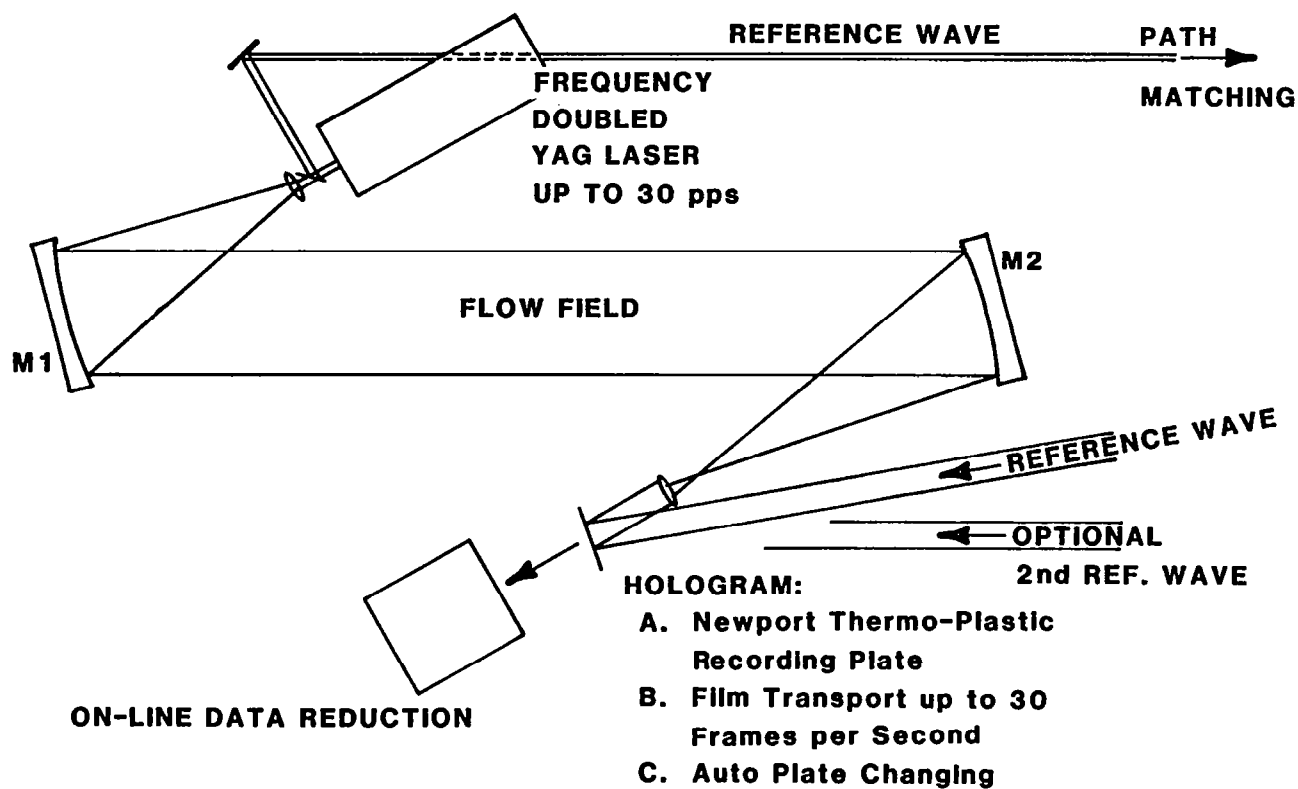


C. HOLOGRAPHIC WAVE SHEARING INTERFEROMETRY

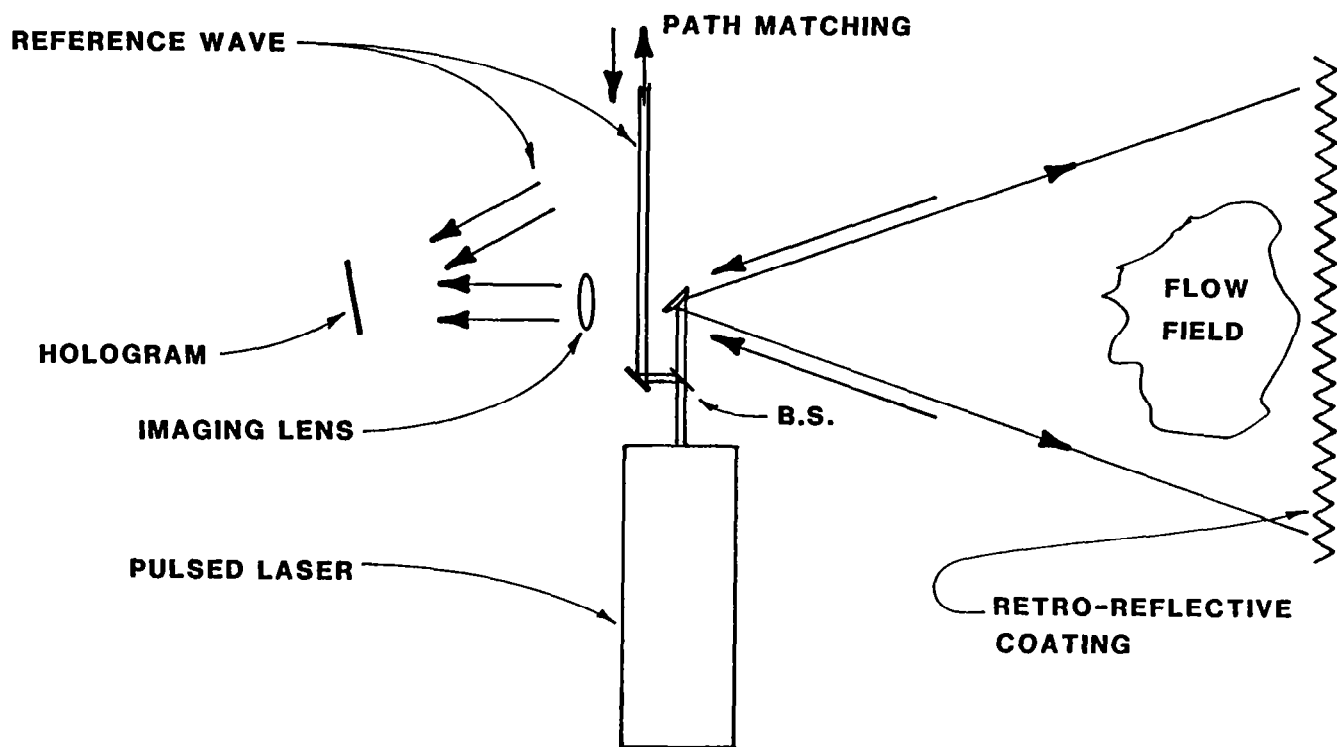


D. TWO REFERENCE WAVE SHEARING

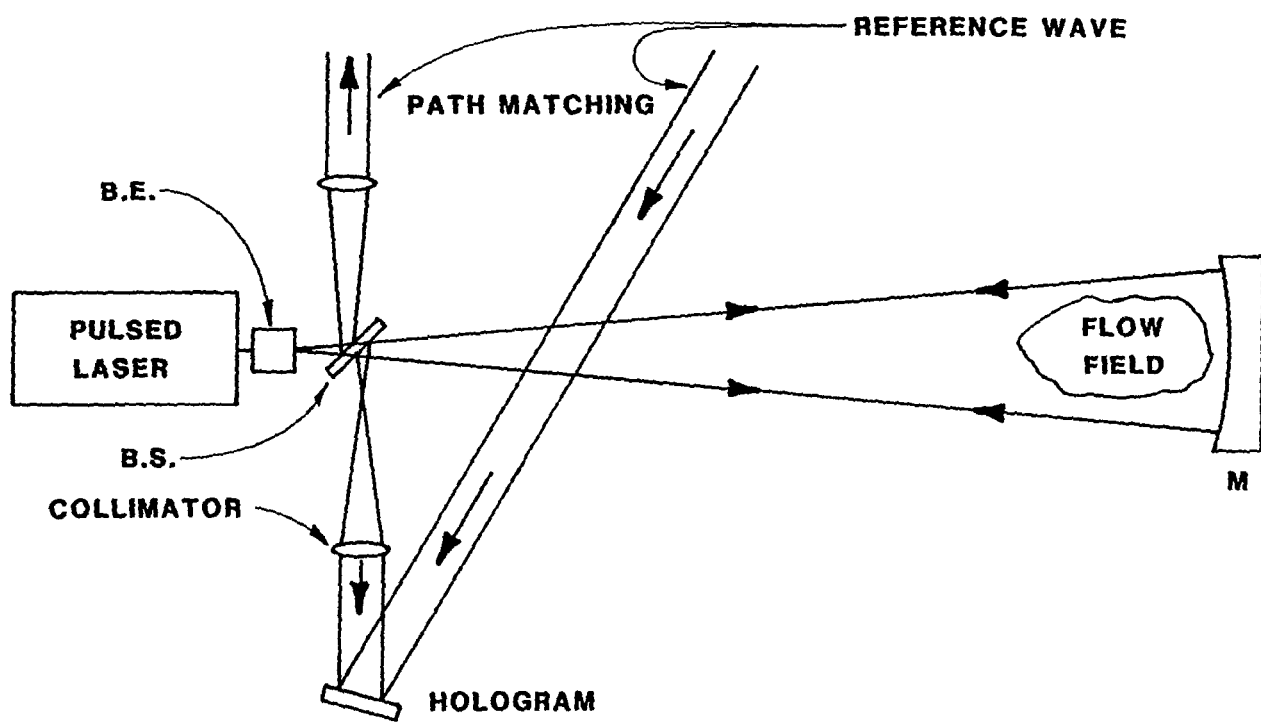
CONCEPTUAL "STATE-OF-THE-ART" HOLOGRAPHIC FLOW VISUALIZATION SYSTEM



LARGE AREA FLOW VISUALIZATION



DOUBLE PASS HOLOGRAPHIC FLOW VISUALIZATION



MEASUREMENT OF THREE-DIMENSIONAL DENSITY
DISTRIBUTIONS BY HOLOGRAPHIC INTERFEROMETRY
AND COMPUTER TOMOGRAPHY

C. M. Vest
Department of Mechanical Engineering
and Applied Mechanics
The University of Michigan

MEASUREMENT OF THREE-DIMENSIONAL DENSITY DISTRIBUTIONS
BY HOLOGRAPHIC INTERFEROMETRY AND COMPUTER TOMOGRAPHY

Traditional Interferometric Techniques for Aerodynamics:

Mach-Zehnder interferometry

Mercury-arc light sources.

These permitted measurement of:

"2-D" boundary layers and shocks

Axisymmetric flows and shocks.

More recent developments include:

Lasers

Holographic Interferometry

Computer tomography.

These permit measurement of:

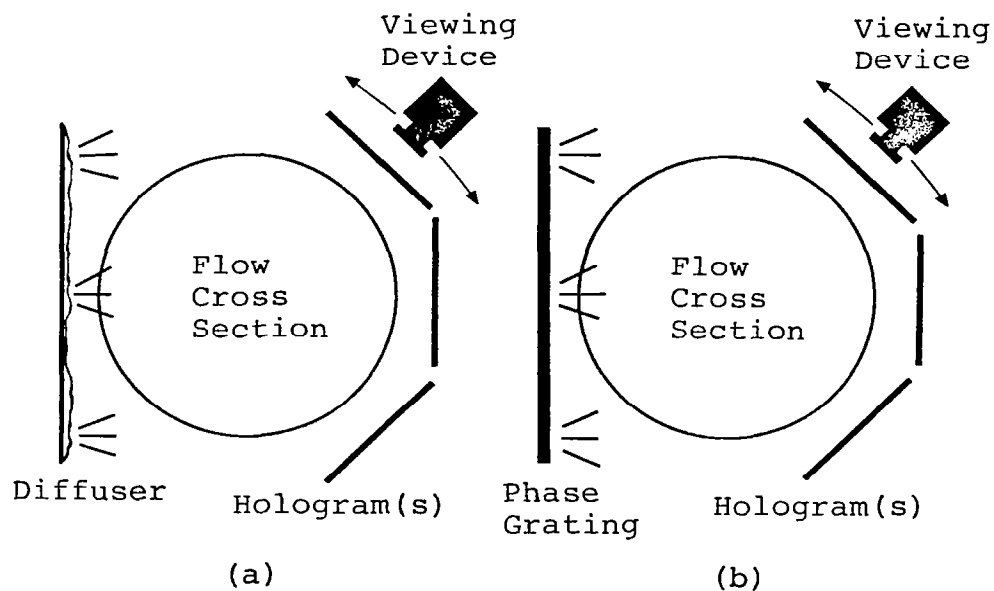
General 2-D and 3-D asymmetrical flows.

Holographic interferometry is described and reviewed by Dr. Trolinger in this workshop.

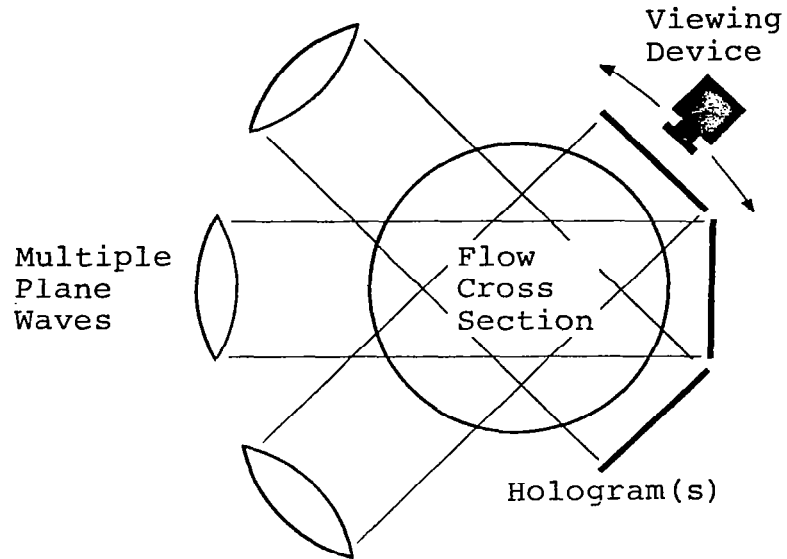
Advantages of the technique include:

- First-order correction for non-flat windows.
- Relative simplicity and ease of alignment.
- Permanent record of wavefront with some post-experiment processing possible.
- Operates readily with pulsed lasers for ~10ns time resolution.
- Multiple viewing directions available when diffused or multi beam illumination is used.

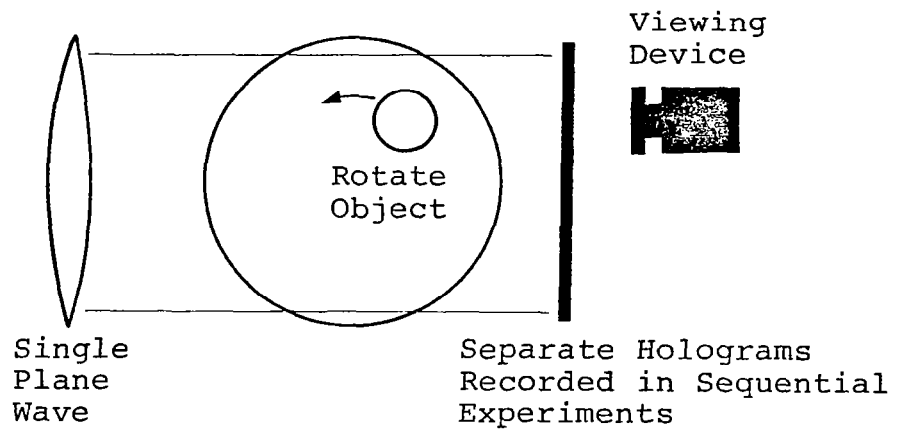
Collection of Multiple Views:



Collection of Multiple Views



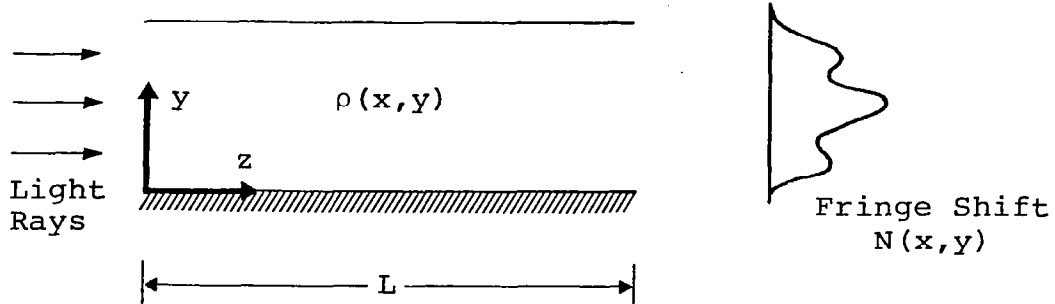
(c)



(d)

Interpretation of multiple-view interferograms requires computer tomography.

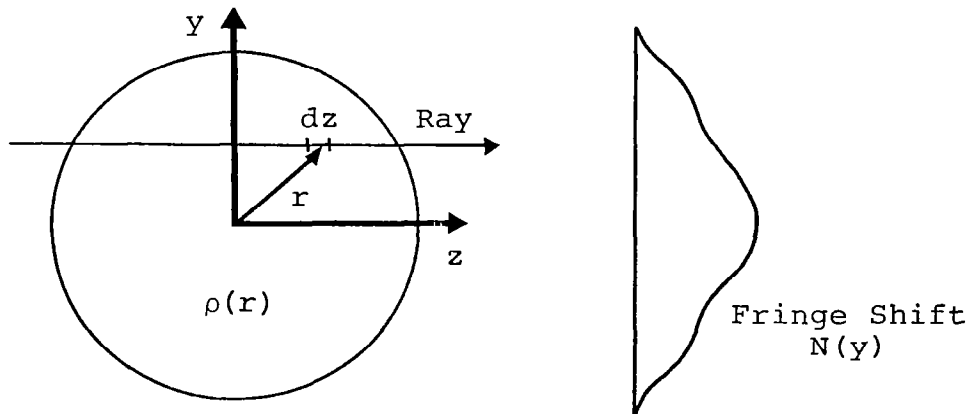
BACKGROUND: "2-D" Fields



$$\lambda N(x, y) = K \int_0^L [\rho(x, y) - \rho_0] dz$$

$$\rho(x, y) - \rho_0 = \frac{\lambda}{KL} N(x, y)$$

BACKGROUND: Axisymmetric Fields

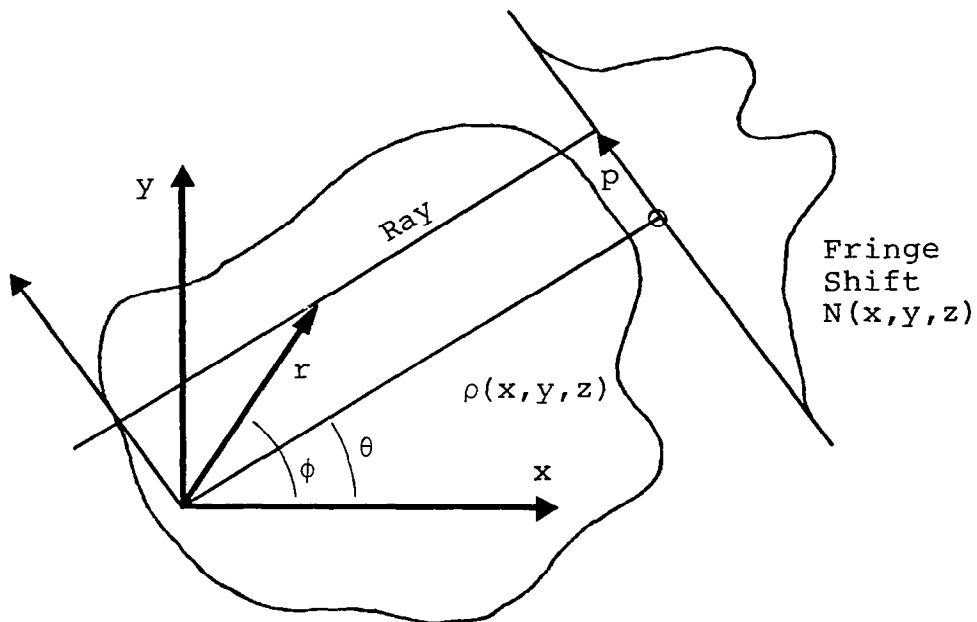


$$\lambda N(y) = 2K \int_y^{\infty} \frac{[\rho(r) - \rho_0] r dr}{(r^2 - y^2)^{1/2}}$$

$$\rho(r) - \rho_0 = -\frac{\lambda}{\pi K} \int_r^{\infty} \frac{(dN/dy) dy}{(y^2 - r^2)^{1/2}}$$

Computer tomography is an important technique for reconstructing 2-D or 3-D fields from measurements of line integrals through the field. It has been under development since the late 1960's. However, its origins are in the mathematical analysis of Radon (1917), work in radio astronomy by Bracewell (1956), and applications to medical imaging by Cormack (1964), and Hounsfield. It is discussed in this workshop in the context of holographic interferometry (Lee, Vest).

BASIC PROBLEM OF TOMOGRAPHY



Line-integral transform:

$$\lambda N(p, \theta) = K \iint [\rho(r, \phi) - \rho_0] \delta[p - r \sin(\phi - \theta)] dx \quad (1)$$

Inversion:

$$\rho(r, \phi) - \rho_0 = \frac{\lambda}{2\pi^2 K} \int_{-\pi/2}^{\pi/2} d\theta \int_{-\infty}^{\infty} \frac{(\delta N / \delta p)}{r \sin(\phi - \theta) - p} \quad (2)$$

The problem of tomography can be stated as a set of linear integral equations. There is an analytical inversion with which continuous and complete data recorded over a 180° range of viewing directions could be used to reconstruct $\rho(r,\phi)-\rho_0$. By doing this for several planes, $z=\text{constant}$, the entire 3-D field could be reconstructed.

In real experiments several difficulties are encountered:

1. Data are discrete and limited in number.
2. Data are recorded for a finite number of viewing directions.
3. Data are incomplete.
 - a. Range of viewing directions may be less than 180° .
 - b. Opaque objects such as test models may block out part of the data.
4. Data contain experimental error.
5. Refractive ray bending may occur.

Therefore, several computational techniques have been developed for computer tomography.

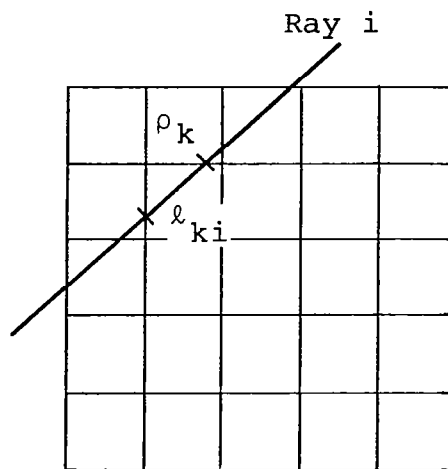
1. IMPLICIT METHODS: The right-hand side of Eq. (1) is approximated and the integral is replaced by a sum. This results in a set of algebraic equations which are solved for unknown coefficients or density values.

a. SERIES EXPANSIONS $\rho - \rho_0 = \sum a_{mn} f_{mn}(r, \phi)$
 where f_{mn} may be Fourier series
 Legendre Polynomial
 Bessel functions
 Sinc functions

This yields a set of equations to solve:

$$\sum A_{ij} f_j = \pi N_i$$

b. DISCRETE ELEMENT REPRESENTATIONS

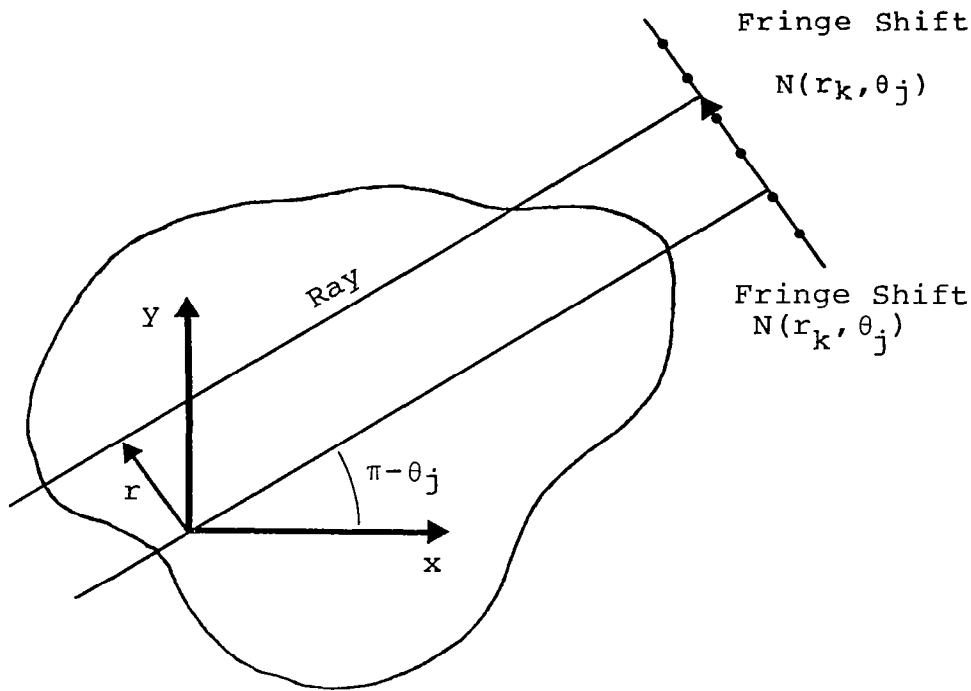


Basic Grid Method
 ART (relaxation)

$$\sum l_{ki} [\rho_k - \rho_0] = \frac{\lambda N_i}{K}$$

2. EXPLICIT METHODS: The right-hand side of Eq. (2) is approximated and the integral is replaced by a sum. This results in a direct representation of $\rho(r, \phi)$ which is obtained by operations entirely in the object domain. The most common method is:

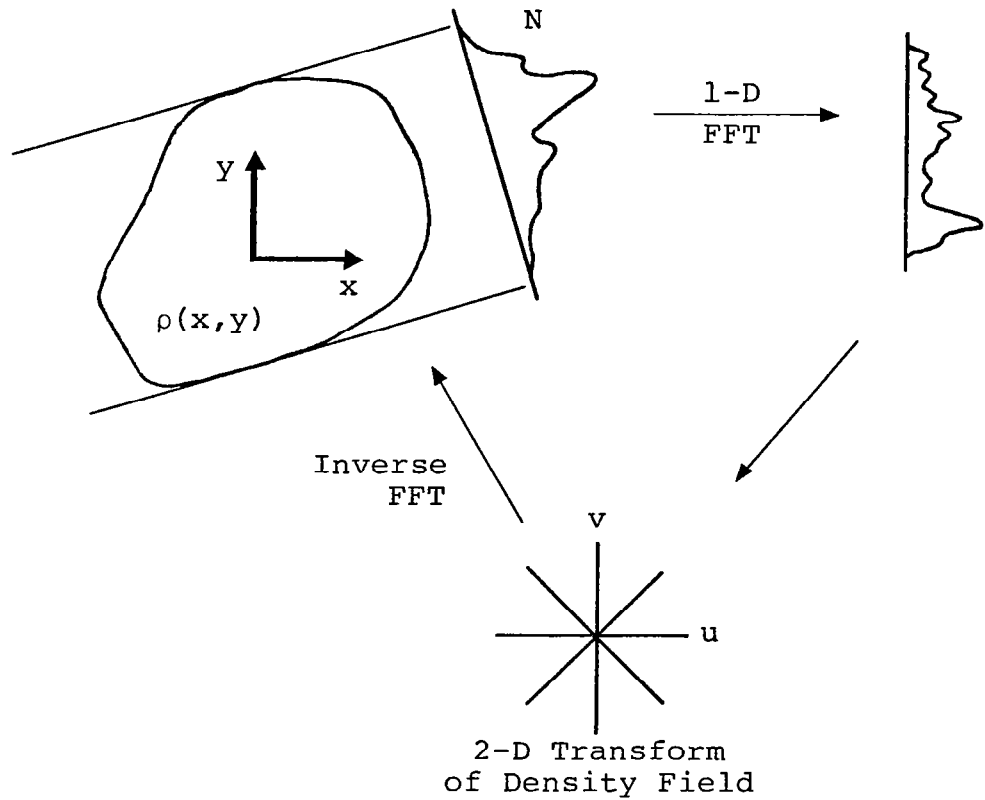
CONVOLUTION METHOD (FILTERED BACKPROJECTION)



$$\rho(x, y) - \rho_0 = \sum \sum N(r_k, \theta_j) w(x \cos \theta_j + y \sin \theta_j - p_k)$$

where w is a weight, or filter, applied to the fringe shift of each ray passing through the point in question.

3. **FOURIER TRANSFORM METHODS:** These are based on the Central Section Theorem of Bracewell which states that the 1-D Fourier transform of a projection, i.e. $N(p;\theta)$ for fixed θ , equals the 2-D Fourier transform along a corresponding radial line in the 2-D Fourier transform of the density field.



SELECTION OF TOMOGRAPHY ALGORITHM

There is no simple way to determine what computer tomography algorithm is "best". The behavior of algorithms is highly dependent on the structure of the density field, the amount and format of available data, the amount of "noise" in the data, and the nature of the desired information about the field.

A few characteristics of the two methods with which we have had the most success are:

1. CONVOLUTION METHODS

- a. Moderately simple to program.
- b. Modest storage requirements.
- c. Low execution time.
- d. Requires 180° range of viewing angles.
- e. Requires equally-spaced data in each view.

2. SERIES EXPANSION METHODS

- a. Can be moderately complex to program.
- b. Storage requirements can be moderately high.
- c. Low execution time if efficiently programmed.
- d. Can be used with limited range of viewing angles.
- e. Does not require equally-spaced data.

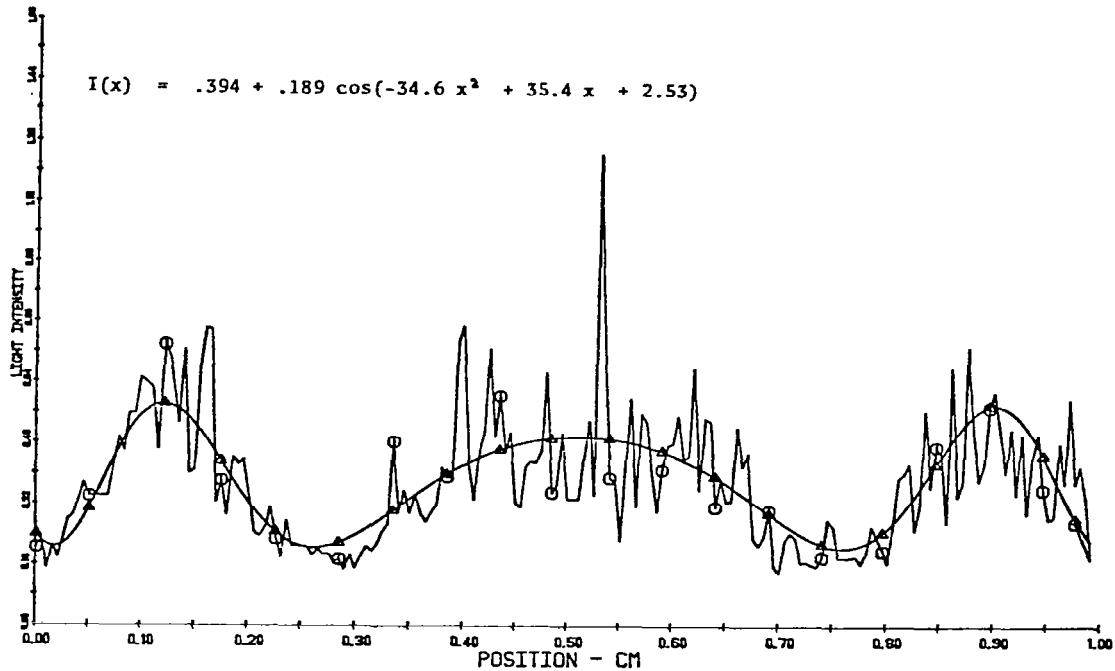
CURRENT AND FUTURE RESEARCH TOPICS

1. Development of automated fringe readout system which permits accurate interpolation.
 - a. Digital TV/Computer systems
 - b. Heterodyne systems
2. Development of optimum reconstruction procedures when an opaque test model is present in the field.
3. Interferometry and tomography with strongly refracting fields and shocks.
4. Gaining experience with well-instrumented experiments.

CURRENT RESEARCH AT THE UNIVERSITY OF MICHIGAN

1. Fringe readout system using a CCD array camera and LSI 11/23 computer. Noisy data are fitted to fringe functions with several degrees of freedom by nonlinear regression analysis. (In progress)

JBS990.DS11 NON-LINEAR PHASE VARIATION, HIGH NOISE

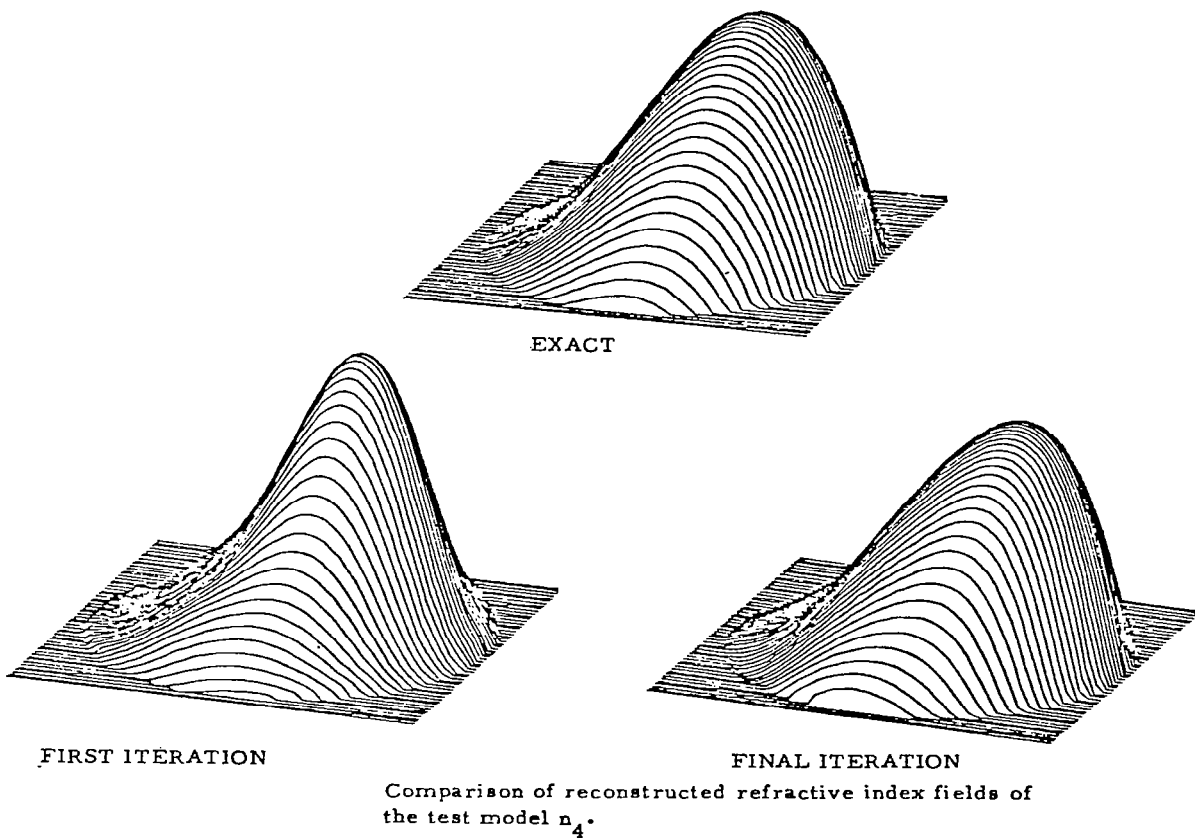


The Sampled Data with the curve that was fit to it for Data Set JBS990.DS11.

2. Reconstruction with an opaque test object in the field (in progress).
 - a. Development of a convolution algorithm which iterates between the line-integral-transform plane and the density field plane to correct for the missing data.
 - b. Development of series-expansion algorithms which meet all criteria for reconstruction of the density field outside a convex region surrounding the opaque object.

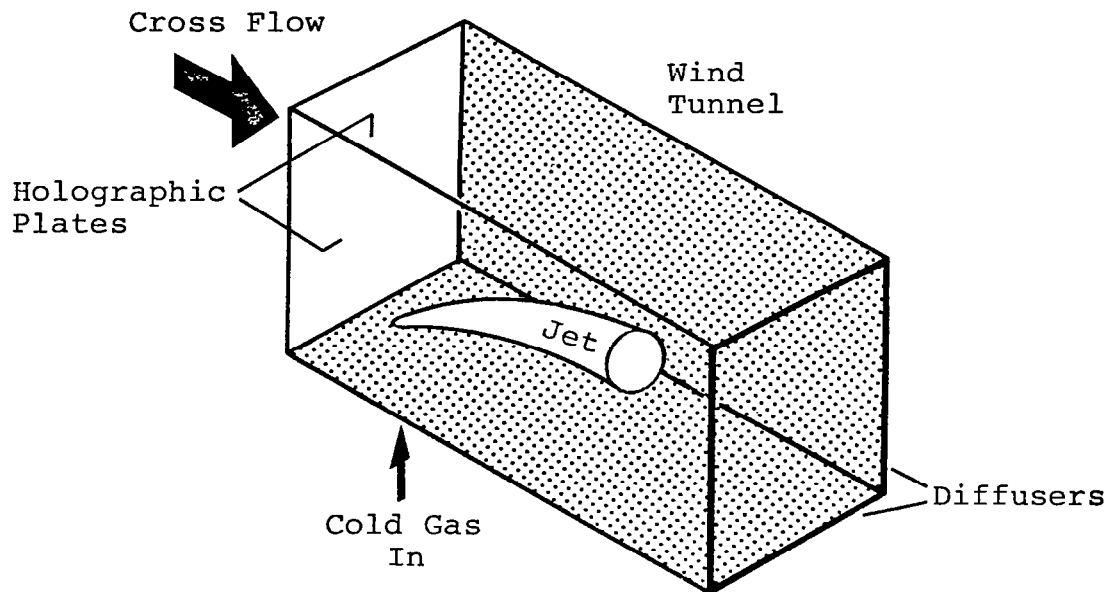
3. Interferometry of strongly-refracting density fields and shocks. (Initial study completed.)

Developed an algorithm which corrects reconstructions for refraction by iteratively using geometric optical ray tracing through estimates obtained by series-expansion tomographic reconstruction.



4. Well-instrumented experiment. (Proposed)

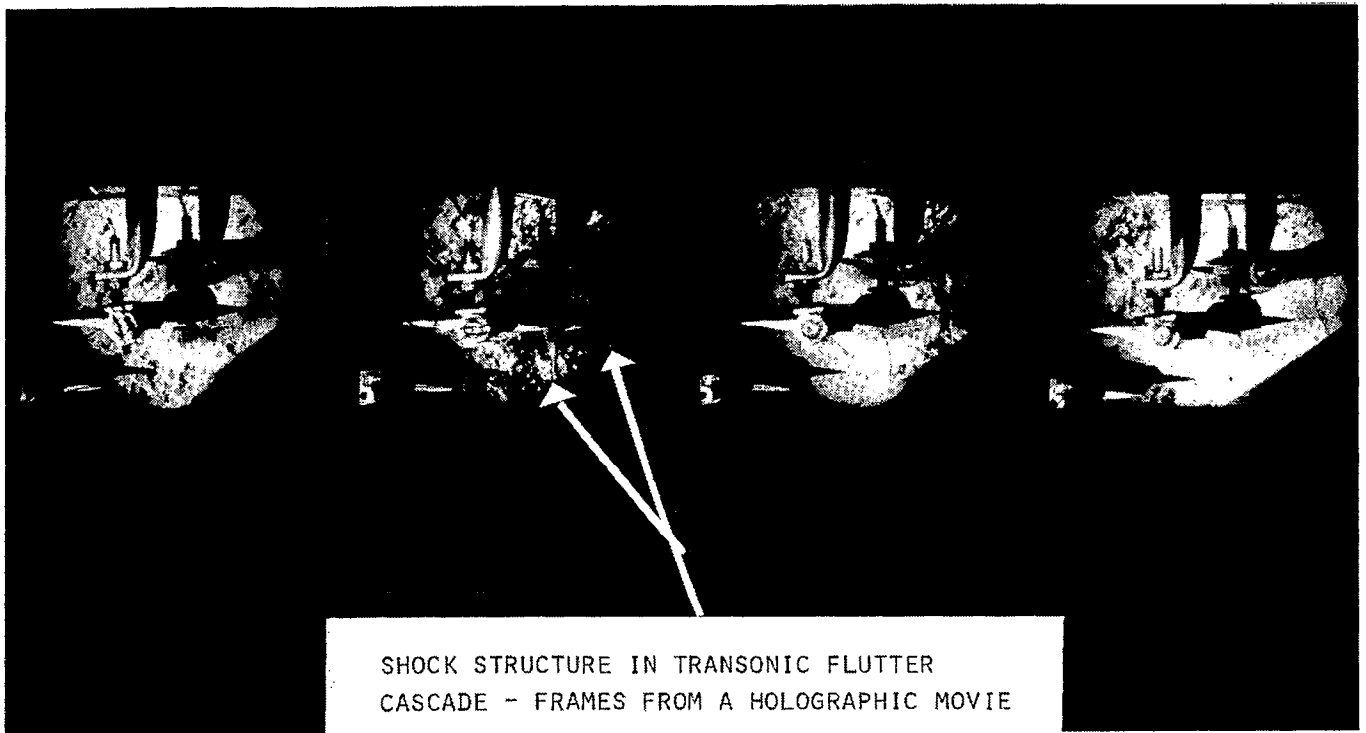
We hope to study the structure of a turbulent jet in a turbulent cross flow in an experiment scaled to model the mixing of dilutant jets in gas turbine engines.



HOLOGRAPHIC CINEMATOGRAPHY AND
OTHER DYNAMIC FLOW VISUALIZATION METHODS

Arthur J. Decker
NASA Lewis Research Center
Cleveland, Ohio

Reconstructed images from four frames of a holographic movie of a three-blade flutter cascade are shown. The holograms were recorded on 70 mm film, Kodak SO 253 emulsion, at 20 double-exposure holograms per second. The film was transported by a Mitchell DA-70 camera body. The object illumination (the second harmonic from a Quantel International Nd:YAG laser) was diffusely reflected from the back end-wall of the tunnel. Other laser operating parameters are: 10 microseconds between exposures, 10 millijoules radiated per frame, and 3 longitudinal modes. Tunnel parameters are: Mach number of 0.81, mean angle of attack of -6 degrees, vibrational amplitude of 1.2 degrees driven at 500 Hz, chord of 6.2 cm, span of 9.9 cm, end-wall boundary layer thicknesses of 1.5 cm, and a blade stagger angle of 30 degrees. The lambda shock waves are seen nearly edge-on, and their 3-D structure is easily viewed in the actual reconstructions.



BIBLIOGRAPHY OF RELATED REPORTS

1. A. J. Decker, "Fringe Localization Requirements for Three-Dimensional Flow Visualization of Shock Waves in Diffuse-Illumination, Double-Pulse Holographic Interferometry," NASA TP-1868, 1982.
2. A. J. Decker, "Holographic Flow Visualization of Time-Varying Shock Waves," *Applied Optics* 20, 3120-3127 (1981).
3. A. J. Decker, "Holographic Cinematography of Time-Varying Reflecting and Time-Varying Phase Objects Using a Nd:YAG Laser," *Optics Letters* 7, 122-123 (1982).
4. D. Weimer, "Pockels Effect Cell for Gas Flow Simulation," NASA TP-2007, to be published.
5. D. R. Boldman, A. E. Buggele, and A. J. Decker, "Three-Dimensional Shock Structure in a Transonic Flutter Cascade," *AIAA Journal*, to be published.

HOLOGRAPHIC INTERFEROMETRY AND TOMOGRAPHY
AT AMES RESEARCH CENTER

GEORGE LEE
NASA, AMES RESEARCH CENTER
MOFFETT FIELD, CALIFORNIA

ABSTRACT

The Aerodynamic Research Branch of NASA, Ames Research Center has been pursuing a program in laser holographic interferometry and tomography for the past three years. A new YAG laser holographic interferometer system and reconstruction laboratory for the Ames 2- by 2-Foot Transonic Wind Tunnel was put into operation last year. This system provides dual plate and double pulse holography for quantitative and qualitative measurements, respectively. The program to date consists of making interferometric measurements of two-dimensional airfoils and three-dimensional bodies of revolution for the tomography feasibility study. The two-dimensional work included supercritical airfoils, an oscillating airfoil undergoing dynamic stall, and a circulation control airfoil. The tomography experiments centered around hemispherical nose and tangent ogive models. In addition, the tomography work covered the development of a Fourier transform code for the retrieval of the three-dimensional density distributions from the interferograms.

The new interferometer gives excellent infinite fringe interferograms in both dual plate and double pulse modes. Quantitative data for surface pressures on a wing were within 1% of those from pressure orifices, see Figure 1. Excellent definitions of shock waves, boundary layers, and wakes can be seen in the interferograms, see Figure 2. The location of flow separation regions can also be readily detected. Figure 3 shows the separated flow line along with oil flow confirmation. Interferograms give density data over the large inviscid regions and the data can be used to verify theoretical calculations, see Figure 4. This technique can be adapted for unsteady flows. Excellent interferograms of an airfoil undergoing dynamic stall are shown in Figure 5. Note the wake flows and the typical hysteresis effects of flow separation and reattachment as the airfoil oscillates. Double pulse interferograms were used to freeze the flow and the vortex shedding process can be seen in Figure 6. Figures 7 and 8 are typical interferograms of hemispherical and tangent ogives used for tomography. These data will be compared with theoretical density contours to evaluate the feasibility of tomography for aerodynamics. Figures 9(a) and 9(b) are computer simulations to check out the accuracy of the Fourier code. Input density contours from a Navier-Stokes code for flow over the tangent ogive are compared with those from the Fourier code. Good results were obtained. Finally, Figure 10 shows a sketch of the interferometer including transmitting and receiving optics.

In summary, a new type of laser holographic interferometer was built and excellent interferograms were obtained. Two-dimensional data can be obtained routinely. A Fourier code for tomography was developed and experiments are under way. This area looks promising.

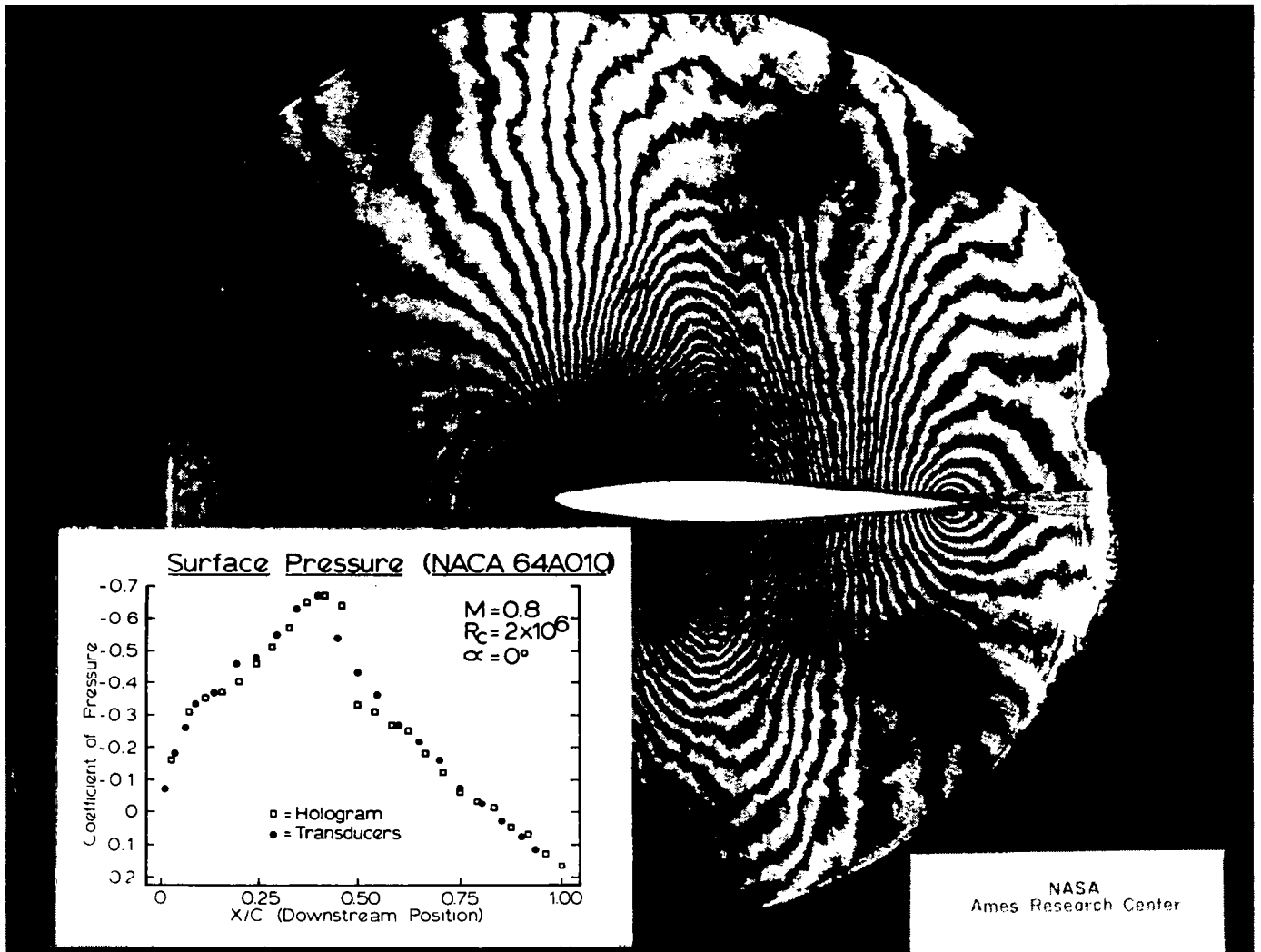


Figure 1.- Comparison of surface pressures on an NACA 64A010 airfoil from interferograms and transducers.

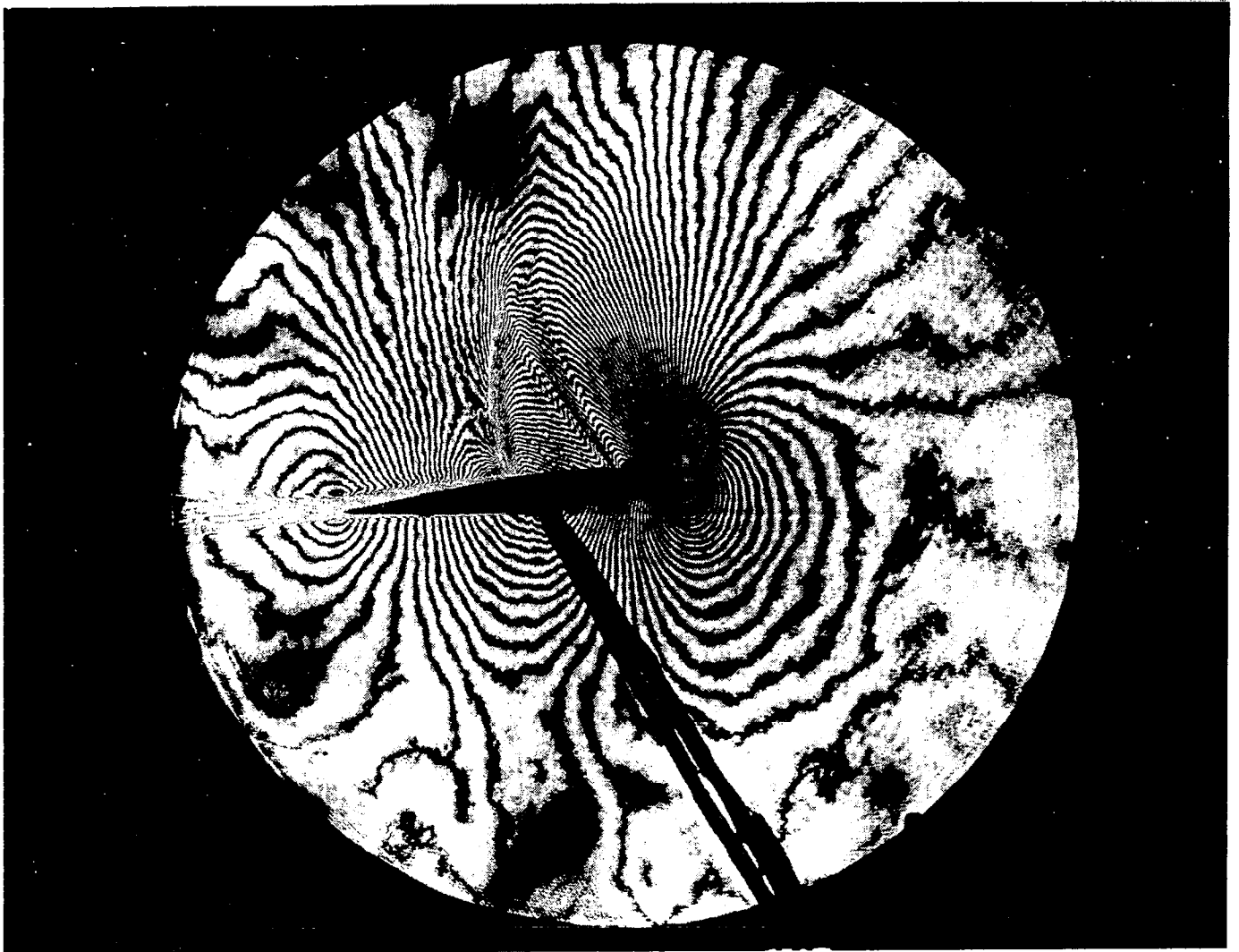


Figure 2.- Interferogram of NACA 64A010 at $M_\infty = 0.8$.

TRANSONIC TURBULENT BOUNDARY LAYER SEPARATION

$M_x = 0.875$

INFINITE - FRINGE
INTERFEROGRAM



OIL FLOW VISUALIZATION



MEAN VELOCITY PROFILES

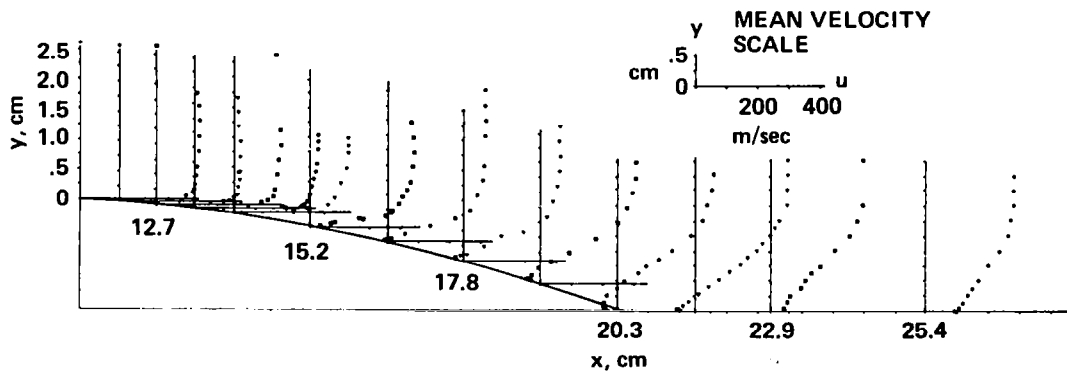
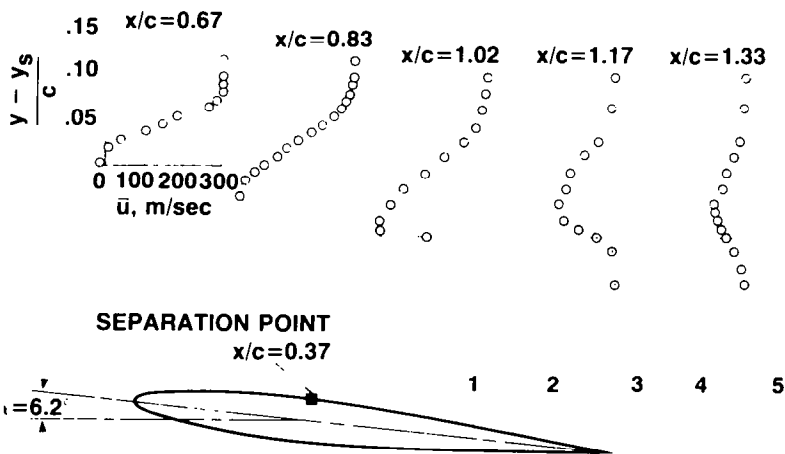
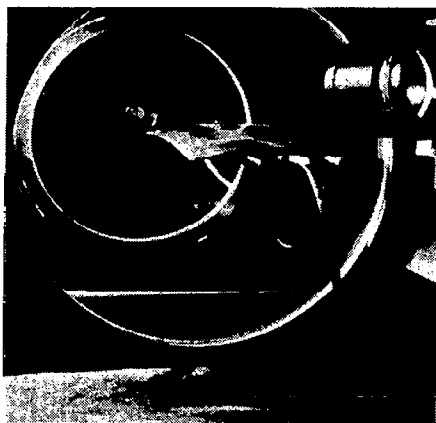


Figure 3.- Comparison of separation region.

UNIQUE DATA FOR AIRCRAFT DESIGN



VERIFICATION OF THEORIES FOR AIRCRAFT DESIGN

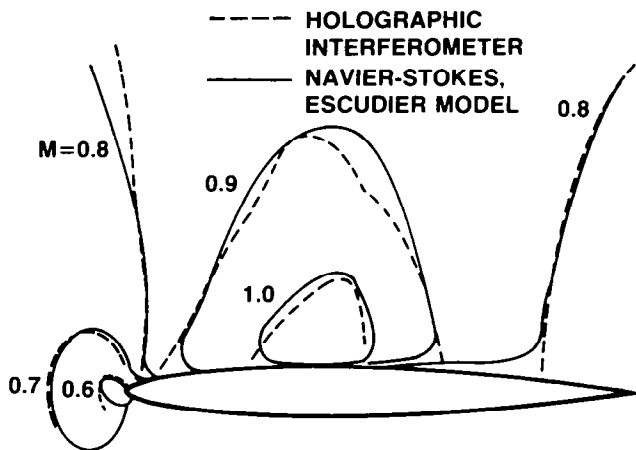
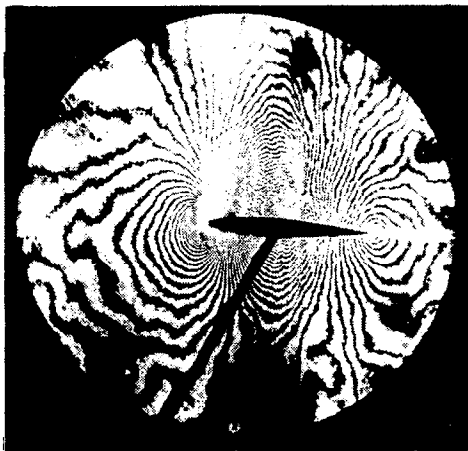
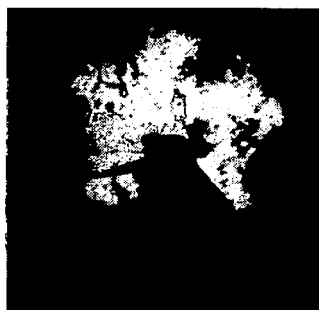
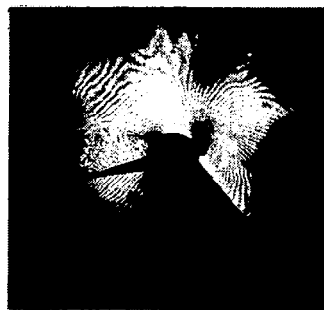


Figure 4.- Comparison of Mach number contours.

LASER HOLOGRAPHIC INTERFEROGRAMS
0012 AIRFOIL IN 2X2 WIND TUNNEL

$M_\infty = 0.6$
 $Re = 4 \times 10^6$
 $f = 21.7 \text{ Hz}$
 $\alpha_{\text{mean}} = 5^\circ \pm 10^\circ$



$\alpha = 15^\circ$

DOUBLE PULSE

AIRFOIL MOVING UP
↑



$\alpha = 12.5^\circ$

↓
AIRFOIL MOVING DOWN



$\alpha = 10^\circ$

Figure 5.- Interferograms of 0012 airfoil undergoing dynamic stall.

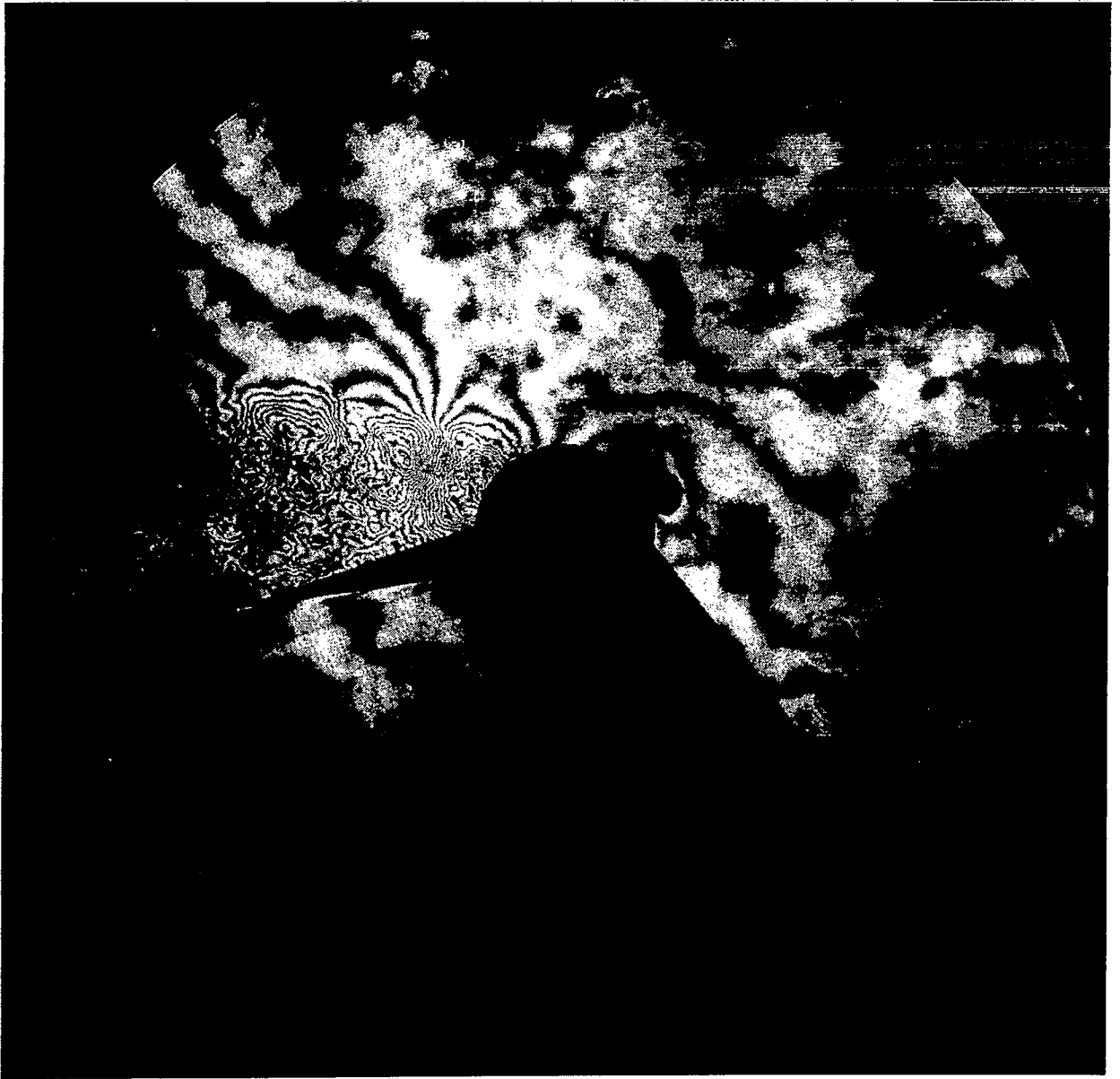


Figure 6.- Double pulse interferogram of 0012 airfoil.

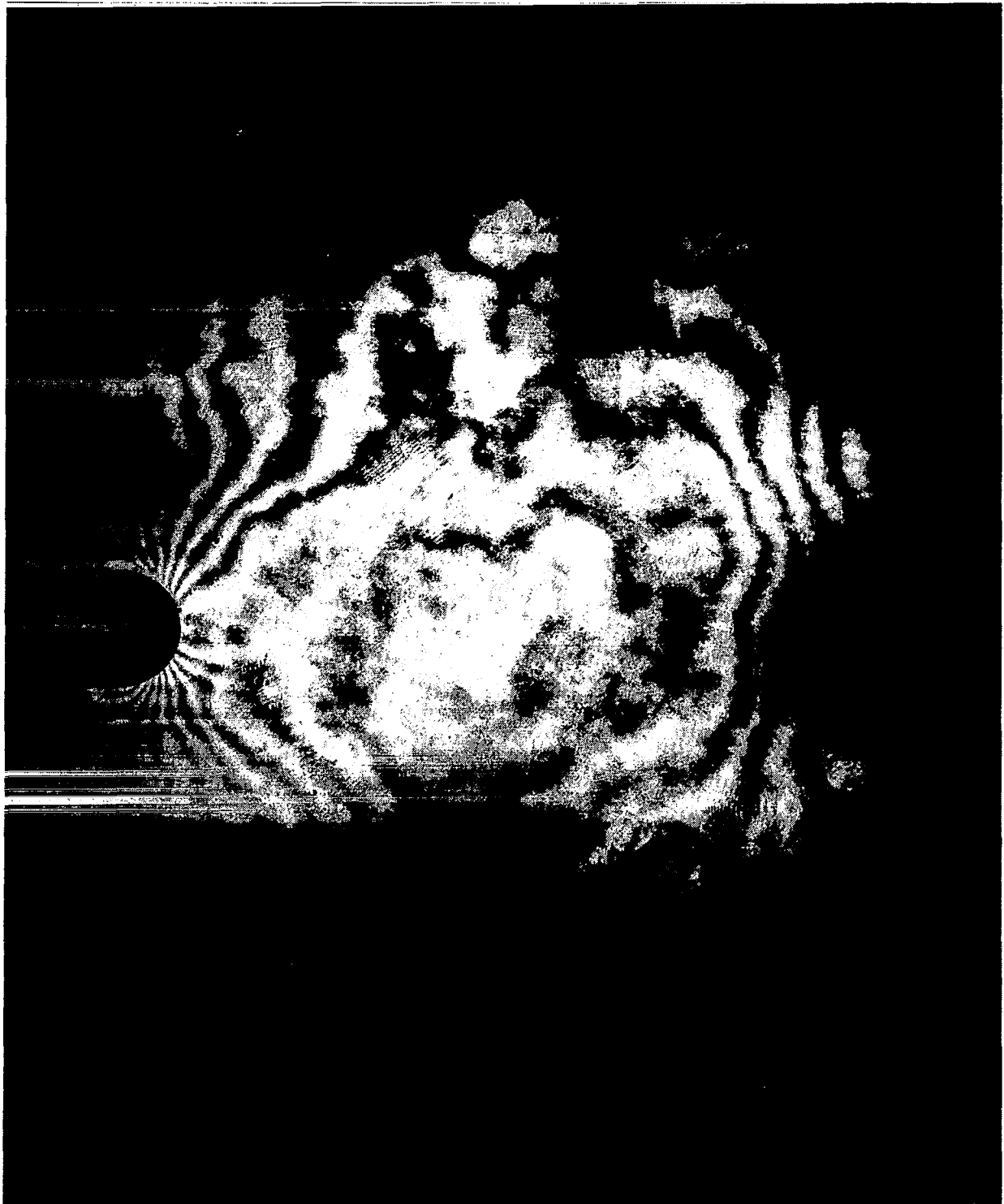


Figure 7.- Hemispherical cylinder at $M_\infty = 0.6$.

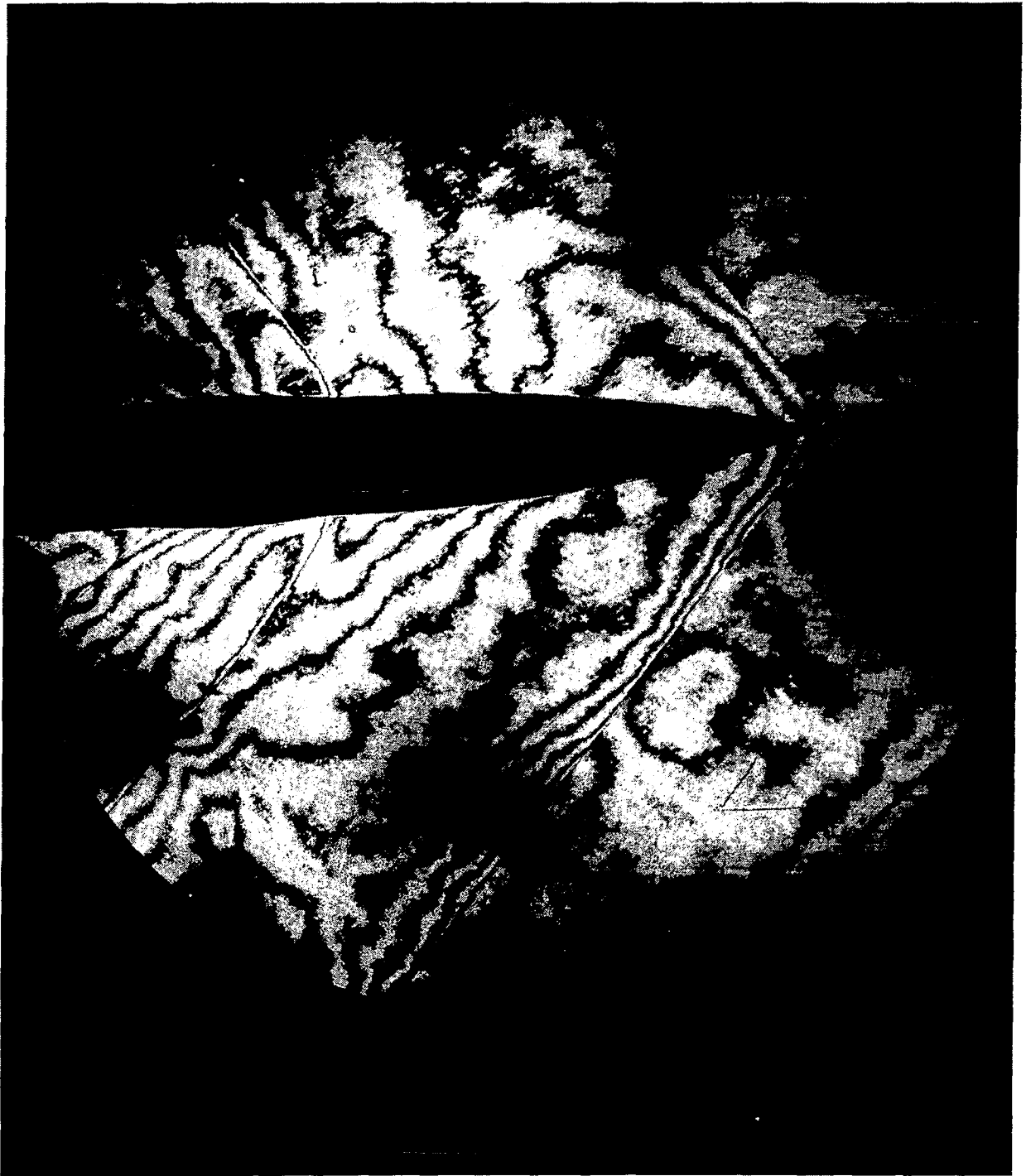
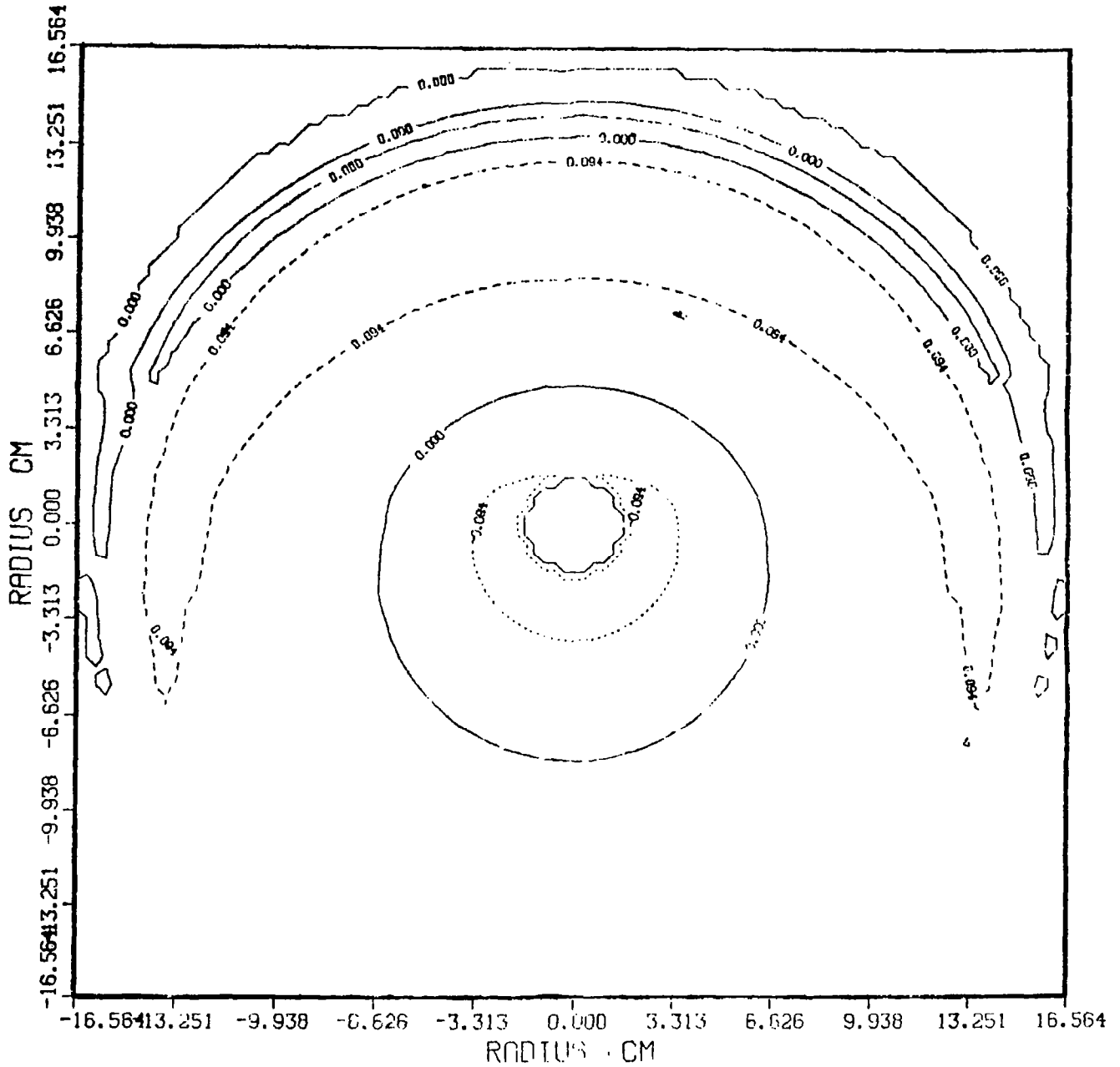


Figure 8.- Tangent ogive at $M_\infty = 1.25$.

DATA F(XY)



CALC F(XY)

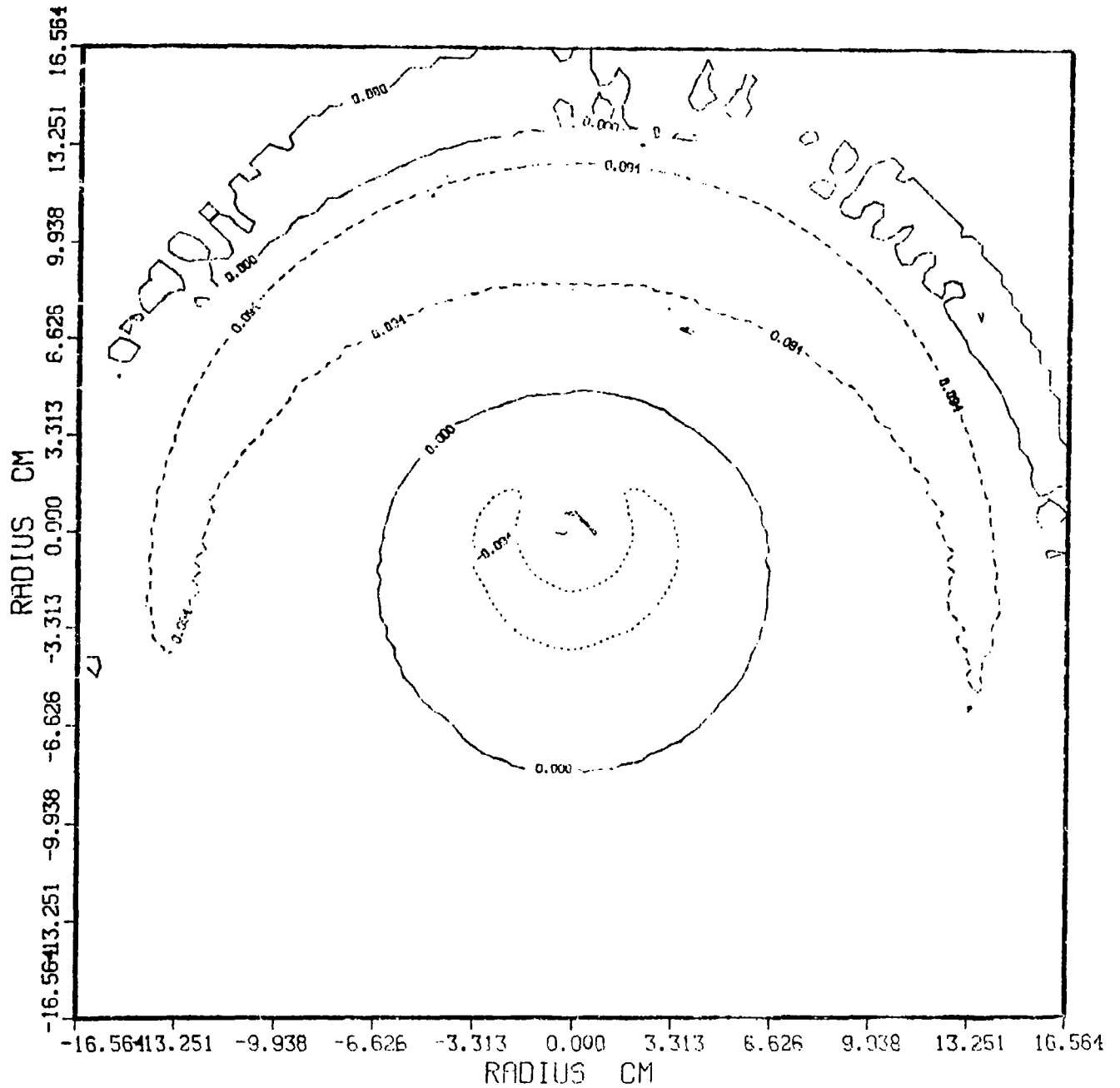
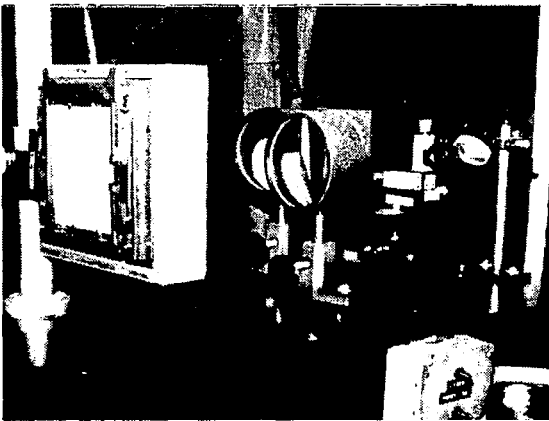
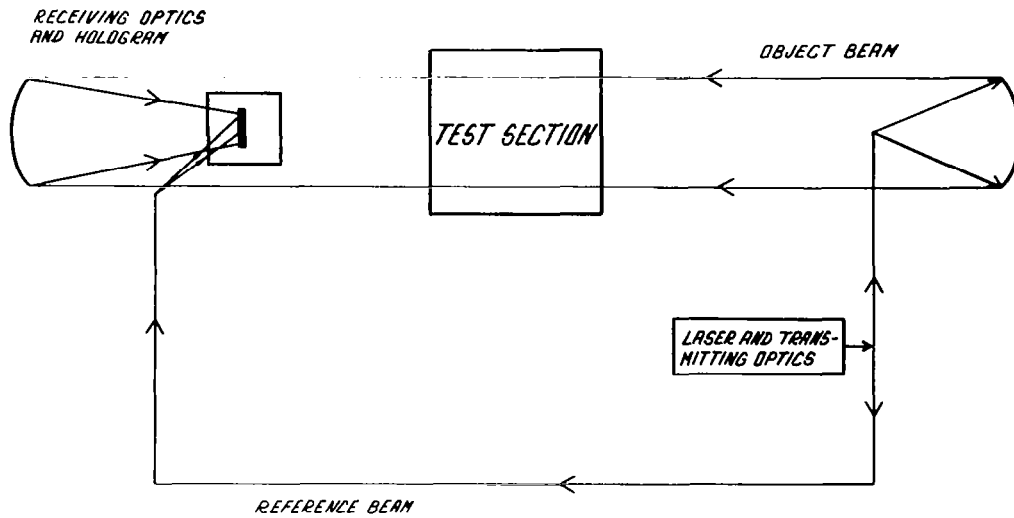


Figure 9(b).- Normalized density contours from the Fourier reconstruction code using data from Navier-Stokes code.



RECEIVING OPTICS AND HOLOGRAM



LASER AND TRANSMITTING OPTICS

Figure 10.- 2×2 laser holographic interferometer.

FLOW FIELD STUDIES USING HOLOGRAPHIC
INTERFEROMETRY AT LANGLEY

A. W. Burner, W. L. Snow, W. K. Goad,
V. T. Helms, and P. B. Gooderum

NASA Langley Research Center
Hampton, Virginia



INTRODUCTION

During the past decade holographic interferometry has largely superseded the classical Mach-Zender interferometer as the interferometric technique with the best potential for measuring density in aerodynamic research facilities. Holographic interferometry is a nonintrusive optical technique which offers the additional capability over conventional interferometry of recording for later reconstruction the flow and no-flow optical fields. It is the interference between these two optical fields which yields fringe shift data necessary for density calculations. This paper traces some of the uses of holographic interferometry at Langley Research Center both for flow visualization and for density field determinations and concludes with the description of recent tests in cryogenic flows at the Langley 0.3-Meter Transonic Cryogenic Tunnel.

HOLOGRAPHIC FLOW VISUALIZATION FROM THE LANGLEY CF_4 TUNNEL

The main use of holography in wind tunnels at Langley has been for flow visualization. Figure 1 is an interferogram made at the Langley Hypersonic CF_4 tunnel of the Shuttle Orbiter nose in Mach 6 flow. The field of view is 40 cm with flow from left to right. Note that the maximum fringe shift is less than 4. Smaller models run at the facility at low freestream density have fringe shifts less than 1.0.

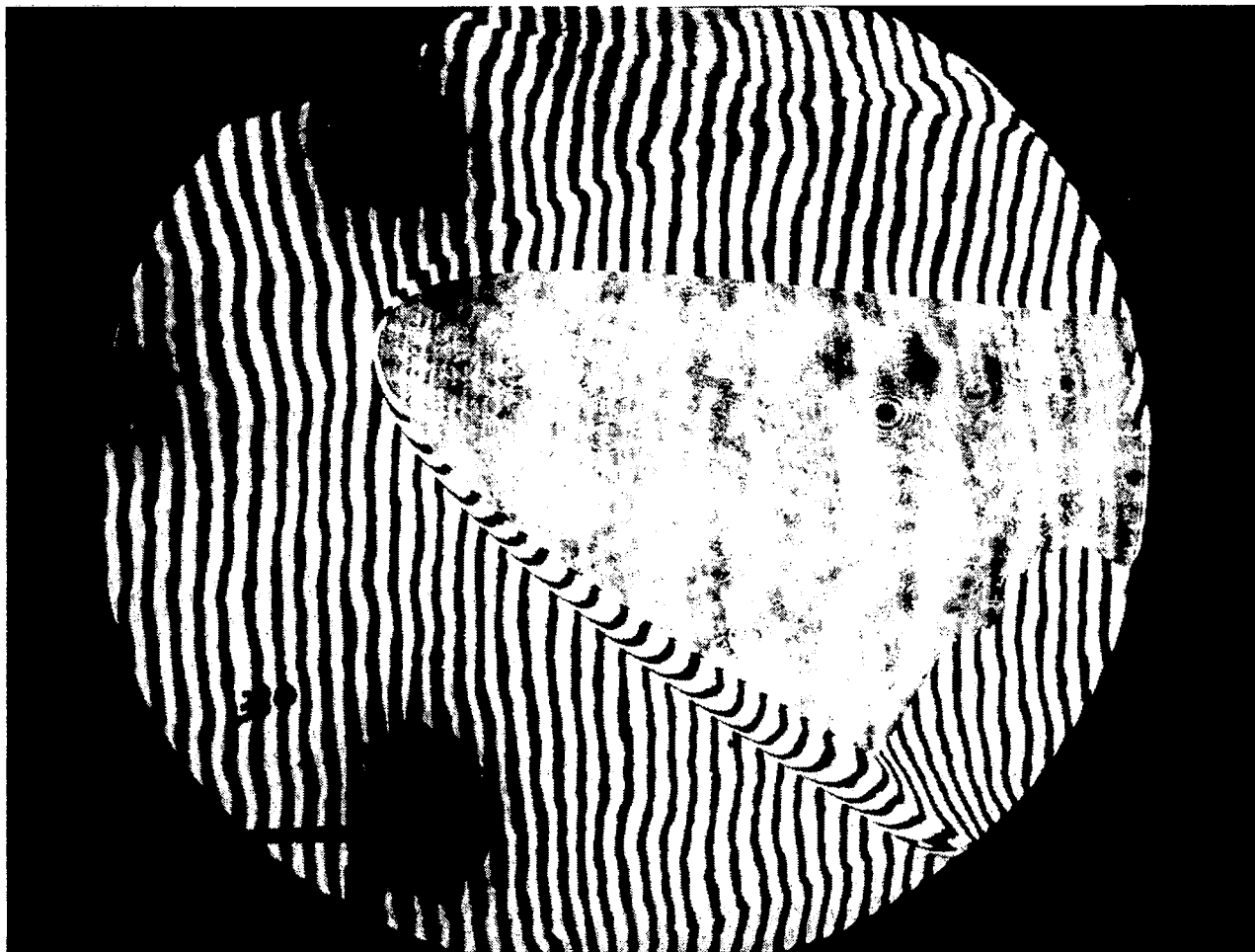
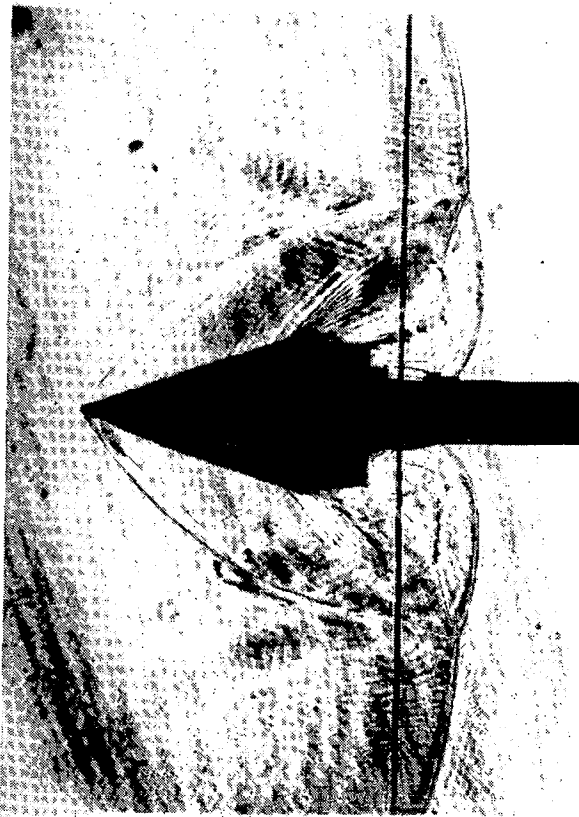


Figure 1

HOLOGRAPHIC FLOW VISUALIZATION FROM THE LANGLEY EXPANSION TUBE

Figure 2 shows a shadowgraph and interferogram of a 20° half-angle wedge from the Langley Expansion Tube. Flow is from left to right. In the expansion tube mode of operation maximum fringe shifts vary from about 0.1 to 2.0. For the hologram of figure 2 the facility was operated as a shock tube which resulted in much higher densities and hence larger fringe shifts than when operated as an expansion tube. The incident shock was recorded before leaving the field of view. Note the formation of a bow shock about the wedge.



(a) Shadowgraph.



(b) Interferogram.

Figure 2

INTERFEROGRAM OF CONE FROM LANGLEY CF_4 TUNNEL

To gain some experience with interferometry, fringe shift measurements have been made on several spheres and sphere-cones run at $0^{\circ}A-0-A$ at the CF_4 tunnel. An interferogram of a 7.6 cm base 45° half-angle cone is shown in figure 3. Note that the maximum fringe shift is less than 1.0. In order to obtain more fringe crossings and also to determine the repeatability of a number of fringe shift measurements, the same flow and no-flow holograms were used to generate seven interferograms of slightly different fringe spacing. Fringe shift measurements were then made on each interferogram at 9 x-stations, where x is the distance in the direction of flow from the nose of the model.

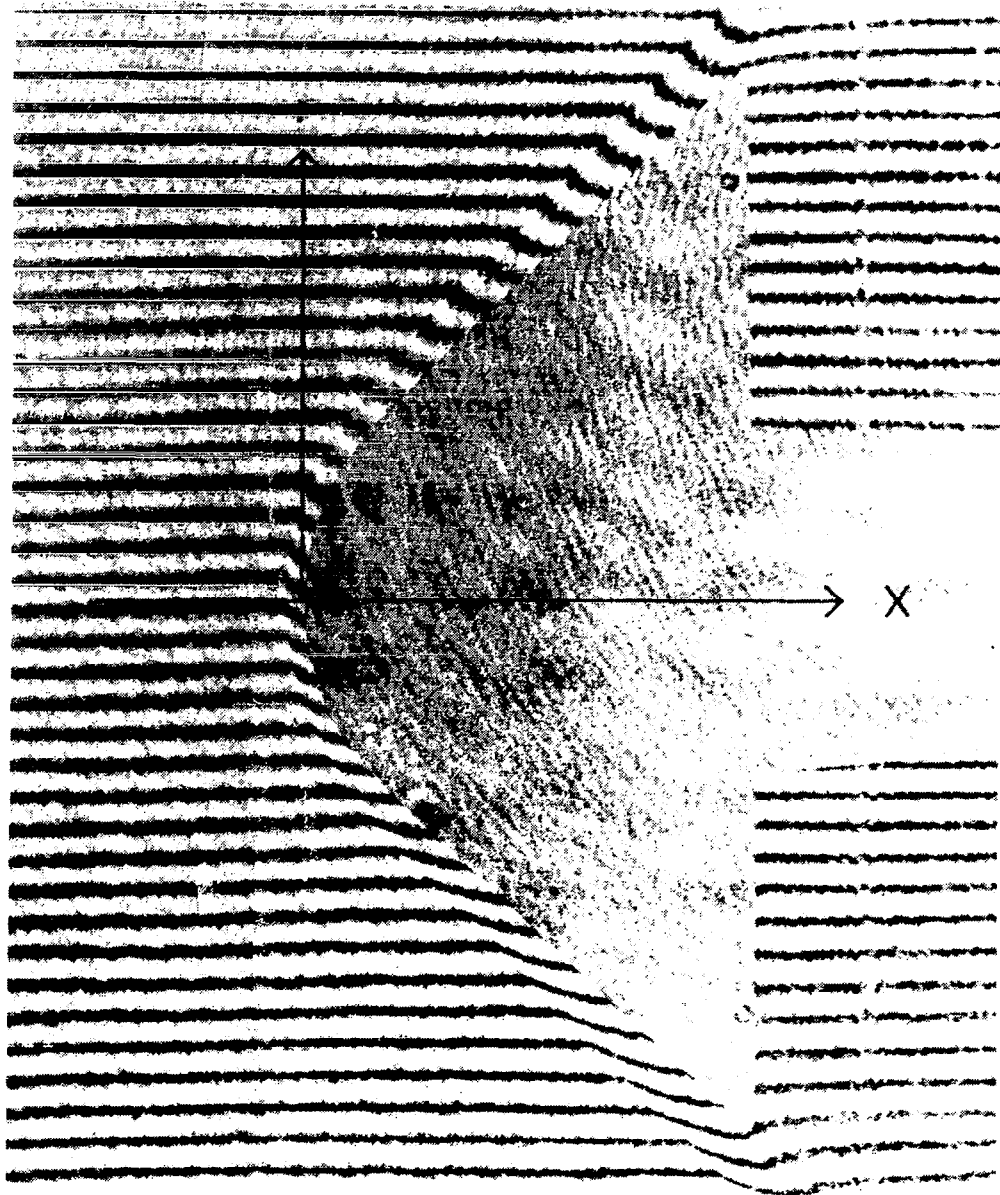


Figure 3

FRINGE SHIFT DATA

In figure 4 fringe shift S is plotted against r , the distance perpendicular to the flow from the model centerline. The plots are for x -stations slightly in front of the nose, 60% of the nose-to-base distance, and 95% of the nose-to-base distance. The solid line on the plots is the theoretical fringe shift curve calculated from the predicted density field. Note that a comparison of experimental and theoretical fringe shift curves is an effective way to verify computer codes which are used to predict density flow fields. This kind of comparison can be made for asymmetrical flows as well. When comparing experimental and theoretical fringe shift data it should be remembered that the fringe shift data is sensitive to interferogram alignment on the digitizing surface, especially so in front of the nose of the model where the slope of the shock can be very large. Also uncertainty in the freestream density will lead to uncertainty in the theoretical fringe shift calculations from the predicted density field. Another consideration in such comparisons is that the tunnel may be operating in a regime where the density predictions are not entirely valid.

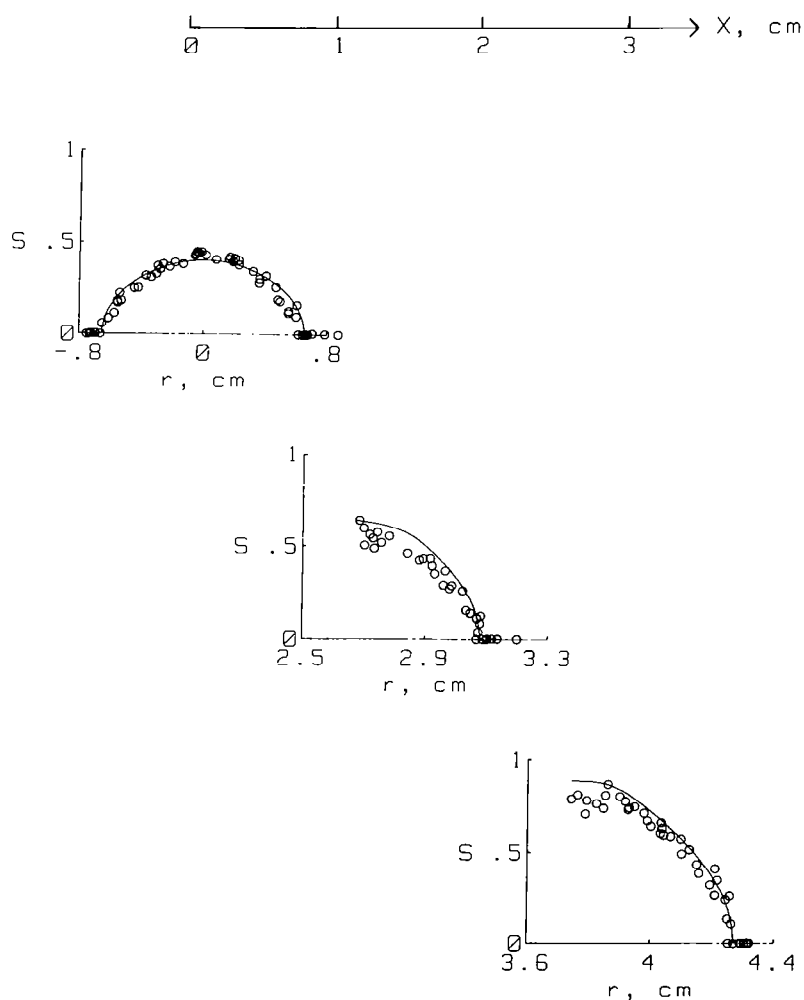


Figure 4

DEPENDENCE OF FRINGE SHIFT SHAPE ON DENSITY FUNCTION

Two density functions and their corresponding fringe shifts are presented in figure 5. The density and fringe shift functions are normalized by their on-axis values for comparison. The relatively large scatter of the data in figure 4 makes it difficult to match experimental fringe shift to a particular shape factor. The same problem occurs when attempting to invert the fringe shift data to obtain density since it is necessary to select a "best fit" curve to the experimental data before inversion. In order to use interferograms in which the maximum fringe shift is only 1 or 2 for determining density functions it is necessary that the interferogram be of much higher quality than required for visualization only.

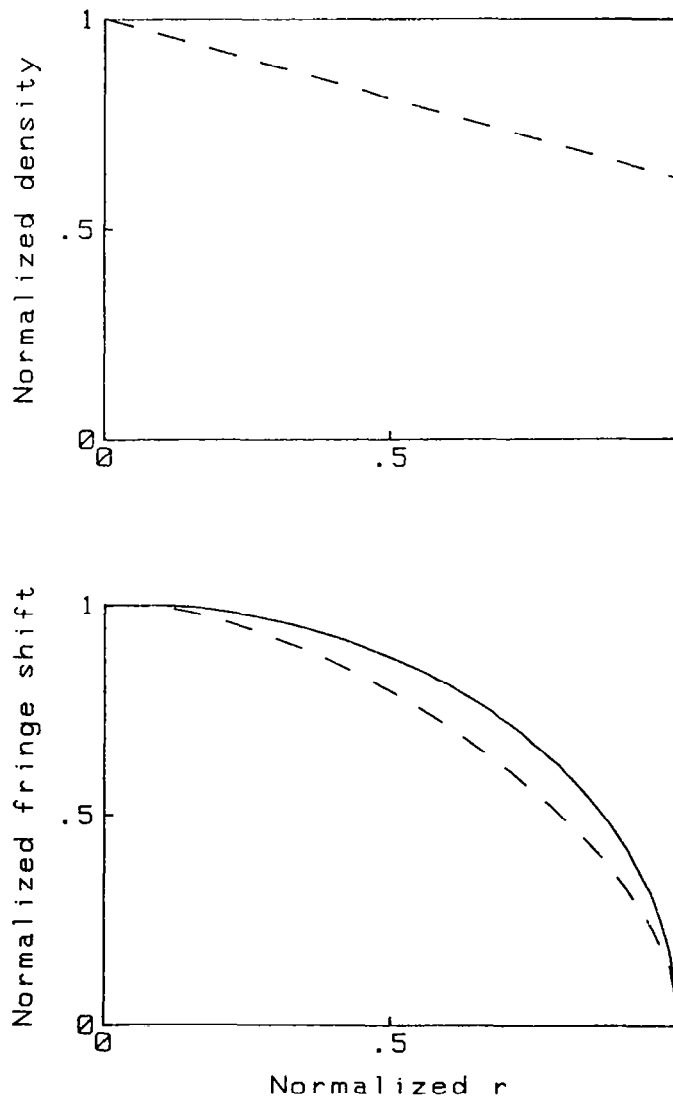


Figure 5

INTERFEROGRAM OF CONE WITH LARGER FRINGE SHIFT

If the fringe shift is larger then requirements on interferogram quality are lessened. Figure 6 is an interferogram of a 13 cm base, 60° half-angle cone for which the maximum fringe shift is about 5 at regions toward the base of the model. The combination of larger base, half-angle, and freestream density resulted in the increased fringe shift for this model.

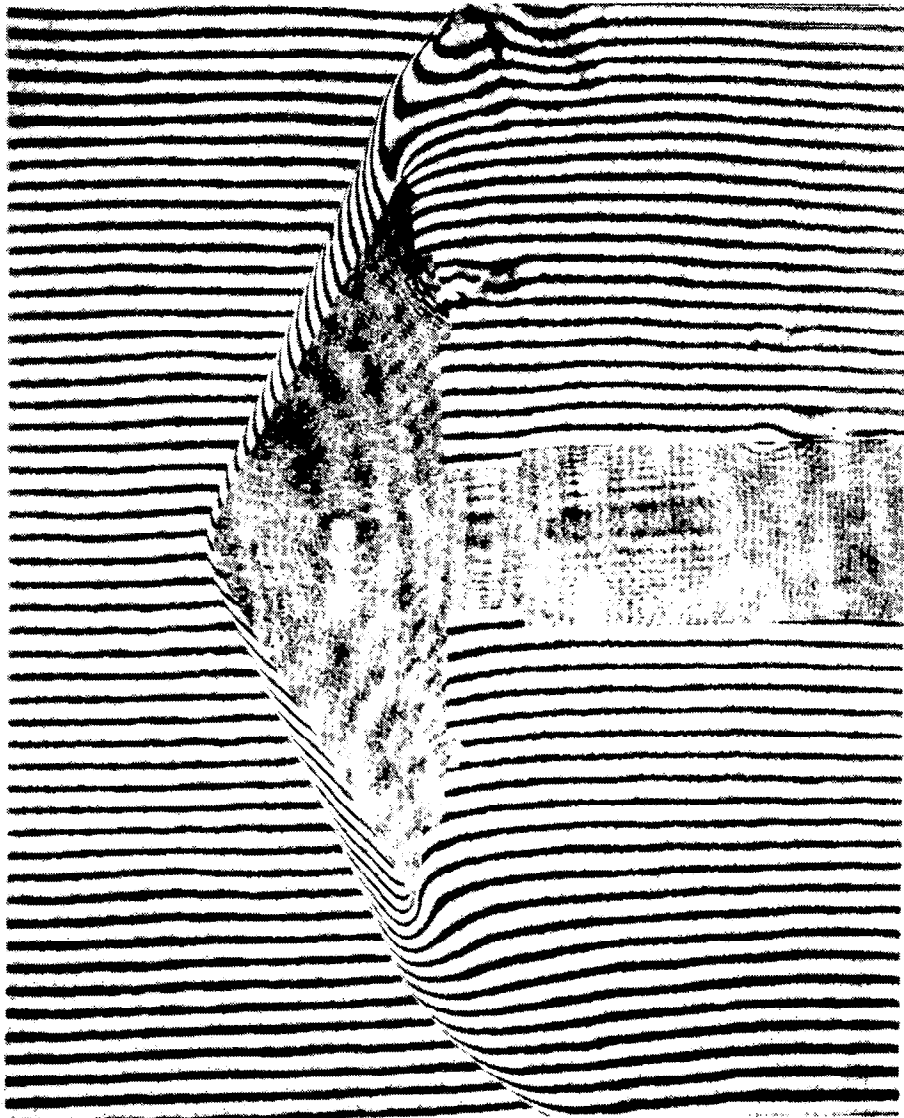


Figure 6

MATCHING OF EXPERIMENTAL FRINGE SHIFT DATA TO SHAPE FACTOR

In figure 7 the experimental fringe shift data taken near the base of the cone of figure 6 is normalized and matched for "best fit" to a theoretical fringe shift shape corresponding to a linear density increase from the shock (located at 7.2 cm from the model centerline) to the model (5.5 cm from model centerline). The density function corresponding to this shape factor is plotted above the fringe shift curve. This density function compared very well with the density function obtained by inverting the fringe shift data. For more complicated density functions a piecewise linear match of fringe shift shape can be made.

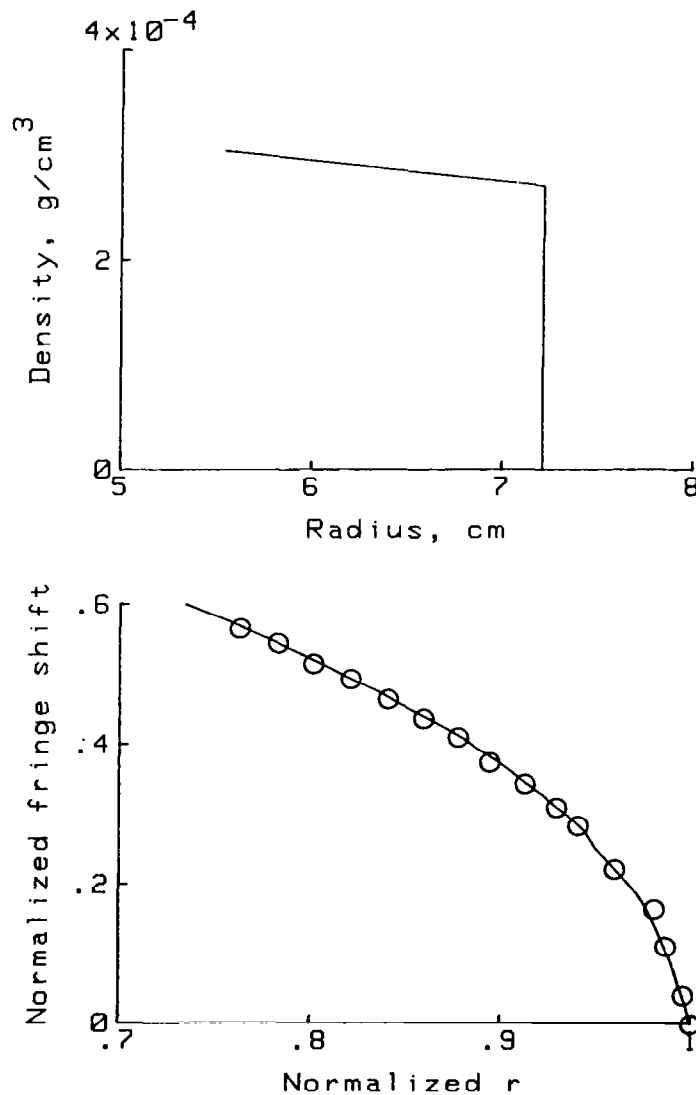


Figure 7

GEOMETRY OF TEST SECTION WINDOWS AND AIRFOIL AT 0.3 METER TCT

The flow field is viewed at the 0.3 meter TCT through "D-Shaped" fused silica test section windows as in figure 8. The lower window edge is 1.9 cm above the centerline of the airfoil so that the airfoil is not visible for flow visualization. For the flow visualization examples in the next two figures, a copper tube purge ring limited the field of view at the top of the photographs. This purge ring vented dry room-temperature N_2 onto the outer plenum windows to prevent condensation on the outer surfaces of the windows as the tunnel temperature was lowered.

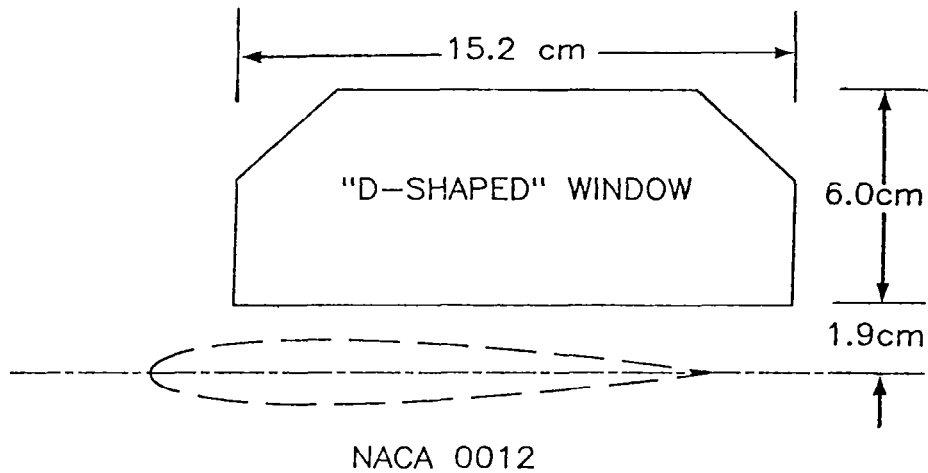


Figure 8

HOLOGRAPHIC FLOW VISUALIZATION FROM THE 0.3 METER TCT

Figure 9 shows a vertical knife-edge schlieren and interferogram from the same flow hologram recorded at the 0.3 meter TCT. The NACA 0012 airfoil was at 0°A-0-A. The Mach number was 0.77, stagnation temperature was 212 K and stagnation pressure was 2 atm. Flow is from left to right. For these relatively mild conditions the holograms are of excellent quality.

212 K 2 ATM M = 0.77

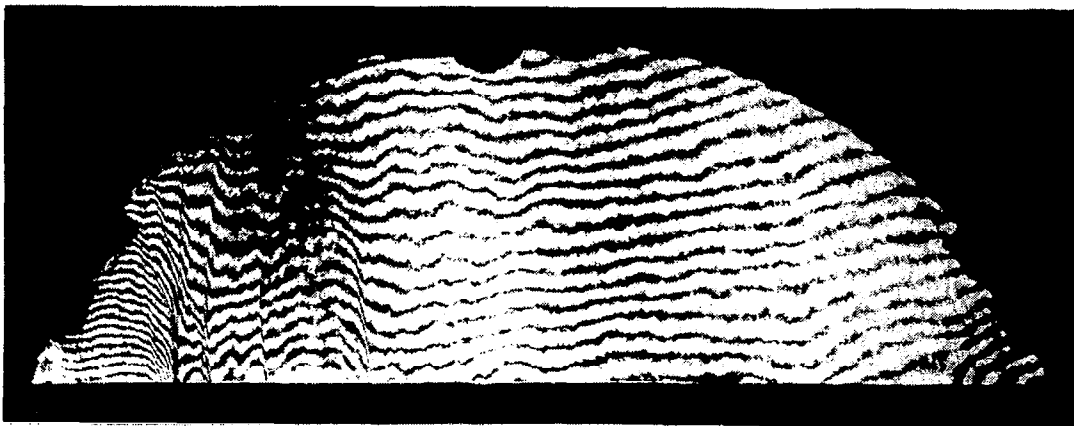
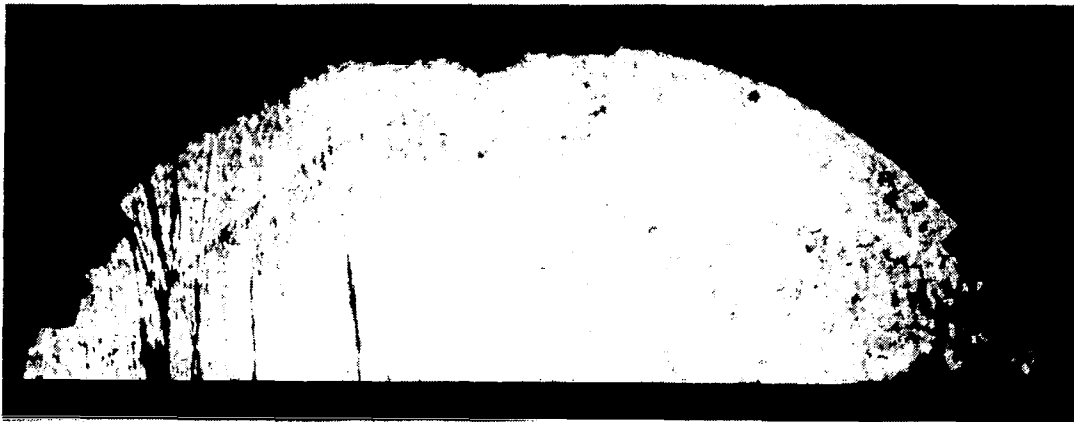


Figure 9

HOLOGRAPHIC FLOW VISUALIZATION AT 100 K

Figure 10 is a focused shadowgraph reconstructed from a hologram made at the 0.3 meter TCT. The NACA 0012 airfoil was at 0°A-0-A. The Mach number was 0.77, stagnation temperature was 100 K, and stagnation pressure was 4 atm. Flow is from left to right. Note the grainy appearance of the reconstruction and the very strong (optically) shock. At this condition it has not been possible to produce interferograms. The lowest temperature at which interferograms have been produced is 125 K at 2 atm pressure. At those conditions where interferograms were not possible the spot size at the schlieren focus was noted to be much larger than for those conditions where interferometry was possible. More work is in progress to determine if the degradation noted for these more severe conditions is due to experimental artifact (e.g., condensation on a window) or if it is a fundamental limitation imposed by the low temperature and high pressure.

100 K 4 ATM M = 0.77

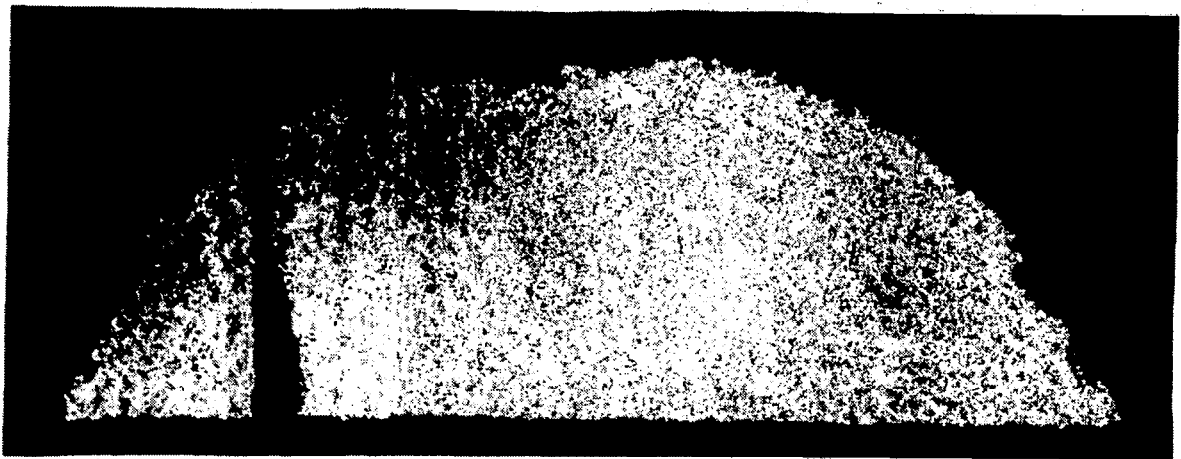
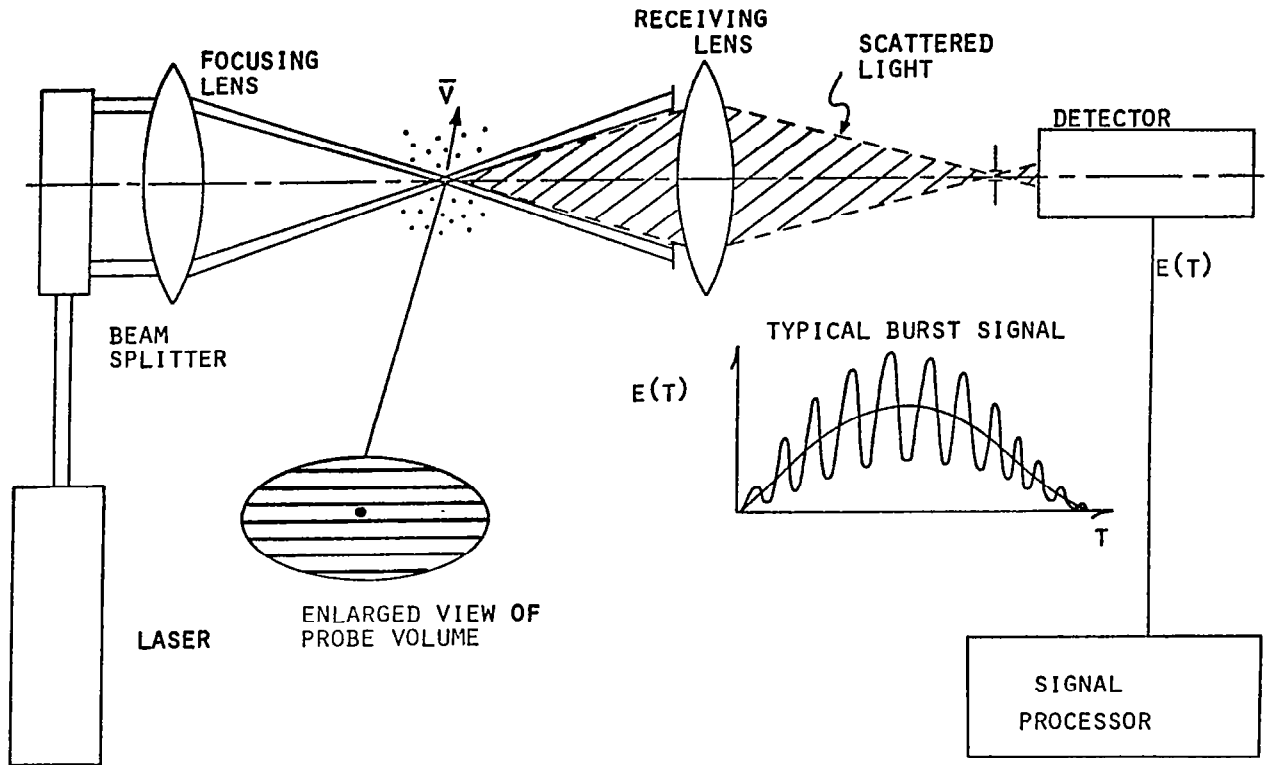


Figure 10

LASER VELOCIMETRY - A STATE-OF-THE-
ART OVERVIEW

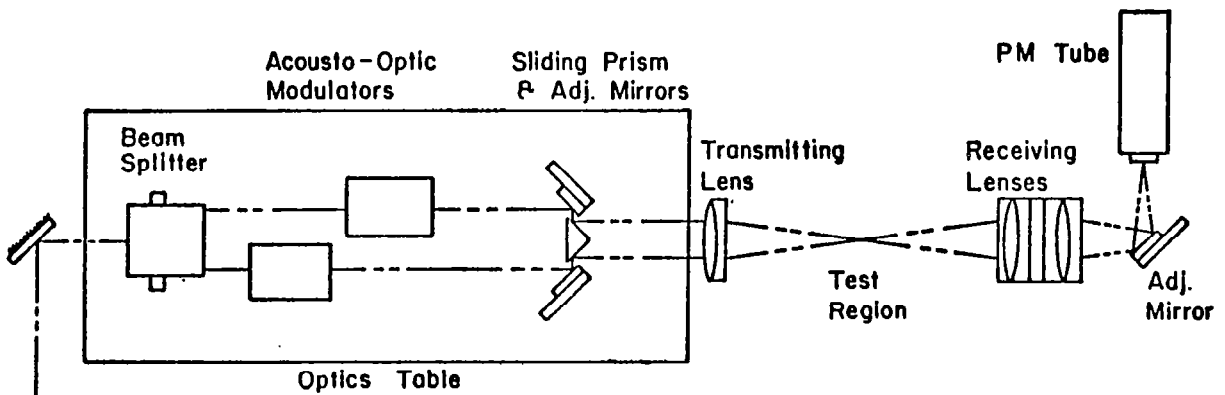
Warren H. Stevenson
School of Mechanical Engineering
Purdue University
West Lafayette, Indiana 47907

TYPICAL DIFFERENTIAL DOPPLER LDV

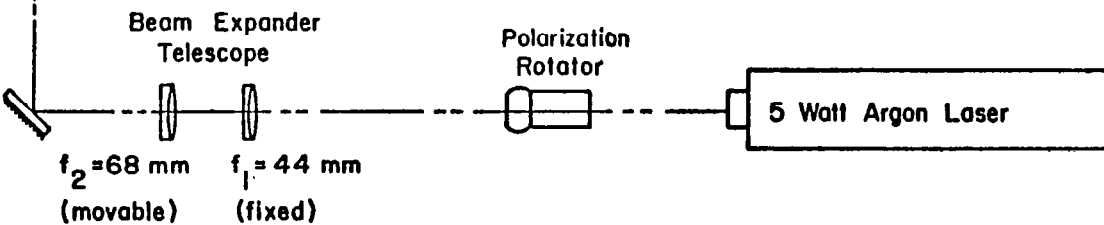


VARIABLE PARAMETER LDV SYSTEM

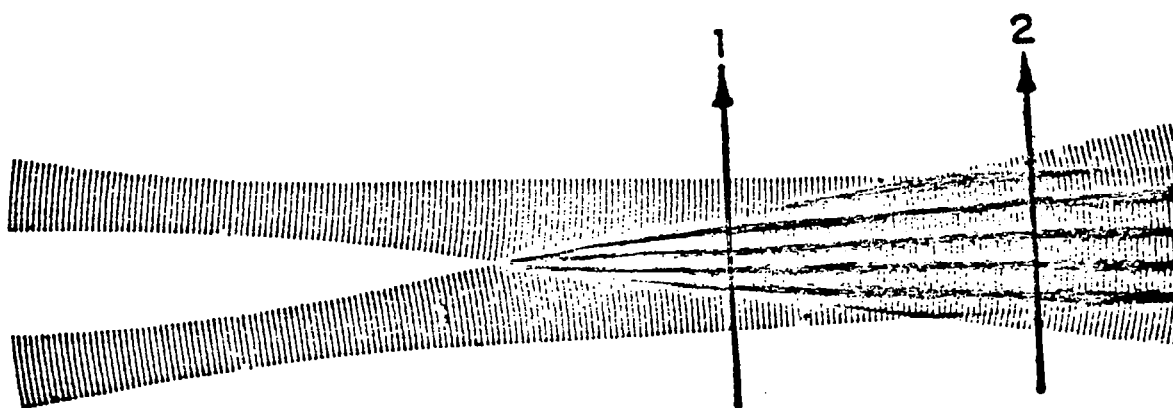
UPPER OPTICS PACKAGE



LOWER OPTICS PACKAGE



FRINGE MODEL



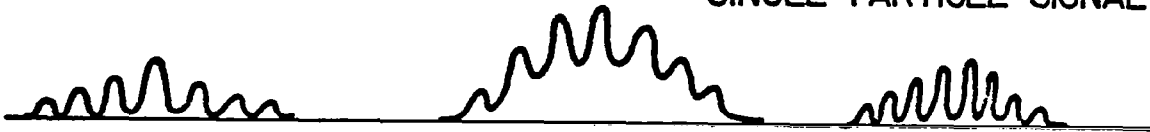
Fringe model indicating variations in Doppler frequency.
Beam waists are on same side of focal plane.

When beam intersection does not occur at the waists, the fringe planes in the probe volume will not be parallel and the observed signal frequency will depend on particle trajectory. This effect, though small, can lead to an increase in the measured turbulence intensity. Perhaps of more significance in most cases is that the beam intensity is higher at the waists than in the probe volume. This results in a lower signal-to-noise ratio.

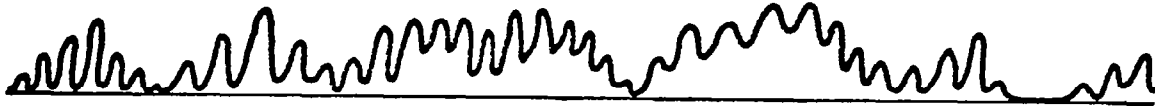
Durst, F. and Stevenson, W. H., "Influence of Gaussian Beam Properties on Laser Doppler Signals," Applied Optics, 18, 516 (1979).

NATURE OF VOLTAGE SIGNAL

SINGLE PARTICLE SIGNAL



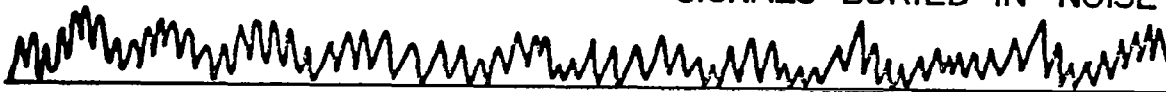
MULTIPARTICLE SIGNAL



PHOTON LIMITED SIGNAL



SIGNALS BURIED IN NOISE



The nature of the voltage signal observed at the detector output will depend on several factors including the laser power, scattering efficiency of the particles, and particle seeding density. In high speed wind tunnels either single particle "burst" signals or photon limited signals will be typical.

SIGNAL PROCESSING DEVICES

SPECTRUM ANALYZER

FREQUENCY TRACKER

BURST PROCESSOR (COUNTER)

PHOTON CORRELATOR

TRANSIENT RECORDER

The parameters usually desired from the sampled velocity data are

Mean Velocities	$\bar{u}, \bar{v}, \bar{w} ?$
Turbulence Intensity	$\overline{u'^2}/U$ etc.
Reynolds Stress	$\overline{u'v'}$
Power Spectrum	$E(\omega)$

COMMENTS ON SEEDING

Experience has shown that particles $\lesssim 1 \mu\text{m}$ are needed to make accurate measurements in gas flows. Below $1 \mu\text{m}$ the scattered intensity drops off rapidly and above $1 \mu\text{m}$ the particles do not follow the flow. However, smaller particles may be necessary in situations where extremely high accelerations are present.

In tunnels where "zero" seeding is allowed, natural contaminants in the tunnel must be used. This can pose severe requirements on the LDV system, both in terms of the optical design and the signal processing.

Various methods of particle generation are available including liquid atomization, solid particle dispersal, and "chemical" seeding with reacting gases.

Yanta, W. J. "The Use of the Laser Doppler Velocimeter in Aerodynamic Facilities," Paper 80-0435, 10th AIAA Aerodynamics Testing Conference (1980).

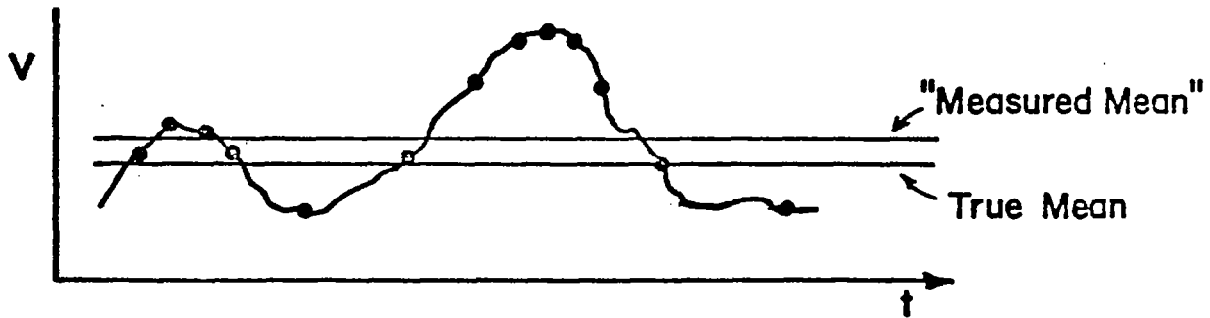
IMPORTANT BIAS ERRORS WHICH OCCUR IN LDV MEASUREMENTS USING BURST (COUNTER) PROCESSORS

<u>BIAS</u>	<u>SOURCE</u>
Particle Lag	Particle Inertia
Directional Ambiguity Bias	Lack of Directional Sensitivity in LDV
Velocity Bias	Particle Controlled Sampling
Incomplete Signal Bias	Signal Validation Based on Fixed Number of Cycles

Both directional ambiguity and incomplete signal bias may be eliminated by frequency shifting.

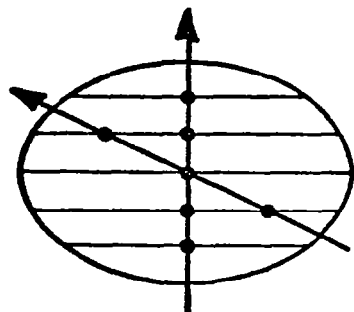
VELOCITY BIAS

ARISES WHEN A PARTICLE (ENSEMBLE) AVERAGE RATHER THAN A TIME AVERAGE OF THE DATA IS USED.

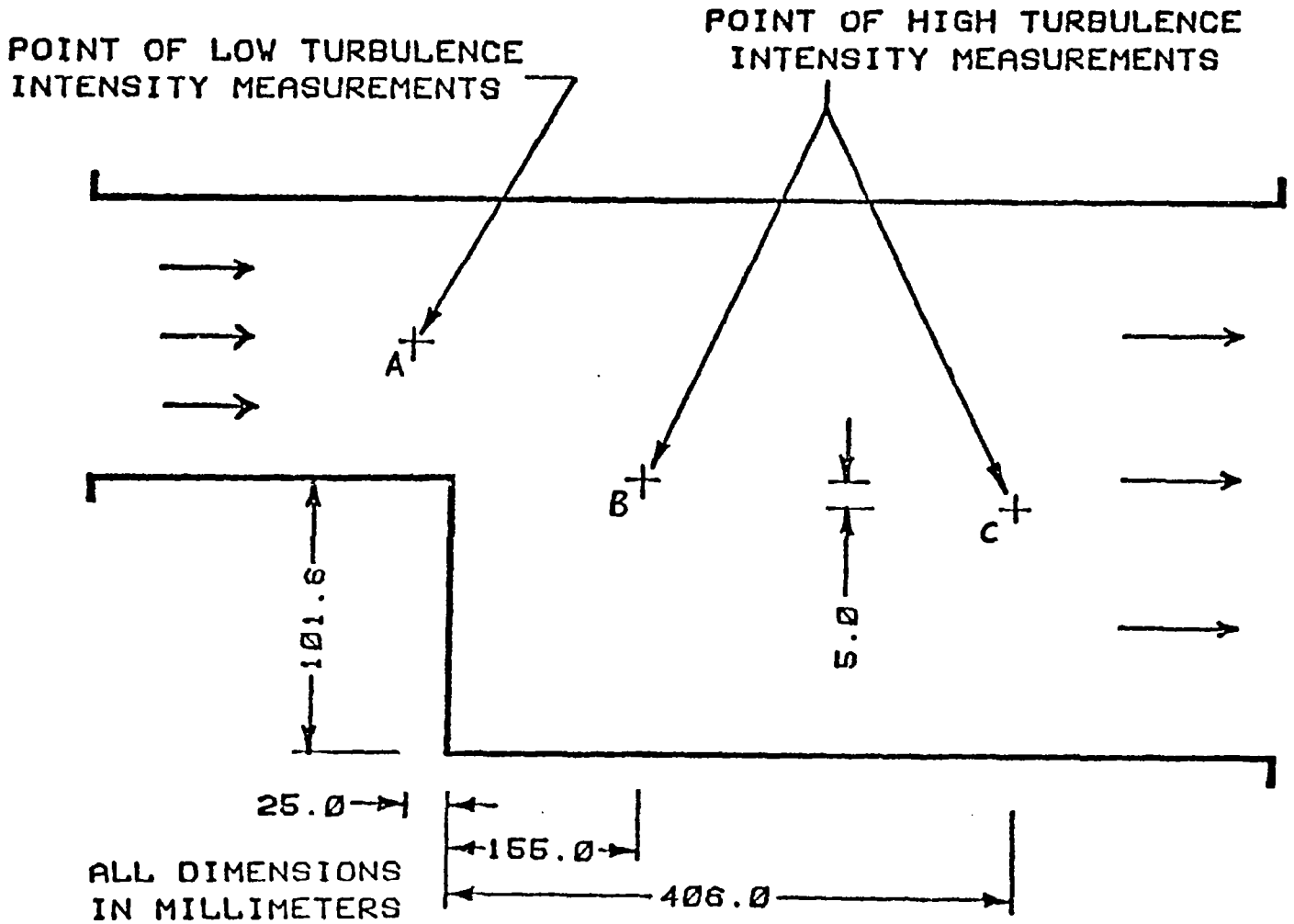


INCOMPLETE SIGNAL BIAS

ARISES IN HIGHLY TURBULENT FLOWS WHEN PARTICLES AT A LARGE "ANGLE OF ATTACK" FAIL TO CROSS THE NUMBER OF FRINGES NEEDED TO TRIGGER AN OUTPUT FROM THE PROCESSOR. THIS LEADS TO AN ERRONEOUSLY HIGH MEASURED MEAN VELOCITY WHEN THE FRINGES ARE ALIGNED PERPENDICULAR TO THE LOCAL MEAN VELOCITY VECTOR.

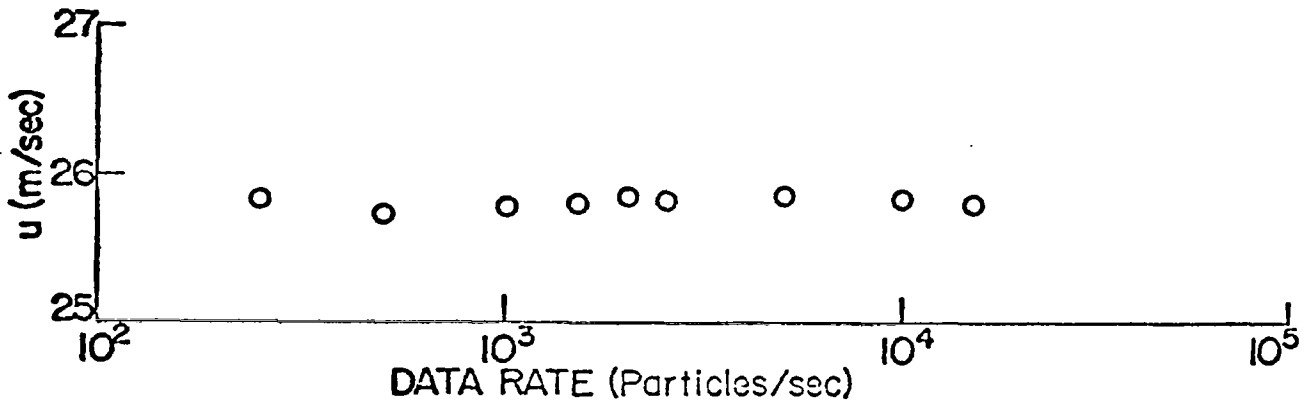


FLOW GEOMETRY OF VELOCITY BIAS STUDY

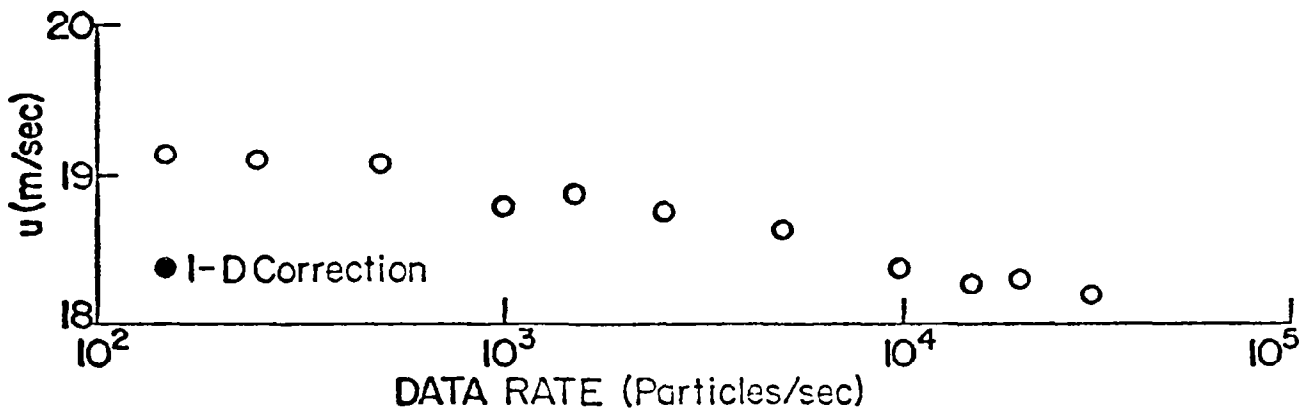


Flow geometry used in Purdue study of velocity bias is shown above. At point A the flow was essentially laminar. At points B and C the turbulence intensity was 20% and 35% respectively.

EFFECT OF DATA RATE ON MEAN VELOCITY



Effect of Data Rate on Mean Velocity at Point A

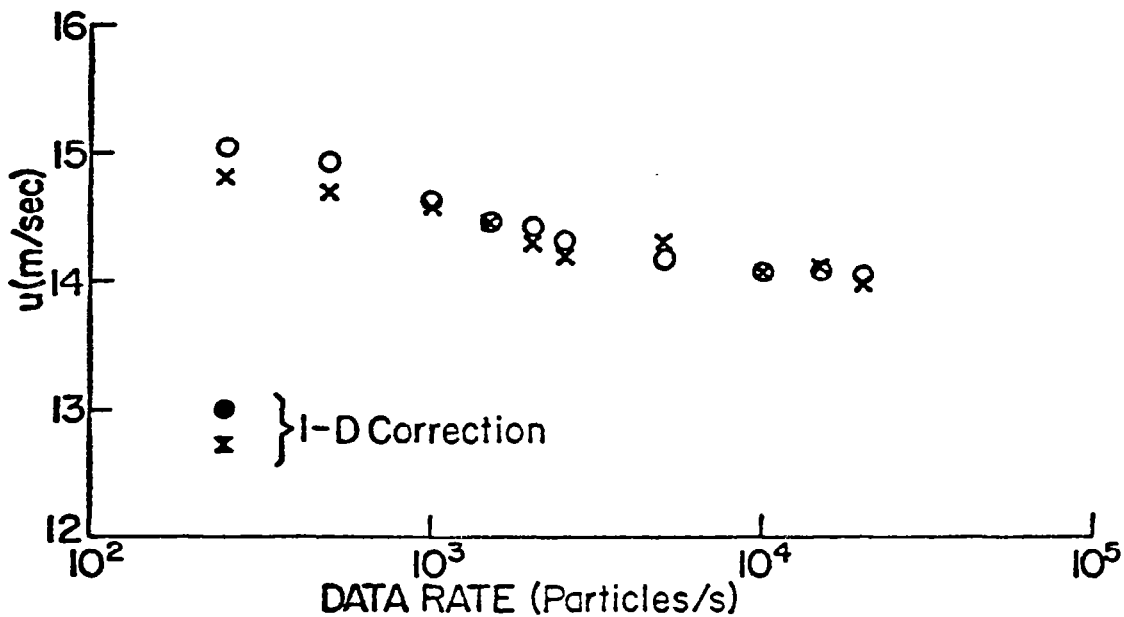


Effect of Data Rate on Mean Velocity at Point B

In the above figures "data rate" refers to the number of validated Doppler signals per second when the processor was uncontrolled. This depends on seeding density. The velocity data shown were taken with the processor controlled by a microcomputer so that a fixed waiting time occurred after a velocity sample was stored before the processor was available to accept a new signal. At the high data rates (high seeding density) this resulted in essentially equal time interval sampling of the velocity at a sample rate of 250 Hz.

The analytically corrected data point shown in the second figure is based on the 1-D correction of McLaughlin and Tiederman.

EFFECT OF DATA RATE ON MEAN VELOCITY (Concluded)



Effect of Data Rate on Mean Velocity at Point C
 x = 25 Hz Sampling Rate
 o = 250 Hz Sampling Rate

Roesler, T. C., Stevenson, W. H., Thompson, H. D.,
 "Investigation of Bias Errors in Laser Doppler
 Velocimeter Measurements," AFWAL-TR-80-2105, December
 1980.

AREAS REQUIRING FURTHER STUDY

Velocity Bias - "The Final Word"
 Improved Designs for 3-D Systems
 Measurements Near Surfaces

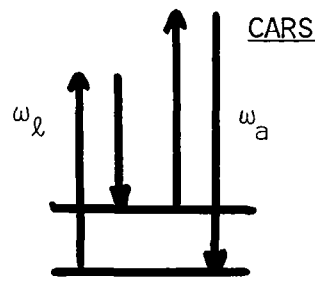
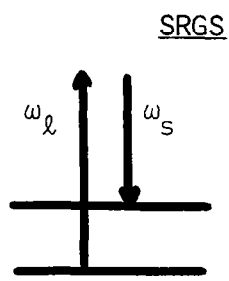
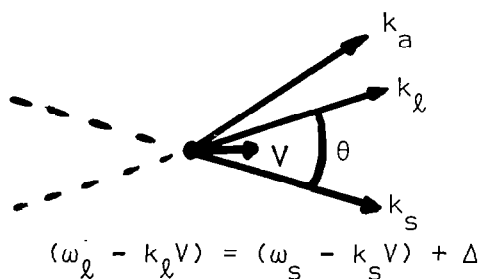
COHERENT RAMAN SPECTROSCOPIES FOR MEASURING
MOLECULAR FLOW VELOCITY

C. Y. She
Department of Physics
Colorado State University
Fort Collins, Colorado 80523

GENERAL

1. Molecular flow velocity can be measured directly by probing the velocity dependent Raman shift (Doppler effect) of the flowing molecules. No seeding is required.
2. Because of the small Doppler shift (~ 1 GHz), high frequency resolution is required. Thus, spontaneous Raman scattering will not work; any type of coherent Raman spectroscopy (SRGS, CARS, IRS, or CSRS) will do.
3. The direction as well as the magnitude of the velocity is measured. The measurement is easier for faster flow which gives a larger Doppler shift.
4. When pressure broadening dominates, backward scattering geometry is preferred ($\theta \sim 180^\circ$).
5. High spatial resolution may be achieved by crossing pump and probe beams.

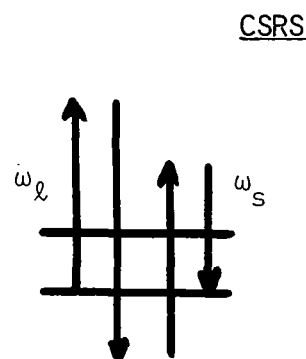
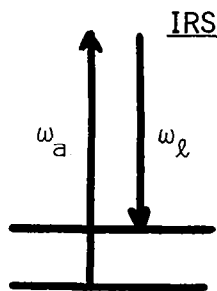
PROCESSES



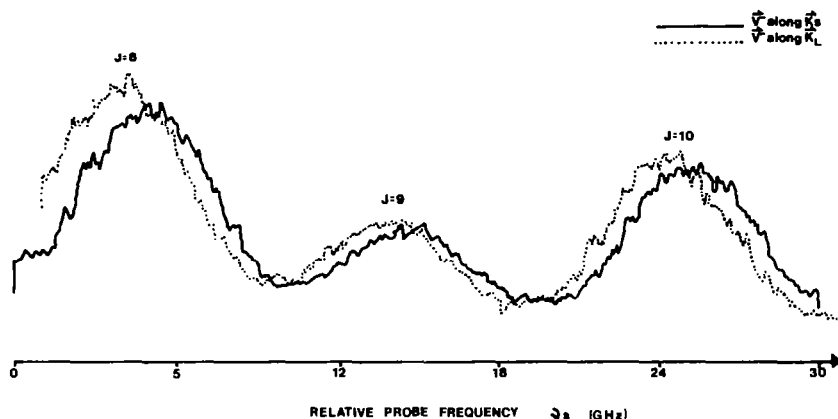
SRGS: $\omega_s = (\omega_l - \Delta) - (k_l - k_s)V$

CARS: $\omega_a = (\omega_l + \Delta) + (k_l - k_s)V$

IRS & CSRS: $(k_l - k_s) \rightarrow (k_a - k_l)$



INITIAL EXPERIMENT



SRGS of the Q-branch N_2 vibrations at 2331 cm^{-1} with oppositely directed flows (backward scattering). Pump: 5 MW, 5320 \AA , Q-switched; Probe: 20 mW, single-frequency dye.

POTENTIAL

1. Much better S/N can be obtained if lasers with lower intensity and frequency fluctuations are used. IRS experiments using a pulsed dye amplifier and a single-frequency argon-ion laser are in progress.
2. Using a 3-D phase matching arrangement, two-dimensional velocity vectors can be measured by CARS and CSRS.
3. With currently available electronic technology, CARS and CSRS spectra can, in principle, be taken on single-shot basis. This will reduce the measurement time from 10 min. to less than 1 sec.
4. Such spectra contain information on species concentration and temperature as well. The proposed method has the potential for measuring all interesting flow parameters.

MEASUREMENT POTENTIAL
OF
LASER SPECKLE VELOCIMETRY

Ronald J. Adrian
University of Illinois at Urbana-Champaign
Department of Theoretical and Applied Mechanics

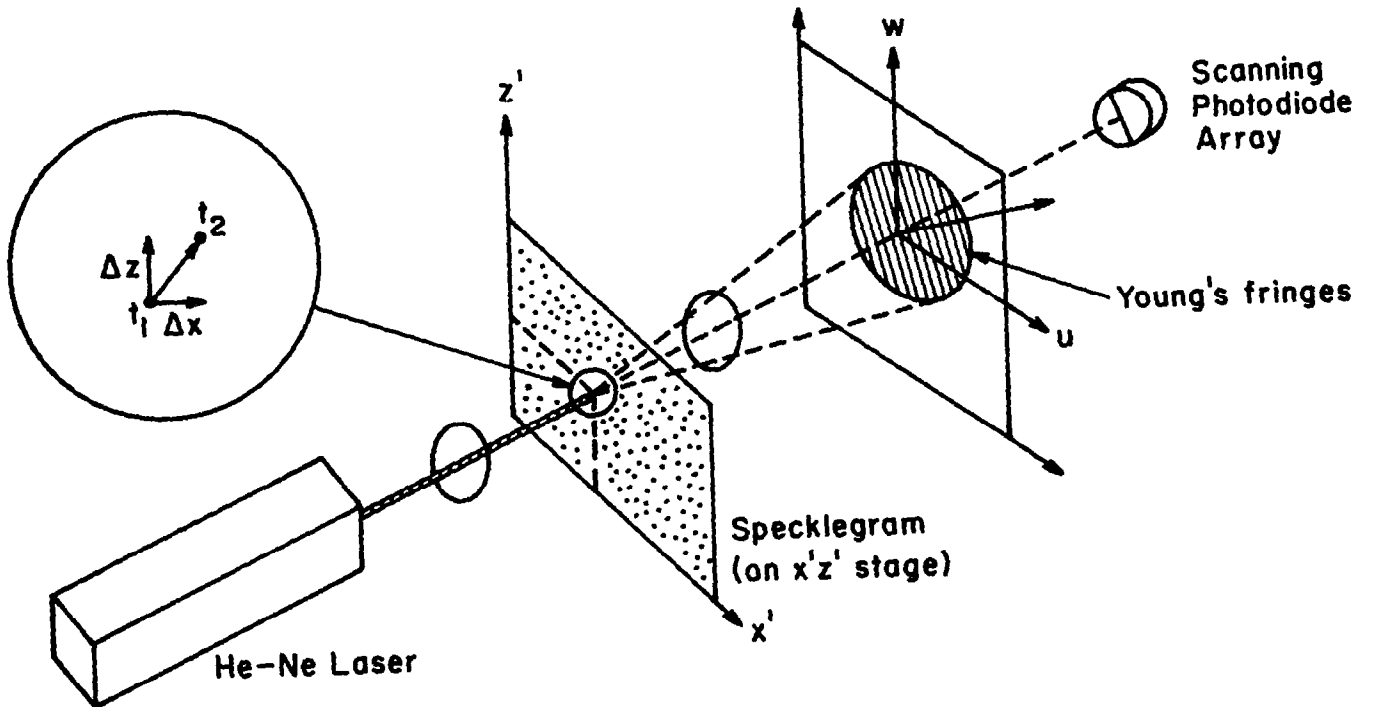
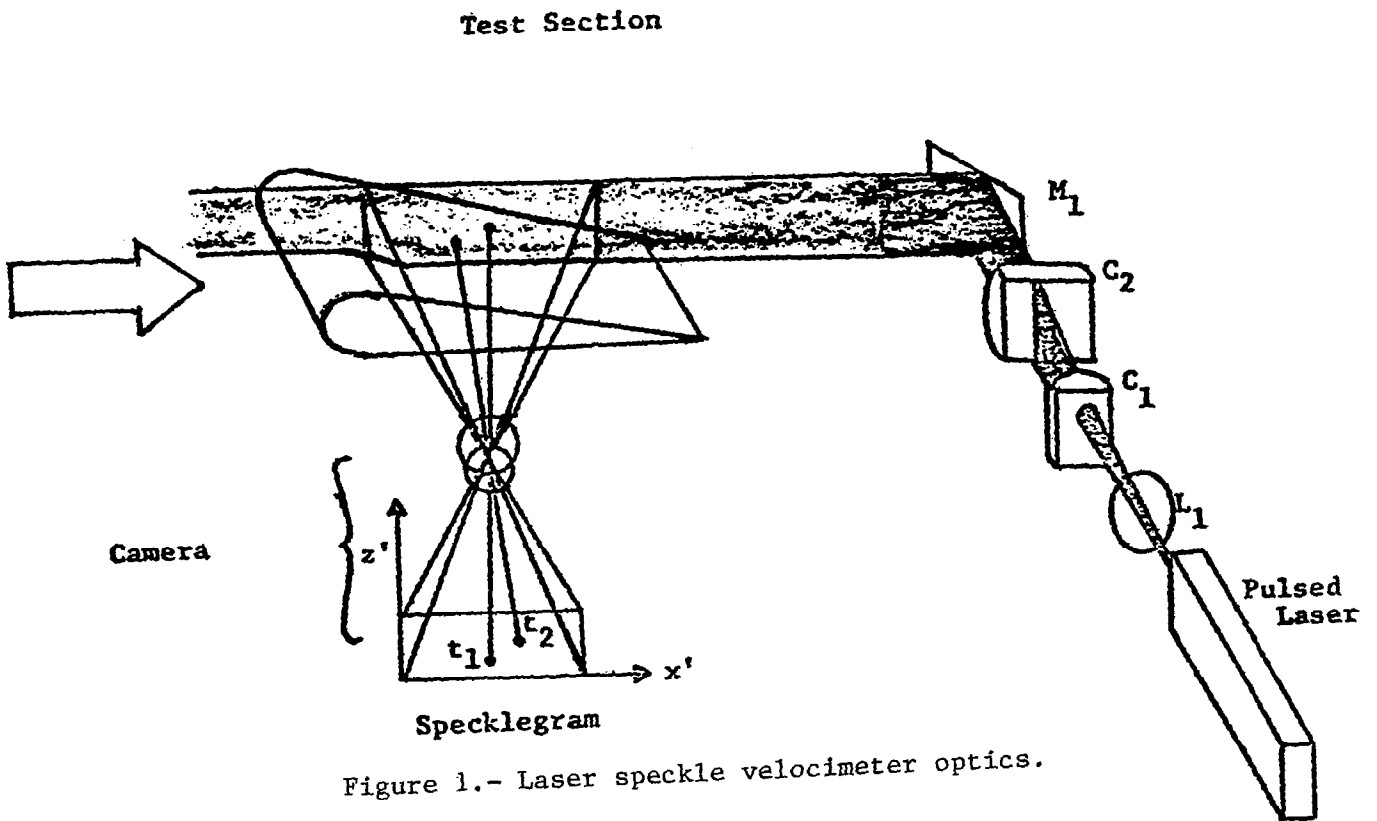
Laser speckle velocimetry, hereafter called "LSV", refers to the measurement of fluid velocity by measuring the translation of speckle patterns, or in the simplest case, individual particles that are moving with the fluid. The measurement is accomplished by illuminating the fluid with consecutive pulses of laser light and recording the images of the particles or the speckles on a double exposed photographic plate, Figs. 1 and 2. The plate contains flow information throughout the image plane so that a single double exposure may provide data at hundreds or thousands of points in the illuminated region of the fluid, as illustrated in Fig. 3 (P.G. Simpkins and T.D. Dudderar, 1978, J. Fluid Mech., 89, 665-71). Conventional interrogation of the specklegram involves illuminating the plate to form Young's fringes, whose spacing is inversely proportional to the speckle separation. Subsequently the fringes are digitized and analyzed in a computer, possibly by 2-D FFT, to determine their frequency and orientation, yielding the velocity magnitude and orientation. The time consumed by this process is one of the major drawbacks of LSV at present. For example, current "fast" processing at the rate of 10 s per point would require more than 3 hours to process 10^3 velocities on a single specklegram.

The Young's fringe technique is equivalent to performing a 2-D spatial correlation of the double exposed specklegram intensity pattern, and this observation suggests that correlation should be considered as an alternative processing method. The principle of the correlation technique is that the correlation of the transmission will have a secondary maximum at separations corresponding to the mean displacement of the fluid within the interrogated spot, Figs. 4 and 5. Two methods have been devised which produce an output proportional to the correlation by superposing the spatially translated image of the interrogated spot back onto the specklegram with unity magnification.

The first one, Fig. 6, uses an oscillating mirror with $1\text{ms}/\text{scan}$, whereas the second uses a dual Bragg cell with about $1\mu\text{s}/\text{scan}$. Figure 7 shows a heterodyne technique employing a 2-D Bragg cell.

Simply scanning and recording the correlogram requires enormous data storage when high velocity resolution is required: 128 K words are needed to store 256 line scans with 512 words each, Fig. 8. Clearly, simplified techniques are essential; one possibility is to scan the entire $s_1 - s_3$ plane but only store the (s_1, s_3) addresses of those points which yield correlation values greater than a threshold value. Those points, presumably fewer than a thousand in number if the threshold is properly set, could then be readdressed to obtain their amplitude values. Other possibilities are to use coarse interval scanning followed by scanning with high resolution the limited region containing the correlation peak, or to scan coarsely until a peak is found, followed immediately by high resolution scanning, Fig.9. The velocity is found by calculating the centroid of the correlator peak, and the width of the peak σ_1 should be of the order of a spot diameter, or a particle image diameter.

Some estimates of the performance parameters of an LSV applied to a high speed wind tunnel measurement are shown in Fig. 10. Spatial resolution is poor because the field of view, $1\text{m} \times 0.75\text{m}$, is large and because a modest $F/10$ lens has been assumed. An $F15$ lens combined with a $200\text{mm} \times 150\text{mm}$ field of view would yield 1mm spatial resolution.



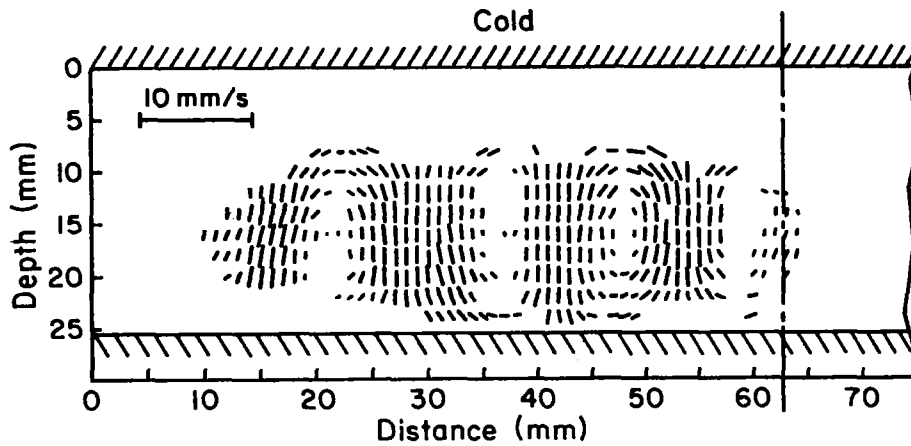
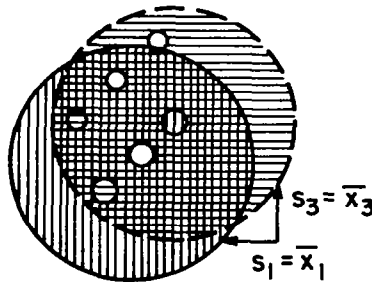


Figure 3.- Two-dimensional velocity field obtained in the unsteady Bénard convection experiment by Simpkins and Dudderar. (From P.G. Simpkins and T.D. Dudderar, Laser Speckle Measurements of Transient Bénard Convection, Journal of Fluid Mechanics, volume 89, part 4, by permission of Cambridge University Press.)

● Transmissivity of Specklegram = $T(x_1, x_3)$

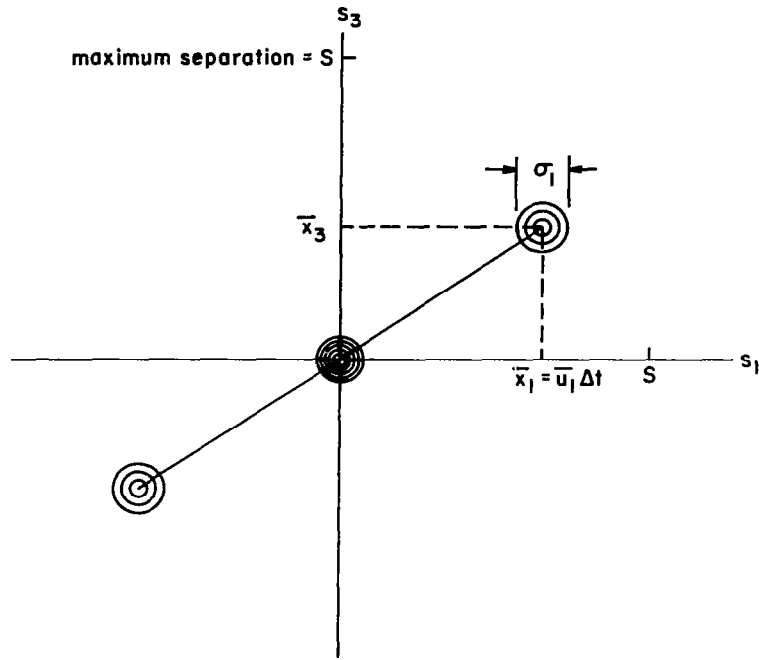


● Correlation Concept



● $J(s_1, s_3) = \int I_0(x_1, x_3) T(x_1, x_3) T(x_1 + s_1, x_3 + s_3) dx_1 dx_3$
 = maximum when $(s_1, s_3) = (u_1 \Delta t, u_2 \Delta t)$

Figure 4.- Interrogation by 2-D correlation.

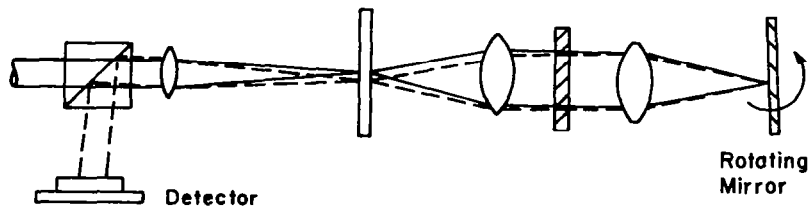


Velocity Resolution $\propto \sigma_1 / \bar{x}_1 > \sigma_1 / S$

Spatial Resolution $\propto S$

Figure 5.- Correlation plane.

- Mirror Deflection (1 ms/scan)
Polarization Splitter



- Bragg Cell Deflection (1 μs/scan)

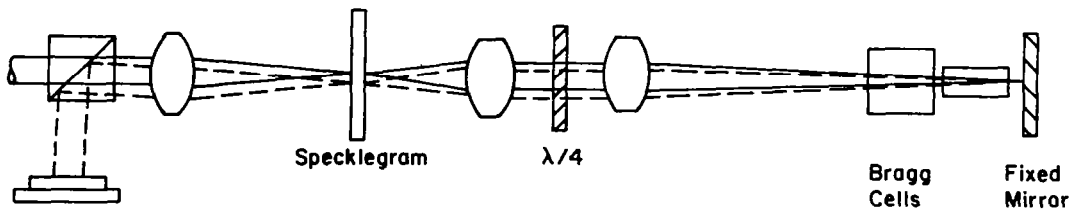
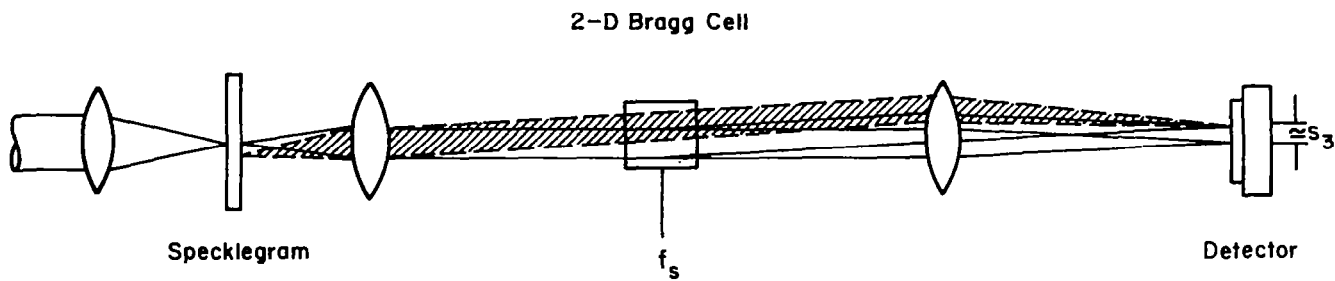


Figure 6.- Fast 2-D transmission correlation.



Maximum Heterodyne Signal Strength When $s_3 = \bar{x}_3$

Figure 7.- Fast 2-D heterodyne correlation.

0.2% full scale requires 512 x 256 points on the specklegram correlation if done blindly, e.g., 256 scans across s_1 with 512 points stored per scan.

Total time at 1 ms/scan = 0.25 s

Total data storage = 128 k words

Smart scanning - store (s_1, s_3) if J exceeds threshold.

Total data storage \cong 1 k words

Total time at 1 ms/scan \cong 0.25 s

Figure 8.- Correlation speed.

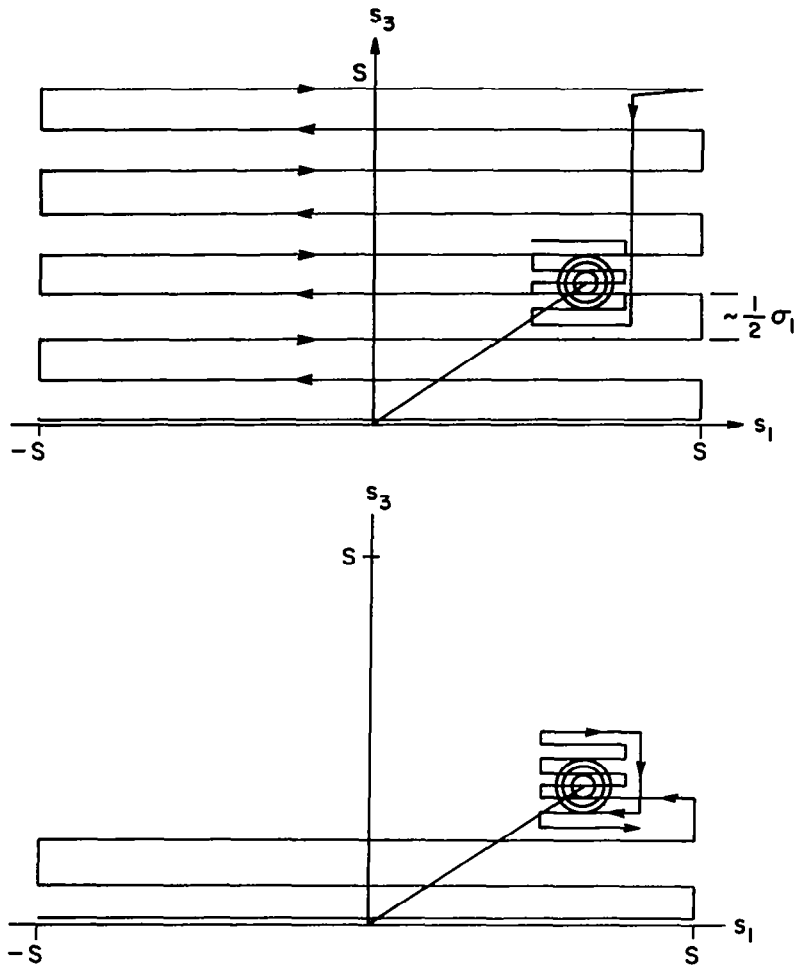
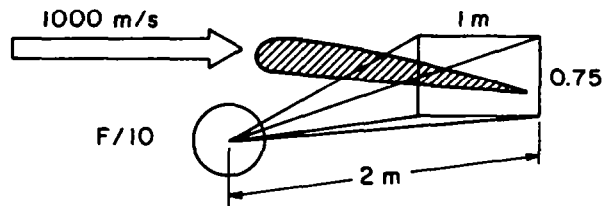


Figure 9.- Search methods.



Spatial Resolution: 10 mm

Temporal Resolution: $1 \mu\text{s} \pm 3 \text{ ns}$

Velocity Resolution: $\pm 0.6\%$ of full scale

Particle Resolution: $1.5 \mu\text{m}$

Figure 10.- Performance.

STATUS OF LASER ANEMOMETRY IN TURBOMACHINERY RESEARCH
AT THE LEWIS RESEARCH CENTER

Richard G. Seasholtz
NASA Lewis Research Center
Cleveland, Ohio

OPTICAL CONFIGURATION FOR FRINGE-TYPE
LASER ANEMOMETERS

Laser anemometer systems have been developed for a full-annular turbine stator cascade facility and for a compressor rotor facility; both are ambient temperature axial-flow facilities with a 20-inch tip diameter. The optical configurations of the two anemometers are similar single-component fringe-type backscatter systems with a probe volume diameter of $125\ \mu\text{m}$ and length of about 2 mm. The effective f-number of the receiving optics is about $f/5$. A rhodamine 6G fluorescent dye aerosol, which fluoresces orange when excited by the 514 nm laser light, is used to allow rejection of unwanted scattered light from surfaces near the probe volume. Measurements can be made to within 1 mm of the hub. The estimated diameter of the particles actually measured is about $1.2\ \mu\text{m}$. For the rotor measurements the data are accepted continuously with the rotor position at the time of each measurement determined by a unique electronic shaft angle encoder.

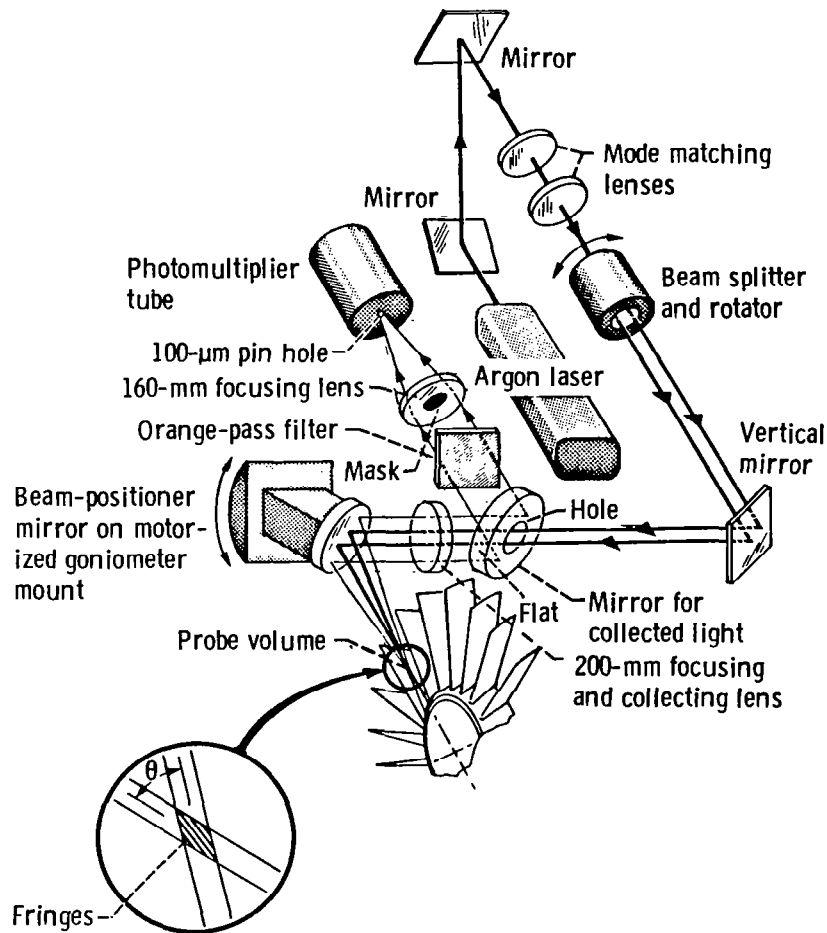
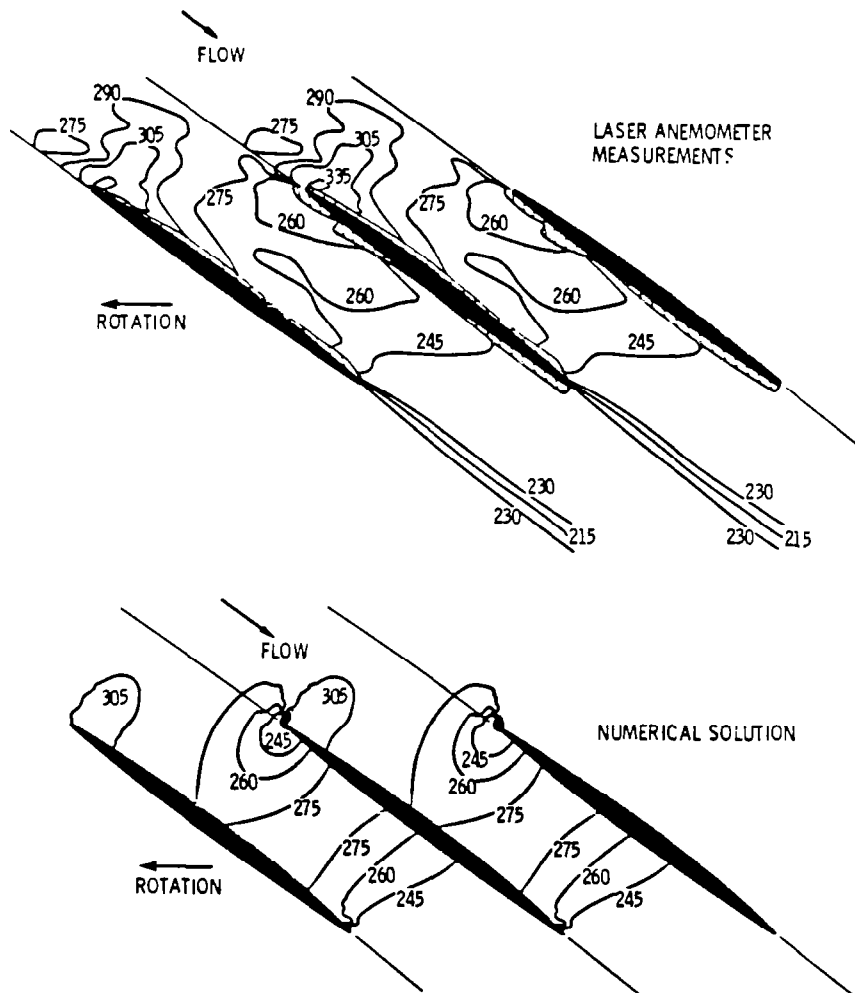


Figure 1

COMPARISON OF LASER ANEMOMETER MEASUREMENTS AND NUMERICAL SOLUTION FOR A TRANSONIC AXIAL-FLOW COMPRESSOR ROTOR

The results of an inviscid computer code are compared with laser anemometer measurements taken at mid-span. The operating point was 70 percent of design speed near maximum efficiency. The cross-hatched areas near the blade denote regions in which no measurements were obtained. The numerical and experimental results display reasonable agreement in the expansion region around the blade leading edge, but the LA measurements indicate less diffusion than predicted by the numerical solution near the pressure side of the blade passage in the rear portion of the passage.



RELATIVE VELOCITY
 CONTOURS IN (M/SEC)
 Figure 2

TURBINE STATOR TEST SECTION

The test section consists of a sector of four vanes, which are part of the full-annular ring of 36 vanes. The vanes, of constant profile from hub to tip, have a height of 1.5 inches and an axial chord of 1.5 inches. All measurements were taken at the design mean-radius exit critical velocity ratio of 0.78. A cutout in the test section outer vane ring provides optical access. The test vanes in this region have been machined to the vane tip radius to permit a cylindrical window to fit flush with the tip endwall. The 1/8-inch thick glass window was formed by sagging it, in a vacuum furnace, onto a machined graphite form. The form was designed so that the window area used for the measurements did not touch the form during the sagging process to avoid creating surface imperfections in the glass.

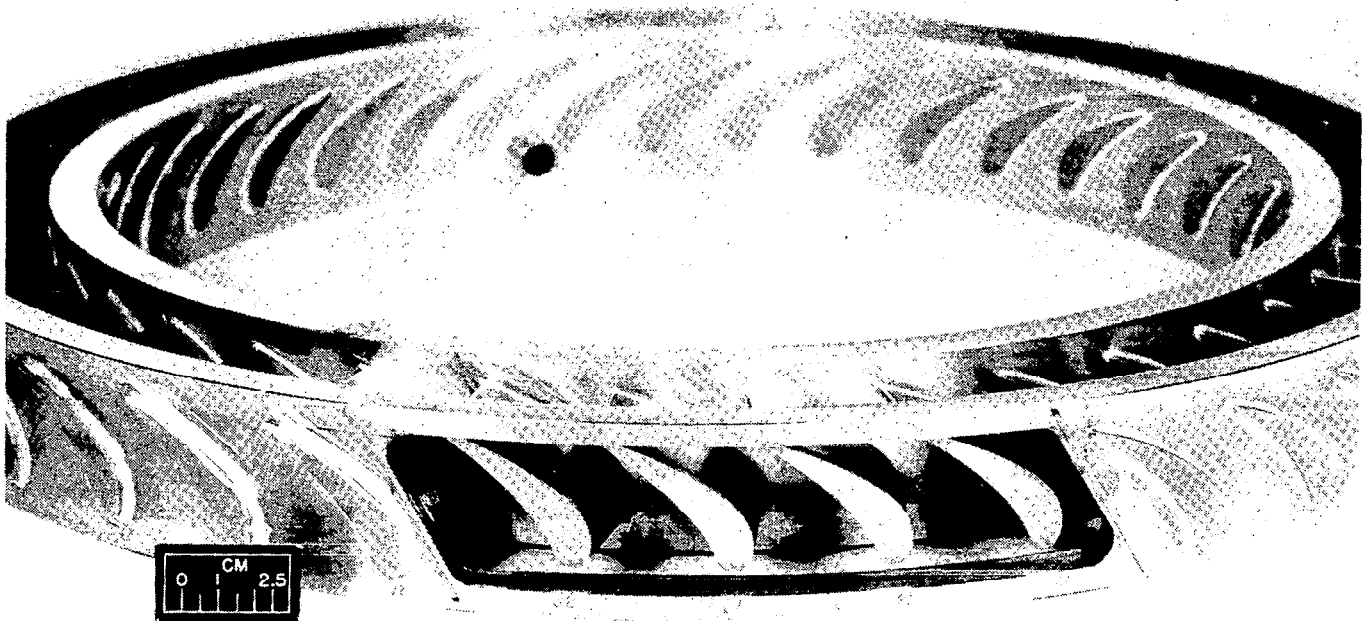


Figure 3

COMPARISON OF LASER ANEMOMETER MEASUREMENTS AND NUMERICAL SOLUTIONS FOR A TURBINE STATOR CASCADE

Typical laser anemometer measurements taken at 80 percent axial chord are shown compared with the results of three turbomachinery computer codes: a quasi three-dimensional inviscid code (Katsanis), a three-dimensional inviscid code (Denton), and a three-dimensional viscous code (Dodge). The agreement between the laser anemometer data and Denton code is considered good, while the comparison with the other two is only fair. The larger differences between the data and the Katsanis and Dodge codes at this axial location are felt to be caused by the modeling of the trailing edge region.

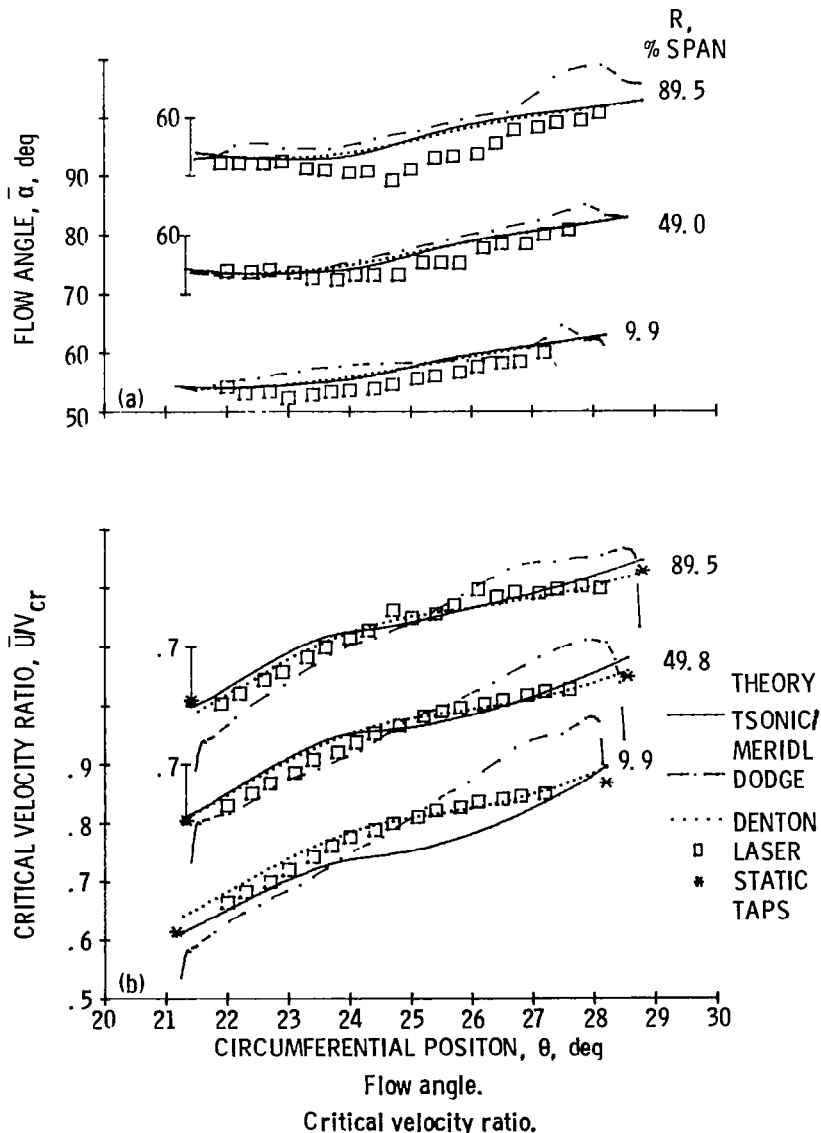


Figure 4

OPTICAL CONFIGURATION OF LASER ANEMOMETER USING FABRY-PEROT INTERFEROMETER FOR MEASUREMENT OF VELOCITY COMPONENT ALONG OPTICAL AXIS

A laser anemometer based on a scanning confocal Fabry-Perot interferometer (2 GHz free spectral range) was built to measure the velocity component along the optical axis. This component, which corresponds to the radial component in axial flow turbomachinery, cannot be directly measured with fringe-type anemometers. The incident and scattered light propagation directions are symmetrically located off the optical axis to reduce the probe volume length while giving a Doppler shift frequency proportional only to the velocity component along the optical axis. A signal with an offset frequency generated by a Bragg cell is used as a reference for scan calibration and for a spectrum stabilization circuit that compensates for frequency drift of the laser. The system was tested in the annular turbine stator cascade previously mapped with the fringe-type anemometer. Because of the high acoustic noise level (105 dB), it was necessary to place the anemometer in an acoustic enclosure for this test to prevent excessive jitter of the laser frequency.

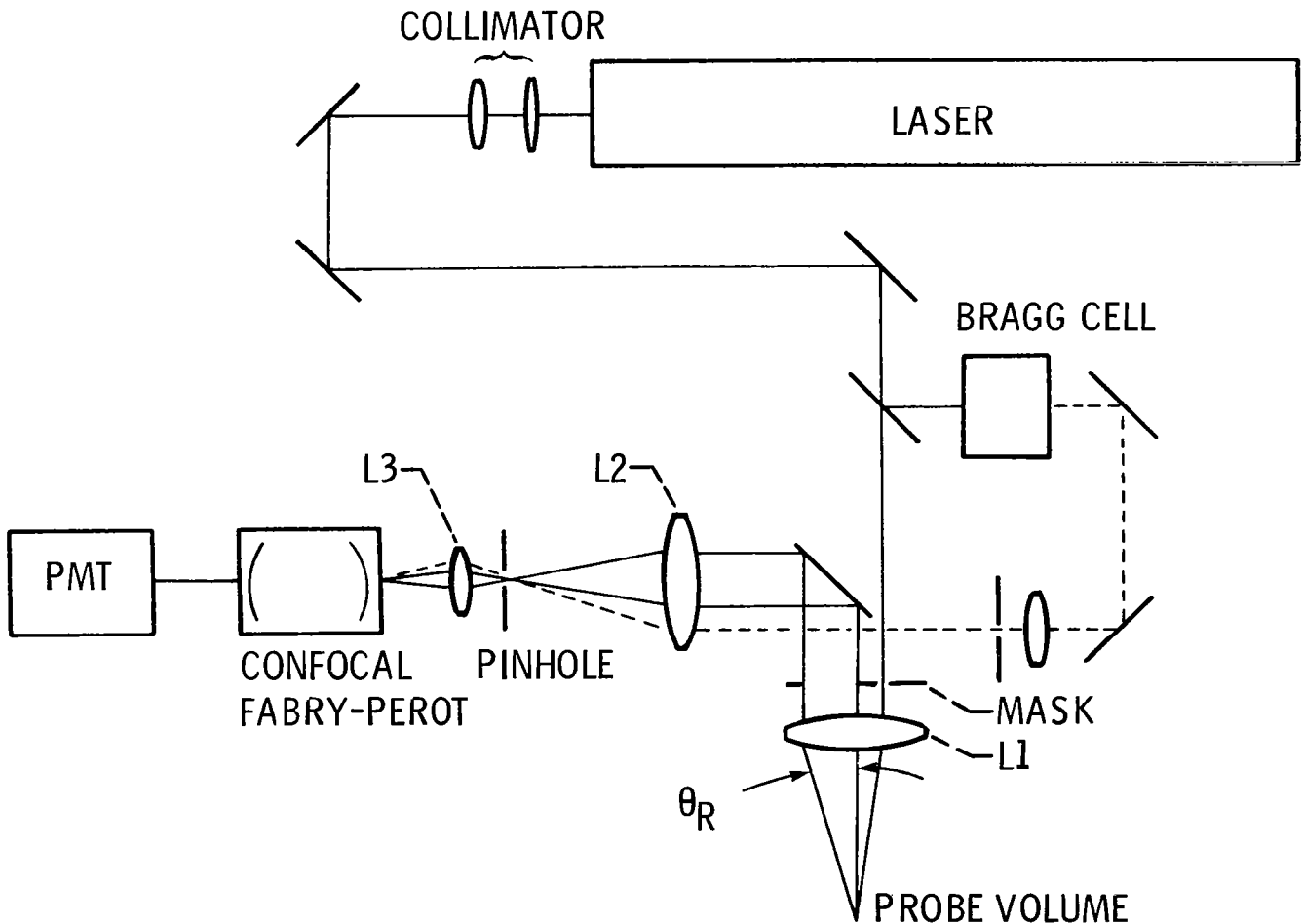
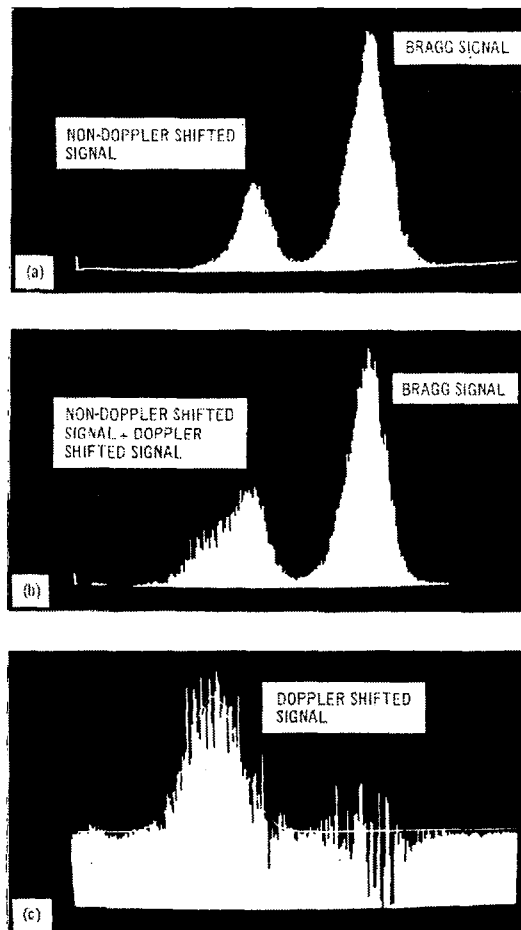


Figure 5

**RADIAL VELOCITY COMPONENT IN ANNULAR TURBINE STATOR CASCADE
MEASURED WITH FABRY-PEROT INTERFEROMETER**

A procedure was developed to measure a small velocity component along the optical axis, where the Doppler shifted signal is masked by the unshifted signal due to light scattered from surfaces near the probe volume. To accomplish this, two multiple scan spectra were recorded using alternate scans of the Fabry-Perot with the flow being seeded for only one of the spectra. The Bragg signal, shifted by 77.7 MHz from the laser frequency, is recorded in each spectrum. Subtracting the unseeded spectrum from the seeded spectrum gives the signal due to just the seed particles. A least-squares fit of the unseeded spectrum to a double Gaussian gives the frequency span, which is used with a fit of the difference spectrum to a single Gaussian to calculate the mean Doppler shift. The width of the difference spectrum is also used to calculate the turbulence intensity. For this example (taken at 50% axial chord, 50% span, and 2.3 degrees from the vane suction surface), the mean radial velocity was 6.3 m/sec toward the hub. The turbulence intensity, relative to the mean velocity magnitude of 243 m/sec, was 2.4%.



- Measured spectra in annular cascade (a) unseeded flow (b) seeded flow (c) difference between seeded and unseeded flow.

Figure 6



BIBLIOGRAPHY

1. Powell, J. A.; Strazisar, A. J.; and Seasholtz, R. G.: Efficient Laser Anemometer for Intra-Rotor Flow Mapping in Turbomachinery. ASME J. Eng. Power, Vol. 103, No. 2, Apr. 1981, pp. 424-429.
2. Strazisar, A. J.; and Powell, J. A.: Laser Anemometer Measurements in a Transonic Axial Flow Compressor Rotor. ASME J. Eng. Power, Vol. 103, No.2, Apr. 1981, pp. 430-437.
3. Powell, J. Anthony; Strazisar, Anthony J.; and Seasholtz, Richard G.: High-Speed Laser Anemometer System for Intrarotor Flow Mapping in Turbomachinery. NASA TP-1663, 1982.
4. Goldman, L. J.; and Seasholtz, R. G.: Laser Anemometer Measurements in an Annular Cascade of Core Turbine Vanes and Comparison With Theory. NASA TP-2018, 1982.

FLOW VISUALIZATION EFFORTS AND
PILOT MEASUREMENTS WITH A LASER-DOPPLER ANEMOMETER
IN BACKSCATTER MODE

K. A. Bütetisch
DFVLR-Institut for Experimental
Fluid Dynamics
Göttingen, West Germany

1. Introduction

At DFVLR flow visualization in wind tunnels has been a field of interest for many years and different techniques have been developed to high standards.

Currently DFVLR has the following techniques in routine use:

1. Schlieren and shadowgraph [1]
2. Smoke flow visualization at low and high speeds [2]
3. Surface flow visualization as oil flow, oil spots, and liquid crystals [3], [4]
4. Hydrogen bubble method [5]
5. Electron-beam-induced afterglow in rarefied gas flow [6]

Digital image processing techniques have been applied to colour-schlieren as well as to liquid-crystal pictures. Density and temperature profiles are the possible objectives. Further, an ultrasonic vortex detection method is presently being developed for low-speed application [7].

Regarding laser techniques, DFVLR started its work in the early 70's. A 1-component laser has been built by Petersen and Maurer [8]. A group in DFVLR-Berlin [9] has successfully used a very simple system for jet and turbulence investigations, and Schodl [10] has developed his dual-focus system for measurements in turbomachinery. The new efforts in Göttingen are concentrated on the installation of an LDA system operated in the backscatter mode in the $3 \times 3 \text{ m}^2$ Low Speed and the $1 \times 1 \text{ m}^2$ Transonic Wind Tunnels. Up to now the optical system allowed 2-D measurements with focal lengths of 250, 750, and 2200 mm, but to become familiar with measurements at large distances, mostly 1-component measurements have been performed. In a final stage, 3-D nonstationary-flow-field measurements in the backscatter mode will be achieved. The arrangement for this 3-D LDA will possibly be the same as that used in the Naval Surface Weapons Center (Yanta and Ausherman) [11].

2. Calibration measurements on a rotating disc

To avoid any difficulties with beam angles and their changes when going through curved windows, the well-known velocity of a rotating disc was used for the calibration of the system. Thereby it was found that it was very important to get a real parallel fringe system. In figure 1 the measured relative-velocity change as a function of the position of the disc surface within the measuring volume is shown. Curve A represents the result when the fringes are not parallel. The measured velocity changes more than $\pm 10\%$, whereby the statistical weight varies about 3 orders of magnitude. Curve B has been achieved when the adjustment has been done very carefully.

3. Turbulent pipe flow measurements

Figure 2 shows the arrangement for measurements in a fully developed turbulent pipe flow at the exit of a pipe with a length of more than 60 diameters. To avoid the influence of curved windows the measurements have been undertaken at the exit of the pipe. The focal length was 750 mm at a total laser power of about 2 watts. The

measurements were made along a horizontal pipe diameter under an angle of about 42° to make possible also measurements in the inner part of the pipe. This seemed to be very important in order to achieve some information about a possible velocity change in the axial direction. Figure 3 shows a measured profile in comparison with an experimental result of Musker et al. [12]. The agreement at this Reynolds number of 3.5×10^5 is rather good. Some values near the axis deviate due to a change in the operating conditions of the pipe facility.

Near the wall the measuring volume was too large so that the local resolution is rather poor. On the other hand the measured values near the axis could be reproduced with a high accuracy. As a consequence we could find a small asymmetry (fig. 4) within the velocity profile, although the pipe had a smoothed length of 60 diameters and a total length of 100 diameters. This asymmetry was confirmed by pitot-probe measurements, as the operation of the pipe facility was controlled very carefully.

4. Local velocity determination in the $3 \times 3 \text{ m}^2$ wind tunnel

As a first step in measuring at low speeds but large distances local velocity measurements in the $3 \times 3 \text{ m}^2$ wind tunnel NWG have been performed. The focal length was 2200 mm. Small olive oil particles produced by a LASKIN nozzle have been introduced alternatively into the settling chamber, the test section, and the diffuser inlet to study different possibilities for later applications.

In the undisturbed flow the agreement of the measured values with the predicted is within an accuracy of $\pm 0.5\%$ (fig. 5). The next step was to measure two components within the flow field of a 6:1 prolate spheroid with a length of 2400 mm at different velocities and angles of incidence. Figure 6 shows a preliminary result of these velocity measurements within the boundary layer of the model. Although the focal length was again 2200 mm the local resolution in the z-direction was quite good.

5. References

- [1] Lawaczeck, O.: High Speed Schlieren-Film of the Pulsating Flow in a Transonic Turbine Cascade. Boundary Layer Effects in Turbomachines, AGARDograph No. 164, London 1972.
- [2] Stahl, W.: Zur Sichtbarmachung von Strömungen um schlanke Deltaflügel bei hohen Unterschallgeschwindigkeiten. AVA-Bericht 70 A 45 (1970).
- [3] Vanino, R.; and Wedemeyer, E.: Wind Tunnel Investigation of Buffet Loads on Four Airplane Models. AGARD CP No. 83, pp. 34-1 - 34-15.
- [4] Schöler, H.: Heat Transfer Measurements with Liquid Crystals in the DFVLR Ludwig Tube. DFVLR-Report 251 80 A 07 (1980).
- [5] Bippes, H. Visualization of Flow Separation and Separated Flows With the Aid of Hydrogen Bubbles. Sym. on Flow Visualization (Bochum), Sept. 9-12, 1980, pp. 225-230.
- [6] Bütetfisch, K. A.: Investigation of Hypersonic Nonequilibrium Rarefied Gas Flow Around a Circular Cylinder by the Electron Beam Technique. Rarefied Gas Dynamics, Band 2, S. 1739-1748, Academic Press, New York, 1969.

- [7] Engler, R. H.; Holst, H.; Schmidt, D. W.; and Wulf, R.: Measurements of Vortices in Wind Tunnel Experiments by Use of Ultrasonic Pulses. IEEE Publication 79 CH 1500-8 AES, Monterey/Calif. (1979), pp. 163-170.
- [8] Petersen, J. C.; and Maurer, F.: A Method for the Analysis of Laser Doppler Signals Using a Computer in Connection With a Fast A/D Converter. LDA Symposium, Technical University of Denmark (1975).
- [9] Lehmann, B.: Experimentelle Methode für die quasimomentan Erfassung mehrdimensionaler Geschwindigkeitsfelder mit Hilfe der Laser-Doppler-Messtechnik. DFVLR IB 22214-81/3.
- [10] Schodl, R.: The Laser-Dual Focus Flow Velocimeter. AGARD Preprint 193, pp. 22-1 - 22-09 (1976).
- [11] Yanta, W. J.; and Ausherman, D. W.: An Improved 3-D Laser Doppler Velocimeter for Use in Supersonic Flow. Proc. 6th U.S. Air Force and the FRG Data Exchange Agreement "Viscous and Interacting Flow Field Effects", Göttingen, DFVLR-AVA-Report IB 222 81 CP 1, 1981.
- [12] Musker, A. J.; Lewkowicz, A. K.; and Preston, J. H.: Investigation of the Effect of Surface Roughness of a Ship on the Wall Friction Using a Pipe Flow Technique. Report No. FM/24/76, University of Liverpool, 1976.

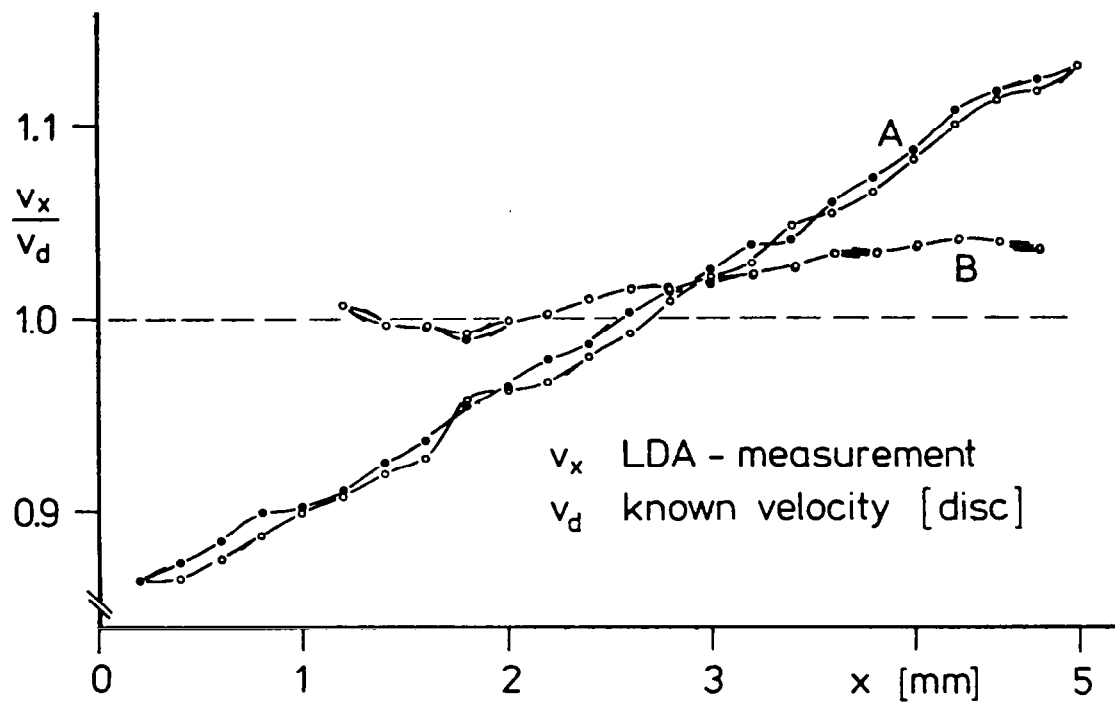


Figure 1.- Relative measured velocities on a rotating disc.
 A - Fringe system nonparallel; B - fringe system well adjusted.

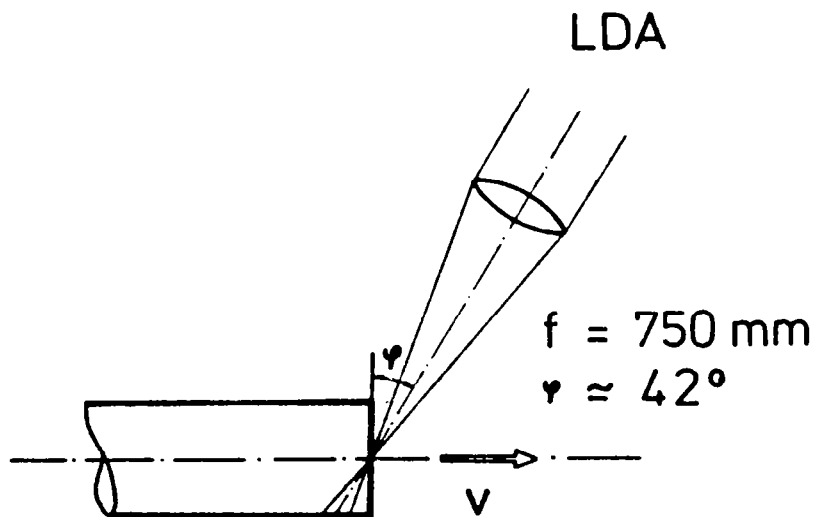


Figure 2.- Arrangement for pipe flow measurements.

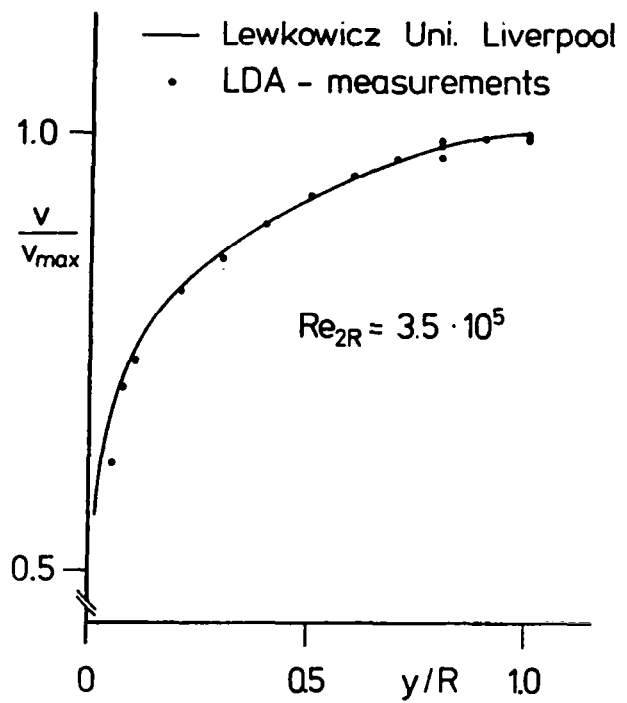


Figure 3.- Velocity profile in turbulent pipe flow.

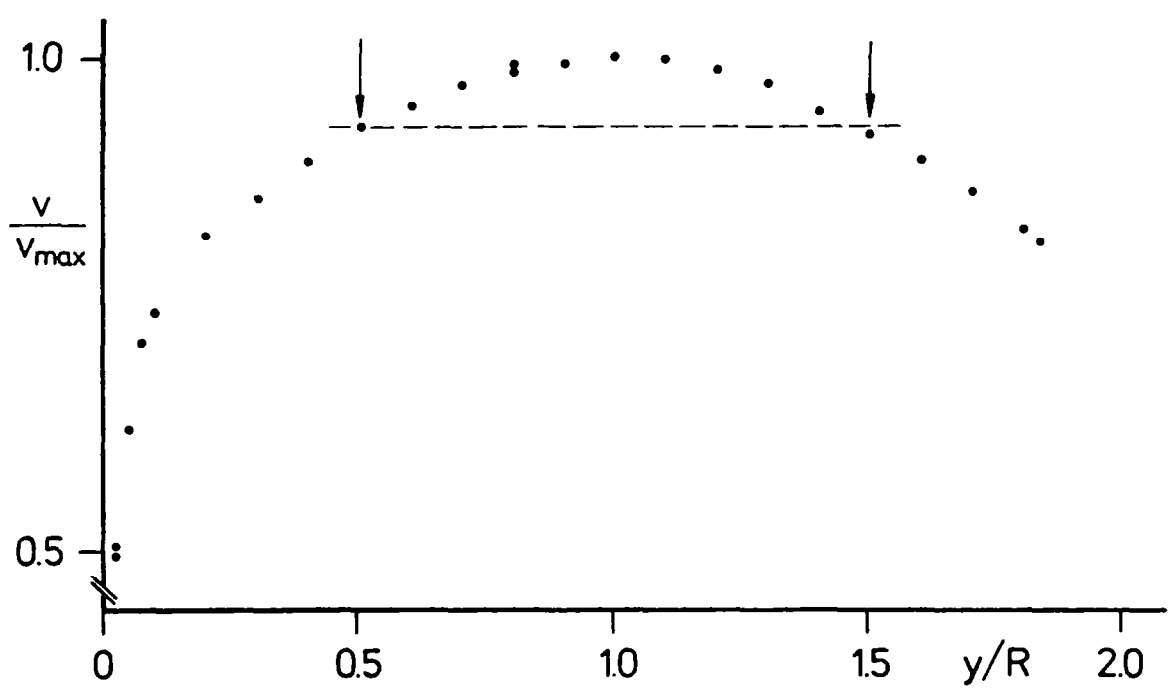


Figure 4.- Asymmetry in turbulent pipe flow.

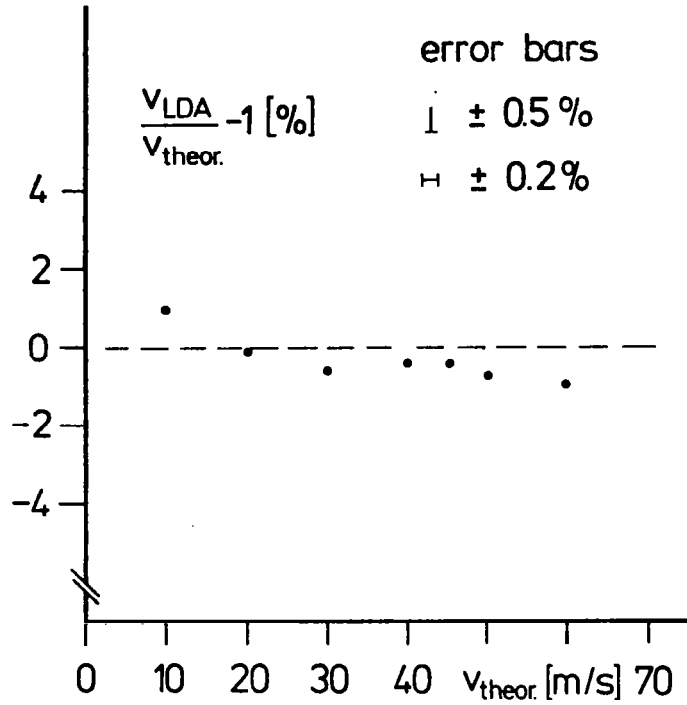


Figure 5.- Local velocity measurements in the $3 \times 3 \text{ m}^2$ Low-Speed Wind Tunnel.

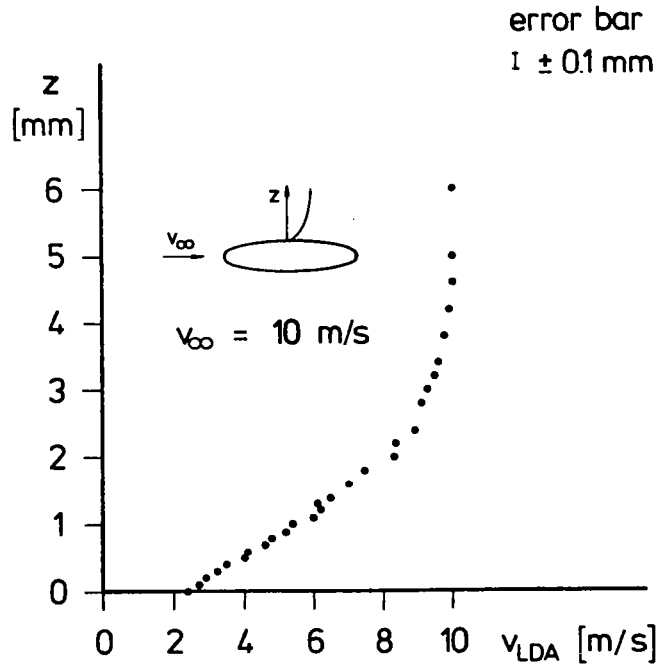


Figure 6.- Profile of the horizontal velocity component in the plane of symmetry for an angle of incidence $\alpha = 0$ within the flow field of a prolate spheroid.



DEVELOPMENT OF A LASER VELOCIMETER FOR A LARGE TRANSONIC WIND TUNNEL

John P. Greissing and Daniel L. Whipple
NASA Lewis Research Center
Cleveland, Ohio

At the Lewis Research Center 8 × 6 Foot Supersonic Wind Tunnel a laser velocimeter (LV) has been utilized in the testing of advanced high speed turbo-propellers (fig. 1). The system, using a 15-W argon-ion laser, a 3-beam 2-axis transmitting-receiving optics package, a zoom lens with 1- to 4-m focal lengths, and a 0.4-m corner mirror was initially assembled and tested in the checkout room shown in fig. 2. During the time the system was located in the checkout area, experience was acquired in the alignment and operation of the system and the data acquisition system and software were developed. By using air jets to simulate tunnel air flow, the system worked quite well.

With the checkout of the system complete, the velocimeter was relocated adjacent to the wind tunnel test section on a 2-axis positioning platform (fig. 3). Because the area surrounding the test section is subjected to reduced atmospheric pressures, elevated temperatures, and high noise levels, access to the velocimeter is impossible during tunnel operations. All controls, instrumentation, and computing equipment are remotely located.

The relocated system again underwent testing using air jets to simulate tunnel flows and worked very well. However, the first attempts to operate the system during actual tunnel runs revealed several unforeseen problems. The laser, when subjected to reduced atmospheric pressures, would cease lasing and intense vibration caused a loss of beam alignment. Consequently, the laser was mounted into a vessel maintained at atmospheric pressure and deflectors were mounted to the external tunnel walls to shield the system from the air blast created by the wall bleed holes. Limited LV data was attainable with this configuration, but the system would become misaligned after 1 or 2 hours of operation. A combination of vibrations induced by the high acoustic pressure loadings and the rise in temperature of about 50°F were suspected to cause the loss of alignment.

The system was remounted to the positioning platform in an enclosure that provides both thermal and acoustic isolation (fig. 4). The enclosure has water cooling lines affixed on all 6 internal surfaces and lead sheet-foam acoustic insulation on all external surfaces. The optical table carrying the LV system is mounted to the base plate of the enclosure on rubber shock mounts.

Concurrent with the installation of the isolation system, a 4-beam 2-axis transmitting-receiving optics package was obtained (fig. 5). This package appeared to be more tolerant of vibrations as well as being easier to align.

The present instrument described above with its isolation system has been successfully operated with runs of 8 hours endurance being routine.

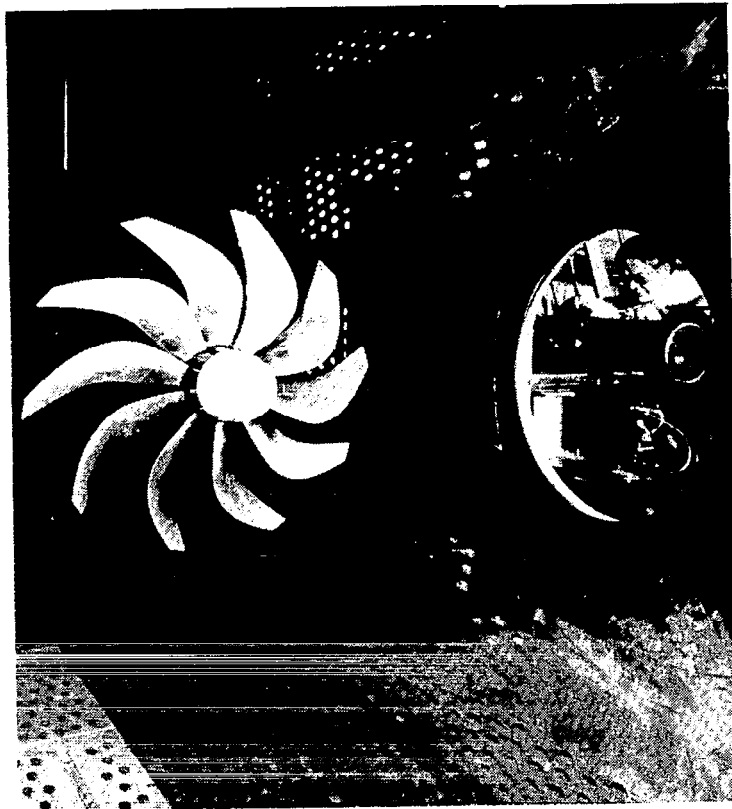


Figure 1.- The NASA Lewis LV system at the 8 x 6 wind tunnel.

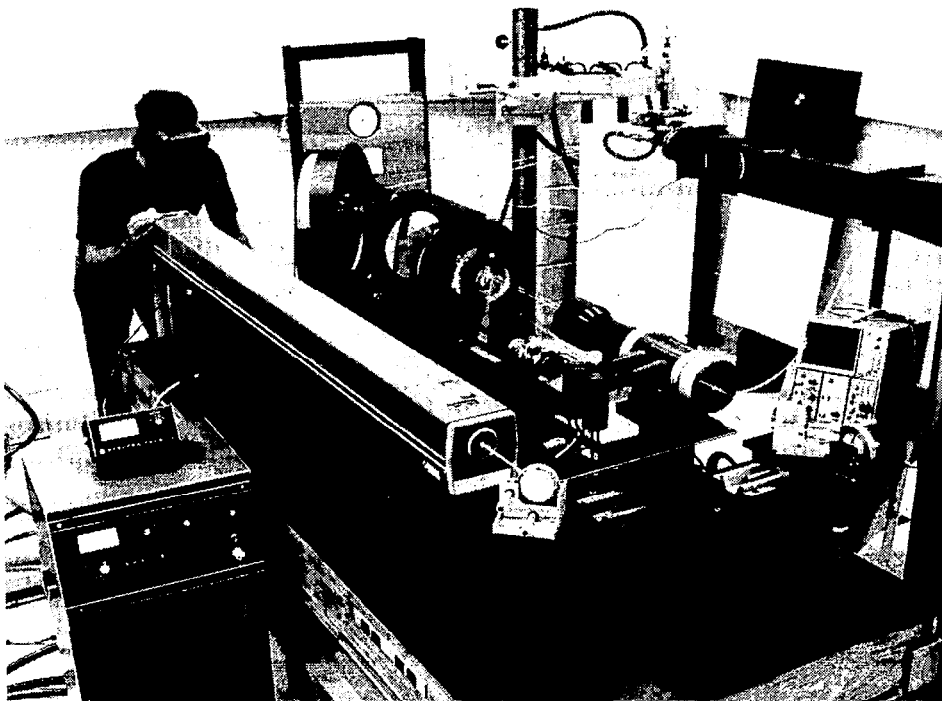


Figure 2.- The LV checkout area.

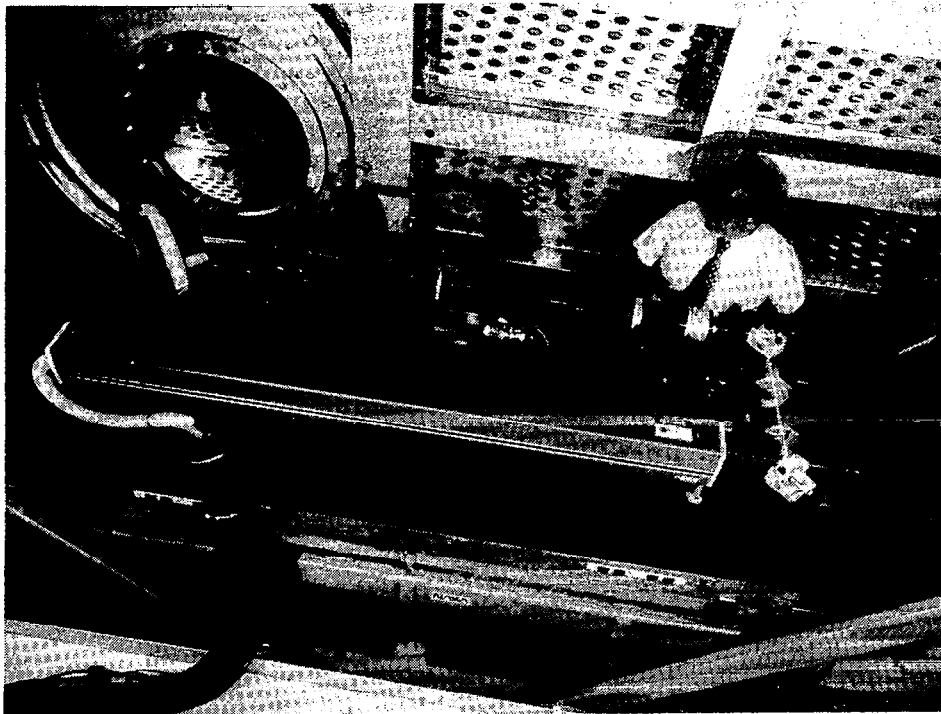


Figure 3.- Initial installation of the LV at the 8 X 6 wind tunnel.

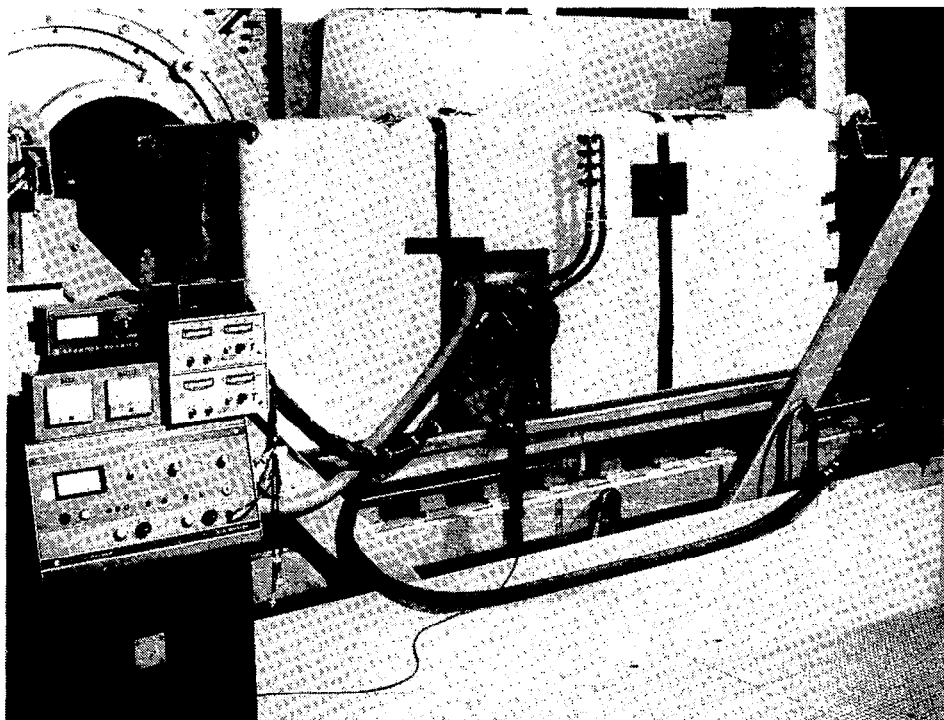


Figure 4.- Laser velocimeter environmental isolation enclosure.

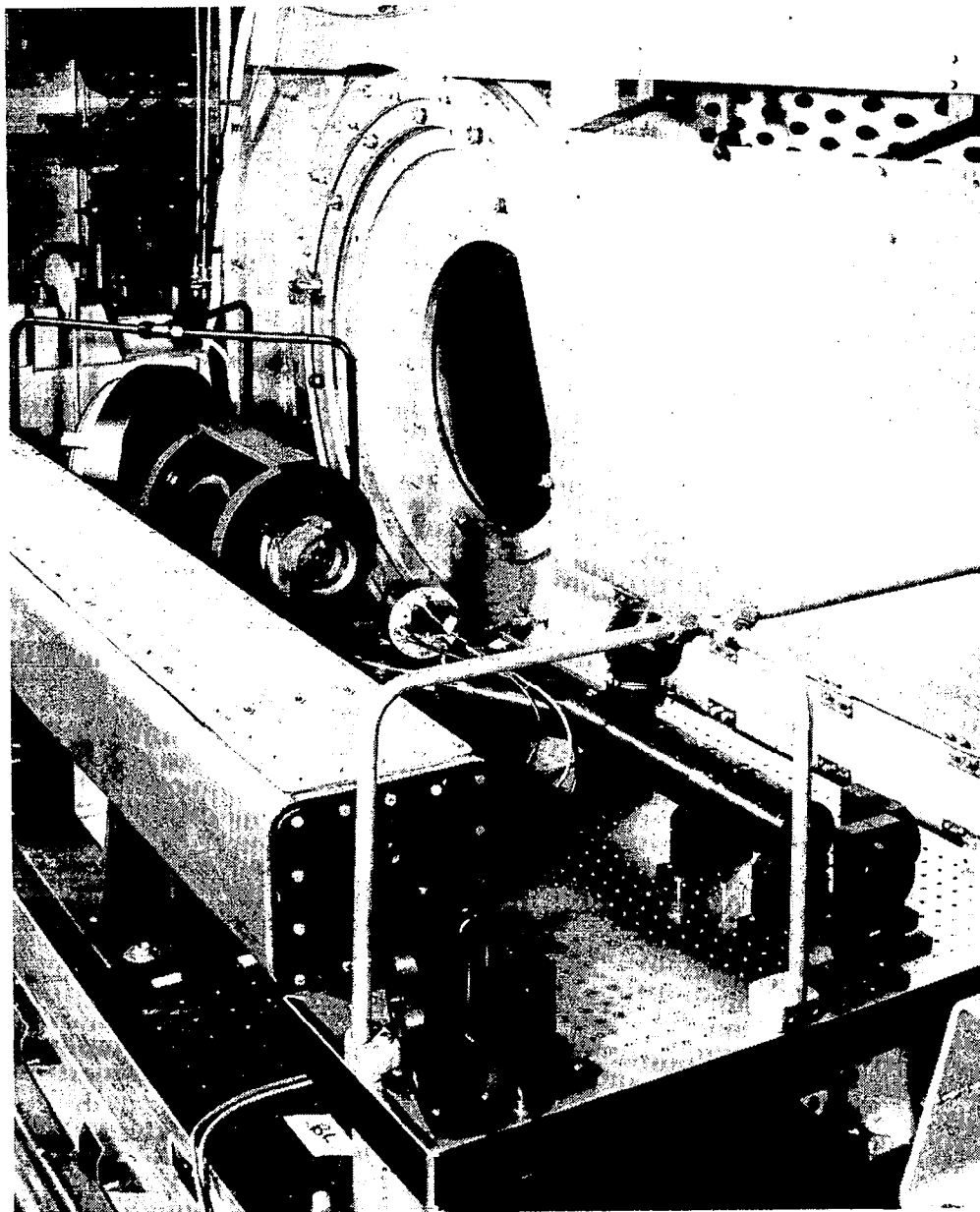


Figure 5.- Laser velocimeter optics system.

SEEDING CONSIDERATIONS FOR AN LV SYSTEM
IN A LARGE TRANSONIC WIND TUNNEL

Robert J. Freedman
NASA Lewis Research Center
Cleveland, Ohio

The results from any laser velocimeter (LV) depend upon the seeding particles. If they are too large they fail to follow the flow, if too small they may be impossible for your system to see. Thus, when we at Lewis decided to use a laser velocimeter to measure the properties of propellers, seeding was a great concern. Many methods were tried and weeded out by using a Malvern particle sizer. The most promising ones were tested in the tunnel and the LV measurements compared to theoretical values of velocity as the particle approached a blunt nose body along a stagnation streamline. Data obtained from the LV system are compared with the one dimensional particle lag calculation in figure 1. This figure shows the theoretical velocity over the blunt nose and a velocity profile for 5 μm particles. This indicates the particles were approximately 5 μm .

Figure 2 shows the seeding method. The seed, DOP, was atomized by 2 seeders run with all 12 available atomizer jets on. The atomizer seed traveled from these two seeders through four 1 inch tubes 20 feet long to the plenum chamber where this cluster of tubes injected the seed into the air stream. The tubes were located 60 feet from the model and could be moved only by shutting the tunnel down.

Figure 3 shows our future seeding plans. The model will be a cylinder with a hemispherical head, about 8 to 12 inches in diameter and properly instrumented with pressure taps. The test would more accurately evaluate our current seeding techniques, evaluate ways to improve these techniques so data rates can be increased in areas of interest like across shocks and between blades, and finally evaluate alternate methods which might be used for other facilities.

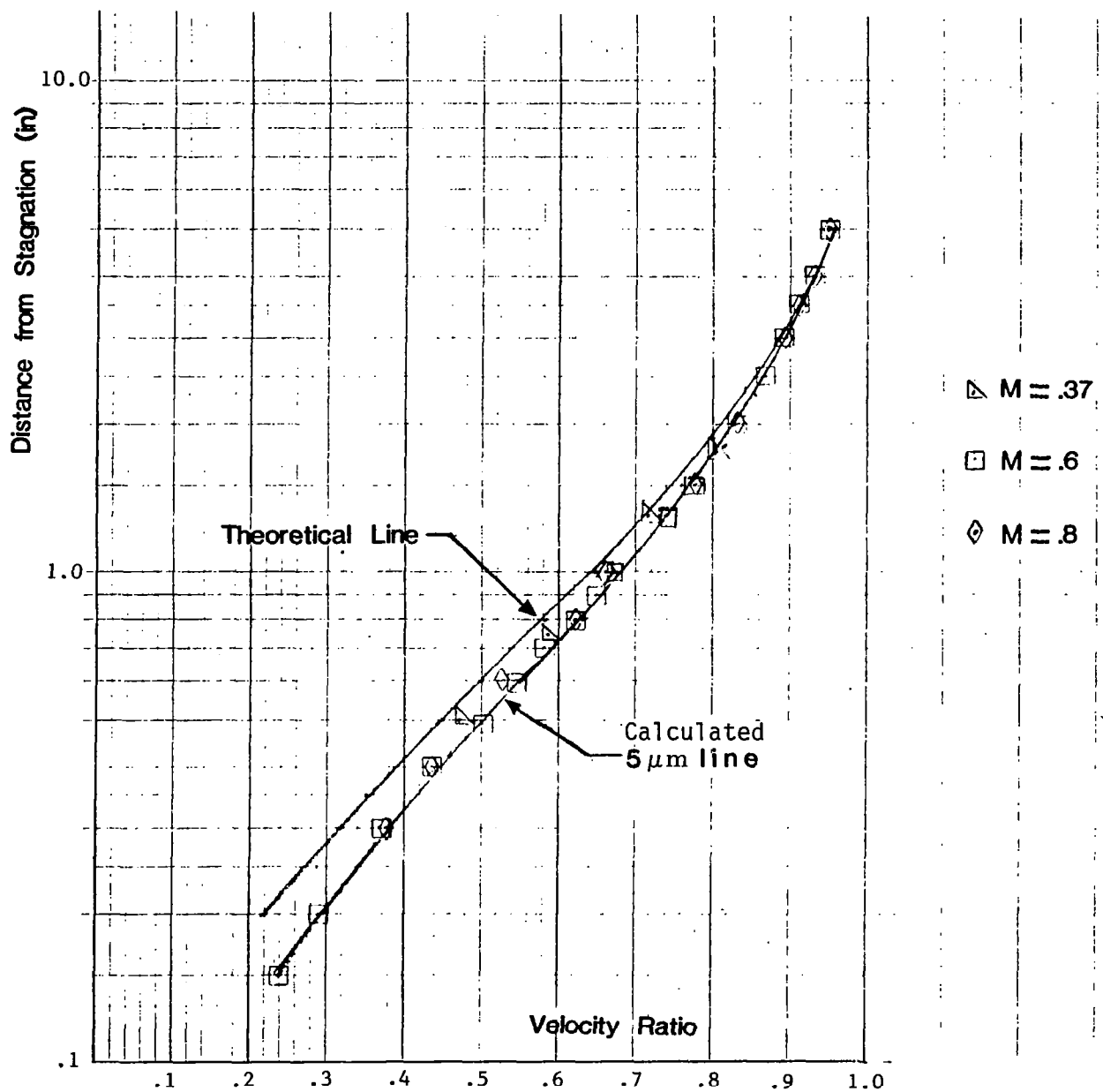


Figure 1.- Comparison of LV measurements to theoretical values of velocity as the particle approached a blunt nose body along a streamline.

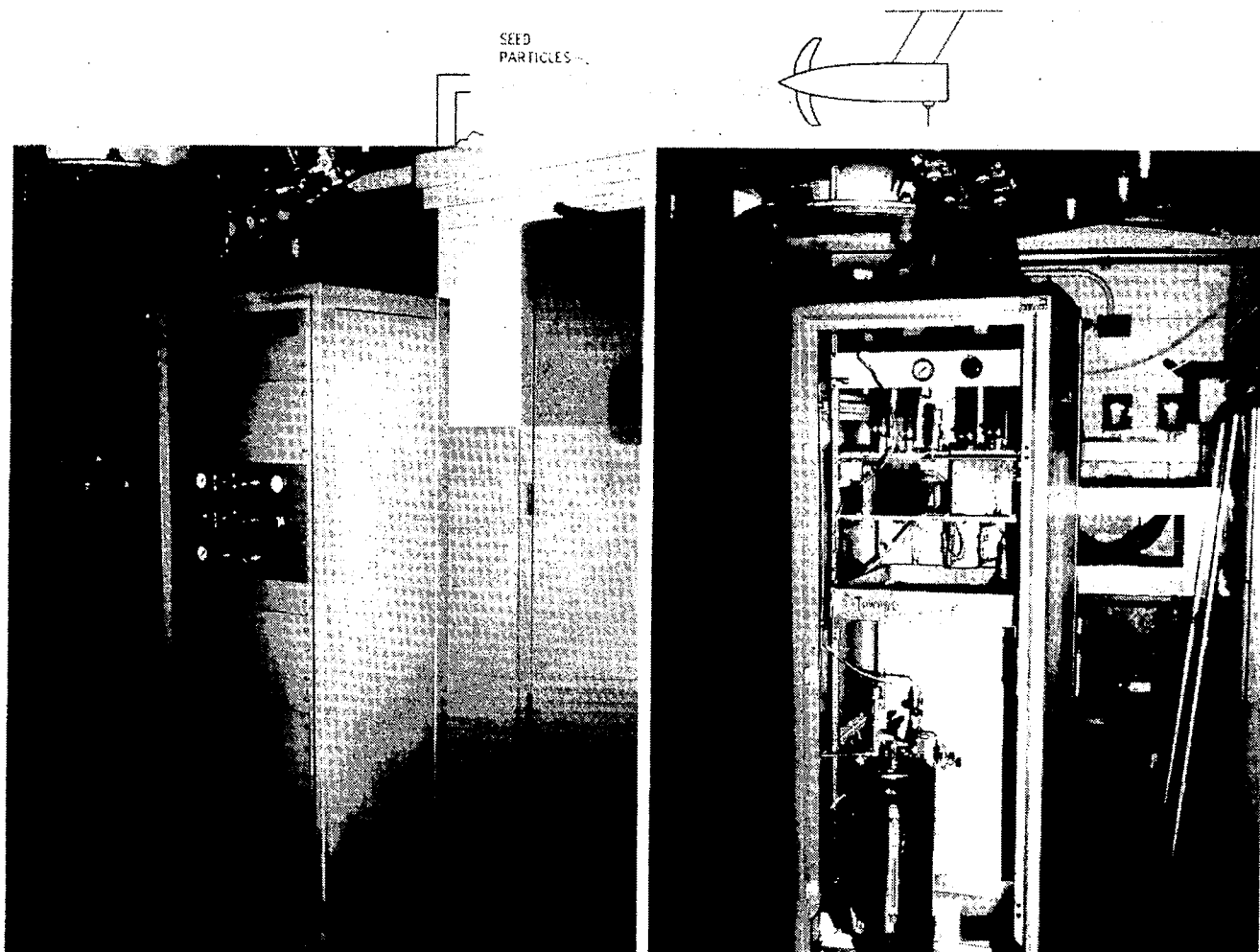


Figure 2.- Propeller particle generator system.

MODEL: Cylinder - Hemispherical Head
PURPOSE: Check Current System
Increase Data Rate Within Blades
Improve System
Evaluate Alternatives

Figure 3.- Future plans.

LV MEASUREMENTS WITH AN ADVANCED TURBOPROP

H. E. Neumann and J. S. Serafini
NASA Lewis Research Center
Cleveland, Ohio

Nonintrusive measurements of velocity about a spinner-propeller-nacelle configuration have been made at a Mach number of 0.8. A laser velocimeter (LV) specifically developed for these measurements in the NASA Lewis 8 x 6 Foot Supersonic Wind Tunnel was used to determine the flow field of the advanced swept SR-3 propeller (fig. 1). The LV system development was previously discussed by J. P. Greissing and D. L. Whipple and by R. J. Freedman (papers 26 and 27 of this compilation). The data will be used to study the flow and to verify computer prediction codes. The purpose of this presentation is to demonstrate the usefulness of the LV data in detecting flow anomalies and to substantiate the data quality.

Some typical results are shown in figure 2. Mach number profiles at the entrance of the propeller are compared with theoretical predictions. The LV data is in excellent agreement with the axisymmetric, compressible, inviscid theory (without blades) ahead of the propeller except near the hub. The data indicate blade blockage near the spinner. Blade to blade variations in axial velocity for four radial positions at the propeller exit are also shown. The large apparent wake near the hub is associated with the hub choking.

Measurements were also made within the blades. An example is shown in figure 3. The blade to blade variation of axial velocity ahead of a shock within the blade passage is shown. This shock was not predicted by the current lifting line propeller analysis.

This data set represents the first opportunity to study the flow field within and about an advanced swept propeller while operating at design operating conditions. The system described by J. P. Greissing and D. L. Whipple and by R. J. Freedman has provided repeatable and consistent data and work is continuing on the application of this data to propeller research.



Figure 1.- SR-3 propeller installed in NASA Lewis 8 x 6 Foot Supersonic Wind Tunnel.

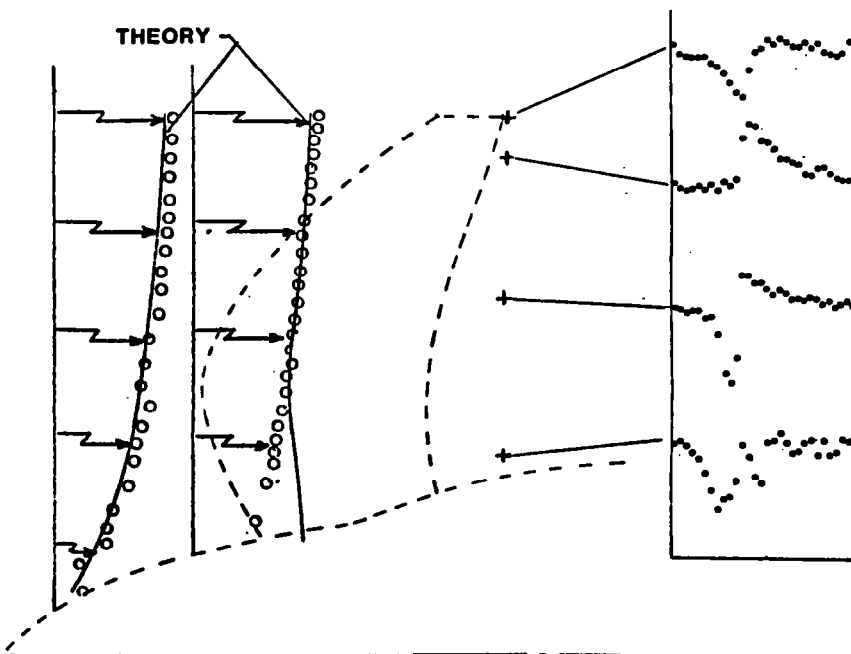


Figure 2.- SR-3 LV velocity measurements.

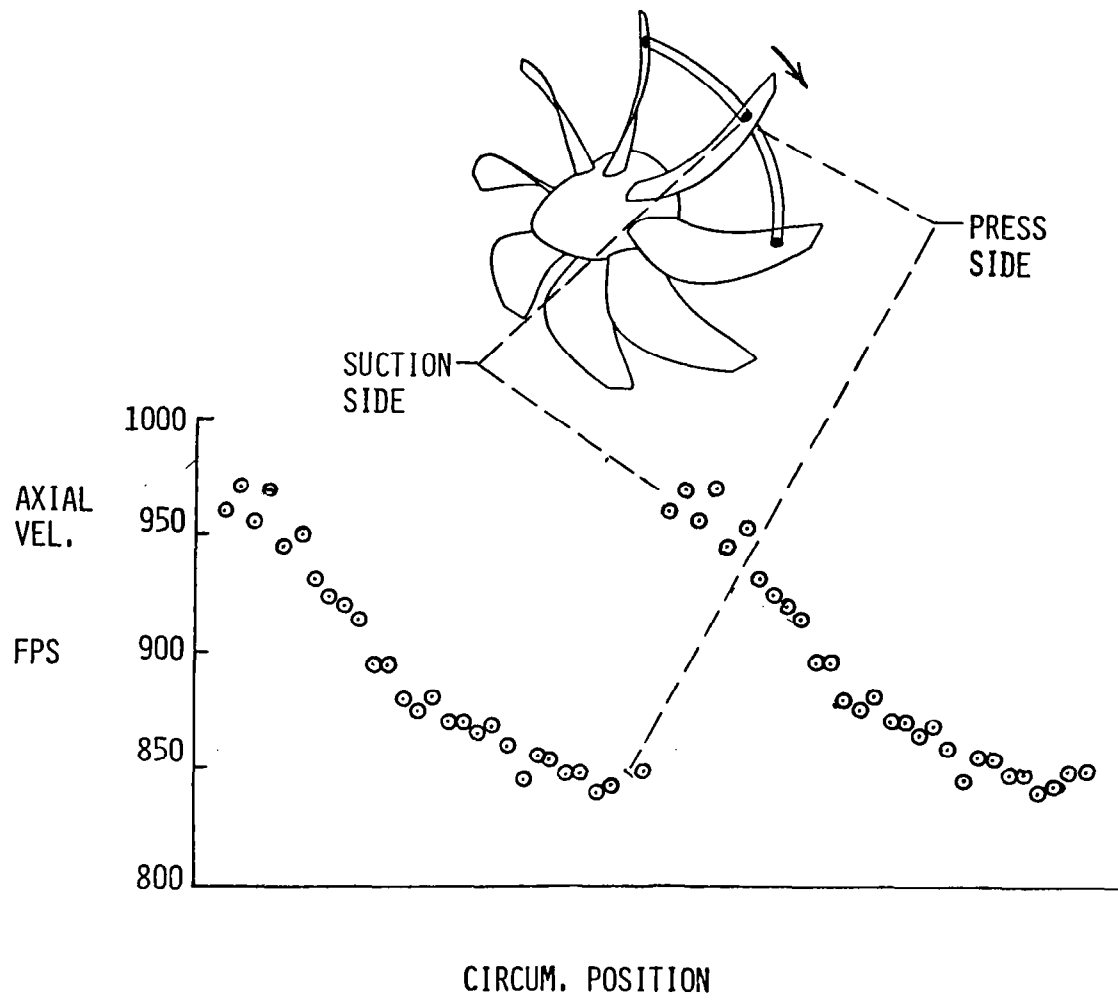


Figure 3.- Laser intrablade velocity for SR-3 propeller.
 $M = 0.8$; $C_p = 1.8$; $J = 3.06$.

16-FOOT TRANSONIC TUNNEL LASER
VELOCIMETER SYSTEM

J. M. Franke
NASA Langley Research Center
Hampton, Virginia

16-FOOT TUNNEL FACILITY

The Langley 16-Foot Transonic Tunnel was originally constructed in 1941 for engine cooling and cowling investigations. The most recent modifications permit operation from Mach 0.2 to 1.3. The tunnel is a single return atmospheric tunnel with slotted test section (figure 1). The test section is vented to the surrounding 9.75 m diameter plenum through slots at the corners of the octagon. The static pressure in the plenum drops from 1 atmosphere at low speeds to 0.36 atmospheres at Mach 1.3 plenum. Temperature can vary from -17°C , in winter, to a maximum of 77°C in summer.

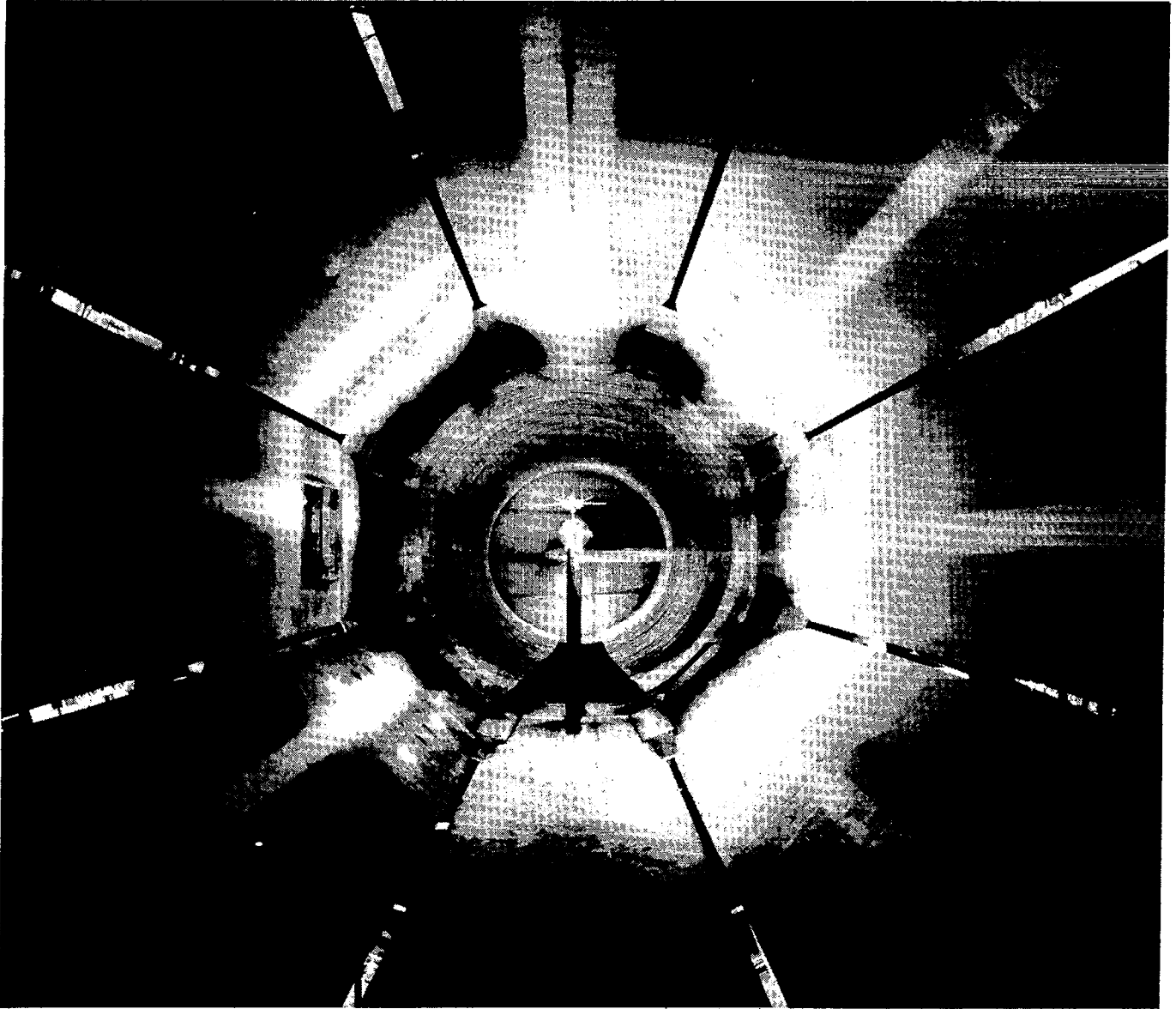


Figure 1

SYSTEM CONFIGURATION

To minimize the separation between the flow and the laser velocimeter, and avoid the losses and cost of a second window, the velocimeter is mounted in the plenum chamber. Figure 2 is an artist's rendition of the installed system. The outer frame is fixed; the next inner frame assembly is driven vertically with stepper motors and jack screws. The innermost frame is translated parallel to the tunnel axis by stepper motors and jack screws. Translation of the sample volume across the tunnel is accomplished with zoom optics.

\bar{U} & \bar{V} VELOCITY COMPONENT INSTALLATION

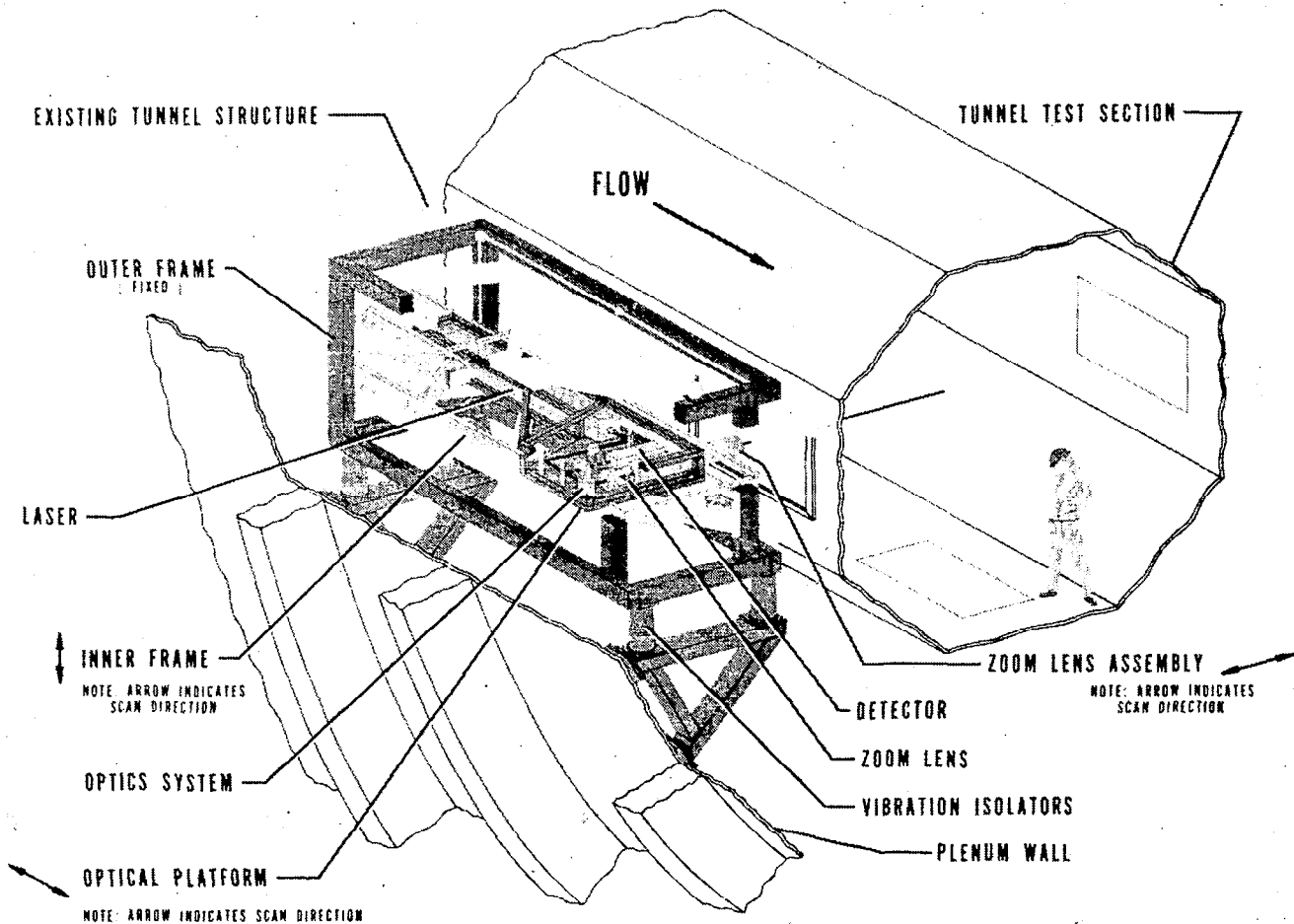


Figure 2

OPTICAL LAYOUT

A schematic of the optical components of the laser velocimeter is shown in figure 3. The system is a two color, two component, Bragg cell, coaxial, back-scatter configuration. A 12 watt argon ion laser is used to supply approximately 2.5 watts on 488 nm and 514.5 nm. The polychromatic output is separated into discrete wavelength beams and the 488 nm and 514.5 nm beams are selected and used to form a two by two matrix of beams. Two 514.5 nm beams form the vertical component system and two 488 nm beams form the u or horizontal component system. The matrix of beams passes through the pierced mirror and is focused into the tunnel by the scanning optics. The final objective has a clear aperture of 250 nm.

The same scanning optics are used to collect the light scattered by smoke particles passing through the sample volume. The collected radiation is relayed, by mirrors, back to the receiver where extraneous light is rejected with a pinhole. The remaining optical signal is separated with a dichroic beamsplitter to isolate the 488 nm and 514.5 nm radiation. Separate photomultiplier tubes are used to detect each wavelength.

A photograph of the assembled optics is shown in figure 4.

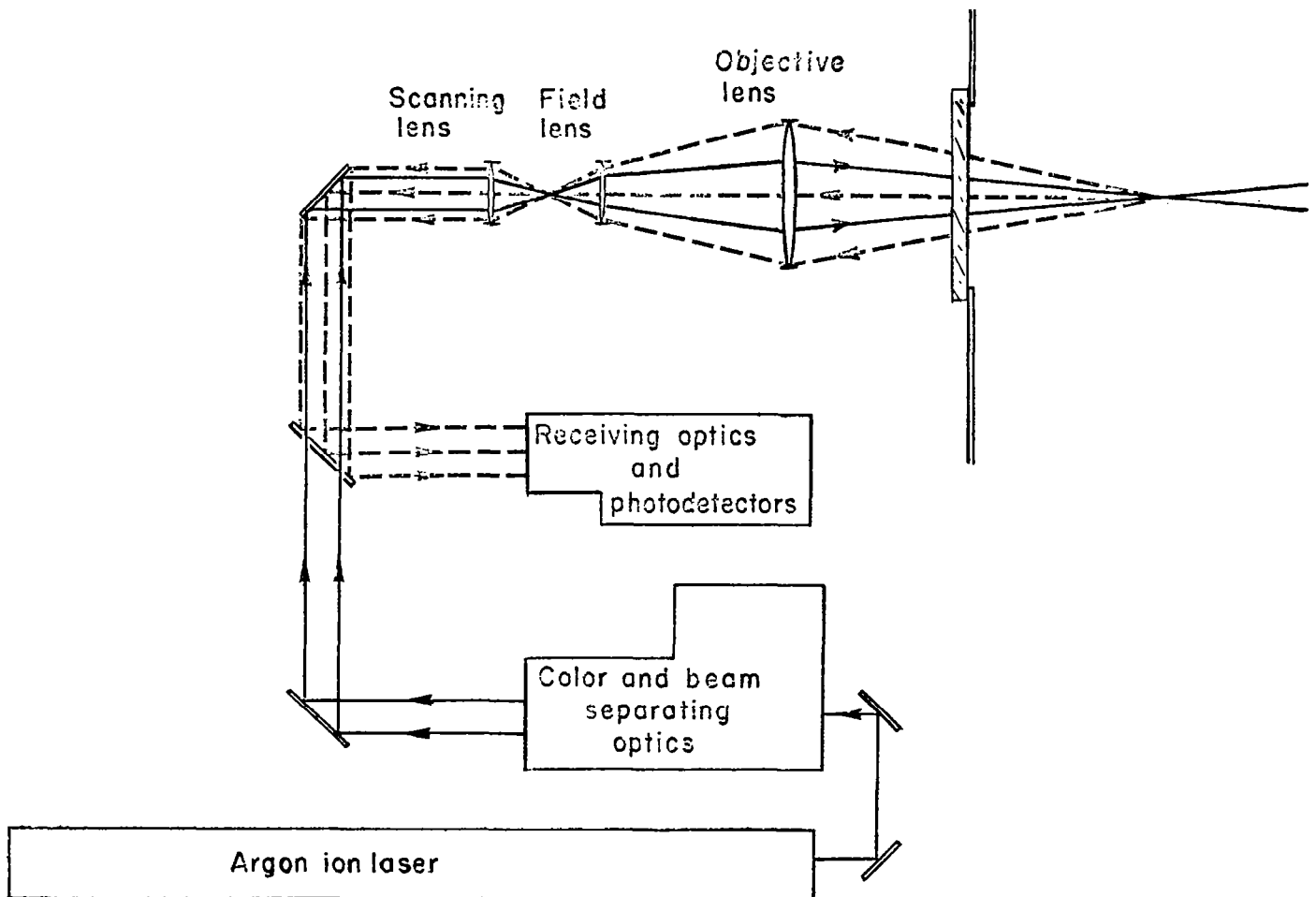


Figure 3

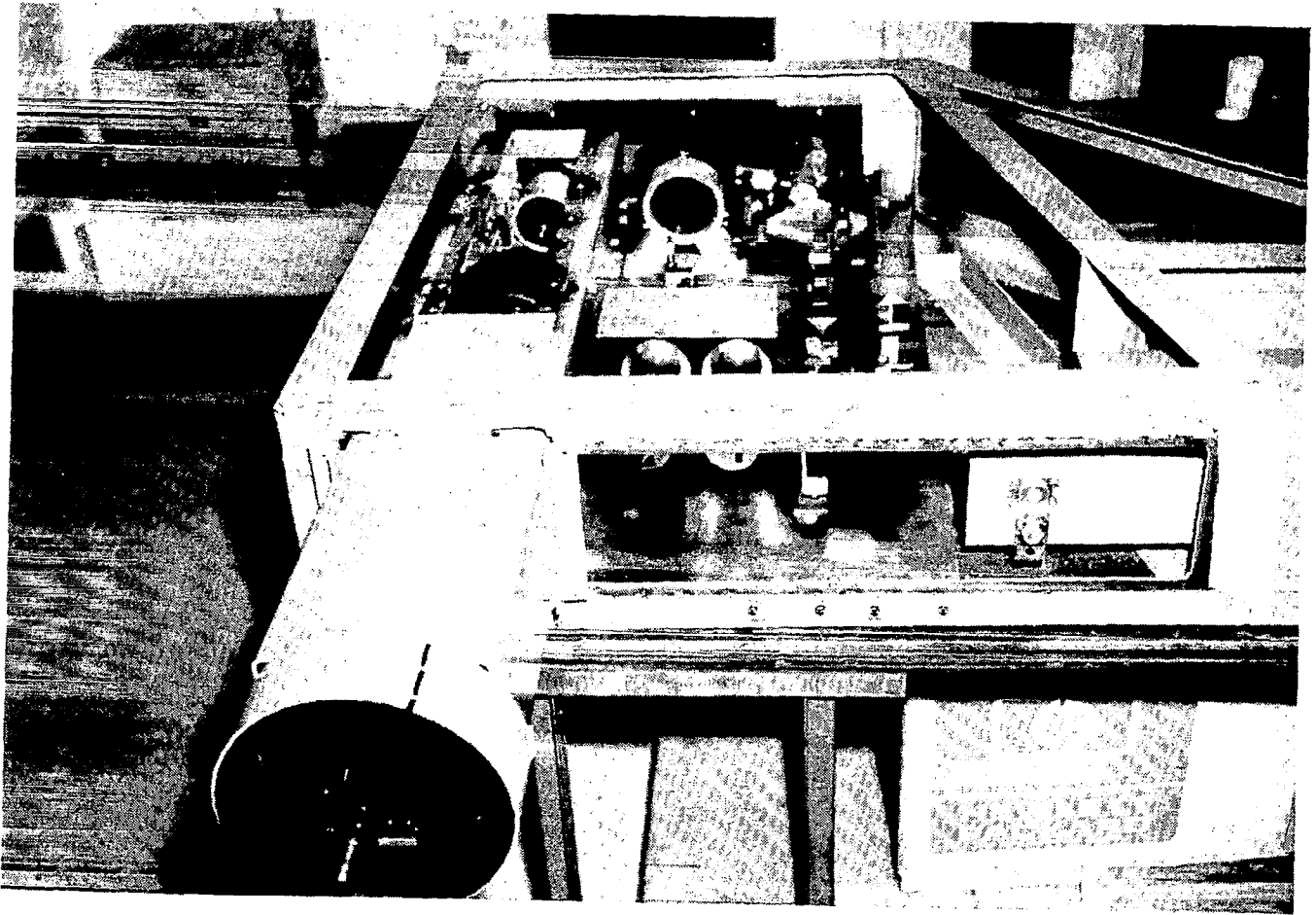


Figure 4.- Assembled optical system.

LASER COLOR SEPARATOR

The color separator is unique to this instrument. It produces parallel monochromatic beams from a multiwavelength laser. The beam to beam separation is easily adjusted and alignment is simple. The optical layout of the separator is depicted in figure 5. The incident beam is dispersed according to wavelength by the two 60° prisms. The dispersed beams are returned parallel to themselves by action of the Porro prism retroreflector. By reciprocity of the dispersing prisms, the beams then exit the color separator parallel to each other and to the incident beam. The beam to beam separation is easily varied by moving the retroreflector closer or farther from the dispersion prisms. Unwanted wavelengths are removed with a simple mask.

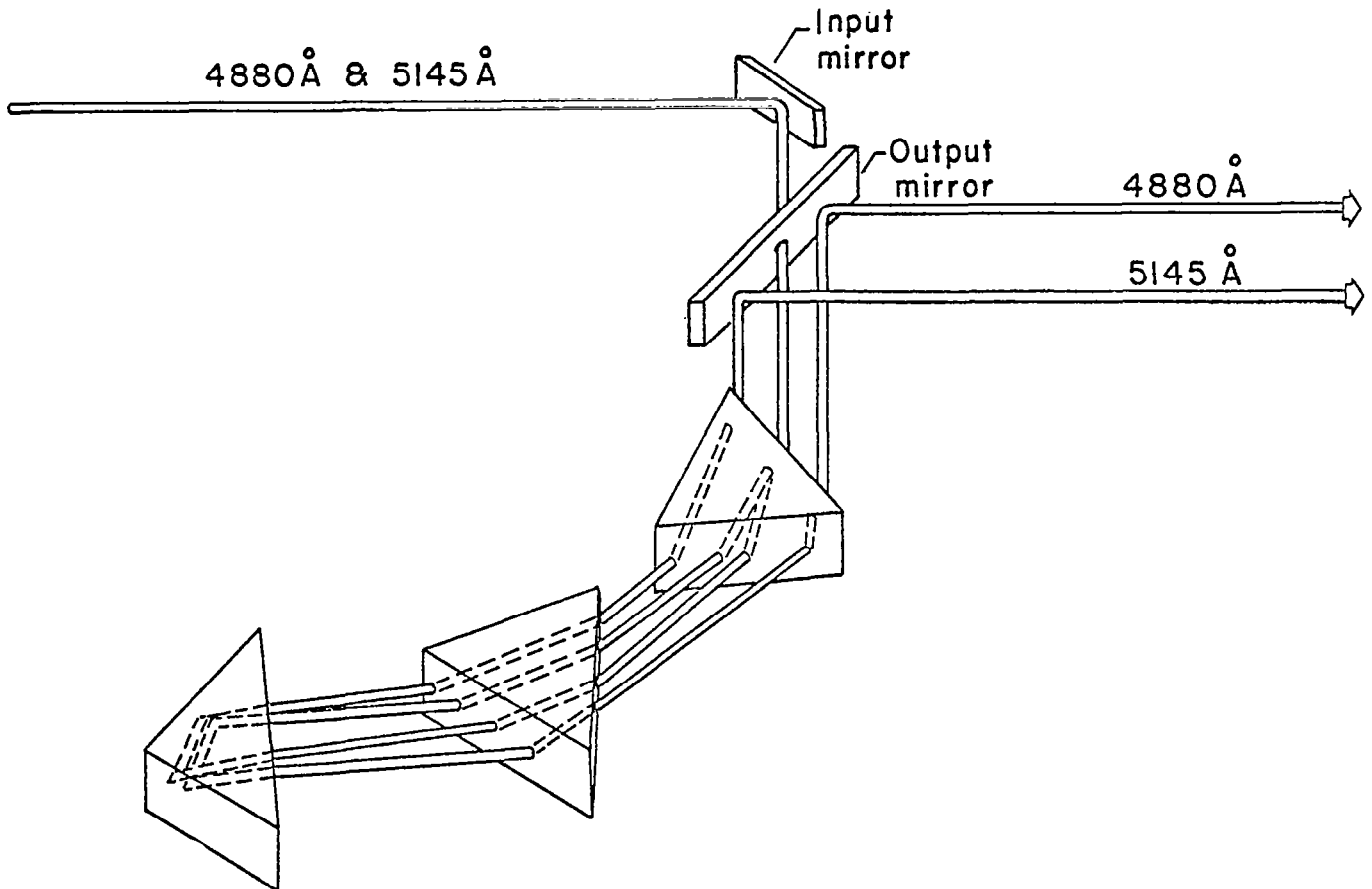


Figure 5

OPTICAL RECEIVER

The optical receiver (figure 6) consists of the input lens, spatial filter, recollimating lens, dichroic beamsplitter, line filters and photomultiplier tubes. The input lens accepts the collimated scattered light from the scanning lenses and focusses it down on the spatial filter. The spatial filter is used to reject stray scattered light and background tunnel lighting. The light is then recollimated with a 10X microscope objective. The dichroic beamsplitter passes the 514.5 nm light and reflects the 488 nm light. Line filters are used to further reduce crosstalk between channels.

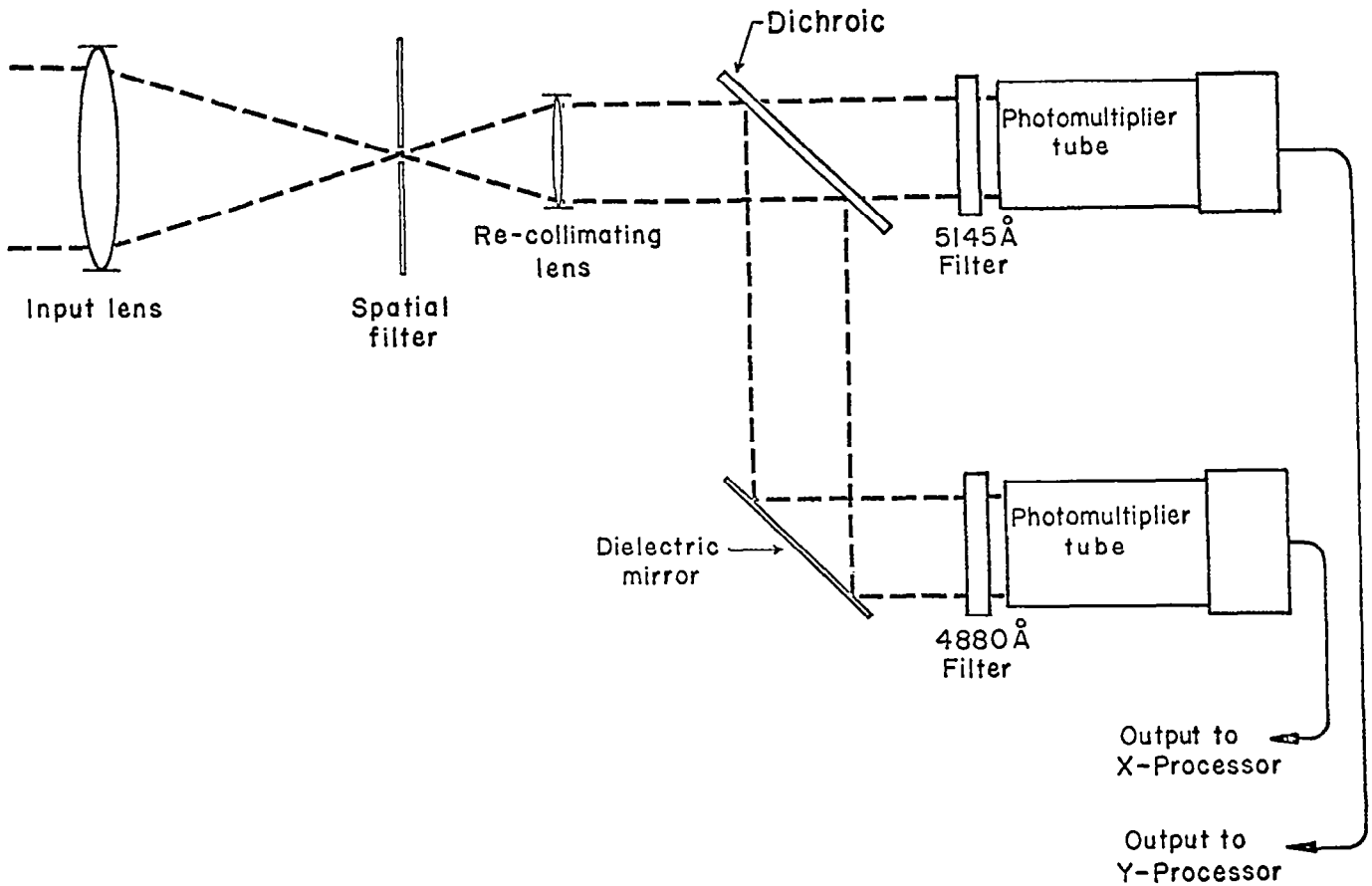


Figure 6

TUNNEL WINDOW

A major optical component that is not normally considered to be a part of the laser velocimeter but which can heavily impact the cost and construction time is the window. The window mounted in the 16-foot tunnel flat measures .965 m by 1.32 m and is 63.5 mm thick. The time between the original order date and delivery (figure 7) was four years. The cost was in excess of \$80,000. The window is mounted in a frame (figure 8) which in turn is mounted behind the tunnel flat. The window is covered by a wooden panel when technicians are working in the test section. Future plans include making a storage vault and steel blank to store and replace the window during periods when the instrument is not being used.



Figure 7

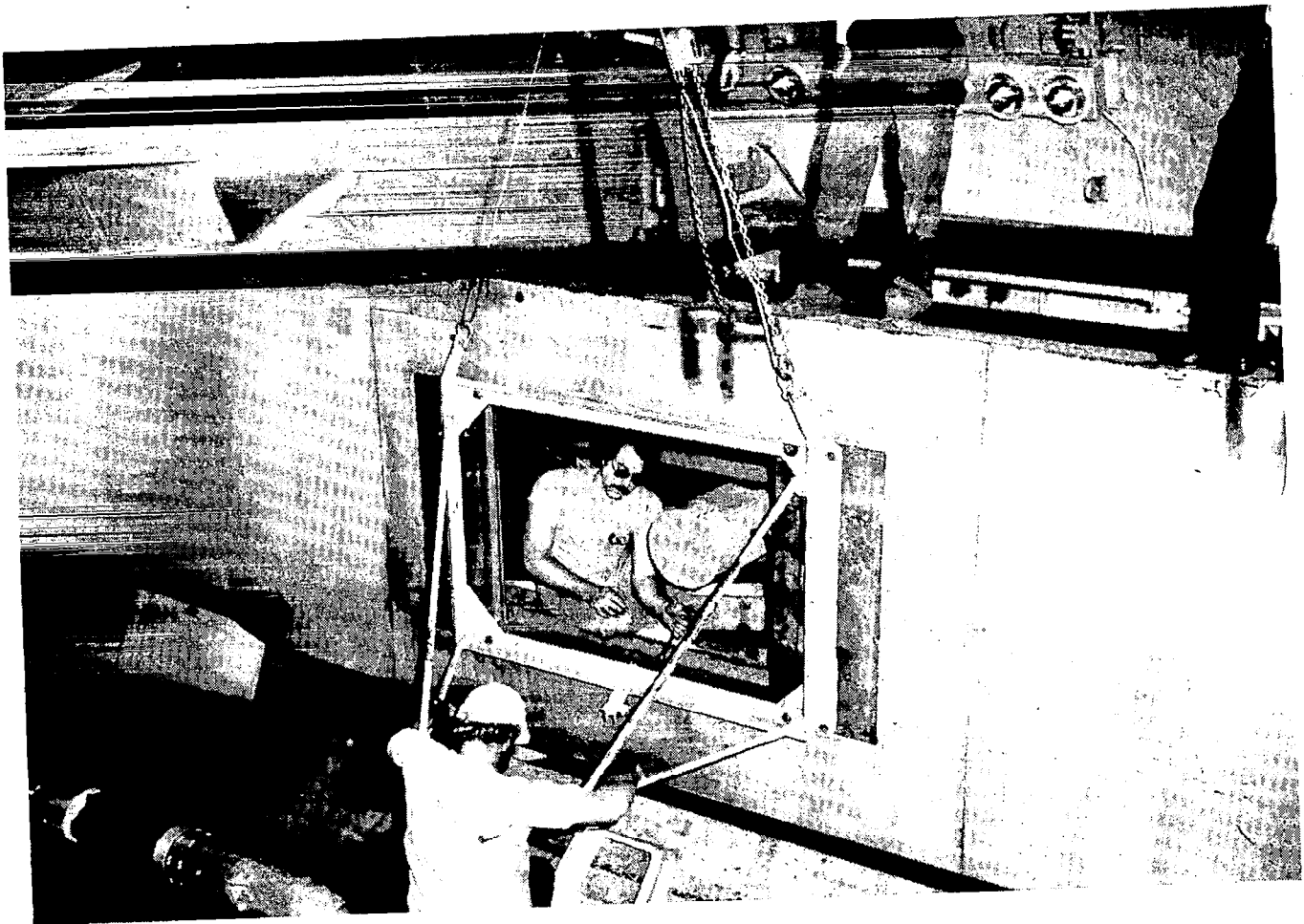


Figure 8.- Installation of tunnel window.

SEEDING GENERATORS

The seeding generators, designed by W. V. Feller, are of the shearing jet design. Operation of the generator is controlled by controlling the high pressure air supply. Figure 9 shows two generators installed on a five generator manifold. This arrangement was mounted on the turning vanes of the tunnel upstream from the test section (figure 10). The final system will employ a matrix of generators with electric solenoid air valves on each. The generators can then be independently turned on or off according to the sample volume position. The fluid used is kerosene, which produces a nominal 1-1.5 micron droplet.



Figure 9

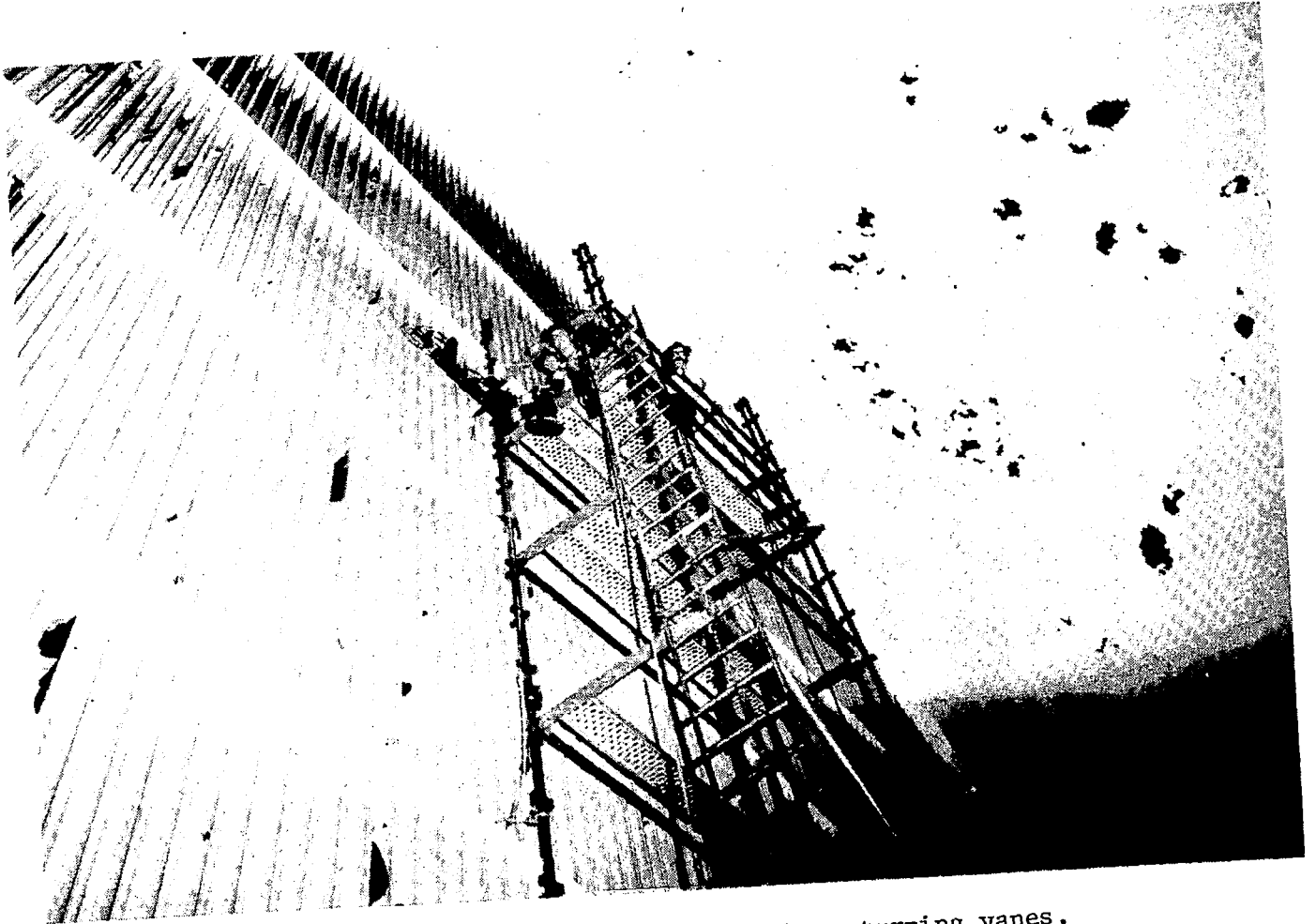


Figure 10.- Installation of bank on turning vanes.

CONDENSATION

A problem with atmospheric tunnels with air exchange is condensation. Tunnel runs made during periods of high ambient dewpoint will result in water vapor condensation in the test section air flow. The probability of fog formation increases with humidity and tunnel Mach number. The condensation occurs first in the annular layer of air adjacent to the test section wall (figure 11). At higher Mach numbers the condensation can occur throughout the test section (figure 12). Presence of large amounts of condensation inhibits operation of the laser velocimeter. By limiting the air exchange, and thereby heating the flow, the condensation can be minimized but not entirely eliminated.



Figure 11

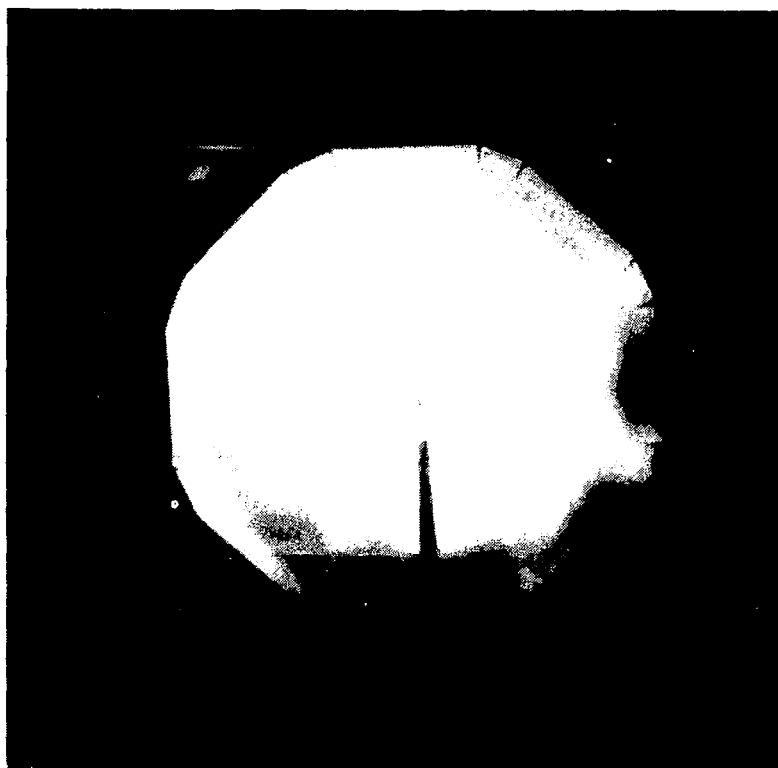


Figure 12.- Condensation at high speeds/humidity.

VIBRATION

The final problem to be discussed is a dominant problem with installation of sensitive optics in any tunnel of this large a scale. The problem is vibration. After the scan rig and optical components had been installed, accelerometer measurements were made on the support frame, optics bed, and laser enclosure. A pneumatic vibration isolator had been installed to support each of the four corners of the scan rig. Accelerometer measurements as a function of Mach number indicate vibration levels were either insignificantly affected by the isolators or in some cases increased (figure 13). The isolators were left in place but are not operational and will eventually be removed. The ineffectiveness of the isolators indicates that the major source of vibration coupling is acoustical. The influence of vibration on the optical components was reduced by mounting all but one of the components on a common plate with short stiff mounts.

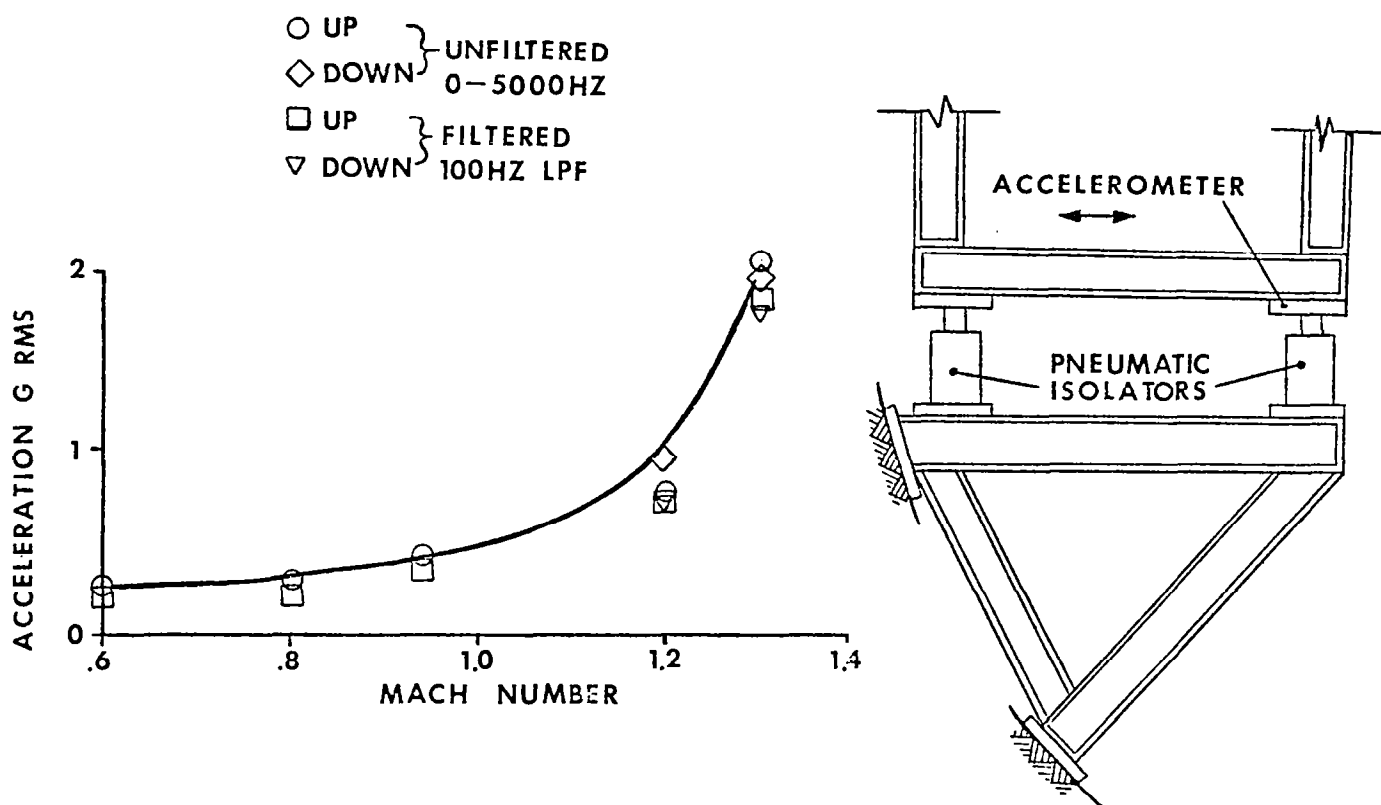


Figure 13

INITIAL RESULTS

A shakedown test was made to check out the instrument and identify areas requiring further work. A simple cone-cylinder-boattail model was mounted at zero angle of attack (figure 14). A limited survey was made above the model. Measurements were made with only the 488 nm u-component channel. Lasing on the 514.5 nm line would cease when the tunnel was operative and return when the tunnel was stopped. This problem is still being investigated. The results from the u-component channel are very encouraging. Figure 15 is a velocity profile measured above the model compared with a profile by William B. Compton, III done in 1975 with a strain gauge pressure transducer rake. The lowest sample volume location was acquired with the beams passing only 0.4 mm above the model.

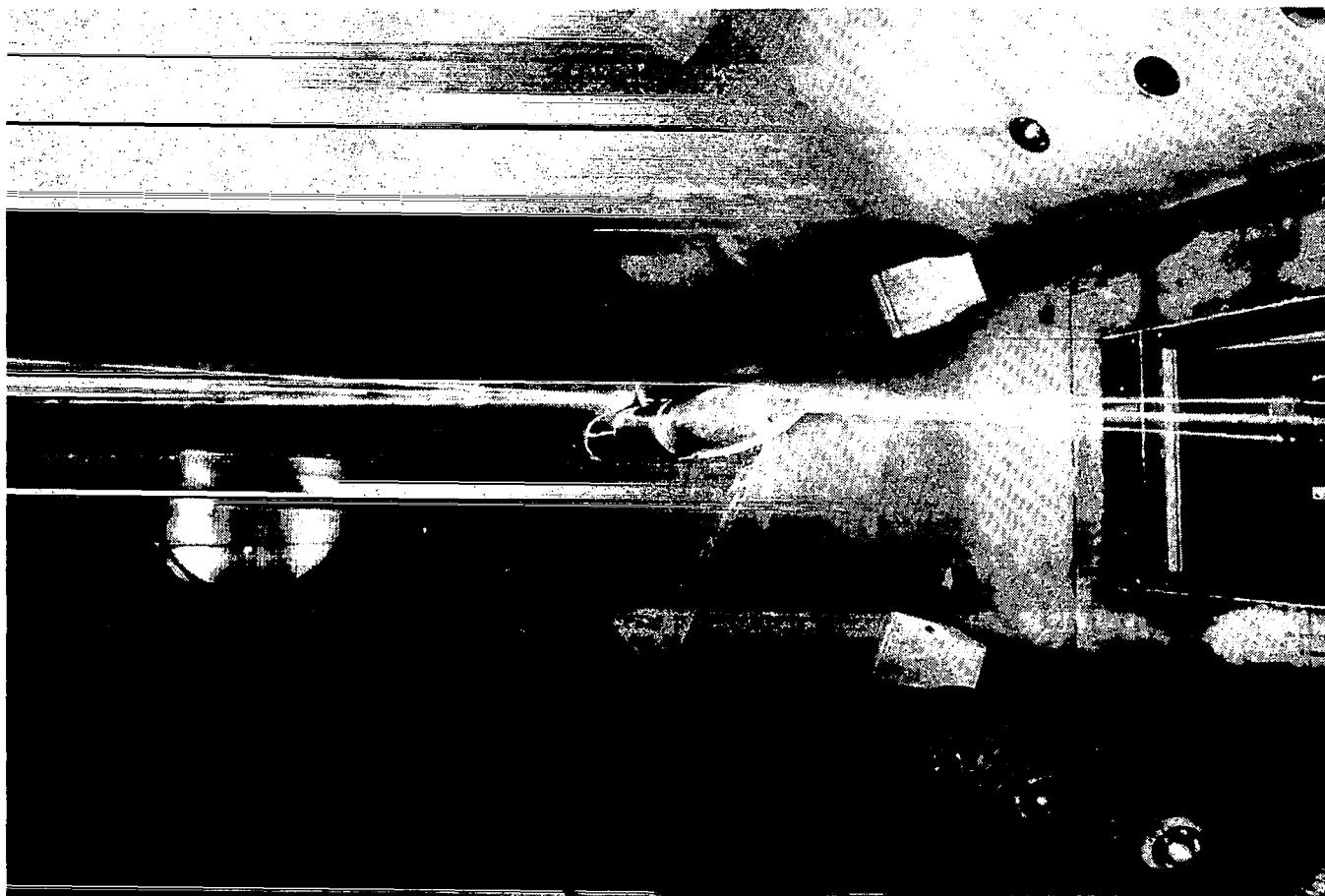


Figure 14

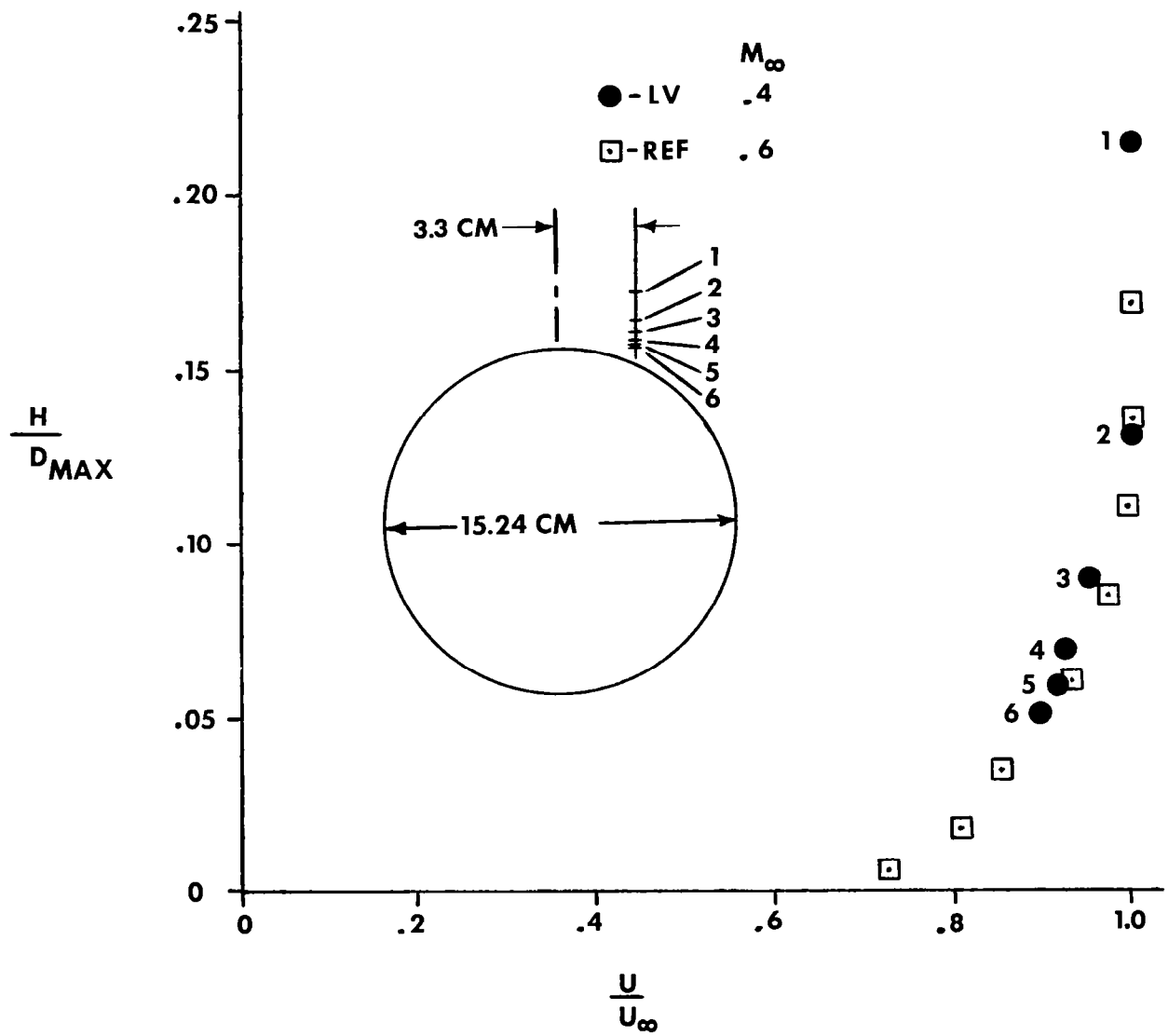


Figure 15.- Test results of vertical profile scan.

LASER VELOCIMETER APPLICATIONS TO HIGH-LIFT RESEARCH

R. R. Whipkey, G. Jones, and J. A. Braden
Lockheed-Georgia Co.
Marietta, Georgia

The subject of this presentation concerns the application of the Lockheed-Georgia 2-D laser velocimeter (LV) burst-counter system to the flow field around a 2- and 3-element high-lift airfoil. This work, performed under contract to NASA Langley Research Center, evaluates, via the LV, the characteristic behavior of the confluent boundary layer (that is, the boundary layer existing downstream of a slot) as it approaches and undergoes separation. In this application, the LV represents all ideal instruments for nonintrusively probing into the narrow slots and cove areas characterizing mechanical high-lift systems. The work is being performed in the Lockheed-Georgia 10 × 30-inch low-speed test facility using a 9-inch (basic) chord section of the general aviation GAW-1 airfoil. Figure 1 shows the test facility and LV-system arrangements used in the experimental work. The LV system (ref. 1) employs a 4-W argon laser and operates in an off-axis, backscatter mode with a focal length of about 30 inches. Smoke is used as the seeding medium and is injected downstream of the model such that particle uniformity and size are constant upon completion of the tunnel circuit into the test area. The LV system (fig. 1) is fully automated by utilizing a MAC-16 minicomputer for positioning, data acquisition, and preliminary data reduction.

Figure 2 summarizes the matrix of airfoil configurations undergoing current study where the behavior of the boundary layer reflects modifications in the slots and angular deflections of the leading- and trailing-edge airfoil elements. With this rather extensive matrix of study configurations it has become expedient to use various devices by which nominal flow surveys can be rapidly acquired and those areas of specific interest (separated flow, vortex formations, and so forth) can be quickly identified for more precise measurements. A highly reliable method for this purpose is represented by a "quick-traverse" LV-analog system which is employed to acquire instantaneous velocity profiles. This is normally done prior to obtaining the more time-consuming digital definition of the boundary layers in terms of mean velocity profiles u and v , Reynolds shear stresses, and turbulence intensities u' and v' . Figure 3 shows a sample output from the analog system as compared to the corresponding digital data (bottom of the figure) for an attached- and separated-flow condition on the airfoil. As noted, the quick-traverse analog trace provides a reliable indication of the position and degree of surface-flow separation as well as the shape and condition of the overall boundary-layer profile.

The extent of LV data acquisition for boundary layers on the individual airfoil configurations is exemplified in figure 4, which shows the airfoil at a post-stall angle of attack of 16° . The corresponding pressure distribution, also shown on figure 4, indicates a trailing-edge type of flow separation on the main airfoil element which is further corroborated by the boundary-layer surveys. Points of general interest in such surveys are the large wake overlying the flap-surface flow, the stationary vortex within the cove area, and the modifications to the main-element, upper-surface flow as introduced by variations in the leading-edge geometry. For most trailing-edge configurations, it has been found that attached flap-surface flow is maintained for all but the most adverse circumstances although the flap load (i.e., lift) is highly sensitive to the separated wake from the forward main element. Corresponding to the velocity profiles displayed in figure 4, the turbulence intensity and Reynolds shearing stress profiles are presented in figures 5 to 7. Figures 5 and 6 show the streamwise and normal (to the airfoil surface) components of the turbulence-intensity measurements representing coincident data points as acquired by the LV system. These data and the shearing stress data of figure 7 show the high level of turbulence within the separated wake and the shear layer near its edges.

To further enhance the visual interpretation of general flow behavior, computer graphics are extensively employed to treat specific areas of the flow field as illustrated in figures 8 to 10. In these figures, the leading-edge, trailing-edge, and wake flow fields are highlighted by enlargement. In many instances of massive flow separation the measured time-averaged velocity profiles will reflect the highly unsteady nature of the flow through slight variations in the magnitude of adjacent velocity vectors and, in isolated instances, through variations in flow direction (wakes primarily). In the leading-edge regions (fig. 8), characterized by high-speed, curvilinear flows, close-to-surface LV measurements become difficult as (it is speculated) the seeding medium tends to be "centrifuged" away from the surface. The generation of seeding particles of specified sizes and distributions using various media represents a current emphasis in further LV-development work at Lockheed, and additional research is needed to fully understand these effects.

Further effective use of computer graphics for interpreting the measured flow fields is illustrated in figure 11, wherein contours of constant velocity components (u) are shown. Such charts, developed for rapid visualization of all LV measurements, facilitate data manipulations as needed for interfacing with theoretical modeling of the flow field. The rapidity and consistency of the LV system for acquiring such data makes it mandatory that an extensive data processing capability be an inherent part of the experimental setup.

RREFERENCE

1. Whiffen, M. C.; and Meadows, D. M.: Two Axis Single Particle Laser Velocimeter System for Turbulence Spectral Analysis. Proc. of the Second International Workshop on Laser Velocimetry, Vol. 1, Mar. 1974, pp. 1-12.

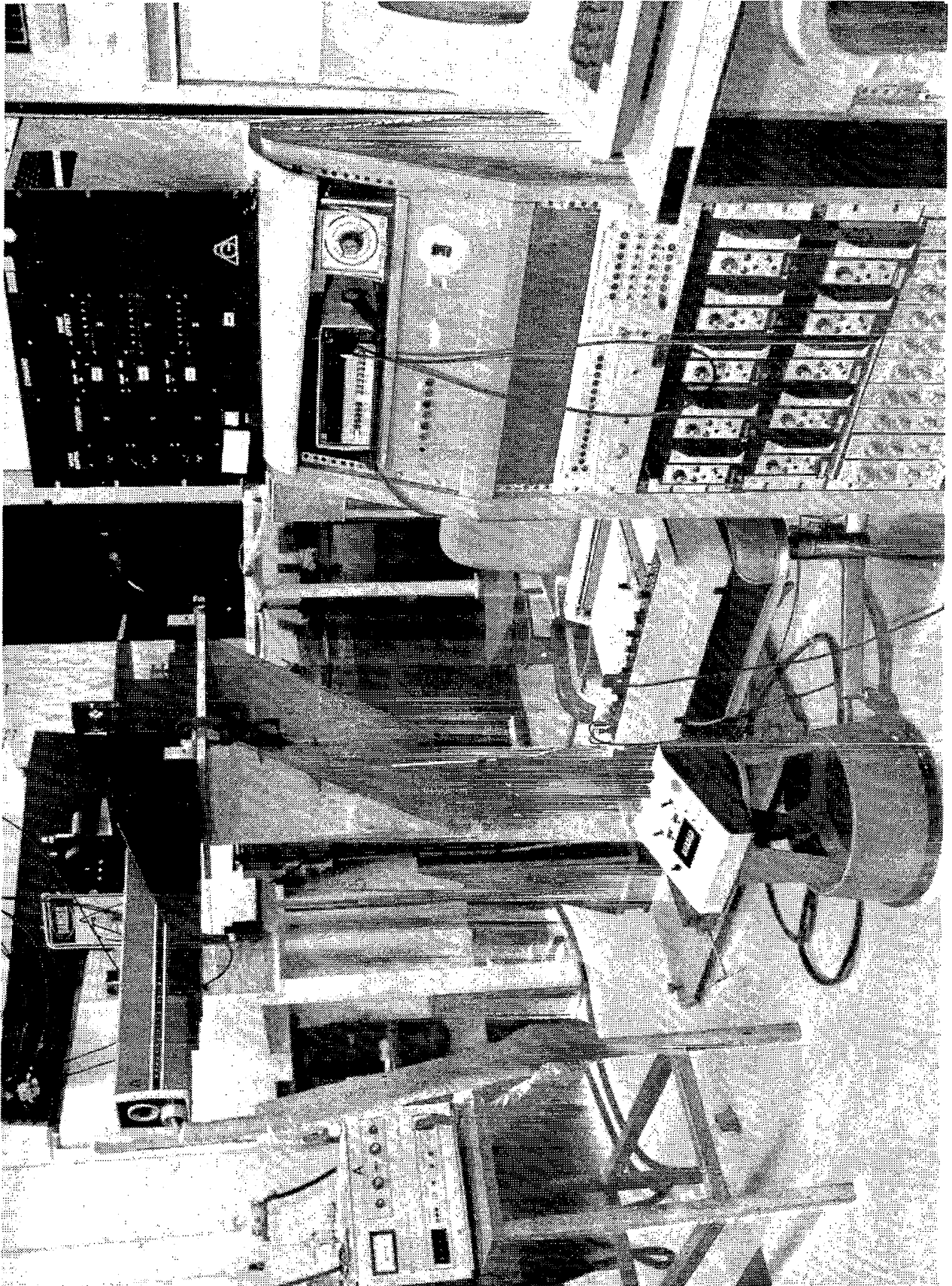


Figure 1.- Experimental arrangement of 2-D LV system in the 10 x 30-inch low-speed test facility.

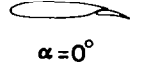
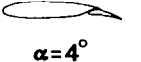
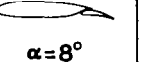
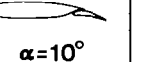
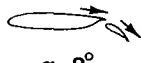
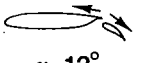
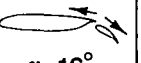
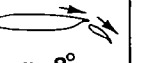
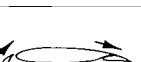
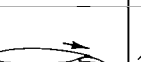
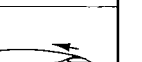
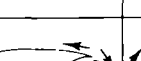
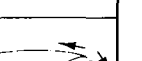
CLEAN AIRFOIL	 $\alpha=0^\circ$	 $\alpha=4^\circ$	 $\alpha=8^\circ$	 $\alpha=10^\circ$	 $\alpha=12^\circ$	 $\alpha=16^\circ$
FLAPPED $\delta_f=20^\circ$	 $\alpha=8^\circ$	 $\alpha=12^\circ$	 $\alpha=16^\circ$	 $\alpha=8^\circ$	 $\alpha=12^\circ$	 $\alpha=16^\circ$
FLAPPED $\delta_f=30^\circ$	 $\alpha=4^\circ$	 $\alpha=8^\circ$	 $\alpha=12^\circ$	 $\alpha=4^\circ$	 $\alpha=8^\circ$	 $\alpha=12^\circ$
FLAPPED $\delta_f=40^\circ$	 $\alpha=4^\circ$	 $\alpha=8^\circ$	 $\alpha=10^\circ$	 $\alpha=4^\circ$	 $\alpha=8^\circ$	 $\alpha=11^\circ$
SLATTED $\delta_s=45^\circ$	 $\alpha=4^\circ$	 $\alpha=8^\circ$	 $\alpha=12^\circ$	 $\alpha=4^\circ$	 $\alpha=8^\circ$	 $\alpha=12^\circ$
FLAPPED & SLATTED $\delta_f=30^\circ \delta_s=45^\circ$	 $\alpha=12^\circ$	 $\alpha=14^\circ$	 $\alpha=16^\circ$	 $\alpha=12^\circ$	 $\alpha=14^\circ$	 $\alpha=16^\circ$

Figure 2.- Applications to high-lift research - separating confluent boundary layer.

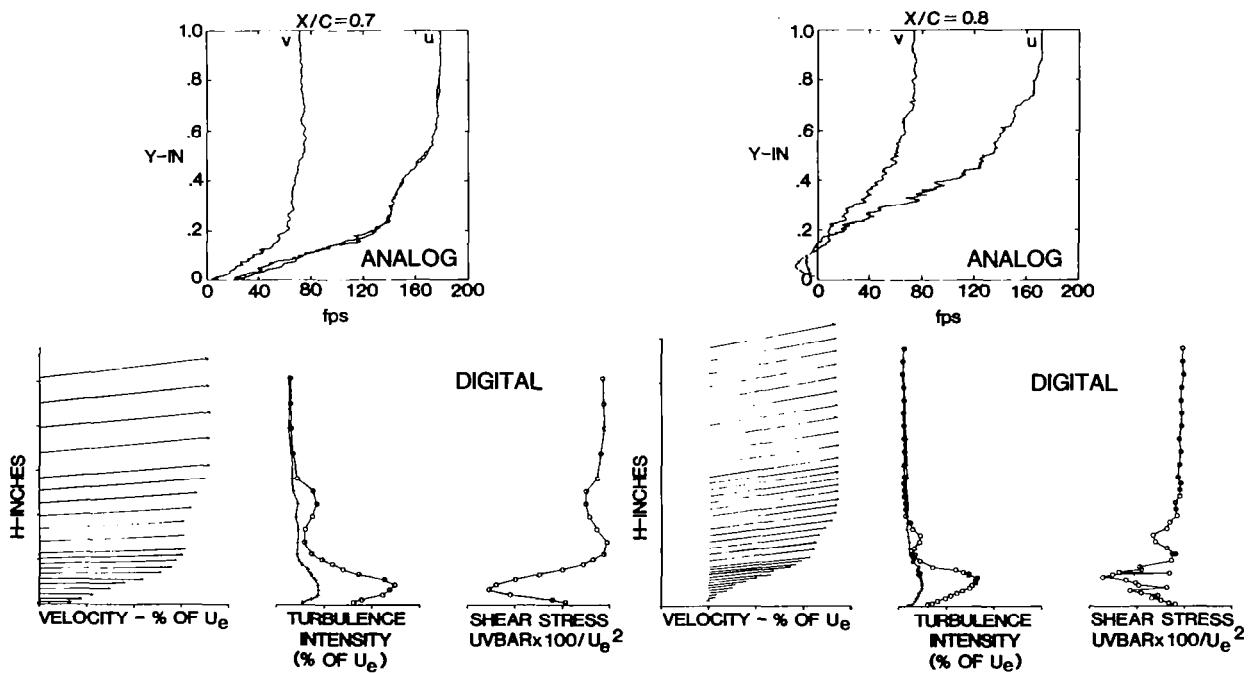


Figure 3.- Analog rapid-scan LV system. GAW-1 airfoil; $\delta_f=30^\circ$; $\alpha=16^\circ$.

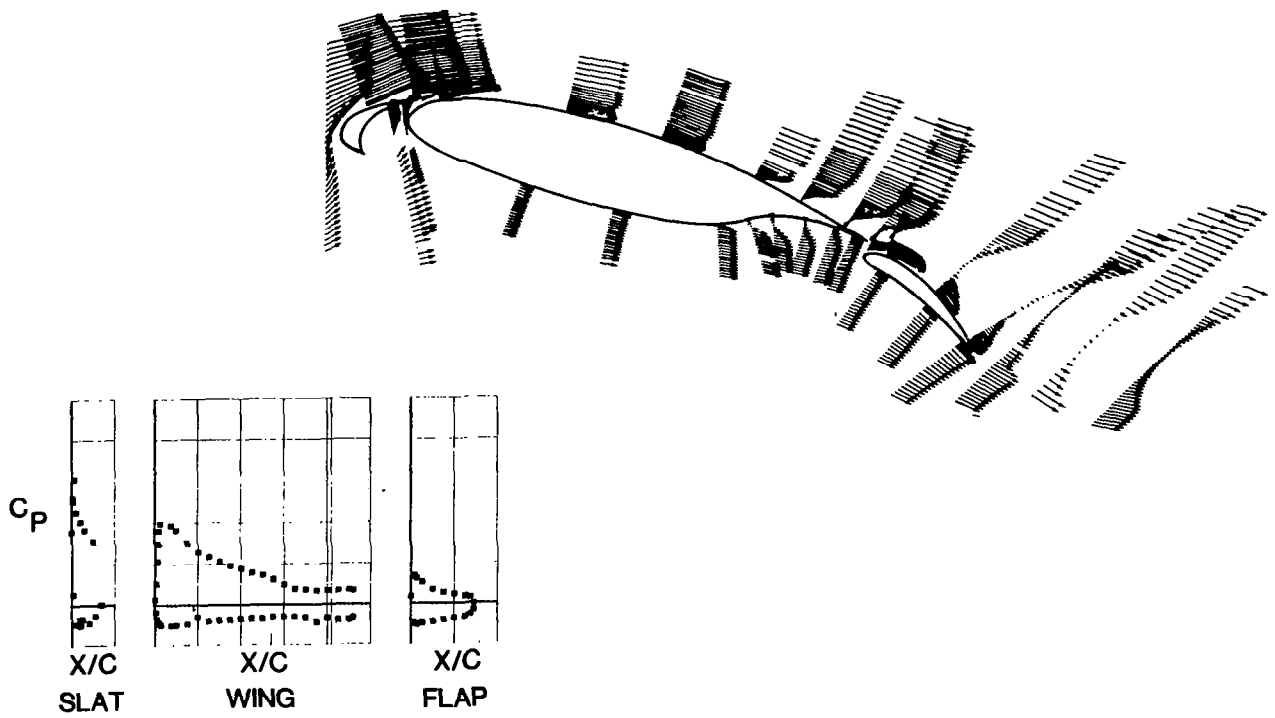


Figure 4.- Example of LV data acquisition for GAW-1 airfoil velocity vectors, $\alpha = 16^\circ$.

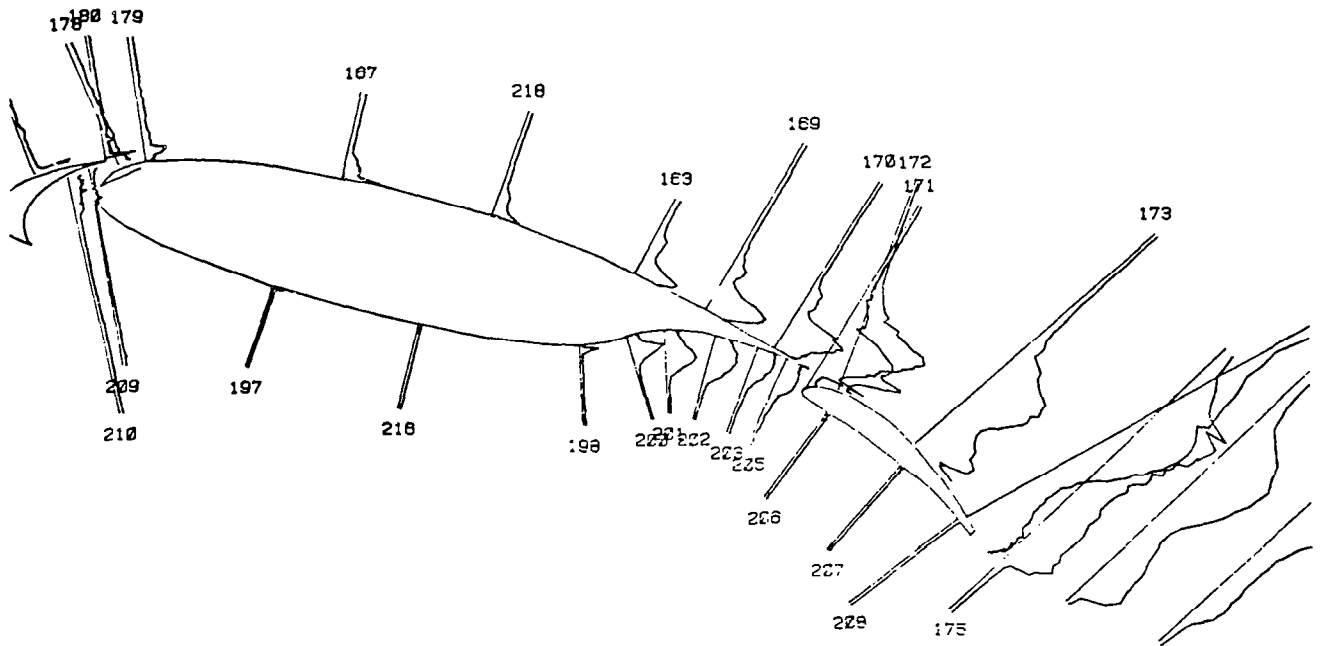


Figure 5.- Streamwise component of turbulence intensity u' , GAW-1 airfoil; $\delta_f = 30^\circ$; $\alpha = 16^\circ$.

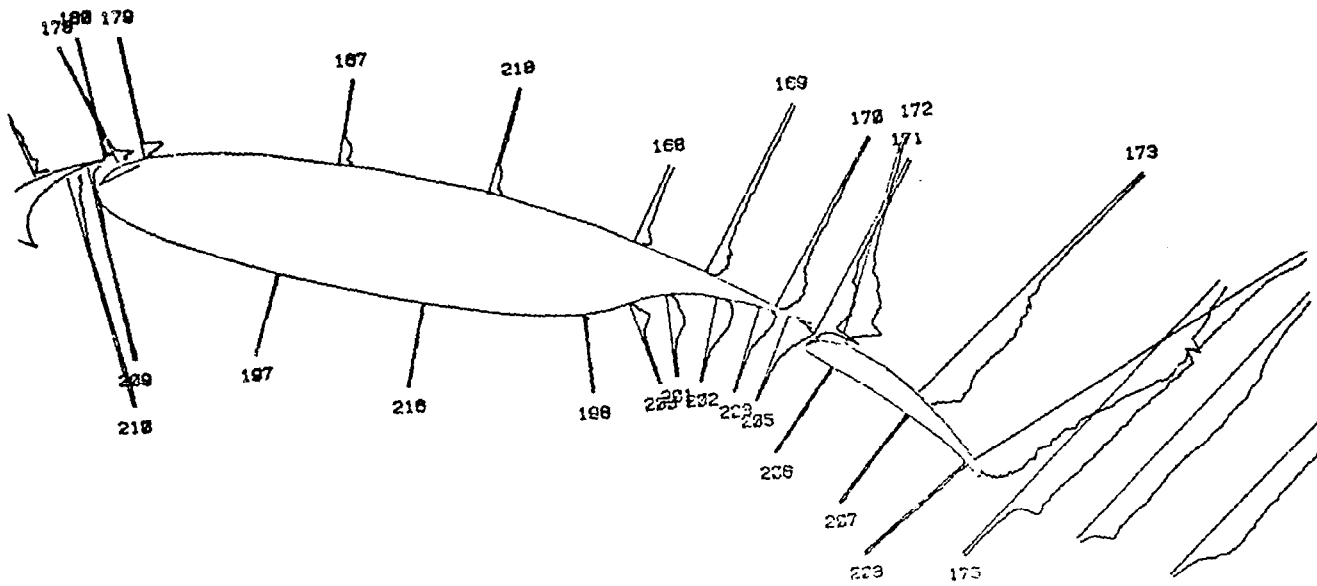


Figure 6.- Normal component of turbulence intensity v' . GAW-1 airfoil; $\delta_f = 30^\circ$; $\alpha = 16^\circ$.

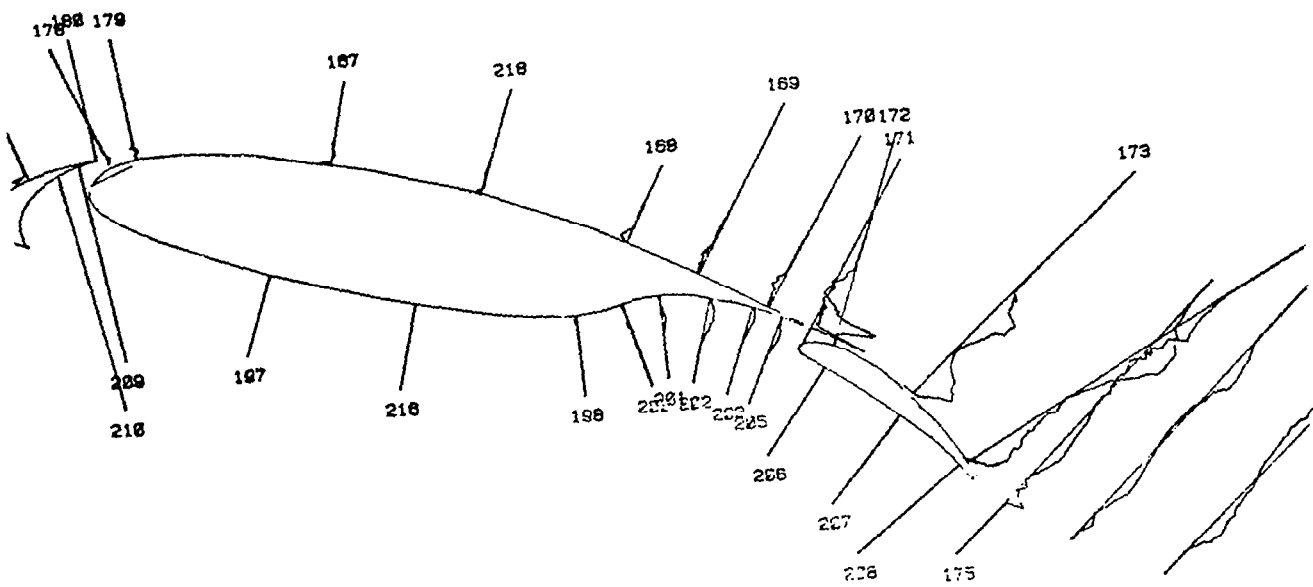


Figure 7.- Reynolds shearing stress profiles $u'v'$. GAW-1 airfoil; $\delta_f = 30^\circ$; $\alpha = 16^\circ$.

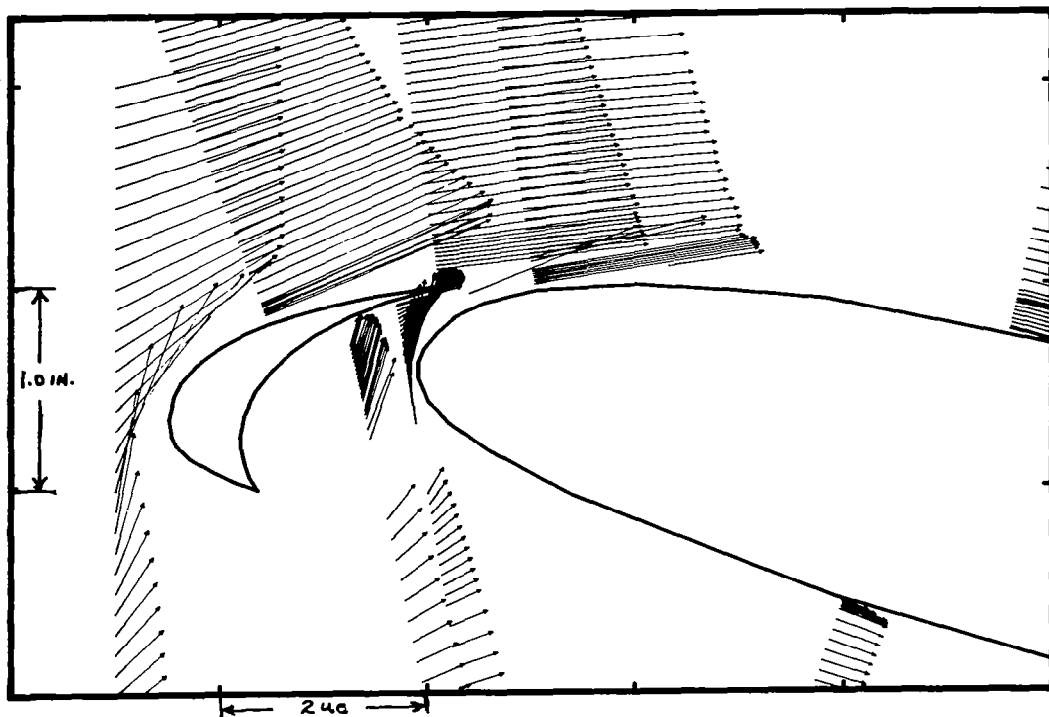


Figure 8.- Leading-edge flow field. GAW-1 airfoil; $\delta_f = 30^\circ$; $\alpha = 16^\circ$.

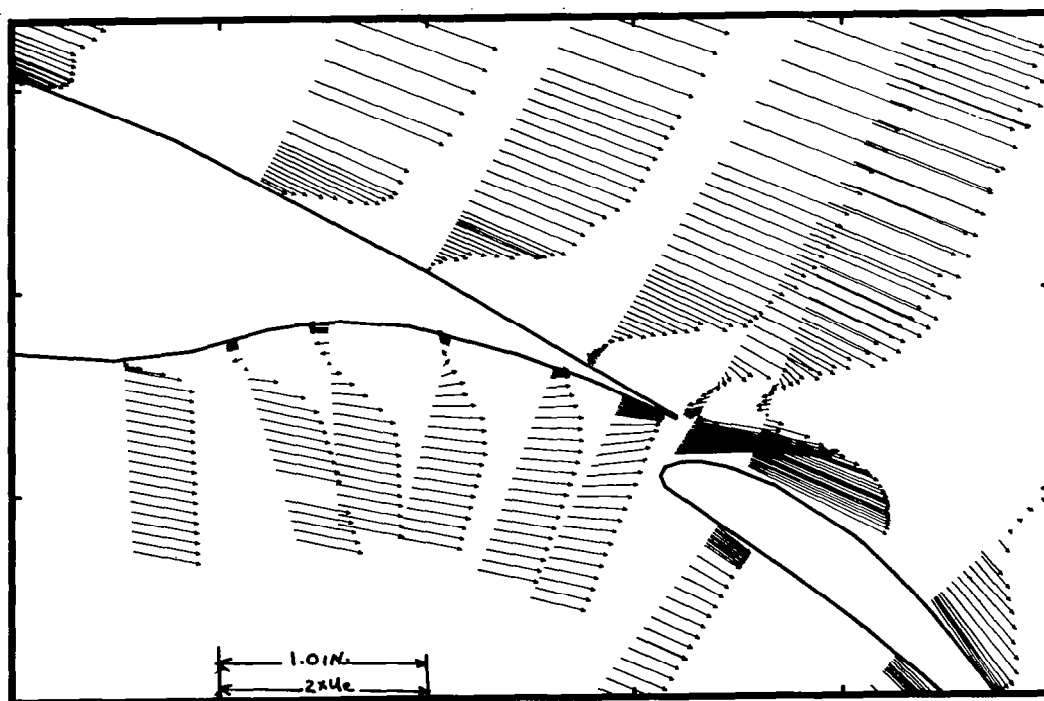


Figure 9.- Trailing-edge flow field. GAW-1 airfoil; $\delta_f = 30^\circ$; $\alpha = 16^\circ$.

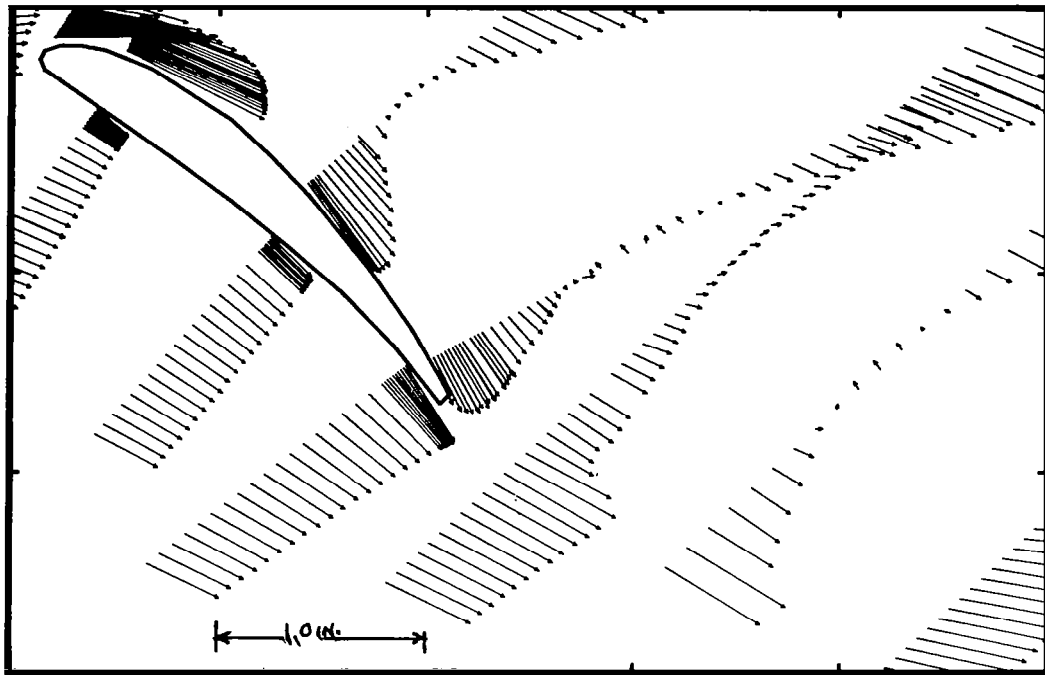


Figure 10.- Wake flow field. GAW-1 airfoil; $\delta_f = 30^\circ$; $\alpha = 16^\circ$.

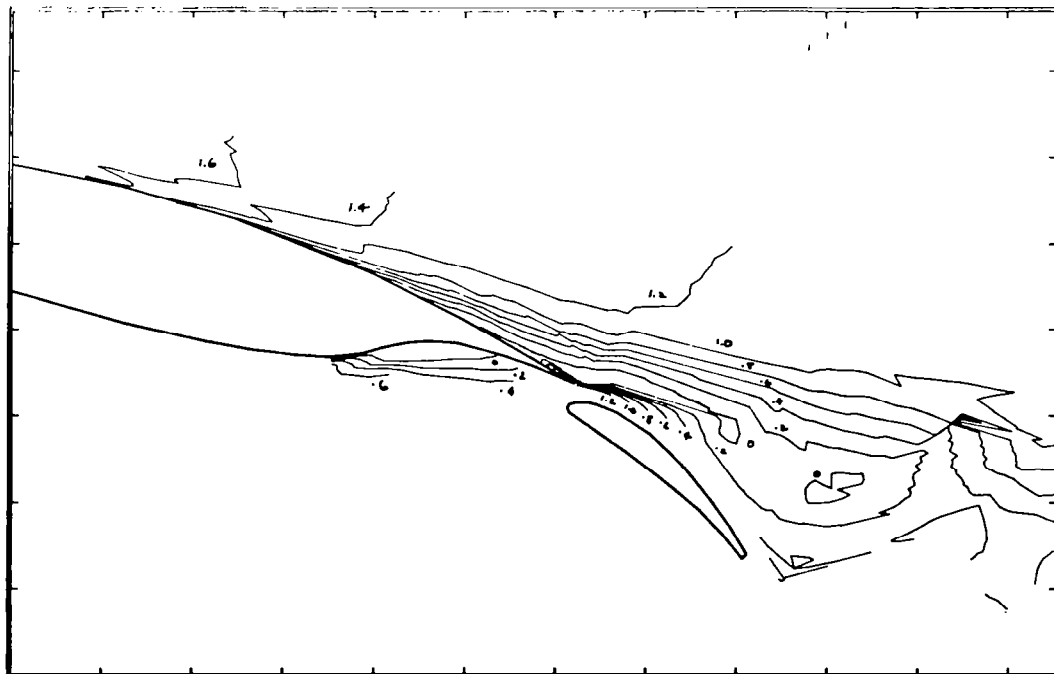


Figure 11.- Contours of constant velocity components u . GAW-1 airfoil;
 $\delta_f = 30^\circ$; $\alpha = 16^\circ$.

APPLICATIONS OF A LASER VELOCIMETER IN THE
LANGLEY 4- BY 7-METER TUNNEL

William L. Sellers
NASA Langley Research Center

Joe W. Elliott
U.S. Army Structures Laboratory (AVRADCOM)

Hampton, Virginia

4- BY 7-METER TUNNEL

This paper will describe the dedicated laser velocimeter (LV) system that has been installed in the Langley 4- by 7-Meter Tunnel and will provide several examples of how an LV has been used to support research in the facility. The 4- by 7-Meter Tunnel is a closed circuit, single-return, atmospheric wind tunnel which can be operated in either an open or closed test section configuration. The test section is 14.5 ft (4.42 m) high, 21.75 ft (6.63 m) wide and 50 ft (15.24 m) long. In the open test section configuration, the side walls and ceiling are raised to the top of the test chamber to form a closed-on-bottom-only configuration as shown in the bottom left photograph.

The tunnel supports several research programs, such as high-lift/wake vortex investigations and aerodynamic and acoustic testing of rotorcraft, as well as providing data for general aerodynamic theory development and validation. Examples of some typical tests are shown in the bottom left and right photographs. In recent years, the tunnel has also been used to test several proof-of-concept LV systems, including a 3-component, coaxial backscatter system, shown in the bottom center photograph.

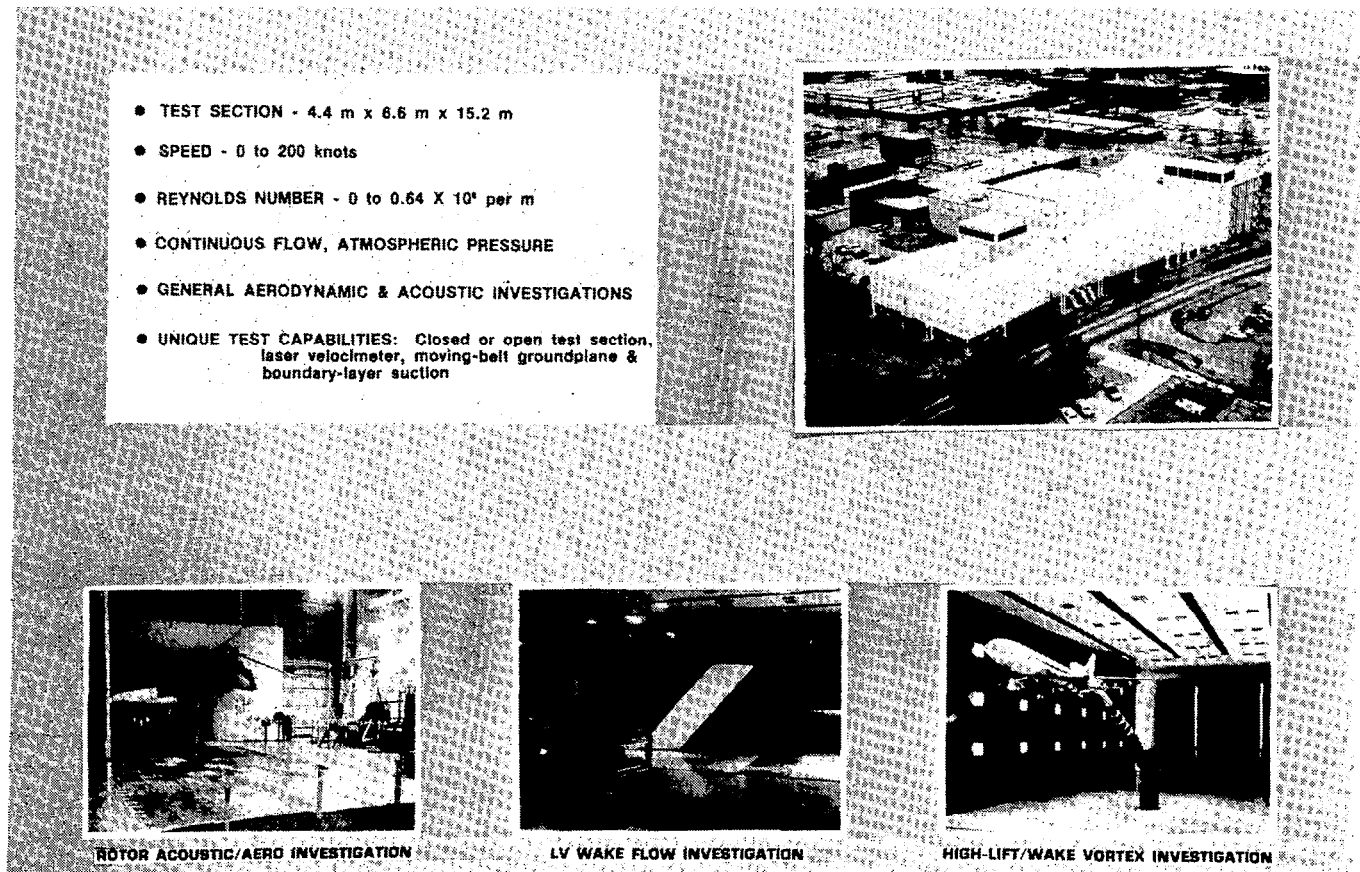


Figure 1

LASER VELOCIMETER SYSTEM

The present LV system has benefited from the knowledge gained from testing earlier proof-of-concept systems. The system was designed to provide mean flow velocity measurements of the longitudinal and vertical velocity components. The LV has a sample volume less than 1 cm long and approximately 0.2 mm in diameter over the 10- to 20-ft focal length of the system. A 12-W argon-ion laser provides the light source and is typically operated at 4 W output (in all lines) at the exit of the laser. The transmitting and receiving optics packages are commercially available, 2-component, 2-color units. The zoom lens system consists of a 3-in. clear aperture negative lens and a 12-in. clear aperture positive lens. The negative lens can be moved under computer control, as shown in the figure, to provide the capability of positioning the sample volume laterally across the test section. In addition, the final folding mirror can be panned and/or tilted under computer control, as shown in the figure, to provide additional traversing capability. Bragg cells are incorporated in the system to alleviate directional ambiguity in each of the velocity components.

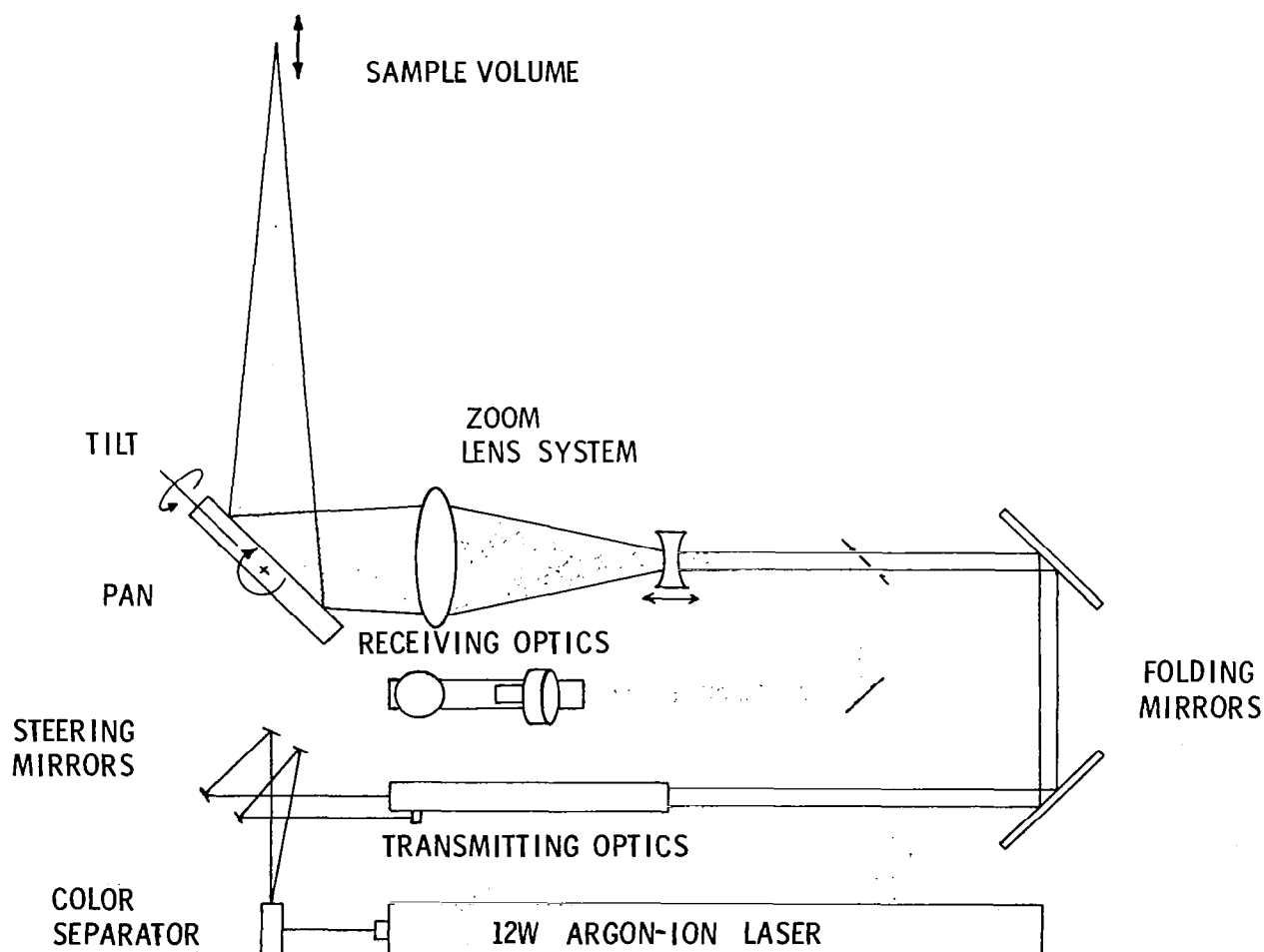


Figure 2

LV DATA ACQUISITION SYSTEM

The existing LV system can acquire two channels of LV data and one channel of auxillary data. During helicopter testing, the auxillary channel typically provides data relating to helicopter rotor position. The signals from the photodetectors are input to high-speed burst counters, which are interfaced to a 16-bit minicomputer by a laser velocimeter autocovariance buffer interface (LVABI). The LVABI can store up to 4096 data points for each channel in individual buffers. When either of the two LV data buffers are filled or a preset kick-out time is exceeded, the LVABI sends the data to the minicomputer via direct memory access (DMA). The minicomputer processes the data, stores it on a disc and magnetic tape, and displays the results on a graphics terminal and line printer.

The LVABI has an additional feature that enhances data processing. The LVABI has the capability of only accepting data from the counters when the measurement of each velocity component occurs within a 1- μ sec coincidence window. The auxillary data channel and the coincidence window provide the capability for conditional sampling during data processing.

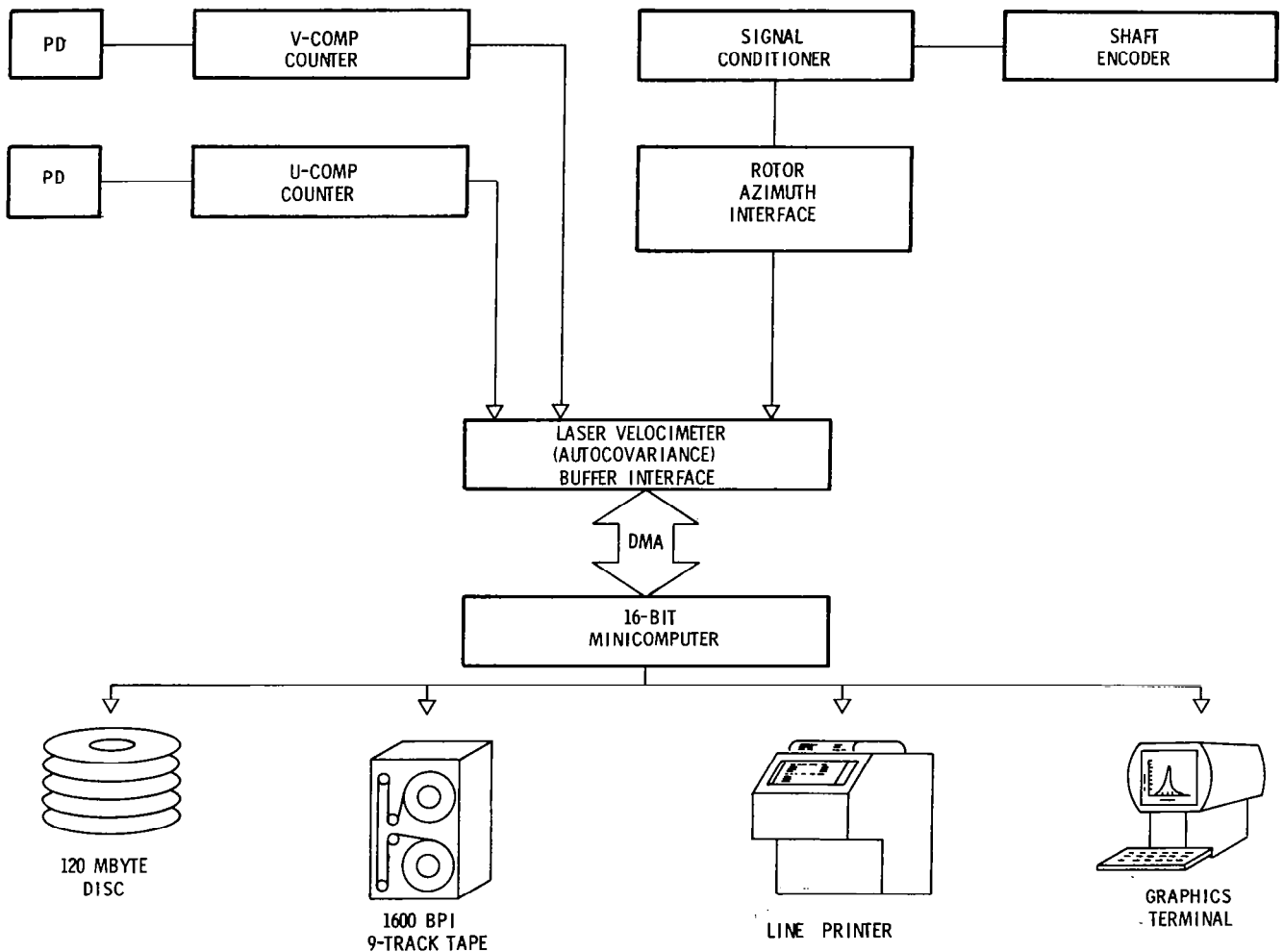


Figure 3

LV TRAVERSING SYSTEM

The LV has its own dedicated, computer controlled traversing system. The majority of the traversing which takes place during an LV test is accomplished with the x-y traversing rig shown in figure 4(a). The optical pan and tilt capability is used to make minor adjustments in sample volume position to provide optical access to critical areas. The unit was designed to provide approximately 7-ft (2.134-m) vertical and \pm 3-ft (0.914-m) horizontal traversing capability of the entire optics package. A unique suspension and control system enables the optics package to be placed, with 0.020-in. (0.051-cm) accuracy, anywhere in the traverse range. The traverse system can be operated either manually or under computer control with a traversing speed of 10 in/min (0.254 m/min). The optics package, shown in the close-up photograph (fig. 4(b)), is mounted under a horizontal platform that moves vertically inside the exterior framework. The entire traverse system is mounted on wheels and can be rolled into various positions along the test section. The unit is 11 ft (3.35 m) high, 16 ft (4.88 m) long, 8.5 ft (2.59 m) wide, and weighs 6000 lb (2721.6 kg).

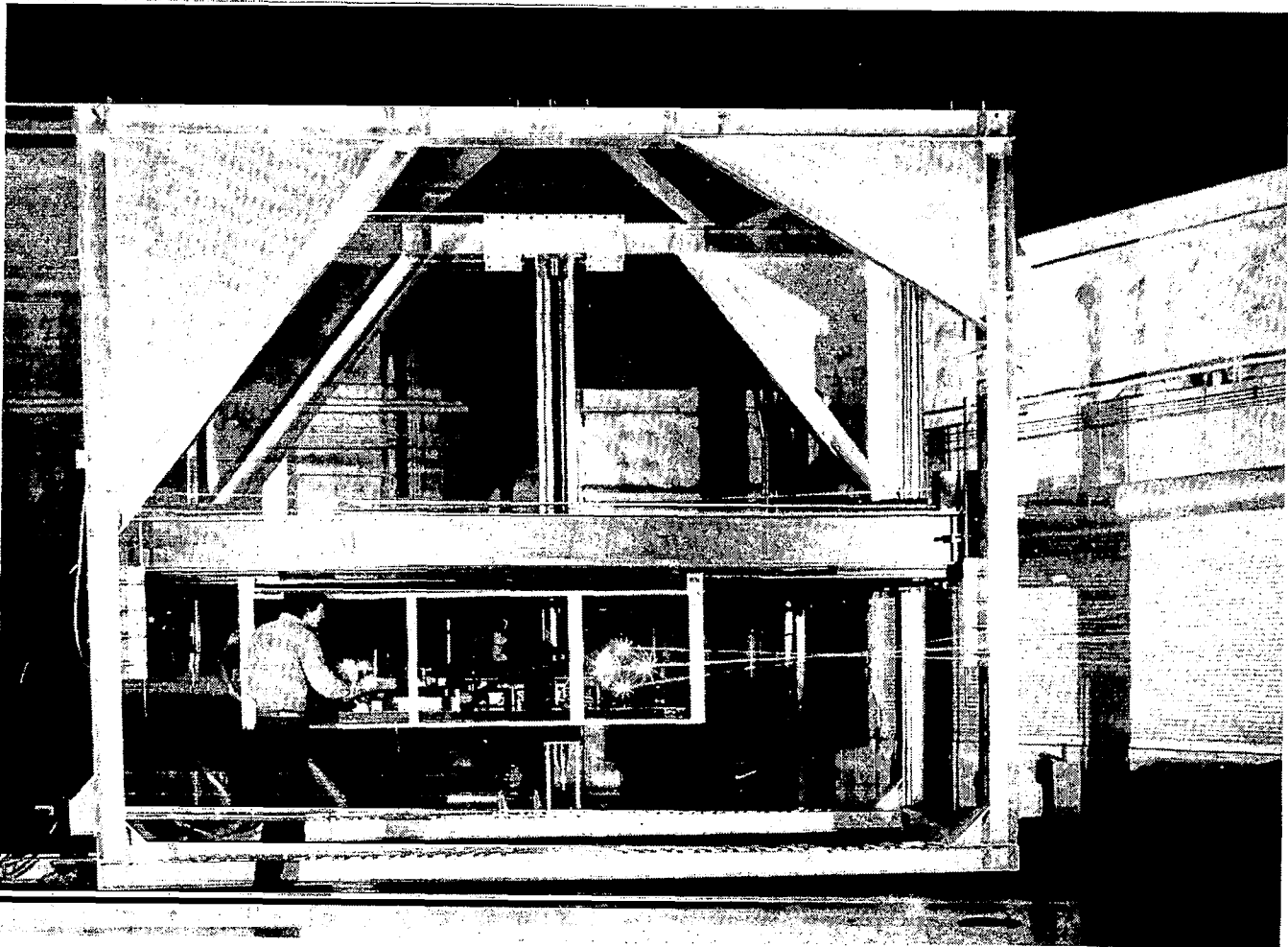


Figure 4(a)

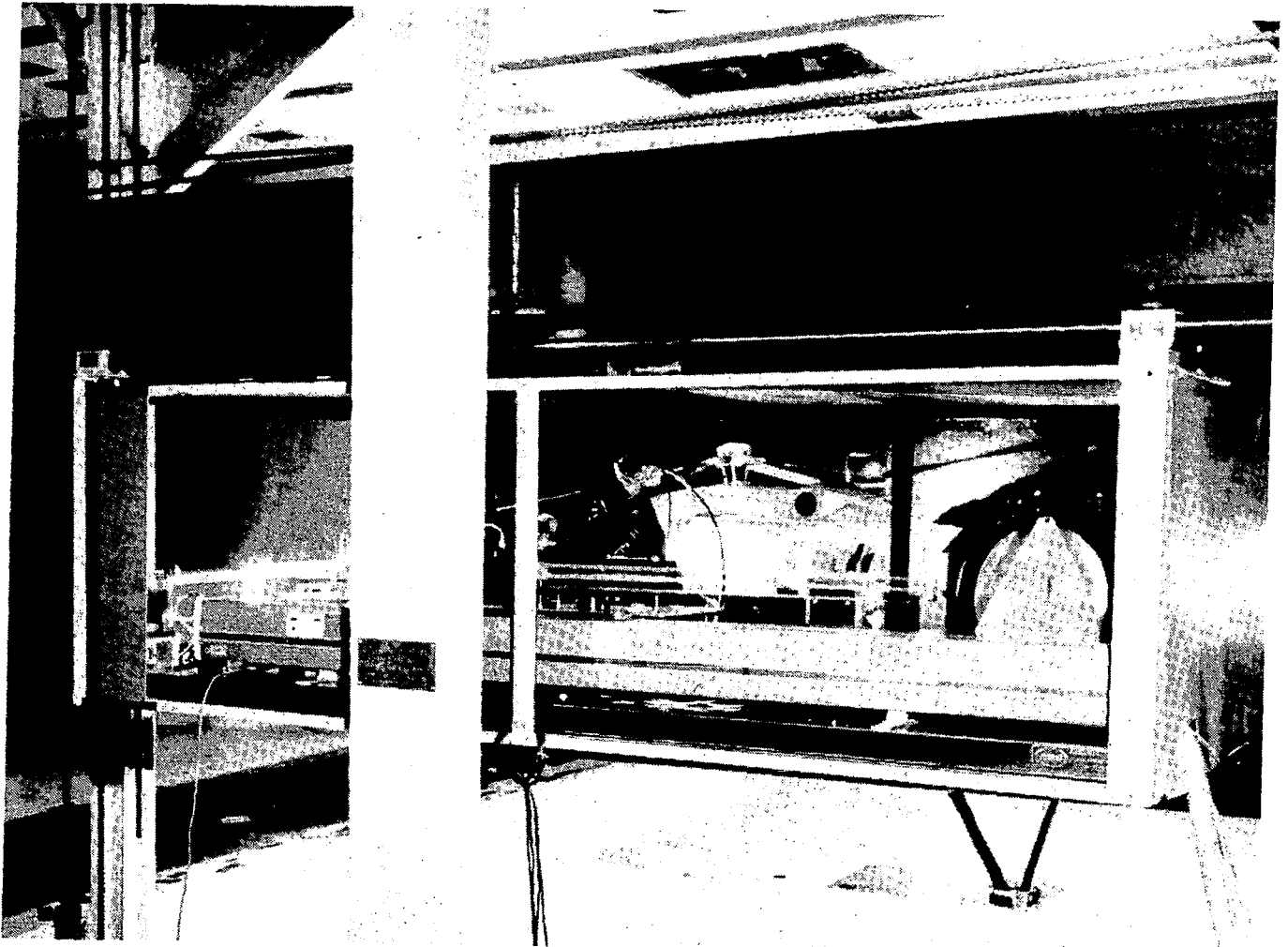


Figure 4(b)

PARTICLE GENERATING SYSTEM

The particle generator currently in use at the facility is a kerosene smoke generator. Liquid kerosene, under pressure from a nitrogen tank, is forced through a wand where it is heated, vaporized, and expelled through a nozzle that was sized to maximize the number of 2- μm particles in the smoke. Positioning of the smoke wand in the settling chamber is accomplished by manually pulling the smoke wand up and down on cables using pulleys mounted on the floor and ceiling of the settling chamber. Particle generation and the placement of the particles in the flow is the most time consuming problem hampering the efficient operation of the laser velocimeter in the 4- by 7-Meter Tunnel.

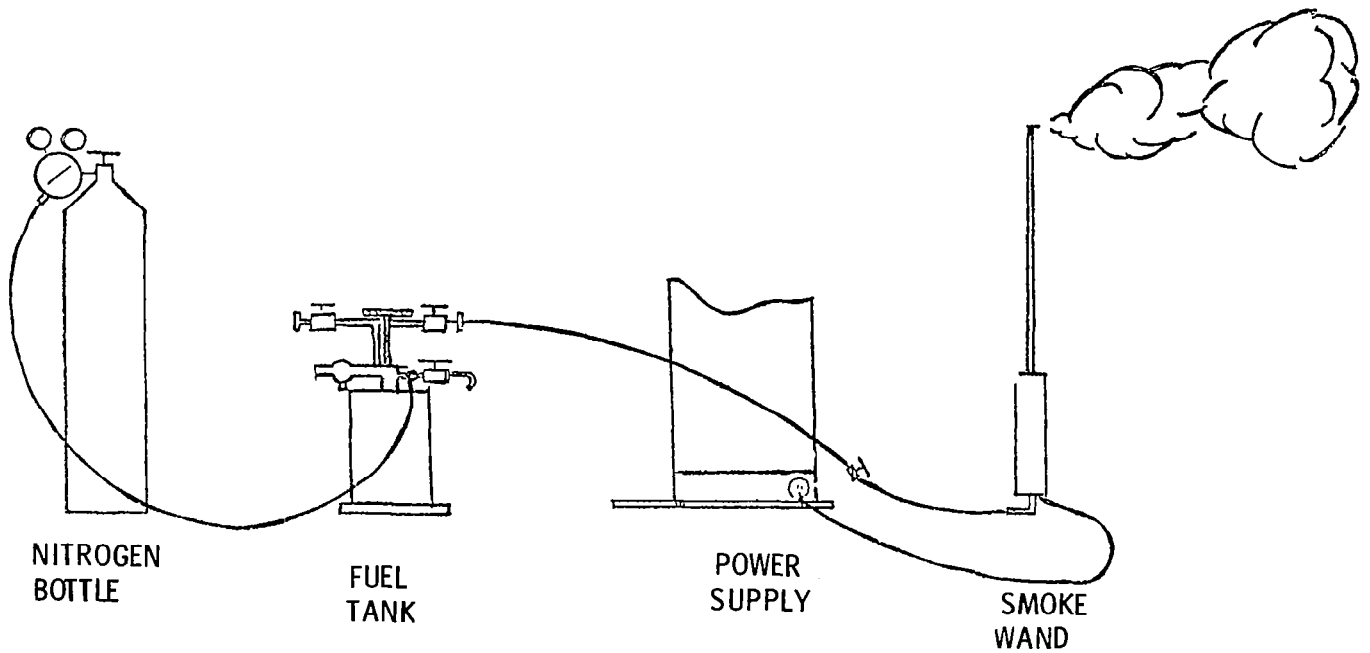


Figure 5

LV APPLICATIONS - NEAR-FIELD WAKE DETAILS

The small sample volume associated with the LV gives the aerodynamicist the capability to probe flow fields in great detail. Of particular interest is the near-field wake generated by lifting surfaces. A very small wake is generated, at low angles of attack, behind the 12-in. (30.48-cm) chord NACA 0012 wing shown in the upper left of figure 6. An example of the wake defect measured by a LV is shown in the graph in the lower left of the figure. A standard 1/4-in. (0.638-cm) pitot-static probe is also shown for a size comparison. The pitot-static probe is too large to measure the steep gradients and would, therefore, provide uncertainty in drag computations based on the wake defect.

The measurement of the flow field around a wing is another application for which the LV is ideally suited. An example of the complex flow field measured around the same NACA 0012 wing, at $\alpha = 19.4^\circ$, is shown in the upper right of the figure. The laser velocimeter was able to measure, in great detail, the broad shear layer dividing the free-stream and the separated flow regions, as well as the reverse flow in the separated region. An enlargement of the trailing edge area of the wing is shown in the lower right of the figure and demonstrates that the LV was able to provide great detail in regions of severe velocity gradients. The above data were obtained from an earlier proof-of-concept LV system as reported by Hoad, Meyers, Young, and Hepner (refs. 1 to 3). The earlier LV system did not have the positional accuracy of the present system; therefore, we expect to be able to provide even more detail in the future.

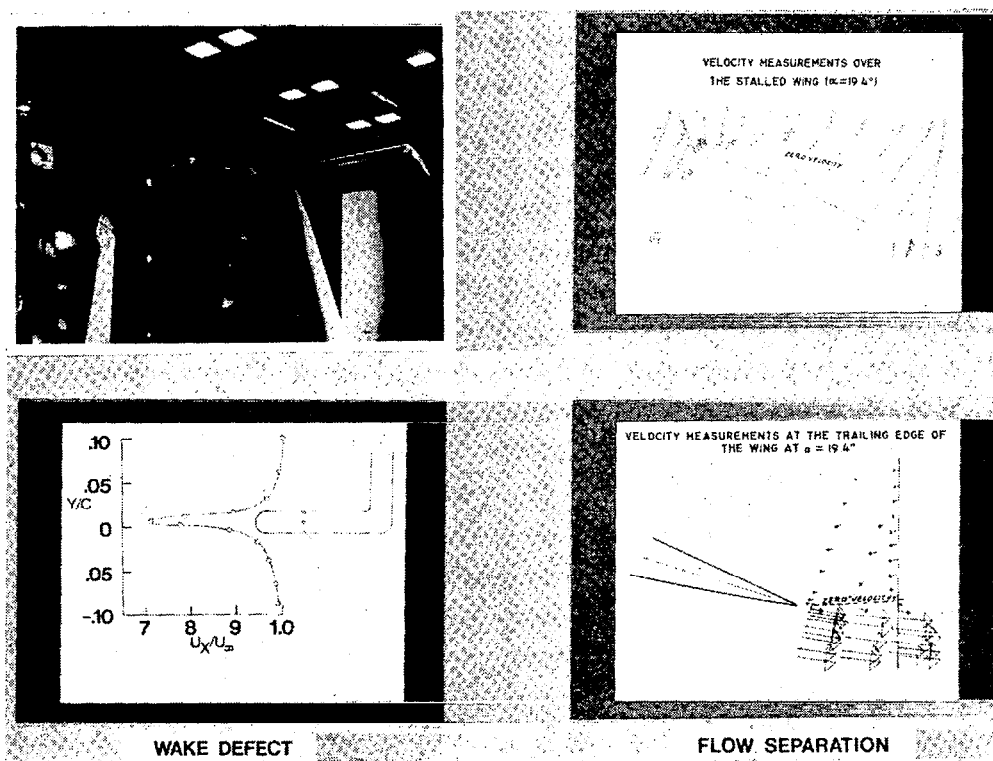


Figure 6

LV APPLICATIONS - ROTOR WAKE SURVEYS

The nonintrusive character of the LV makes the measurement of complex flow fields possible in places where conventional measurement techniques are not practical. An example of this capability and of the type of data obtained with the LV are shown in figure 7.

A test was conducted in the Langley 4- by 7-Meter Tunnel to measure the flow field in several longitudinal planes ahead of the vertical fin of a helicopter. The model used in the test was a 1/4-scale UH-60 helicopter as shown in the upper left of the figure. A sketch of the measurement grid is shown in the upper right of the figure to show the relative position of the helicopter blades, body, and fin to the region where measurements were taken. Data were obtained on the model centerplane and 6 and 12 in. off the centerplane, with the tunnel operating at a free-stream velocity of 41.19 m/sec (80 knots).

The centerplane data were taken in two configurations. In the first configuration, the blades were rotating at 1200 rpm with an advance ratio of 0.219. In the second configuration, the blades were off and a scaled rotor hub was rotating at 600 rpm. The data taken off the centerplane were obtained with the rotating hub only. Typical data obtained during the test included flow-field velocity vectors and probability histograms of the u and v components of velocity. The histograms are plotted on-line using a graphics terminal to enable the operator to assess data quality and assist in setting thresholds in the high-speed burst counters.

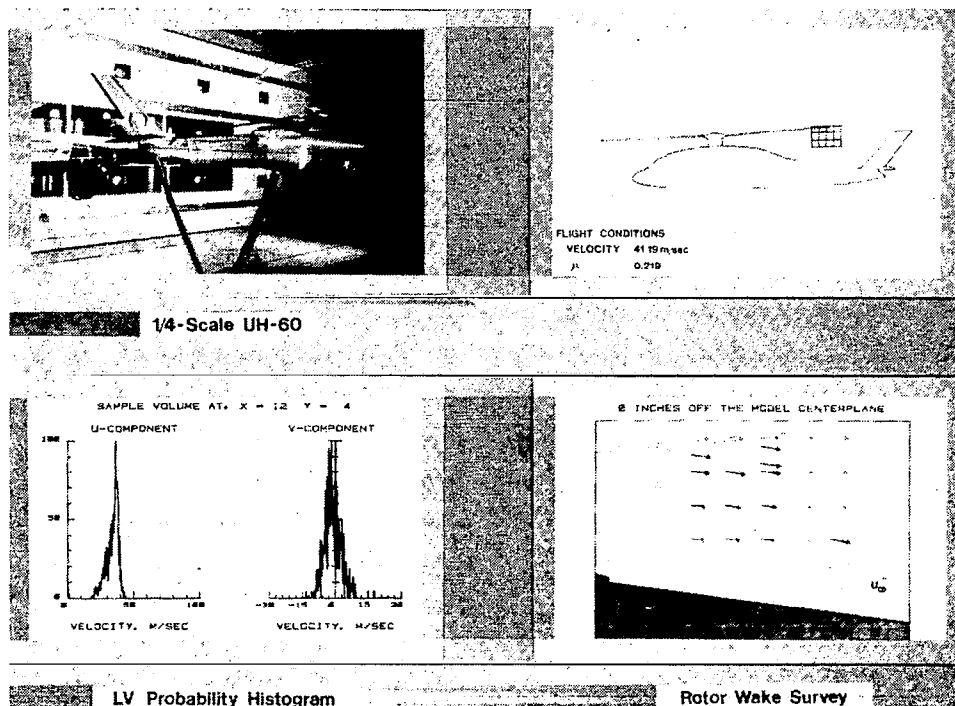


Figure 7

ROTOR WAKE SURVEY

Figure 8 shows a comparison between the flow field measured at the model centerplane with the blades on and off. The dashed arrows represent the velocity vectors measured with the blades off, and the solid arrows represent the velocity vectors obtained with the blades on. The sizes of the diamond and square symbols represent the turbulence intensity. The squares represent the blades on data, and the diamonds represent blades-off data. Reference symbols and vectors are included at the lower left to illustrate a free-stream velocity of 41.19 m/sec and 25 percent turbulence intensity.

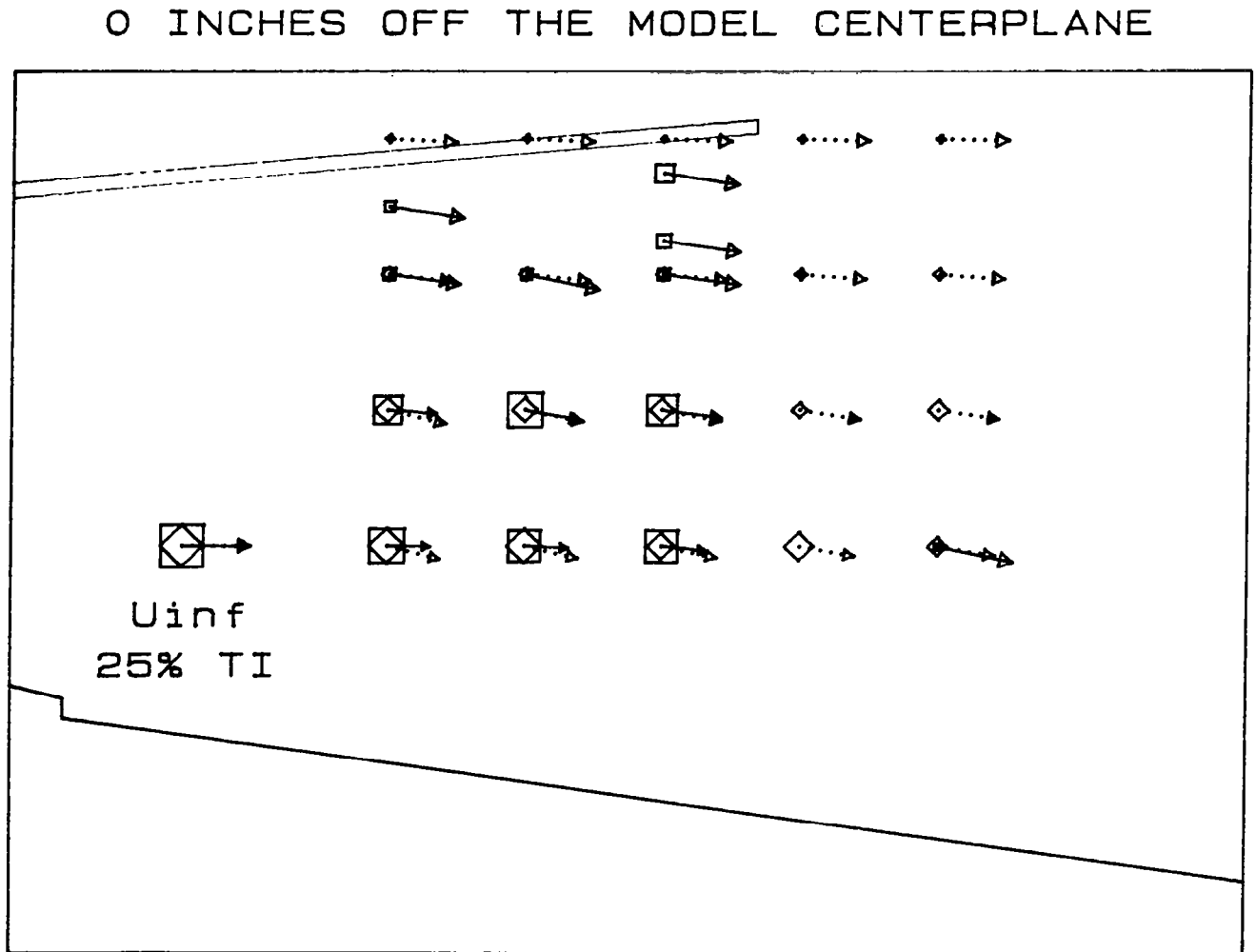


Figure 8

CONCLUSIONS

A dedicated LV system is operational at the Langley 4- by 7-Meter Tunnel facility. Improvements are needed to further enhance the operation, however. These include improved particle generation and enhancements to the LVABI.

The goal is to provide the facility with a nonintrusive velocity measurement capability around arbitrary shapes.

REFERENCES

1. Hoad, Danny R.; Meyers, James F.; Young, Warren M., Jr.; and Hepner, Timothy E.: Correlation of Laser Velocimeter Measurements With Results of Two Prediction Techniques. NASA TP-1168, 1978.
2. Young, Warren H., Jr.; Meyers, James F.; and Hoad, Danny R.: A Laser Velocimeter Flow Survey Above a Stalled Wing. NASA TP-1266, 1978.
3. Meyers, James F.; and Hoad, Danny R.: Turbulent Wake Measurements With Laser Velocimeter. AIAA Paper 79-1087, June 1979.

APPLICATION OF THE LASER DOPPLER VELOCIMETER
IN AERODYNAMIC FLOWS

William J. Yanta
Donald W. Ausherman

Naval Surface Weapons Center
Aerodynamics Branch, K24
White Oak
Silver Spring, Maryland 20920

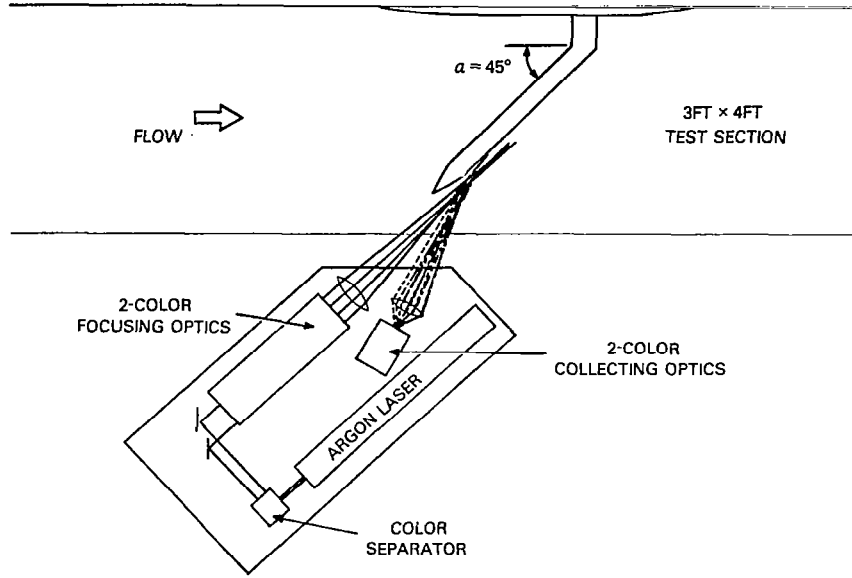
Measurements have been made of the flowfield around a tangent-ogive model in a low turbulent, incompressible flow at an incidence of 45° . The free-stream velocity was 80 ft/sec. The flowfield velocities in several cross-flow planes were measured with a 2-D, two-color LDV operated in a backscatter mode (Figure 1a). Measurements were concentrated in the secondary separation region. A typical survey is shown in Figure 1b. This survey was taken at a model location where the maximum side force occurs. This figure shows the overall character of the leeward flowfield with the influence of the two body vortices. S_a' and S_s' are attachment and separation points, respectively. Figures 1c and 1d show in more detail the characteristics of the secondary flow region. Details of the experiment are described in AIAA paper 82-0343, "The Secondary Separation Region on a Body at High Angles of Attack" by W. J. Yanta and A. B. Wardlaw, Jr. presented at AIAA 20th Aerospace Sciences Meeting, 11-14 January 1982/Orlando, Florida.

Measurements of the velocity and density flowfields in the shock-layer region of a reentry-vehicle indented nose configuration have been carried out at Mach 5. The velocity flowfield was measured with a 2-color, 2-D, forward-scatter LDV system shown schematically in Figure 2a. Because of the need to minimize particle lag in the shock-layer region, polystyrene particles with a mean diameter of 0.312 microns were used for the scattering particles. The model diameter was 6 inches. A typical LDV survey is shown in Figure 2b. It is seen that there is some particle lag in approximately the first 0.2 inches after which, the particles are in equilibrium with the flow. Separation and flow reversal are very obvious in the indented part of the nose shape thus verifying the existence of a separation region on this type of nose shape. Details of the experiment can be found in the paper "The Hypersonic Flowfield Over a Reentry Vehicle Indented Nose Configuration" by A. M. Morrison, W. J. Yanta, and R. L. P. Voisinet, AIAA paper 81-1060, presented at the AIAA Thermophysics Conference, 23-25 June 1981, Palo Alto, California.

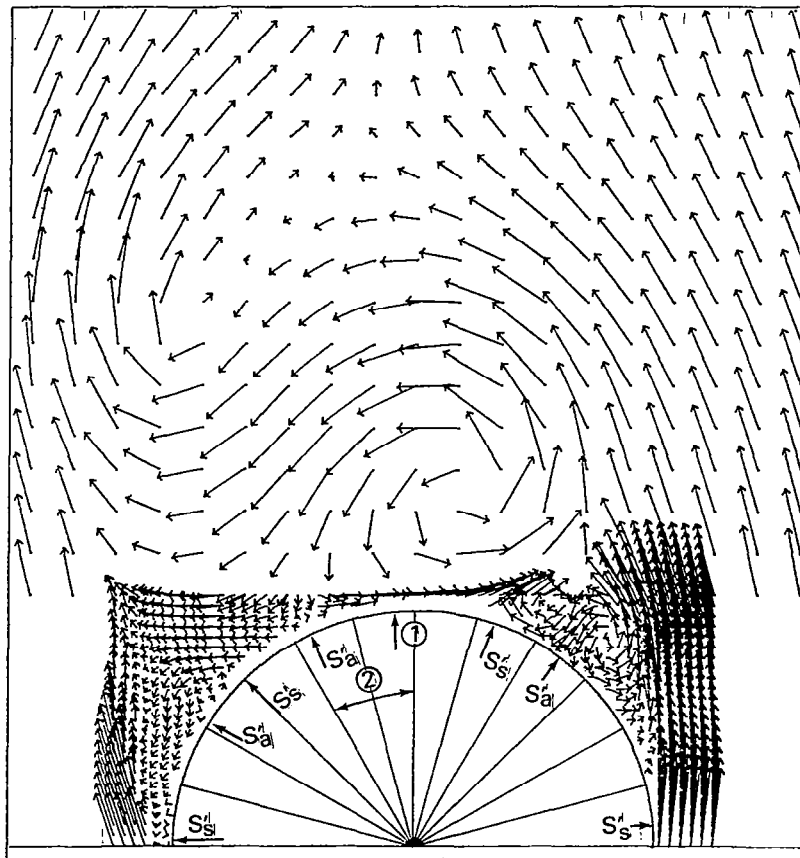
Three-dimensional velocity measurements were carried out in the boundary layer of a 7° -semivortex angle sharp cone for angles of attack of 0° , 2° , and 4° in NSWC Supersonic Tunnel 2 at a free-stream Reynolds number of $2.3 \times 10^6/\text{ft}$ ($7.5 \times 10^6/\text{m}$) and a Mach number of 3. The mean U, V, and W velocity components were measured for seven circumferential locations around the body at one axial station using a 3-D LDV system as shown in Figure 3a and described in Proceedings from the Seventh Biennial Symposium on Turbulence, "A 3-D Laser Doppler Velocimeter For Use In High Speed Flows," by W. J. Yanta and D. W. Ausherman, presented at the University of Missouri, Rolla, Missouri, September 1981. The system was capable of measuring the cross-flow velocity directly while still utilizing three nonorthogonal 1-D LDV components.

The development of the flow around the body at an angle of attack of 4° is shown in Figures 3b, 3c, and 3d for the U, V, and W velocity components, respectively. All velocities have been transformed into model coordinates so that U, V, and W are the velocity parallel to the model surface, velocity perpendicular to the model surface and the cross-flow velocity component, respectively. Also, all measurements have been nondimensionalized by the free-stream speed of sound. The V component is highly dependent on the circumferential position on the windward side of the model to about 135° but shows negligible change from 135° to 180° . The U velocity undergoes a larger change on the leeward side of the model. W appears to be proportional to $U \sin \phi$ from $\phi = 0^\circ$ to $\phi = 180^\circ$. A more complete description of the mean velocity data can be found in AIAA paper 82-0289, "Measurements of a Three-Dimensional

Boundary Layer on a Sharp Cone at Mach 3¹¹ by W. J. Yanta, D. W. Ausherman, and E. Hedlund, presented at the AIAA 20th Aerospace Sciences Meeting, 11-14 January 1982/Orlando, Florida.

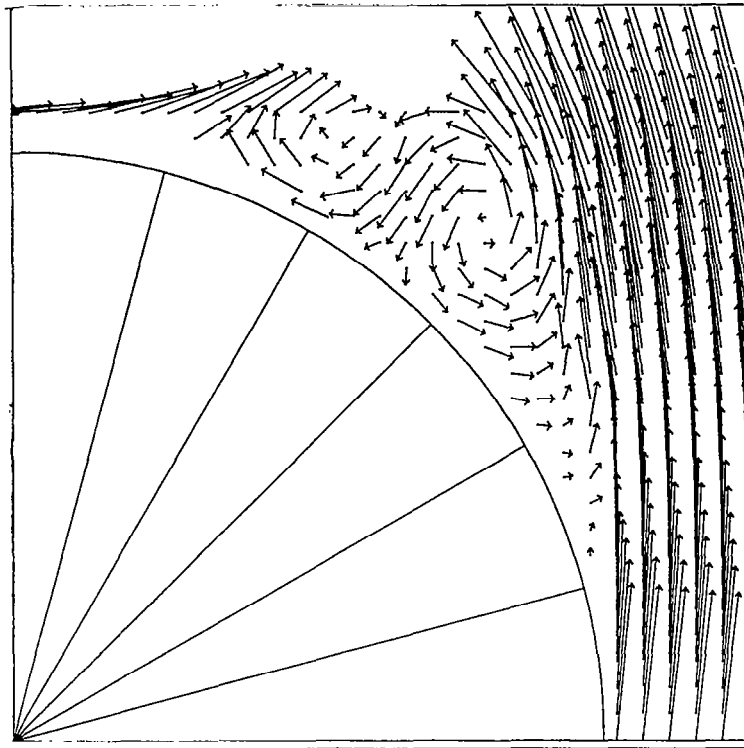


(a) 2-D backscatter LDV.

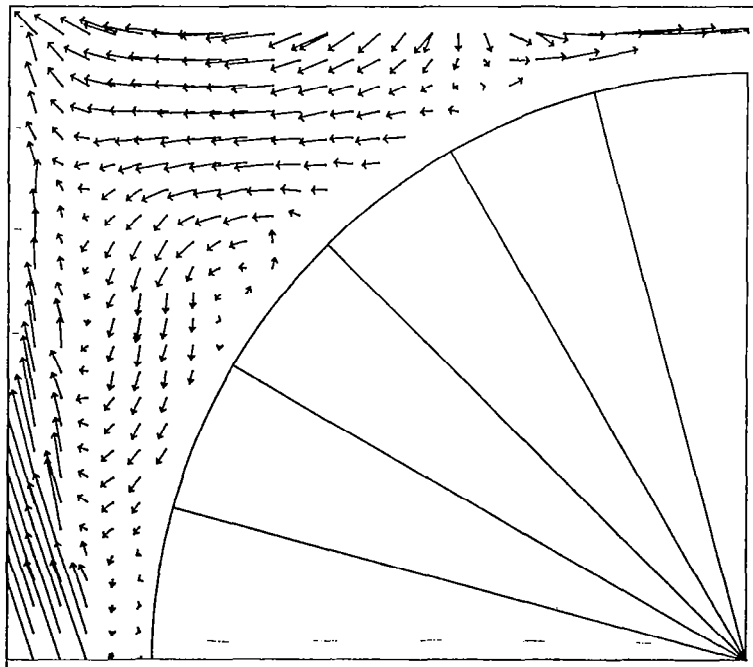


(b) Typical survey

Figure 1.- Measurements of flowfield velocities.

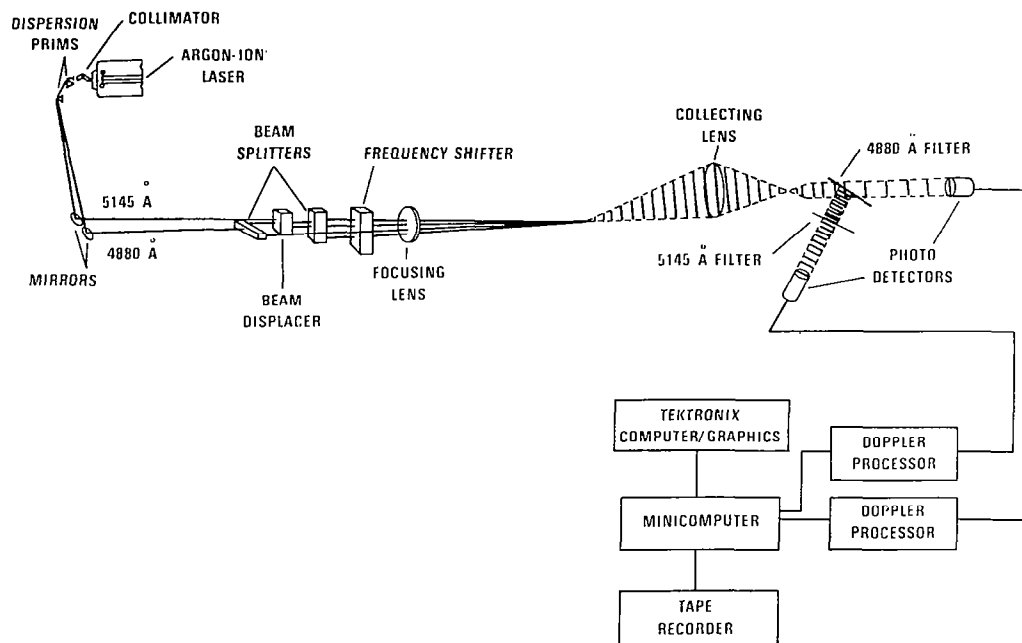


(c) Survey details, right side

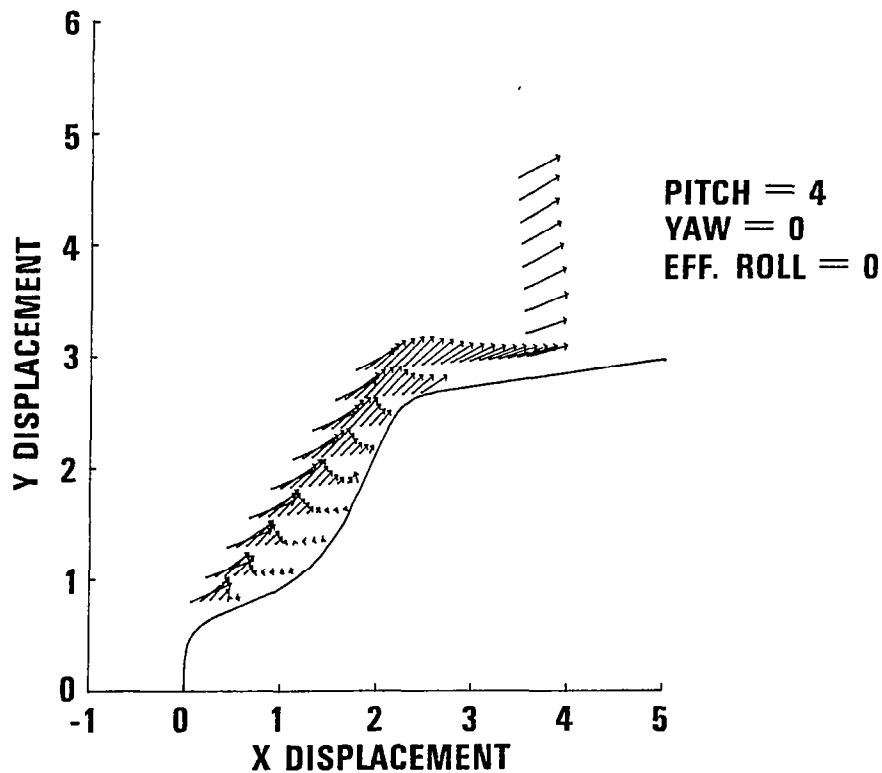


(d) Survey details, left side

Figure 1.- Concluded.

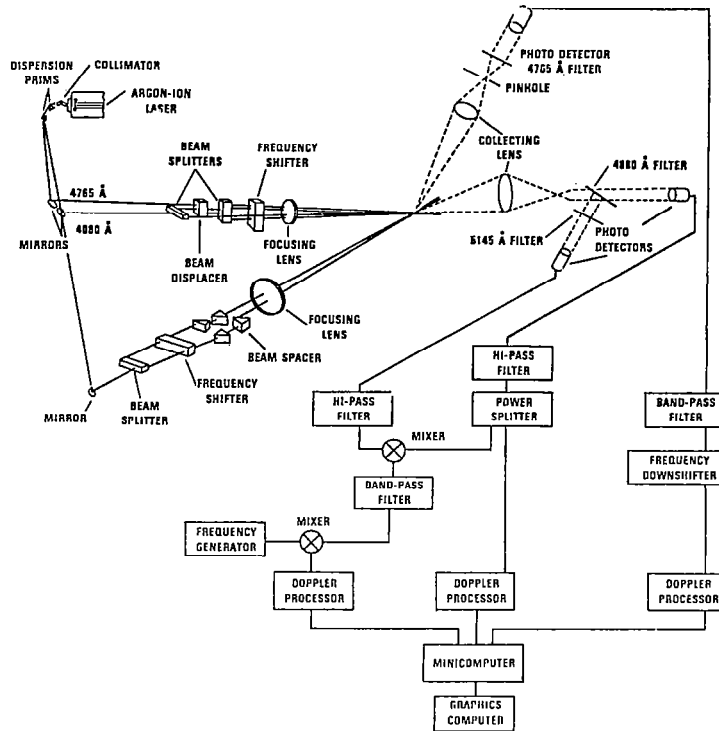


(a) Schematic of 2-D LDV

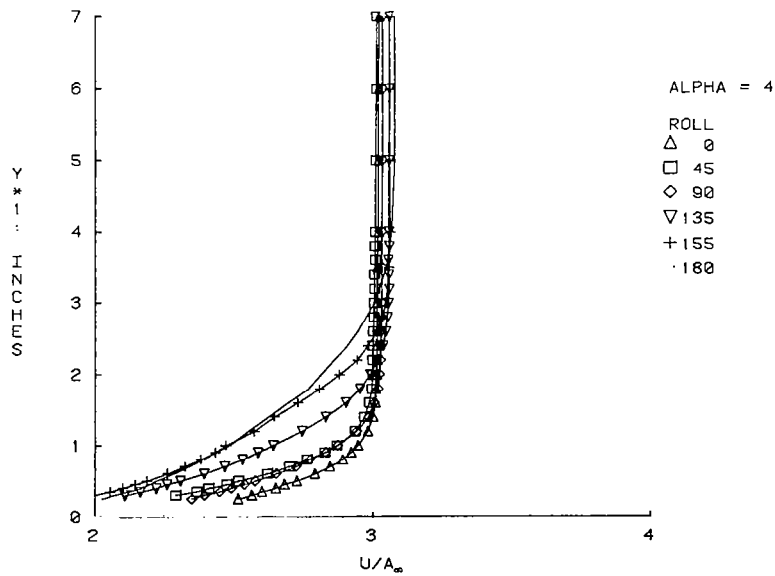


(b) Indented nose flowfield

Figure 2.- Measurements of velocity and density flowfields.

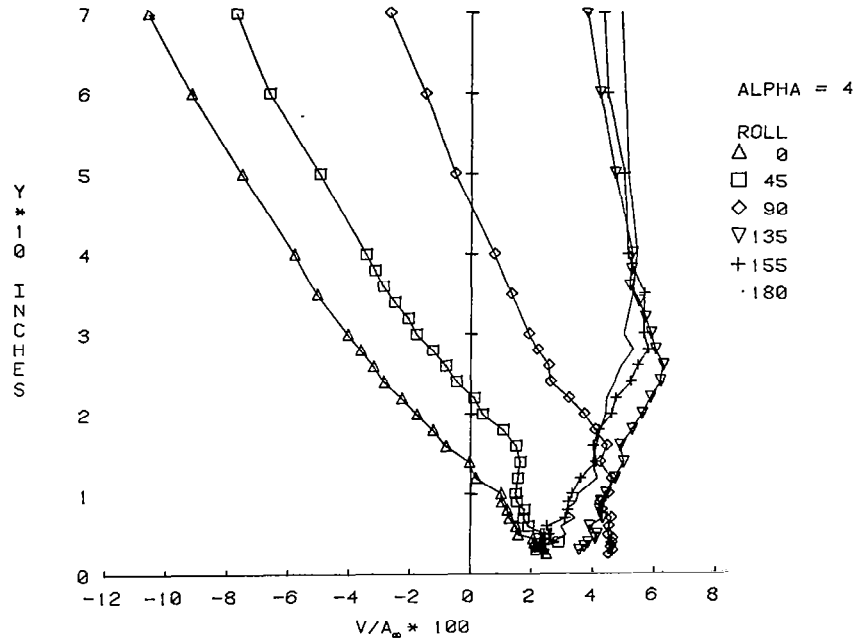


(a) 3-D LDV schematic

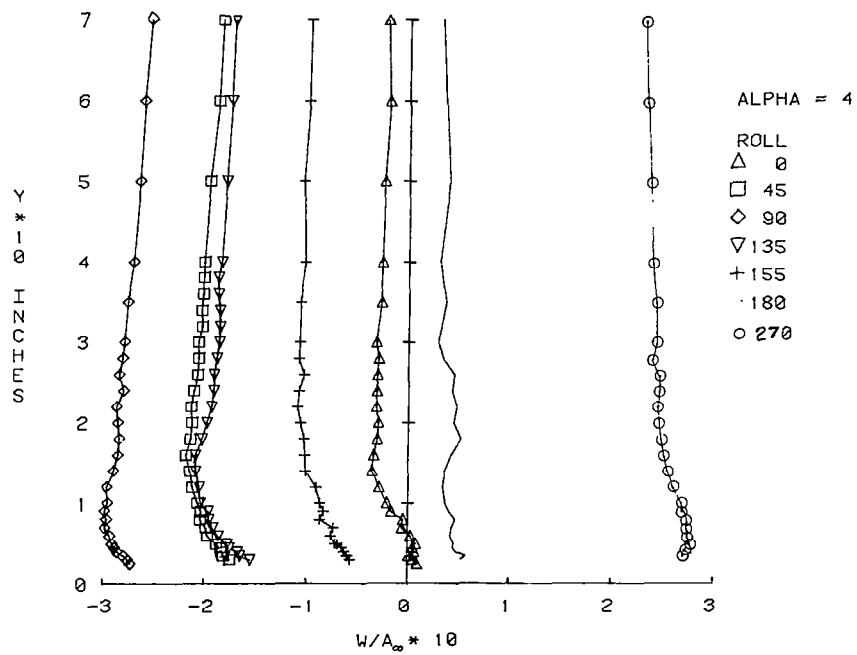


(b) U velocity component

Figure 3.- Three-dimensional velocity measurements.



(c) V velocity component



(d) W velocity component

Figure 3.- Concluded.

COMPARISON OF HOT WIRE/LASER VELOCIMETER TURBULENCE
INTENSITY MEASUREMENTS

J. F. Meyers and S. P. Wilkinson
NASA Langley Research Center
Hampton, Virginia

OBJECTIVE

Since the development of the laser velocimeter as a flow diagnostic tool in the early 1960's, researchers have thought of the laser velocimeter as a novel technique which could be used to measure the basic flow field characteristics in situations where classic probe techniques could not be used, were difficult to implement, or the results were suspect because of probe effects. Over the years a basic confidence level has been established in the use of the laser velocimeter to measure mean velocity. This confidence level does not exist, however, with the application of the laser velocimeter to measure turbulence intensity. The lack of confidence seems to have evolved from the question of whether a random measure of particle velocities yields a good statistical estimate of the stationary condition of the turbulence flow field. This question was further enhanced by the early attempts to compare the results from the laser velocimeter with a hot wire in which there always seemed to be an approximate 10-percent bias of the turbulence intensity measurements from the laser velocimeter, references 1 and 2. In an attempt to satisfy this question, the present comparative study was performed.

Great care was taken in the present study to insure that the instrument precision of both the laser velocimeter and hot wire was maximized. In this attempt to reduce the measurement uncertainties in the hot wire, direct digitization of the analog output signal was performed with point-by-point conversion to velocity through a spline fit calibration curve and the turbulence intensity function was calculated statistically. Frequent calibrations of the hot wire were performed using the laser velocimeter as the velocity standard to account for the presence of the small seed particles in the air flow and signal drift in the hot wire. A low velocity flow was also chosen because of the high confidence level in the hot wire measurements at low speeds. Measurement uncertainties in the laser velocimeter were reduced by using 0.35 - 0.55 micrometer polystyrene particles to remove the particle lag problem, forward-scatter was used to maximize signal-to-noise in the output signal, an off-axis receiver location was used to minimize the sample volume length, and velocity bias corrections were applied to the data along with calculating the time average quantities.

DEVELOP A BASE LEVEL OF CONFIDENCE IN LASER VELOCIMETRY TO MEASURE TURBULENCE INTENSITY

MINIMIZE ERRORS IN HOT WIRE MEASUREMENT

- Direct Digitization**
- Point-by-Point Velocity Conversion**
- Frequent Calibrations**
- Low Velocity Flow**
- Calibrate with Particles**

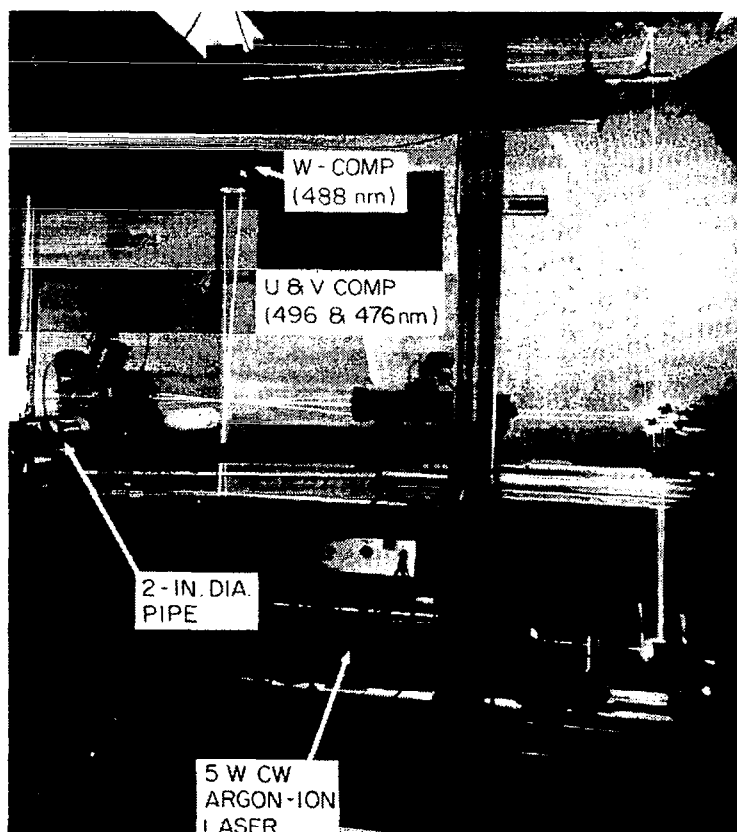
MINIMIZE ERRORS IN LV MEASUREMENT

- Small Particles**
- Forward Scatter**
- Off-Axis Receiver**
- Velocity Bias Correction**
- Time Average**

LASER VELOCIMETER SYSTEM

The laser velocimeter (LV) was an orthogonal three component fringe type system used in an off-axis, forward scatter mode. For the purposes of the present study, only one component was used to compare with the results from the hot wire. A Bragg cell was not used in the LV in order to maintain compatibility with the hot wire, since the hot wire is not sensitive to flow reversal. A 5.0 W Argon-ion laser was used as the light source with the 496.5 nm output line being selected. The output power at 496.5 nm was set to 0.2 W. The focal length was 0.38 m and the cross beam angle was 7.52 degrees, which yielded a fringe spacing of 3.78 micrometers with a sample volume diameter of 160 micrometers. The collecting optics were rotated 37 degrees off of the optical centerline in the plane of the laser beams, which reduced the sample volume length (measured to the points where the collected scattered light intensity value was $1/e^2$ of the peak) to 0.62 mm. The receiving optical system had a focal length of 0.38 m with a 7.5 cm clear aperture. The collected light was converted to electrical energy using a photomultiplier with a quantum efficiency of 0.21. This configuration yielded signal levels of approximately 0.2 V, peak-to-peak, from 0.35 - 0.55 micrometer polystyrene particles.

The output signals from the photomultiplier were processed by a high-speed burst counter which contained a double threshold triggering circuit and a 5/8 count comparison error detection circuit set to 2 percent. The digital output from the counter was input to a high-speed buffer memory, references 3 and 4, which will accept up to 4096 velocity measurements, and the associated measured interarrival times. The data contained within this buffer system was then transferred to a 16-bit minicomputer for data processing and analysis.

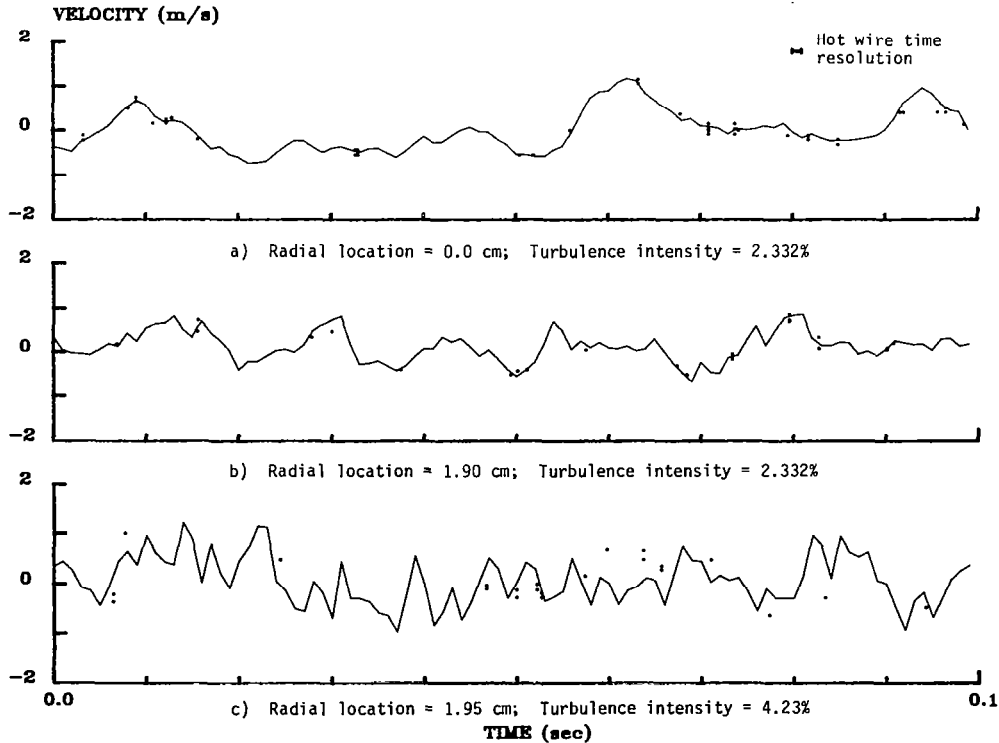


LV/HOT WIRE TIME HISTORY — CAL RIG

In the present study, two free turbulent flows were tested: the exit flow from the convergent nozzle (calibration facility), and the exit flow from a fully developed turbulent pipe. The convergent nozzle was fan driven with velocity controllable over a range of 0 m/s to 30 m/s by a gate valve located at the fan exit. The nozzle settling chamber contained a honeycomb and screens with an 8:1 convergent, 4.0-cm diameter output nozzle.

The seeding particles used by the laser velocimeter were 0.35 - 0.55 micrometer polystyrene particles suspended in a water-alcohol solution. This solution was atomized using an air jet atomizer whose output was directed into the fan inlet of the convergent nozzle and into the settling chamber of the pipe. The water and alcohol evaporated leaving the particles to follow the air flow. Since the resulting signals from the LV were nominally the same voltage level, it was concluded that agglomeration was not a problem.

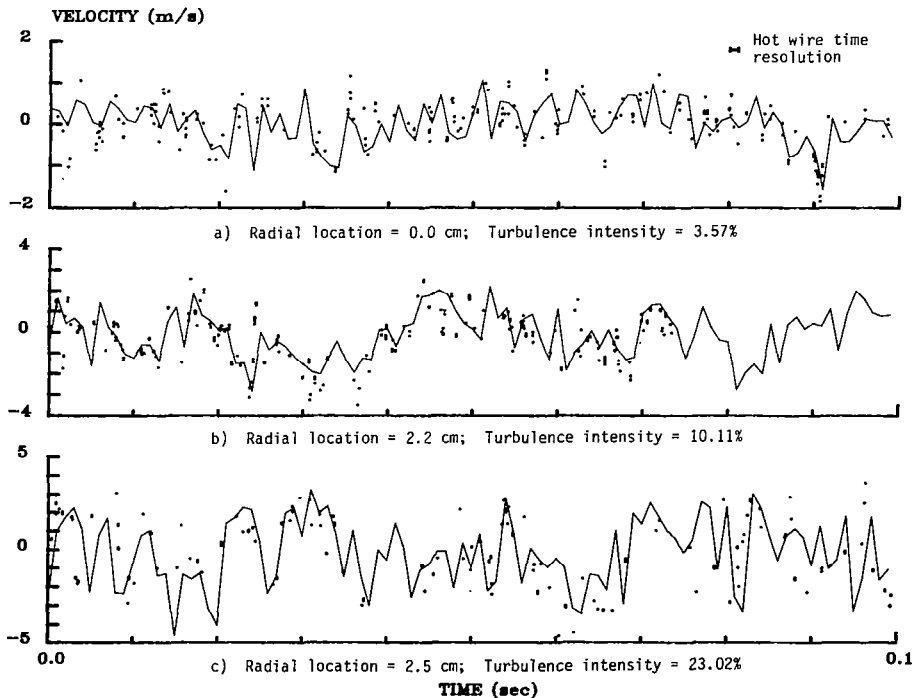
The effect of the seeded flow on the hot wire response was first examined by comparing the instantaneous hot wire and LV output. This was done by comparing the hot wire output obtained with the digital oscilloscope with the measured particle velocities from the LV. The hot wire (continuous trace) and the laser velocimeter (each dot is a single particle velocity) velocity time histories in the convergent nozzle jet flow are shown in the figure. Since the LV sample volume and the hot wire were axially displaced by 2 mm and since the LV yields instantaneous point measurements within the sample volume whereas the hot wire yields instantaneous spatial averages over the length of the wire, it would not be expected that the two signal traces would be identical. Referring, however, to the figure, it is seen that the two signals follow each other well and there is no evident erratic hot wire response due to particle impingement.



LV/HOT WIRE TIME HISTORY — PIPE

The pipe flow was driven from nominal 80 psi shop air via an adjustable regulator and a 1.25 cm diameter tube. The air from this tube expanded into a 1.35 m long, 5.0 cm diameter pipe which expanded again into a 38 cm long, 15.0 cm diameter settling chamber which contained a honeycomb and screens. The flow then contracted back into a 5.0 cm diameter pipe and exited into the atmosphere 6.60 m downstream. The pipe flow temperature was within 2 degrees Fahrenheit of the calibration facility temperature. Typical velocity time histories from the hot wire (continuous trace) and the laser velocimeter (each dot is a single particle velocity) obtained in the exit flow from the fully developed turbulent pipe are shown in the figure. Any significant deviation between the two measurements is due to the relatively low time resolution of 0.001 second of the hot wire due to the sample rate of the oscilloscope whereas the LV time resolution is one microsecond.

To examine the effect of the combined particle/water-alcohol mixture on hot wire response, the hot wire output was recorded with the air flow on, with and without the particle mixture in both the calibration facility and the pipe. In both cases the mass flow addition due to the seeding mixture was less than 1-percent of the total mass flow. In the calibration facility, switching the mixture on and off had no effect on the mean hot wire output. In the pipe, however, an apparent 3-percent increase in the mean output was noted, although no change was noted in the measure of turbulence intensity. This discrepancy is due to the fact that the calibration facility recirculated the surrounding particle-laden air. In the pipe, however, the source air was particle free and originated from a source away from the experiment. Two conclusions can be drawn from these results: first, while the seeded flow does not appear to influence the dynamic response of the hot wire, the overall level of the signal is influenced by a slight amount due to the slightly altered thermal properties of the seeded flow; and secondly, when the calibration and subsequent measurements were both carried out in the seeded flow, the level shift is effectively cancelled out.



VELOCITY MEASUREMENTS FOR AXIAL SCAN OF CAL RIG

The mean velocity measurements from the laser velocimeter for an axial scan along the 75-percent radial line in the calibration facility are shown in the top figure. The results indicate a smooth decay of the mean velocity as the axial distance is increased. This data was then corrected for velocity bias, reference 5, using the following equation:

$$\bar{U}_b = \frac{\sum A_i U_i}{\sum A_i} \quad \text{where } A_i = \frac{1}{U_i}$$

and compared with the uncorrected data, i.e., $C_m = \frac{\bar{U}_b - \bar{U}}{\bar{U}}$

The results of this comparison are shown in the lower figure. Since the times between velocity measurements were measured, a time average of the laser velocimeter data could be made:

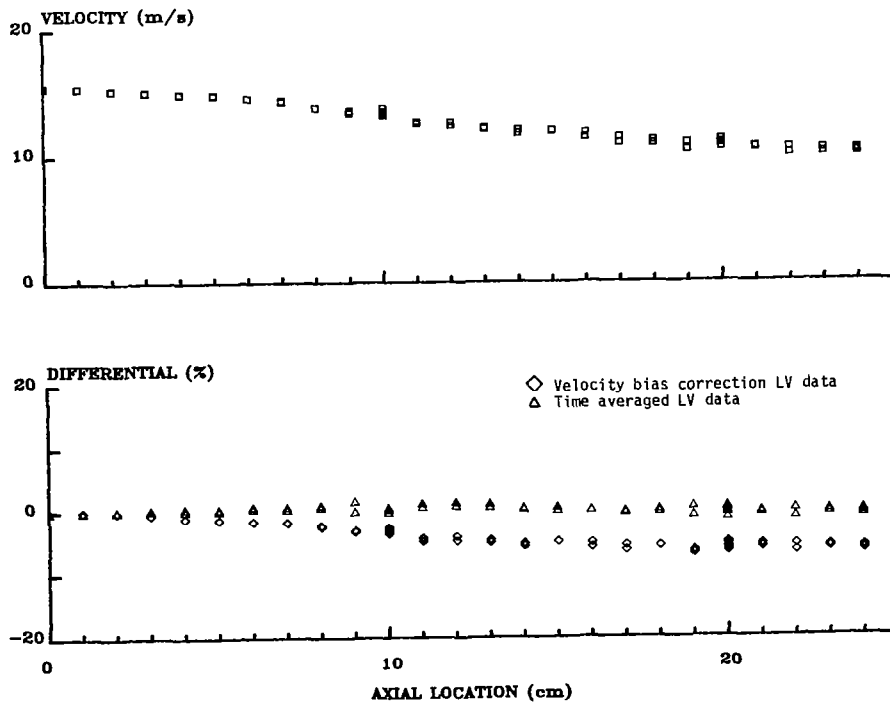
$$\bar{U}_t = \frac{\sum B_i \Delta t_i}{\sum \Delta t_i} \quad \text{where } B_i = \frac{(U_i + U_{i-1})}{2}$$

Δt_i = time between the i th velocity measurement and the $i-1$ th velocity measurement.

A comparison of these results with the uncorrected data, i.e.,

$$C_m = \frac{\bar{U}_t - \bar{U}}{\bar{U}}$$

is shown in the lower figure.

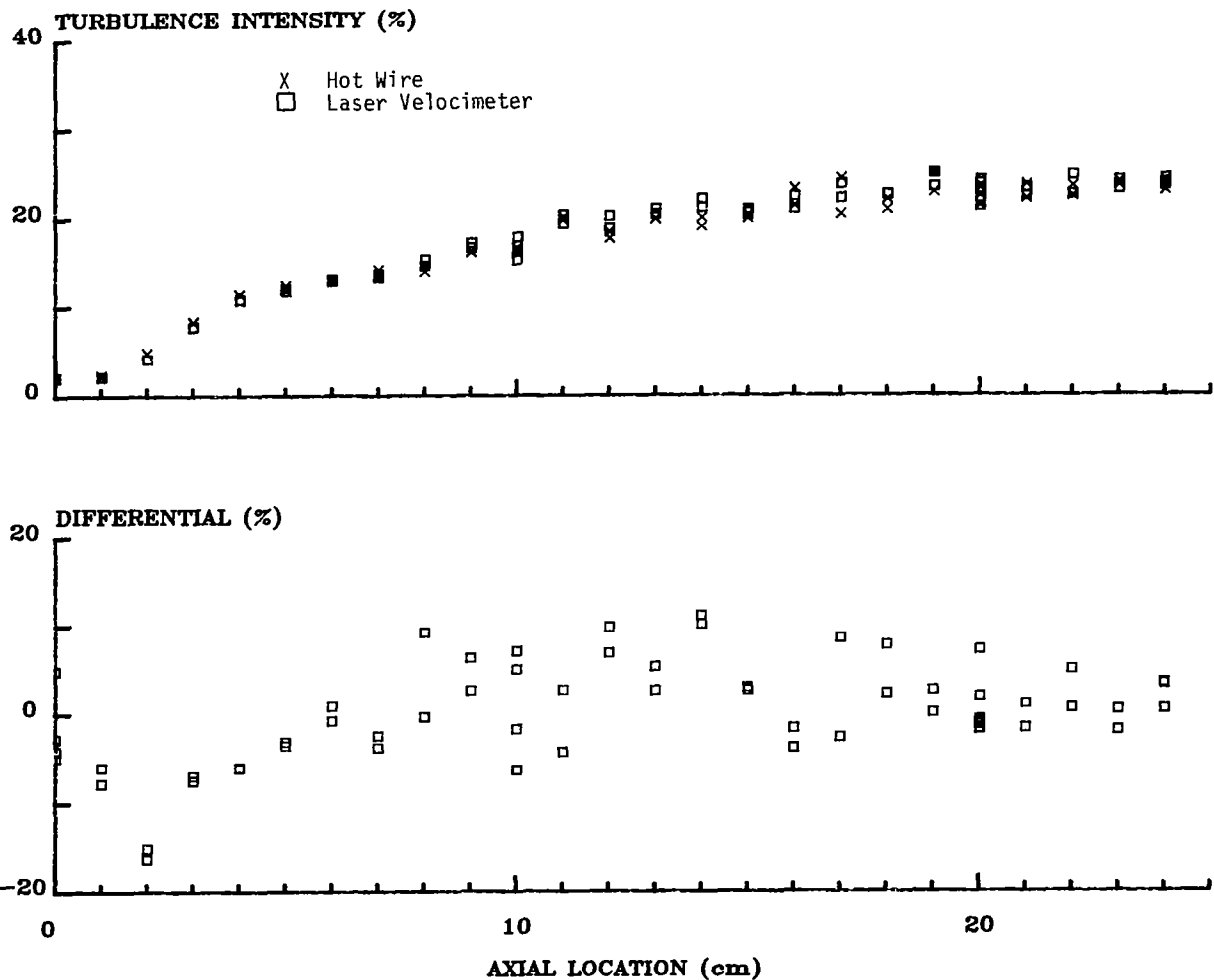


TURBULENCE INTENSITY FOR AXIAL SCAN OF CAL RIG — COMPARISON OF HOT WIRE/LV DATA

The turbulence intensity measurements from the hot wire and the laser velocimeter for an axial scan along the 75-percent radial line in the calibration facility are shown in the top figure. The results show a turbulence intensity of about 2 percent within the potential core, which begins to break down between 1 and 2 cm downstream. A large turbulence intensity gradient exists until approximately 5 cm downstream where the mixing region is entered. Due to the large gradient in turbulence intensity, the axial spacing of 2 mm between the hot wire and the laser velocimeter will cause the measurements from the laser velocimeter to be lower than the measurements from the hot wire since the hot wire is further downstream. With the exception of the data obtained in the large turbulence intensity gradient region, the comparison of the data from the hot wire with the data from the laser velocimeter, i.e.,

$$C_{ti} = \frac{TI_{lv} - TI_{hw}}{TI_{hw}}$$

yields a bias of 1.7 percent with the laser velocimeter measuring high with a standard deviation of 4.3 percent (lower figure).



TURBULENCE INTENSITY FOR AXIAL SCAN OF CAL RIG — COMPARISON
OF HOT WIRE/BIAS CORRECTED LV DATA

The turbulence intensity measurements from the hot wire and velocity bias corrected laser velocimeter data for an axial scan along the 75-percent radial line in the calibration facility are shown in the top figure. The velocity bias correction was made to the data by computing the standard deviation with the following equation:

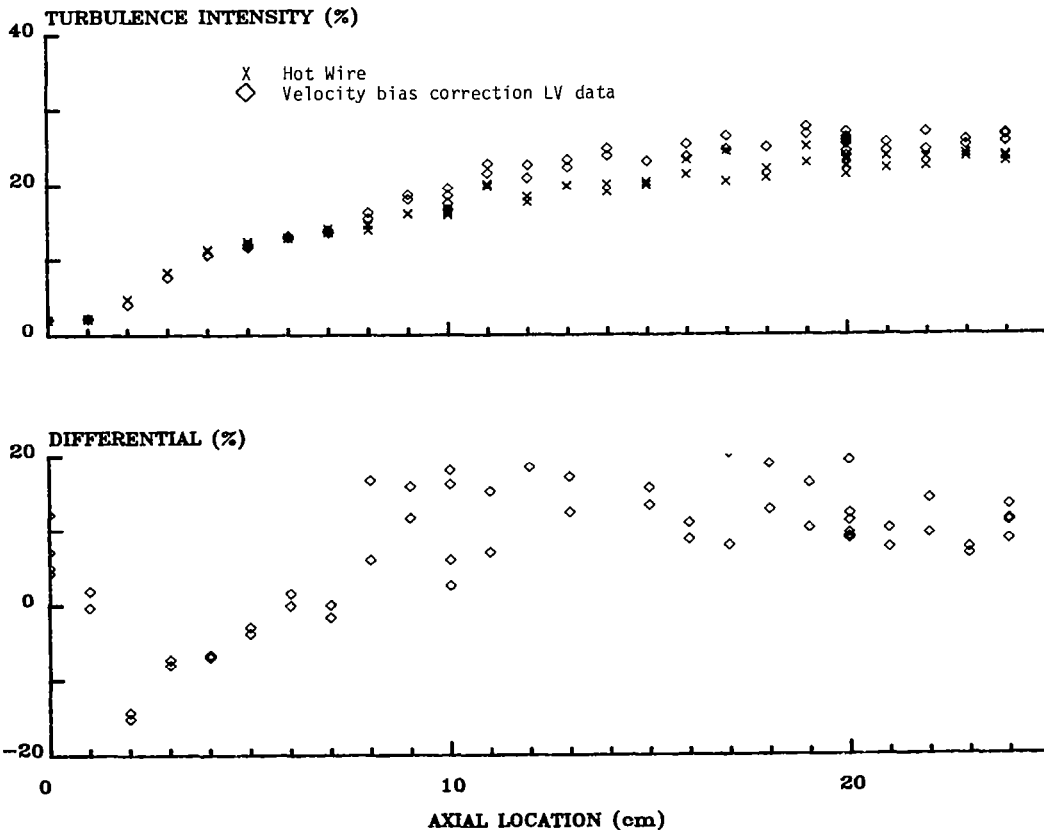
$$\sigma_b = \sqrt{\frac{\sum A_i (U_i - \bar{U}_b)^2}{\sum A_i}}$$

where $A_i = \frac{1}{U_i}$ and $\bar{U}_b =$ velocity bias corrected mean

and dividing the result by the velocity bias corrected mean to obtain turbulence intensity. With the exception of the data obtained in the large turbulence intensity gradient region, discussed previously, the comparison of the data from the hot wire with the velocity bias corrected data from the laser velocimeter, i.e.,

$$C_{ti,b} = \frac{TI_{lv,b} - TI_{hw}}{TI_{hw}}$$

yields a bias of 11.1 percent with the laser velocimeter measuring high with a standard deviation of 6.7 percent (lower figure).



TURBULENCE INTENSITY FOR AXIAL SCAN OF CAL RIG — COMPARISON
OF HOT WIRE/TIME AVERAGED LV DATA

The turbulence intensity measurements from the hot wire and time averaged laser velocimeter data for an axial scan along the 75-percent radial line in the calibration facility are shown in the top figure. The time average was made to the data by computing the standard deviation with the following equation:

$$\sigma_t = \sqrt{\frac{\sum (B_i - \bar{U}_t)^2 \Delta t_i}{\sum \Delta t_i}}$$

where $B_i = \frac{(U_i - U_{i-1})}{2}$

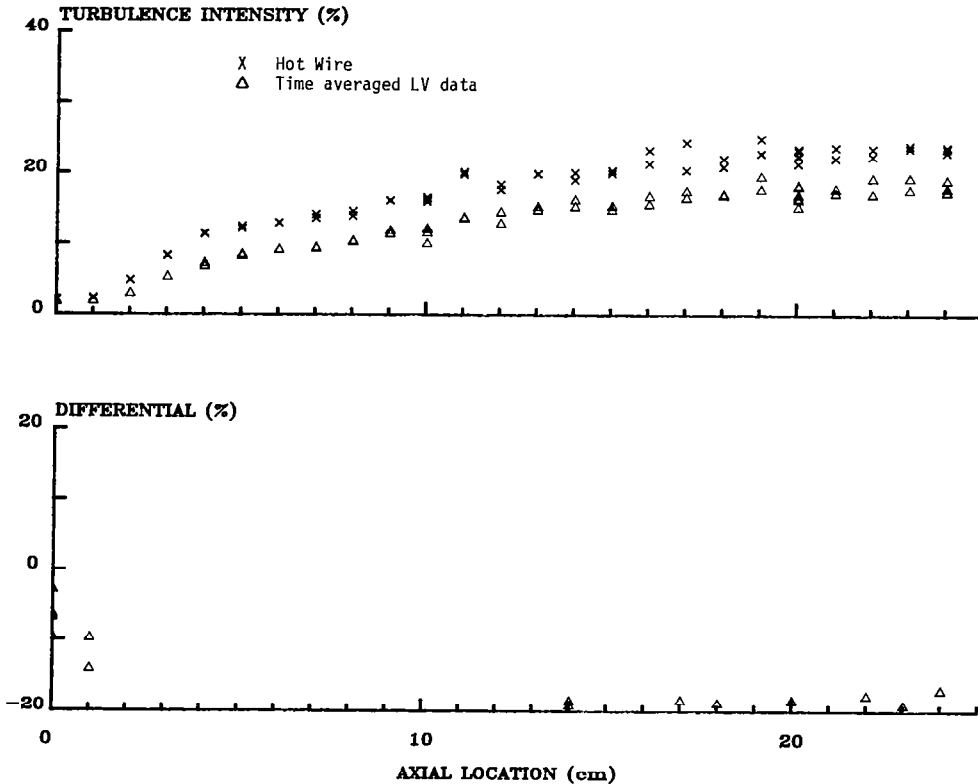
\bar{U}_t = time averaged mean velocity

Δt_i = time between the i th measurement and the $i-1$ th measurement

and dividing the result by the time averaged mean velocity to obtain turbulence intensity. With the exception of the data obtained in the large turbulence intensity gradient region, discussed previously, the comparison of the data from the hot wire with the time averaged data from the laser velocimeter, i.e.,

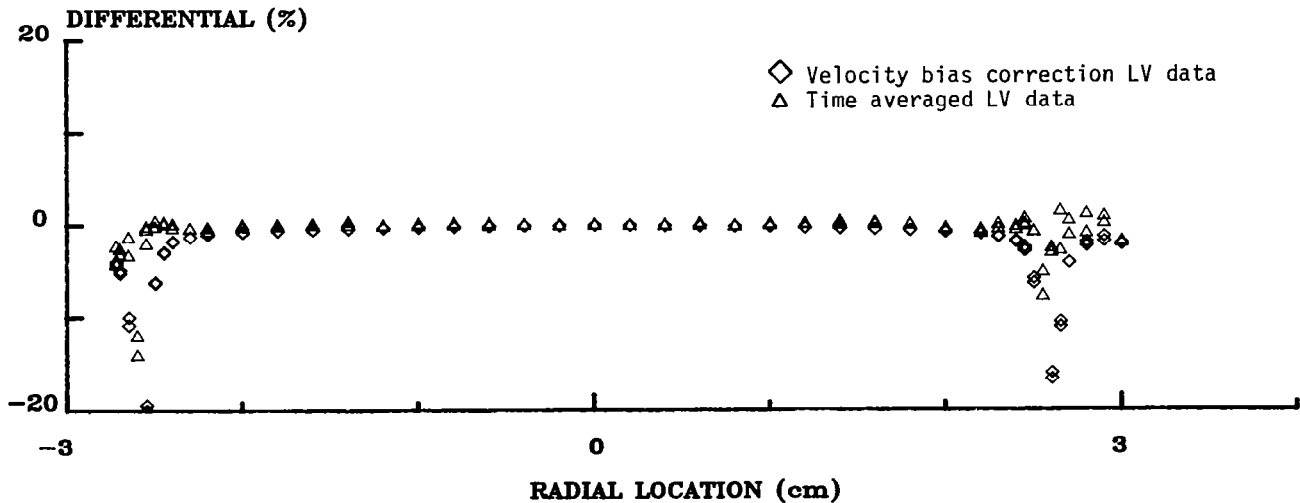
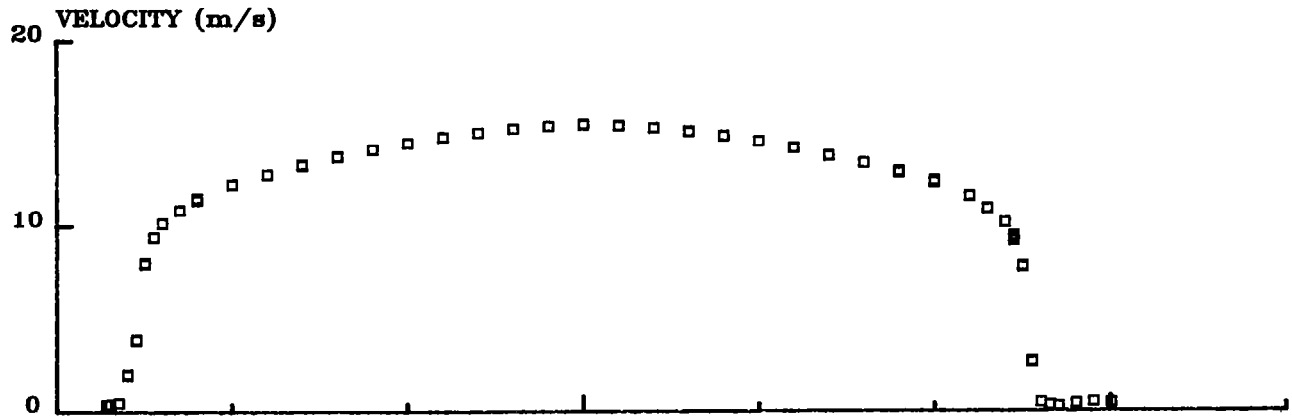
$$C_{ti,t} = \frac{TI_{lv,t} - TI_{hw}}{TI_{hw}}$$

yields a bias error of 25.0 percent with the laser velocimeter measuring low with a standard deviation of 4.5 percent (lower figure).



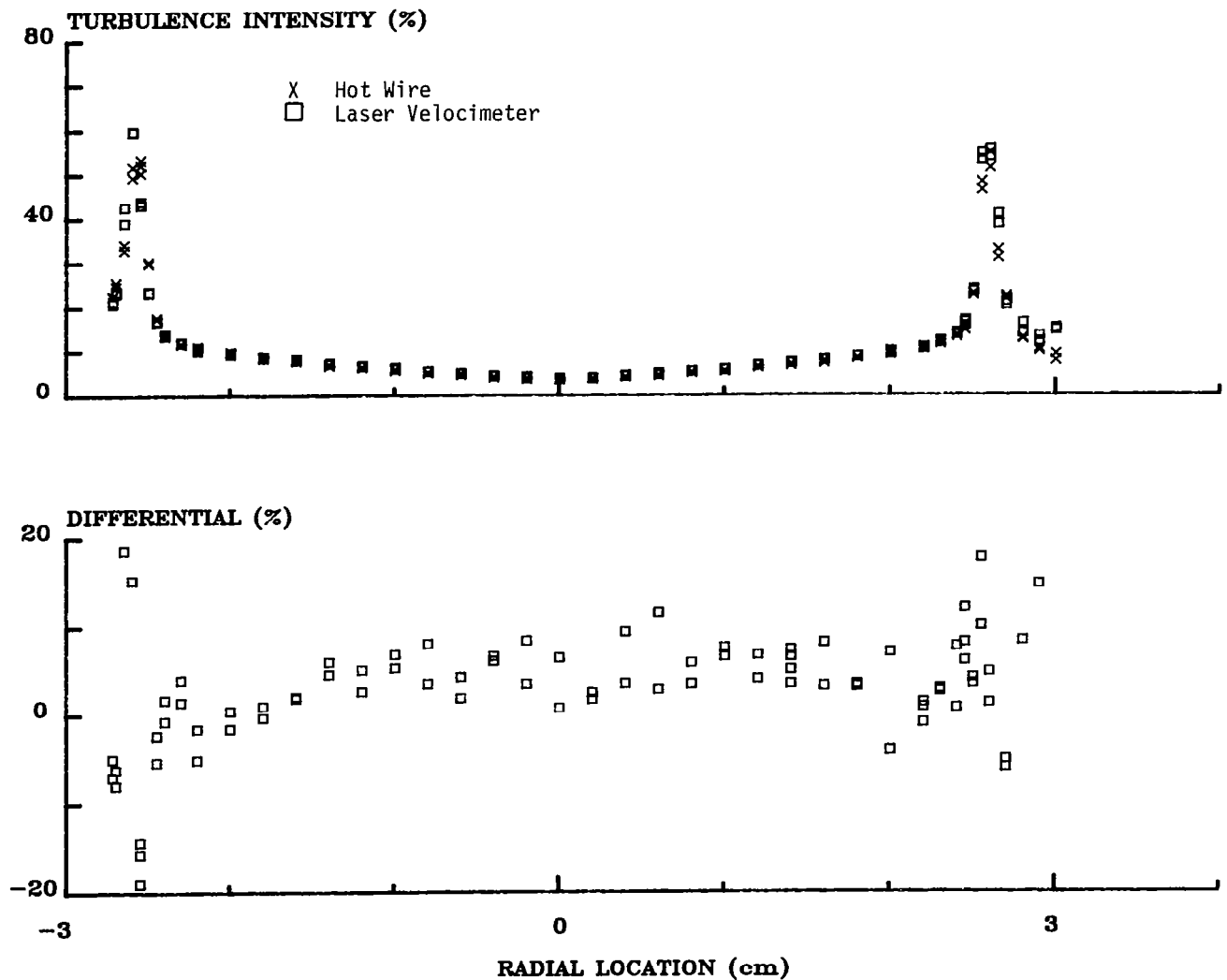
VELOCITY MEASUREMENTS FOR RADIAL SCAN OF PIPE (EXIT)

The mean velocity measurements from the laser velocimeter for a radial scan at the exit of the fully developed turbulent pipe are shown in the top figure. Velocity bias corrected data and time averaged data are compared to the uncorrected data in the lower figure.



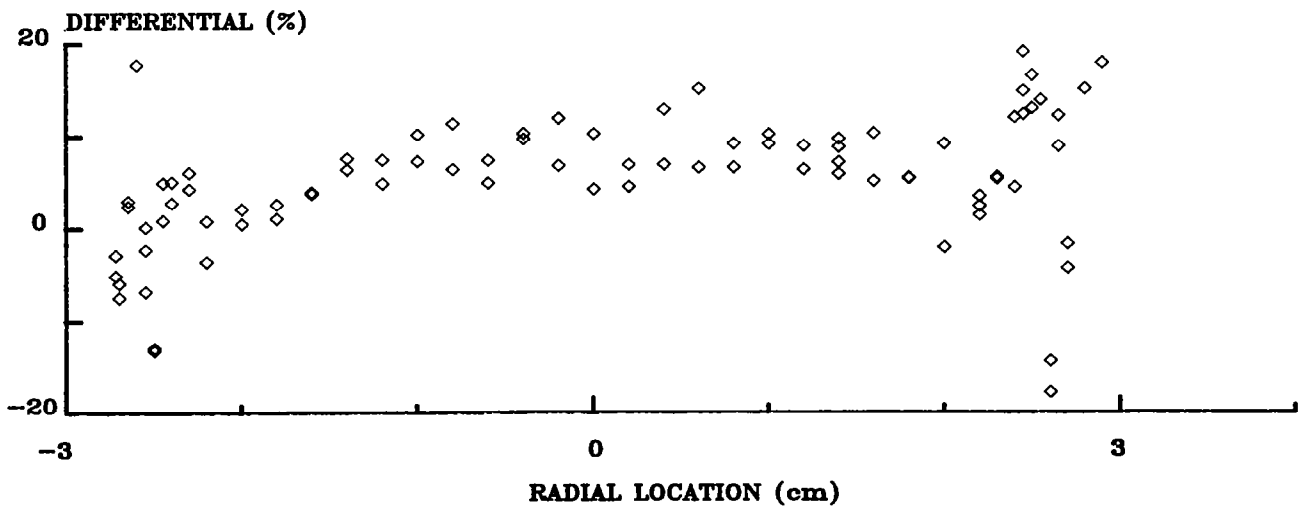
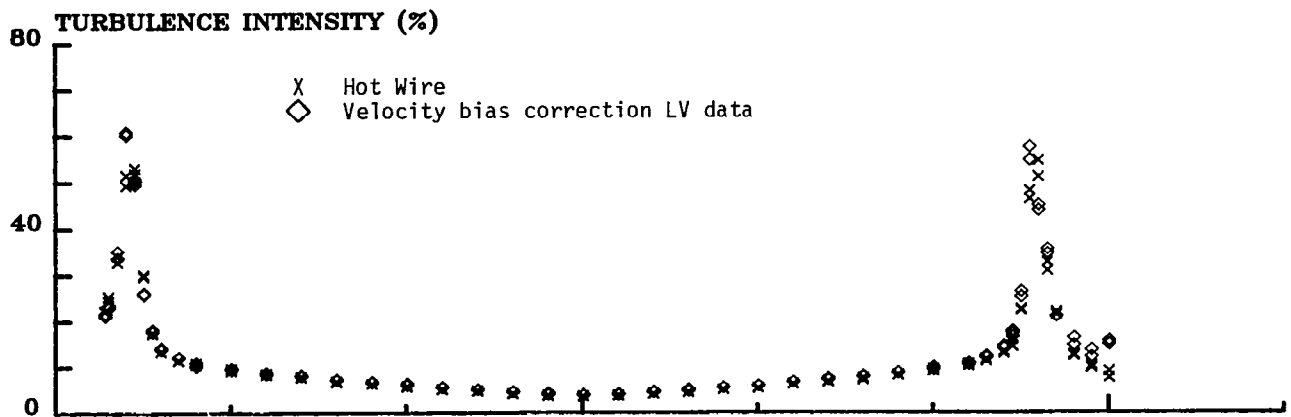
TURBULENCE INTENSITY FOR RADIAL SCAN OF PIPE (EXIT) — COMPARISON
OF HOT WIRE/LV DATA

The turbulence intensity measurements from the hot wire and the laser velocimeter for a radial scan at the exit of the fully developed turbulent pipe are shown in the top figure. With the exception of the data obtained in the free shear region (radial locations greater than 2.5 cm), the comparison of the data from the hot wire with the data from the laser velocimeter (lower figure) yields a bias of 3.5 percent with the laser velocimeter measuring high and a measurement standard deviation of 3.6 percent. The turbulence intensity measurements within the free shear regions yielded results of up to 75-percent turbulence intensity by both instruments; however their agreement is not as good. This may be accounted for by several reasons: 1) the 2 mm axial spacing between the two probe volumes causing the instruments to measure different parts of the flow; 2) the averaging effect of the hot wire along its length, not present in the LV; 3) the increase in flow angle causing the hot wire approximations of being a one-component measurement device to no longer be accurate; and 4) seeding density gradients along the LV sample volume caused by the entrainment of cleaner ambient air causing the measurements to be inaccurate because of a biased sampling of the flow field.



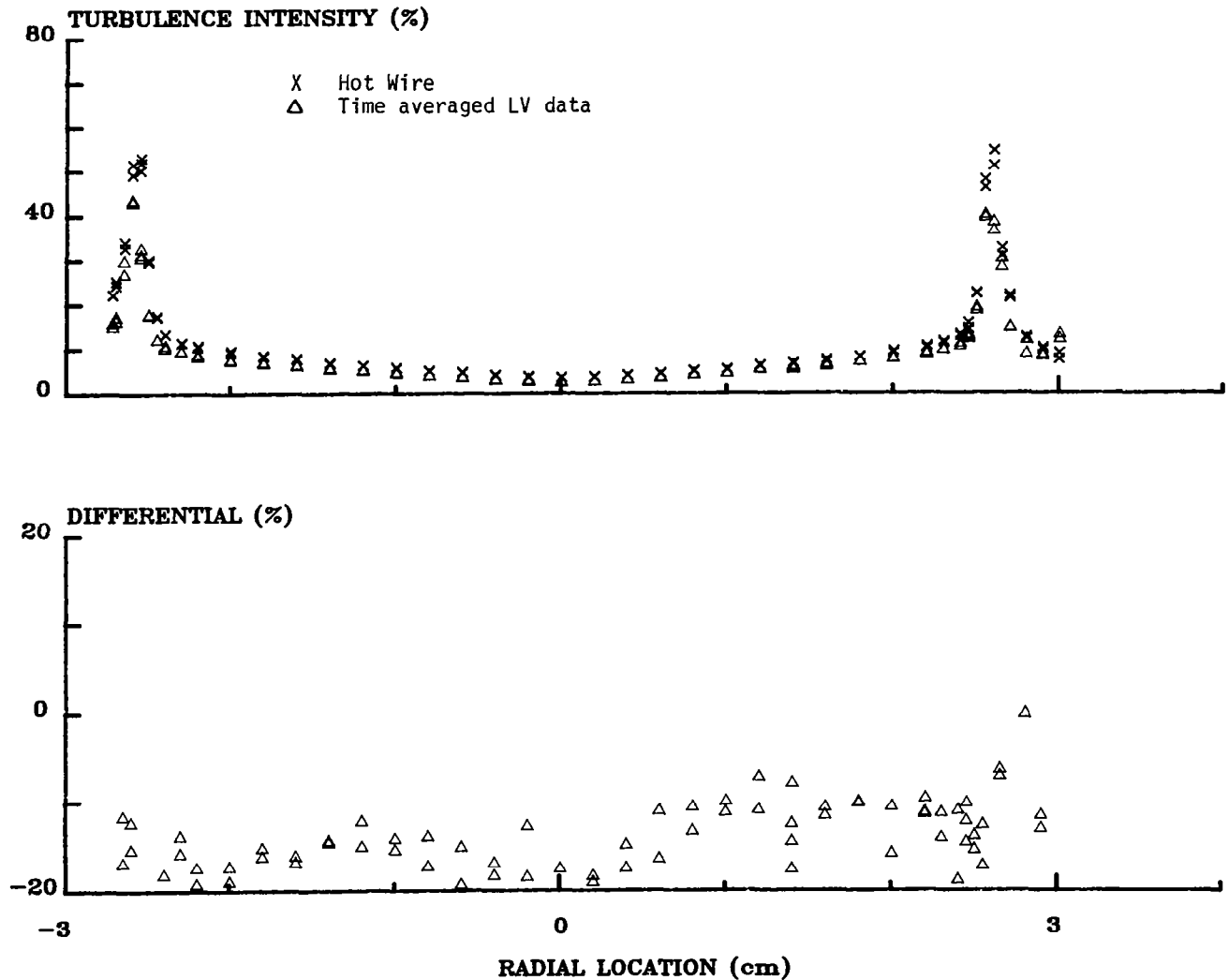
TURBULENCE INTENSITY FOR RADIAL SCAN OF PIPE (EXIT) - COMPARISON
OF HOT WIRE/BIAS CORRECTION LV DATA

The turbulence intensity measurements from the hot wire and velocity bias corrected laser velocimeter data for a radial scan at the exit of the fully developed turbulent pipe are shown in the top figure. With the exception of the data obtained in the free shear region (radial locations greater than 2.5 cm), the comparison of the data from the hot wire with the data from the laser velocimeter (lower figure) yields a bias of 6.8 percent with the laser velocimeter measuring high and a measurement standard deviation of 4.3 percent.



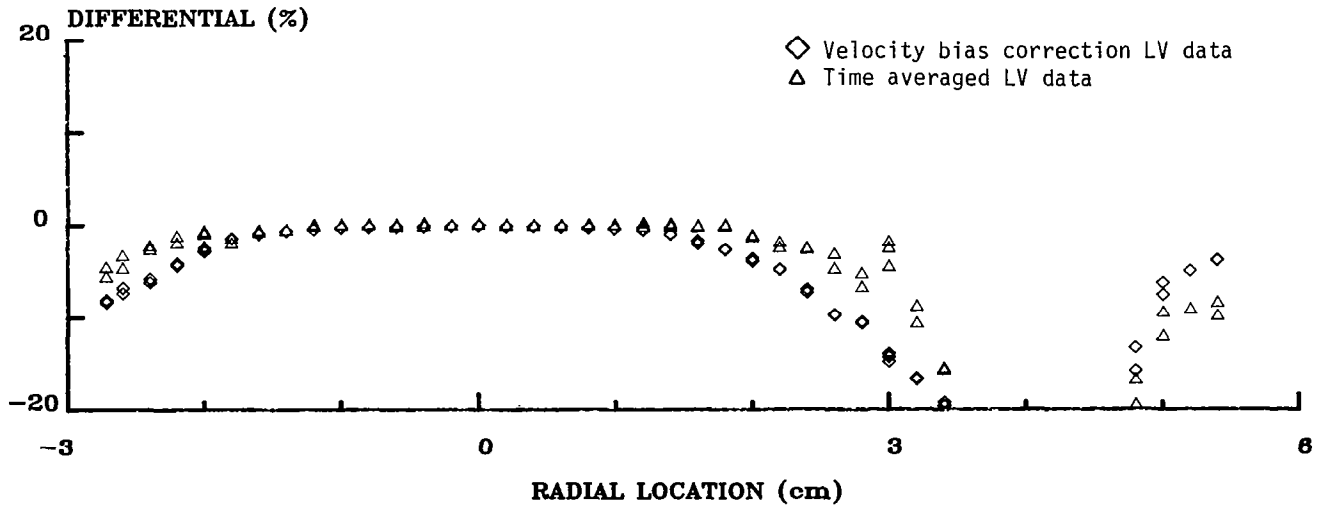
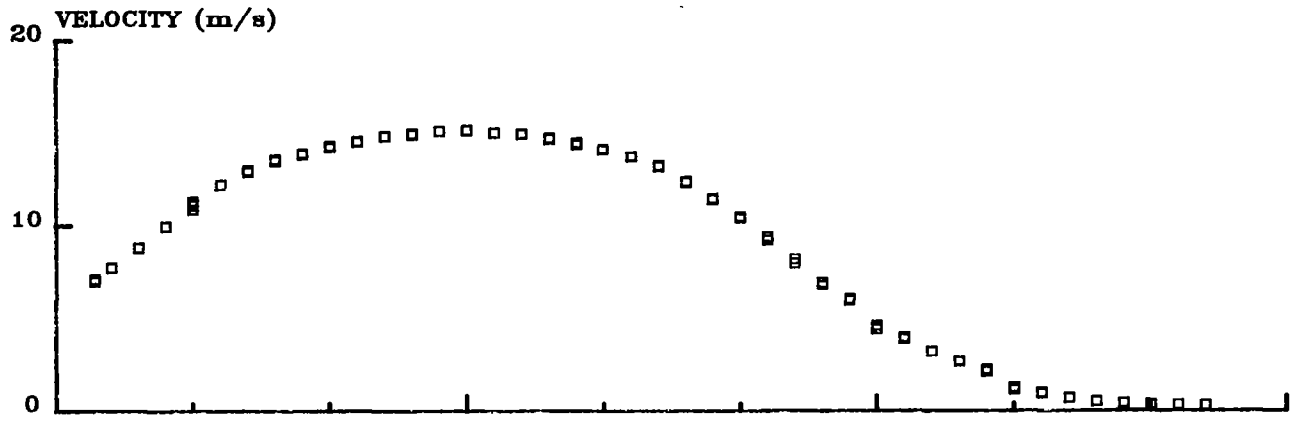
TURBULENCE INTENSITY FOR RADIAL SCAN OF PIPE (EXIT) — COMPARISON
OF HOT WIRE/TIME AVERAGED LV DATA

The turbulence intensity measurements from the hot wire and time averaged laser velocimeter data for a radial scan at the exit of the fully developed turbulent pipe are shown in the top figure. With the exception of the data obtained in the free shear region (radial locations greater than 2.5 cm), the comparison of the data from the hot wire with the data from the laser velocimeter (lower figure) yields a bias of 14.8 percent with the laser velocimeter measuring low and a measurement standard deviation of 4.1 percent.



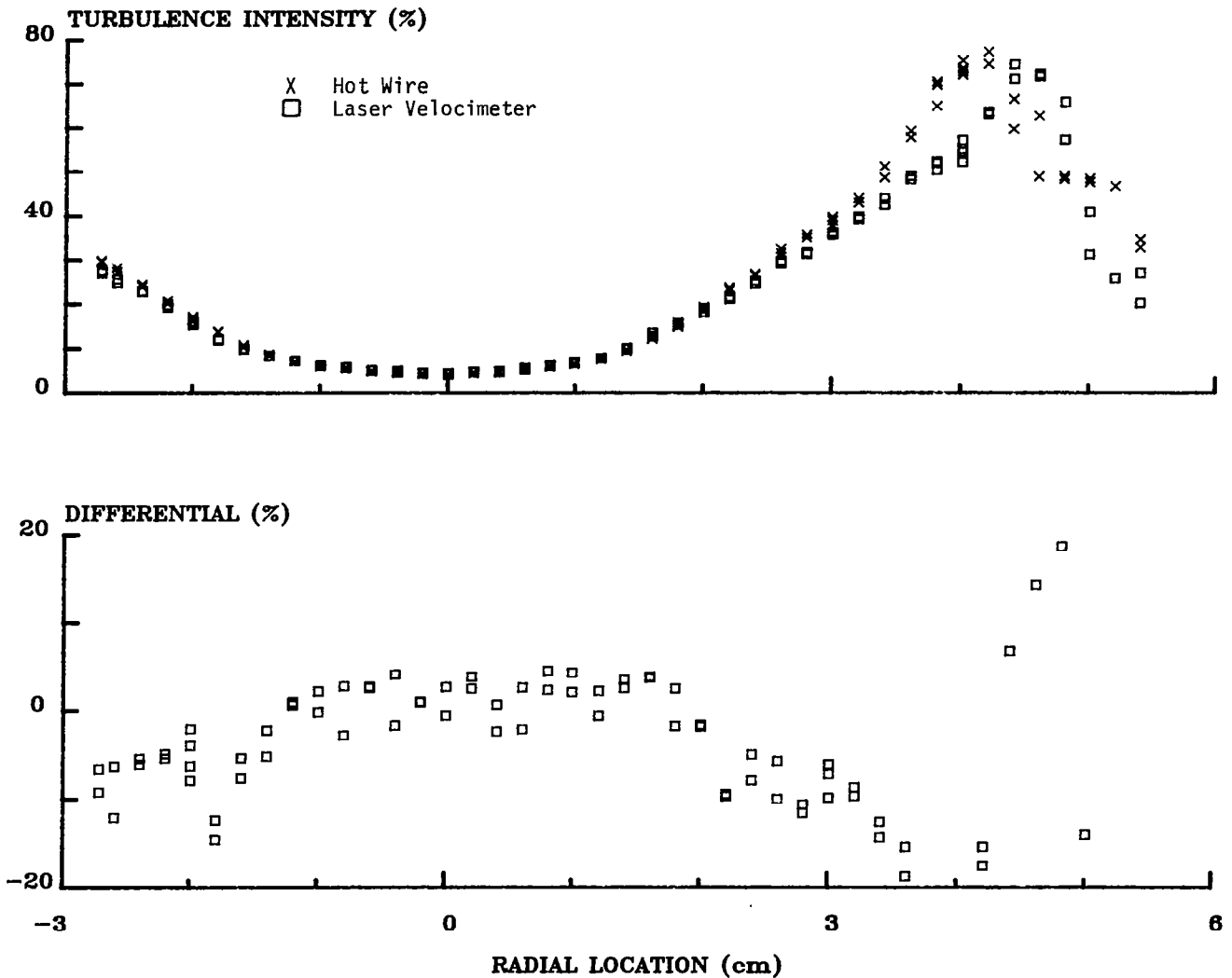
VELOCITY MEASUREMENTS FOR RADIAL SCAN OF PIPE (12 cm)

The mean velocity measurements from the laser velocimeter for a radial scan 12.0 cm downstream from the exit of the fully developed turbulent pipe are shown in the top figure. Velocity bias corrected data and time averaged data are compared to the uncorrected data in the lower figure.



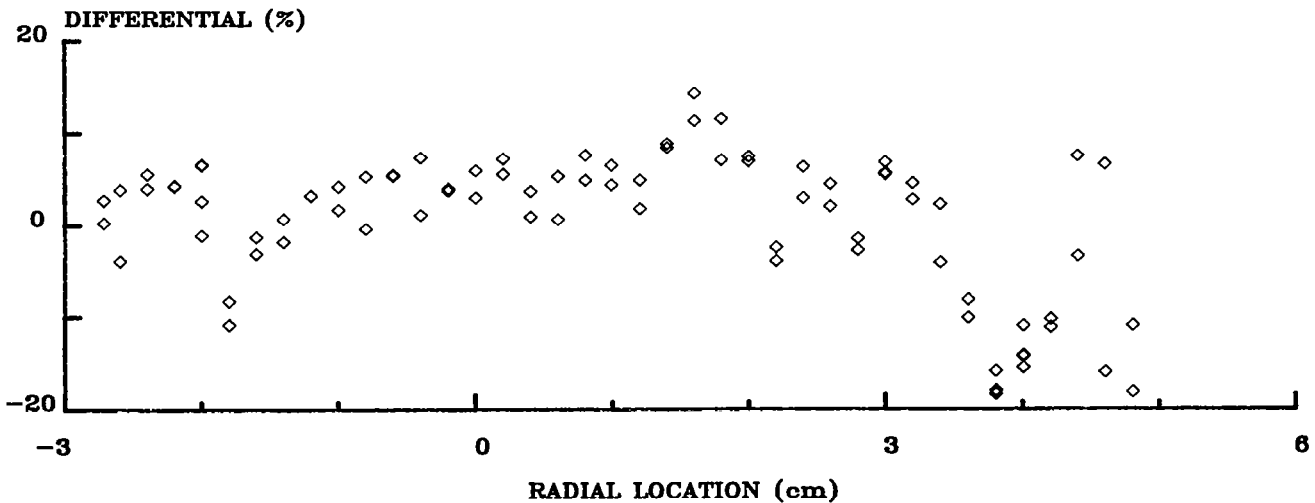
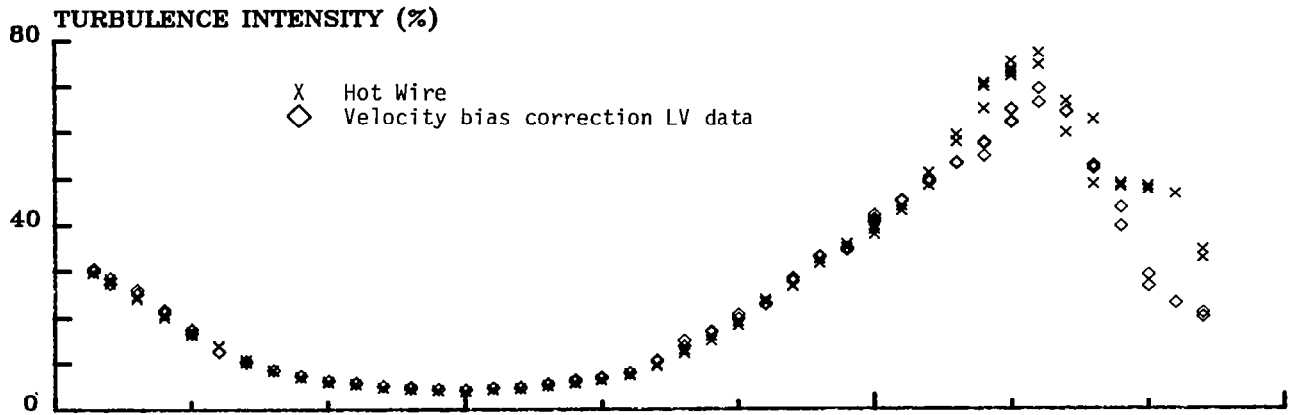
TURBULENCE INTENSITY FOR RADIAL SCAN OF PIPE (12 cm) – COMPARISON
OF HOT WIRE/LV DATA

The turbulence intensity measurements from the hot wire and the laser velocimeter for a radial scan 12.0 cm downstream from the exit of the fully developed turbulent pipe are shown in the top figure. With the exception of the data obtained in the free shear region (radial locations greater than 2.0 cm), the comparison of the data from the hot wire with the data from the laser velocimeter (lower figure) yields a bias of 0.6 percent with the laser velocimeter measuring low and a measurement standard deviation of 4.3 percent. As the free shear region is entered, the turbulence intensity from the laser velocimeter rises at a much lower rate than the hot wire, due probably to the entrainment of clean ambient air. However, when the flow field is derived from the entrained air to a greater degree (radial locations greater than 4.0 cm), the comparisons with the hot wire become better since the bias due to seeding effects becomes weaker.



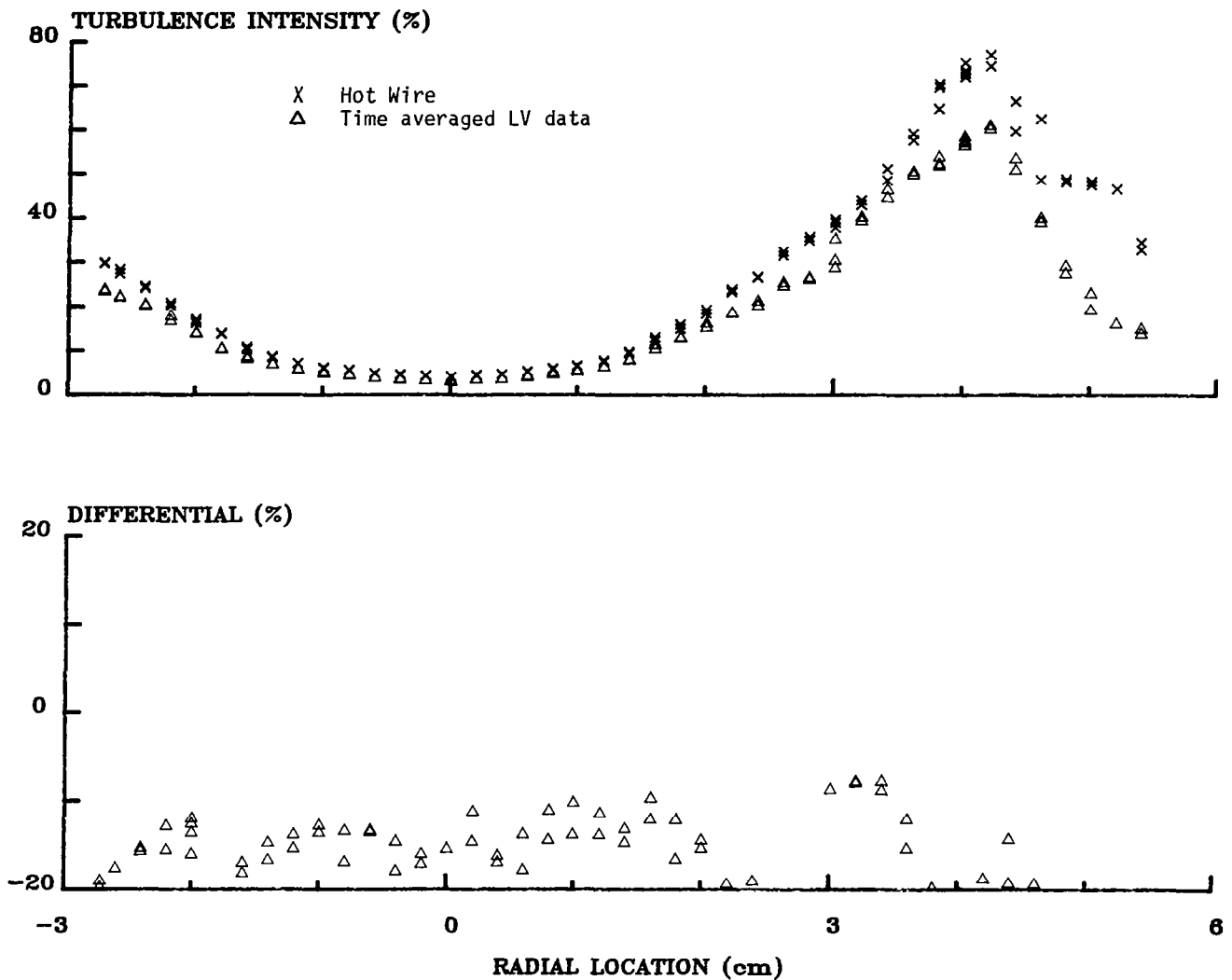
TURBULENCE INTENSITY FOR RADIAL SCAN OF PIPE (12 cm) — COMPARISON
OF HOT WIRE/BIAS CORRECTION LV DATA

The turbulence intensity measurements from the hot wire and velocity bias corrected laser velocimeter data for a radial scan 12.0 cm downstream from the exit of the fully developed turbulent pipe are shown in the top figure. With the exception of the data obtained in the free shear region (radial locations greater than 2.0 cm), the comparison of the data from the hot wire with the data from the laser velocimeter (lower figure) yields a bias of 3.8 percent with the laser velocimeter measuring high and a measurement standard deviation of 4.7 percent. As the free shear region is entered, the velocity bias corrected data tracks the hot wire results better than the uncorrected data in the previous figure. Although the differences between the hot wire results and the corrected laser velocimeter data are large at radial locations greater than 4.0 cm, the overall turbulence intensity profile through the free shear region is much smoother than the uncorrected data or the hot wire data.



TURBULENCE INTENSITY FOR RADIAL SCAN OF PIPE (12 cm) — COMPARISON
OF HOT WIRE/TIME AVERAGED LV DATA

The turbulence intensity measurements from the hot wire and time averaged laser velocimeter data for a radial scan 12.0 cm downstream from the exit of the fully developed turbulent pipe are shown in the top figure. With the exception of the data obtained in the free shear region (radial locations greater than 2.0 cm), the comparison of the data from the hot wire with the data from the laser velocimeter (lower figure) yields a bias of 14.7 percent with the laser velocimeter measuring low and a measurement standard deviation of 2.8 percent. The time averaged profile through the free shear region seems to have the lower slope of the uncorrected data but with the smoothness of the velocity bias corrected data.



RESULTS

A comparative study was conducted between a laser velocimeter and a single component hot wire in two free jet flows to determine if the LV could be used reliably to measure flow turbulence intensity. Great care was taken to reduce the known measurement uncertainties in both instruments. The possible measurement uncertainties in the hot wire were reduced by direct digitization of the hot wire signal and point-by-point conversion of the voltage to velocity, frequent calibrations of the hot wire, low velocity flows chosen to maintain isothermal conditions, and the determination of the effects of seeded flows. The possible errors in the laser velocimeter were reduced by using very small particles as the seed material, forward-scatter system to increase the output signal-to-noise, and off-axis receiver location to decrease the length of the sample volume.

The results of this study show good agreement between the hot wire turbulence intensity measurements and the measurements made with the laser velocimeter, thus indicating that indeed the laser velocimeter may be used to obtain reliable turbulence intensity measurements. An unexpected result of this study was that the velocity bias correction, which has been the accepted standard for several years, was found to be very questionable for turbulence intensity measurements.

BASE LEVEL OF CONFIDENCE ESTABLISHED IN LV MEASUREMENT OF TURBULENCE INTENSITY

**TURBULENCE INTENSITY MEASUREMENTS FROM
1% TO OVER 75%**

VELOCITY BIAS CORRECTION QUESTIONABLE

TIME AVERAGE DATA IS UNACCEPTABLE

REFERENCES

1. Yanta, W.J.; and Smith, K.A.: Measurements of Turbulence - Transport Properties with a Laser Doppler Velocimeter. AIAA 11th Aerospace Sciences Meeting, Washington, DC, January 10-12, 1973.
2. Lau, J.C.; Whiffen, M.C.; Fisher, M.J.; and Smith, D.M.: A Note on Turbulence Measurements with a Laser Velocimeter. J. Fluid Mech., vol. 102, pp. 353-366, 1981.
3. Meyers, J.F.; and Clemmons, J.I., Jr.: Processing Laser Velocimeter High-Speed Burst Counter Data. Third International Workshop on Laser Velocimetry, Purdue University, July, 1978.
4. Clemmons, J.I., Jr.: Laser Velocimeter (Autocovariance) Buffer Interface. NASA Technical Memorandum 83110, May, 1981.
5. Tiederman, W.G.; McLaughlin, D.K.; and Reischman, M.M.: Individual Realization Laser Doppler Technique Applied to Turbulent Channel Flow. Proceedings of Symposium on Turbulence in Liquids, Rolla, MO, 1973.

LASER DOPPLER VELOCIMETRY APPLICATION
IN THE
LANGLEY 0.3-METER TRANSONIC CRYOGENIC TUNNEL

Luther R. Gartrell
NASA Langley Research Center
Hampton, Virginia

INTRODUCTION

The discussion given herein describes the work done in the Langley 0.3-Meter Transonic Cryogenic Tunnel (TCT), i.e., the beginning efforts toward fulfilling the flow velocity instrumentation requirement. A diagram illustrating the flow of events for accomplishing this task is given in figure 1. The purpose of the initial tunnel tests was to investigate the problems and the potential use of a nonintrusive flow velocity measuring technique in this facility. The approach used was the laser velocimeter (LV), a well-known method that has become widely used by researchers as a supplementary flow diagnostic tool (refs. 1 and 2). Some of the main features of the LV are as follows:

(1) It can obtain, nonintrusively, flow velocities directly without the need for calibrations or the knowledge of other flow parameters such as temperature and pressure.

(2) It has good spatial resolution and local-flow velocity response for turbulence intensity studies.

Some of the anticipated problems were maintaining optical alignment due to inherent vibration effects, preventing the test section window from frosting during the cold temperature runs, and detecting enough natural occurring particulates present in the flow to make a velocity measurement. Tests were conducted for the tunnel condition as given without a model. After the completion of these tests, a faulty liquid nitrogen (LN₂) injector was found. As a result of this finding, it was suspected that the particulates detected were primarily due to the malfunctioning LN₂ injector. A second test was conducted in the tunnel to investigate the presence of particles in the flow and measure their velocity after the LN₂ injector had been corrected.

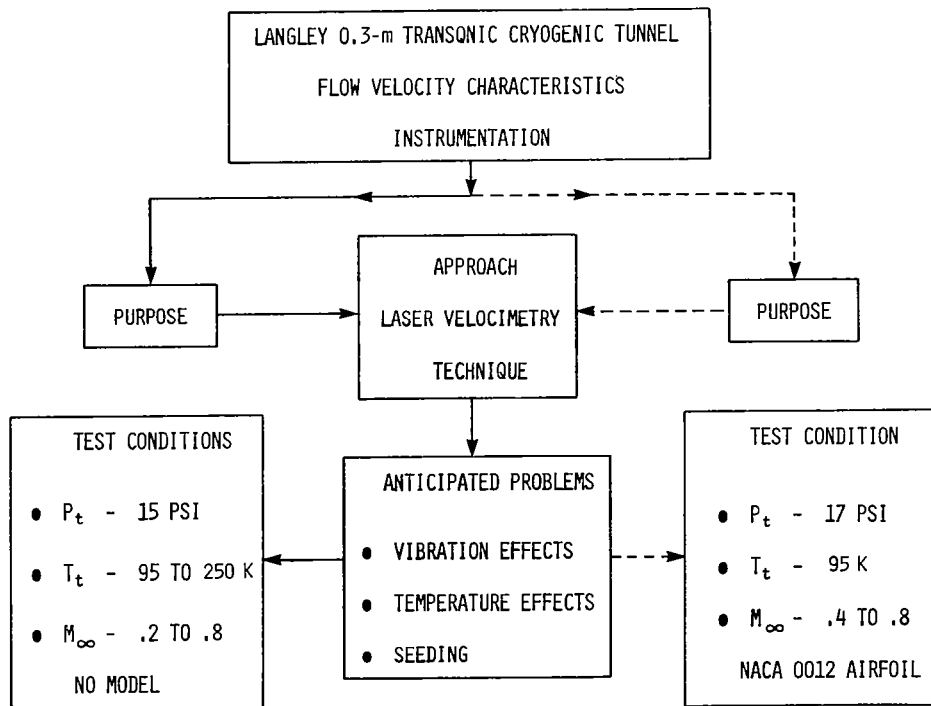


Figure 1

LASER VELOCIMETER SYSTEM CHARACTERISTICS

The LV system used in these tests (fig. 2) was configured to operate in the forward-scatter mode and to measure the axial component of the flow velocity. It uses a He-Ne laser operating in the TEM_{00} mode and providing 15 mW of continuous power at a wavelength of 632.8 nm. The laser beam is divided into two parts by a 50:50 beam splitter prism which yields a beam separation of 50 mm. The transmitter lens with focal length of 47.62 cm was used to focus the beams to a spot size (sample volume) 0.2 mm in diameter by 3 mm long. The fringe spacing was approximately 6 μm . The light scattered by particles in the sample volume is collected by an F1:2 lens and imaged on a high-gain, low-noise photomultiplier tube (PMT) with an S-20 wavelength response by a 10x (0.25 numerical aperture) microscope objective lens.

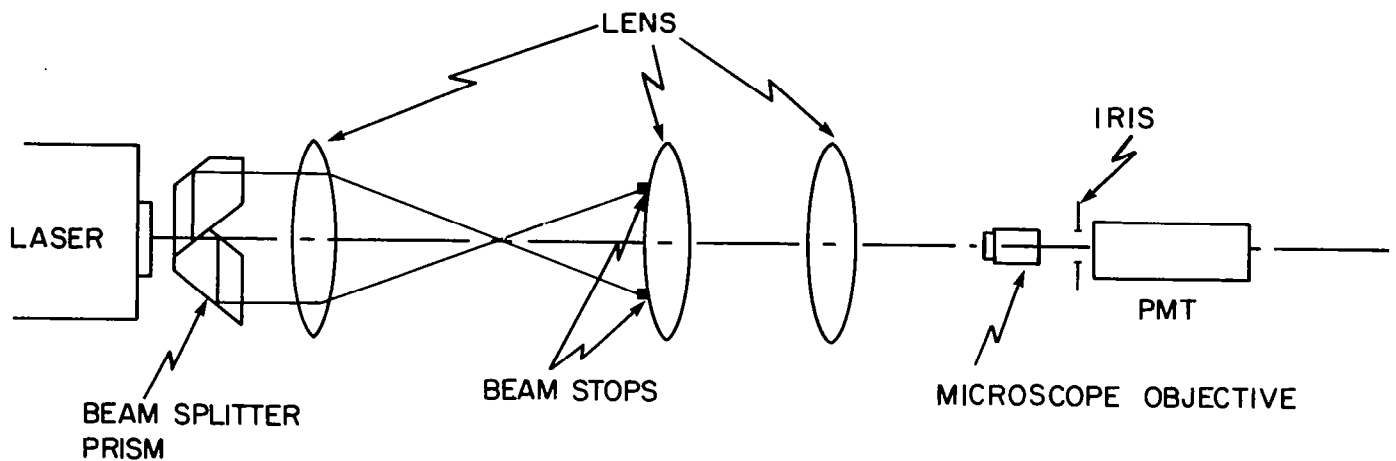


Figure 2

DATA ACQUISITION AND PROCESSING SYSTEM

The data acquisition and processing system (fig. 3) consisted of signal conditioning electronics (10-dB-gain wide-band amplifier/high-speed burst counter) and a 16-bit minicomputer with its peripheral devices. The processed data includes the basic statistical calculations for an ensemble of velocity measurements, i.e., events produced by particles moving through the sample volume.

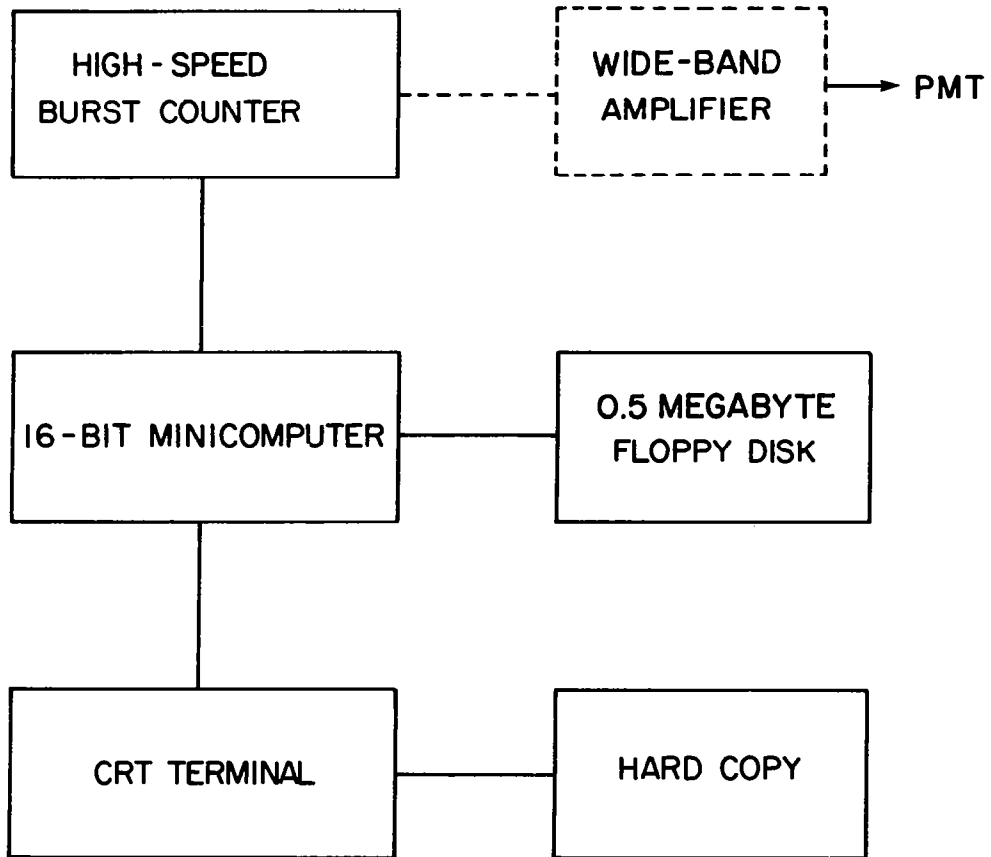


Figure 3

TEST PROCEDURE

The LV system is mounted in metal enclosures, originally used to house a schlieren system, and attached directly to the tunnel test section (fig. 4). These enclosures are purged with dry nitrogen to prevent the windows from frosting during the cold temperature runs. Accelerometers were mounted on the optics enclosures approximately 0.5 m from the test section wall to measure the inherent tunnel vibration levels. The tunnel is cooled prior to operation by running the drive motor and fan at a low speed and injecting LN₂ at a low rate. After reaching the desired operating temperature, the tunnel flow is brought to the desired Mach number and pressure. For the tests discussed herein, the nominal free-stream pressure was 18 psi, the temperature range from 95 to 250 K and free-stream Mach numbers from 0.2 to 0.8. Tests are made with and without an airfoil model. For the tunnel test conditions discussed herein, the inherent tunnel vibrations on the order of 0.3g at 100 Hz, had very little effect on the optical alignment. Dry nitrogen gas purged through the optics enclosures kept the viewing ports free of condensation.

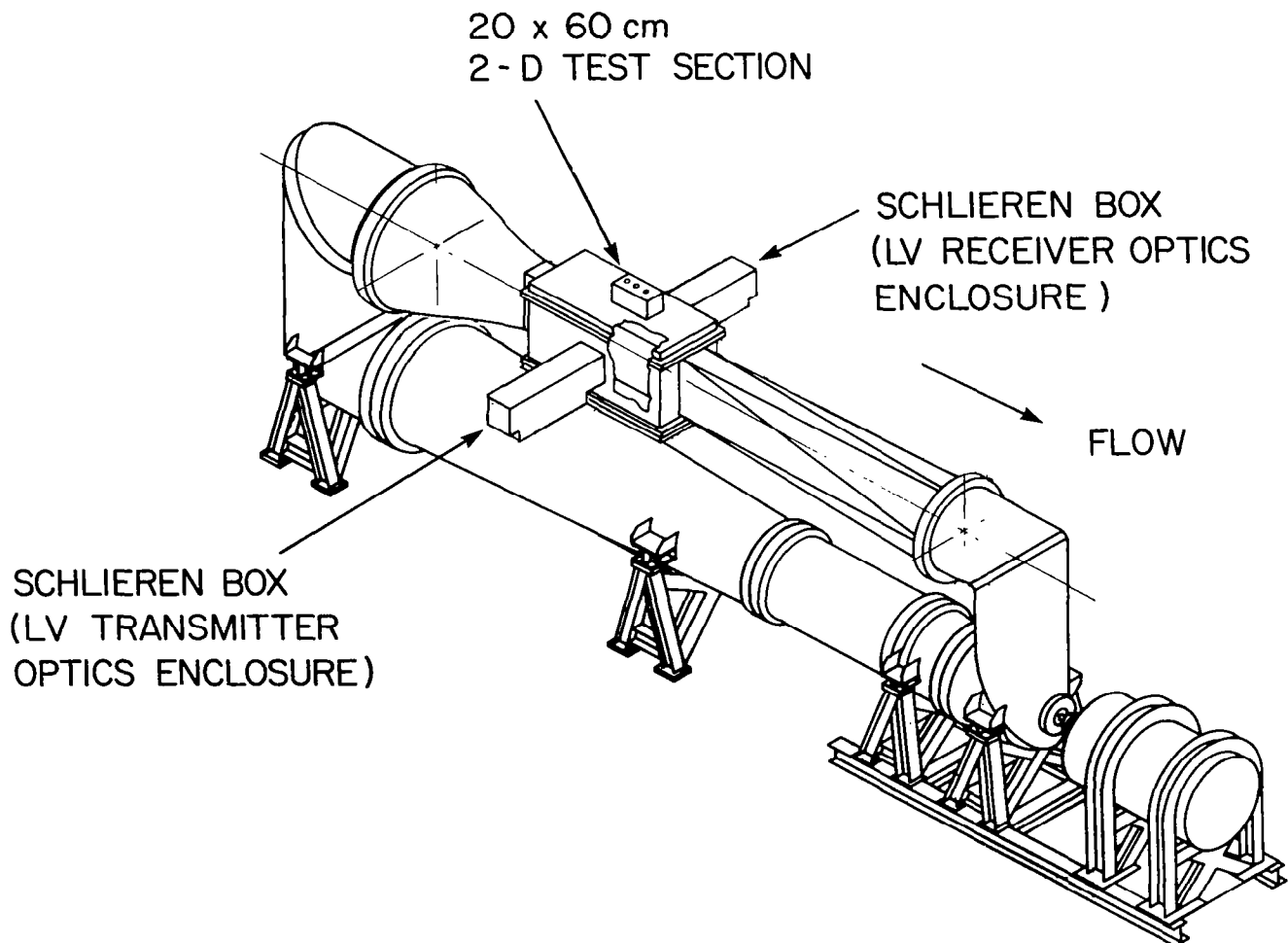


Figure 4

FREE-STREAM VELOCITY MEASUREMENT

Free-stream mean flow velocity as a function of Mach number and temperature are shown in figure 5. The most consistent measurements were below a temperature of 250 K and Mach numbers ranging from 0.3 to ~0.8.

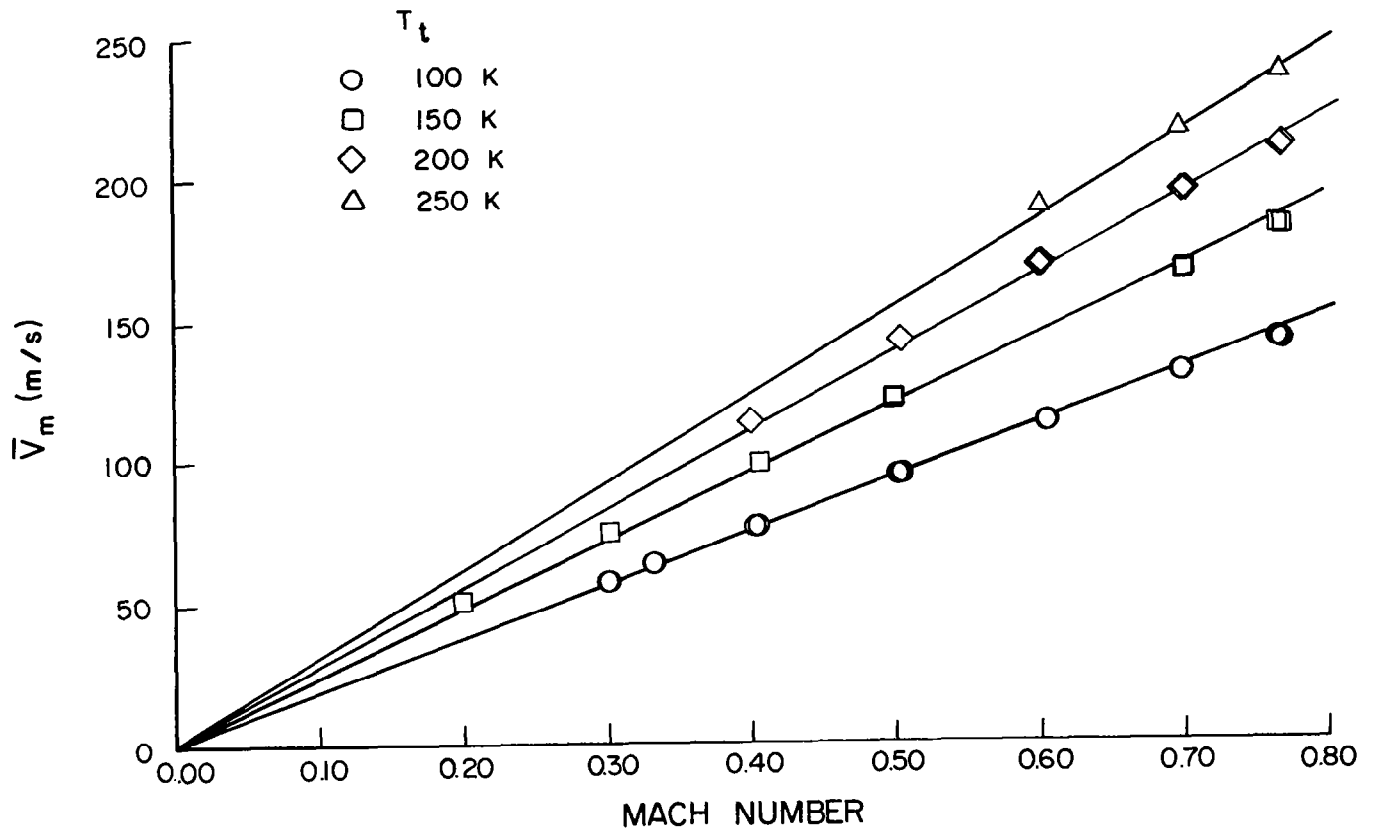


Figure 5

MEASURED MEAN VELOCITY VERSUS CALCULATED MEAN VELOCITY

In comparing these test results (fig. 5) to those calculated from tunnel parameters \bar{V}_c (shown in fig. 6), the agreement was typically better than 1 percent. The standard deviations for this plot cannot be shown because they would appear within the test-point symbols.

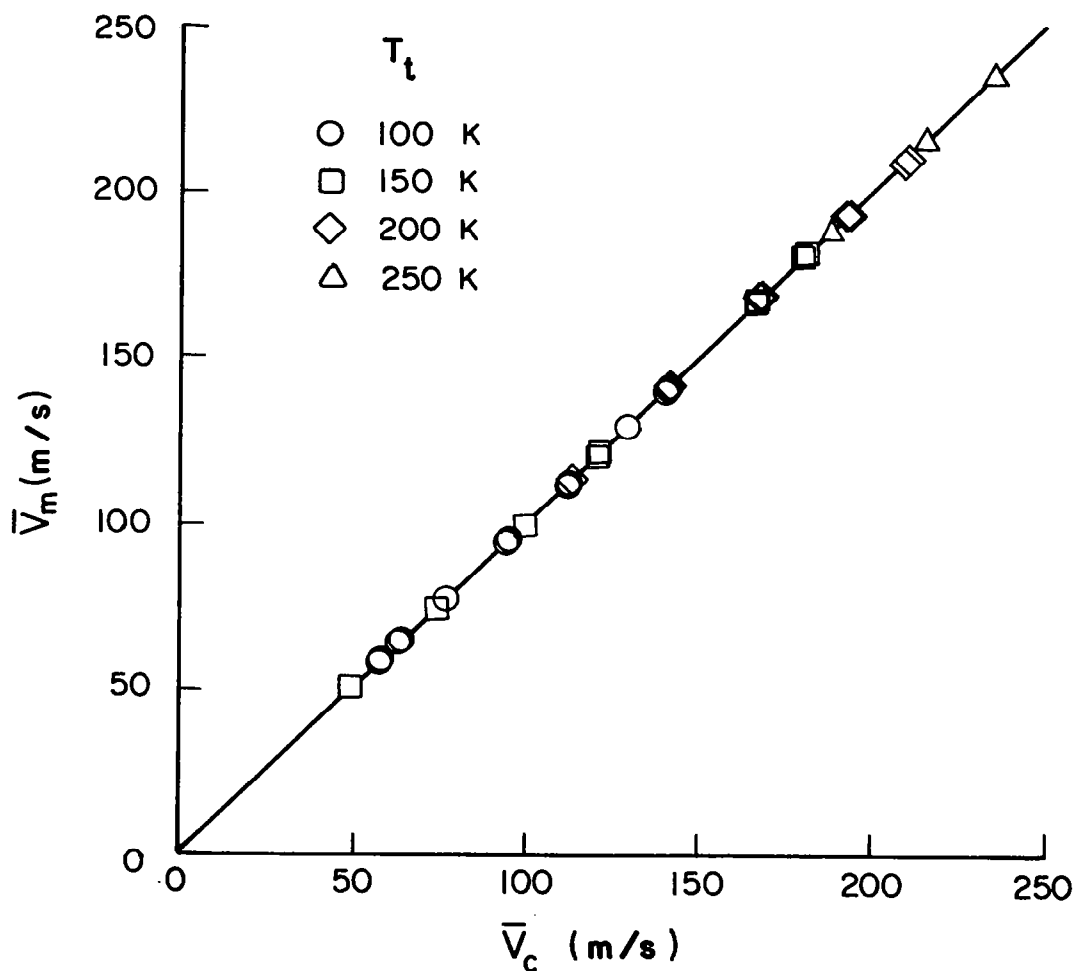


Figure 6

NORMALIZED STANDARD DEVIATION

A plot of the normalized standard deviation σ_m/V_m is shown in figure 7, where σ_m and V_m are the measured standard deviation and velocity, respectively. Over the test Mach number and temperature range, the normalized standard deviation was usually less than 1 percent.

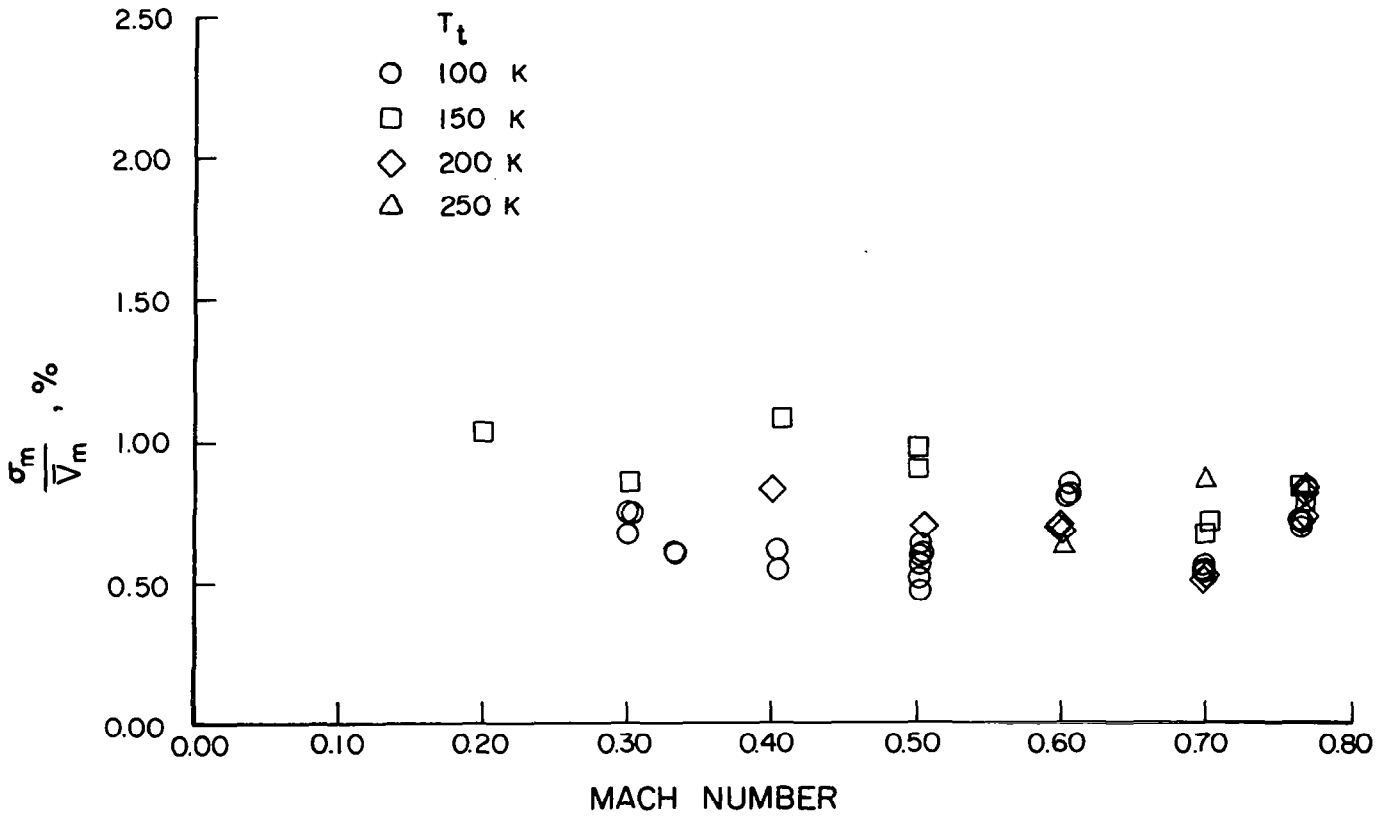


Figure 7

AIRFOIL MODEL VELOCITY MEASUREMENT

The test results for the velocity measurements at a point above an airfoil are shown in figure 8. At a Mach number of 0.8 the normal shock generated was located approximately 2 cm ahead of the measurement point (verified from flow visualization data). The corresponding velocity measured in the subsonic region was within a 10-percent agreement with the predicted value. The particle concentration based on the data rates shown was in the order of $10^6 / \text{m}^3$.

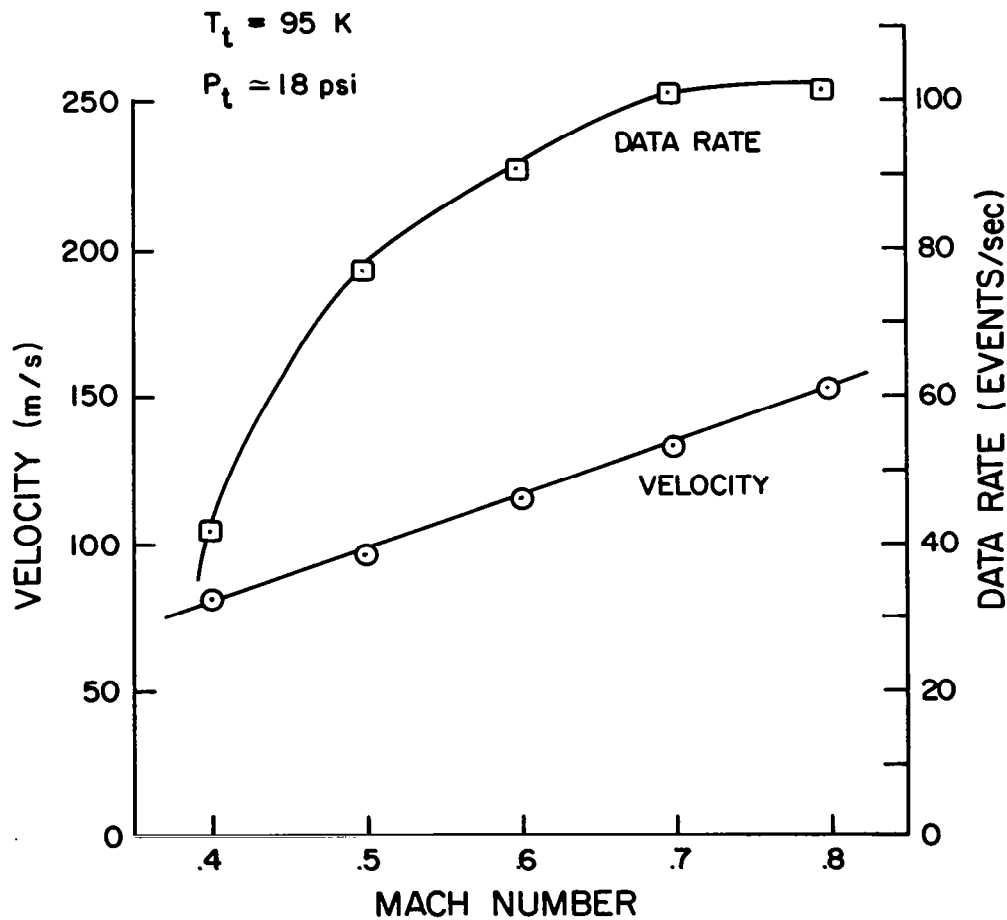
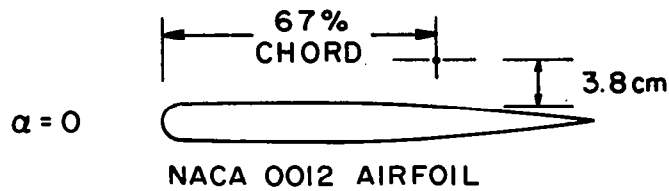


Figure 8

VELOCITY HISTOGRAM

A typical velocity histogram is shown in figure 9. Each velocity ensemble consisted of 1024 measurements and the average data acquisition time was approximately 15 seconds.

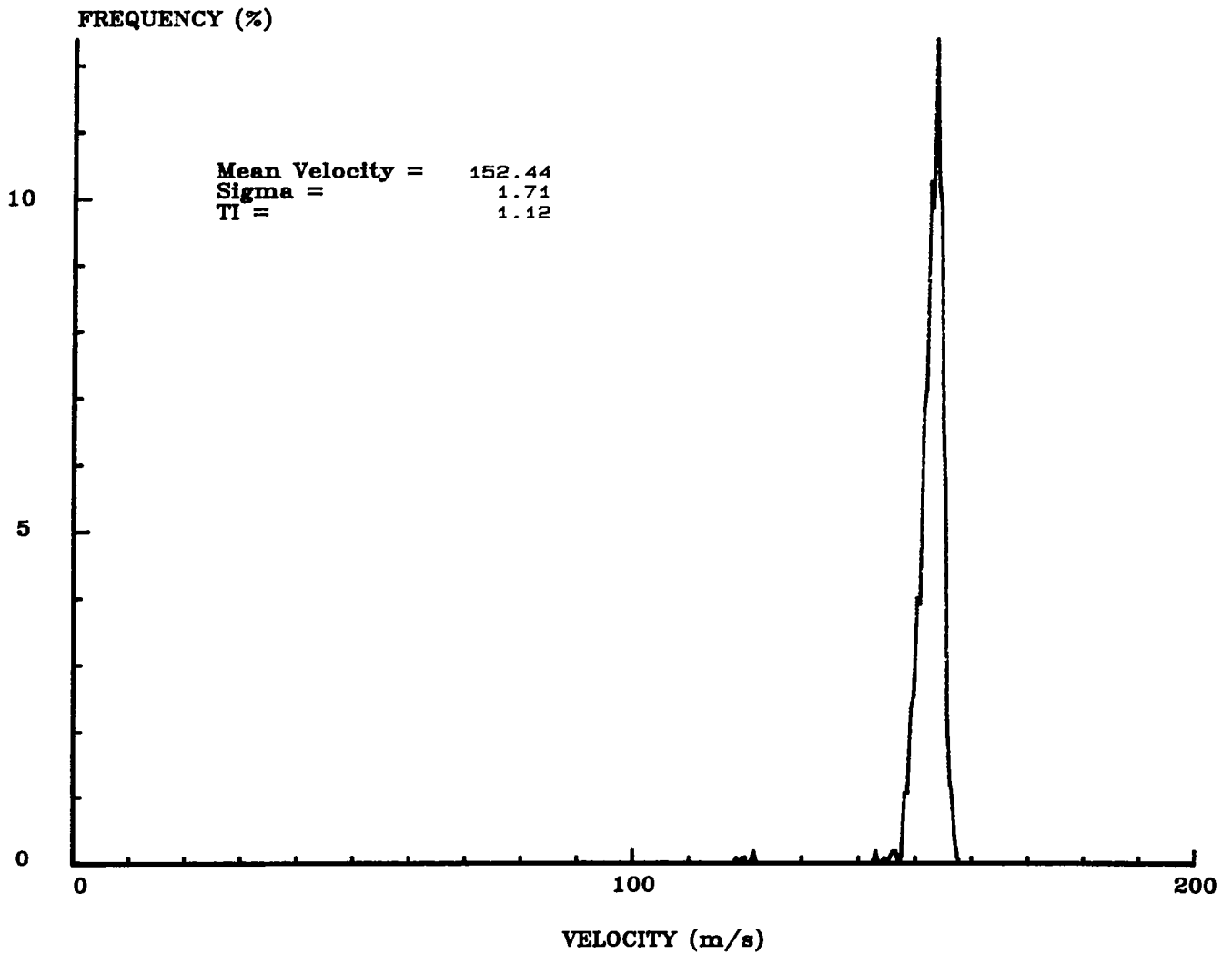


Figure 9

PARTICLE VELOCITY LAG VERSUS PARTICLE SIZE

At the present time, no quantitative data for particle size has been obtained. However in viewing the particle behavior in a moving fluid, the deceleration of a particle passing through a shock in a supersonic flow field is smaller than the deceleration of the fluid. Consequently, a finite relaxation distance behind the shock is traveled before the particle reaches the fluid velocity. This phenomenon depends on the particle size and velocity and the Reynolds number of the flow. Figure 10 (a severe gradient case) illustrates the particle velocity lag (percent) versus particle size at 2 cm behind a normal shock. This spline fitted curve is based on calculations given in reference 3 for a temperature of 95 K, a pressure of 18 psi, and a Mach number of 1.2 ahead of the normal shock. The symmetry of the velocity histogram (fig. 9) shows that the particle size could be in the order of 5 μm or less. In addition, observations of the Doppler burst pattern on an oscilloscope indicated that a majority of the particles (contributors to the flow velocity measurement) are smaller than the fringe spacing ($\approx 6 \mu\text{m}$) for the test conditions shown in figure 8. The velocity survey across the shock using a laser transient anemometer (LTA) revealed a 27-percent velocity change (within 3 percent of theoretical calculations). This measurement further indicates that the particles are probably small enough to track the flow reasonably well.

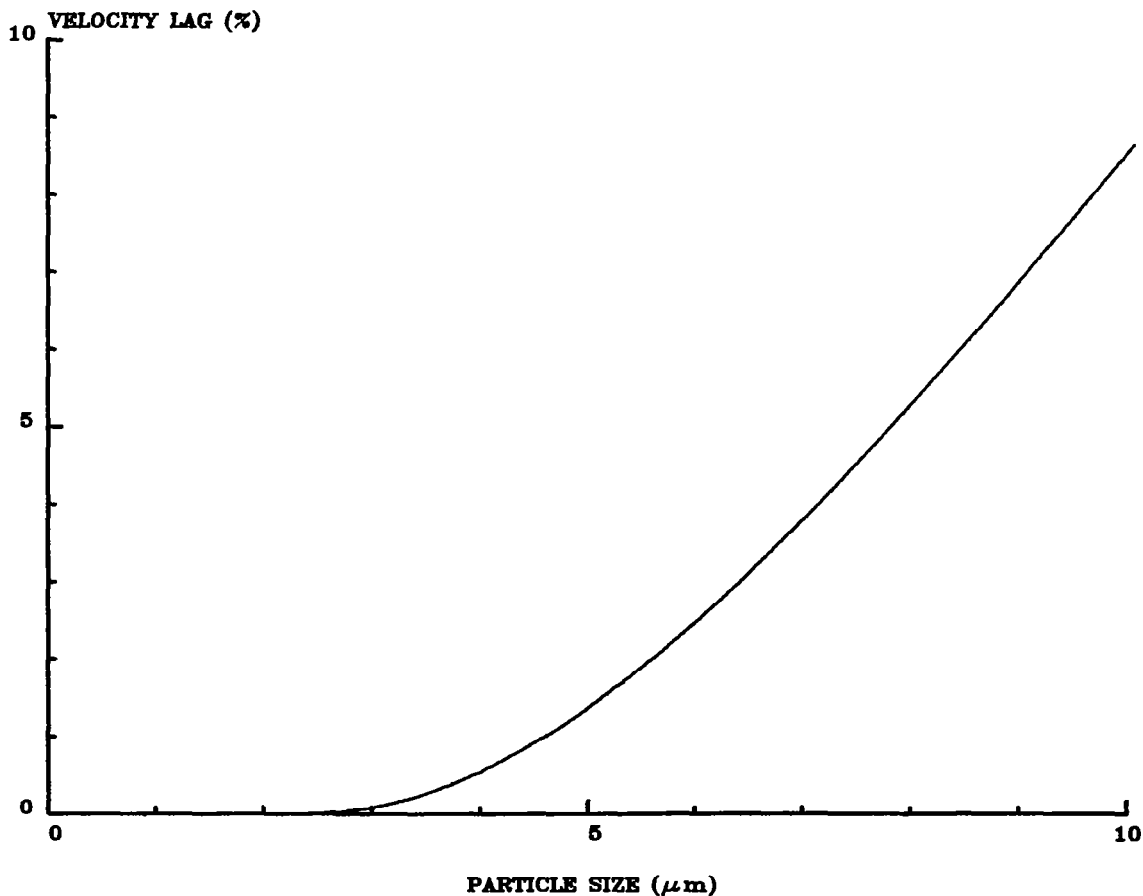


Figure 10

CONCLUSIONS

In view of the test results obtained, the following conclusions are made:

1. Free-stream velocity measurements can be successfully made in the Langley 0.3-m TCT using a low-power (15-mW) LV system.
2. The measured and calculated mean velocities typically agreed within 1-percent.
3. The overall normalized standard deviation (σ_m/V_m) was less than 1 percent.
4. The concentration of the detected particles were in the order of $10^6/m^3$.
5. Tunnel vibration and temperature had no detrimental effects on the optical system.
6. It is recommended that the LV work should be further investigated for future use in the Langley 0.3-m TCT.

REFERENCES

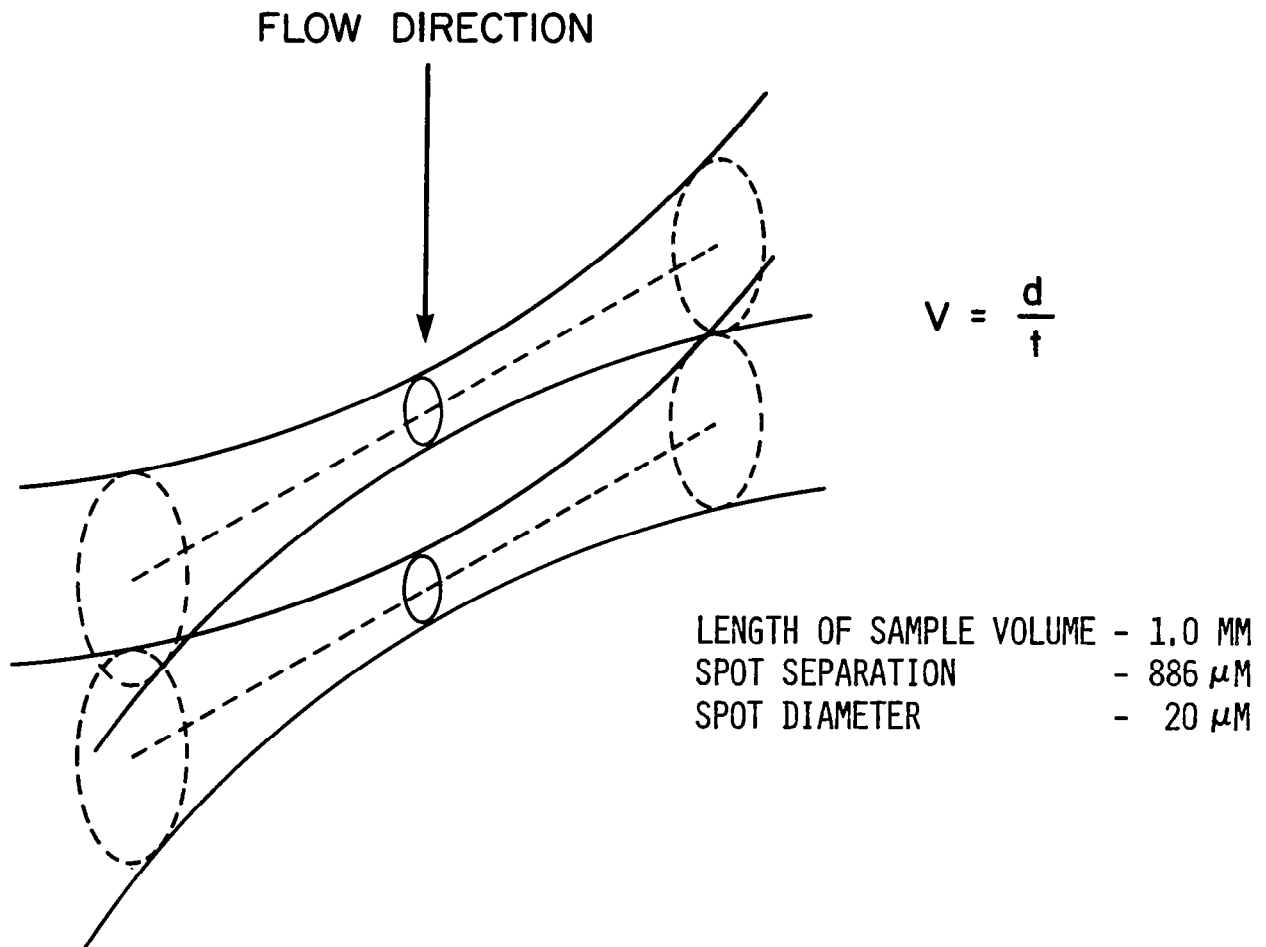
1. Eckert, E. R. G.; ed: Proceedings of the Minnesota Symposium on Laser Anemometry. Continuing Education and Extension, University of Minnesota, Jan. 1976.
2. Thompson, H. D.; and Stevenson, W. H., eds.: Laser Velocimetry and Particle Sizing. Hemisphere Publishing Corp., C. 1979.
3. Walsh, Michael J.: Influence of Drag Coefficient Equations on Particle Motion Calculations. Symposium on Laser Anemometry, University of Minnesota, October 22-24, 1975.

VELOCITY AND FLOW ANGLE MEASUREMENTS IN THE
LANGLEY 0.3-METER TRANSONIC CRYOGENIC
TUNNEL USING A LASER TRANSIT ANEMOMETER

W. C. Honaker
NASA Langley Research Center
Hampton, Virginia

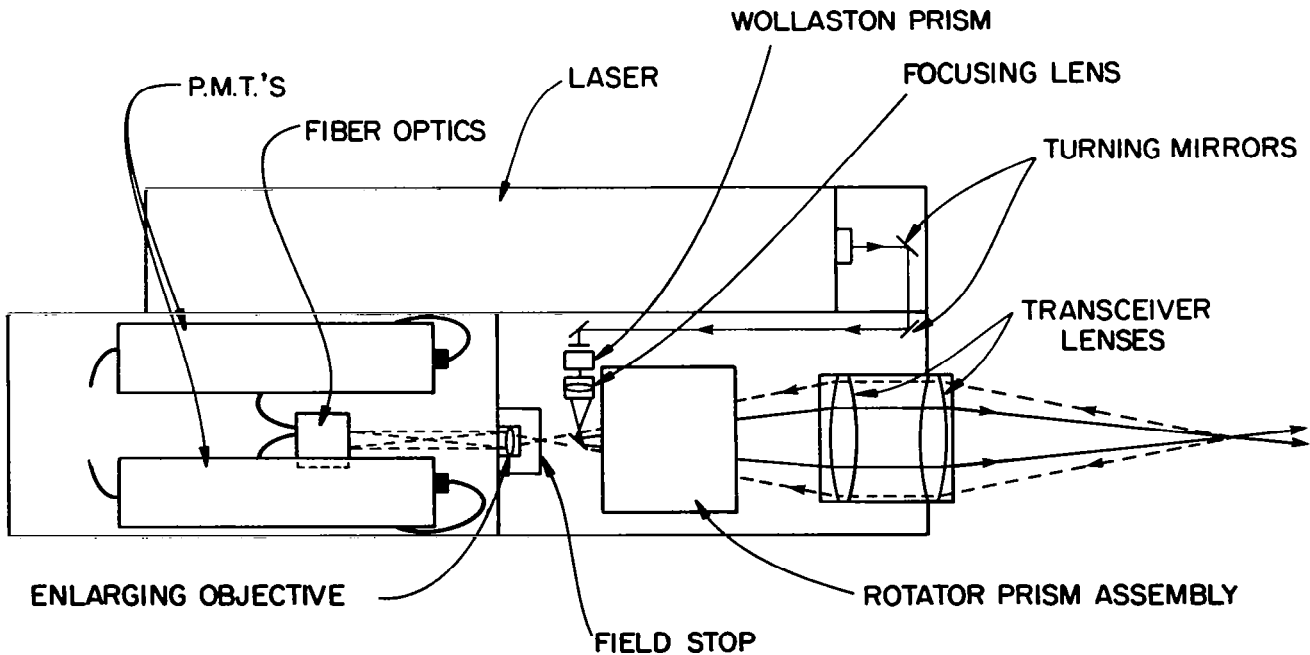
LASER TRANSIT ANEMOMETER

The Laser Transit Anemometer (LTA), or "2-spot" system, is an outgrowth of difficulties encountered by using the more familiar fringe system (e.g., measurements inside turbomachinery). In the LTA system two parallel laser beams of known separation and cross sectional area are focussed at the same location or plane. When a particle in a flow field passes through both beams and the time is recorded for its transit (time of flight), its velocity can be calculated knowing the distance between the beams. By rotating the two beams (spots) around a common center and recording the number of valid events (a particle which passes through both spots in the proper sequence) at each angle the flow angle can be determined by curve fitting a predetermined number of angles or points and calculating the peak of what should be a gaussian curve. The best angle or flow angle is defined as the angle at which the maximum number of valid events occurs.



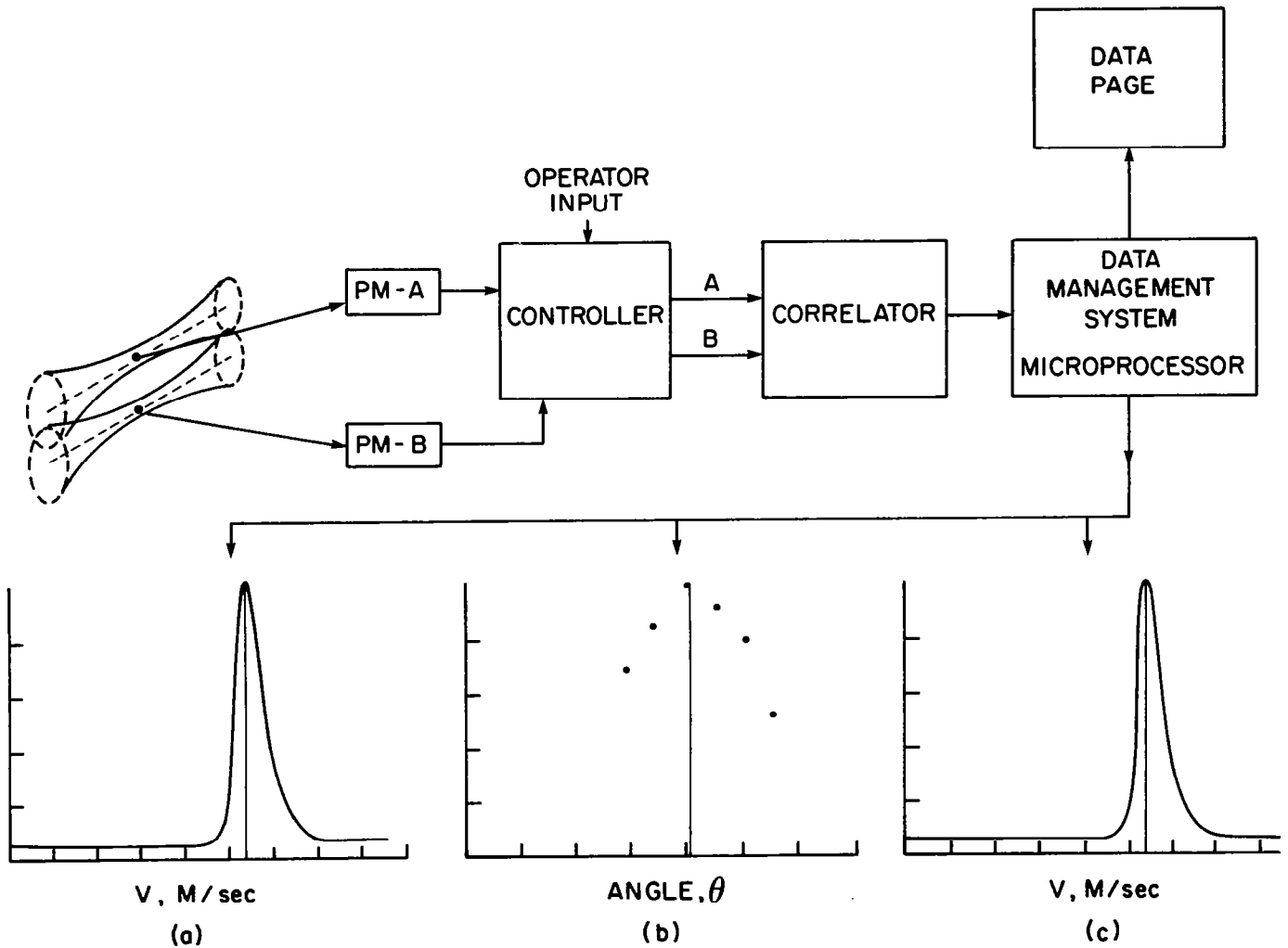
LTA OPTICAL HEAD

The LTA optical head consists of a one watt laser, two channels of electronics for the photomultiplier, beam splitting optics and transceiver optics, and spot rotation system and control circuits. Laser power is provided by a one watt Lexel laser. Four turning mirrors are used to transport the laser beam to the lower half of the optics head. The beam is split by a Wollaston prism inclined to the polarization axis to give equal intensity beams (polarized at right angles to each other). The image is relayed by the central part of the output system, the transceiver mirror, the rotator prism and inner and outer transceiver lenses to produce the illuminated region in front of the system. The sample volume is reimaged by the outer annulus of the transceiver lenses and rotator prism and the small transceiver mirror now behaves as a stop. The field stop contains two holes conjugate with the spots to reject flare. These stops are magnified on to the ends of optical fibers which act as secondary stops and further reduce flare and channel cross talk before transmitting the light to two photomultiplier tubes. The rotator prism allows the plane containing the two spots and the optical axis to be rotated such that the spots orbit a common center.



LTA ELECTRONIC SYSTEM FUNCTIONAL BLOCK DIAGRAM

The major components of the LTA are: Optics head, controller, correlator and data management system. To make velocity and flow angle measurements with the system one must be familiar with the equipment and the flow field of interest. An initial correlogram is taken to assure that all instrument settings are correct to give a reasonable peak at approximately 60 percent of full scale on plot (a) ((a) is a plot of data rate vs velocity). After a successful first correlogram has been taken a best angle search is made in (b) ((b) is a plot of data rate vs angle). From this best angle search the data system will choose a best angle if a valid peak is found. The system will then orientate the spots at that angle and take a best angle correlogram (c) ((c) is a plot of data rate vs velocity). From this correlogram velocity, flow angle and turbulence intensity are calculated and displayed on a data page. All of the plots and data page can then be printed or stored on diskette at the option of the operator.



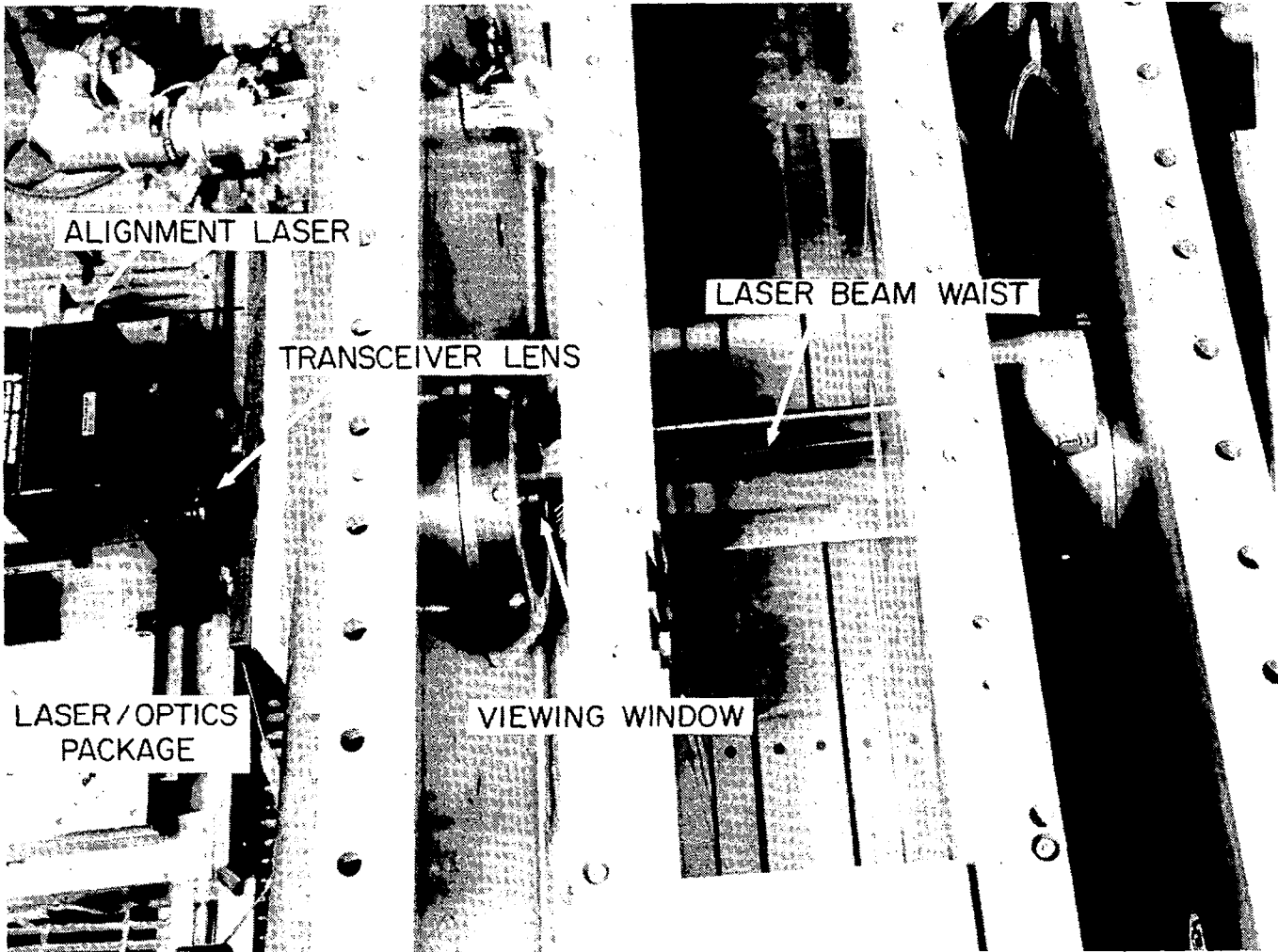
LTA - DATA PAGE

Information required to run the system and the program is entered into the data management system by a data page. To run the complete program, items 1-13 must be entered by the keyboard input. Items 1-13 can then be recorded on diskette and changes made as the operator desires. After a data point is completed the results are recorded in items 14-22 and can be printed or stored on diskette for future and further analyses by a large computer.

1NO OF STORES	***	14VEL(M/S)	****,**
2SPOT SEP(MM)	****	15TURB(%)	**,**
3DURATION	*	16DATA RATE	*****
4DT(NS)	****	17BACK RATE	*****
5PTS ABT PEAK	**	18D/B RATIO	****,**
6DISC RANGE	*	19ANGLE	****,**
7NO ANGLES	*	20RATE A/S	*****
8THETA(NOW)	***.*	21RATE B/S	*****
9THETA(ASK)	***.*	22DTHETA	**,**
10THETA(GET)	***.*		
11EXPT NO	****		
12RUN NO	****		
13DTHETA	**,**		

0.3 METER TRANSONIC CRYOGENIC TUNNEL (TCT) SETUP

This is a top view of the TCT experimental arrangement showing the inside of the test section and the position of the LTA system. The laser beam waist was located 3.5 centimeters above the surface of a NACA-0012 airfoil for the majority of the experimental data points. The LTA system was mounted on a scan rig in order to make measurements over the entire surface of the model. An alignment laser and photodiode system was used to track the relative position of the test section as the tunnel was cooled and moved with respect to the LTA. As the tunnel cooled the viewing window frosted. This problem was solved by purging the outside surface with dry nitrogen and keeping a positive pressure between that surface and a window of plate glass located about 15 centimeters to the left of the viewing window. In turn the plate glass window was kept free of condensation by a low velocity hair dryer (no heat).



RANGE OF PARAMETERS USED DURING TCT EXPERIMENT

The reason for this entry into the TCT was to further evaluate the LTA system and to determine if there was enough natural particulates in the flow to make velocity and flow angle measurements. Listed below is the range of temperatures, pressures, Mach numbers, velocities, data rate and flow angles used and measured during this experiment. Also shown is the velocity change measured during a scan across the shock for one of the conditions.

T_t - 95 TO 285K

P_t - 17 TO 60 PSIA

M_∞ - 0.11 TO 0.85

VELOCITY - 42 TO 320 M/SEC

DATA RATE - 2-898 CTS/SEC

ANGLE - 91 - 94°

VELOCITY CHANGE ACROSS SHOCK - 318 TO 232 M/SEC

COMPARISON OF LTA MEASURED VELOCITY WITH FLOW FIELD CALCULATIONS

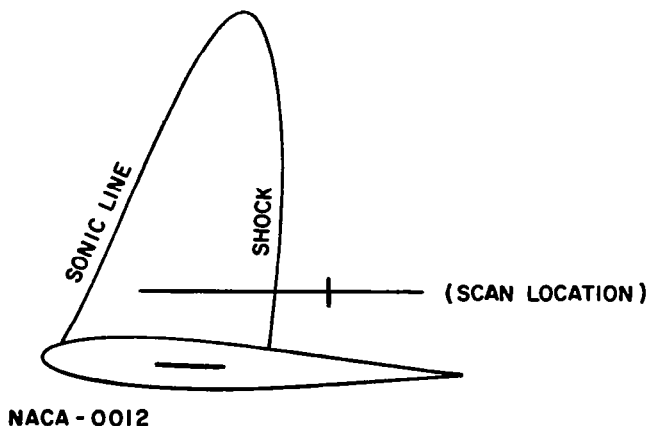
This sketch shows the airfoil used (NACA-0012) with the location of the sonic line and shock position when the tunnel parameters are those listed to the left of the sketch. A horizontal scan was made at the position of the horizontal line on the sketch and at zero angle of attack. A calculation was made of Mach Number around the airfoil using a 2-dimensional transonic code developed by Korn and Garabedian. Shown in the table are values obtained from the calculation as well as values measured with the LTA system. The calculations assume free air and no real gas effects were considered. Further calculations are being made which, including these factors, should bring the two values into closer agreement.

CONCLUSIONS

- o The LTA system functioned properly although conditions were less than desirable. (Transceiver through 3 windows and the laser head was at a 6° angle to eliminate flare)
- o Particle concentration remained at levels high enough to make velocity and flow angle measurements at all tunnel conditions used in this experiment.

	AHEAD SHOCK		DOWNSTREAM SHOCK		RATIO
	M	VEL M/SEC	M	VEL M/SEC	V_2/V_1
2D TRANSONIC AIRFOIL CODE	1.25	306	0.813	214	.700
MEASURED VELOCITY-LTA		317		232	.732
% DIFF		4		8	5

$M = 0.85$
 $T_t = 192K$
 $P_t = 30 \text{ PSIA}$
 $R = 8 \times 10^6$



SOME NTF LASER VELOCIMETER
INSTALLATION AND OPERATION
CONSIDERATIONS

W. W. Hunter, Jr.
L. R. Gartrell
W. C. Honaker

NASA Langley Research Center
Hampton, Virginia

INTRODUCTION

Installation and effective utilization of a laser velocimeter system in the National Transonic Facility (NTF) has been advocated by a variety of technical panels (ref. 1) . The purpose of these panels is to make recommendations to ensure maximum research information is realized from this unique modern facility. Throughout the NTF's development high priority program requirements have continued to push consideration of a laser velocimeter system into the future. A need exists to measure and monitor flow field angularity during the calibration and shakedown of the NTF; providing a near term requirement for laser velocimetry.

Two velocimeter techniques were considered as possible candidates to meet this flow field angularity measurement requirement. The two approaches considered were the "fringe" laser Doppler velocimeter and the "two spot" laser transit anemometer. The purpose of this paper is to present the performance and system considerations in selecting the "two-spot" approach.

REQUIREMENT

The initial requirement was to make a non-intrusive measurement of flow field angularity at a point on the centerline displaced some distance upstream of a potential model location. The angle range and required resolution were estimated to be 0.2 and 0.01 degrees, respectively. Maximum velocity for design considerations was 250 m/sec. Spatial resolution was not initially specified, other than it should be small compared with model and flow field scale so that a two-dimensional measurement in the plane perpendicular, coincident, and parallel to tunnel centerline would not be significantly in error due to a three-dimensional flow field.

VELOCIMETER TECHNIQUES

Two velocimeter techniques were considered as potential candidates for achieving the flow field angularity measurements. The first was the "fringe" laser Doppler velocimeter, (LDV). A great deal of experience has been obtained with this approach at Langley and the literature is rich with papers describing many experimental applications and system performance details (refs. 2 and 3). That is, many velocity flow field measurements have been conducted with the LDV but not with high resolution precise angularity measurements. The second candidate considered was the "two-spot" laser transit anemometer, (LTA). This approach has not been as extensively used as the LDV technique but literature does contain experimental applications and system performance details (refs. 4 and 5). Again, a lack of high resolution, high precision angularity measurements is noted for the LTA.

REQUIREMENT

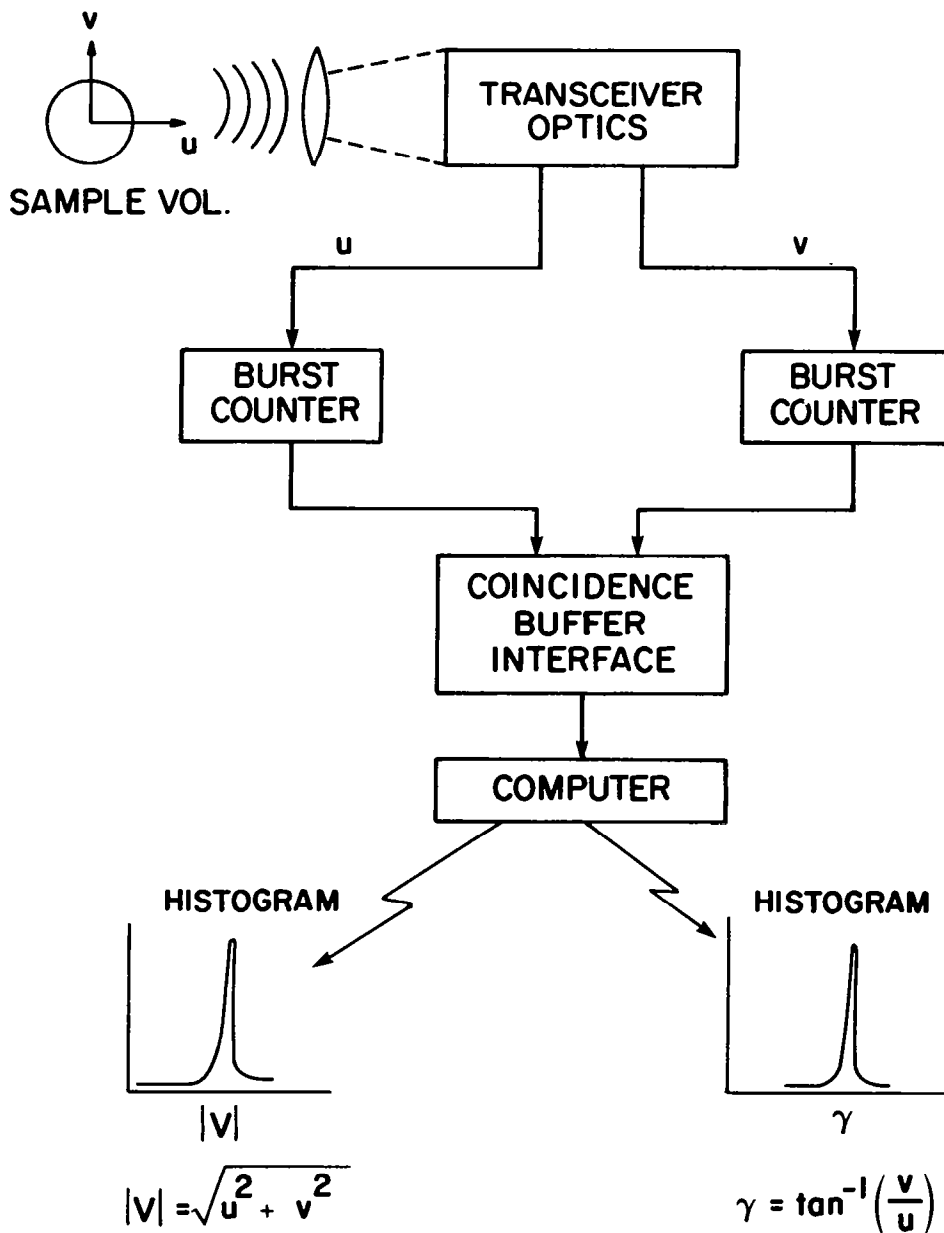
MEASURE FLOW FIELD ANGULARITY WITH AN ACCURACY OF 0.01 DEGREE
NON-INTRUSIVELY

APPROACHES CONSIDERED

- o LASER DOPPLER VELOCIMETER (LDV)
- o LASER TRANSIT ANEMOMETER (LTA)

LDV FUNCTIONAL DIAGRAM

The approach considered for the measurement of the flow field angularity in a perpendicular plane parallel and coincident with the tunnel centerline was to require simultaneous two-velocity component measurements, u and v . The imposition of the condition of coincident measurements allows for the separation and measurement of the mean flow field velocity magnitude and angularity and their respective higher order statistical moments.



LASER DOPPLER VELOCIMETER COORDINATE SYSTEM

Fundamentals of the "fringe" laser Doppler velocimeter are well known and numerous articles and conferences have explored its capabilities and limitations. Conceptually the technique is embodied in this simple expression:

$$f_D = \frac{2V \sin \theta/2}{\lambda}$$

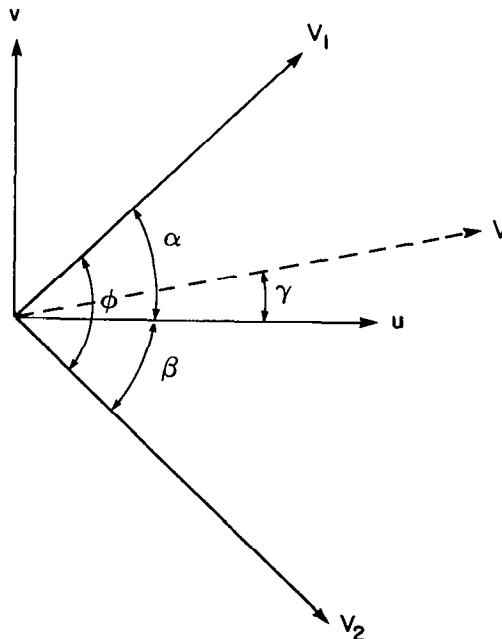
The Doppler frequency, f_D , is related to the velocity component, V , in the plane of two laser beams which cross with an angle θ and whose wavelength is λ .

The Coordinate system shown below and the following expressions permit the development of the relations between the measured values and the two-dimensional flow field magnitude and angle:

$$\begin{aligned} V_1 &= V \cos (\alpha-\gamma) \\ V_2 &= V \cos (\phi-\alpha+\gamma) \\ \beta &= \phi-\alpha \end{aligned}$$

The flow field angularity is given by:

$$\gamma = \tan^{-1} \left[\frac{V_1 \cos (\phi-\alpha) - V_2 \cos \alpha}{V_1 \sin (\phi-\alpha) + V_2 \sin \alpha} \right]$$



ESTIMATE OF THE ALLOWED SYSTEM UNCERTAINTIES

To achieve an estimate of the uncertainty to be expected in the measurement of γ or to achieve an estimate of the uncertainties that can be tolerated in the parameters V_1 , V_2 , ϕ , and α , an analysis based on the propagation of errors was performed (ref. 6). For the specific case indicated and the assumptions that the uncertainties in the quantities V_1 , V_2 , ϕ and α are independent and the velocity, V , of the scattering particulate is constant during the measurement transition the following expression for the standard deviation, σ , or variance, σ^2 , of the flow angle, γ , and velocity were derived. Note the potentially significant amplification of the variance of the cross beam angle, θ , by the cotangent squared term.

$$\begin{aligned} \text{FOR CASE} \quad \phi &= 90^\circ \\ \alpha &= 45^\circ \end{aligned}$$

$$\begin{aligned} \text{THEN} \quad V_2 &\cong V_1 \\ \sigma_{V_1} &\cong \sigma_{V_2} \end{aligned}$$

$$\text{AND ASSUMING} \quad \sigma_\alpha \cong \sigma_\phi$$

$$\sigma_\gamma = \left[\frac{\sigma_V^2}{2V^2} + \frac{5\sigma_\phi^2}{4} \right]^{1/2}$$

$$\text{WHERE} \quad \frac{\sigma_V^2}{V^2} = \left[\frac{\sigma_{fD}^2}{fD^2} + \frac{\text{COT}^2 \theta/2}{4} \sigma_\theta^2 \right]$$

RESULT OF UNCERTAINTY ANALYSIS

Assuming that the angles, θ , and ϕ can be determined with equal precision and noting that the cotangent squared term dominates the case considered, the contribution to the uncertainty by the detected Doppler frequency was neglected. To achieve the flow angle, γ , uncertainty of 0.01 degree requires that the uncertainty in the cross beam angle be restricted to no more than 1.3 seconds of arc.

$$\sigma_{\gamma} = \left[\frac{\sigma_{fD}^2}{2fD^2} + \frac{\text{COT}^2 \theta/2}{8} \sigma_{\theta}^2 + \frac{5}{4} \sigma_{\phi}^2 \right]^{1/2}$$

ASSUMING

$$\sigma_{\theta} = \sigma_{\phi} \equiv \sigma_{<}$$

AND NEGLECTING

$$\sigma_{fD}^2/2fD^2$$

$$\sigma_{<} = \left[\frac{\sigma_{\gamma}}{\frac{\text{COT}^2 \theta/2}{8} + \frac{5}{4}} \right]^{1/2}$$

REQUIRE: $\sigma_{\gamma} \leq 0.01^{\circ}$ OR 1.74×10^{-4} RAD.

AND LET: $\theta = 1.5^{\circ}$

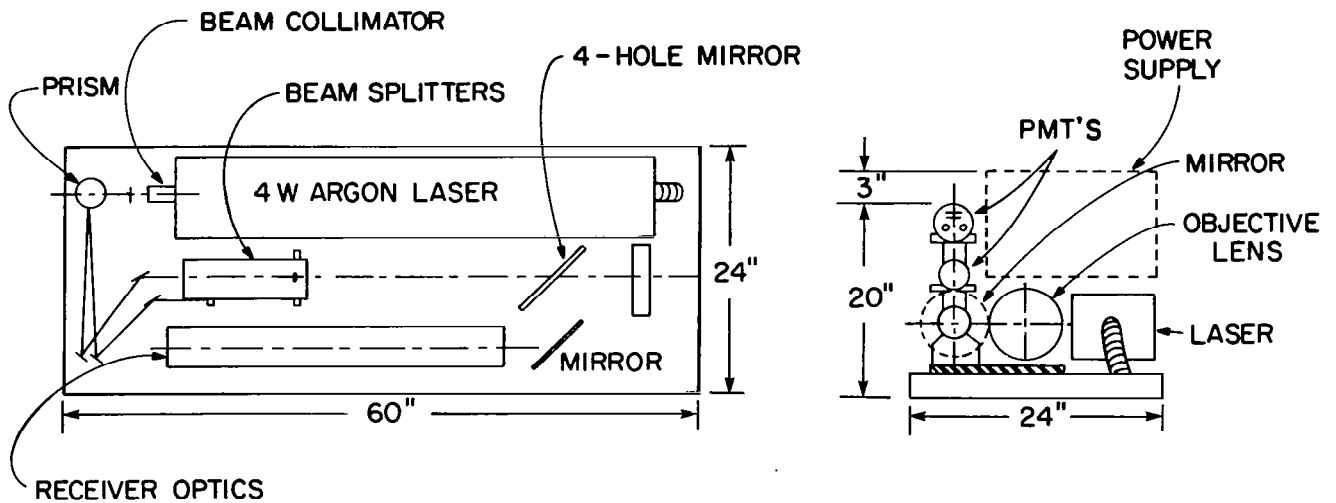
THE ALLOWED UNCERTAINTY OF $\sigma_{<}$ IS

6.44×10^{-6} RAD. OR 1.3 SECONDS

LDV LASER/OPTICS CONFIGURATION

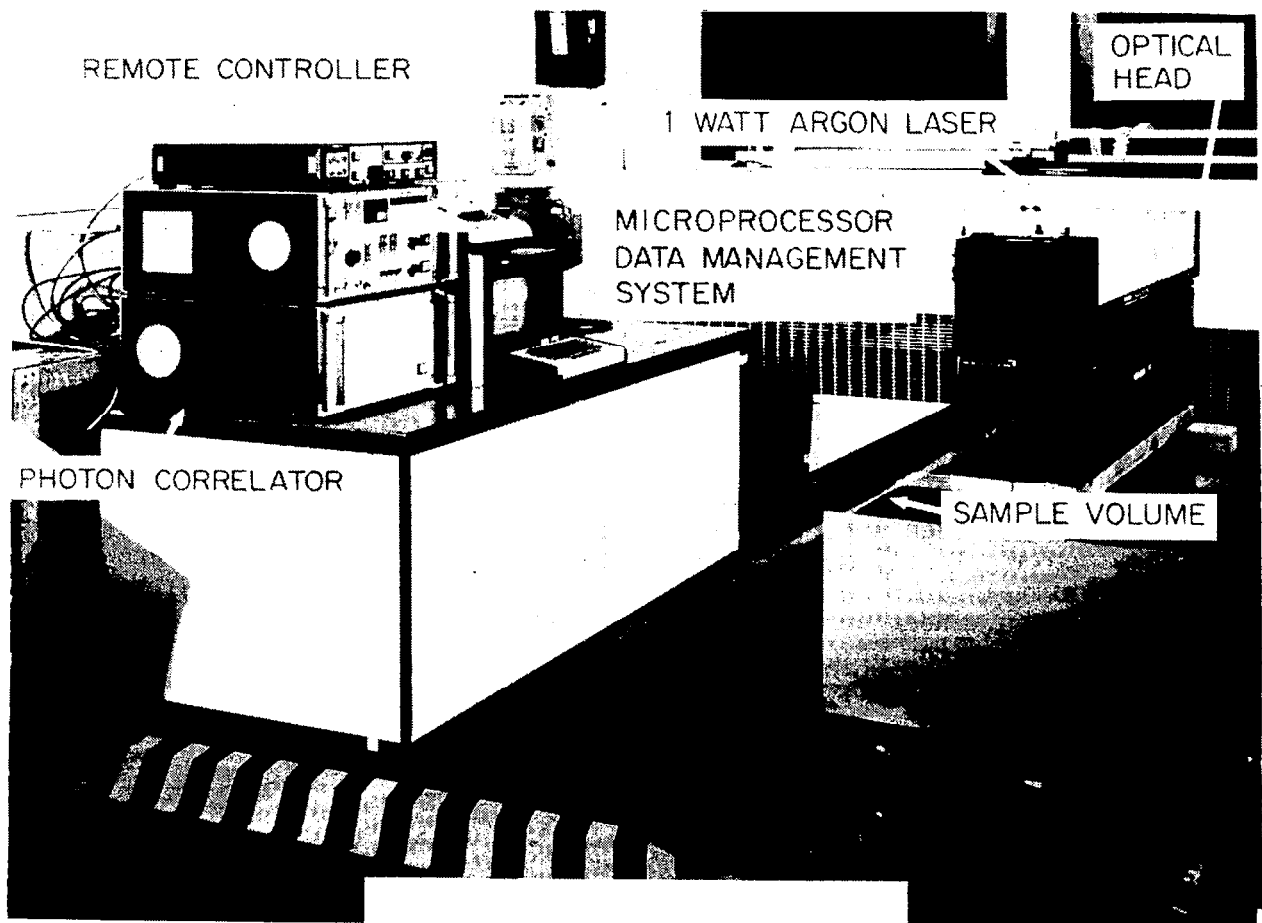
The only optical access to the NTF test section is through ports in the side walls. There are no optical ports in the plenum vessel wall, so installation of any velocimeter system would have to be in the plenum chamber. Any optical package installed in the plenum chamber must have the proper enclosure to protect it from the high pressures and cryogenic temperatures. A schematic diagram of a LDV system configuration and the minimum internal dimensions for the protective enclosure are shown below. Installation of this configuration and its enclosure would be very difficult.

Consideration of equipment and installation cost plus the inability to ensure that once a system has been aligned to the required precision at ambient conditions that this alignment would hold at the high pressures and cryogenic temperatures it was decided to consider another approach. This approach was the laser transit anemometer.



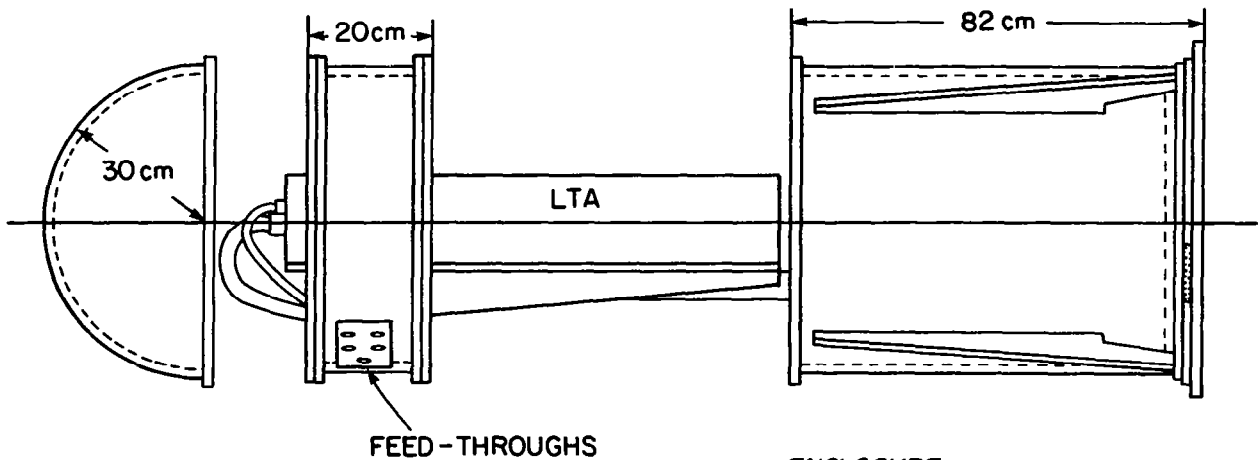
LASER TRANSIT ANEMOMETER

Langley's laser transit anemometer system (LTA) is a Spectron Development Laboratories, Inc., model 104 which is equipped with a one-watt cw argon-ion laser and a 100mm diameter objective lens. An attribute of this system that the fringe velocimeter does not have is its compact laser/optics package.



LTA ENCLOSURE

Because of the limited optical access and the necessity to achieve the minimum optical path length, consideration was given to mounting the LTA laser/optics package on the tunnel test section wall. This creates an operational problem. The side walls of the test section retract into the floor area of the plenum vessel to allow access to the test section. Any device mounted to either side wall must not obstruct side wall operations, i.e., must clear structures about the wall or be easily removed. To provide sufficient clearance the LTA laser/optics package enclosure was designed so that it can be easily disassembled.



ENCLOSURE

ALUMINUM - 6061

WALL THICKNESS - 95 mm

WT. - 123 kg

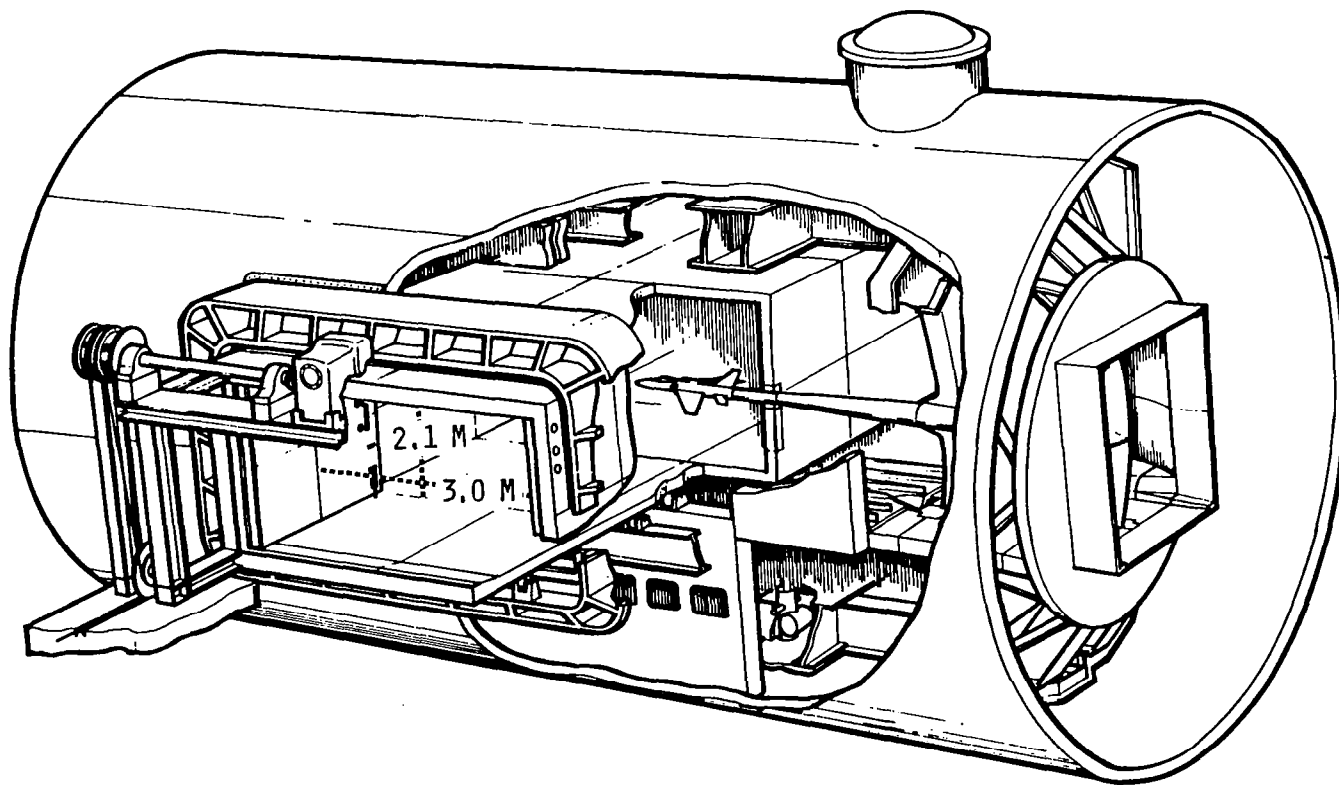
INSULATION - 5 cm, G.E. CRYO FOAM

WINDOW - QUARTZ, ~15cm DIA. x 3.8cm

MODEL ACCESS SYSTEM

An additional operational problem exists. To achieve access to the test section for disassembling of the LTA enclosure, a tunnel warm-up period of five hours is required. Operationally, to reduce this excessive warm-up time the use of portable enclosures is planned which can be installed through the plenum side wall into the test section permitting access to the test models. With this procedure, tunnel warm-up and subsequent cool-down periods are reduced to half-hour periods. These enclosures also require clear access and side walls must be free for retraction.

The preceding operational problems have not been resolved at this time. An additional installation problem is the provision of water for laser thermal control. It is a paradox, i.e., with the enormous amount of cooling gas present, that efforts must be made to maintain ambient conditions for the optics and at the same time provide cooling water for the laser. Obviously, it is highly desirable to decouple the laser from the optics package and transmit the laser radiation to the optics by some means such as fiber optics. This problem is being pursued.



CONCLUDING COMMENTS

At the present time, the ability to achieve flow field angularity measurements with an absolute 0.01 degree accuracy appears, at best, very difficult. But, because of the unique installation and operation requirements presented by the NTF an entry with a laser velocimeter is necessary to obtain the experience to achieve optimum performance capability. Also, because the present existing velocimeter systems are capable of obtaining state-of-the-art velocity measurements it appears to be appropriate to recommend the installation of a system in NTF. This initial entry should be accomplished at a minimum cost. Based on the preceding considerations it was decided to recommend the use of an existing "two-spot" system for the initial tests. The LTA "two-spot" system has a compact laser/optics package which should keep the initial installation cost to a minimum plus the system is capable of comparable performance with a larger LDV "fringe" system. If it is decided a "fringe" system would be more appropriate at a later time, the experience gained with the "two-spot" and related performance data should be applicable or can be related with a minimum of effort.

THE RESULTS OF THIS STUDY, 0.3 M TCT LDV AND LTA TESTS AND OTHER EFFORTS HAVE NOT REVEALED ANY FUNDAMENTAL PROBLEMS THAT WOULD SUGGEST THAT LASER VELOCIMETRY IS NOT A VIABLE DIAGNOSTIC TECHNIQUE FOR NTF. HOWEVER, THERE ARE A NUMBER OF ENGINEERING PROBLEMS THAT NEED TO BE SOLVED, E.G.,:

- 1) AN INSTALLATION SCHEME THAT IS COMPATIBLE WITH THE PLANNED TUNNEL OPERATION PROCEDURES
- 2) MEANS TO SIMPLIFY THE INSTALLATION, FOR EXAMPLE, RELOCATION OF THE LASER OUTSIDE OF THE TUNNEL AND REMOTE FROM THE OPTICS PACKAGE (FIBER OPTICS?)
- 3) AN EFFICIENT SEEDING TECHNIQUE AND RELATED SYSTEM SO THAT POINT MEASUREMENT TIME IS ON THE ORDER OF A SECOND
- 4) DEVELOP HARDWARE AND TECHNIQUES TO ACHIEVE THE 0.01 DEGREE ACCURACY GOAL

SYMBOLS

f - frequency, Hertz

u - reference direction

v - reference direction, normal to u

V - velocity magnitude, meters per second

α - angle between velocity component V_1 and reference direction u , radians

β - angle between velocity component V_2 and reference direction u , radians

γ - flow field angularity with respect to reference direction u , radians

Δ - finite difference

ϕ - angle between velocity components V_1 and V_2 , radians

θ - laser cross beam angle, radians

λ - laser radiation wavelength, meters

σ - standard deviation

σ^2 - variance

Subscripts

D - Doppler

1, 2 - velocity components

α - angle

REFERENCES

1. McKenney, L. W.; and Baals, D. D., eds.: Proceedings of the Workshop on High Reynolds Number Research. NASA 2183, 1981.
2. Thompson, H. D.; and Stevenson, W. H., eds.: Laser Velocimetry and Particle Sizing. Hemisphere Publishing Corp., C. 1979.
3. Eckert, E. R. G.; ed.: Proceedings of the Minnesota Symposium on Laser Anemometry. Continuing Education and Extension, University of Minnesota, Jan. 1976.
4. Mayo, W. T., Jr.; and Smart, A. E.; eds.: Proceedings from the 4th International Conference on Photon Correlation Techniques in Fluid Mechanics. Stanford, University, Aug. 1980.
5. Ross, M. M.: Transit Laser Anemometry Data Reduction for Flow In Industrial Turbo Machinery. Optica Acta, Vol. 27, No. 4, pp. 511-528 (1980).
6. Pugh, Emerson M.; and Winslow, George H.: The Analysis of Physical Measurements. Addison-Wesley, 1966.

ATTENDEES

NASA Headquarters
Washington, DC

Lana Couch (Aerodynamics)

Ames Research Center
Moffett Field, CA

George Lee

Langley Research Center
Hampton, VA

Ralph J. Muraca
S. L. Ocheltree
James Scheiman
A. W. Burner
W. L. Snow
Maynard C. Sandford
S. M. Mangalam (NRC)
R. J. Exton
Charles C. Laney, Jr.
David R. Johnson
Jag J. Singh
Frank Jordan
W. B. Jones
David B. Rhodes
J. M. Franke
P. J. Bobbitt
Robert A. Kilgore
Bill Corlett
W. C. Honaker
J. T. Foughner
David S. Shaw
John M. Seiner
Ruth Martin
Perry Hanson
J. W. Elliott
Sharon Stack
Odell Morris
David Reubush
James C. Ferris
James Yu
Jim Meyers
Luther Gartrell
William Goad
Dan Banks
Murthy Annageri (NRC)
Rayapalya Gopinath (NRC)
Wayne McKinney
William W. Hunter, Jr.

Langley (Continued)

John Hoppe
Pete Jacobs
Warren Young
T. E. Hepner
G. Thomas Holbrook
P. Calvin Stainback
Charles B. Johnson
John C. Wilson
Thomas F. Brooks
Pierce L. Lawing
Blair Gloss
Dennis Fuller
W. L. Sellers

Lewis Research Center
Cleveland, OH

Arthur J. Decker
Robert J. Freedman
Richard G. Seasholtz
William C. Nieberding
George Stefko
Warren Hingst
John Greissing
Harvey Neumann

British Embassy
Washington, DC

Michael M. Shaw

Boeing Co.
Seattle, WA

Donald J. Bernitt

Boeing Commercial Airplane Co.
Seattle, WA

James P. Crowder

Boeing Aerodynamic Labs
Seattle, WA

Ronald L. Bengelink

Naval Surface Weapons Center
Silver Spring, MD

Mark M. Roberts

DSMA International, Inc.
Toronto, ON

Sergio Raimondo
G. M. Elfstrom

TSI, Inc.
St. Paul, MN

Leroy Fingerson
R. Sathyakumar

General Electric Co.
Cincinnati, OH

John T. Kutney

DFVLR
Gottingen, Germany

Wolfgang Lorenz-Meyer

Aircraft Research Association, Ltd.
Bedford, England

Peter G. Hutton

Lockheed-Georgia Co.
Marietta, GA

John A. Braden
Robert Whipkey
K. K. Ahuja
M. C. Whiffen
Greg Jones

Douglas Aircraft Co.
Long Beach, CA

J. D. Cadwell
Michael F. Fancher

Calspan Field Services
Arnold AFS, TN

Fred L. Heltsley

Rockwell International
Los Angeles, CA

Milton H. Cohen

Princeton University
Princeton, NJ

Gary S. Settles

University of Michigan
Ann Arbor, MI

Charles M. Vest

University of Notre Dame
Notre Dame, IN

Thomas J. Mueller

University of Tennessee Space Institute
Tullahoma, TN

J. M. Wu

University of Maryland
College Park, MD

Allen E. Winkelmann
Alfred Gessow

Purdue University
Lafayette, IN

Warren H. Stevenson

University of Illinois
Urbana, IL

Ronald Adrian

George Washington University
Langley Research Center
Hampton, VA

Ulf Michel

Colorado State University
Ft. Collins, CO

C. Y. She

1. Report No. NASA CP-2243		2. Government Accession No.		3. Recipient's Catalog No.	
4. Title and Subtitle FLOW VISUALIZATION AND LASER VELOCIMETRY FOR WIND TUNNELS				5. Report Date September 1982	
				6. Performing Organization Code 505-31-53-05	
7. Author(s) William W. Hunter, Jr., and Jerome T. Foughner, Jr., Editors				8. Performing Organization Report No. L-15498	
				10. Work Unit No.	
9. Performing Organization Name and Address NASA Langley Research Center Hampton, VA 23665				11. Contract or Grant No.	
				13. Type of Report and Period Covered Conference Publication	
12. Sponsoring Agency Name and Address National Aeronautics and Space Administration Washington, DC 20546				14. Sponsoring Agency Code	
15. Supplementary Notes					
16. Abstract This report is a compilation of papers presented at the Workshop on Flow Visualization and Laser Velocimetry for Wind Tunnels held March 25-26, 1982, at the Langley Research Center. The workshop was structured to provide: (1) a state-of-the-art overview of flow visualization, holography/tomography, and laser velocimetry, (2) a forum for industry, universities, and government agencies to address problems in developing useful and productive flow visualization and laser velocimetry measurement techniques, and (3) a report of recent developments and applications of flow visualization and laser velocimetry measurement techniques and instrumentation systems for Langley wind tunnels including the 0.3-Meter Transonic Cryogenic Tunnel and plans for the National Transonic Facility.					
17. Key Words (Suggested by Author(s)) Flow visualization Cryogenic Laser velocimetry Holography/tomography Wind tunnel National Transonic Facility			18. Distribution Statement Unclassified - Unlimited Subject Category 35		
19. Security Classif. (of this report) Unclassified		20. Security Classif. (of this page) Unclassified		21. No. of Pages 368	22. Price A16

National Aeronautics and
Space Administration

Washington, D.C.
20546

Official Business

Penalty for Private Use, \$300

SPECIAL FOURTH CLASS MAIL
BOOK

Postage and Fees Paid
National Aeronautics and
Space Administration
NASA-451



6 1 10, D, 820816 S00903DS
DEPT OF THE AIR FORCE
AF WEAPONS LABORATORY
ATTN: TECHNICAL LIBRARY (SUL)
KIRTLAND AFB NM 37117

NASA

POSTMASTER: If Undeliverable (Section 158
Postal Manual) Do Not Return
